Universidad Autónoma de Madrid
Programa de Doctorado en Biociencias Moleculares

Stress kinases in the regulation of inter-organ communication in obesity comorbidities

Leticia Herrera Melle
Madrid, 2021

DEPARTAMENTO DE BIOQUÍMICA

FACULTAD DE MEDICINA

UNIVERSIDAD AUTÓNOMA DE MADRID

Stress kinases in the regulation of inter-organ communication in obesity comorbidities

Tesis doctoral presentada por:

Leticia Herrera Melle

Graduada en Biología Sanitaria por la Universidad de Alcalá

Máster en Biomedicina Molecular por la Universidad Autónoma de Madrid

Dirigida por:

Dra. Guadalupe Sabio Buzo

Dr. Alfonso Moral Corral

Laboratorio “Papel de las quinasas activadas por el estrés en el desarrollo de enfermedades cardiovasculares, diabetes y cáncer”

Centro Nacional de Investigaciones Cardiovasculares Carlos III (CNIC)

Dra. Guadalupe Sabio Buzo, jefa del grupo “Papel de las quinasas activadas por el estrés en el desarrollo de enfermedades cardiovasculares, diabetes y cáncer”, del área de Fisiopatología del Miocardio del Centro Nacional de Investigaciones Cardiovasculares Carlos III (CNIC), como **directora**,

Dr. Alfonso Mora Corral, investigador del grupo “Papel de las quinasas activadas por el estrés en el desarrollo de enfermedades cardiovasculares, diabetes y cáncer”, del área de Fisiopatología del Miocardio del Centro Nacional de Investigaciones Cardiovasculares Carlos III (CNIC), como **co-director**,

Dra. Benilde Jiménez Cuenca, profesora titular del Departamento de Bioquímica de la Universidad Autónoma de Madrid, como **tutora**,

CERTIFICAN

Que la Tesis Doctoral titulada “Stress kinases in the regulation of inter-organ communication in obesity comorbidities” ha sido realizada en el Centro Nacional de Investigaciones Cardiovasculares Carlos III (CNIC) y tutelada por el Departamento de Bioquímica de la Universidad Autónoma de Madrid.

El trabajo realizado por Doña Leticia Herrera Melle reúne todas las condiciones requeridas por la legislación vigente, así como la originalidad y la calidad científica para poder ser presentada y defendida ante el Tribunal Calificador con el fin de optar al grado de Doctor.

Y para que conste, se extiende el presente certificado,

Madrid, 1 de junio de 2021.

VºBº Directora	VºBº Co-director	VºBº Tutora
Dra. Guadalupe Sabio Buzo	Dr. Alfonso Mora Corral	Dra. Benilde Jiménez Cuenca

This PhD Thesis has been carried out by Leticia Herrera Melle at the “Stress kinases in cardiovascular disease, diabetes and cancer” laboratory from the Myocardial Pathophysiology Area at Centro Nacional de Investigaciones Cardiovasculares Carlos III (CNIC) in Madrid, under the supervision of Dr. Guadalupe Sabio Buzo and Dr. Alfonso Mora Corral.

The support received from the following grants and fellowships has permitted to develop this PhD work:

- Programa de ayudas predoctorales para la formación de profesorado universitario (FPU) 2015 del Ministerio de Educación, Cultura y Deporte (FPU2015-05802).

- Programa de ayudas para estancias breves del programa FPU del Ministerio de Ciencia, Innovación y Universidades (EST18/00100).

- European Molecular Biology Organization (EMBO) Short-Term Fellowship Program (8245).

- European Foundation for the Study of Diabetes (EFSD) Albert Renold Travel Fellowship Program 2019 (94431).

- European Union Seventh Framework Programme (FP7/2007-2013) under grant agreement; n° European Research Council 260464.

- The key role of muscle in obesity-induced diabetes: a new function for p38 family. EFSD/Lilly European Diabetes Research Programme 2016-2017.

- Redes de señalización de MKK3/6 en homeostasis y enfermedad. Ministerio de Economía y Competitividad (SAF2016-79126-R).

- Inhibición de p38gamma como possible diana terapéutica para el cáncer hepático. Leonardo Grant for Researchers and Cultural Creators BBVA Foundation (Investigadores-BBVA-2017; IN [17]_BBM_BAS_0066).

- p38s en metabolismo, cuatro quinasas que comparten nombre pero ejercen diferentes funciones. Ministerio de Economía y Competitividad (EUIN2017-85875).

- Inmunidad tumoral e inmunoterapia del cáncer. IMMUNOTHERCAN-CM (2017/BMD-3733).

- Role of muscle stress kinases in obesity-related diseases. Ministerio de Ciencia e Innovación (PID2019-104399RB-I00).

Dana-Farber Cancer Institute

Bruce M. Spiegelman, Ph.D.
Stanley J. Korsmeyer Professor
of Cell Biology and Medicine

Dana-Farber Cancer Institute
Harvard Medical School

450 Brookline Avenue, LC 6214
Boston, Massachusetts 02215-5450
617.632.3567 tel
617.582-7014 fax
bruce_spiegelman@dfci.harvard.edu
www.dana-farber.org

May 26, 2021

To Whom It May Concern:

It is my great pleasure to provide my full support to the Doctoral work of Ms. Leticia Herrera Melle entitled “Stress kinases in the regulation of inter-organ communication in obesity comorbidities”. This is an impressive body of work that will undoubtedly have long-lasting impact in the field. In this work, Leticia highlighted a crucial role for the stress-activated protein kinases in the modulation of inter-organ crosstalk. This work has opened new avenues for the treatment of obesity, diabetes and hepatocellular carcinoma.

During her PhD, Leticia did a short stay in my lab for 3 months, in which she learned very well the tools and skills to work with mouse primary myoblasts and adenovirus overexpressing p38alpha and p38gamma active kinases. She learned how to make these myoblasts grow in the best possible conditions, and to differentiate and to transduce them with the viruses. She used these cells to check the phosphorylation of PGC-1alpha protein by p38alpha and p38gamma by different techniques. She also processed the myotubes and the medium secreted by them for doing proteomics and phosphoproteomics analyses. She had enough time to learn all the techniques required to get the samples ready for mass spectrometry, which is a really useful knowledge for her and her future research. Leticia also analyzed part of the mitochondrial profile of these myotubes and the role of PGC-1alpha in some of the changes observed. She obtained very interesting results that have guided her towards understanding the connection between p38s and PGC-1alpha. The stay of Leticia in my laboratory has been very productive and successful, and a really useful experience to help her advance in the understanding of the connection between skeletal muscle p38 MAPKs and type 2 diabetes. We enjoyed having her with us!

Leticia has done an exceptional work during her PhD with the projects about the role of muscle p38s in metabolism and JNKs in inter-organ crosstalk in the context of liver cancer. Leticia has earned my highest recommendation. I am pleased to offer my enthusiastic support for her graduation and her application to the International PhD.

Please do not hesitate to contact me if I can provide more information.

Sincerely,

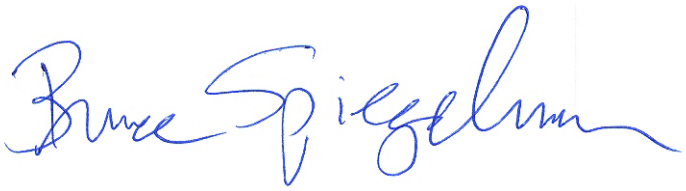

Bruce M. Spiegelman, Ph.D.

Roger J. Davis, Ph.D. F.R.S.
H. Arthur Smith Professor & Chair,
Program in Molecular Medicine

University of Massachusetts Medical School
373 Plantation Street, Biotech II, Suite 309
Worcester, MA 01605
Tel: 508 856-6054 Fax: 508 856-3210

May 19, 2021

Dear Sir or Madam,

It is with great pleasure that I write a letter of support for the Doctoral Thesis of Leticia Herrera Melle entitled “Stress kinases in the regulation of inter-organ communication in obesity comorbidities”. I believe this research study on stress kinases signaling is a breakthrough in the field.

Ms. Herrera´s outstanding curriculum already speaks for itself, as a reflection of a student who has had exceptional performance throughout her entire career. I have had the pleasure of being part of her Thesis Committee. My involvement in this Committee has allowed me to gain further insights on Ms. Herrera´s career and to have knowledge of the projects she has been working on during her PhD studies. She has obtained many results regarding her PhD project. She has described that the activation of p38α or p38γ in skeletal muscle has different effects on metabolism and whole-body homeostasis, being beneficial in the case of p38γ. Additionally, Ms. Herrera has described that the activation of JNK in the white adipose tissue is involved in adipose tissue-to-liver crosstalk by its role in the regulation of the secretion of adiponectin, which protects against the development of hepatocellular carcinoma. In fact, she has a paper as a co-first author in the *Journal of Experimental Medicine*.

In my opinion, Ms. Herrera has combined the best qualities of a pre-doctoral student, such as motivation, perseverance, hard-work, dedication and discipline, which have allowed her to obtain very relevant and valuable results during her PhD.

For all the above reasons, I consider that Ms. Herrera´s thesis represents a visionary contribution to the field, and I am pleased to offer my strong support for her graduation and her application for the International PhD.

Sincerely,

Roger J. Davis, Ph.D. F.R.S.
H. Arthur Smith Professor & Chair,
Program in Molecular Medicine

A mis padres y a mi hermano.

“Take the first step […].
You don’t have to see the whole staircase,
just take the first step.”

— Martin Luther King Jr.

AGRADECIMIENTOS

Dicen que gran parte de lo que somos se debe a las personas de las que nos rodeamos. Y yo no podría ser más afortunada. Durante todos estos años, he aprendido de todas y cada una de las personas que me han acompañado en este camino, y a todos vosotros debo agradeceros haber llegado hasta aquí.

En primer lugar, mis agradecimientos van hacia **Guadalupe**. Resumir 7 años de agradecimientos en unas palabras resulta complicado, especialmente si han venido acompañados de tantas oportunidades como las que he tenido en tu laboratorio. Muchas gracias por confiar en mí desde el primer momento, por permitirme aprender y crecer personal y profesionalmente, y por brindarme tantas oportunidades que han hecho que hoy, en el fin de la tesis, pueda mirar atrás con una sonrisa por cada recuerdo y cada lección aprendida. Gracias por tu apoyo, por tus consejos, y por enseñarme que por muchos obstáculos que encontremos en el camino, siempre hay que levantarse y superarse cada día.

En segundo lugar, debo agradecer a **Alfonso** todo su apoyo, sus ideas, su experiencia, su paciencia y sus consejos. He aprendido y disfrutado mucho trabajando contigo, y siempre me llevaré grandes recuerdos de tantas conversaciones y experimentos compartidos.

Gracias al **Ministerio de Educación, Cultura y Deporte** por su financiación FPU para realizar el doctorado. Gracias también a la **Organización Europea de Biología Molecular (EMBO)** y a la **Fundación Europea para el Estudio de la Diabetes (EFSD)** por su ayuda para mi estancia en Boston.

Gracias a la **Universidad Autónoma de Madrid (UAM)** por permitirme hacer el doctorado, y por las diversas oportunidades que me ha ofrecido durante estos años y de las que tanto he disfrutado, incluyendo cursos, docencia, seminarios y simposios. En especial, gracias a la **Dra. Benilde Jiménez** por su aportación a este trabajo en calidad de tutora de la UAM. Gracias también a aquellos profesores de la UAM que me permitieron colaborar en prácticas docentes, y de los que tanto he aprendido.

A todos los que han formado o forman parte del laboratorio de Guadalupe Sabio: ¡GRACIAS! Gracias, **Luis**, por ponerle salsa y alegría a cada día, por tantas conversaciones y risas, y por aportar toda tu experiencia. Conocerte ha sido un auténtico regalo. Y a ti, **Eli**, gracias por hacerme sentir como una más desde el principio, y por apoyarme siempre que lo he necesitado, allá donde nos hayamos encontrado. Gracias por darme la oportunidad de compartir un proyecto tan bonito contigo y haberme ayudado a llegar hasta aquí. **Edgar**, de ti me llevo gran parte de mi forma de trabajar, mis primeros recuerdos científicos, y grandes enseñanzas que no se me olvidarán nunca. Gracias por toda tu ayuda. **Toñi**, siempre cargada

de luz. No me cansaré de repetirte el gran ejemplo que has sido para mí, y cómo cada conversación contigo me ha dado siempre esa energía para superarme y amar lo que hago. **Nuria**, muchas gracias por tu ayuda, y por haberme hecho sentir tan bien en todo momento; eres una gran científica y una persona increíble. **Bárbara**, muchas gracias por transmitir tanta pasión y energía; eres admirable. **Elena**, gracias por enseñarme tanto durante estos años y echarme una mano siempre que lo he necesitado. **Valle**, mi compañera de habitación de congresos, gracias por tu apoyo. **Ivana**, estoy muy orgullosa de haberte tenido a mi lado durante todo este tiempo; en ti he descubierto un gran apoyo y una gran persona, siempre tan polifacética. Gracias por escucharme y apoyarme en los proyectos, y por aportarme tantas cosas bonitas. Y gracias también a ti, **Magda**, por haber sido siempre tú, una persona auténtica y dispuesta a ayudarme en todo momento y a hacerme reír tanto con tu faceta de actriz de doblaje y tus tics nerviosos. Y a ti, **Ainoita**, gracias por tu apoyo, por cada conversación, por cada carcajada. Aunque te haya echado de menos, no se me olvida nunca la felicidad que aportas al mundo. **Aye**, me llevo grandes conversaciones y momentos gracias a ti, incluidas todas tus recomendaciones gastronómicas y cinematográficas. Gracias por todo. Gracias también a **Rafa**, por ser tan buen compañero siempre. A **María**, por tu gran apoyo y por haberme acompañado en aventuras que aún continúan. A **Cintia**, con quien tenía una conexión desde antes de conocernos y que vino al laboratorio a compartir su cerebro. Eres la que tiene una solución para cada problema, un imán para la buena suerte. Mil gracias por ofrecerte siempre a ayudarme, por tu optimismo, y por enseñarme tanto. **Bea**, sé que te va a ir genial en el laboratorio, y te deseo toda la suerte del mundo. **Arancha**, gracias por el tiempo que hemos pasado juntas y por inculcarme una vida sana. **Víctor**, gracias por haber estado siempre tan dispuesto a ayudar. Y gracias a tantos otros que han pasado por el laboratorio: las **Lauras**, **Delia**, **Álex**, **Natalia**, **Marta**, **Cris**, **Pablo**, **Chusa**, **Paula**…

Gracias al resto de grupos del CNIC. Gracias al laboratorio de **Toño Enríquez**, en especial a **Sara Cogliati**. Gracias también al laboratorio de **David Sancho**, al de **Mercedes Ricote**, al de **Pura Muñoz**, al de **María Ángeles Moro**, y a tantos otros. Gracias a las múltiples unidades técnicas del CNIC, incluyendo **Animalario**, **Proteómica**, **Genómica**, **Vectores Virales**, **Imagen Avanzada**, **Bioinformática** y **Microscopía**. Soy muy afortunada de haber podido trabajar en un centro con tan grandes profesionales. Gracias en especial a **Juan Antonio** y **Jesús Vázquez** por su ayuda con la Proteómica. Gracias a **Marta León**, a quien admiro y agradezco enormemente su apoyo, por ser tan ordenada, tan trabajadora, y facilitarme la vida siempre. También tengo que agradecer al resto de **trabajadores del CNIC**, que habéis hecho de esta una experiencia inmejorable. En especial, a **Cristina Giménez**, **Laura Grau** y **Almudena Fernández** por toda vuestra ayuda. Gracias a **Mari**, **Javi**, **Compras**,

Departamento de Comunicación, **RR.HH.** e **Informática** por su ayuda con la logística. Gracias a mis compañeras del máster que continuaron su aventura en el CNIC: **Ana**, **Irenes**, **Sofía**, **Ester, Silvia**… Y también a mis compañeros del **PhDay**, con los que compartí esta experiencia tan bonita.

A big THANK YOU to Dr. Bruce Spiegelman's lab. Thank you, **Bruce**, for giving me the opportunity to learn from some of the best scientists that I could ever imagine, and for always treating me as part of your lab family. Special thanks to **Phillip**, one of the best scientists and mentors that I have ever had, and a person that I really admire. Thank you for being so kind, for showing me an invaluable amount of knowledge and making my stay at Dana-Farber so nice and productive. Thanks also to **Mark** and **John** from Dr. Gygi's lab for all your help with Proteomics experiments. And thank you to the rest of Dr. Bruce Spiegelman's lab, who were always willing to help, as well as to the whole **Dana-Farber Cancer Institute** and **Harvard Medical School** staff, which made my experience at Boston an incredible one.

Gracias a todos los **grandes científicos** que me han inspirado con sus ponencias, sus conversaciones y sus consejos, y que me han hecho amar la Ciencia cada vez más. A todos los que han colaborado en estos proyectos, tanto del CNIC como de otros centros, en especial al laboratorio del **Dr. Rubén Nogueiras** en el CiMUS, especialmente a **Daniel Beiroa** y **Begoña Porteiro**; al del **Dr. Javier Cubero** de la Universidad Complutense de Madrid, en especial a **Laura Morán**; al del **Dr. Miguel Marcos** en el Hospital Universitario de Salamanca; al laboratorio de la **Dra. Sisi Seoane**; al del **Dr. Roger Davis**, en especial a **Myoung Sook**; a la **Dra. Clara Álvarez**; y al **Servicio de Microscopía del Centro Nacional de Biotecnología**, entre otros. Gracias a los miembros de mi Comité de Tesis, **Roger Davis**, **Toño Enríquez** y **Rebeca Acín**, por sus valiosas aportaciones. Thank you, **Roger**, for all your support with several applications and your really helpful advice during the thesis.

Gracias a las **personas** que con sus muestras biológicas han contribuido a este trabajo, así como a todos los **animales** que han hecho posible esta tesis, y gracias a los cuales se puede avanzar en la cura de infinitas enfermedades.

Tampoco puedo olvidar agradecer a mis mentores y compañeros de IPLS-Spain, en especial a **Armando**, **Miguel**, **Fernando**, **Omar** y **Javi**, por abrirme la mirada a otros campos y dejarme participar con ellos en este proyecto, que ha sido un reto para mí. Gracias también a **IMFAHE** por las maravillosas oportunidades que me ha ofrecido, y a mis compañeros de **MySweetHealth**, con quienes he aprendido y sigo aprendiendo tanto.

Gracias a mis amigos de toda la vida: **Patri**, **Natalia**, **Míriam**, **Alvir**… Gracias por tantos años de amistad, por apoyarme y acompañarme en todo el camino que me ha llevado hasta aquí. **Sergio**, **Caño** y **Álex**, gracias por ser un apoyo tan importante. Gracias también a **Sandra**, **Elena**, **Sofía** y **Dunia**. **Ángela**, gracias por darme una amistad tan bonita, por escucharme, apoyarme y comprenderme durante todo este proceso y tantos otros. Y gracias también a esos **vecinos** que han estado presentes en cada paso de mi vida.

Gracias a mi familia por hacerme tan afortunada. A mis **tíos** y **primos**, por estar siempre a mi lado, acompañarme y apoyarme en cada paso que he dado. A mi **abuela Feli**, que no pudo llegar a ver el resultado de la tesis, pero a quien tengo y tendré presente en todo momento. Gracias por haberme dado tanto cariño y apoyo, por alegrarte de cada logro, y por haber creado una familia tan maravillosa. A mi **abuela Paca**, ojalá hubieras estado en este momento. Gracias a **Laura** por formar parte de mi vida y contribuir a ella de una forma tan bonita. Gracias a mi **hermano** por ser inmejorable. No hay palabras para describir lo mucho que te admiro y te quiero. Gracias por ser tan paciente, tan increíble, por ayudarme en todo, y por enseñarme siempre las cosas que realmente merecen la pena en la vida.

Y, por último, GRACIAS a las personas más maravillosas de mi vida, mis **padres**. Sois los principales responsables de que haya llegado hasta aquí. Jamás encontraré palabras suficientes para agradeceros todo lo que me dais cada día. Ojalá algún día llegue a ser la mitad de maravillosa de lo que sois vosotros. Gracias por ser pilar, promotores de mis sueños, amor puro y apoyo incondicional. Por aguantarme. Por permitirme soñar y soñar conmigo. Por hacer que la vida sea tan bonita.

A todos vosotros, que habéis formado parte de esta increíble aventura:

¡GRACIAS!

Leticia

ABSTRACT/RESUMEN

Obesity is characterized by the excessive fat accumulation that develops when energy intake exceeds energy expenditure. Lifestyle changes have increased the prevalence of obesity, which has become a major health problem. In fact, obesity is a well-known risk factor for several chronic diseases, including type 2 diabetes and the most common type of liver cancer, hepatocellular carcinoma (HCC). Therefore, understanding the mechanisms that lead to the development of obesity comorbidities is paramount to decrease their incidence and mortality.

One of the signaling pathways that participate in obesity and its adverse consequences is the stress-activated protein kinases (SAPKs) pathway. These proteins include c-Jun NH_2-terminal kinases (JNKs) and p38s. While the role of some SAPKs in obesity and its associated pathologies has been studied, the systemic implications of their activation in specific tissues is starting to be addressed. Our main aim in this thesis is to better understand the participation of SAPKs in inter-organ communication in the context of obesity and its associated diseases.

Using a conditional mouse model lacking p38α in striated muscle, we observed that muscle p38α deletion protects mice against high-fat diet (HFD)-induced obesity by increasing energy expenditure. This phenotype is accompanied by an increase in mitochondrial oxidative metabolism in skeletal muscle due to the upregulation of peroxisome proliferator-activated receptor gamma coactivator 1 alpha (PGC1α). Importantly, lack of p38α results in the hyperactivation of p38γ, which improves glucose and energy homeostasis through an increase in locomotor activity, a process in which interleukin-15 (IL-15) might be involved. This effect decreases the risk of developing diabetes and liver steatosis, therefore linking local and systemic manifestations of muscle p38α deficiency.

Apart from obesity, the incidence of HCC is also higher in men, and both obesity and male sex are characterized by reduced levels of the adipokine adiponectin. We found that the decrease in plasma adiponectin in males is responsible for their increased liver cancer risk. Testosterone activates JNK in white adipocytes, which inhibits adiponectin secretion. Since adiponectin protects against HCC development through the activation of AMP-activated protein kinase (AMPK) and p38α in the liver, JNK-mediated inhibition of adiponectin secretion increases liver cancer cell proliferation.

The results from this thesis provide insight into novel roles of stress signaling in skeletal muscle and white adipose tissue, which regulates inter-organ communication in the context of obesity and its comorbidities, opening new research avenues that might be crucial for the prevention and treatment of these diseases.

La obesidad se caracteriza por la acumulación excesiva de grasa cuando la ingesta calórica es mayor que el gasto energético. Los cambios en el estilo de vida han provocado un aumento en la prevalencia de la obesidad, que se ha convertido en un problema de salud prioritario. De hecho, la obesidad es un factor de riesgo para algunas enfermedades crónicas, como la diabetes de tipo 2 y el cáncer de hígado más común, el carcinoma hepatocelular (HCC). Por ello, es preciso comprender los mecanismos que conducen al desarrollo de las enfermedades asociadas a la obesidad, para así disminuir su incidencia y mortalidad.

Entre las vías de señalización que desempeñan un papel en la obesidad y sus efectos adversos destaca la vía de las proteínas quinasas activadas por estrés (SAPKs). Estas proteínas incluyen a las quinasas c-Jun NH_2-terminal (JNKs) y a las p38s. Aunque se ha estudiado el papel de algunas SAPKs en obesidad y sus patologías, se desconocen muchas de las implicaciones sistémicas que conlleva su activación en determinados tejidos. Nuestro principal objetivo en esta tesis es comprender mejor el papel de las SAPKs en la comunicación entre órganos en el contexto de la obesidad y sus enfermedades asociadas.

Hemos observado que la deficiencia de p38α en el músculo estriado en ratones protege frente a la obesidad inducida por dieta rica en grasa (HFD) al aumentar su gasto energético. La ausencia de p38α incrementa el metabolismo oxidativo mitocondrial en el musculo esquelético a través de la activación del coactivador PGC1α. Asimismo, estos músculos presentan una hiperactivación de p38γ, que ocasiona un aumento de la interleuquina-15 (IL-15) y de la actividad locomotora, mejorando así la homeostasis energética y de la glucosa, y disminuyendo el riesgo de padecer diabetes y esteatosis hepática.

Tanto los varones como las personas con obesidad presentan menores niveles plasmáticos de la adipoquina adiponectina y una mayor incidencia de HCC. Hemos comprobado que los menores niveles de adiponectina en machos son responsables de la mayor incidencia de HCC debido a que la testosterona activa a JNK en adipocitos que, a su vez, inhibe la secreción de adiponectina. Puesto que la adiponectina protege frente al HCC por la activación de la proteína quinasa activada por AMP (AMPK) y p38α en el hígado, la inhibición de su secreción por JNK aumenta la proliferación de las células cancerígenas hepáticas.

Los resultados de esta tesis muestran la relevancia de la señalización del estrés en músculo esquelético y tejido adiposo blanco en el desarrollo de la obesidad y sus comorbilidades, modulando la comunicación entre órganos. Estos resultados indican que estas quinasas podrían ser potenciales dianas terapéuticas para la prevención y el tratamiento de las enfermedades asociadas a la obesidad.

INDEX

Content

ABBREVIATIONS

A

AAV	Adeno-associated virus
A/BA	Acrylamide/Bis-acrylamide
ACN	Acetonitrile
Acrp30	Adipocyte complement-related protein of 30 kDa
AdipoQ	Adiponectin
AdipoR1	Adiponectin receptor 1
AdipoR2	Adiponectin receptor 2
AGPAT1	1-acylglycerol-3-phosphate O-acyltransferase 1
AGPAT3	1-acylglycerol-3-phosphate O-acyltransferase 3
AKT	Protein kinase B
ALT	Alanine aminotransferase
AMP	Adenosine monophosphate
AMPK	AMP-activated protein kinase
AMPKα	AMP-activated protein kinase α
ANOVA	Analysis of variance
AP	Antero-posterior
AP-1	Activator protein-1
aP2	Adipocyte Protein 2
APS	Ammonium persulfate
ASK	Apoptosis signal-regulating kinase
AST	Aspartate aminotransferase
ATF1	Activating transcription factor 1
ATF2	Activating transcription factor 2
ATP	Adenosine triphosphate
ATP5O	ATP synthase subunit O

B

BAIBA	β-aminoisobutyric acid
BAT	Brown adipose tissue
BCA	Bicinchoninic acid
BCL-2	B-cell lymphoma-2
bFGF	Basic fibroblast growth factor
BMI	Body mass index
BSA	Bovine serum albumin

C

CI	Mitochondrial complex I (NADH dehydrogenase)
CII	Mitochondrial complex II (succinate dehydrogenase)
CIII	Mitochondrial complex III (ubiquinol-cytochrome c reductase)
CIV	Mitochondrial complex IV (cytochrome c oxidase)
CV	Mitochondrial complex V (ATP synthase)
CCA	Cholangiocarcinoma
CD36	Cluster of differentiation 36
CDK	Cyclin-dependent kinase
cDNA	Complementary DNA
CHOP	CCAAT/enhancer-binding protein (C/EBP) homologous protein
c-Jun	Cellular-Jun
c-Myc	Cellular-Myc
CoA	Coenzyme A
COVID-19	Coronavirus disease 2019
COX5B	Cytochrome c oxidase subunit 5B
CREB	Cyclic AMP response element-binding
CRP	C-reactive protein
CTL	Cytotoxic T lymphocyte

CYCS	Cytochrome c

D

DEG	Differentially expressed gene
DEN	Diethylnitrosamine
DEPTOR	DEP domain-containing mTOR-interacting protein
DLK	Dual leucine zipper-bearing kinase
DMEM	Dulbecco’s Modified Eagle Medium
DNA	Deoxyribonucleic acid
DNase	Deoxyribonuclease
DTT	Dithiothreitol
DUSP	Dual-specificity phosphatase
DV	Dorsal-ventral

E

E2F	Eukaryotic transcription factor 2
EC	Endothelial cell
ECL	Enhanced chemiluminescence
EDL	Extensor digitorum longus
EDTA	Ethylenediaminetetraacetic acid
EE	Energy expenditure
eEF2K	Eukaryotic elongation factor 2 kinase
EGTA	Ethylene glycol tetraacetic acid
ELK1	Ets-like protein 1
EMT	Epithelial-mesenchymal transition
EPPS	4-(2-hydroxyethyl)-1-piperazinepropanesulfonic acid
ER	Endoplasmic reticulum
ERK	Extracellular signal-regulated kinase
Esrra	Estrogen-related receptor α

eWAT	Epididymal white adipose tissue

F

FA	Formic acid
FABP4	Fatty acid-binding protein 4
FAHFA	Fatty acid ester of hydroxy fatty acid
FASP	Filter aided sample preparation
FBS	Fetal bovine serum
FC	Fold change
FDR	False discovery rate
FFA	Free fatty acid
FGF2	Fibroblast growth factor 2
FGF21	Fibroblast growth factor 21
Fndc5	Fibronectin type III domain-containing 5
FWER	Family-wise error rate

G

GAPDH	Glyceraldehyde-3-phosphate dehydrogenase
GBSS	Gey’s Balanced Salt Solution
GFP	Green fluorescent protein
Glu	Glutamic acid
GLUT4	Glucose transporter 4
Gly	Glycine
GSEA	Gene set enrichment analysis
GTT	Glucose tolerance test

H

HCC	Hepatocellular carcinoma
HDL	High-density lipoprotein
HEK	Human embryonic kidney

He-NK	Hepatic-Natural Killer
HEPES	4-(2-hydroxyethyl)-1-piperazineethanesulfonic acid
HFD	High-fat diet
H&E	Hematoxylin and eosin
HMW	High molecular weight
H_2O_{mq}	Milli-Q water
HOMA-IR	Homeostasis model assessment of insulin resistance
HRP	Horseradish peroxidase
HS	Horse serum
HSC	Hepatic stellate cell
HSP27	Heat shock protein 27

I

IBMX	3-isobutyl-1-methylxanthine
IDF	International Diabetes Federation
Ig	Immunoglobulin
IGF-1	Insulin-like growth factor-1
IKK-β	Inhibitor of nuclear factor-κB kinase-β
IL	Interleukin
IL-15	Interleukin-15
IL-15Rα	Interleukin-15 receptor, alpha subunit
IL-1β	Interleukin-1 β
IL-6	Interleukin-6
IP	Immunoprecipitation
i.p.	Intraperitoneal
IPA	Ingenuity Pathway Analysis
IPAKB	Ingenuity's proprietary knowledge-base
IRS	Insulin receptor substrate

IRS1	Insulin receptor substrate 1
ITT	Insulin tolerance test
IU	International unit
iWAT	Inguinal white adipose tissue

J

JNK	c-Jun NH_2-terminal kinase
JNK1	c-Jun NH_2-terminal kinase 1
JNK2	c-Jun NH_2-terminal kinase 2
JNK3	c-Jun NH_2-terminal kinase 3
JunD	JunD proto-oncogene

K

KC	Kupffer cell
KO	Knockout

L

LA	Locomotor activity
LC-MS/MS	Liquid chromatography with tandem mass spectrometry
LDL	Low-density lipoprotein
LIF	Leukemia inhibitory factor
LMW	Low molecular weight
LoxP	Locus of crossover in P1
LPA	Lysophosphatidic acid
Lys-C	Lysine-C

M

M1	Primary motor cortex
M2	Secondary motor cortex
MAPK	Mitogen-activated protein kinase
Mapk8	MAPK 8 (JNK1)

Mapk9	MAPK 9 (JNK2)
Mapk10	MAPK 10 (JNK3)
Mapk11	MAPK 11 (p38β)
Mapk12	MAPK 12 (p38γ)
Mapk13	MAPK 13 (p38δ)
Mapk14	MAPK 14 (p38α)
MAP2K	MAPK kinase
Map2k3	MAPK kinase 3
Map2k6	MAPK kinase 6
MAP3K	MAPK kinase kinase
MAPKAPK2	MAPK-activated protein kinase 2
MAPKAPK3	MAPK-activated protein kinase 3
MAPKK	MAPK kinase
MAPKKK	MAPK kinase kinase
MCK	Muscle creatine kinase
MCP-1	Monocyte chemoattractant protein-1
MEF2A/C	Myocyte enhancer factor 2 A/C
MEK1	MAPK/ERK kinase 1
MEK2	MAPK/ERK kinase 2
MEKK	MAPK/ERK kinase kinase
MHC	Myosin heavy chain
MK2	MAPK-activated protein kinase 2
MK3	MAPK-activated protein kinase 3
MKK3	MAPK kinase 3
MKK4	MAPK kinase 4
MKK6	MAPK kinase 6
MKK7	MAPK kinase 7

MKP	MAPK phosphatase
MKP-1	MAPK phosphatase-1
ML	Medial-lateral
MLK	Mixed lineage kinase
MMLV	Moloney murine leukemia virus
MMW	Middle molecular weight
MOI	Multiplicity of infection
mRNA	Messenger RNA
MS	Mass spectrometry
MS/MS	Tandem mass spectrometry
mTOR	Mammalian target of rapamycin
mTORC1	mTOR complex 1
mTORC2	mTOR complex 2
Myh7	Myosin heavy chain 7

N

NADH	Nicotinamide adenine dinucleotide
NAFL	Non-alcoholic fatty liver
NAFLD	Non-alcoholic fatty liver disease
NASH	Non-alcoholic steatohepatitis
ND	Normal chow diet
NDUFB5	NADH dehydrogenase (ubiquinone) 1 beta subcomplex subunit 5
NDUFV2	NADH dehydrogenase (ubiquinone) flavoprotein 2
NES	Normalized enrichment score
NGS	Normal goat serum / Next-generation sequencing
NIH	National Institutes of Health
NMR	Nuclear magnetic resonance
NRF2	Nuclear factor erythroid 2-related factor 2

NRG4	Neuregulin 4

O

OCT	Optimal cutting temperature

P

P	Phospho / Postnatal day (if followed by a number)
PADM	Preadipocytes differentiation medium
PAGE	Polyacrylamide gel electrophoresis
PAI1	Plasminogen activator inhibitor 1
PBS	Phosphate-buffered saline
PCR	Polymerase chain reaction
PDA	Photodiode array
PDK1	3-phosphoinositide-dependent protein kinase-1
PGC1α	Peroxisome proliferator-activated receptor gamma coactivator 1 α
PGC1α-a	PGC1α-isoform a
PGC1α-b	PGC1α-isoform b
PGC1α-c	PGC1α-isoform c
PGC1β	Peroxisome proliferator-activated receptor gamma coactivator 1 β
PI3K	Phosphatidylinositol 3-kinase
PIP_2	Phosphatidylinositol-4,5-bisphosphate
PIP_3	Phosphatidylinositol-3,4,5-triphosphate
PKB	Protein kinase B
PKC	Protein kinase C
PKD1	Protein kinase D1
PMSF	Phenylmethylsulfonyl fluoride
Ppargc1a	Peroxisome proliferator-activated receptor gamma coactivator 1 α
Ppargc1b	Peroxisome proliferator-activated receptor gamma coactivator 1 β
Pro	Proline

P/S	Penicillin/streptomycin

Q

qPCR	Quantitative PCR
qRT-PCR	Quantitative real-time-PCR

R

Rb	Retinoblastoma protein
RIN	RNA Integrity Number
RNA	Ribonucleic acid
RNase	Ribonuclease
RNA-seq	RNA-sequencing
ROS	Reactive oxygen species
Rps18	Ribosomal protein S18
RQ	Respiratory quotient
RSEM	RNA-seq by Expectation Maximization
RT	Room temperature

S

SAP90	Synapse-associated protein 90
SAP97	Synapse-associated protein 97
SAPK	Stress-activated protein kinase
SAPK2a	SAPK 2a (p38α)
SAPK2b	SAPK 2b (p38β)
SAPK3	SAPK 3 (p38γ)
SAPK4	SAPK 4 (p38δ)
SDS	Sodium dodecyl sulfate
SEM	Standard error of the mean
Ser (S)	Serine
shRNA	Short hairpin RNA

SOCS3	Suppressor of cytokine signaling 3
SPARC	Secreted protein acidic and rich in cysteine
SPE	Solid-phase extraction
STAT3	Signal transducer and activator of transcription 3
STAT5	Signal transducer and activator of transcription 5

T

T3	Triiodothyronine
TAA	Thioacetamide
TAB1	TAK1-binding protein 1
TAK1	Transforming growth factor-β-activated protein kinase 1
Tbp	TATA-box-binding protein
TCA	Tricarboxylic acid
TEAB	Triethylammonium bicarbonate
TEMED	N,N,N',N'-Tetramethylethylenediamine
Tfam	Mitochondrial transcription factor A
Thr (T)	Threonine
TL	Tibia length (for organ's weight figures) / Total lysate (for IP figures)
TMM	Trimmed mean of M-values
TMT	Tandem mass tag
TNFα	Tumor necrosis factor α
TNFR1	Tumor necrosis factor receptor 1
TREM1	Triggering receptor expressed on myeloid cells 1
TWEAK	Tumor necrosis factor-like weak inducer of apoptosis
Tyr (Y)	Tyrosine

U

UV	Ultraviolet

W

WAT	White adipose tissue
WHO	World Health Organization
WSPP	Weighted spectrum, peptide and protein
WT	Wild-type

INTRODUCTION

1. Obesity

1.1. Energy balance and obesity

Energy balance is the result of the equilibrium between energy intake and energy expenditure (Romieu et al., 2017). This equilibrium needs to be properly regulated for the adequate maintenance of whole-body homeostasis and body weight, which will therefore depend on the total amount of calories that are taken from food and drinks, and the energy expended (Figure I1). Metabolism provides such energy to conduct cellular functions, mainly through the conversion of nutrients into smaller units through catabolism. In contrast, energy is required for the transformation of simpler structures into macromolecules through anabolism (Chandel, 2015). Total energy expenditure is composed by the basal metabolic rate, which is the requirement for sustaining general cellular processes in complete inactivity; the energy expended by physical activity; and the one dissipated by thermogenesis, which is defined as heat production in response to environmental cues, such as temperature or diet (Lowell & Spiegelman, 2000). When energy intake exceeds energy expenditure, the excess energy is deposited as body fat, which can lead to the appearance of obesity (Hotamisligil, 2006). An individual is considered obese when the body mass index (BMI), which is calculated by dividing the weight in kilograms by the height in meters squared, is greater than or equal to 30 (World Health Organization [WHO], 2020). The excess of lipids can be stored in adipose tissue, but also in other metabolic organs, such as the liver and the skeletal muscle, impairing their function and causing serious complications (Donohoe et al., 2020; Speakman, 2004).

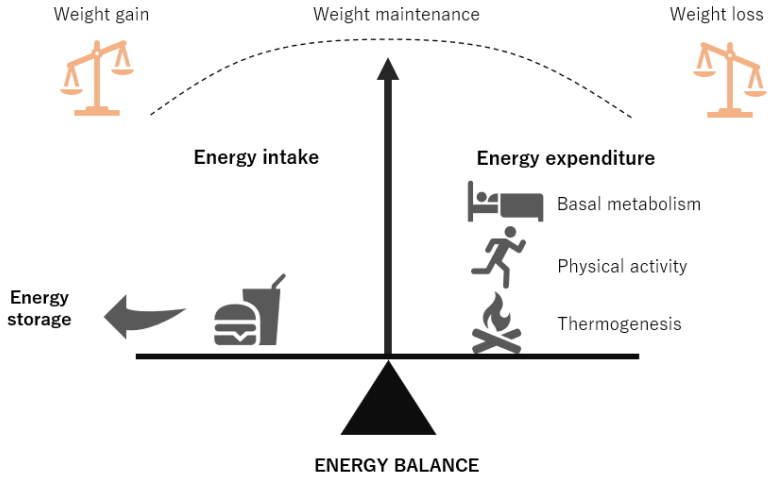

Figure I1. Energy balance. Energy enters an organism through food and drink consumption, and it can be released as heat and work. The excess energy intake can be stored in adipose depots, from where it can be mobilized when needed. Total energy expenditure is the sum of energy expenditure attributed to basal metabolism required for the proper function of cells and organs, and expenditure derived from physical activity and thermogenesis. An equilibrium between energy intake and energy expenditure is required for body weight maintenance; if energy intake exceeds energy expenditure, body weight increases, while the opposite outcome is achieved when the organism expends more energy than ingested.

Obesity is the most common metabolic disorder worldwide, with growing incidence and prevalence as reflected by the over 650 million obese adults in 2016 (Figure I2) (WHO, 2020). Globally, there has been a change from a context of nutrient scarcity and high caloric needs to a situation with increased energy intake and physical inactivity, leading to this energy imbalance. However, there is also a genetic component in the predisposition to obesity (S. E. Kahn et al., 2006; Speakman, 2013). Current trends predict that the prevalence of obesity will increase and reach up to around 60% of the global population by 2030 (Kelly et al., 2008), which urges the need for finding new preventive and therapeutic strategies for its treatment.

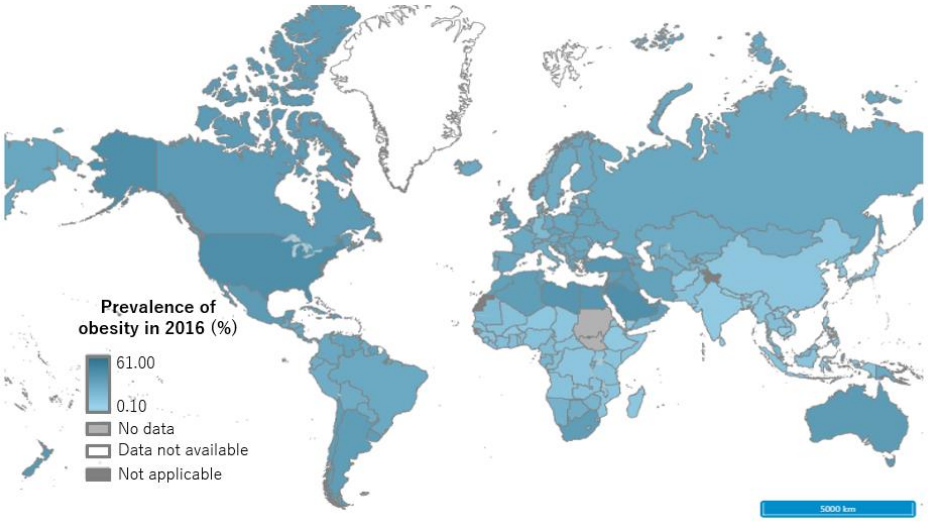

Figure I2. Prevalence of obesity in 2016. World map representing the prevalence of obesity (%) among male and female adults (≥ 18 years old) in 2016 (age-standardized estimate). Obesity refers to body mass index (BMI) ≥ 30 kg/m^2. Source: modified from World Health Organization, 2021.

Considering the future predictions about the prevalence of obese people, several strategies for the prevention and treatment of obesity have been proposed so far. First, diverse methods to decrease food intake or diminish nutrient absorption have been designed (Montan et al., 2019). Second, adaptive thermogenesis, the dissipation of energy through the regulated heat production in response to environmental temperature and diet, is another strategy (Lowell & Spiegelman, 2000). This is due to the capacity of brown adipose tissue (BAT) to uncouple mitochondrial respiratory chain from adenosine triphosphate (ATP) generation, leading to energy dissipation as heat (Lowell et al., 1993), which contrasts with the properties of white adipose tissue (WAT) depots (Betz & Enerbäck, 2018). Recently, several molecular targets for achieving an increase in thermogenesis have been described, especially through an increase in BAT thermogenesis (Betz & Enerbäck, 2018) or in WAT browning, a phenotypic switch from energy-storing white adipocytes to thermogenic beige/brite adipocytes (Matesanz et al., 2017, 2018). Importantly, the ability to induce browning is diminished in obese individuals (Saito et al., 2009; van Marken Lichtenbelt et al., 2009). In addition, increased thermogenesis can also be achieved by promoting energy-consuming futile cycles in skeletal muscle (Betz & Enerbäck,

2018). However, one of the most ancient and relevant strategies for the maintenance of energy balance is through physical activity (Westerterp, 2017), which is more effective than other solutions such as pharmacological intervention for the treatment and prevention of obesity-associated diseases (Egan & Zierath, 2013). In fact, sedentary behavior is associated with decreased insulin sensitivity, increased visceral adiposity and muscle atrophy (Whitham & Febbraio, 2016). Remarkably, the benefits of physical activity in disease prevention are not only attributed to weight loss, maintenance of muscle mass and cardiorespiratory fitness, but also to the communication between the different organs in response to exercise (Murphy et al., 2020; Neufer et al., 2015). In fact, this inter-organ communication is not only relevant in the context of exercise, but also in the general maintenance of system homeostasis (Priest & Tontonoz, 2019).

1.2. Inter-organ communication in metabolism and obesity

Both food intake and energy expenditure need to be tightly regulated by different homeostatic mechanisms that involve inter-communication between several organs (Nogueiras & Sabio, 2021). Dysfunction of this crosstalk can result in metabolic diseases and lead to the development of many disorders. Therefore, it is paramount to coordinate the work among the multiple organ systems to maximize the efficiency of homeostatic processes that regulate energy intake and disposition, which may subsequently affect cellular mechanisms, such as cell death and proliferation.

Apart from the traditional functions attributed to key metabolic organs, such as skeletal muscle, adipose tissue or liver, recent evidence has helped classify them as endocrine organs due to their role in the production and secretion of factors that can participate in inter-organ communication. These secreted factors include protein hormones, small molecules, lipids and other factors such as exosomes (Priest & Tontonoz, 2019). This secretory function can be modified in response to physiological or pathological stimuli that can alter cellular signaling, which might explain why changes in one organ can affect distant tissues and have a systemic impact.

1.2.1. Skeletal muscle as an endocrine organ

Skeletal muscle is an essential contributor to exercise-induced changes in metabolism, which is now considered to be an endocrine organ (Ahima & Park, 2015). Indeed, alterations in skeletal muscle signaling can compromise metabolic homeostasis (Rodríguez-Fdez et al., 2020). The humoral factors secreted by the muscle are termed myokines and mediate communications of this organ with the adipose tissue, liver and brain, among others. Many myokines are secreted in response to exercise, thus mediating some of the beneficial effects

of exercise on health (Ahima & Park, 2015). Indeed, physical inactivity causes altered myokine response and/or resistance to the effects of myokines, which has been related to increased risk of several chronic diseases (Pedersen & Febbraio, 2012).

Some important myokines and their main functions are shown in Figure I3. Most of them are released upon exercise, except myostatin (Allen et al., 2011), and their secretion can also be altered in obesity. There are examples of myokines promoting adipose tissue oxidation (e.g., interleukin-6, IL-6) (van Hall et al., 2003), thermogenesis (e.g., irisin, meteorin-like) (Boström et al., 2012; Rao et al., 2014), increasing insulin sensitivity and pancreatic function (e.g., IL-6) (Ellingsgaard et al., 2011; Ikeda et al., 2016), driving bone formation (e.g., leukemia inhibitory factor, LIF; insulin-like growth factor-1, IGF-1; fibroblast growth factor 2, FGF2) (Dazai et al., 2000; Hamrick, 2011), promoting endothelial cell function (e.g., follistatin-related protein 1) (Ouchi et al., 2008), or even protecting against tumor development (e.g., secreted protein acidic and rich in cysteine, SPARC) (Aoi et al., 2013) or cognitive decline (e.g., cathepsin B) (Pedersen, 2019). In addition, some myokines can also act locally by inducing or repressing muscle hypertrophy (e.g., interleukin-15, IL-15; myostatin) (Carbó et al., 2001; McPherron et al., 1997).

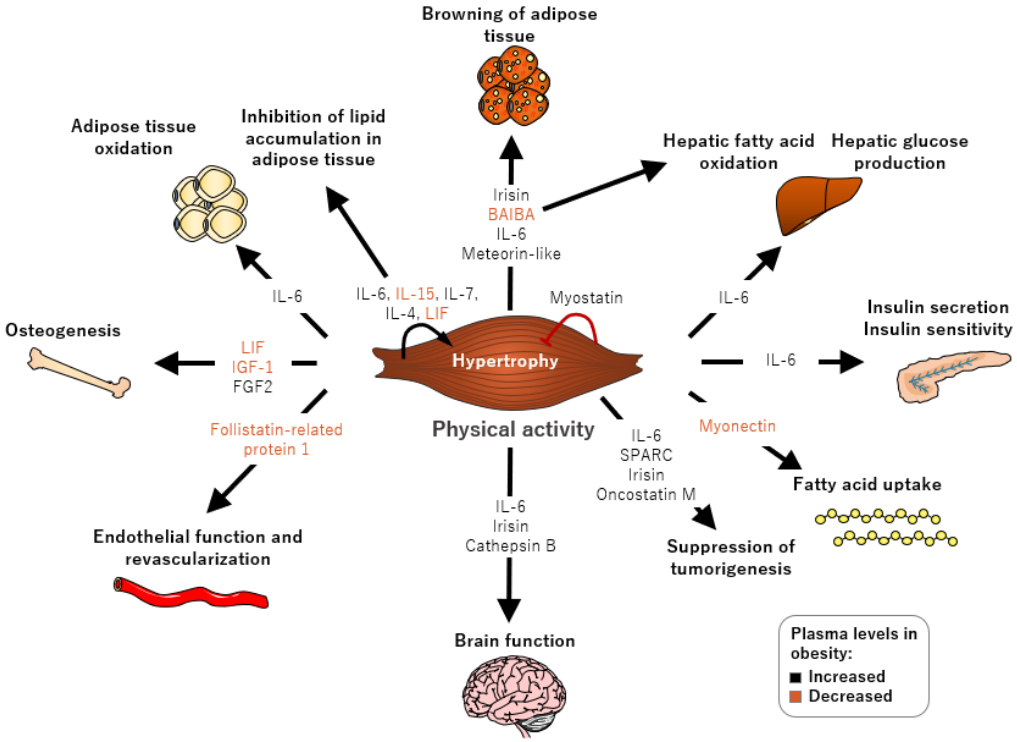

Figure I3. Myokines affected by physical activity. Some of the most important myokines whose expression is altered upon exercise training are indicated, together with some of their effects in distant organs or in skeletal muscle. Myokines in black are usually increased in plasma in obesity, whereas those in orange tend to decrease in obese subjects. IL, interleukin; BAIBA, β-aminoisobutyric acid; LIF, leukemia inhibitory factor; IGF-1, insulin-like growth factor-1; FGF2, fibroblast growth factor 2; SPARC, secreted protein acidic and rich in cysteine.

1.2.2. White adipose tissue as an endocrine organ

While the adipose tissue was originally viewed as an organ committed only to energy storage, it has been demonstrated to be an endocrine organ that synthesizes and secretes diverse signaling molecules termed adipokines (Funcke & Scherer, 2019). Alterations in adiposity can modify the circulating levels of adipokines, therefore affecting systemic energy homeostasis by regulating energy metabolism in distant organs. In fact, changes in the production of adipokines have been linked to obesity, diabetes, inflammation, and cardiovascular and liver disease (Scheja & Heeren, 2019).

Since obesity is characterized by an increase in adipose tissue mass and altered function of the adipocytes, it has been demonstrated that it modifies the production and secretion of adipokines (Rosen & Spiegelman, 2014). Some of these adipokines are pro-inflammatory factors, like tumor necrosis factor α (TNFα) or IL-6, whose secretion rises with the increased number of inflammatory cells infiltrated in this tissue, as occurs in obesity (Barchetta et al., 2019). Some examples of typical adipokines whose expression is altered in obesity and their main functions are shown in Figure I4.

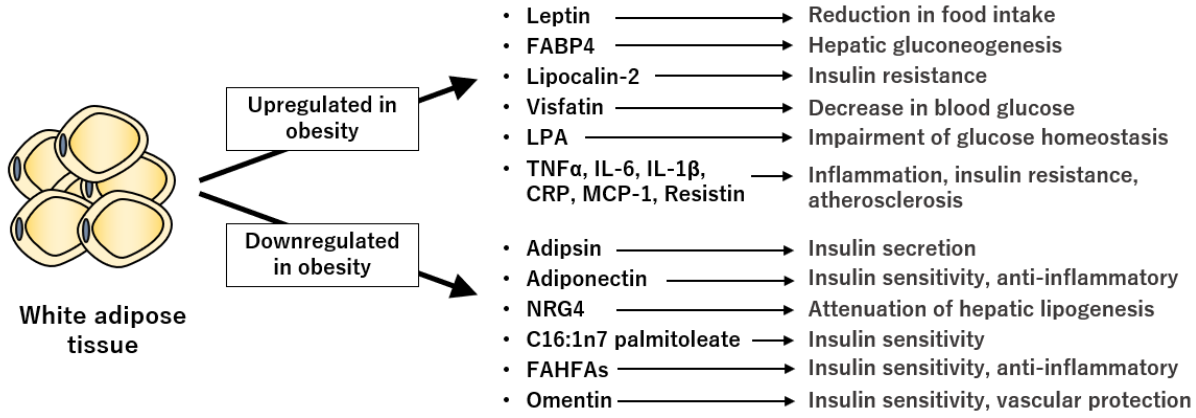

Figure I4. Adipose tissue-secreted factors. There are several adipokines that increase in obesity, including leptin, fatty acid-binding protein 4 (FABP4), lipocalin-2, visfatin, lysophosphatidic acid (LPA), or many pro-inflammatory cytokines. However, others, such as adipsin, adiponectin, neuregulin 4 (NRG4), omentin or some lipokines including C16:1n7 palmitoleate and branched fatty acid esters of hydroxy fatty acids (FAHFAs), are significantly suppressed. The main functions of these endocrine factors are indicated. TNFα, tumor necrosis factor α; IL, interleukin; CRP, C-reactive protein; MCP-1, monocyte chemoattractant protein-1.

One of the most relevant adipokines whose expression is significantly reduced in obesity is adiponectin (Arita et al., 1999; Hu et al., 1996). Adiponectin, previously known as adipocyte complement-related protein of 30 kDa (Acrp30) or AdipoQ, was first described in rodents (Hu et al., 1996; Scherer et al., 1995) and later in humans (K. Maeda et al., 1996; Nakano et al., 1996). It is one of the most abundant adipokines in plasma (Pajvani et al., 2003), and both its transcription and translation are strongly induced by adipocyte differentiation (Hu et al., 1996).

Mouse adiponectin is a 247-amino acid polypeptide with a N-terminal sequence, followed by a hyper-variable region, a collagenous domain and a C-terminal globular domain. It can exist as low-molecular-weight (LMW, trimer), middle-molecular-weight (MMW, hexamer), and high-molecular-weight (HMW, 12-18mer) complex forms, although a smaller form consisting of only the globular domain can be found in small amounts (Schraw et al., 2008). Adiponectin folding and assembly regulate plasma levels and complex distribution, a process which involves the endoplasmic reticulum (ER) and the Golgi apparatus (M. Liu et al., 2015; Z. V. Wang et al., 2007).

Adiponectin is a critical mediator of the crosstalk between the adipose tissue and other metabolic organs. It increases insulin sensitivity in key metabolic tissues, suppresses hepatic gluconeogenesis and enhances fatty acid oxidation in skeletal muscle (Yamauchi et al., 2001). It also protects kidney podocytes from cell death (Rutkowski et al., 2013), it acts on the brain to decrease body weight (Qi et al., 2004), and it also has anti-inflammatory and vascular protective actions (Shibata et al., 2005). Due to its diverse functions, adiponectin has been implicated in the protection against obesity, diabetes, inflammation, cardiovascular disease and cancer. In fact, adiponectin negatively influences the growth of most obesity-related cancer types, although its role in some of them is controversial (Dalamaga et al., 2012). Several studies have reported an inverse association between adiponectin levels and some types of cancer (Mantzoros et al., 2004; Mitsiades et al., 2011; Nakajima et al., 2009; Ohbuchi et al., 2014; Petridou et al., 2006; Spyridopoulos et al., 2007; Wei et al., 2005), whereas others have found increased levels of this adipokine (Dalamaga et al., 2009; Kerenidi et al., 2013; Kosova et al., 2013; Liao et al., 2013; Petridou et al., 2010) or no association (Petridou et al., 2007) with certain cancers. Despite these discrepancies, it is known that adiponectin acts on cancer cells by activating specific signaling pathways downstream of adiponectin receptors (AdipoR1 and AdipoR2) that have a relevant role in the control of cell proliferation or apoptosis (Hebbard & Ranscht, 2014). It can also suppress tumor angiogenesis, and its role in improving whole-body insulin sensitivity and reduction of inflammation is also beneficial for cancer prevention (Parida et al., 2019).

1.3. Obesity-associated diseases

In spite of the plethora of available strategies for the control of obesity epidemic, the increased incidence that is predicted to occur in the next decades justifies the need for increasing knowledge about new approaches and identification of new therapeutic targets for its control. Health consequences of global obesity epidemic are significant, as obesity is a predisposing factor for many non-communicable diseases, including type 2 diabetes mellitus, cardiovascular diseases, fatty liver disease, musculoskeletal disorders and cancer (Speakman, 2004), which

constitute the dominant health burden on developed and developing countries (Speakman, 2013). Moreover, it may also aggravate other pathologies, such as the global pandemic Coronavirus disease 2019 (COVID-19) (Stefan et al., 2020; J. Yang et al., 2021).

1.3.1. Type 2 diabetes

Diabetes is a metabolic disease characterized by altered glucose homeostasis caused by impaired insulin action, either due to an insufficient production by pancreatic β-cells (type 1 diabetes) or to reduced insulin sensitivity of peripheral tissues (type 2 diabetes). Both types affect insulin-mediated effects, such as glucose uptake into cells, the promotion of many anabolic reactions and blockade of catabolic ones.

As occurs with obesity, diabetes is also increasing at an alarming rate: over 463 million people worldwide were estimated to have diabetes in 2019, and this number will rise to 700 million by 2045 (International Diabetes Federation [IDF], 2019). Several mechanisms that are altered in obesity can induce insulin resistance, a major risk factor for type 2 diabetes (S. E. Kahn et al., 2006). Insulin resistance in the peripheral tissues results in increased blood glucose levels (hyperglycemia), which may lead to a rise in insulin levels, as pancreatic β-cells secrete more insulin to compensate it. This can lead to β-cell dysfunction, decreased insulin secretion and impaired glucose tolerance, followed ultimately by the development of type 2 diabetes (S. E. Kahn et al., 2006).

The main mechanisms that induce insulin resistance in obesity act through impairing insulin signaling pathway (Figure I5). This pathway is initiated by the binding of insulin to its receptor and the subsequent tyrosine phosphorylation of both the receptor and the insulin receptor substrate (IRS), being IRS1 the one involved in insulin signaling in skeletal muscle and adipose tissue (White, 2002). IRS then activates phosphatidylinositol 3-kinase (PI3K), which converts phosphatidylinositol-4,5-bisphosphate (PIP_2) into phosphatidylinositol-3,4,5-triphosphate (PIP_3). One essential target of PIP_3 is the serine/threonine kinase protein kinase B (AKT/PKB) (Hassan et al., 2014), which is recruited to the plasma membrane, where it is activated by phosphorylation on both threonine (Thr) 308 and serine (Ser) 473 residues by 3-phosphoinositide-dependent protein kinase-1 (PDK1) and mammalian target of rapamycin complex 2 (mTORC2), respectively (Alessi et al., 1997; Sarbassov et al., 2005). As a consequence, insulin promotes glucose uptake into cells due to the translocation of glucose transporter 4 (GLUT4) to the plasma membrane in some tissues, including skeletal muscle and adipose tissue, and it also affects cell growth, cell survival and metabolism (C. R. Kahn et al., 2005).

Obesity causes alterations that may lead to the development of insulin resistance (Figure I5). Increased free fatty acids (FFAs) concentrations in obesity can activate proteins like protein kinase C (PKC), mitogen-activated protein kinases (MAPKs) and the inhibitor of nuclear factor-κB kinase-β (IKK-β), or phosphatases, leading to insulin resistance (Qatanani & Lazar, 2007). One of the main mechanisms for insulin resistance is the inhibitory phosphorylation of IRS1 on serine residues (Petersen & Shulman, 2018), which might also be induced by proteins such as mammalian target of rapamycin (mTOR) and suppressor of cytokine signaling 3 (SOCS3) (Gual et al., 2005). Moreover, the chronic low-grade inflammatory state that characterizes obesity recruits immune cells to metabolic organs, which produce pro-inflammatory cytokines that can also induce insulin resistance (Wellen & Hotamisligil, 2005). In addition, the alterations in adipokine production during obesity can also impair insulin signaling (Qatanani & Lazar, 2007), as occurs with oxidative stress (Blair et al., 1999), mitochondrial dysfunction (Chomentowski et al., 2011) and ER stress (Özcan et al., 2004). Interestingly, the distribution of body fat can also determine insulin sensitivity (Cnop et al., 2002).

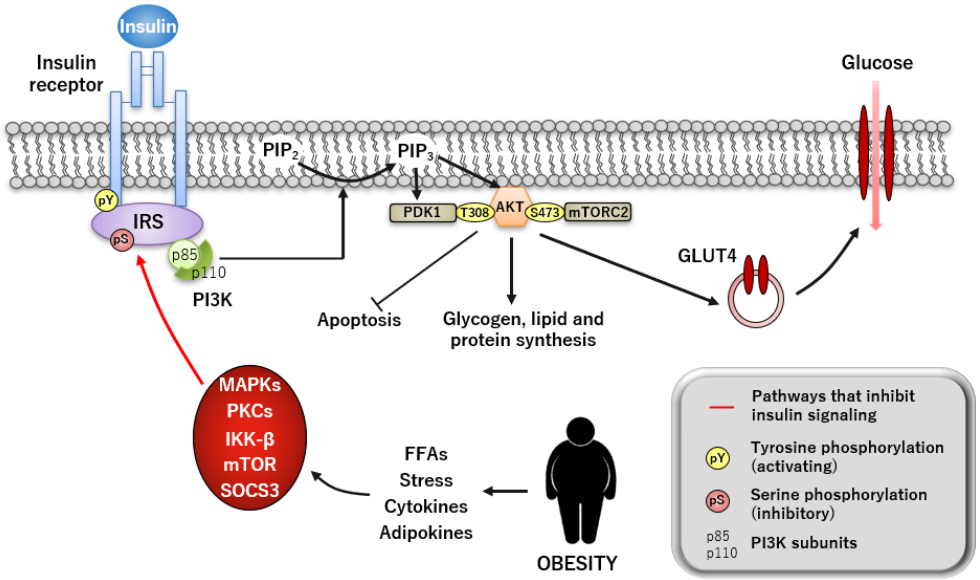

Figure I5. Mechanisms for obesity-induced insulin resistance. Obesity is characterized by an increase in FFAs, stress factors, cytokines and adipokines, among other factors, which activate some proteins that inhibit insulin signaling, mainly by inhibitory phosphorylation of IRS on serine residues.

Among the different organs, skeletal muscle is the major site of insulin-stimulated glucose uptake (Bouskila et al., 2008). In fact, exercise impacts glucose homeostasis by improving whole-body insulin sensitivity (Egan & Zierath, 2013). This essential role can be impaired due to skeletal muscle insulin resistance in obesity (S. E. Kahn et al., 2006).

1.3.2. Cancer

Cancer is a group of diseases characterized by uncontrolled growth of abnormal cells which can invade other parts of the body (Hanahan & Weinberg, 2011). It is the second leading cause

of death globally, and the number of new cases is expected to rise by about 50% over the next two decades (Sung et al., 2021). According to the WHO, around one third of deaths from cancer are due to the five leading behavioral and dietary risks, including high BMI and lack of physical activity, which are commonly associated with obesity (WHO, 2020). In fact, epidemiological data have demonstrated a link between obesity and multiple types of cancer (Arnold et al., 2015; Lauby-Secretan et al., 2016) (Figure I6). Obesity causes a disruption in the role of the adipocytes in energy homeostasis, resulting in chronic low-level inflammation, increasing the secretion of several inflammatory cytokines by the immune cells that infiltrate the adipose tissue, such as TNFα, IL-6 or plasminogen activator inhibitor 1 (PAI1) (Gregor & Hotamisligil, 2011). These cytokines, in turn, promote cancer development by increasing proliferation, angiogenesis and metastasis (Khandekar et al., 2011). In addition, adipokine signaling is also altered. For instance, leptin, which seems to promote cell proliferation, is increased in obesity (Onuma et al., 2003), while levels of adiponectin, which may have antiproliferative effects, decrease (Cnop et al., 2003). Moreover, the proliferation of adipose tissue progenitors in obesity may contribute to tumorigenesis (Y. Zhang et al., 2010). Importantly, the alterations that occur in obesity can also cause secondary changes that may have tumorigenic roles, including increased macrophage infiltration in several tissues (Pollard, 2004), or the negative impact on several immune cell populations that are essential in immune surveillance in cancer (O'Shea et al., 2010, 2013). In addition, impaired insulin signaling and hyperinsulinemia are related to proliferation and metastasis (Lu et al., 2017), and the lipid deregulation observed in obesity may also foster cancer development, either directly through the increased levels of FFAs within tumor cells (Nomura et al., 2010), or due to the excess lipid accumulation in peripheral tissues that may promote reactive oxygen species (ROS) generation, thus causing DNA damage (Panieri & Santoro, 2016).

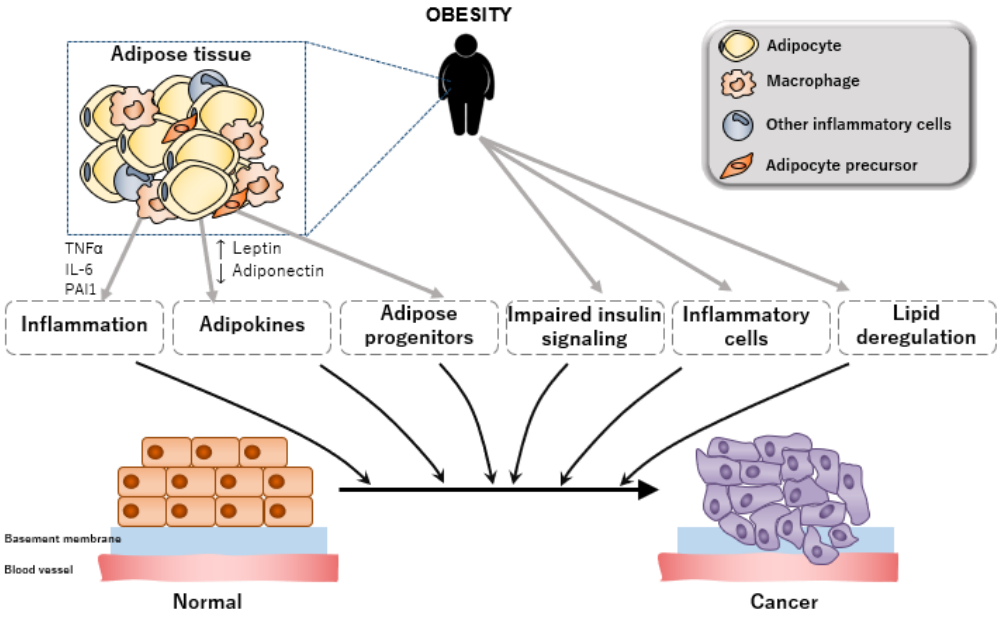

Figure I6. Mechanisms linking obesity to cancer development. Obesity increases adipocyte number and size and causes increased infiltration of inflammatory cells into the adipose tissue. These modifications alter adipokine secretion and promote the release of inflammatory cytokines, as well as the proliferation of adipocyte progenitors. These alterations, along with the secondary consequences of obesity, namely hyperinsulinemia, systemic inflammation, and hyperlipidemia, contribute to the increased incidence of cancer observed in the obese state.

1.3.2.1. Hepatocellular carcinoma

Liver cancer is predicted to be the sixth most commonly diagnosed cancer, and it was the third leading cause of cancer death worldwide in 2020 (Sung et al., 2021). Several studies have demonstrated an association between excess body weight and increased risk of primary liver cancer (Calle et al., 2003; Campbell et al., 2016; Y. Chen et al., 2012; Larsson & Wolk, 2007). In fact, limitation of body weight gain by caloric restriction prevents hepatic tumor formation in mice (Ploeger et al., 2017), and the absence of excess body fatness also lowers the risk of liver cancer in humans (Lauby-Secretan et al., 2016).

The most common primary liver cancer is hepatocellular carcinoma (HCC), which is generated by the uncontrolled proliferation of hepatocytes and accounts for 75-85% of liver cancers (Sung et al., 2021). Other types of liver cancer are caused by the abnormal proliferation of non-parenchymal cells, such as bile duct cells (cholangiocytes) in the case of intrahepatic cholangiocarcinoma (Sung et al., 2021).

Therapeutic options for HCC are limited, and the prognosis is very poor, making it one of the deadliest cancers (Gallage et al., 2021). For this reason, better preventive, diagnostic, and therapeutic tools are urgently needed, particularly in view of the important contribution of obesity to HCC incidence worldwide (Bakiri & Wagner, 2013). As happens with other tumors, the alterations in the adipose tissue in obesity, together with the increased inflammation and high levels of glucose, insulin and FFAs, are major drivers in HCC development. These alterations might lead to non-alcoholic fatty liver disease (NAFLD), a wide spectrum of disorders which can progress to HCC (El-Serag & Rudolph, 2007; Parekh & Anania, 2007). NAFLD can be characterized by simple steatosis (fatty liver), which has a more benign course, or it can progress to nonalcoholic steatohepatitis (NASH), which occurs when there is inflammation in the liver, in addition to fat accumulation. Inflammation and liver cell damage in NASH can further progress to fibrosis, which may lead to cirrhosis. Cirrhosis is characterized by scarring of the liver caused by long-term liver damage, and it may ultimately lead to HCC (Starley et al., 2010) (Figure I7).

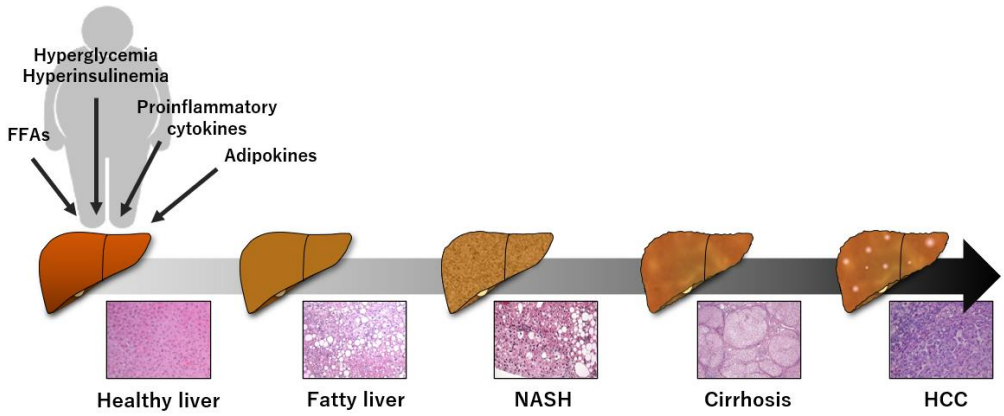

Figure I7. Progression from a healthy liver to NAFLD and HCC in obesity. Obesity is characterized by an excess of FFAs, glucose and insulin levels, as well as proinflammatory cytokines and altered adipokine secretion. These and other factors can cause NAFLD, which is characterized by fat accumulation in the liver (fatty liver). This fatty liver can lead to NASH when it is accompanied with inflammation, a condition which can progress to fibrosis and cirrhosis, and finally to HCC. Histological images of each hepatic condition are represented. Source for NASH and cirrhosis images: Carey, 2020; source for HCC image: Kodama et al., 2018.

Epidemiological studies have shown a higher incidence of HCC in men than in women (Bosch et al., 2004), a dimorphism also observed in mouse models (Ghebranious & Sell, 1998; Naugler et al., 2007). Although several explanations for this phenomenon have been proposed, including differences in sex hormones as well as X or Y chromosomes-linked genes, many mechanisms explaining these discrepancies are still unknown (Clocchiatti et al., 2016; Rubin et al., 2020).

Cancer is linked to general alterations in organ homeostasis and systemic processes, such as the regulation of metabolism. Therefore, gender disparities in key metabolic organs, such as the adipose tissue, may also contribute to the gender dimorphism observed in HCC. In fact, the adipose tissue responds differently in males and females, due to the different genetic make-up and differences in the inputs that act on it (Fuente-Martín et al., 2013). This differential functionality of the adipose tissue can affect the liver, since relevant inter-communications have been found between both organs (Azzu et al., 2020). Remarkably, adipokines are key mediators in this adipose tissue-liver crosstalk, and some of them have relevant gender disparities, like adiponectin, which is significantly reduced in men and male mice compared to women or female rodents (Combs et al., 2003; Yannakoulia et al., 2003). Importantly, the lower adiponectin levels in obese individuals correlate with their higher incidence of HCC, while the reduced HCC development in females correlates with their higher circulating adiponectin levels. Moreover, the role of adiponectin in the crosstalk between the adipose tissue and the liver has been described (Gatselis et al., 2014; Moschen et al., 2012). These evidences point at adiponectin as a potential candidate for mediating the gender dimorphism observed in HCC development.

2. Stress-activated protein kinases (SAPKs)

2.1. Introduction

The response of cells to extracellular and intracellular stimuli is mediated in part by the action of protein kinases and phosphatases that control protein phosphorylation. This post-translational modification of proteins is involved in many cellular processes, including cell cycle, growth, apoptosis and signal transduction (Engin, 2017; Paul et al., 1997). In fact, protein kinase-mediated protein phosphorylation plays an essential role in a variety of cell signaling responses in both physiological and pathological conditions (Cohen, 2002). For this reason, an appropriate control of the activity of these protein kinases is fundamental for the maintenance of cellular and whole-body homeostasis. Indeed, their activity can be easily altered due to changes in extracellular stimuli, such as those that appear in obesity.

One of the most widely studied protein kinases that help cells in sensing diverse stimuli are the MAPKs (Engin, 2017). The MAPKs are serine/threonine kinases which play important roles in stress, the immune response as well as in the regulation of cell survival and differentiation (Kyriakis & Avruch, 2012). MAPKs are activated in response to diverse stimuli by dual phosphorylation on threonine (Thr) and tyrosine (Tyr) residues within a Thr-X-Tyr phosphorylation motif, where X can be glutamic acid (Glu), proline (Pro) or glycine (Gly) (Dérijard et al., 1995). Based on these dual phosphorylation motifs, three groups of MAPKs have been identified in mammals: ERKs (extracellular signal-regulated kinases), JNKs (c-Jun NH_2-terminal kinases), and p38s, for Thr-Glu-Tyr, Thr-Pro-Tyr, and Thr-Gly-Tyr, respectively (Cargnello & Roux, 2011). Each MAPK plays a relevant role in signal transduction by transforming the external stimulation into the appropriate response through the phosphorylation of specific substrates, including transcription factors, cytoskeletal proteins, proteins involved in translation and other kinases. These substrates are phosphorylated by MAPKs in motifs with a Ser or a Thr followed by a Pro (Ser/Thr-Pro), thus causing alterations in their activity, structure, function, localization or interaction with other molecules (Chang & Karin, 2001).

MAPKs signaling pathways share a common structure formed by three sequentially acting protein kinases, including the MAPK kinase kinases (MAPKKKs or MAP3Ks), the MAPK kinases (MAPKKs or MAP2Ks) and the MAPKs. The canonical mechanism of MAPKs activation is caused by MAP2Ks-mediated phosphorylation of the Thr-X-Tyr motif: ERK is activated by MEK1 and MEK2; JNK, by MKK4 and MKK7; and p38, by MKK3 and MKK6, although MKK4 may also contribute to p38α activation (Cuadrado & Nebreda, 2010). Each MAP2K, in turn, is phosphorylated by the MAP3Ks. This organization promotes signal

amplification and fidelity (Raman et al., 2007). In addition, several scaffolding proteins assure the tight regulation of the pathway by clustering specific MAPK cascade components with their substrates at specific subcellular locations (Morrison & Davis, 2003). Apart from the canonical mechanisms for p38 activation, some MAP2K-independent mechanisms for their activation have been described, including mechanisms involving protein interaction, small molecules and both Tyr- and autophosphorylation of p38 (Ge et al., 2002, 2003; Gills et al., 2007; Lanna et al., 2014; Salvador et al., 2005).

Duration and magnitude of MAPKs activation is crucial for the biological outcome (Marshall, 1995). Therefore, there are various negative regulatory mechanisms whereby MAPKs can be inactivated, including termination of stimuli, inactivation of upstream signaling events, transcriptional feedback, or dephosphorylation mediated by MAPK phosphatases (MKPs) (Patterson et al., 2009). MKPs are dual-specificity phosphatases (DUSPs) that attenuate MAPKs signaling by dephosphorylating both Thr and Tyr residues within the MAPK activation loop (Caunt & Keyse, 2013). Importantly, MKPs have substrate preference for one or more MAPKs (Patterson et al., 2009). In addition, activation of some MAPKs may affect the activation of specific substrates mediated by other members of the family, which makes cell responses to extracellular cues highly dependent on the activation pattern of the different MAPKs, which is not exclusive but combinatorial (Kirsch et al., 2020).

Several stimuli can activate MAPKs. In general, ERKs are activated by mitogens and differentiation signals, while the JNK and p38 MAPKs are activated by stress and cytokines (Sabio & Davis, 2014). For this reason, among the MAPKs, the JNKs and p38s are collectively named stress-activated protein kinases (SAPKs) (Figure I8). SAPKs are evolutionarily conserved in all eukaryotes (Li et al., 2011). Apart from inflammatory cytokines, there is a huge number of stimuli that can activate SAPKs, such as ceramides, G protein-coupled receptors, vasoactive peptides, hypoxia, cell stretching, ischemia/reperfusion, oxidative stress, ultraviolet (UV) radiation and osmotic stress, contributing to diverse cellular responses through several intracellular targets (Nikolic et al., 2020).

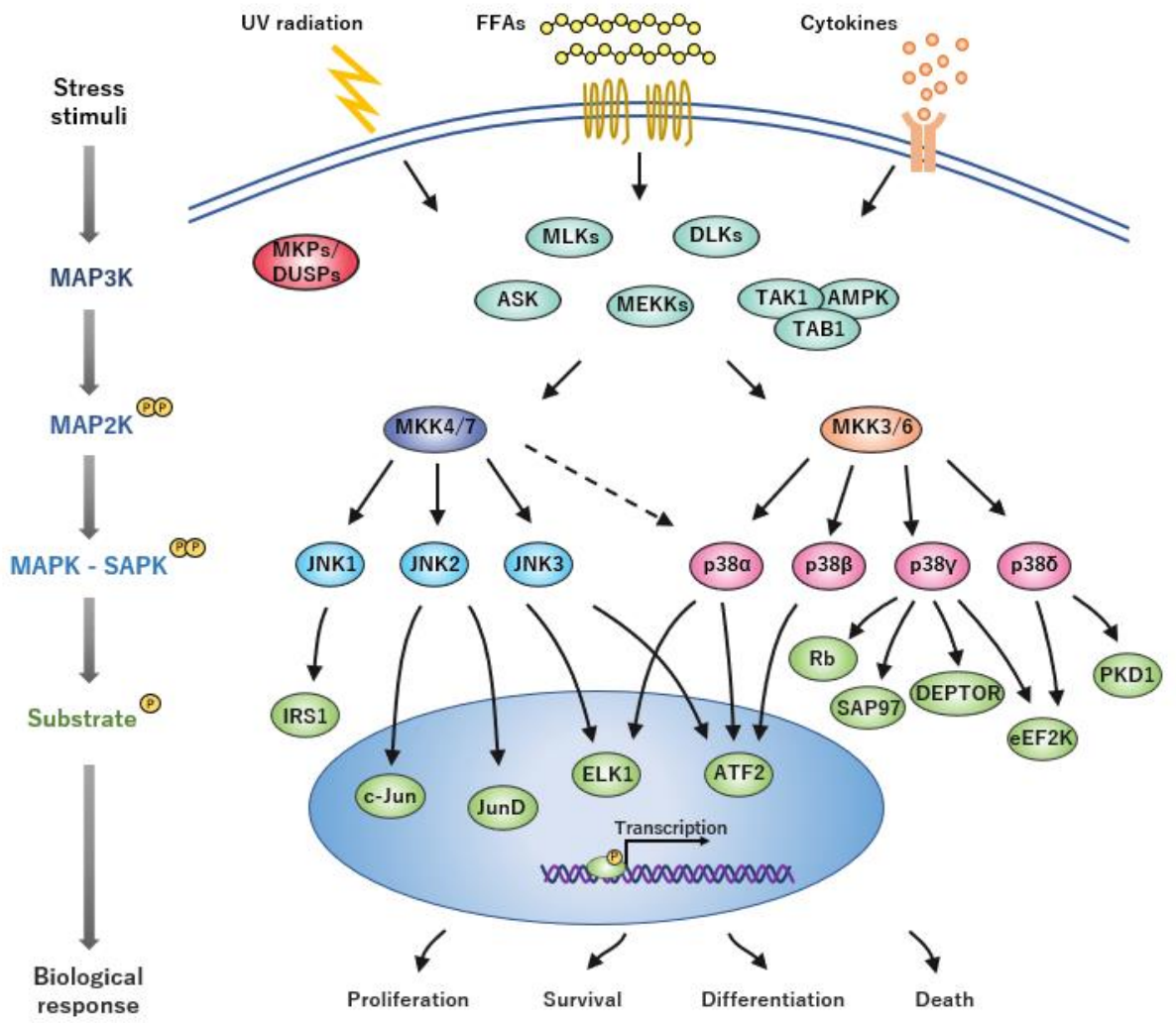

Figure I8. Stress-activated protein kinases signaling pathways. SAPKs family, which includes JNKs and p38s, is activated by stress stimuli, such as ultraviolet (UV) radiation, free fatty acids (FFAs) and cytokines, some of which are usually increased in the obese state. Like other MAPKs, SAPKs are activated by a phosphorylation cascade that involves MAP3Ks and MAP2Ks, which culminates with SAPKs-mediated activation of several targets involved in diverse biological responses, including cell proliferation, survival, differentiation, or death. The inhibitory function of MAPK phosphatases (MKPs/DUSPs) over all SAPKs is also depicted. MLKs, mixed lineage kinases; DLKs, dual leucine zipper-bearing kinases; ASK, apoptosis signal-regulating kinase; MEKKs, MAPK kinase kinases; TAK1, transforming growth factor-β-activated protein kinase 1; TAB1, TAK1-binding protein 1; AMPK, adenosine monophosphate-activated protein kinase; MKPs, MAPK phosphatases; DUSPs, dual-specificity phosphatases; IRS1, insulin receptor substrate 1; c-Jun, cellular-Jun; ELK1, Ets-like protein 1; ATF2, activating transcription factor 2; Rb, retinoblastoma protein; SAP97, synapse-associated protein 97; DEPTOR, DEP domain-containing mTOR-interacting protein; eEF2K, eukaryotic elongation factor 2 kinase; PKD1, protein kinase D1.

2.1.1. p38s

The p38 MAPKs family is composed by four members which are encoded by distinct genes located in tandem in two chromosomes (Li et al., 2011): p38α/SAPK2a (*Mapk14*), p38β/SAPK2b (*Mapk11*), p38γ/SAPK3 (*Mapk12*) and p38δ/SAPK4 (*Mapk13*). Each of these kinases displays different patterns of expression and different roles in a cell type-dependent

and context-specific manner: p38α is ubiquitously expressed; p38β is more restricted to brain, thymus and spleen (Beardmore et al., 2005); p38γ is expressed in all tissues and at high levels in skeletal muscle and BAT (Beardmore et al., 2005; Matesanz et al., 2018); and p38δ is mainly expressed in neutrophils, endocrine glands and BAT (González-Terán et al., 2016b; Ittner et al., 2012; Matesanz et al., 2018; Sumara et al., 2009).

The p38 MAPKs family can be sub-divided into two sub-groups based on their homology, substrate specificity and sensitivity to chemical inhibitors: p38α and p38β, on one side; and p38γ and p38δ, on the other (Cuenda & Rousseau, 2007). Classic downstream targets of p38α and p38β include transcription factors such as activating transcription factor 1/2 (ATF1/2) (Tan et al., 1996), C/EBP homologous protein (CHOP) (Wang & Ron, 1996), myocyte enhancer factor 2 A/C (MEF2A/C) (S. H. Yang et al., 1999) or p53 (Perfettini et al., 2005). These kinases also activate other signaling factors, such as MAPK-activated protein kinase 2/3 (MAPKAPK2/3, MK2/3) leading to the activation of cAMP response element-binding (CREB) (Tan et al., 1996) or the chaperone heat shock protein 27 (HSP27) (L. Xu et al., 2006). Moreover, p38s can also phosphorylate cytoskeletal regulators, such as stathmin and tau protein (Asih et al., 2020). Specifically, p38γ docks directly to proteins with PDZ domains, like synapse-associated protein (SAP)90 and SAP97, and phosphorylates them (Sabio et al., 2004, 2005). Interestingly, p38γ acts as a cyclin-dependent kinase (CDK)-like kinase by phosphorylating retinoblastoma (Rb) tumor suppressor protein (Tomás-Loba et al., 2019). Moreover, both p38γ and p38δ target eukaryotic elongation factor 2 kinase (eEF2K) (González-Terán et al., 2013; Knebel et al., 2001) and the mTOR complex 1 (mTORC1) and complex 2 (mTORC2) inhibitor DEP domain-containing mTOR-interacting protein (DEPTOR) (González-Terán et al., 2016a), whereas p38δ phosphorylates protein kinase D1 (PKD1) (Sumara et al., 2009).

Although it was initially thought that the different members had redundant roles in the cells, it is now known that each p38 plays different roles, and different p38 family members can even serve opposing functions within the same tissue (Nikolic et al., 2020). Genetic modification of individual p38s has been essential for uncovering non-redundant functions of individual p38 kinases (Asih et al., 2020). p38α is the most widely studied isoform, and it is implicated in tissue homeostasis and several pathologies from inflammation and the immune response to cancer, heart and neurodegenerative diseases (Canovas & Nebreda, 2021). Mice with a constitutive deletion of p38α die during embryonic development owing to a defect in placental organogenesis (Adams et al., 2000). For this reason, the roles of p38α in adult mice have been investigated using conditional alleles. p38α has been proposed to regulate the differentiation and proliferation of various cell types (Jirmanova et al., 2009; Ventura et al., 2007), and several

studies support the role of p38α as a tumor suppressor (L. Hui et al., 2007) or with a tumor-promoting function (Vitos-Faleato et al., 2020). Moreover, p38α also plays a role in cognitive functions (Asih et al., 2020). In contrast, the role of p38β, p38γ and p38δ is starting to be elucidated (Cuenda & Sanz-Ezquerro, 2017). Global deletion of p38 genes different from p38α results in viable offspring (Beardmore et al., 2005; González-Terán et al., 2016a, b; Ittner et al., 2016; Loonat et al., 2019; Sumara et al., 2009). p38β has a relevant role in bone formation (Greenblatt et al., 2010) and neuronal function (Loy et al., 2011), and it has been related to cardiac hypertrophy (S. Zhang et al., 2003), neurodegenerative disorders (M. Yu et al., 2017) and cancer (Roche et al., 2020). In contrast, p38γ and p38δ are implicated in inflammation (González-Terán et al., 2013; Risco et al., 2012), cardiac pathophysiology (González-Terán et al., 2016a; Loonat et al., 2019; Rajamäki et al., 2016), cancer (Del Reino et al., 2014; F. Wang et al., 2020; Zur et al., 2015) and neuropathology (Feijoo et al., 2005; Ittner et al., 2016). For instance, p38γ and p38δ promote cardiac hypertrophy (González-Terán et al., 2016a), and p38δ decreases insulin secretion from pancreatic β-cells (Sumara et al., 2009).

2.1.2. JNKs

There are three JNK family members encoded by three different genes located in different chromosomes: JNK1 (*Mapk8*) and JNK2 (*Mapk9*), which are ubiquitously expressed, and JNK3 (*Mapk10*), whose expression is mainly restricted to brain, heart and testis (Davis, 2000). There are several alternatively spliced variants derived from these three genes of each JNK member, which can be separated in two groups based on their size: the short forms of about 46 kDa (JNK1α1, JNK1β1, JNK2α1, JNK2β1, JNK3α1) and the long forms of about 54 kDa (JNK1α2, JNK1β2, JNK2α2, JNK2β2, JNK3α2) (Gupta et al., 1996). These diverse variants have different specificity of interaction between JNK and transcription factors, but their function and exact mechanism of modulation are still unsolved (Vernia et al., 2016a).

Typical targets of JNKs include transcription factors like cellular-Jun (c-Jun), JunD and ATF2 (Ip & Davis, 1998). Since these transcription factors are part of the activator protein-1 (AP-1) transcription factor family, their activation by JNK also affects AP-1 activity (Bogoyevitch & Kobe, 2006). Moreover, JNKs also target other transcription factors such as ETS-like protein 1 (ELK1) (S. H. Yang et al., 1998), p53 (Buschmann et al., 2001), cellular-Myc (c-Myc) (Alarcon-Vargas & Ronai, 2004) and IRS1 (Aguirre et al., 2000), and they can also phosphorylate members of the B-cell lymphoma-2 (BCL-2) family, which are involved in apoptosis (Liu & Lin, 2005).

Disruption of the JNK1, JNK2 or JNK3 genes renders fertile mice of normal size (Dong et al., 1998; D. D. Yang et al., 1997, 1998). JNK1 and JNK2 have been involved in the differentiation of immune cells (Dong et al., 1998, 2000; D. D. Yang et al., 1998). While JNK1 has been mainly implicated in obesity, insulin sensitivity and hepatic steatosis (Hirosumi et al., 2002; Schattenberg et al., 2006), JNK2 has demonstrated to have a role in type 1 diabetes (Jaeschke et al., 2005). In contrast, JNK3 has been mainly studied in the central nervous system, where it participates in neuronal death (D. D. Yang et al., 1997). Moreover, as happens with p38s, JNKs have been shown to play a dual role in cancer, either as oncogenes or tumor suppressor genes (Herrera-Melle et al., 2021). Interestingly, although JNK1/JNK3 and JNK2/JNK3 double mutants survive normally (Kuan et al., 1999), JNK1/JNK2 double knockouts are embryonic lethal due to defects in early brain development (Kuan et al., 1999; Sabapathy et al., 1999).

2.2. SAPKs in obesity

Obesity causes chronic low-grade inflammatory responses that lead to the activation of stress pathways that play critical roles in the etiology of obesity-associated complications, like SAPKs signaling (Nikolic et al., 2020). Several mechanisms of obesity-induced SAPKs activation have been described, which mainly involve pro-inflammatory cytokines and saturated FFAs (Nikolic et al., 2020). The relevance of SAPKs in obesity and its associated comorbidities justifies the need of understanding their role and regulation for the design of future therapies (Manieri & Sabio, 2015).

Increased SAPKs activation is found in WAT from type 2 diabetic patients (Carlson et al., 2003). While JNK is more activated in WAT from obese humans (Boden et al., 2008; Carvalho et al., 2013; Khadir et al., 2015) and mice (Hirosumi et al., 2002; Sabio et al., 2008; Sabio et al., 2010a, b; Tuncman et al., 2006), reduced p38 activity or expression is found in the WAT or BAT from obese mice (J. Lee et al., 2011; Matesanz et al., 2018), and decreased p38α/β expression is found in WAT of obese humans, where the upstream MAP2Ks MKK3 and MKK6 are more expressed (Bernardo, 2017; Matesanz et al., 2017, 2018). In contrast, SAPKs expression or activation is increased in livers of patients with NAFLD (González-Terán et al., 2016b; Koliaki et al., 2015; X. Zhang et al., 2019), as happens with liver JNK activity in obese humans (Carvalho et al., 2013) and mice (Hirosumi et al., 2002; Sabio et al., 2008; Sabio et al., 2010a, b; Singh et al., 2009; Tuncman et al., 2006; Vernia et al., 2014). Similarly, high levels of active SAPKs are found in skeletal muscle from obese (Carvalho et al., 2013; Chung et al., 2008) or type 2 diabetic patients (Koistinen et al., 2003), as well as in obese mice (Hirosumi et al., 2002; Pal et al., 2013; Prada et al., 2005; Sabio et al., 2008; Sabio et al., 2010a, b; Tuncman et al., 2006). Conversely, other studies found overexpression of MKP-1, a MAPK phosphatase which inactivates both JNK and p38 (Patterson et al., 2009), in

subcutaneous WAT, liver and skeletal muscle of obese humans or mice, with concomitant downregulation of p38 (Khadir et al., 2015; Lawan et al., 2015, 2018; J. Lee et al., 2011).

Systemic deletion of p38α is lethal (Adams et al., 2000), and the phenotypes observed in whole-body knockout mice for other SAPKs might be the result of the functions of the protein in specific tissues and their crosstalk, as happens with the decreased adiposity and improved insulin sensitivity observed in mice with systemic ablation of JNK1 ($JNK1^{-/-}$) (Hirosumi et al., 2002). Therefore, the use of conditional knockout mice is crucial to achieve a comprehensive understanding of the functions of SAPKs in a cell- and tissue-specific manner (Figure I9).

2.2.1. Role of p38s in main metabolic organs

2.2.1.1. Role of p38s in adipose tissue

The p38 pathway is known to control the secretion of different adipokines, and p38 kinases have a key role in the regulation of BAT thermogenesis and WAT browning in a fat depot-specific manner (Leiva et al., 2020). In visceral WAT, p38α can promote browning (Cao et al., 2004; Matesanz et al., 2017), while it reduces browning of subcutaneous WAT, possibly through p38γ inhibition (Matesanz et al., 2018). Accordingly, MKK6 in WAT reduces triiodothyronine (T3)-induced thermogenesis and energy expenditure through a decrease in p38α activity (Matesanz et al., 2017), whereas MKK3 protects against insulin resistance (Bernardo, 2017). In contrast, the kinase in charge of BAT activation is p38δ, which is inhibited by p38α (Matesanz et al., 2018). Moreover, p38 activity also alters the activity of GLUT4 (Carlson et al., 2003; Fujishiro et al., 2001; Somwar et al., 2002).

2.2.1.2. Role of p38s in liver

Hepatocyte p38α has been shown to protect against obesity and NASH by the induction of lipolysis and the inhibition of lipogenesis and pro-inflammatory cytokine production (Xiong et al., 2007; X. Zhang et al., 2019). However, opposite results have been published (Tang et al., 2019). In addition, p38α is a pivotal regulator of hepatic gluconeogenesis (Jing et al., 2015). While p38β is known to inhibit glycogen synthase (Kuma et al., 2004), p38δ is thought to activate this enzyme to promote hepatic glycogen storage (Montalvo-Romeral, 2019). Importantly, inhibition of p38γ and p38δ reduces NASH (G. Chen et al., 2019; González-Terán et al., 2016b). Moreover, p38α is known to suppress HCC development (L. Hui et al., 2007; Sakurai et al., 2008, 2013), whereas p38γ activation promotes it (Tomás-Loba et al., 2019). In fact, while p38α and MKK6 activities are reduced in human HCC (Iyoda et al., 2003), p38γ expression is increased (Tomás-Loba et al., 2019).

2.2.1.3. Role of p38s in skeletal muscle

p38 MAPKs signaling pathway is essential for myogenesis, the formation of new muscle fibers: while p38α promotes this process, p38γ is thought to inhibit it (Lluís et al., 2006; Lovett et al., 2010). p38s have been related to the regulation of fiber type determination (Schiaffino & Reggiani, 2011) and muscle hypertrophy (Norrby & Tågerud, 2010). In addition, exercise induces p38s activation (Boppart et al., 2000; Coffey et al., 2006; M. Yu et al., 2001, 2003), which are thought to modulate part of the adaptation of the exercising skeletal muscle, as is the case of p38γ (Bengal et al., 2020; Pogozelski et al., 2009). Moreover, while p38γ has been shown to promote basal glucose uptake (Ho et al., 2004), the activation of p38s in skeletal muscle has also been linked to the development of insulin resistance, mainly through IRS1 Ser307 phosphorylation mediated by p38β (de Alvaro et al., 2004). Hence, different p38s may lead to diverse responses in skeletal muscle, and their contributions to the metabolic adaptation of skeletal muscle are not clear. Moreover, only some *in vivo* studies have reported conclusive results regarding the role of these kinases in skeletal muscle. Although some studies have suggested the implications of p38s activation in myokines production and inter-organ communication (Chan et al., 2004; M. Yang et al., 2013), none of them has focused on the systemic metabolic implications of the muscle-specific p38 deficiency.

2.2.2. Role of JNKs in main metabolic organs

2.2.2.1. Role of JNKs in adipose tissue

Activation of adipose tissue JNK is known to promote insulin resistance (M. T. Nguyen et al., 2005; Sabio et al., 2008). Inactivation of JNK1 and JNK2 in adipose tissue reduces weight gain and improves glucose homeostasis and liver steatosis (X. Zhang et al., 2011), and it is thought to promote adipose tissue thermogenesis (Han et al., 2021). Accordingly, JNK1 activation in the adipose tissue can trigger insulin resistance in the liver through the JNK1-dependent release of the inflammatory cytokine IL-6 by the adipose tissue, which then causes hepatic insulin resistance by increasing liver SOCS3 (Sabio et al., 2008). However, although alternative splicing of adipose JNK contributes to the development of obesity (Vernia et al., 2016a), deletion of JNK1 from adipose tissue does not affect it (Sabio et al., 2008).

2.2.2.2. Role of JNKs in liver

Hepatic JNK induces insulin resistance (Y. Nakatani et al., 2004; R. Yang et al., 2007). Whereas ablation of JNK1 in hepatocytes impairs glucose homeostasis and causes hepatic steatosis (Sabio et al., 2009), deletion of JNK1/2 protects mice against both alterations (Vernia et al., 2014). In fact, hepatic JNK decreases fatty acid oxidation and ketogenesis (Vernia et al., 2014; Vernia et al., 2016c). Moreover, hepatocyte-specific deletion of both JNK1/2 or JNK2

alone protects against obesity (Vernia et al., 2014). Interestingly, JNK1 activation in hepatic stellate cells (HSCs), a cell type involved in collagen secretion, promotes liver fibrosis (G. Zhao et al., 2014).

The role of JNK in liver cancer is controversial (Herrera-Melle et al., 2021). JNK activation is increased in primary HCCs (L. Hui et al., 2008), and it is thought that JNK in Kupffer cells (KCs), the resident macrophages of the liver, promotes the development of HCC by promoting the expression of pro-tumorigenic cytokines (Das et al., 2011; Han et al., 2016). Although JNK in the hepatocyte can induce HCC under several conditions, it is known to prevent cholangiocarcinogenesis (Cubero et al., 2020; Manieri et al., 2020).

2.2.2.3. Role of JNKs in skeletal muscle

JNK activation in skeletal muscle has been linked to insulin resistance (Henstridge et al., 2012; Sabio et al., 2010b; Santos et al., 2012). However, JNK1 activation in skeletal muscle does not influence HFD-induced obesity (Pal et al., 2013; Sabio et al., 2010b). Interestingly, physical exercise also activates JNK in skeletal muscle (Boppart et al., 2000, 2001), which regulates the increase in skeletal muscle IL-6 expression (Whitham et al., 2012).

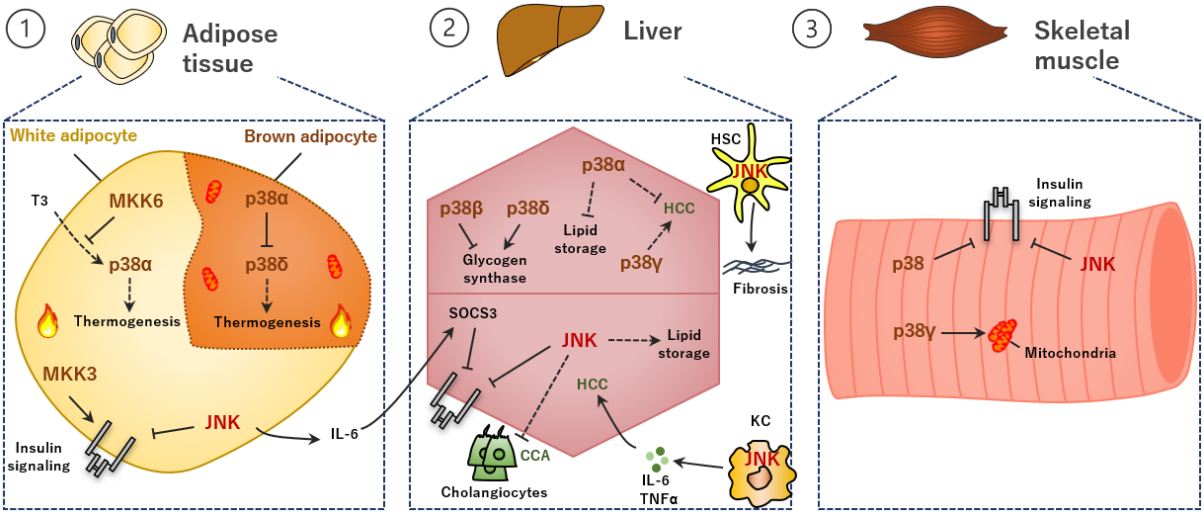

Figure I9. Tissue-specific role of SAPKs in the development of obesity, insulin resistance and NAFLD-HCC. In WAT, MKK6 inhibits the p38α-mediated browning and energy expenditure induced by T3 hormone, whereas p38α inhibits p38δ-mediated thermogenesis in BAT. MKK3 improves insulin signaling in adipose tissue, whereas JNK inhibits it in different organs. Hepatic p38α is thought to protect against liver steatosis and hepatocellular carcinoma (HCC), while p38γ promotes HCC. Hepatic p38δ promotes glycogen storage, while p38β is thought to inhibit it. Hepatocyte JNK promotes liver steatosis but protects against cholangiocarcinoma (CCA), whereas its activation in Kupffer cells (KCs) or hepatic stellate cells (HSCs) promotes HCC or liver fibrosis, respectively. p38s in skeletal muscle are thought to impair insulin signaling, although p38γ is involved in mitochondrial biogenesis. The main functions of JNK in this figure refer to JNK1.

OBJECTIVES

Obesity is a global health problem, and the activation of SAPKs in metabolic organs has demonstrated to have either positive or negative effects in the development of obesity and its comorbidities. The main objective of this thesis is to broaden our knowledge about the implications of specific SAPKs activation in metabolic organs —p38α in striated muscle and JNK1 in white adipose tissue— in the development of obesity or its associated pathologies, namely type 2 diabetes, NAFLD and HCC. To that end, the specific objectives of this work are the following:

1. **Understand the role of skeletal muscle p38α in the control of energy balance:**
    1.1. Analyze the role of muscle p38α in the development of obesity, type 2 diabetes and hepatic steatosis.
    1.2. Evaluate the function of p38α in skeletal muscle metabolism.
    1.3. Decipher the molecular mechanisms by which skeletal muscle p38α controls metabolism and energy balance.

2. **Evaluate the implications of adipose tissue JNK1 and adiponectin in gender predisposition to HCC:**
    2.1. Study adipose tissue and liver crosstalk by determining the role of adipose tissue JNK1 and adiponectin in HCC development.
    2.2. Elucidate the mechanisms linking gender, adipose tissue JNK1 activation and adiponectin secretion.
    2.3. Unveil the molecular mechanism responsible for the effect of adiponectin on HCC development.

MATERIALS AND METHODS

1. Muscle p38α in the control of energy balance

1.1. Mouse experiments

1.1.1. Mice

Mice carrying the floxed p38α alleles (B6.129-*Mapk14*$^{tm2.1}$/N) were generated by Boehringer Ingelheim Pharmaceuticals and have been described previously (L. Hui et al., 2007). The p38α floxed allele was generated by homologous recombination in embryonic stem cells (Lexicon) in which the first exon was flanked by two locus of crossover in P1 (loxP) sites (Engel et al., 2005). These mice were crossed to mice expressing the Cre recombinase under the muscle creatine kinase (MCK) promoter (FVB-*Tg(Ckmm-cre)5Khn*/N; MCK-Cre in the text) to conditionally delete p38α from striated muscle (*Mapk14*$^{MCK\text{-}cre}$; designated as p38α$^{MCK\text{-}KO}$ in the text) (Figures M1A, C).

To generate double knockout mice for p38α and p38γ, p38α$^{MCK\text{-}KO}$ mice were crossed to whole-body knockout mice for p38γ (B6.129-*Mapk12*^{tm1}), generating full-body knockout mice for p38γ and conditional for p38α in striated muscle (p38α/γ$^{MCK\text{-}KO}$ in the text) (Figure M1D).

Mice with a specific deletion of peroxisome proliferator-activated receptor gamma coactivator 1 alpha (PGC1α) in striated muscle were generated by breeding animals harboring a floxed PGC1α allele (Lin et al., 2004) with mice transgenically expressing a Cre recombinase under the control of the MCK promoter (PGC1α$^{MCK\text{-}KO}$; Figure M1B, E). These mice were crossed with mice with the floxed p38α alleles to generate mice with a conditional deletion of both p38α and PGC1α in striated muscle (p38α/PGC1α$^{MCK\text{-}KO}$ in the text) (Figure M1E).

Mice were backcrossed for at least 10 generations to the C57BL/6N background and genotyped by PCR analysis of genomic DNA isolated from mouse tails. All studies were performed using male mice (8-29 weeks old). Mice were housed randomly in a pathogen-free animal facility and maintained on a 12-h light/dark cycle at constant temperature and humidity. Mice were fed a normal chow diet (ND) (breeding and maintenance diets: D183, SAFE; and 1410, Altromin) or a high-fat diet (HFD) (high-fat diet with 60% kcal fat and 1.5% cholesterol: D11103002i, Research Diets, Inc.) *ad libitum* for 8-29 weeks. Experiments in HFD started at 8 weeks of age. All animal procedures conformed to European Union Directive 2010/63/EU and Recommendation 2007/526/EC regarding the protection of animals used for experimental and other scientific purposes, enforced in Spanish law under Real Decreto 53/2013. All experiments were approved by the Spanish National Center for Cardiovascular Research Carlos III (CNIC) Animal Care and Use Committee and Comunidad de Madrid.

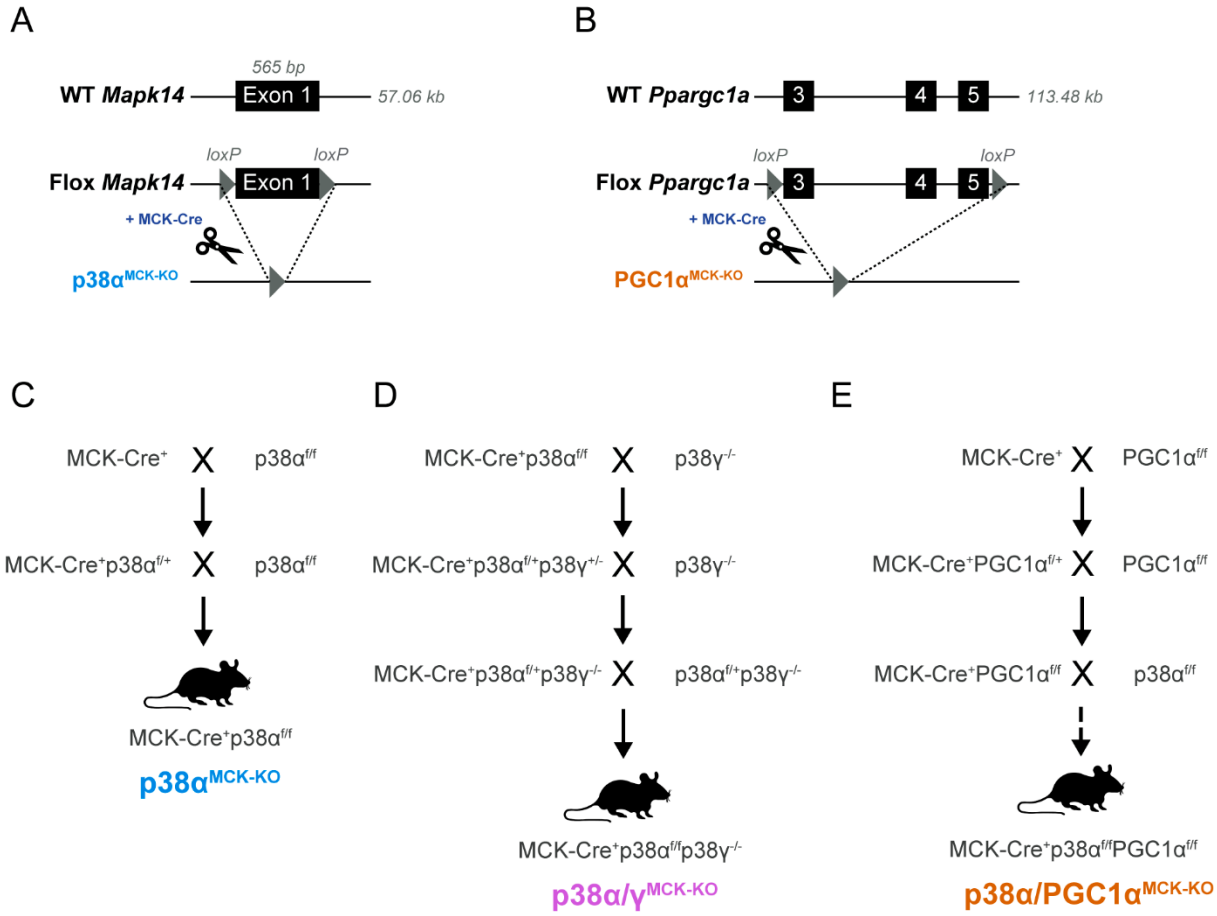

Figure M1. Generation of knockout mice. (A) Schematic depicting *Mapk14* and floxed (f) *Mapk14* alleles. Exon 1 of *Mapk14* is flanked by loxP sites and it is excised upon Cre-lox recombination using Cre recombinase under the muscle creatine kinase (MCK) promoter. (B) Schematic depicting *Ppargc1a* and floxed *Ppargc1a* alleles. Exons 3 to 5 of *Ppargc1a* are flanked by loxP sites and are excised upon Cre-lox recombination using Cre recombinase under the MCK promoter. (C) Schematic representation of mouse lines crossing to generate p38α^{MCK-KO} mice. Control mice are MCK-Cre^{+} (MCK-Cre), while striated muscle-specific p38α knockout mice are MCK-Cre^{+}p38α$^{f/f}$ (p38α^{MCK-KO}). (D) Schematic representation of mouse lines crossing to generate p38α/γ^{MCK-KO} mice. Whole-body knockouts for p38γ and conditional for p38α are MCK-Cre^{+}p38α$^{f/f}$p38γ$^{-/-}$ (p38α/γ^{MCK-KO}). (E) Schematic representation of mouse lines crossing to generate p38α/PGC1α^{MCK-KO} mice. Striated muscle-specific p38α and PGC1α knockout mice are MCK-Cre^{+}p38α$^{f/f}$PGC1α$^{f/f}$ (p38α/PGC1α^{MCK-KO}).

1.1.2. Determination of body composition and energy balance

Whole body composition was measured using nuclear magnetic resonance (NMR) imaging (Whole Body Composition Analyzer EchoMRI 500, EchoMRI), obtaining data about fat mass, lean mass and water in each mouse. For determination of energy expenditure, food intake, locomotor activity and respiratory quotient (RQ), animals were monitored in a custom 12-cage indirect calorimetry, food intake and locomotor activity monitoring system (TSE LabMaster, TSE Systems; and Panlab, Harvard Apparatus) as previously described (Czyzyk et al., 2010). Mice were acclimated during 48 h to the metabolic cages and then were monitored for an

additional 48 h. The indirect calorimetry system collected information about food intake, locomotor activity and respiratory gas exchange (oxygen consumption, vO_2, and carbon dioxide production, vCO_2) every 30 min. Data collected from the last 48 h were used to calculate all parameters for which results are reported. RQ was calculated by dividing vCO_2 produced by vO_2 consumed (vCO_2/vO_2), thus determining the preferential macronutrient oxidation. Energy expenditure was calculated from O_2 consumption and CO_2 production measurements with standard analysis software provided with the calorimeter system. Energy expenditure (kcal/48 h) was normalized to body weight measured at the end of the procedure (energy expenditure/kg body weight). Locomotor activity was determined with infrared sensors that register horizontal and vertical movements. The total number of beam breaks was determined and normalized to body weight measured at the end of the procedure (locomotor activity/kg body weight).

1.1.3. Temperature measurement

Body temperature was measured by a rectal thermometer (AZ 8851 K/J/T Handheld Digital Thermometer-Single from AZ Instruments Corp.; and BAT-12 Microprobe Thermometer from Physitemp). For determination of interscapular temperature as a representation of BAT temperature, mice were shaved in the interscapular region, and a thermographic camera was used to capture images (E60bx: Compact Infrared Thermal Imaging Camera, FLIR). Images were analyzed with FLIR Tools software.

For cold exposure test, temperature was measured with a rectal thermometer (BAT-12 Microprobe Thermometer, Physitemp), and mice were placed in a cold room at 4 °C. Rectal temperature was measured every 60 min, being the last measurement 6 h after the beginning of the test.

1.1.4. *In vivo* metabolic tests

Glucose tolerance test (GTT), insulin tolerance test (ITT) and insulin release test were performed as described (Sabio et al., 2009).

GTT

Mice were fasted overnight (16 h), and basal glucose levels were measured by collecting blood from the tail tip and using a glucometer (Ascensia BREEZE 2 from Bayer and Contour Next One from Ascensia). Then, mice were injected intraperitoneally (i.p.) with glucose (1 g/kg body weight) (D(+)-glucose monohydrate, Merck) dissolved in phosphate-buffered saline (PBS), and blood glucose concentration was measured at 15, 30, 60, 90 and 120 min post-injection.

ITT

Mice were fed *ad libitum*, and basal glucose levels were measured as described for GTT. Then, mice were injected i.p. with insulin (0.75 U/kg body weight) (Lilly). Blood glucose concentration was measured at 15, 30, 60, 90 and 120 min after insulin injection. Glucose levels were normalized to basal glucose and shown as percentage.

Insulin release test

Mice were fasted overnight (16 h), and 100 µl of blood samples from the submandibular vein were collected in ethylenediaminetetraacetic acid (EDTA) blood collection tubes (Microvette). Mice were injected i.p. with glucose (2 g/kg), and 100 µl of blood were collected using the same procedure, 10 and 30 min after glucose injection. Plasma samples were obtained by centrifuging the samples at 9,600 x *g* for 20 min at 4 °C.

1.1.5. Determination of homeostasis model assessment of insulin resistance (HOMA-IR)

The homeostasis model assessment of insulin resistance (HOMA-IR) was calculated as described (Akagiri et al., 2008). Glucose and insulin concentrations obtained after 16 h of food withdrawal were measured as described in other sections and used in the following formula:

$$\text{HOMA-IR} = \frac{\text{Fasting blood glucose (mg/dl) x Fasting insulin (µU/ml)}}{405}$$

1.1.6. Muscle strength test

Muscle strength test was performed as described (Deacon, 2013), with minimum modifications. Briefly, mice were acclimated to the experimental room for 15 min. A series of six weights was made, each consisting of a 7 g fine wire mesh (scale collector) attached to a series of steel chain links of increasing weight (13 g per chain link). Each mouse was hold by the middle of the tail and allowed to grasp the scale collector only with its forelimbs (first weight). A hold of three seconds for each weight was the criterion to test the next weight by adding one chain link. Every mouse was given three chances to hold the corresponding weight for 3 s, with a 10 s rest between them, and the maximum time and weight achieved was annotated. A final total score was calculated as the product of the score given to the corresponding number of links in the heaviest chain held for the full 3 s, multiplied by the time (3 s) it was held (Table M1). The link scores were 0.5 for the wire mesh, and 1.5, 2.5, 3.5 and 4.5 for the wire mesh attached to 1, 2, 3 or 4 chain links, respectively. If the heaviest weight was dropped before 3 s, an appropriate intermediate value was calculated by adding the time the animal was able to hold it to the previous score. For instance, a mouse successfully lifting

the first three weights for 3 s each but dropping the three-link chain after 1 s, scores (2.5 x 3) + 1.

Chain links	Link score	Final score
0 (wire mesh)	0.5	(0.5 x 3) + s holding 1 chain links
1	1.5	(1.5 x 3) + s holding 2 chain links
2	2.5	(2.5 x 3) + s holding 3 chain links
3	3.5	(3.5 x 3) + s holding 4 chain links
4	4.5	(4.5 x 3) + s holding 5 chain links

Table M1. Possible scores based on the number and time of chain links hold.

1.1.7. Tail suspension test

Tail suspension test was performed as previously described (Can et al., 2012), with minor modifications. Mice were acclimated to the experimental room for 15 min. A white 42 cm height x 56 cm width x 17.5 cm depth tail suspension box was used, which was divided in 4 three-walled rectangular compartments (42 cm height x 14 cm width x 17.5 cm depth) to prevent mice from observing other animals. A suspension bar (1 cm height x 1 cm width x 60 cm length) was placed on the top of the box. A 17 cm tape was used to adhere the end of mouse's tail at one end and the suspension bar at the other end in a parallel way. Hollow cylinders (4 cm length, 1.6 cm outside diameter, 1.2 cm inside diameter, 4.15 g) were placed around the tails of mice to prevent climbing behavior. Mice were suspended by the tail in the middle of their compartments with an approximate distance between their noses and the apparatus floor of 15 cm. A digital camera was used to record 6 min sessions with 4 mice tested simultaneously. An on-screen stopwatch software (Xnote Stopwatch, dnSoft Research Group) was used to measure the time that each mouse spends as mobile, excluding small movements confined to the front legs but without involvement of the hind legs, as well as oscillations due to the momentum gained during the earlier mobility, which were considered as immobility. Immobility time was calculated by subtracting the time the mouse spends as mobile to the total 6 min of the session. All analyses were done in a blinded fashion.

1.1.8. Treadmill exercise

Prior to exercise training, blood was obtained from the submandibular vein of 7-8-week-old ND-fed mice and collected in EDTA blood collection tubes (Microvette). Then, mice were exercised during 30 min with forced treadmill running training at a speed of 10 cm/s for 5 min,

15 cm/s for 20 min and 20 cm/s for 5 min, at a 20° uphill inclination of the treadmill (5-lane LE8710 treadmill, Harvard Apparatus, Panlab). Intensity of the electrical stimulation was set to 0.2 mA. The same exercise protocol was repeated two days later, and blood was collected immediately after exercise, following the same procedure. Plasma was obtained after centrifugation at 9,600 x *g* for 20 min at 4 °C.

1.1.9. Lentivirus vector production and stereotaxic microinjections

Lentiviruses were produced as described (Urso et al., 2011), with some modifications. Human embryonic kidney (HEK)-293T cells were plated at 25-35% confluence in Dulbecco's Modified Eagle Medium (DMEM) (Gibco) supplemented with 10% fetal bovine serum (FBS) (Sigma), 200 mM L-glutamine (Lonza), and 10,000 U/ml penicillin/streptomycin (1:1, Lonza). Transient calcium phosphate co-transfection of HEK-293T cells was done with the pGIPZ empty vector or short hairpin RNAs (shRNAs) against the alpha subunit of IL-15 receptor (pGIPZ.shIL15Rα vector, V3LMM_451921, Dharmacon), together with pΔ8.9 and pVSV-G packaging plasmids. The supernatants containing the lentiviral particles were collected 48 h after removal of the calcium phosphate precipitate, filtered through 0.45-µm filters and concentrated by ultracentrifugation at 115,500 x *g* for 2 h at 4 °C (Ultra-Clear Tubes, SW28 rotor and Optima L-100 XP Ultracentrifuge; Beckman Coulter).

Mice were injected in the primary motor cortex (M1) with 1 µl of lentiviral particles suspended in sterile PBS, with a speed of 100 nl/min. For that, mice were placed in a stereotaxic frame (World Precision Instruments) under ketamine-xylazine anesthesia injected i.p. (42.5% ketamine [Richter Pharma AG] and 20% xylazine hydrochloride [Bayer] in NaCl). A longitudinal incision in the skin over the cranium was performed, and lentiviruses were injected stereotaxically in M1 area with a 32-gauge needle (Hamilton) connected to a 1 µl syringe. The coordinates used to reach the M1 area were: anterior to the bregma (AP), +1.1 mm; lateral to the sagittal suture (ML), ±1.2 mm; and ventral from the surface of the skull (DV), -1.5 mm. The incision was closed with sutures, and buprenorphine (0.1 mg/kg body weight) (Richter Pharma AG) was injected i.p. after surgery as a painkiller.

1.1.10. Blood and organs collection

At sacrifice, blood samples were obtained from the submandibular vein and collected in EDTA blood collection tubes (Microvette), and plasma was obtained after centrifugation at 9,600 x *g* for 20 min at 4 °C. Mice were fasted overnight for most of the experiments, euthanized by cervical dislocation, and organs were removed, weighed and frozen in liquid nitrogen. For insulin signaling analysis, mice were injected i.p. with 1.5 U/kg insulin (Lilly) 15 min prior to

removal of the organs. For histological examination of skeletal muscles, samples were immediately frozen in liquid nitrogen-cooled isopentane (2-Methylbutane, Sigma-Aldrich) following extraction and kept on dry ice until finally stored at -80 ºC. Liver samples were collected in 10% formalin (Bio-Optica) for hematoxylin and eosin (H&E) staining, or frozen in dry ice after being embedded in optimal cutting temperature (OCT) compound (Tissue-Tek) for Oil Red staining. Tibia lengths were determined with a digital caliper (Ratio) to normalize organ's weight. Brain samples were frozen in dry ice to preserve their anatomy. The primary and secondary motor cortex (M1 and M2) were removed from the whole brain by cutting at the caudal part of the hippocampus parallel to the base of the hypothalamus and 1.2 mm to each lateral side of the corpus callosum. The depth of each section isolated was around 1 mm thick and according to the Allen Brain reference Atlas (Allen Institute for Brain Science, 2004).

1.2. Protein analyses

1.2.1. Plasma analysis

Plasma insulin, leptin, ghrelin and IL-15 concentrations were measured by magnetic bead-based multiplex assay (Bio-Rad) with a Luminex 200 analyzer, following manufacturer's instructions. IL-15 was also detected in plasma samples by Western blot. Samples were diluted in PBS (1/5), Milli-Q water (H_2O_{mq}), and Laemmli Sample Buffer, and separated by sodium dodecyl sulfate (SDS)-polyacrylamide gel electrophoresis (PAGE) using AnykD Criterion TGX Precast gels (Bio-Rad) as indicated in immunoblot analysis (section 1.2.2).

1.2.2. Immunoblot analysis

Tissue or HEK-293T cells extracts were prepared in lysis buffer (50 mM Tris-HCl pH 7.5, 1 mM ethylene glycol tetraacetic acid [EGTA], 1 mM EDTA, 50 mM NaF, 1 mM sodium glycerophosphate, 5 mM sodium pyrophosphate, 0.27 M sucrose, 1% Triton X-100, 0.1% β-mercaptoethanol, 0.1 mM phenylmethylsulfonyl fluoride [PMSF], 1 mM sodium orthovanadate, 1 µg/ml leupeptin, and 1 µg/ml aprotinin) by using T 10 Ultra-Turrax (IKA). For myotubes, the following lysis buffer was used: 20 mM Tris pH 7.6, 150 mM NaCl, 1% Triton X-100, 1 mM EGTA, 1 mM EDTA, 50 mM NaF, adding one cOmplete EDTA-free tablet and one PhosStop *EASY*pack tablet (protease and phosphatase inhibitors) per 10 ml. Lysates were centrifuged at 19,000 x *g* for 20 min at 4 °C, and protein concentration in supernatants was quantified by Bradford method (Bradford, 1976) (Bio-Rad Protein Assay) or bicinchoninic acid (BCA) assay (Thermo Fisher Scientific BCA Protein Assay). Samples were denatured in loading buffer (0.24 M Tris-HCl pH 6.8, 40% glycerol, 8% SDS, 5% β-mercaptoethanol, 0.04% bromophenol blue) at 95 °C for 5 min. Equal amounts of protein (20-50 µg) were loaded in

10% polyacrylamide gels (30% Acrylamide/Bis Solution, 29:1, Bio-Rad) (Table M2) or AnykD Criterion TGX Precast gels for IL-15 detection (Bio-Rad) and separated by SDS-PAGE at 150 V. Gels were transferred to 0.2 µm pore-size nitrocellulose membranes (Bio-Rad) (100 V, 2 h, 4 °C), blocked with 10% fat-free milk powder for 45 min, and probed overnight with the primary antibodies prepared in 5% bovine serum albumin (BSA) in PBS-0.1% Tween (Table M3). Horseradish peroxidase (HRP)-conjugated goat anti-rabbit and sheep anti-mouse from GE Healthcare were used as secondary antibodies (1:5,000 in 5% BSA in PBS-0.1% Tween) for a 1-h incubation at room temperature (RT). Membranes were washed with PBS-0.1% Tween, and reactive bands were detected by enhanced chemiluminescence (ECL, GE Healthcare) and quantified by ImageJ software (National Institutes of Health, NIH). In certain instances, membranes probed for phospho-proteins were stripped by incubating them at 55 °C for 15 min with stripping buffer (68 mM Tris-HCl pH 6.8, 1% SDS, 0.7% β-mercaptoethanol) and reprobed for total protein. Results were normalized to the non-phosphorylated form.

Reagents	Acrylamide solution 10%	Stacking
A/BA 29:1	5 ml	670 µl
Tris buffer pH 8.8 + SDS	3.8 ml	-
Tris buffer pH 6.8 + SDS	-	1 ml
H_2O_{mq}	6.1 ml	2.3 ml
APS (20% stock solution)	150 µl	40 µl
TEMED	6 µl	4 µl

Table M2. Recipes for stacking and resolving SDS-PAGE gels. A/BA, Acrylamide/Bis-acrylamide; SDS, Sodium dodecyl sulfate; H_2O_{mq}, Milli-Q water; APS, Ammonium persulfate; TEMED, N,N,N',N'-Tetramethylethylenediamine.

Antibody	Company	Reference	Dilution
Phospho-p38 (T180/Y182)	Cell Signaling	9211	1:1,000
p38α	Santa Cruz Biotechnology	sc-535	1:1,000
p38γ	Cell Signaling	2307	1:1,000
Phospho-MKK3 (S189)/MKK6 (S207)	Cell Signaling	9231	1:1,000
MKK3b	Cell Signaling	9238	1:1,000
MKK6	Enzo Life Sciences	ADI-KAP-MA014-E	1:1,000
Phospho-MK2 (T334)	Cell Signaling	3007	1:1,000
MK2	Cell Signaling	3042	1:1,000

Phospho-HSP27 (S82)	Cell Signaling	9709	1:1,000
Phospho-JNK (T183/Y185)	Cell Signaling	4668	1:1,000
JNK	Cell Signaling	9252	1:1,000
Phospho-AKT (T308)	Cell Signaling	2965	1:1,000
Phospho-AKT (S473)	Cell Signaling	9271	1:1,000
AKT	Cell Signaling	9272	1:1,000
Phospho-Thr-Pro	Cell Signaling	9391	1:1,000
Phospho-Ser-Pro-Pro	Cell Signaling	14390	1:1,000
FLAG	Sigma-Aldrich	F1804	1:1,000
PGC1α	Calbiochem	ST1202	1:1,000
PGC1β	Abcam	ab176328	1:1,000
IL-15	Abcam	ab273625	1:1,000
Phospho-ERK1/2 (T202/Y204)	Cell Signaling	9101	1:1,000
ERK1/2	Cell Signaling	9102	1:1,000
Phospho-STAT3 (Y705)	Cell Signaling	9145	1:1,000
STAT3	Cell Signaling	12640	1:1,000
Phospho-STAT5 (Y694)	Cell Signaling	9359	1:1,000
STAT5	Cell Signaling	94205	1:1,000
Vinculin	Sigma-Aldrich	V4505	1:2,000

Table M3. List of primary antibodies and dilutions used for western blotting.

1.2.3. Immunoprecipitation (IP)

PGC1α detection required immunoprecipitation (IP) prior to immunoblotting (Ruas et al., 2012). Cells were lysed by mechanical homogenization in lysis buffer (recipes indicated in section 1.2.2). After a centrifugation at 19,000 x *g* for 20 min at 4 °C, the supernatant was used for protein quantification and subsequent IP. For IP in HEK293 cells, protein G-Sepharose beads (GE Healthcare) were washed four times with PBS, and 20 µl were rotated with 2 µg anti-PGC1α antibody per IP (Table M4) at 4 °C for 1 h. Beads and antibody were washed 4 times with PBS, and 1 mg total protein was added to each IP in 600 µl lysis buffer and rotated at 4 °C overnight. Next day, samples were centrifuged at 9,600 x *g* for 1 min, and unbound fraction was collected. Precipitated beads were washed 4 times with lysis buffer and denatured at 95 ºC for 5 min in loading buffer. Both unbound fraction and samples derived from precipitated beads were loaded on 4-12% acrylamide precast gels (GenScript) and transferred

as described in SDS-PAGE procedure (1.2.2). For IP in myotubes, 1 mg total protein was used for each IP, or 200-250 µg total protein in pools of 4 samples for Phos-tag gels, and 2 µg anti-PGC1α or 0.5 µg peroxisome proliferator-activated receptor gamma coactivator 1 beta (PGC1β) antibodies (Table M4) were added in 600 µl lysis buffer, followed by overnight rotation at 4 °C. The next day, agarose beads (Pierce™ Protein G Agarose, Thermo Scientific) were washed twice with lysis buffer, and 100 µl were added to each IP, followed by rotation at 4 °C for 2 h. Samples were washed 3 times in lysis buffer, and immunoprecipitated protein was eluted in loading buffer incubating at 95 ºC for 5 min. Samples were loaded on 4-12% acrylamide precast gels (Invitrogen) or SuperSep Phos-tag gels (Fujifilm) and transferred as described in SDS-PAGE procedure (section 1.2.2). Phospho-Thr-Pro (9391, Cell Signaling), Phospho-Ser-Pro-Pro (14390, Cell Signaling), PGC1α (ST1202, Calbiochem) and PGC-1β (ab176328, Abcam) antibodies were used for immunoblotting (Table M3).

Antibody	Company	Reference	Use per IP
PGC1α (H-300)	Santa Cruz Biotechnology	sc-13067	2 µg
PGC1α (D-5)	Santa Cruz Biotechnology	sc-518025	2 µg
PGC1β	Abcam	ab176328	0.5 µg

Table M4. List of antibodies and amounts used for immunoprecipitation (IP).

1.2.4. Isobaric tandem mass tag (TMT) quantitative analysis

A quantitative proteomic analysis was performed in collaboration with the Proteomics Unit of CNIC (Figure M2). Gastrocnemius muscle samples from HFD-fed mice were homogenized by using the MagNA Lyser. 120 µg of total protein for each sample were digested using the filter aided sample preparation (FASP) protocol as previously described (Cardona et al., 2015). The dried peptides were dissolved in 100 mM triethylammonium bicarbonate (TEAB) buffer. Equal amounts of each peptide sample were labeled using the 10-plex tandem mass tag (TMT) Kit (Thermo Fisher Scientific). Labeled peptides were subjected to liquid chromatography with tandem mass spectrometry (LC-MS/MS) analysis using a C-18 reversed phase EASY nano-column (75 µm I.D. x 50 cm, 2 µm particle size, Acclaim PepMap RSLC, 100 C18; Thermo Scientific) in a continuous gradient consisting of 0-30% B in 360 min, 50-90% B in 3 min (A = 0.5% formic acid; B = 90% acetonitrile, 0.5% formic acid). Peptides were eluted from the reverse-phase nano-column to an emitter nanospray needle for real time ionization and peptide fragmentation on an Orbitrap Trybrid Fusion mass spectrometer (Thermo Fisher). An enhanced Fourier transform-resolution spectrum (resolution = 70,000) followed by the MS/MS spectra from the 15 most intense parent ions was performed. All spectra were analyzed with

Proteome Discoverer (version 2.1, Thermo Fisher Scientific) using SEQUEST-HT (Thermo Fisher Scientific). Data were searched against a Uniprot database (48,644 sequences), and peptide identification was performed as described previously (Navarro & Vázquez, 2009). Identified peptides had a false discovery rate (FDR) equal or lower than 1% FDR. Protein quantification and statistical analysis were performed using QuiXoT based on the weighted spectrum, peptide and protein (WSPP) statistical model. Proteins were annotated using Ingenuity Knowledge Database (Ingenuity Pathway Analysis, IPA).

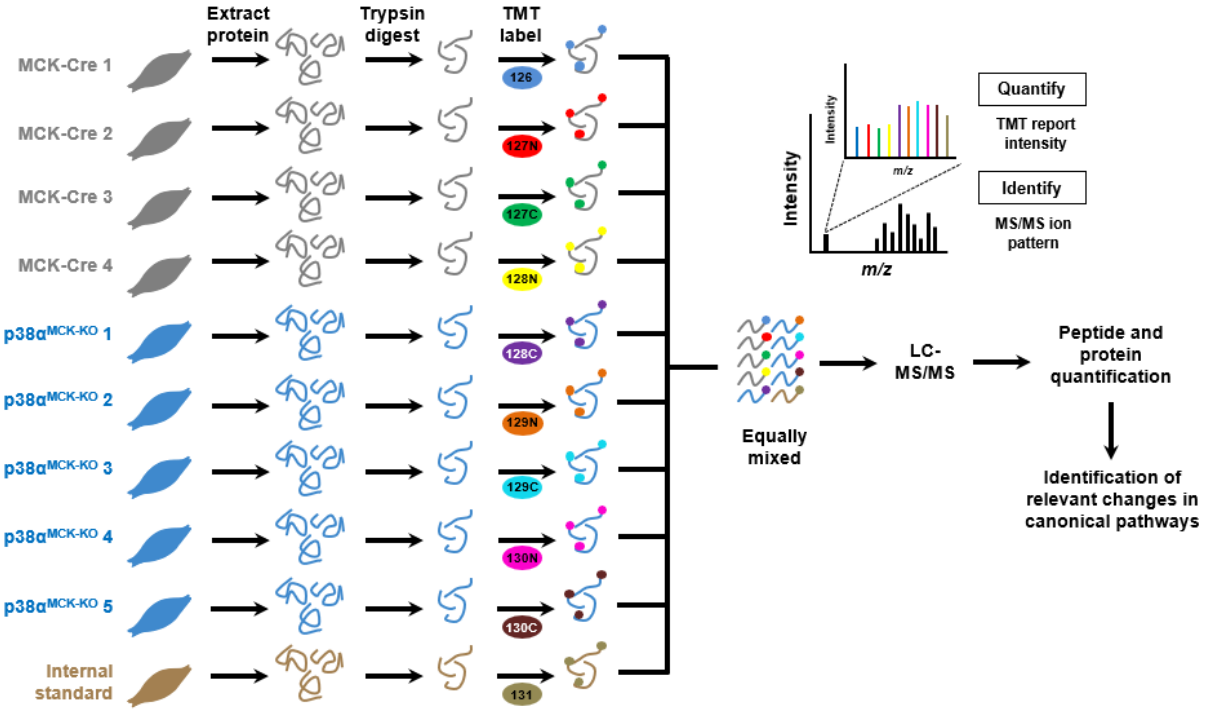

Figure M2. Isobaric TMT quantitative analysis in skeletal muscle. Gastrocnemius samples were obtained, proteins were digested, and 10-plex peptide isobaric labeling was performed. Peptides were subjected to LC-MS/MS, quantified, and IPA or gene set enrichment analysis (GSEA) analyses were performed (see sections 1.6.1 and 1.6.2).

1.3. Nucleic acids analyses

1.3.1. RNA isolation and quantitative real-time-PCR analyses (qRT-PCR)

RNA from gastrocnemius samples was extracted with RNeasy Fibrous Tissue Mini kit (Qiagen) following manufacturer's instructions. T 10 Ultra-Turrax (IKA) was used to homogenize muscles. For RNA extraction from myotubes, RNeasy Mini Kit (Qiagen) was used. RNA concentration was measured with a NanoDrop 1000 spectrophotometer (Thermo Fisher Scientific). From 200 ng to 1 µg RNA were retrotranscribed using High-Capacity cDNA Reverse Transcription Kit (Applied Biosystems) following manufacturer's instructions. The following program was used: 10 min at 25 °C, 2 h at 37 °C, 5 min at 85 °C. Samples were

diluted 1/5, and the expression of mRNA was examined by qRT-PCR using a 7900HT Fast Real-Time PCR System and FAST SYBR GREEN assays (Applied Biosystems). For that, 2 µl of diluted complementary DNA (cDNA) were added to 384-well MicroAmp Optical plates (Applied Biosystems), together with the following mix per well: 4 µl Fast SYBR Green Master Mix (Applied Biosystems), 0.16 µl each primer and 2 µl ribonuclease (RNase)-free water. An 8-point standard curve created by 5-fold serial dilution was included. The following PCR program in SDS 2.4 software was used: 1 cycle of 20 s at 95 °C and 40 cycles of 1 s at 95 °C plus 20 s at 60 °C. A dissociation curve was used after each reaction to verify primer specificity and purity of the PCR products. Relative mRNA expression was normalized to ribosomal protein S18 (*Rps18*), glyceraldehyde-3-phosphate dehydrogenase (*Gapdh*) or TATA-box-binding protein (*Tbp*) mRNA measured in each sample. The genes indicated in Table M5 were amplified using primers purchased from Sigma-Aldrich or Integrated DNA Technologies.

Gene	Forward primer (5'→3')	Reverse primer (5'→3')
Map2k3	GCCTCAGACCAAAGGAAAATCC	GGTGTGGGGTTGGACACAG
Map2k6	ATGTCTCAGTCGAAAGGCAAG	TTGGAGTCTAAATCCCGAGGC
Mapk12	ATGCGCTACACGCAGACA	TGGTCATTGCCTTTGAACAG
Ppargc1a	TATGGAGTGACATAGAGTGTGCT	CCACTTCAATCCACCCAGAAAG
Ppargc1a-a	GGGACATGTGCAGCCAAGA	AAGAGGCTGGTCCTCACCAA
Ppargc1a-b	GACATGGATGTTGGGATTGTCA	ACCAACCAGAGCAGCACATTT
Ppargc1a-c	TGAGTAACCGGAGGCATTCTCT	TGAGAACCGCTAGCAAGTTTG
Ppargc1b	GCTCTGACGCTCTGAAGGAC	AAGGGCTTGGGCAATCCTC
Gfp	CTTCTTCAAGTCCGCCATGC	AAGTCGATGCCCTTCAGCTC
Tbp	GAAGCTGCGGTACAATTCCAG	CCCCTTGTACCCTTCACCAAT
Rps18	CAGCTCCAAGCGTTCCTGG	GGCCTTCAATTACAGTCGTCTTC
Gapdh	TGAAGCAGGCATCTGAGGG	CGAAGGTGGAAGAGTGGGA
Tfam	CAAGTCAGCTGATGGGTATGG	TTTCCCTGAGCCGAATCATCC
Esrra	GCAGGGCAGTGGGAAGCTA	CCTCTTGAAGAAGGCTTTGCA
Il15	CATCCATCTCGTGCTACTTGTG	GCCTCTGTTTTAGGGAGACCT

Table M5. Primers used in qRT-PCR.

1.3.2. RNA-sequencing (RNA-seq) library preparation, sequencing and generation of FastQ files

Total RNA was isolated from gastrocnemius samples of mice fed a HFD for 6 weeks using the RNeasy Fibrous Tissue Mini Kit (Qiagen) as previously described (section 1.3.1). RNA quality was verified using Agilent 2100 Bioanalyzer, and individual samples with RNA Integrity Number (RIN) > 8 were included in the study. Samples were pooled from two individual samples to obtain 200 ng of total RNA (100 ng from each pooled sample) in 100 µl RNase-free water. RNA sequencing was performed in the CNIC Genomics Unit. Total RNA was used to generate barcoded RNA-seq libraries using the NEBNext Ultra II Directional RNA Library preparation kit (New England Biolabs) according to manufacturer's instructions. First, poly A+ RNA was purified using poly-T oligo-attached magnetic beads followed by fragmentation and first and second cDNA strand synthesis. Next, cDNA ends were repaired and adenylated. The NEBNext adaptor was then ligated followed by second strand removal, uracile excision from the adaptor and PCR amplification. The size of the libraries was checked using the Agilent 2100 Bioanalyzer, and the concentration was determined using the Qubit® fluorometer (Thermo Fisher Scientific). Libraries were sequenced on a HiSeq2500 (Illumina) to generate 60 bases single reads. FastQ files for each sample were obtained using CASAVA v1.8 software (Illumina).

RNA-seq data analysis was performed by the Bioinformatics Unit of CNIC. The number of reads per sample was between 25 and 30 million. After evaluating their quality with FastQC (Andrews, n.d.), reads were mapped against mouse transcriptome GRCm38.76, and gene expression levels were estimated with RNA-seq by Expectation Maximization (RSEM) (Li & Dewey, 2011). Parameter "strandedness reverse" was included to calculate expression from directional RNA-seq data. The percentage of aligned reads was between 91% and 94% for all samples. Expression count matrices were then processed with an analysis pipeline that used Bioconductor package limma (Ritchie et al., 2015) for normalization (using trimmed mean of M-values [TMM] method) and differential expression testing, taking into account only those genes expressed with at least one count per million in at least three samples (the number of samples available for each condition). Three pairwise contrasts were performed: $p38\alpha^{MCK\text{-}KO}$ vs. MCK-Cre, $p38\alpha/\gamma^{MCK\text{-}KO}$ vs. MCK-Cre, and $p38\alpha^{MCK\text{-}KO}$ vs. $p38\alpha/\gamma^{MCK\text{-}KO}$. Changes in gene expression were considered significant if associated to Benjamini and Hochberg adjusted *p*-value < 0.05.

Data were analyzed using IPA and gene set enrichment analysis (GSEA) (see section 1.6).

1.4. Histology

1.4.1. Histological analysis

Liver tissue samples were fixed in 10% formalin (Bio-Optica) for 48 h, dehydrated and embedded in paraffin. 8 µm sections were cut and stained with H&E (American Master Tech Scientific) following the next protocol: 3 changes of 100% xylol (Sigma), 5 min each; 2 changes of 100% ethanol (BDH Prolabo), 5 min each; 95%, 70% and 50% ethanol, 2 min each; distilled water, 2 min; hematoxylin (Harris), 40 s; rinse in tap water; Bluing solution (Thermo Scientific), 4 dips; quick rinse in water; 95% ethanol, 1 min; eosin (Thermo Scientific), 1 min; 2 changes of 95% ethanol, 1 min each; 2 changes of 100% ethanol, 1 min each; 3 changes of xylol, 1 min each.

For Oil Red staining, 8 µm sections were prepared from tissue frozen in OCT compound (Tissue-Tek) using a cryostat (Leica CM 1950). Sections were fixed in 10% formalin (Bio-Optica) during 10 min at 4 °C and rinsed with distilled water. Sections were embedded in propylene glycol (Sigma-Aldrich) for 5 min at RT, changed to new propylene glycol and left 5 additional min. Samples were stained with pre-warmed (60 °C) Oil Red O solution (7 mg/ml Oil Red O from Sigma-Aldrich in propylene glycol) for 10 min. 85% propylene glycol was added for 3 min, and samples were rinsed in distilled water and embedded in hematoxylin for 1 min, washed in water and introduced in Bluing solution. Sections were washed in tap water, rinsed in distilled water and mounted in aqueous mounting agent Aquatex (Merck).

All samples were examined in Leica DM2500 microscope at different magnifications and imaged using the software Leica Application Suite v4.3 (LAS v4.3).

1.4.2. Fiber-typing

Soleus muscle samples previously frozen in liquid nitrogen-cooled isopentane were cut into 8 µm thick cryosections with a cryostat (Leica CM 1950) on microscope slides (Superfrost Plus, Thermo Fisher Scientific) maintained at -20 ºC. Fiber-type analysis was determined by indirect immunofluorescence as described previously (Bloemberg & Quadrilatero, 2012), with some modifications. Briefly, slides were allowed to come to RT. Blocking solution (3% BSA + 10% normal goat serum [NGS] + 0.4% Triton X-100, in PBS) was applied for 1 h at RT, followed by two consecutive washes with PBS-Triton X-100 (0.1%) and one wash with PBS alone for 5 min each. Primary antibodies against myosin heavy chain (MHC)-I (BA-D5) and MHC-IIA (SC-71) were diluted in 1% BSA + 3.3% NGS + PBS-Triton X-100 (0.1%) (Table M6). These primary antibodies were purchased from the Developmental Studies Hybridoma Bank (University of Iowa). Muscle sections were incubated with these antibodies at 4 ºC overnight. Next morning,

three consecutive washes with PBS-Triton X-100 (0.1%) and one with PBS at RT for 5 min each were followed by sequential incubation with Alexa Fluor-conjugated goat-anti mouse immunoglobulin (Ig)G/IgM secondary antibodies (Invitrogen) at RT for 1 h in the dark. The list of secondary antibodies and the dilutions used are indicated in Table M6. Muscle sections were then washed three times with PBS-Triton X-100 (0.1%) and once with PBS at RT for 5 min each. Then, sections were incubated with Hoechst 33342 (Sigma) (1:5,000 in PBS) at RT in the dark for 30 min, and then washed three times with PBS, 5 min each. Slides were mounted in VECTASHIELD mounting medium (Palex) and visualized with a Leica TCS-SP5 confocal scanning laser unit attached to an inverted epifluorescence DMI6000B microscope fitted with an HCX PL APO lambda blue 63x/1.4-numerical-aperture oil immersion objective, using Las-AF acquisition software (Leica Microsystems). Images were analyzed with ImageJ software (NIH).

Primary antibody concentrations	MHC reactivity	Secondary antibody concentrations
BA-D5 (5 µg/ml)	I	Alexa Fluor 647 IgG_{2b} 1:100 (white)
SC-71 (1:600)	IIA	Alexa Fluor 488 IgG_1 1:500 (green)

Table M6. List of antibodies used for MHC staining of mouse skeletal muscle.

1.4.3. Transmission electron microscopy

Transmission electron microscopy analysis was performed at the Electron Microscopy Unit of the Spanish National Center for Biotechnology (CNB-CSIC). Gastrocnemius muscle samples were harvested from mice fed a HFD for 21 weeks. Tissue fragments (1-2 mm^3) were fixed in 2.5% glutaraldehyde/4% paraformaldehyde in PBS for 4 h at RT, with one change of fresh fixative, followed by overnight incubation at 4 °C. After PBS washes, samples were postfixed for 1 h at 4 °C in a solution with 1% osmium tetroxide and 0.8% potassium ferrocyanide. Samples were rinsed in distilled H_2O and treated with 2% uranyl acetate for 1 h at 4 °C. Following distilled H_2O washes, tissues were dehydrated through a graded acetone series (30-100%) at 4 °C, embedded in epoxy resin (Epon 812, Sigma) and polymerized at 60 °C for 48 h. Ultra-thin sections (70 nm) were obtained by Leica EM UC6 ultramicrotome, mounted on formvar/carbon coated grids and stained with uranyl acetate and lead citrate following conventional protocols. Samples were examined on a JEOL JEM 1011 (100 kV) transmission electron microscope and imaged with a ES1000W Erlangshen CCD digital camera (Gatan). ImageJ (NIH) (1.8v) was used for image analysis. Mitochondria (10 images per animal) were traced manually in electron micrographs, and the area of a total of 100 intermiofibrillar

mitochondria per mouse was quantified. The number of lipid droplets (≥ 9 images per animal) was quantified in at least nine random and separated view fields per muscle. The investigator was blinded to the group allocation when assessing the outcome.

1.5. Cell culture experiments

1.5.1. Kinase assay

HEK-293T cells were plated at 50% confluence in DMEM (Gibco) supplemented with 10% FBS (Sigma), 200 mM L-glutamine (Lonza), and 10,000 U/ml penicillin/streptomycin (1:1, Lonza), 8 h before transfection. Cells were transfected using the calcium phosphate precipitation method (Rodriguez & Flemington, 1999) with the next cDNA expression plasmids: pcDNA-f:PGC1 (plasmid #1026, Addgene); and pBABE-p38α$^{D176A/F327S}$, pBABE-p38β^{D176A}, pCEFL-Flag-p38γ^{D179A}, pCMV-HA-Flag-p38δ^{F324S} and pCEFL-empty vector (Diskin et al., 2004), which were kindly provided by Dr. David Engelberg (The Hebrew University of Jerusalem, Israel). The culture medium was replaced 14 h after transfection with fresh complete medium, and cells were harvested 48 h later. Cellular extracts were prepared as described in section 1.2.3.

1.5.2. Adenovirus production

For adenovirus production, the cDNA of *Ppargc1a* (GenBank: NM_008904.2) cloned from a brown fat cDNA library was used (Dumesic et al., 2019). pcDNA3-HA-p38α$^{D176A/F327S}$ and pCEFL-Flag-p38γ^{D179A} plasmids (Diskin et al., 2004) were kindly provided by Dr. David Engelberg (The Hebrew University of Jerusalem, Israel), and green gluorescent protein (GFP) was used as a control. GFP, PGC1α, p38α and p38γ adenoviral expression systems were created with Gateway® Technology (Invitrogen). First, the full-length cDNAs, amplified by PCR, were cloned into the pDONR221 vector (donor vector), using BP clonase (Invitrogen), following manufacturer's instructions. After purification of the plasmids from transformed DH5α competent cells (Invitrogen), cDNA inserts (entry clone) were transferred into the pAd/CMV/V5-DEST vector (destination vector) by means of the ViraPower™ Adenoviral Expression System using LR clonase (Invitrogen), following manufacturer's instructions. The recombination product was transformed in DH5α cells to confirm the presence of the expression clone. Once purified, the newly constructed pAd/CMV/V5-DEST vector (expression clone) was linearized by digestion with *Pac* I (New England Biolabs), purified and transfected into 90-95% confluent 293A cells with Lipofectamine® 2000 (Invitrogen). For this, 1 µg expression plasmid and lipofectamine were incubated for 20 min at RT and added to 293A cells for incubation at 37 °C overnight in culture medium composed by DMEM (Corning) and

10% FBS (BenchMarkTM, Gemini Bio-Products). The next day, medium was replaced to fresh medium supplemented with 2x penicillin/streptomycin (Corning), which was changed every 2-3 days. After 1-2 weeks of culture, when an approximately 80% cytopathic effect was observed, the culture medium and cells were harvested together, frozen-thawed three times (-80 °C for 30 min, 37 °C for 15 min), and centrifuged at 1,000 x *g* during 15 min to obtain adenovirus-enriched supernatants. Aliquots of the supernatants were added to fresh 293A cells, and the culture was grown for 48 h to amplify adenoviruses. Same freeze-thaw cycles and centrifugation were repeated with these adenoviral amplification stocks. Viral titers were determined using the Adeno-X Rapid Titer Kit (Clontech) in 293A cells, following manufacturer's instructions.

1.5.3. Isolation, growth and differentiation of mouse primary myoblasts

Skeletal muscles were obtained from lower limbs (gastrocnemius, quadriceps, tibialis anterior and soleus) of 2-4-week-old C57BL6 mice, and isolation and growth of mouse primary myoblasts were done as previously reported (Springer et al., 2002), with some modifications. Digestion was performed at 37 °C during 20 min using 2 ml of freshly prepared digestion solution (1.5 U/ml collagenase D [Boehringer Mannheim Corp.], 2.4 U/ml dispase II [Boehringer Mannheim Corp.] and 2.5 mM $CaCl_2$) per gram of tissue. The slurry was filtered through an 80-µm filter and centrifuged at 350 x *g* during 5 min. Pellet was resuspended in 2-4 ml of F-10-based primary myoblast growth medium (Ham's F-10 [Gibco], supplemented with 20% FBS [BenchMarkTM, Gemini Bio-Products], 2.5 ng/ml basic fibroblast growth factor [bFGF, Gibco] and 2x penicillin/streptomycin [Corning]). Cells were cultured in collagen-coated plates (BioCoat) at 37 °C and 5% CO_2, and medium was changed every other day. Splitting was performed by rinsing twice with PBS (Corning) and hitting firmly the plate to dislodge the myoblasts and leave the fibroblasts on the plate. This process was repeated until fibroblasts were no longer visible in the culture, when the medium was changed to F-10/DMEM-based primary myoblast growth medium (Ham's F-10/DMEM [Corning] 1:1 supplemented with 20% FBS, 2.5 ng/ml bFGF and 2x penicillin/streptomycin). Myoblasts were induced to differentiate by cultivating in differentiation medium (fusion medium) (DMEM, 5% horse serum [HS, GemCell; Gemini Bio-Products], 2x penicillin/streptomycin and 1 mM sodium pyruvate [Corning]). The composition of the different cell culture media used is indicated in Table M7.

Solution	Ham's F-10	DMEM	FBS	HS	bFGF	Sodium pyruvate	P/S
F-10-based primary myoblast growth medium	✓	-	20%	-	2.5 ng/ml	-	2x
F-10/DMEM-based primary myoblast growth medium	✓ (1:1 with DMEM)	✓ (1:1 with DMEM)	20%	-	2.5 ng/ml	-	2x
Fusion medium	-	✓	-	5%	-	1 mM	2x

Table M7. Composition of different cell culture media used for myoblasts and myotubes. DMEM, Dulbecco's Modified Eagle Medium; FBS, fetal bovine serum; HS, horse serum; bFGF, basic fibroblast growth factor; P/S, penicillin/streptomycin. ✓, included in the medium; -, not included in the medium.

1.5.4. Adenovirus transduction *in vitro*

Mouse primary myoblasts were seeded in 6-well plates (5 x 10^5 cells/well) or 10 cm plates (3.6 x 10^6 cells), and differentiation to myotubes was initiated 24 h later by changing to fusion medium. 24 h after differentiation, myotubes were transduced with GFP, PGC1α, p38α or p38γ adenoviruses at multiplicities of infection (MOIs) of 50 viral particles per cell. 24 h after transduction, the virus-containing medium was replaced by new fusion medium. 24 and 48 h postransduction, cell transduction was assessed by calculating the percentage of GFP-positive cells under a fluorescence microscope. Cells were collected 48 h after transduction, 9-10 h after serum deprivation with a medium composed by DMEM (without phenol red for proteomics experiments) supplemented with 1 mM sodium pyruvate, 584 mg/l L-glutamine and 2x penicillin/streptomycin. The expression of p38α and p38γ recombinant proteins was assayed by Western blot analysis and by MS, together with PGC1α expression. GFP reporter gene expression was assessed by qRT-PCR.

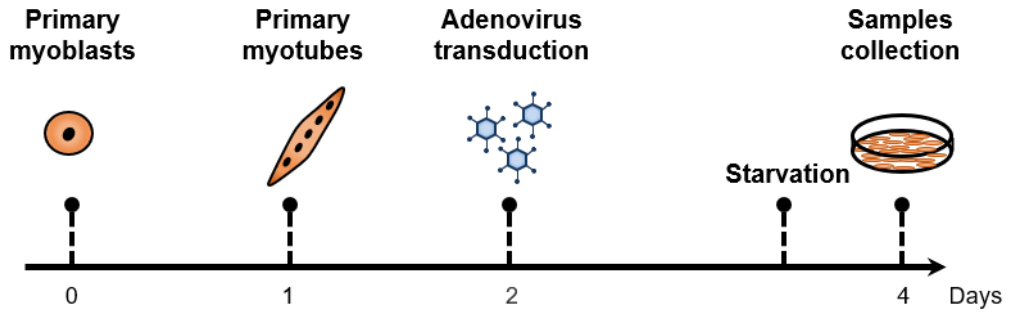

Figure M3. Adenoviral infection procedure of mouse-derived myotubes. Differentiation of myoblasts was initiated 24 h after seeding cells and consisted of a change from F-10/DMEM-based

primary myoblast growth medium to fusion medium. Transduction with adenoviruses was performed 24 h after initiation of differentiation, and cells were harvested 48 h after adenoviral transduction, following 9-10 h of serum starvation.

1.5.5. Cell proteome analysis

After washing the plates with PBS, myotubes were harvested using lysis buffer composed of 50 mM 4-(2-hydroxyethyl)-1-piperazineethanesulfonic acid (HEPES) pH 8.5, 150 mM NaCl, 5 mM dithiothreitol (DTT), 2% SDS, phosphatase inhibitors (PhosStop *EASY*pack, Roche) and EDTA-free protease inhibitor cocktail (Roche). Cells were homogenized and placed at 60 °C for 30 min. Reduced lysates were incubated with iodoacetamide (14 mM) in the dark for 45 min. Alkylation was quenched by addition of DTT to a final concentration of 5 mM in the dark for 15 min. Protein purification was performed by methanol-chloroform precipitation (Methanol/Chloroform/H_2O, 3:1:2.5). First, samples were centrifuged at 4,000 x *g* for 10 min at RT after adding Methanol/Chloroform/H_2O (3:1:2.5). Then, methanol phase was removed, and three consecutive washes with cold methanol were performed. Samples were further lysed with a mechanical homogenizer after adding 8 M urea, 50 mM HEPES pH 8.5. Lysates were centrifuged at 4,000 x *g* for 5 min, and protein content in the supernatant was measured using a BCA assay (Thermo Scientific). 225 µg protein were digested with endoproteinase lysine-C (Lys-C) (Wako, Japan) in a 1:100 enzyme/protein ratio in 4 M urea and digestion buffer (10 mM HEPES, pH 8.5 and 1 mM $CaCl_2$) in rotation at 37 °C for 2 h. Further digestion was performed with new Lys-C (1:100) and with trypsin (ThermoFisher Scientific) in a 1:100 enzyme/protein ratio, in 2 M urea and digestion buffer in rotation at 37 °C overnight. Samples were diluted to 1 M urea and further digested with trypsin (1:100) at 37 °C for 6 h. Digests were acidified with 25% acetic acid to a pH of ~2.0 and subjected to C18 solid-phase extraction (10 mg SPE) (Sep-Pak, Waters). Samples were resuspended in 200 mM 4-(2-hydroxyethyl)-1-piperazinepropanesulfonic acid (EPPS) pH 8.0, and micro-BCA was performed. Then, isobaric labeling of the peptides was performed using 11-plex TMT reagents (Thermo Fisher Scientific). Reagents were dissolved in 256 µl acetonitrile (ACN), and 1/16 of the solution was added to 70 µg of peptides dissolved in 100 µl of 200 mM EPPS pH 8.0. After 1 h at RT, the reaction was quenched by adding 8 µl of 5% hydroxylamine. 15 min later, labeled peptides were combined and acidified with formic acid (FA) prior to C18 SPE on Sep-Pak cartridges (50 mg).

TMT labeled peptides were solubilized in 600 µl solution containing 5% ACN/10 mM ammonium bicarbonate pH 8.0, and 300 µl of TMT labeled peptides were separated by an Agilent 300 Extend C18 column (3.5 µm particles, 4.6 mm I.D. and 250 mm in length). An Agilent 1260 binary pump coupled with a photodiode array (PDA) detector (Thermo Scientific)

was used to separate the peptides. A 45 min linear gradient from 10% to 40% ACN in 10 mM ammonium bicarbonate pH 8.0 (flow rate of 0.6 ml/min) separated the peptide mixtures into a total of 96 fractions (36 s). A total of 96 fractions were consolidated into 24 samples in a checkerboard fashion, acidified with 25 µl of 20% FA and vacuum dried. Samples were then resuspended in 100 µl 0.5% FA/3% ACN. Each sample was desalted via StageTips and re-dissolved in 12 µl 5% FA/5% ACN, prior to LC-MS/MS analysis. Labeled peptides were subjected to LC-MS/MS analysis using an Orbitrap Fusion Lumos mass spectrometer (Thermo Fisher Scientific) coupled with a Proxeon EASY-nLC 1200 LC pump (Thermo Fisher Scientific). LC-MS/MS and peptide quantification were performed as previously described (Dumesic et al., 2019) (Figure M4).

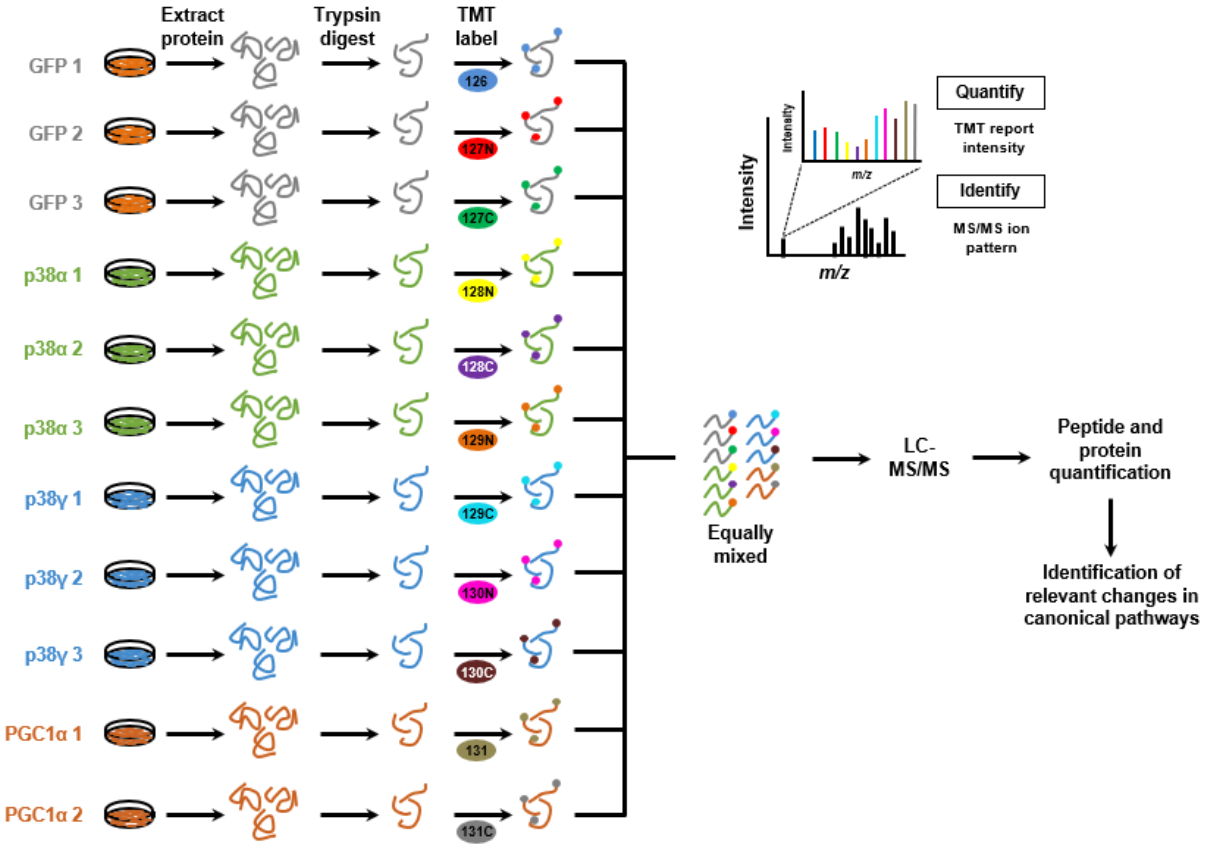

Figure M4. Isobaric TMT quantitative analysis in myotubes. Cells transduced with the indicated adenoviruses were harvested, proteins were digested, and 11-plex peptide isobaric labeling was performed. Peptides were subjected to LC-MS/MS, quantified, and GSEA was performed.

1.6. Bioinformatics and statistics

1.6.1. Gene set enrichment analysis (GSEA)

Fold change (FC) values were used to generate pre-ranked protein or gene lists for gene set enrichment analysis (Subramanian et al., 2005). GSEA was done using GSEA software version 4.0.1, which uses predefined gene sets from the Molecular Signatures Database

(MSigDB v7.2) (Liberzon et al., 2015). For unbiased discovery of enriched gene sets in RNA-seq and *in vitro* proteomics studies, we used the HALLMARK gene sets as queries and a list of ranked proteins or genes based on a score calculated as log2 fold changes for each protein or gene (log2FC) for every comparison. The minimum and maximum criteria for selection of gene sets from the collection were 15 and 500 genes, respectively. "Classic" mode was used for enrichment statistic calculation. The same conditions were used for GSEA of proteomics from *in vivo* data; however, due to the logarithmic nature and values of Zq, difference between Zq means instead of ratio was used for every comparison.

In a separate query, muscle gene expression data from RNA-seq were examined using a custom gene set: "PGC1α muscle gene set". This gene set contains all genes upregulated > 2-fold in the gastrocnemius muscle of MCK-PGC1α transgenic mice (Lin et al., 2002) (Appendix I, Table S1). Muscle gene expression was also examined using a custom protein set: "PGC1α myotubes". This protein set was generated with data from the experiments with adenovirus-infected myotubes and corresponds to all proteins upregulated > 1.4-fold in myotubes overexpressing PGC1α (Appendix I, Table S2).

All GSEA graphs were replotted using replot GSEA package in R.

1.6.2. Ingenuity Pathway Analysis (IPA)

The list of differentially expressed genes or proteins in RNA-seq or proteomics analyses of skeletal muscles, containing gene or protein identifiers and corresponding expression values, was uploaded into the IPA software (Qiagen) to discover overrepresented gene lists derived from Ingenuity's proprietary knowledge-base (IPAKB). Enrichments associated to a p-value < 0.05 were considered statistically significant and included. Each gene or protein identifier was mapped to its corresponding gene object in the Ingenuity Pathway Knowledge Base. The "core analysis" function included in the software was used to interpret the differentially expressed data, which included biological processes, canonical pathways, upstream transcriptional regulators, and gene networks. Importantly, IPA issues predictions on the activation state of pathways or regulators in the form of a parameter called z-score; activation or inhibition is indicated by positive or negative values, respectively.

1.6.3. Identification of secreted proteins

All potential p38γ-induced genes as judged from gene expression analysis in the comparison of muscles from p38α^{MCK-KO} or p38α/γ^{MCK-KO} mice with MCK-Cre controls with a p-value < 0.05 were filtered for those encoding for secreted proteins by using the SignalP, SecretomeP and

TargetP software (http://www.cbs.dtu.dk/services/) as described (Emanuelsson et al., 2007). Heatmap representation was created using Heatmapper tool.

1.6.4. Statistical analysis

Values are presented as means ± standard error of the mean (SEM). Differences between groups were examined for statistical significance using two-tailed unpaired Student's *t*-test (with Welch's correction when variances were different), one- or two-way analysis of variance (ANOVA) coupled to Bonferroni's post-test, Kruskal-Wallis test, or Mann-Whitney test. Statistical significance was determined as a two-sided p-value < 0.05 (GraphPad Prism 8.0). Family-wise error rate (FWER) p-values are displayed for GSEA to correct for multiple hypothesis testing. Statistical details and experimental n are specified in figure legends.

2. Adipose tissue JNK1 and adiponectin in gender predisposition to hepatocellular carcinoma

2.1. Human samples

2.1.1. Study population and sample collection

For the analysis of human levels of blood adiponectin, individuals were recruited among patients who underwent laparoscopic cholecystectomy for gallstone disease. Data were collected on demographic information (age and sex), anthropometric measurements (BMI), and coexisting medical conditions. Fasting blood samples were collected for adiponectin, glucose, total bilirubin, albumin, aspartate aminotransferase (AST), alanine aminotransferase (ALT), alkaline phosphatase and lipid analysis. Blood was extracted using straight needles (21G butterfly) and Vacuette Z Serum Sep Clot Activator tubes. After 30 min, these tubes were centrifuged at 1,500 rpm for 10 min at RT to separate serum, which was divided into aliquots and stored at -80 °C until further analysis. The study was approved by the Ethics Committee of the University Hospital of Salamanca, and all subjects provided written informed consent to participate. Patients were excluded if they had a history of alcohol use disorders or excessive alcohol consumption (> 30 g/day in men and > 20 g/day in women), or chronic hepatitis C or B (Table M8).

Variable	Women (*n* = 9)	Men (*n* = 10)	*p*-value
Age (years)	49.7 (14.3)	58.1 (14.3)	0.278
Hypertension (n)	1 (11.1)	2 (20)	0.542
Diabetes mellitus (n)	0	0	-
BMI (kg/m^2)	25.8 (3.5)	26.8 (4.5)	0.905
Fasting blood sugar (mg/dl)	86.1 (12.8)	99 (10.5)	0.046
AST (IU/l)	24.3 (12.9)	21.1 (5.1)	0.798
ALT (IU/l)	32.5 (32.2)	30.3 (20.7)	0.878
Alkaline phosphatase (IU/l)	77.4 (21.4)	95.3 (35.3)	0.536
Bilirubin (mg/dl)	0.5 (0.3)	0.9 (0.5)	0.059
Albumin (mg/dl)	4.5 (0.3)	4.5 (0.6)	0.607
Total cholesterol (mg/dl)	205.9 (50)	189.9 (47.9)	0.383
Triglycerides (mg/dl)	118.7 (67.5)	116 (49.7)	0.902
LDL-cholesterol (mg/dl)	121.7 (44.5)	123.7 (43.7)	0.945
HDL-cholesterol (mg/dl)	62.1 (14.6)	42.9 (12.7)	0.035
Adiponectin (µg/ml)	19.69 (2.663)	14.18 (3.620)	0.0016

Table M8. Characteristics of women and men. Variables are presented as mean (standard deviation) or absolute frequency (%) and are compared by means of Mann-Whitney U test or χ^2 test. ALT, alanine aminotransferase; AST, aspartate aminotransferase; IU, international units; BMI, body mass index; HDL, high-density lipoprotein; LDL, low-density lipoprotein.

2.2. Animal and cell culture experiments

2.2.1. Animals

C57BL/6J mice (Jackson Laboratory) were used as wild-type (WT) male and female mice. Sprague-Dawley rats from Universidad de Santiago de Compostela were used as WT male and female rats. Adiponectin knockout mice (B6;129-Adipoq^{tm1Chan}/J; Adipoq$^{-/-}$ in the text) and Fabp4 cre mice (B6.Cg-Tg(Fabp4-cre)1Rev/J) were purchased from the Jackson Laboratory and backcrossed to the C57BL/6 background for 10 generations. Mice with specific deletion of JNK1 in adipocytes (JNK1$^{Fabp\text{-}KO}$) were generated as described (Sabio et al., 2008). Briefly, mice with exon 7 of *Jnk1* gene flanked by loxP sequences (JNK1$^{f/f}$) were generated in Dr. Roger J. Davis' laboratory (JNK1$^{f/f}$) and crossed with mice expressing the Cre recombinase under the control of the adipose tissue-specific Fabp4 promoter (Fabp4-Cre+). To get a better depletion of the *Jnk1* gene, these mice were crossed with whole-body knockout *Jnk1* mice (Jackson Laboratories; B6.129S1-*Mapk8*^{tm1Flv}/J, here called Jnk1$^{-/-}$), obtaining Fabp4-Cre^{+}Jnk1$^{f/-}$ mice (JNK1$^{Fabp\text{-}KO}$). Littermates without conditional *Jnk1* allele (Fabp4-Cre^{+}Jnk1$^{+/-}$) were used as controls (Fabp-Cre) (Figures M5A, B). Adiponectin knockout mice (Adipoq$^{-/-}$) were crossed with Fabp4-Cre^{+}Jnk1$^{f/f}$ and Jnk1$^{-/-}$ to generate JNK1$^{Fabp\text{-}KO}$ Adipoq$^{-/-}$ and Fabp-Cre Adipoq$^{-/-}$ models (Figure M5C). Mice were housed randomly in a pathogen-free animal facility and maintained on a 12-h light/dark cycle at constant temperature and humidity. Rodents were fed a ND (D183, SAFE, for mice; A04, SAFE, for rats) *ad libitum*. Genotypes were identified by PCR analysis of genomic DNA isolated from mouse tails. All animal procedures conformed to European Union Directive 2010/63/EU and Recommendation 2007/526/EC regarding the protection of animals used for experimental and other scientific purposes, enforced in Spanish law under Real Decreto 53/2013. All experiments were approved by CNIC Animal Care and Use Committee or from Universidad de Santiago de Compostela and Comunidad de Madrid.

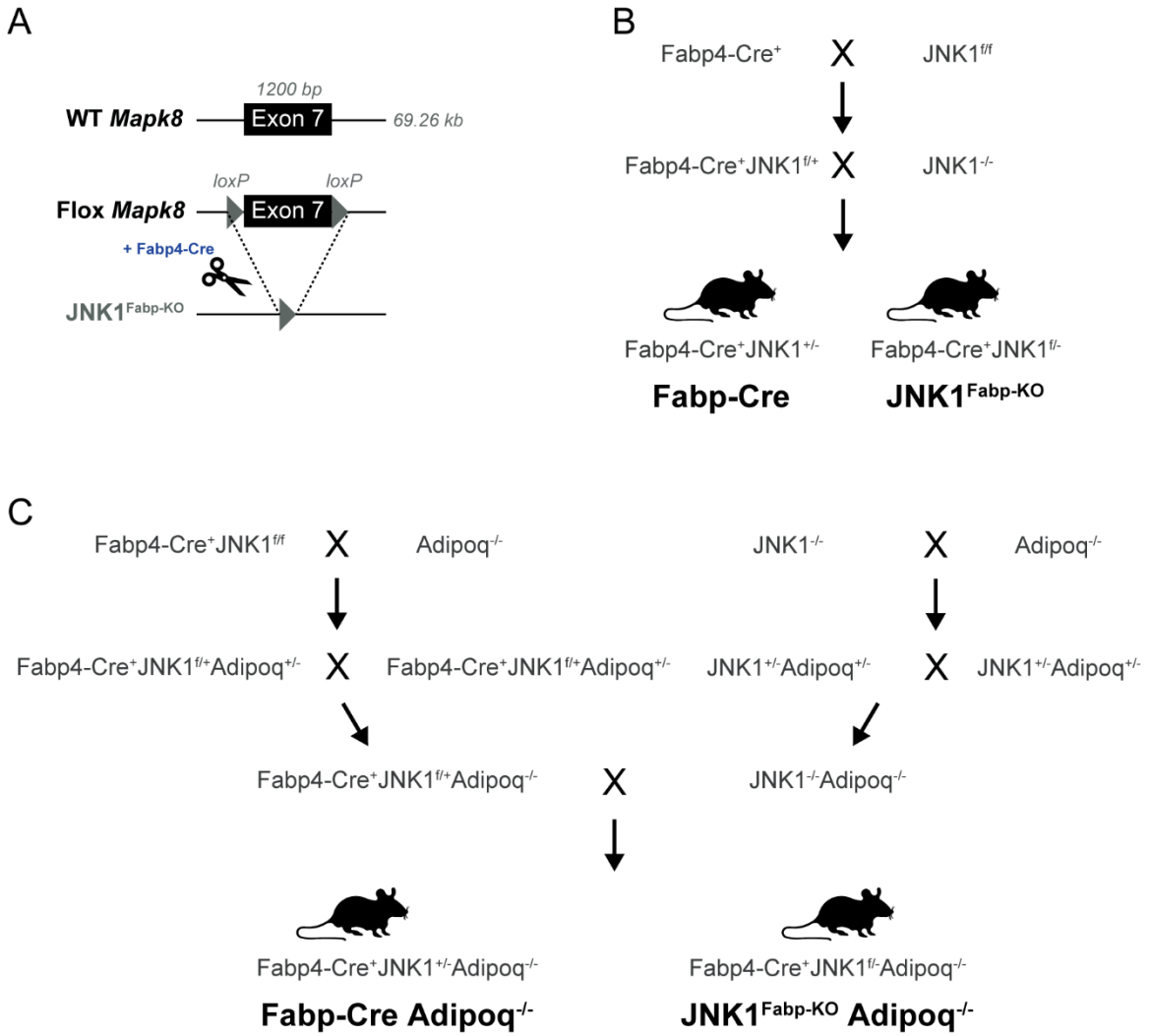

Figure M5. Generation of knockout mice. (A) Schematic depicting *Mapk8* and floxed (f) *Mapk8* alleles. Exon 7 of *Mapk8* is flanked by loxP sites and it is excised upon Cre-lox recombination using Cre recombinase under the fatty acid-binding protein 4 (Fabp4) promoter. (B) Schematic representation of mouse lines crossing to generate Fabp-Cre and JNK1$^{Fabp\text{-}KO}$ mice. Control mice are Fabp4-Cre^{+}JNK1$^{+/-}$ (Fabp-Cre), while adipose tissue-specific JNK1 knockout mice are Fabp4-Cre^{+}JNK1$^{f/-}$ (JNK1$^{Fabp\text{-}KO}$). (C) Schematic representation of mouse lines crossing to generate Fabp-Cre Adipoq$^{-/-}$ and JNK1$^{Fabp\text{-}KO}$ Adipoq$^{-/-}$ mice. Adiponectin knockout control mice are Fabp4-Cre^{+}JNK1$^{+/-}$Adipoq$^{-/-}$ (Fabp-Cre Adipoq$^{-/-}$), while whole-body knockouts for adiponectin and adipose tissue specific for JNK1 are Fabp4-Cre^{+}JNK1$^{f/-}$ Adipoq$^{-/-}$ (JNK1$^{Fabp\text{-}KO}$ Adipoq$^{-/-}$).

2.2.2. HCC induction, castration and testosterone administration

For tumor studies, mice at postnatal day (P) 14 received one i.p. injection of diethylnitrosamine (DEN) (Sigma-Aldrich) at 50 mg/kg body weight dissolved in saline. After 8 months, tumors were extracted, counted and measured with a caliper (Mitutoyo 7301). For specific cell signaling experiments, mice were sacrificed 15 days or 1 month after DEN injection. In all cases, mice were euthanized after overnight starvation.

For healthy and tumor hepatocytes analysis, C57BL/6J mice were injected with a single dose of DEN at P14, followed by administration of thioacetamide (TAA; 300 µg/l) in the drinking water during 26 weeks, as described (Salguero Palacios et al., 2008). Control mice received a single injection of PBS at P14 and normal drinking water. The parenchymal and the non-parenchymal compartments were isolated from vehicle (healthy) or DEN/TAA (tumor) mice.

For testosterone deprivation studies, castration or sham operations were performed in mice at 4-5 weeks of age, as previously described (Nishizawa et al., 2002). 23 days after castration, testosterone propionate (Desma) diluted in corn oil (5 µg/g body weight) (Sigma) or vehicle alone was subcutaneously injected in castrated or sham-operated mice, every other day for 3 weeks. Blood samples were collected 2 weeks after the first injection, and testosterone propionate (50 µg/g body weight) was injected into some castrated mice 30 min before sacrifice, at the end of the experiment.

2.2.3. Adeno-associated virus (AAVs) production and infection of mice

Male mice were injected intravenously at P1 with 0.5 x 10^{11} viral particles of a serotype 8 adeno-associated virus (AAV) overexpressing adiponectin under the control of the adipocyte-specific adipocyte Protein 2 (aP2) mini promoter (vector tailor-designed and purchased from Vector Builder) or carrying an empty control vector. These AAVs were produced by the Viral Vector Unit at CNIC as described (González-Terán et al., 2016a).

2.2.4. Retrovirus production

Retroviruses expressing p38α$^{D176A/F327S}$ were produced in HEK-293 Phoenix-ECO cell line, which is stably transfected to express Moloney murine leukemia virus (MMLV) viral packaging proteins. Transient calcium phosphate co-transfection of these cells was done with 20 µg of pBABE.p38α$^{D176A/F327S}$ (kindly provided by Dr. Ángel Nebreda) or pBABE.Empty vector, together with 2.5 µg of packaging virus DNA, as previously described (Rodriguez & Flemington, 1999). The supernatants containing the retrovirus particles were collected 48 and 72 h after removal of the calcium phosphate precipitate and filtered through 0.45-µm filters. Viruses were concentrated by ultracentrifugation at 49,000 x *g* for 90 min at 4 °C (Ultra-Clear Tubes, SW28 rotor and Optima L-100 XP Ultracentrifuge; Beckman Coulter). Viruses were resuspended in cold sterile PBS.

2.2.5. Tumor cells culture

The Hep53.4 cell line was purchased from CLS-Cell Lines Service GmbH and tested against *Mycoplasma* (MycoAlert Detection Kit; Lonza). Cells were cultured in DMEM (Gibco) supplemented with 10% FBS (Sigma), 200 mM L-glutamine (Lonza), and 10,000 U/ml penicillin/streptomycin (1:1, Lonza). The MC-38 and B16-F10 cell lines were kindly provided by Dr. David Sancho and were originally tested against *Mycoplasma*. MC-38 cells were cultured in DMEM supplemented with 10% FBS, non-essential amino acids, sodium pyruvate, HEPES pH 7.5, 200 mM L-glutamine, and 10,000 U/ml penicillin/streptomycin, whereas B16-F10's culture medium only contained DMEM supplemented with 10% FBS, sodium pyruvate, and antibiotics.

2.2.6. Lentivirus vector production and cell infection

Lentiviruses were produced as described (Urso et al., 2011). HEK-293T cells were plated at 25-35% confluence in DMEM (Gibco) supplemented with 10% FBS (Sigma), 200 mM L-glutamine (Lonza), and 10,000 U/ml penicillin/streptomycin (1:1, Lonza). Transient calcium phosphate co-transfection of HEK-293T cells was carried out with the pGIPZ empty vector shRNAs against AdipoR1 (pGIPZ.shAdipoR1, V2LMM_84583), AdipoR2 (pGIPZ.shAdipoR2, V2LMM_95355) or AMPK (pGIPZ.shAMPK, V2LMM_70372) from Dharmacon, together with pΔ8.9 and pVSV-G packaging plasmids. The supernatants containing the lentiviral particles were collected 48 and 72 h after removal of the calcium phosphate precipitate and were centrifuged at 600 x *g* for 5 min at 4 °C and filtered through 0.45-µm filters (Corning). Once filtered, the virus-containing medium was added to Hep53.4 culture medium (1:1 volume) with 8 µg/ml polybrene (Sigma). After incubation at 37 °C and 5% CO_2 for 24 h, the medium was changed, and puromycin selection (2 µg/ml puromycin dihydrochloride, Sigma) was initiated 48 h after infection. The selection medium was changed every 2 days for 1 week, and the cells were subsequently used for experiments.

2.2.7. Allografts

For allograft assays, Hep53.4 cells (5 x 10^4 cells for usual experiments, or 1 x 10^6 for shRNA experiments) were mixed 1:1 with Matrigel Matrix (Corning) and subcutaneously injected into each flank of anesthetized 8-14-week-old mice. For MC-38 or B16-F10 allograft assays, 5 x 10^5 cells without Matrigel were subcutaneously injected into each flank. In both cases, tumor growth was monitored by measuring length and width every 3-4 days with a digital caliper (Ratio) for a period of 2, 3, or 5 weeks. At the end of the experiment, mice were sacrificed,

tumors extracted, and length, width and thickness were measured to determine tumor volume. Allograft samples were frozen in liquid nitrogen.

To study AMPKα activation by metformin, mice were treated with metformin (Merck) dissolved in drinking water (300 mg/day/kg body weight), starting 1 week before allograft injection, and changing water every day. In allografts treated with active p38α, pBABE.p38α$^{D176A/F327S}$ retrovirus or control virus was injected intratumorally on days 9 and 22.

2.2.8. Blood and organs collection

At sacrifice or specific time points, blood samples were obtained from the submandibular vein of mice and collected in EDTA blood collection tubes (Microvette). Plasma was obtained after centrifugation at 9,600 x *g* for 20 min at 4 °C. Trunk blood from rats was collected in EDTA blood collection tubes (BD Vacutainer) and centrifuged at 2,500 x *g* for 15 min at 4 °C. For other tissue collection, animals were euthanized by cervical dislocation, and organs were removed and frozen in liquid nitrogen. For histological examination, liver samples were collected in 10% formalin (Bio-Optica) to perform H&E staining.

2.2.9. Adipocytes cell culture

Immortalized white preadipocytes from C57BL/6 male mice were maintained in DMEM-F12 medium (Gibco) with 8% FBS (Sigma), 200 mM L-glutamine (Lonza), and 10,000 U/ml penicillin/streptomycin (1:1, Lonza). These cells were differentiated to white adipocytes for 10 days with the previous medium supplemented with 5 µg/ml insulin (Sigma), 25 µg/ml 3-isobutyl-1-methylxanthine (IBMX, Sigma), 1 µg/ml dexamethasone (Sigma), and 1 µM troglitazone (Tocris). All mentioned compounds were added for the first day of differentiation, and medium was changed every other day, but omitting IBMX and dexamethasone in the first change, and only including insulin supplementation in the following changes. After adipocytes were differentiated, they were starved overnight (5% FBS) and treated with 300 nM testosterone (Sigma) or vehicle for 2 h (Figure M6).

Human visceral white preadipocytes were purchased from Innoprot, and culture was set up following the manufacturer's instructions. Preadipocytes were cultured in poly-L-lysine-coated plates (Sigma) with supplier's preadipocyte medium. Preadipocytes differentiation medium (PADM) from Innoprot was used for the differentiation to white adipocytes during 8 days, followed by an overnight starvation and treatment with 1.2 µM testosterone or vehicle for 30 min.

Figure M6. Mouse-derived preadipocytes differentiation procedure. Differentiation of preadipocytes consists of medium changes that start with IBMX, dexamethasone, troglitazone and insulin for 48 h, followed by a medium change with insulin and troglitazone for 48 h, and subsequent changes of medium with insulin every 48 h. Differentiated adipocytes were starved overnight and treated with testosterone or vehicle. A similar procedure was done with human preadipocytes, but PADM from Innoprot was used for their differentiation.

2.2.10. Liver cell populations isolation

To isolate the different hepatic cell types, a perfusion was performed in a C57BL/6 mouse. The liver was perfused with each solution (A, B, and C; Table M9.1) separately for 5 min or 25 ml. After the final solution C, the perfusion was stopped, and the liver was dissected and transferred into solution D and incubated for 20 min at 37 °C. To ensure proper digestion of the liver, solution D was inverted several times during the incubation time. Next, solution D containing the digested liver was filtered through a 70-µm cell strainer, and the filtered solution was centrifuged at 50 x *g* for 1 min at 4 °C. The pellet containing hepatocytes was kept for further analysis, and the supernatant was transferred to a new conical tube and subsequently centrifuged at 720 x *g* for 8 min at 4 °C. The supernatant was removed, and the pellet was resuspended in 10 ml Gey's Balanced Salt Solution buffer (GBSS-B) solution containing 150 µl deoxyribonuclease (DNase) I stock solution, and the conical tube was filled up to 50 ml with GBSS-B solution. In the next step, the solution was centrifuged at 720 x *g* for 8 min at 4 °C, and the supernatant was removed. Next, the pellet was resuspended in 10 ml GBSS-B containing 150 µl DNase I stock solution. In addition, 24 ml GBSS-B and 14 ml of Nycodenz 1 solution were added, and the solution was carefully mixed. Then, 4 ml of Nycodenz 2 solution was transferred into six 15-ml Falcon tubes. Next, 8.3 ml of the mixed cell solution containing GBSS-B, DNase, and Nycodenz 1 was carefully laid onto Nycodenz 2 solution, and the GBSS-B solution was used to gently overlay the cell suspension to obtain a final volume of 15 ml. Consequently, the gradient solution was centrifuged without brakes at 3,000 x *g* for 20 min at 4 °C. After the centrifugation step, HSCs are found in the upper gradient phase as a white ring, and KCs are found in the lower gradient phase. Each cell type was carefully transferred to a new tube and washed with GBSS-B solution and subsequently centrifuged at 720 x *g* for 8 min at 4 °C to pellet the cells. The supernatant was removed, and the cells were

checked for their purity under a microscope and subsequently frozen in liquid nitrogen and stored at -80 °C for further RNA isolation. Tables M9.1 and M9.2 indicate the solutions used for the isolation of different hepatic cell types.

Solution (ml)	A	B	C	D
SC-1	100	-	-	-
SC-2	-	100	100	100
DNase I (2 mg/ml in GBSS-B)	-	-	-	1
Collagenase D (mg)	-	-	110	80
Pronase E (mg)	-	40	-	50

Table M9.1. Solutions for hepatic perfusion.

Stock solution (mg)	SC-1	SC-2	GBSS-A	GBSS-B
EGTA	95	-	-	-
Glucose	450	-	495.5	495.5
HEPES	1,190	1,190	-	-
KCl	200	200	185	185
$Na_2HPO_4 \cdot 2\ H_2O$	75.5	75.5	37.5	37.5
NaCl	4,000	4,000	-	4,000
$NaH_2PO_4 \cdot H_2O$	39	39	-	-
$NaHCO_3$	175	175	113.5	113.5
Phenol red	3	3	3	3
$CaCl_2 \cdot 2\ H_2O$	-	280	112.5	112.5
KH_2PO_4	-	-	15	15
$MgCl_2 \cdot 6\ H_2O$	-	-	105	105
$MgSO_4 \cdot 7\ H_2O$	-	-	35	35
H_2O up to (ml)	500	500	500	500

Table M9.2. Stock solutions for hepatic cell isolation. For the density gradient medium, the following solutions were prepared before starting the perfusion of the liver: Nycodenz 1 (5.18 g/total volume 15 ml GBSS-A) and Nycodenz 2 (3.63 g/total volume 25 ml GBSS-A).

2.3. Protein analyses

2.3.1. Plasma analysis

Plasma cytokine concentrations were measured by magnetic bead-based multiplex assay (Merck Millipore) in a Luminex 200 analyzer, following manufacturer's instructions. Adiponectin was detected in plasma samples by Western blot. Samples were diluted in PBS (1/10) and buffered with 2x Native Tris-Glycine Sample Buffer (Invitrogen). Diluted samples were loaded on precast native gels to preserve adiponectin multimers (NativePAGE Bis-Tris gel system; Thermo Fisher Scientific) and run with Novex Tris-Glycine Native Running Buffer (Invitrogen). In other cases, plasma samples were prepared as described, but diluted in PBS, Milli-Q water, and Laemmli Sample Buffer and separated by SDS-PAGE. Gels were transferred to 0.2 µm pore-size nitrocellulose membranes (Bio-Rad) (100 V, 2 h, 4 °C), which were blocked with 10% milk prepared in PBS without detergents (in the first case) or with PBS-0.1% Tween (in the second case) and probed with a primary antibody to adiponectin (1:500 dilution, #PA1-054; Thermo Fisher Scientific). After washing, membranes were incubated with a fluorescent secondary antibody (goat anti-rabbit 680 nm, #926-32221, 1:5,000 dilution; LI-COR) or an HRP-conjugated goat anti-rabbit secondary antibody (1:5,000 dilution; GE Healthcare) for 1 h at RT. Membranes were washed, and proteins were visualized and quantified using the Odyssey Imaging System (LI-COR) or an ECL substrate (Clarity Western ECL substrate; Bio-Rad), respectively. The specificity of the antibody was assured by using plasma from adiponectin knockout mice. Results were normalized to the control group (male rodents, Fabp-Cre mice, or control mice, as indicated in the figure legends).

2.3.2. Immunoblot analysis

Tissue or cell extracts were prepared in lysis buffer (50 mM Tris-HCl pH 7.5, 1 mM EGTA, 1 mM EDTA, 50 mM NaF, 1 mM sodium glycerophosphate, 5 mM sodium pyrophosphate, 0.27 M sucrose, 1% Triton X-100, 0.1% β-mercaptoethanol, 0.1 mM PMSF, 1 mM sodium orthovanadate, 1 µg/ml leupeptin, and 1 µg/ml aprotinin) by using T 10 Ultra-Turrax (IKA) (except for cells). Lysates were centrifuged at 19,000 x *g* for 20 min at 4 °C, and protein concentration in supernatants was quantified by Bradford method (Bio-Rad Protein Assay). Samples were denatured in loading buffer (0.24 M Tris-HCl pH 6.8, 40% glycerol, 8% SDS, 5% β-mercaptoethanol, 0.04% bromophenol blue) at 95 °C for 5 min. Equal amounts of protein (20-50 µg) were loaded in 10% polyacrylamide gels (30% Acrylamide/Bis Solution, 29:1, Bio-Rad) and separated by SDS-PAGE at 150 V. Gels were transferred to 0.2 µm pore-size nitrocellulose membranes (Bio-Rad) (100 V, 2 h, 4 °C), blocked with 10% fat-free milk powder for 45 min, and probed overnight with the primary antibodies prepared in 5% BSA in PBS-0.1%

Tween (Table M10). HRP-conjugated goat anti-rabbit and sheep anti-mouse from GE Healthcare were used as secondary antibodies (1:5,000 in 5% BSA in PBS-0.1% Tween) for a 1-h incubation at RT. Membranes were washed with PBS-0.1% Tween, and reactive bands were detected by ECL (GE Healthcare) and quantified by ImageJ software (NIH). In certain instances, membranes probed for phospho-proteins were stripped by incubating them at 55 °C for 15 min with stripping buffer (68 mM Tris-HCl pH 6.8, 1% SDS, 0.7% β-mercaptoethanol) and reprobed for total protein. Results were normalized to the non-phosphorylated form.

Antibody	Company	Reference	Dilution
Phospho-JNK (T183/Y185)	Cell Signaling	4668	1:1,000
JNK	Cell Signaling	9252	1:1,000
Phospho-AMPKα (T172)	Cell Signaling	2531	1:1,000
AMPKα	Cell Signaling	2603	1:1,000
Phospho-p38 (T180/Y182)	Cell Signaling	9211	1:1,000
p38α	Santa Cruz Biotechnology	sc-535	1:1,000
GAPDH	Santa Cruz Biotechnology	sc-25778	1:1,000
Vinculin	Sigma-Aldrich	V4505	1:2,000

Table M10. List of primary antibodies and dilutions used for western blotting.

2.4. Nucleic acids analyses

2.4.1. RNA isolation and qRT-PCR analyses

Total RNA was isolated from healthy or tumorigenic hepatocytes, other cell populations in the liver (KCs; endothelial cells, ECs; and HSCs) and different tumor cell lines (Hep53.4, MC-38, and B16-F10) using the RNeasy Mini Kit (Qiagen), following manufacturer's instructions. RNA concentration was measured with a NanoDrop 1000 spectrophotometer (Thermo Fisher Scientific). 2 µg RNA were retrotranscribed using High-Capacity cDNA Reverse Transcription Kit (Applied Biosystems), according to manufacturer's instructions. The following program was used: 10 min at 25 °C, 2 h at 37 °C, 5 min at 85 °C. Samples were diluted 1/5-1/20, and the expression of mRNA was examined by qRT-PCR using a 7900HT Fast Real-Time PCR System and FAST SYBR GREEN assays (Applied Biosystems). For that, 2 µl of diluted cDNA were added to 384-well MicroAmp Optical plates (Applied Biosystems), together with the following mix per well: 4 µl Fast SYBR Green Master Mix (Applied Biosystems), 0.16 µl each primer and 2 µl RNase-free water. An 8-point standard curve created by 5-fold serial dilution was included. The following PCR program in SDS 2.4 software was used: 1 cycle of 20 s at

95 °C and 40 cycles of 1 s at 95 °C plus 20 s at 60 °C. A dissociation curve was used after each reaction to verify primer specificity and purity of the PCR products. Relative mRNA expression was normalized to *Gapdh* mRNA measured in each sample. The genes indicated in Table M11 were amplified using primers purchased from Sigma-Aldrich.

Gene	Forward primer (5'→3')	Reverse primer (5'→3')
AdipoR1	AATGGGGCTCCTTCTGGTAAC	GGATGACTCTCCAACGTCCCT
AdipoR2	GGCCCATCATGCTATGGAAC	GTGAGGGATCACTCGCCATC
Gapdh	TGAAGCAGGCATCTGAGGG	CGAAGGTGGAAGAGTGGGA

Table M11. Primers used in qRT-PCR.

2.5. Histology

2.5.1. Histological analysis

Liver tissue samples were fixed in 10% formalin (Bio-Optica) for 48 h, dehydrated and embedded in paraffin. 8 µm sections were cut and stained with H&E (American Master Tech Scientific) following the next protocol: 3 changes of 100% xylol (Sigma), 5 min each; 2 changes of 100% ethanol (BDH Prolabo), 5 min each; 95%, 70% and 50% ethanol, 2 min each; distilled water, 2 min; haematoxylin (Harris), 40 s; rinse in tap water; Bluing solution (Thermo Scientific), 4 dips; quick rinse in water; 95% ethanol, 1 min; eosin (Thermo Scientific), 1 min; 2 changes of 95% ethanol, 1 min each; 2 changes of 100% ethanol, 1 min each; 3 changes of xylol, 1 min each. Histopathological examination of H&E-stained livers was performed in an Eclipse CiL light microscope (Nikon), using 10-20x magnification with a numerical aperture of 0.25-0.40 of the optic lenses. Microphotographs were taken with a Nikon Camera DS-Fi3 and acquired using the NIS-Elements Microscope Imaging Software (Nikon). Histopathological grading of chronic liver disease was assessed based on the score system previously published (Goodman, 2007), but modified for NAFLD and HCC. No insult (−) or different grades of injury (mild [+], moderate [++], or marked [+++]) were noted in at least seven view fields per slide.

2.6. Statistics

2.6.1. Statistical analysis

Values are presented as means ± SEM. Differences between groups were examined for statistical significance using two-tailed unpaired Student's *t*-test (with Welch's correction when variances were different), or one- or two-way ANOVA coupled to Bonferroni's or Dunnett's

post-test. Statistical significance was determined as a two-sided *p*-value < 0.05 (GraphPad Prism 8.0). Statistical details and experimental *n* are specified in figure legends.

RESULTS

1. Muscle p38α in the control of energy balance

Stimuli which are frequently elevated in obesity or type 2 diabetes, such as insulin or FFAs, have been described to induce the activation of p38s in skeletal muscle (Kadotani et al., 2009; Koistinen et al., 2003). Interestingly, exercise is also known to activate muscle p38s (Coffey et al., 2006). Therefore, we wanted to understand the consequences of p38α activation in striated muscle in the control of metabolism and energy homeostasis. For that, we generated conditional knockout mice for p38α in this tissue by expressing the Cre recombinase under the MCK promoter in mice with the first exon of p38α gene flanked by loxP sequences (p38α^{MCK-KO}). Mice expressing this Cre recombinase without floxed p38α alleles were used as controls (MCK-Cre). Immunoblot images confirmed the deficiency of p38α in the skeletal muscles analyzed (quadriceps, gastrocnemius, soleus and extensor digitorum longus [EDL]) and in the heart of p38α^{MCK-KO} mice, whereas no changes in the level of p38α were observed in other tissues (Figure R1). These results indicate that these mice are an appropriate model for the analysis of striated muscle p38α deficiency.

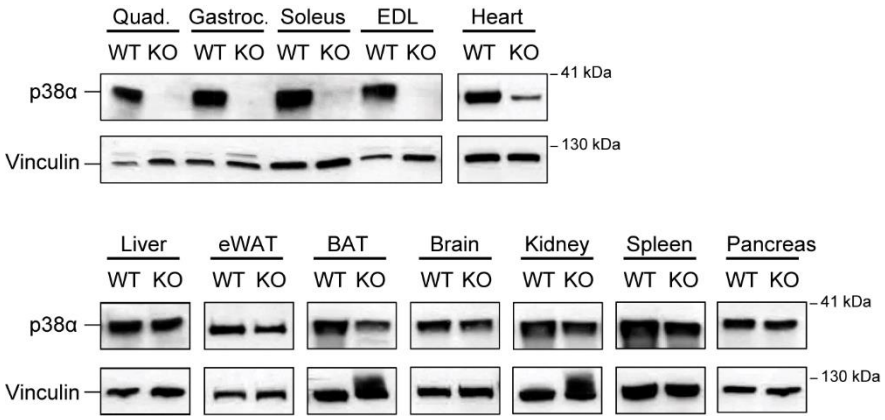

Figure R1. Analysis of p38α expression in tissues derived from MCK-Cre or p38α^{MCK-KO} mice. p38α expression in tissues from MCK-Cre and p38α^{MCK-KO} mice was examined by immunoblot analysis using antibodies against p38α and vinculin as loading control. *n* = 2-4. Quad., quadriceps; Gastroc., gastrocnemius; EDL, extensor digitorum longus; eWAT, epididymal white adipose tissue; BAT, brown adipose tissue; WT, MCK-Cre; KO, p38α^{MCK-KO}.

1.1. p38α^{MCK-KO} mice have decreased body weight and improved glucose homeostasis in normal chow diet

When fed a ND, mice lacking p38α in striated muscle presented reduced body weight (Figures R2A, B). Indeed, measurement by NMR demonstrated that this reduction in body weight was due to lower lean and fat mass in p38α^{MCK-KO} mice (Figures R2C, D), which correlated with a decrease in adipose tissue, liver and skeletal muscle weight at sacrifice (gastrocnemius, quadriceps, soleus and EDL muscle weight are shown as representative), while no significant differences were found in heart weight (Figure R2E).

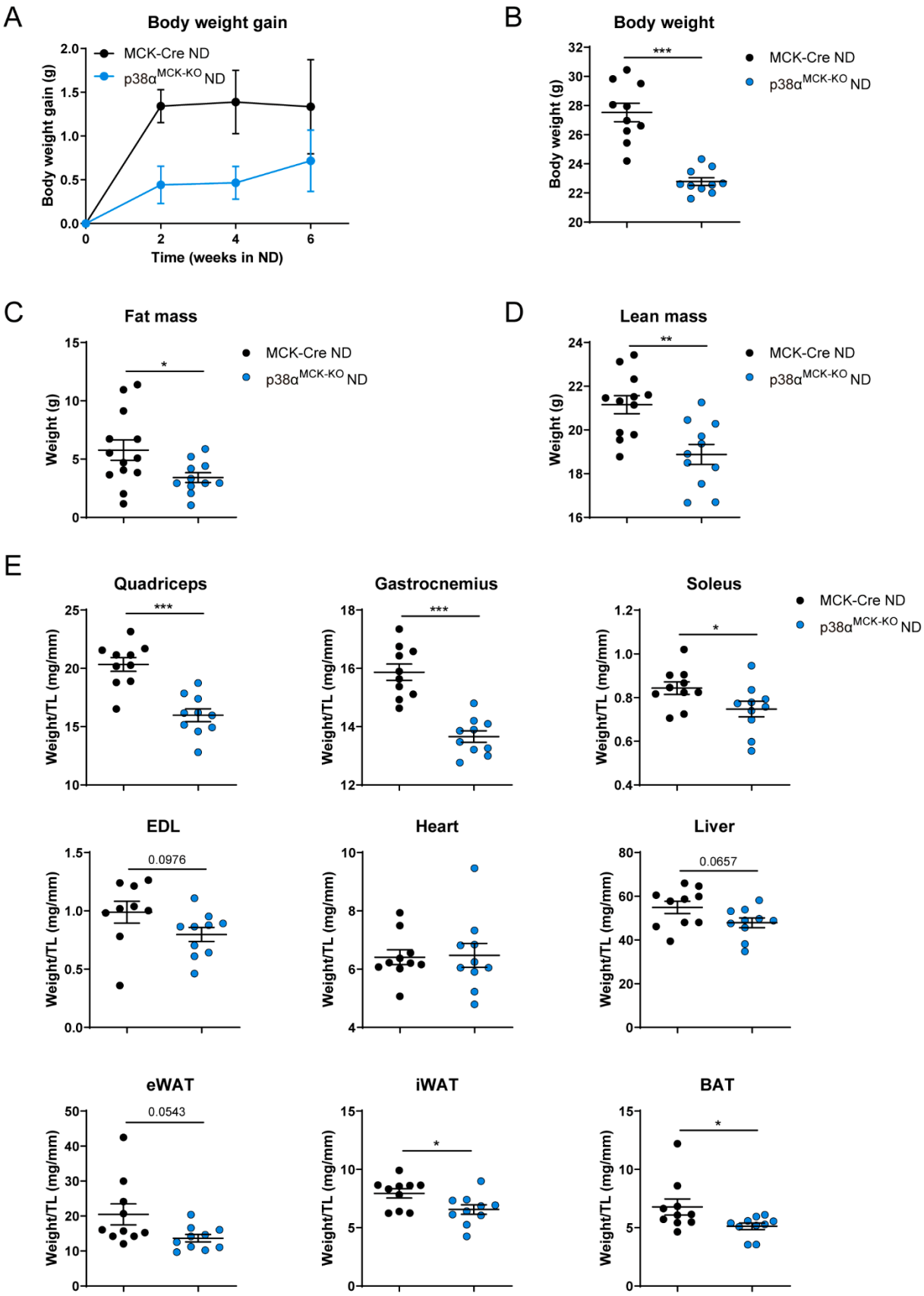

Figure R2. Lack of p38α in striated muscle decreases body weight in mice fed a normal chow diet. 8-week-old p38α^{MCK-KO} and MCK-Cre mice were fed a ND, and body weight was monitored for 6 weeks. (A) Body weight gain measured at the indicated times during ND treatment. (B) Body weight

measured at sacrifice. (C, D) Fat mass and lean mass determined by NMR after body weight gain measurement. (E) Relative weight of organs at sacrifice (measurements standardized to tibial length). Data are shown as means ± SEM; *p < 0.05; **p < 0.01; ***p < 0.001; two-way ANOVA coupled to Bonferroni's multiple comparisons test (body weight gain); Student's t-test (Figures B-E), with Welch's correction for body weight, fat mass, eWAT and BAT; n = 10-13. TL, tibia length; EDL, extensor digitorum longus; eWAT, epididymal white adipose tissue; iWAT, inguinal white adipose tissue; BAT, brown adipose tissue.

The lower body weight of p38α^{MCK-KO} mice correlated with decreased blood glucose levels both in the fasted and fed state (Figure R3A), as well as improved glucose tolerance (Figure R3B).

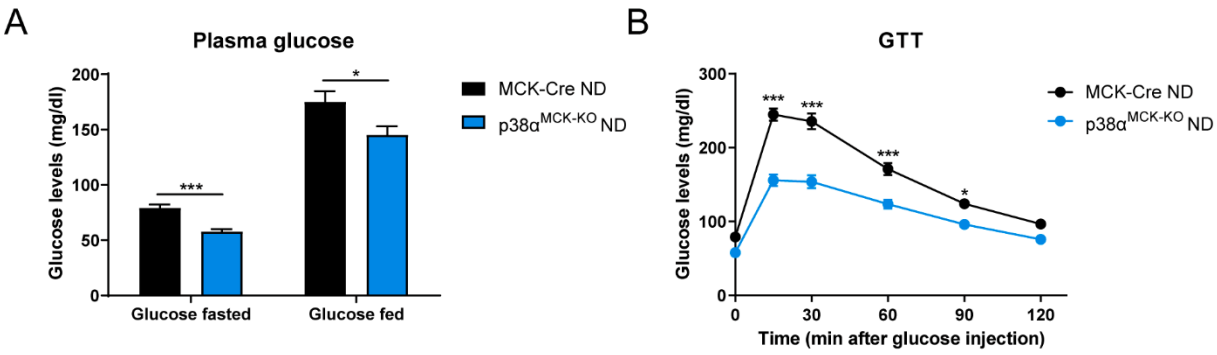

Figure R3. Lack of p38α in striated muscle improves glucose homeostasis in mice fed a normal chow diet. p38α^{MCK-KO} and MCK-Cre mice were fed a ND, and glucose parameters were measured at 16 weeks old. (A) Fasting and fed plasma glucose levels. (B) Glucose tolerance test (GTT). Mice fasted overnight were injected i.p. with glucose (1 g/kg) and blood glucose concentration was measured at the indicated time points. Data are shown as means ± SEM; *p < 0.05; ***p < 0.001; Student's t-test (plasma glucose); two-way ANOVA coupled to Bonferroni's multiple comparisons test (GTT); n = 10.

1.2. Mice deficient for p38α in striated muscle are protected against HFD-induced obesity

The decreased body weight and lower glucose levels found in ND-fed mice led us to check whether the absence of p38α in striated muscle protected mice against HFD-induced obesity. To that end, MCK-Cre and p38α^{MCK-KO} mice were fed a HFD. p38α^{MCK-KO} mice showed decreased body weight gain and, consequently, presented lower weight at sacrifice (Figures R4A, B). Indeed, measurement of lean mass and fat mass by NMR demonstrated that this reduction in body weight was again due to lower lean and fat mass in p38α^{MCK-KO} mice (Figures R4C, D), which correlated with a decrease in adipose tissue, liver and skeletal muscle weight at sacrifice, while no significant differences were found in heart weight (Figure R4E). These data indicate that muscle-specific p38α deficiency protects mice against HFD-induced obesity.

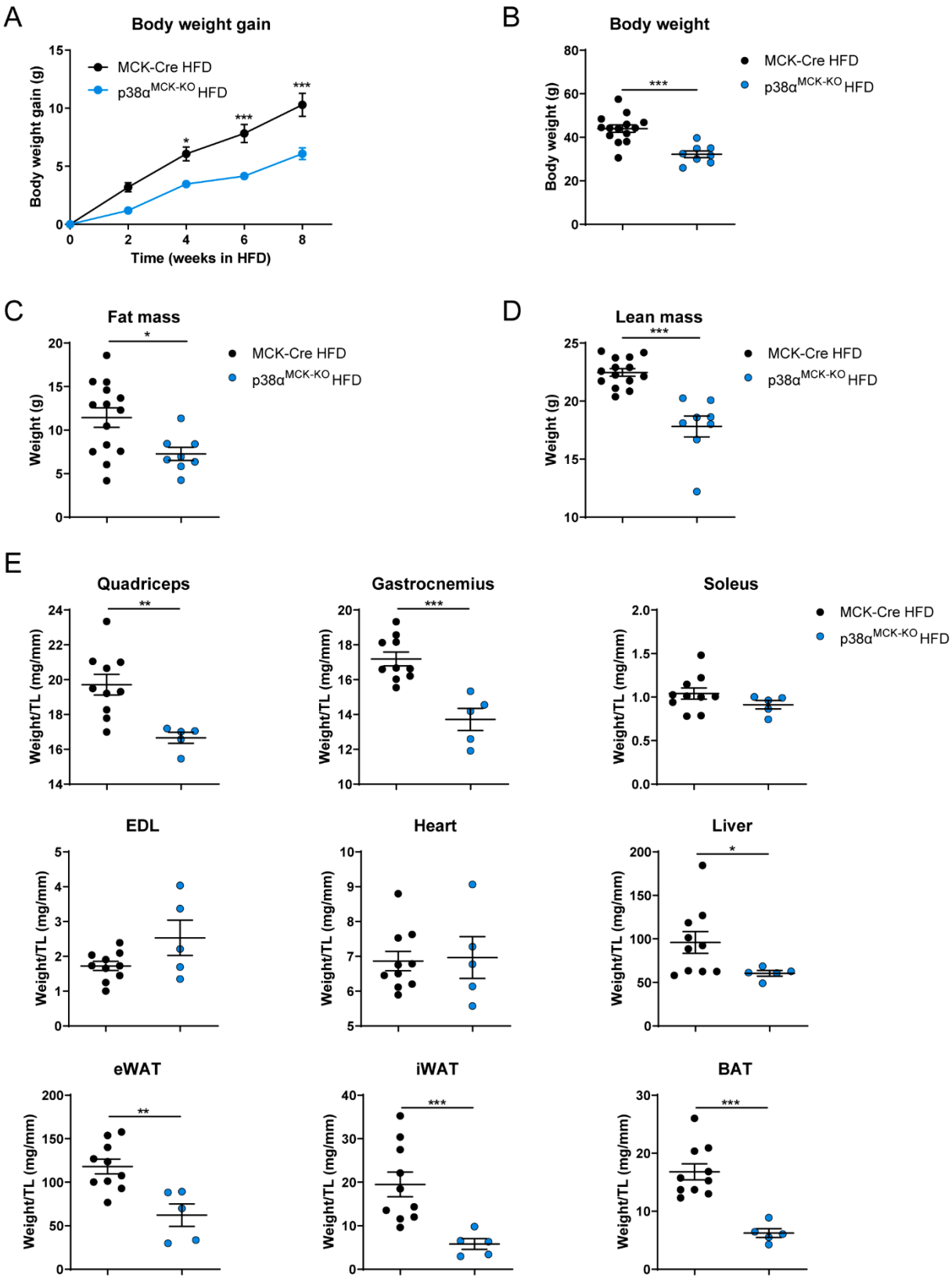

Figure R4. Lack of p38α in striated muscle protects against HFD-induced obesity. p38α^{MCK-KO} and MCK-Cre mice were fed a HFD, and body weight was monitored for 8 weeks. (A) Body weight gain measured at the indicated times during HFD treatment. (B) Body weight measured at sacrifice. (C, D) Fat mass and lean mass determined by NMR after 12 weeks on HFD. (E) Relative weight of organs at sacrifice (measurements standardized to tibial length). Data are shown as means ± SEM; *p < 0.05;

**$p < 0.01$; ***$p < 0.001$; two-way ANOVA coupled to Bonferroni's multiple comparisons test (body weight gain); Student's *t*-test (Figures B-E), with Welch's correction for lean mass, EDL, liver and iWAT; $n = 5$-14. TL, tibia length; EDL, extensor digitorum longus; eWAT, epididymal white adipose tissue; iWAT, inguinal white adipose tissue; BAT, brown adipose tissue.

1.3. Deletion of p38α in striated muscle increases energy expenditure in HFD-fed mice

Body weight is a balance between energy intake and energy expenditure (Speakman, 2004). In order to elucidate the reason for the reduced body weight of p38α^{MCK-KO} mice, we used metabolic cages in HFD-fed animals. p38α^{MCK-KO} mice presented higher energy expenditure than MCK-Cre mice, with no differences in the RQ (Figures R5A, B), indicating that lack of muscle p38α increases energy expenditure without affecting nutrient partitioning. In concordance with increased energy expenditure, locomotor activity was also higher in p38α^{MCK-KO} mice (Figure R5C), while no differences were found in body or interscapular temperature (Figures R5D, E). These data suggest that increased energy expenditure was due to higher locomotor activity. Surprisingly, despite their lower body weight, p38α^{MCK-KO} mice showed a significant increase in food intake (Figure R5F). To find the mechanism underlying this higher food intake, we analyzed plasma levels of the anorexigenic hormone leptin and the orexigenic hormone ghrelin. p38α^{MCK-KO} mice presented lower leptin levels in fasted condition, which correlated with their increased food intake, whereas no differences were observed in ghrelin (Figure R5G). In summary, the results presented here support a role for muscle p38α in the regulation of energy balance in HFD.

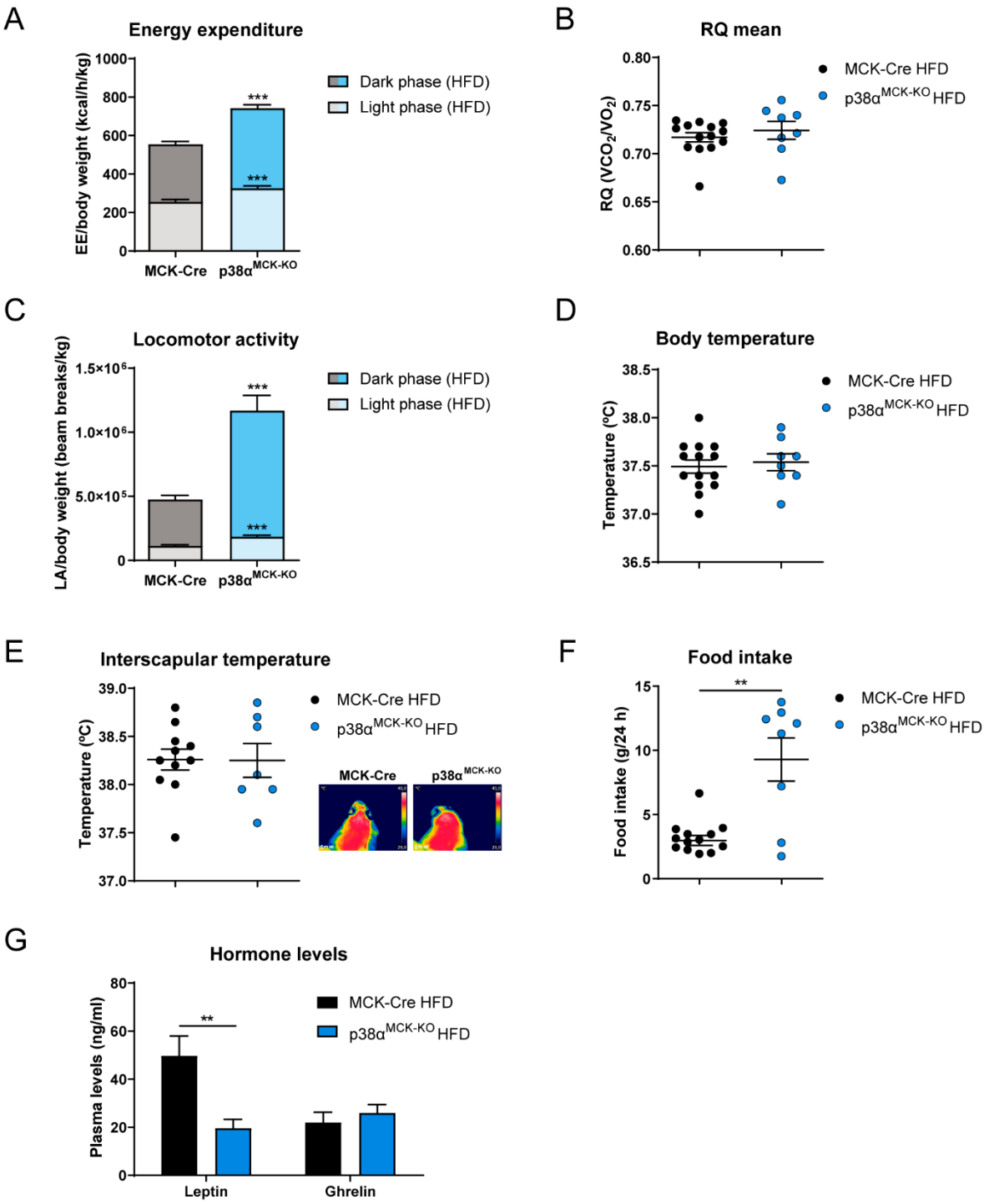

Figure R5. HFD-fed p38α^{MCK-KO} mice present higher energy expenditure and locomotor activity. p38α^{MCK-KO} and MCK-Cre mice were fed a HFD for 12 weeks, and metabolic parameters were assayed at the end of this period. (A) Energy expenditure (EE) corrected by body weight. (B) Average of respiratory quotient (RQ) measured during 48 h. (C) Locomotor activity (LA) corrected by body weight during a 48 h period. (D) Rectal temperature measurement. (E) Interscapular temperature measurement and representative infrared thermal images. Scale range: 29 °C (lowest, blue)-40 °C (highest, white). (F) Total food intake in 24 h. (G) Fasting leptin and ghrelin levels in plasma. Data are shown as means ± SEM; **$p < 0.01$; ***$p < 0.001$; Student's *t*-test (with Welch's correction for LA-dark phase, food intake and leptin); n = 7-14.

In fact, although differences were milder, similar results were found in ND-fed p38α^{MCK-KO} mice compared to MCK-Cre controls, which did not show significant differences in body or interscapular temperature, or cold exposure test (Figures R6A-F). The only relevant difference compared to HFD-fed mice was found in food intake, which was decreased in the case of ND-fed p38α^{MCK-KO} mice (Figure R6G), probably due to a tendency towards higher leptin levels (Figure R6H).

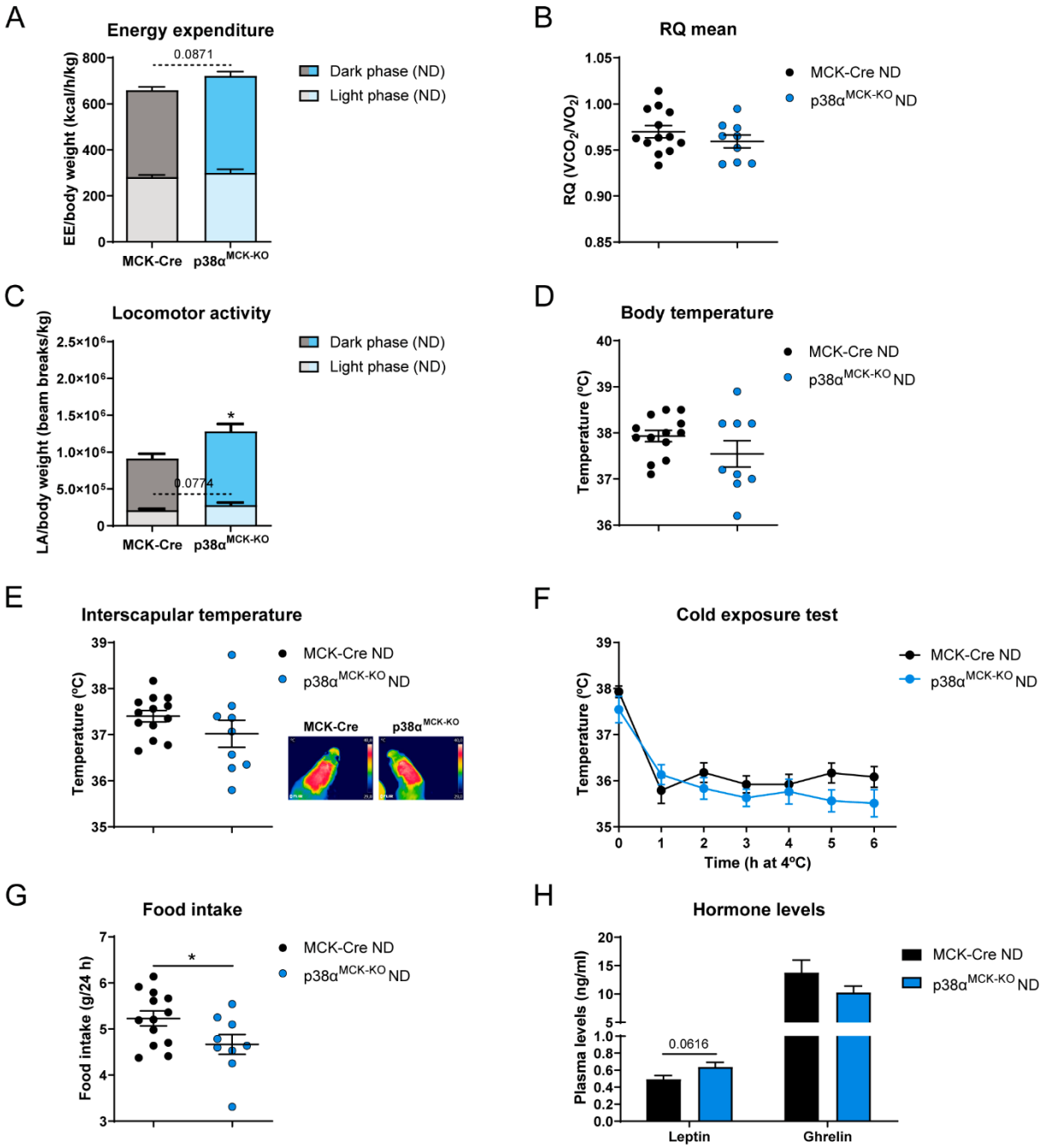

Figure R6. ND-fed p38α^{MCK-KO} mice present higher locomotor activity. p38α^{MCK-KO} and MCK-Cre mice were fed a ND, and metabolic parameters were assayed in 21-week-old mice. (A) Energy expenditure (EE) corrected by body weight. (B) Average of respiratory quotient (RQ) measured during 48 h. (C) Locomotor activity (LA) corrected by body weight during a 48 h period. (D) Rectal temperature

measurement. (E) Interscapular temperature measurement and representative infrared thermal images. Scale range: 29 °C (lowest, blue)-40 °C (highest, white). (F) Effect of cold exposure (4 °C during 6 h) on body temperature at different time points. (G) Total food intake in 24 h. (H) Fasting leptin and ghrelin levels in plasma. Data are shown as means ± SEM; *$p < 0.05$; Student's *t*-test (Figures A-E, G-H), with Welch's correction for body and interscapular temperature; two-way ANOVA coupled to Bonferroni's multiple comparisons test (cold exposure test); n = 9-13.

1.4. Striated muscle p38α-deficient mice are protected against diet-induced diabetes

Feeding of a HFD causes hyperglycemia and hyperinsulinemia in mice, which can increase the propensity of developing insulin resistance and diabetes (S. E. Kahn et al., 2006). The reduced fat accumulation in p38α^{MCK-KO} mice prompted us to investigate whether these mice were also protected against HFD-induced diabetes. Analysis of plasma samples indicated that p38α^{MCK-KO} mice had significantly lower levels of HFD-induced hyperglycemia and hyperinsulinemia than control mice (Figure R7A, B), as well as a decreased HOMA-IR index, indicative of lower insulin resistance (Figure R7C). Moreover, HFD-fed p38α^{MCK-KO} mice showed enhanced glucose tolerance (Figure R7D), correlating with higher glucose-induced insulin release (Figure R7E). In addition, higher insulin sensitivity in knockout mice was corroborated by insulin tolerance test (Figure R7F). These data indicate that p38α deficiency protects against HFD-induced diabetes.

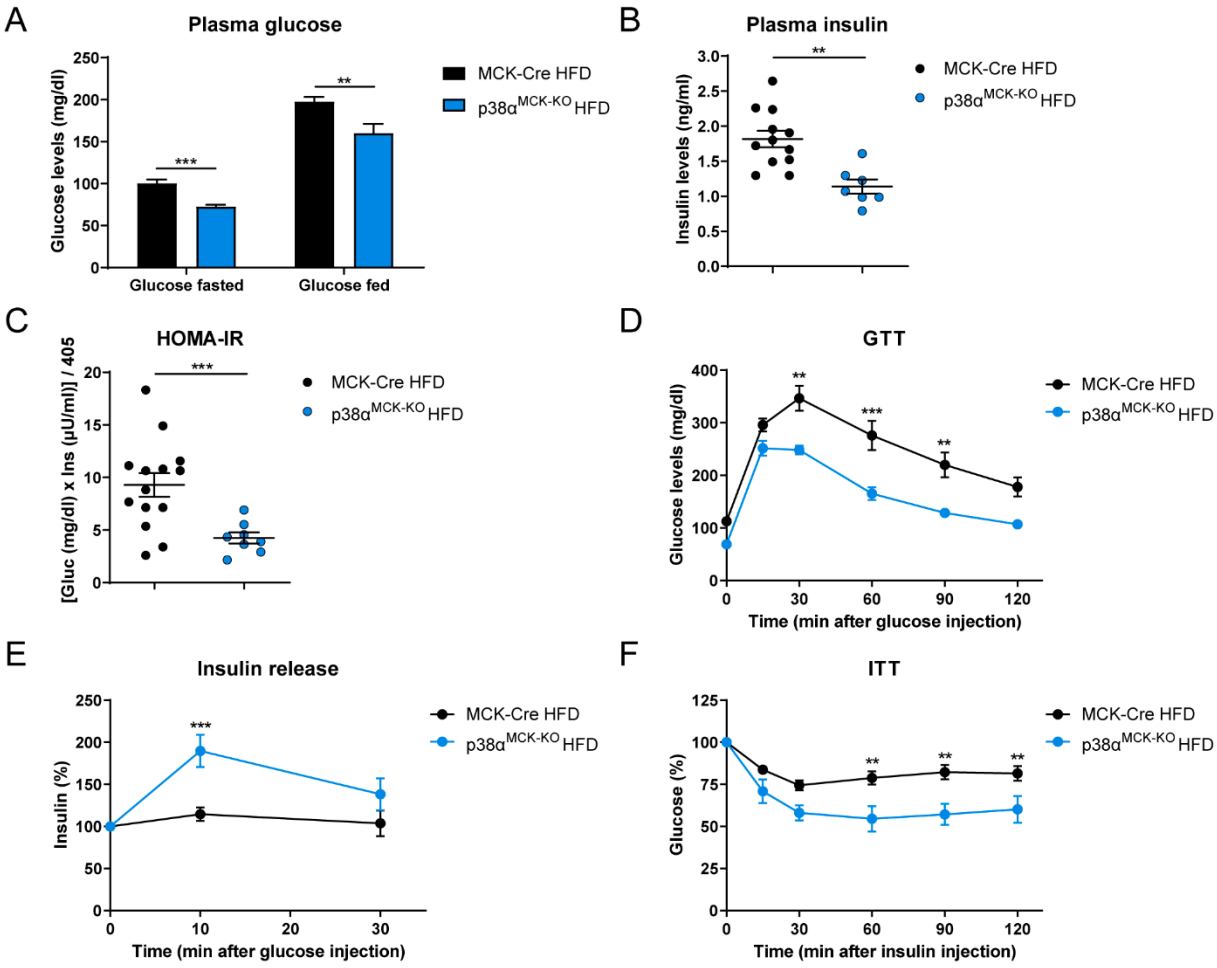

Figure R7. HFD-fed p38α^{MCK-KO} mice present improved glucose metabolism. p38α^{MCK-KO} and MCK-Cre mice were fed a HFD for 8 weeks. (A) Fasting and fed plasma glucose levels. (B) Fasting plasma insulin levels. (C) Insulin resistance rate calculated as HOMA-IR ratio. (D) Glucose tolerance test (GTT). Mice fasted overnight were injected i.p. with glucose (1 g/kg). (E) Insulin release assay. Mice fasted overnight were injected i.p. with glucose (2 g/kg) and insulin levels were measured at the indicated points. (F) Insulin tolerance test (ITT). Mice fed *ad libitum* were injected i.p. with insulin (0.75 U/kg). Blood glucose concentration was measured at the indicated points in GTT and ITT. Data are shown as means ± SEM; $^{**}p < 0.01$; $^{***}p < 0.001$; Student's *t*-test (Figures A-C), with Welch's correction for glucose (fasted) and HOMA-IR; two-way ANOVA coupled to Bonferroni's multiple comparisons test (Figures D-F); n = 7-14. Gluc, glucose; Ins, insulin.

Considering the crucial role of AKT in insulin signaling pathway, its phosphorylation state represents an appropriate method to assay insulin resistance (S. E. Kahn et al., 2006). For this reason, to further analyze insulin resistance at the tissue level, we checked AKT phosphorylation in both Thr308 and Ser473 residues as a measurement of its activation. Biochemical analyses showed that p38α^{MCK-KO} mice presented higher AKT phosphorylation after insulin injection in liver and skeletal muscle compared to MCK-Cre mice, indicative of protection against insulin resistance (Figure R8A, B), partial protection in heart (Figure R8C), while not in white fat (Figure R8D). These results indicate that p38α^{MCK-KO} mice are protected against HFD-induced insulin resistance in liver and skeletal muscle, being therefore protected against diabetes.

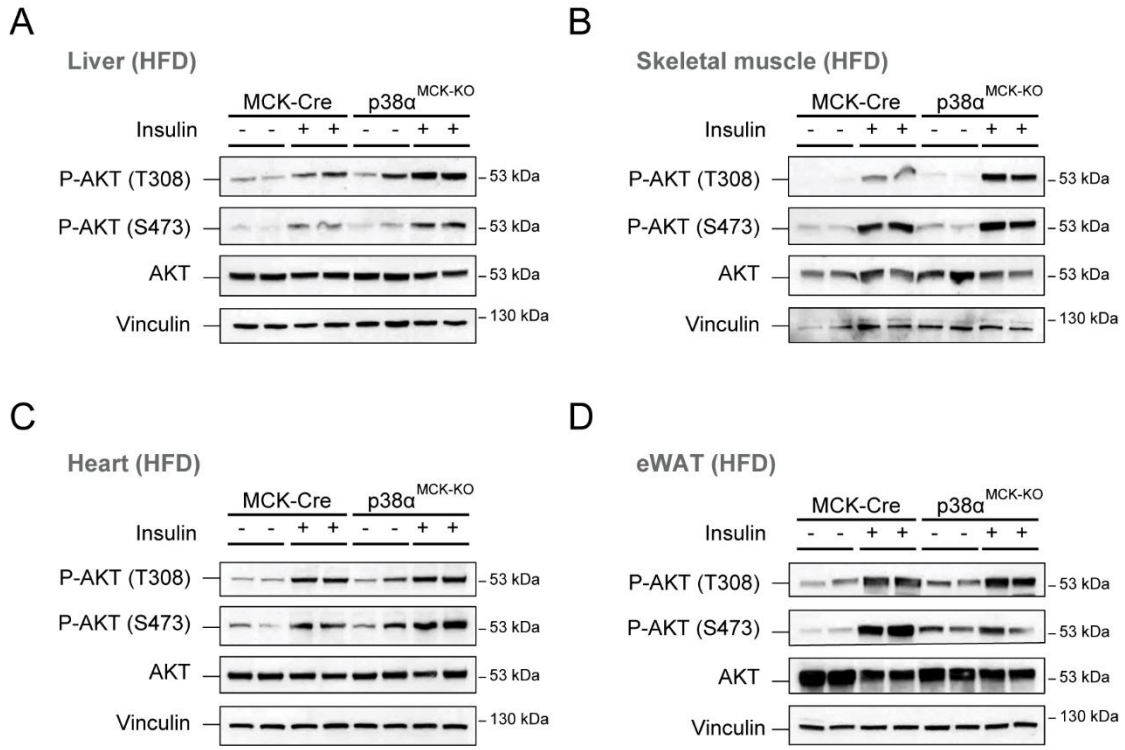

Figure R8. Mice lacking p38α in striated muscle are protected against insulin resistance in liver and skeletal muscle under HFD condition. p38α^{MCK-KO} and MCK-Cre mice were fed a HFD for 14 weeks, fasted overnight and injected (+) or not (-) with insulin (1.5 U/kg) before sacrifice. Extracts prepared from liver (A), quadriceps (B), heart (C) and epididymal white adipose tissue (eWAT) (D) at

15 min post-injection were examined by immunoblot analysis with antibodies against phospho (P)-AKT and total AKT. Vinculin protein expression was monitored as a loading control. *n* = 4.

1.5. Striated muscle p38α deficiency leads to decreased liver steatosis

Obesity is associated with hepatic steatosis, characterized by excessive lipid accumulation in the liver, which is a characteristic of NAFLD that may induce insulin resistance (Farese et al., 2012). To check whether the deficiency of p38α in muscle also protected against HFD-induced liver steatosis, therefore decreasing hepatic insulin resistance, we performed histological analyses of the liver. Our results revealed a milder hepatic steatosis in p38α^{MCK-KO} mice as evaluated by H&E and Oil Red staining (Figure R9). These results suggest that the deficiency of p38α in striated muscle protected against HFD-induced hepatic steatosis.

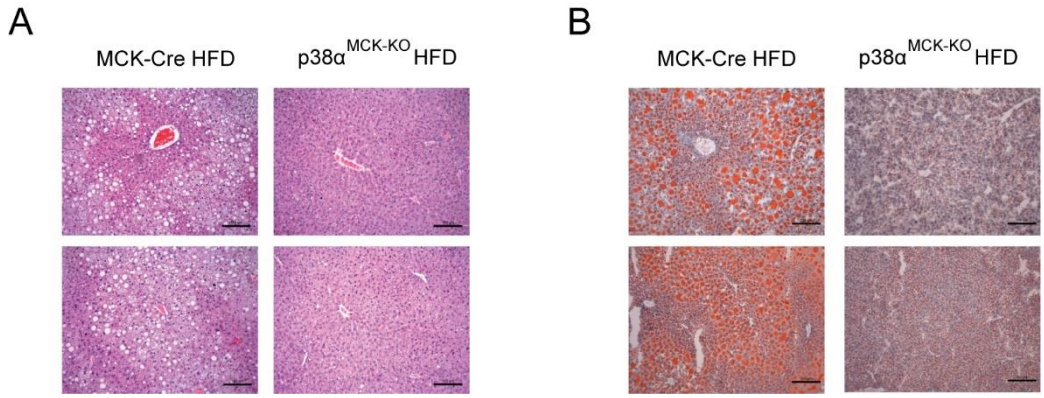

Figure R9. HFD-fed p38α^{MCK-KO} mice present reduced hepatic steatosis. p38α^{MCK-KO} and MCK-Cre mice were fed a HFD for 14 weeks, fasted overnight and sacrificed. Representative H&E- (A) and Oil Red O- (B) stained liver sections are presented. Scale bar: 150 μm. *n* = 5.

1.6. Lack of p38α in skeletal muscle increases its mitochondrial metabolism

Changes in muscle metabolism have been linked to insulin sensitivity (Pinti et al., 2019). To gain further insights into the altered protein expression caused by the lack of p38α that could influence insulin signaling, we performed a quantitative proteomics analysis, using TMT labeling and subsequent LC-MS/MS analysis of gastrocnemius muscles from HFD-fed mice (Figure R10A). A total of 188 statistically significant pathways were detected by IPA ($p < 0.05$). The most enriched pathway associated with upregulated proteins in p38α^{MCK-KO} mice compared to control mice was mitochondrial oxidative phosphorylation (Figure R10B), while glycolysis was the most enriched one associated with downregulated proteins (Figure R10C). Similar results were found by GSEA (Figure R10D). A further analysis revealed that 61 proteins of oxidative phosphorylation, 14 of tricarboxylic acid (TCA) cycle and 13 of fatty acid β-oxidation were significantly upregulated in p38α^{MCK-KO} mice, while 17 glycolytic proteins and 13 gluconeogenic proteins were downregulated in comparison with MCK-Cre mice (Figure R10E). These data suggest that p38α-deficient myocytes rely on the production of ATP by mitochondrial metabolic pathways rather than by glycolysis.

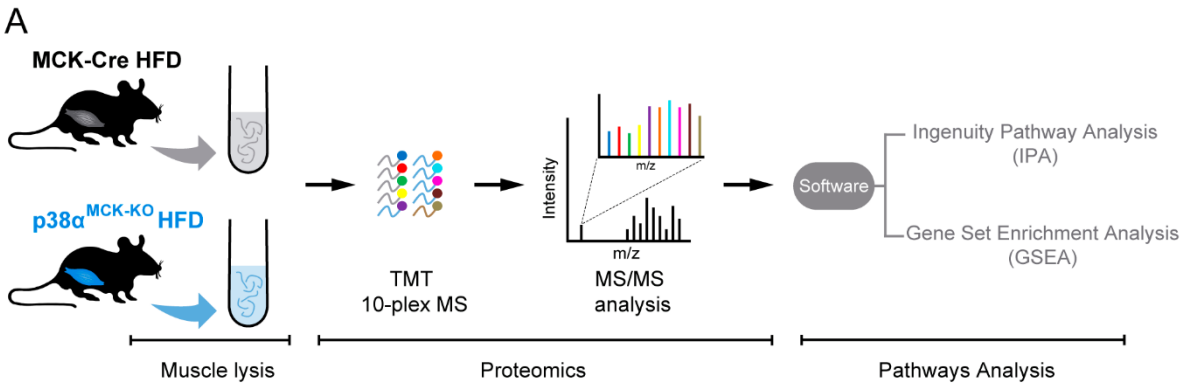

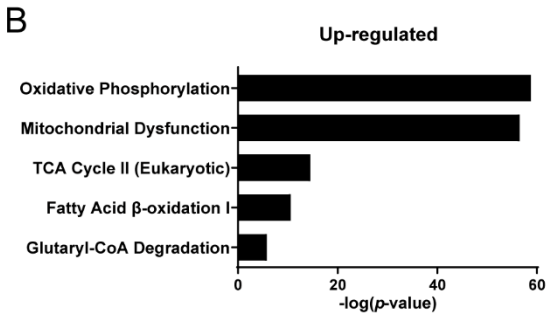

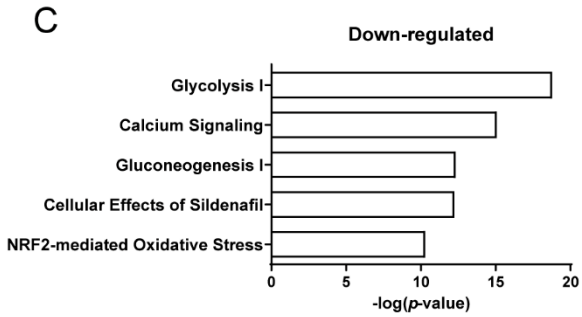

D

p38α MCK-KO vs. MCK-Cre
HALLMARK pathways

Pathway	NES	p-value
Oxidative phosphorylation	3.27	<0.001
Fatty acid metabolism	2.54	0.001
Protein secretion	2.27	0.012
Glycolysis	-2.53	0.001
Myogenesis	-2.20	0.016

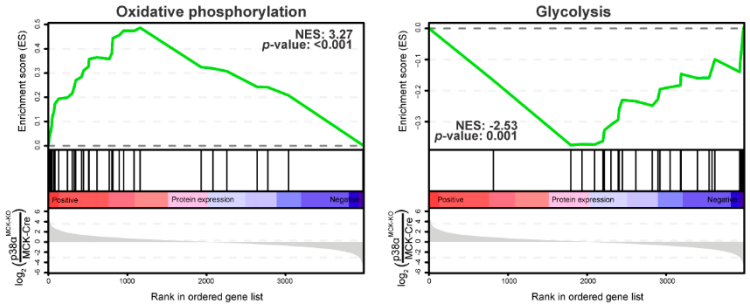

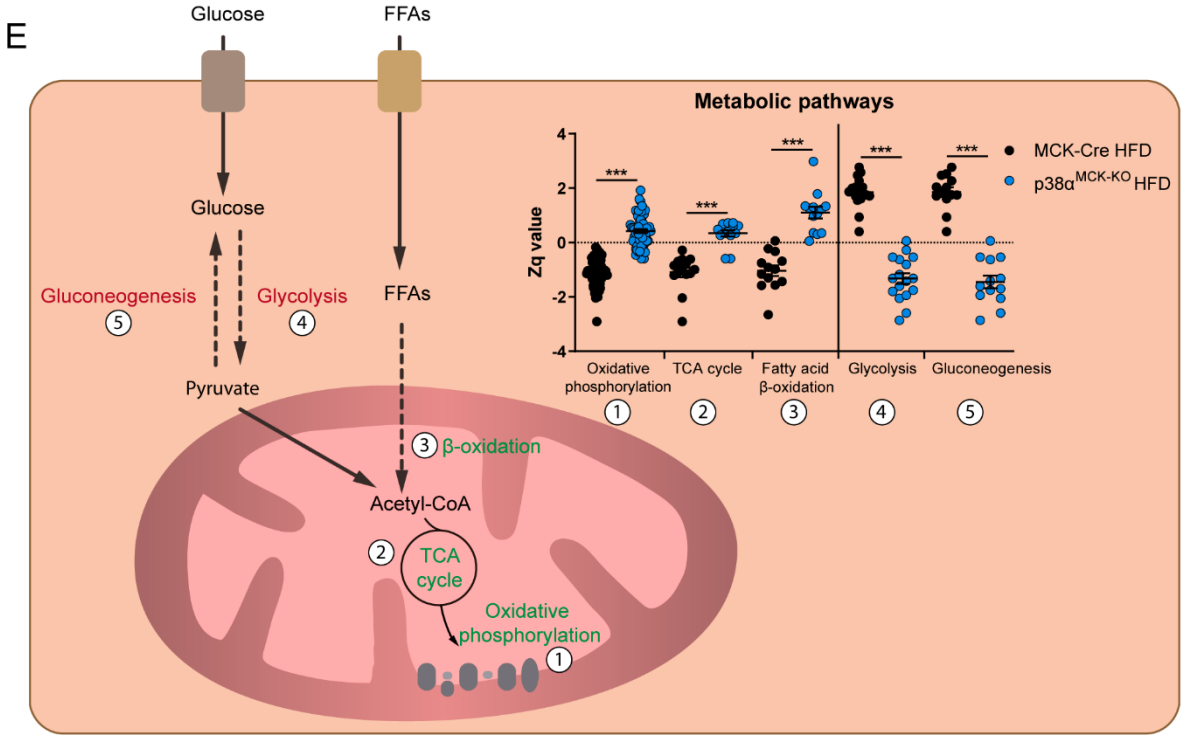

Figure R10. Pathway enrichment analysis of differentially expressed proteins between p38α^{MCK-KO} and MCK-Cre mice. p38α^{MCK-KO} and MCK-Cre mice were fed a HFD for 14 weeks, fasted overnight and sacrificed. A quantitative proteomics analysis with gastrocnemius samples was performed. (A) Schematic representation of the proteomics experimental layout. (B, C) Top 5 significantly enriched pathways shown by Ingenuity Pathway Analysis derived through comparison of proteins differentially expressed between MCK-Cre and p38α^{MCK-KO} mice. Bars show enriched pathways for upregulated (B) or downregulated (C) proteins in p38α^{MCK-KO} mice compared to controls. NRF2, nuclear factor erythroid 2-related factor 2; CoA, coenzyme A. (D) MS analysis by GSEA and gene set enrichment plots of HALLMARK oxidative phosphorylation and glycolysis of p38α^{MCK-KO} and MCK-Cre mice. Proteins detected in MS were ranked based on relative amount in muscles from p38α^{MCK-KO} mice versus MCK-Cre mice, with the first ranked protein corresponding to the protein most upregulated in those conditions (log2 scale). GSEA was used to determine whether any HALLMARK gene sets were enriched among proteins upregulated or downregulated in p38α^{MCK-KO} mice compared with MCK-Cre controls. All gene sets enriched with an absolute value of normalized enrichment score (NES) greater than 2 are shown. Hash marks represent positions in the ranked list corresponding to members of oxidative phosphorylation (left) or glycolysis (right) HALLMARK gene sets. NES indicates whether these members are enriched towards the upregulated end of this list (positive NES) or downregulated end of this list (negative NES) as compared to chance expectation. (E) Analysis of proteins of oxidative phosphorylation, TCA cycle, fatty acid β-oxidation, glycolysis and gluconeogenesis in MCK-Cre and p38α^{MCK-KO} mice. Each point in the graph corresponds to a protein of the pathway. Zq values represent units of standard deviation according to the estimated variances. Data are shown as means ± SEM; ***$p < 0.001$; Student's *t*-test; $n = 4$-5.

1.7. p38α-deficient muscles hyperactivate p38γ and MAP2Ks

Signal transduction is well known to drive metabolic changes in cells (Chandel, 2015). To unveil the mechanism linking p38α deficiency and the metabolic remodeling observed in skeletal muscle, we analyzed p38 activation by its state of phosphorylation in skeletal muscle samples of MCK-Cre and p38α^{MCK-KO} mice. Results showed a hyperactivation of p38γ in different skeletal muscles of HFD-fed p38α^{MCK-KO} mice (Figures R11A-D), which was conserved both in ND and HFD (Figure R11E). This increase was not accompanied by an increase in total p38γ mRNA (Figure R11F) or protein levels (Figures R11A-E). We selected gastrocnemius muscle to further analyze these effects. As expected, MK2, a well-known specific p38α/β substrate (Cuenda et al., 1997), was not phosphorylated in HFD-fed p38α^{MCK-KO} mice, suggesting that p38β kinase activity was not compensating for p38α loss (Figure R11G). This correlated with lower MK2 kinase activity, shown by the reduced phosphorylation of its substrate HSP27 (Figure R11G). In addition, JNK was more phosphorylated in p38α-deficient muscles, suggesting a possible compensation for the deficiency of p38α (Figure R11G). Moreover, in concordance with the higher p38γ activation, the deficiency of p38α resulted in the hyperactivation of the two main MAP2Ks of p38s signaling pathway, MKK3 and MKK6, linked to an increase in their mRNA and total protein levels (Figures R11H-J), suggesting a negative feedback regulation of p38α over its upstream kinases. Taken together, these results indicate that lack of muscle p38α results in higher activation of its upstream kinases and subsequent p38γ hyperphosphorylation.

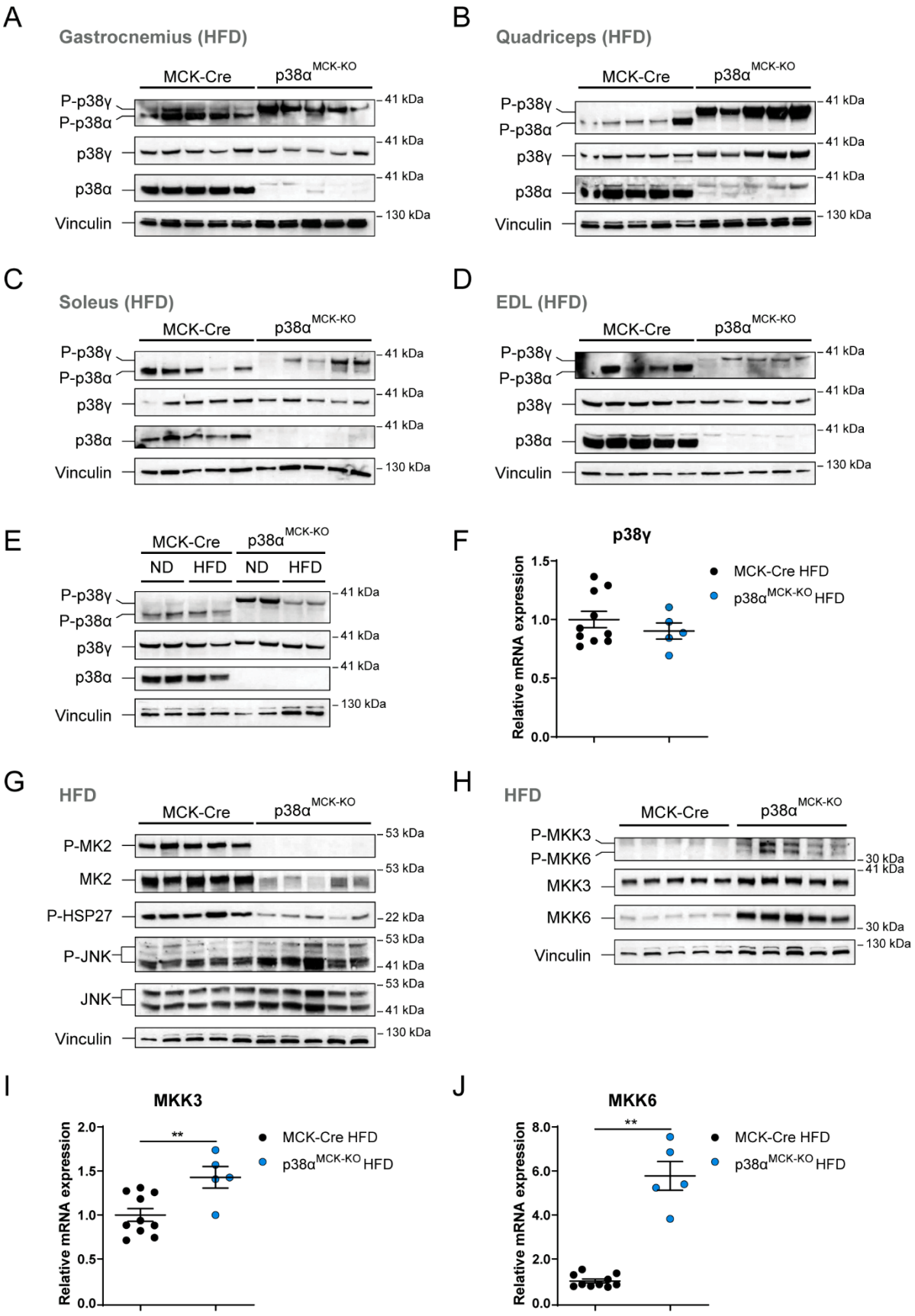

Figure R11. Biochemical analysis of the p38 signaling pathway and JNK in p38α^{MCK-KO} and MCK-Cre mice. 8-week-old p38α^{MCK-KO} and MCK-Cre mice were fed a HFD or a ND (E) for 14 weeks,

fasted overnight and sacrificed. Extracts prepared from gastrocnemius (A, E, G, H), quadriceps (B), soleus (C) and extensor digitorum longus (EDL) (D) muscles were examined by immunoblot analysis with antibodies against phospho (P)-p38, P-MK2, P-Hsp27, P-JNK, P-MKK3/6 and total protein levels. Vinculin protein expression was monitored as a loading control. *n* = 4-5. (F, I-J) qRT-PCR analysis of *Mapk12* (p38γ), *Map2k3* (MKK3) and *Map2k6* (MKK6) genes in gastrocnemius samples. mRNA expression was normalized to the amount of *Gapdh* mRNA in each sample. Data are normalized to MCK-Cre mice and shown as means ± SEM; ***p* < 0.01; Student's *t*-test (with Welch's correction for MKK6); *n* = 5-10.

1.8. PGC1α expression is increased in p38α-deficient muscles

p38γ has been shown to regulate metabolic adaptation in skeletal muscle, increasing mitochondrial biogenesis (Pogozelski et al., 2009). Therefore, we decided to check the possible implications of p38γ hyperactivation in the metabolic remodeling of p38α-deficient muscles. For that, we created striated muscle p38α-deficient mice that also lacked p38γ (p38α/γ^{MCK-KO}) and performed an RNA-seq in gastrocnemius samples from HFD-fed p38α^{MCK-KO}, p38α/γ^{MCK-KO} and MCK-Cre mice (Figure R12A). Pathways analysis revealed that oxidative phosphorylation was one of the upregulated pathways in both knockout mice compared to MCK-Cre controls (Figures R12B-E).

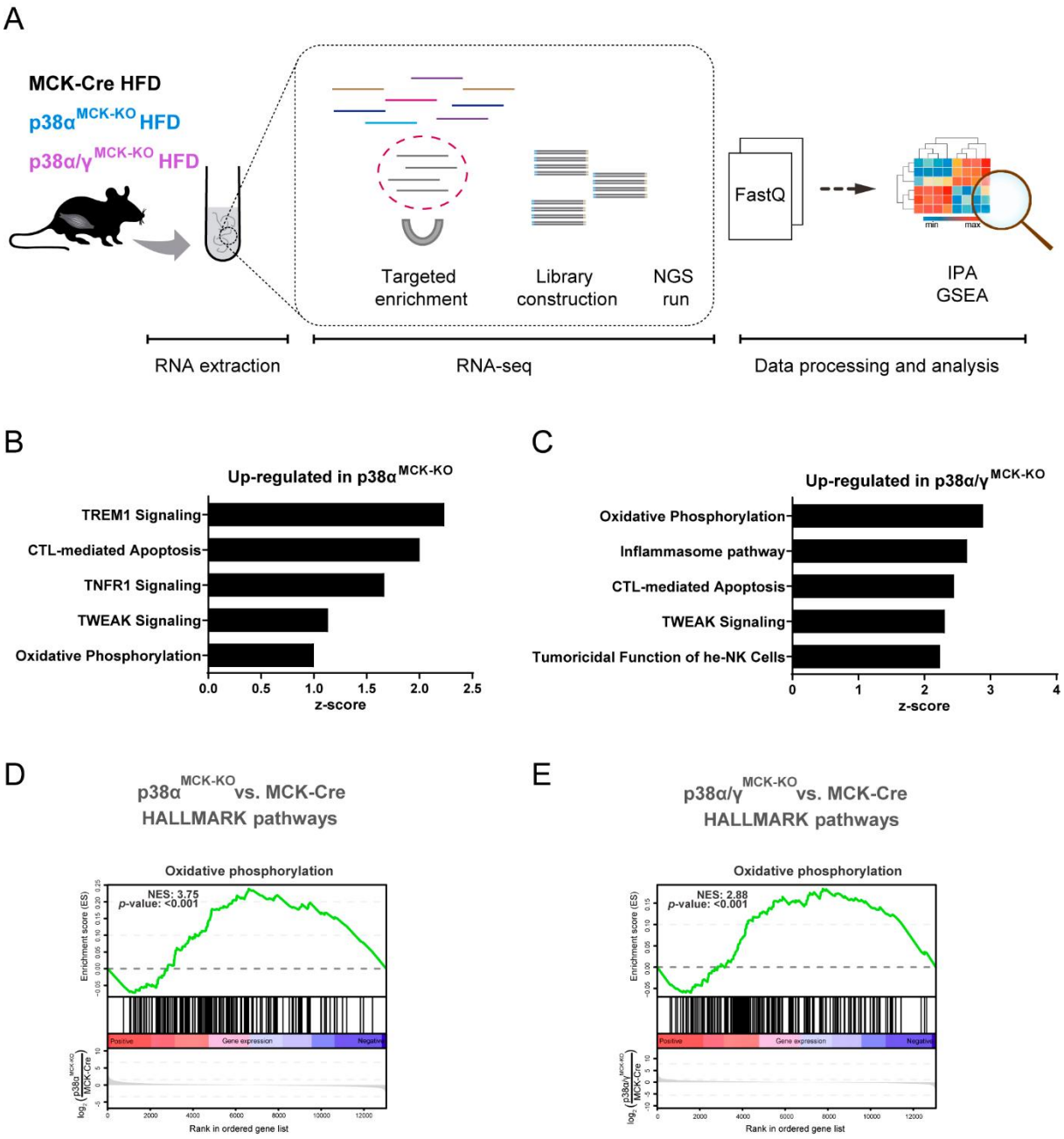

Figure R12. Oxidative phosphorylation is upregulated in muscles from p38α^{MCK-KO} and p38α/γ^{MCK-KO} mice. p38α^{MCK-KO}, p38α/γ^{MCK-KO} and MCK-Cre mice were fed a HFD for 6 weeks, fasted overnight and sacrificed, and an RNA-seq analysis with gastrocnemius samples was performed. (A) Schematic representation of the RNA-seq experimental layout. NGS, next-generation sequencing. (B, C) Pathway enrichment analysis of differentially expressed genes between p38α^{MCK-KO}, p38α/γ^{MCK-KO} and MCK-Cre mice. (B) Top 5 selected significantly enriched pathways shown by Ingenuity Pathway Analysis (IPA) derived through comparison of genes differentially expressed between MCK-Cre and p38α^{MCK-KO} mice. (C) Top 5 significantly enriched pathways shown by IPA derived through comparison of genes differentially expressed between MCK-Cre and p38α/γ^{MCK-KO} mice. TREM1, Triggering receptor expressed on myeloid cells 1; CTL, Cytotoxic T lymphocyte; TNFR1, Tumor necrosis factor receptor 1; TWEAK, Tumor necrosis factor-like weak inducer of apoptosis; he-NK, Hepatic-Natural Killer. (D, E) Gene set enrichment plots of HALLMARK oxidative phosphorylation when comparing p38α^{MCK-KO} (D) or p38α/γ^{MCK-KO} (E) mice versus MCK-Cre controls. Hash marks represent positions in the ranked list corresponding to members of oxidative phosphorylation HALLMARK gene set. NES indicates whether

these members are enriched towards the upregulated end of this list (positive NES) or downregulated end of this list (negative NES) as compared to chance expectation. *n* = 3.

According to the metabolic changes observed in p38α-deficient muscles, the key metabolic regulator PGC1α (Handschin & Spiegelman, 2006) appeared as one of the upstream regulators in the proteomics analysis from gastrocnemius muscles of p38α^{MCK-KO} mice (*p*-value < 0.001). In fact, some known PGC1α targets (Choi et al., 2008; Handschin et al., 2007b) were upregulated in p38α-deficient gastrocnemius (Figure R13A). Thus, we checked PGC1α mRNA expression, which was increased in skeletal muscles from p38α^{MCK-KO} mice, but also in p38α/γ^{MCK-KO} mice (Figure R13B). Since PGC1β also upregulates mitochondrial proteins (Islam et al., 2020), we checked its expression in skeletal muscle. Interestingly, neither PGC1β mRNA expression nor total protein levels were altered in muscles from p38α^{MCK-KO} and p38α/γ^{MCK-KO} mice (Figures R13C, D). To further verify the relevant role of PGC1α in the gene expression of p38α-deficient muscles, we performed a deeper analysis comparing the gene expression-based signatures of gastrocnemius from mice overexpressing PGC1α in striated muscle ("PGC1α muscle"; MCK-PGC1α transgenic mouse) (Lin et al., 2002) or the MS-based signatures of PGC1α-overexpressing myotubes ("PGC1α myotubes") with our RNA-seq data (see Appendix I). Results revealed that *in vivo* PGC1α signature (upregulated genes) was significantly enriched in gastrocnemius from both p38α^{MCK-KO} (Figure R13E) and p38α/γ^{MCK-KO} (Figure R13F) compared to MCK-Cre mice, as also occurred with *in vitro* PGC1α signature (Figures R13E, F). These results suggest that PGC1α is responsible for the metabolic alterations of p38α-deficient muscles and that although p38γ has been described as a regulator of PGC1α (Pogozelski et al., 2009), the absence of p38α, but not the hyperactivation of p38γ, is responsible for the increase in PGC1α expression. These results indicate that p38γ hyperactivation is not responsible for changes in oxidative phosphorylation in mice lacking p38α in striated muscle, and it foresees the existence of a different inhibitory mechanism of p38α over PGC1α.

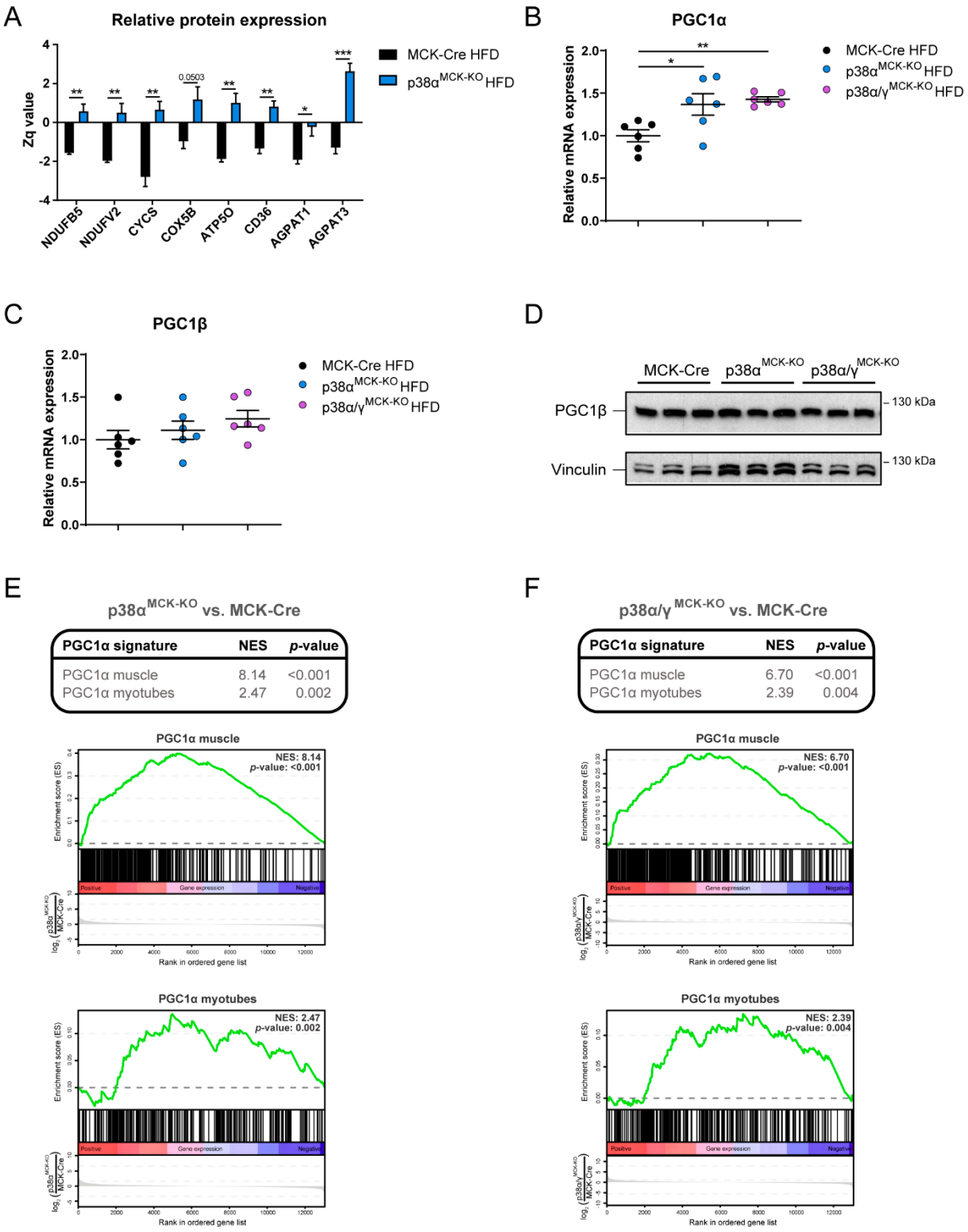

Figure R13. p38α-deficient skeletal muscles show increased PGC1α expression under HFD. (A) p38α^{MCK-KO} and MCK-Cre mice were fed a HFD for 14 weeks, fasted overnight and sacrificed. Relative protein expression of known PGC1α targets in quantitative proteomics analysis of gastrocnemius samples is shown. Zq values represent units of standard deviation according to the estimated variances. Data are shown as means ± SEM; *p < 0.05; **p < 0.01; ***p < 0.001; Student's t-test; n = 4-5. NDUFB5, NADH dehydrogenase (ubiquinone) 1 beta subcomplex subunit 5; NDUFV2, NADH dehydrogenase (ubiquinone) flavoprotein 2; CYCS, Cytochrome c; COX5B, Cytochrome c oxidase subunit 5B; ATP5O,

ATP synthase subunit O; CD36, Cluster of differentiation 36; AGPAT1, 1-acylglycerol-3-phosphate O-acyltransferase 1; AGPAT3, 1-acylglycerol-3-phosphate O-acyltransferase 3. (B-D) p38α^{MCK-KO}, p38α/γ^{MCK-KO} and MCK-Cre mice were fed a HFD for 6 weeks, fasted overnight and sacrificed. qRT-PCR analysis of *Ppargc1a* (PGC1α) (B) and *Ppargc1b* (PGC1β) (C) genes in gastrocnemius samples is shown. mRNA expression was normalized to the amount of *Rps18* mRNA in each sample. Data are normalized to MCK-Cre mice and shown as means ± SEM; **p* < 0.05; ***p* < 0.01; one-way ANOVA coupled to Bonferroni's multiple comparisons test; *n* = 6. (D) Immunoblot analysis of PGC1β in gastrocnemius. Vinculin protein expression was monitored as a loading control. *n* = 3. (E, F) p38α^{MCK-KO}, p38α/γ^{MCK-KO} and MCK-Cre mice were fed a HFD for 6 weeks, fasted overnight and sacrificed, and an RNA-seq analysis with gastrocnemius samples was performed. Gene set enrichment plots and quantification are shown. Genes detected in RNA-seq of gastrocnemius were ranked based on the relative amount in p38α^{MCK-KO} versus MCK-Cre (E), or p38α/γ^{MCK-KO} versus MCK-Cre mice (F). A comparison was done between these RNA-seq data and the signature of upregulated genes in gastrocnemius of PGC1α transgenic mice (PGC1α muscle) or the signature of upregulated proteins in myotubes overexpressing PGC1α (PGC1α myotubes) obtained by MS. The first ranked gene is the most upregulated in p38α^{MCK-KO} muscle (E) or p38α/γ^{MCK-KO} muscle (F) (log2 scale). Hash marks represent positions in the ranked list corresponding to members of a given gene/protein set. The normalized enrichment score (NES) indicates whether these members are enriched towards the upregulated end of this list (positive NES) or downregulated end of this list (negative NES) as compared to the chance expectation. Up: PGC1α muscle gene set contains genes upregulated > 2-fold in MCK-PGC1α transgenic mice. Down: PGC1α myotubes protein set contains proteins up-regulated > 1.4-fold in PGC1α-overexpressing myotubes.

Since PGC1α is widely known as the master regulator of mitochondrial biogenesis and many mitochondrial pathways were altered in muscle p38α-deficient mice, we decided to check mitochondria in skeletal muscles from HFD-fed mice. Transmission electron microscopy images revealed increased individual mitochondrial area in gastrocnemius from p38α^{MCK-KO} mice (Figures R14A, B). Similar results were found in p38α/γ^{MCK-KO} mice, further corroborating that this mitochondrial phenotype was not dependent on p38γ (Figures R14A, B). To verify that the increase in mitochondrial area was dependent on PGC1α protein, we used muscles from mice lacking both p38α and PGC1α in striated muscle, which showed a reduction in mitochondrial area compared to muscles from p38α^{MCK-KO} and p38α/γ^{MCK-KO} mice (Figures R14A, B). In addition, a higher number of lipid droplets was found in p38α- and p38α/γ-deficient muscles, but only when PGC1α was present (Figures R14A, C). Indeed, increased levels of proteins involved in fatty acid uptake and reesterification, such as cluster of differentiation 36 (CD36) and 1-acylglycerol-3-phosphate O-acyltransferases 1 (AGPAT1) and 3 (AGPAT3), were previously found in muscles from p38α^{MCK-KO} mice (Figure R13A), being a possible explanation for the increase in intramyocellular fat, as previously described (Choi et al., 2008). Moreover, some genes found to be upregulated in gastrocnemius from p38α^{MCK-KO} mice compared to MCK-Cre mice were decreased in p38α/PGC1α^{MCK-KO} mice related to controls (Figure R14D-E). These results indicat that PGC1α is a relevant factor for the mitochondrial phenotype observed in p38α-deficient muscles.

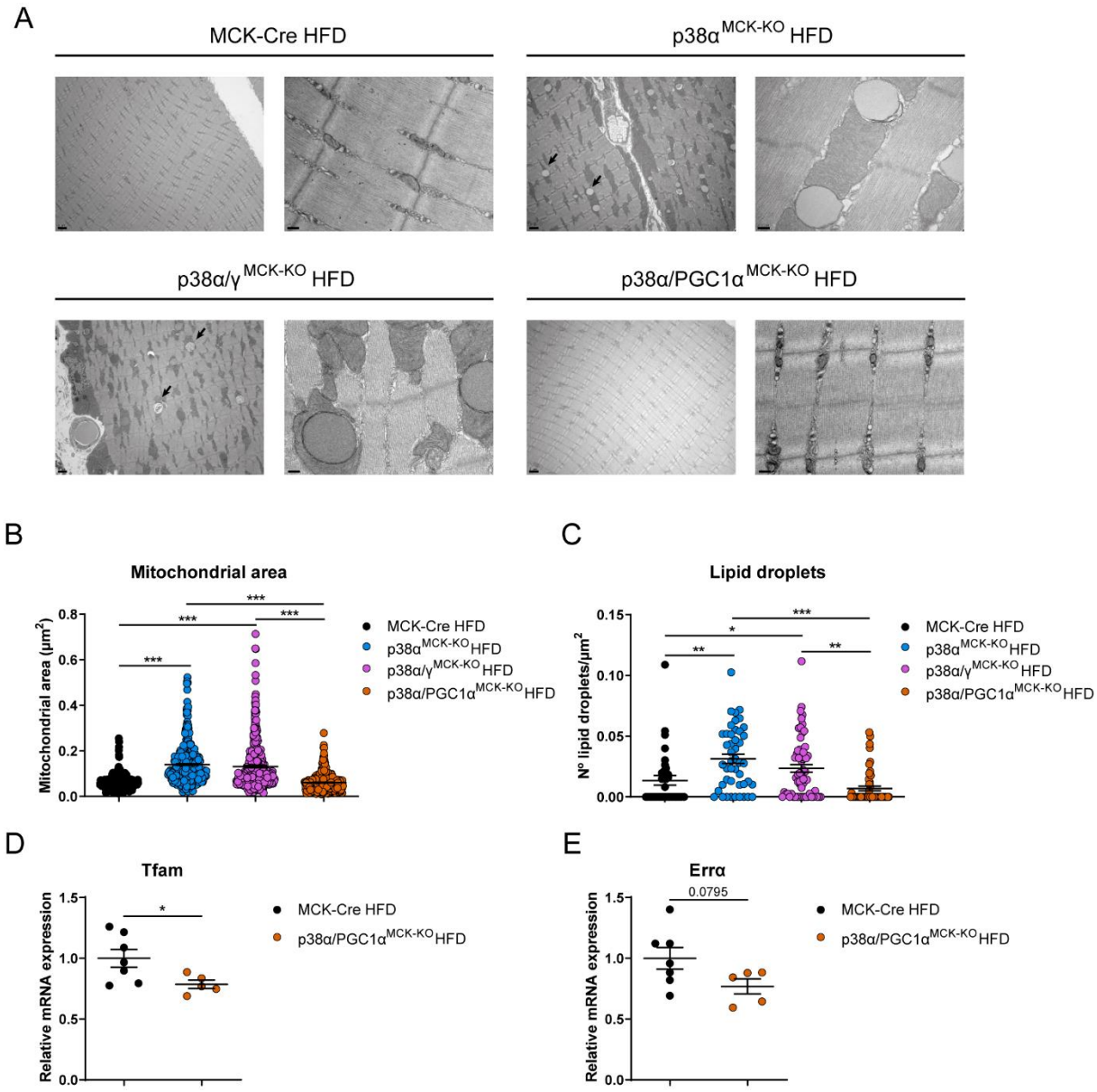

Figure R14. Lack of p38α in skeletal muscle increases mitochondrial area and the number of lipid droplets. MCK-Cre, p38α^{MCK-KO}, p38α/γ^{MCK-KO} and p38α/PGC1α^{MCK-KO} mice were fed a HFD for 21 weeks, fasted overnight and sacrificed. (A) Representative transmission electron microscopy images of mitochondria in gastrocnemius muscle from MCK-Cre, p38α^{MCK-KO}, p38α/γ^{MCK-KO} and p38α/PGC1α^{MCK-KO} mice. Low magnification (*left* in each genotype): 7,500x; scale bars, 1 μm. High magnification (*right* in each genotype): 50,000x; scale bars, 0.2 μm. Arrows: lipid droplets. (B) Individual mitochondrial area. The area of 100 intermiofibrillar mitochondria from 10 randomly distributed areas per mouse was measured. (C) Total number of lipid droplets per area of gastrocnemius muscle, counted in at least 9 random and separated view fields per muscle. For B and C, data are shown as means ± SEM; **p* < 0.05; ***p* < 0.01; ****p* < 0.001; one-way ANOVA coupled to Bonferroni's multiple comparisons test; *n* = 4. (D, E) qRT-PCR analysis of *Tfam* (mitochondrial transcription factor A) and *Esrra* (estrogen-related receptor alpha, Errα) genes in gastrocnemius samples. mRNA expression was normalized to the amount of *Rps18* mRNA in each sample. Data are normalized to MCK-Cre mice and shown as means ± SEM; **p* < 0.05; Student's *t*-test; *n* = 5-7.

A deeper analysis of proteins from mitochondrial electron transport chain revealed that 39 subunits in mitochondrial complex I (CI: NADH dehydrogenase), 4 in complex II (CII: succinate dehydrogenase), 9 in complex III (CIII: ubiquinol-cytochrome c reductase), 13 in complex IV (CIV: cytochrome c oxidase) and 14 in complex V (CV: ATP synthase) were detected in the muscle proteome, being a good coverage across the electron transport system. The majority of them were increased in muscles from p38α^{MCK-KO} mice, being statistically significant in 58.97% of the subunits in CI, 100% in CII, 55.56% in CIII, 38.46% in CIV and 71.43% in CV (Figure R15). However, there was a clear tendency towards increased expression in p38α^{MCK-KO} mice where no significant changes were detected. This suggested conserved stoichiometry of respiratory subunits.

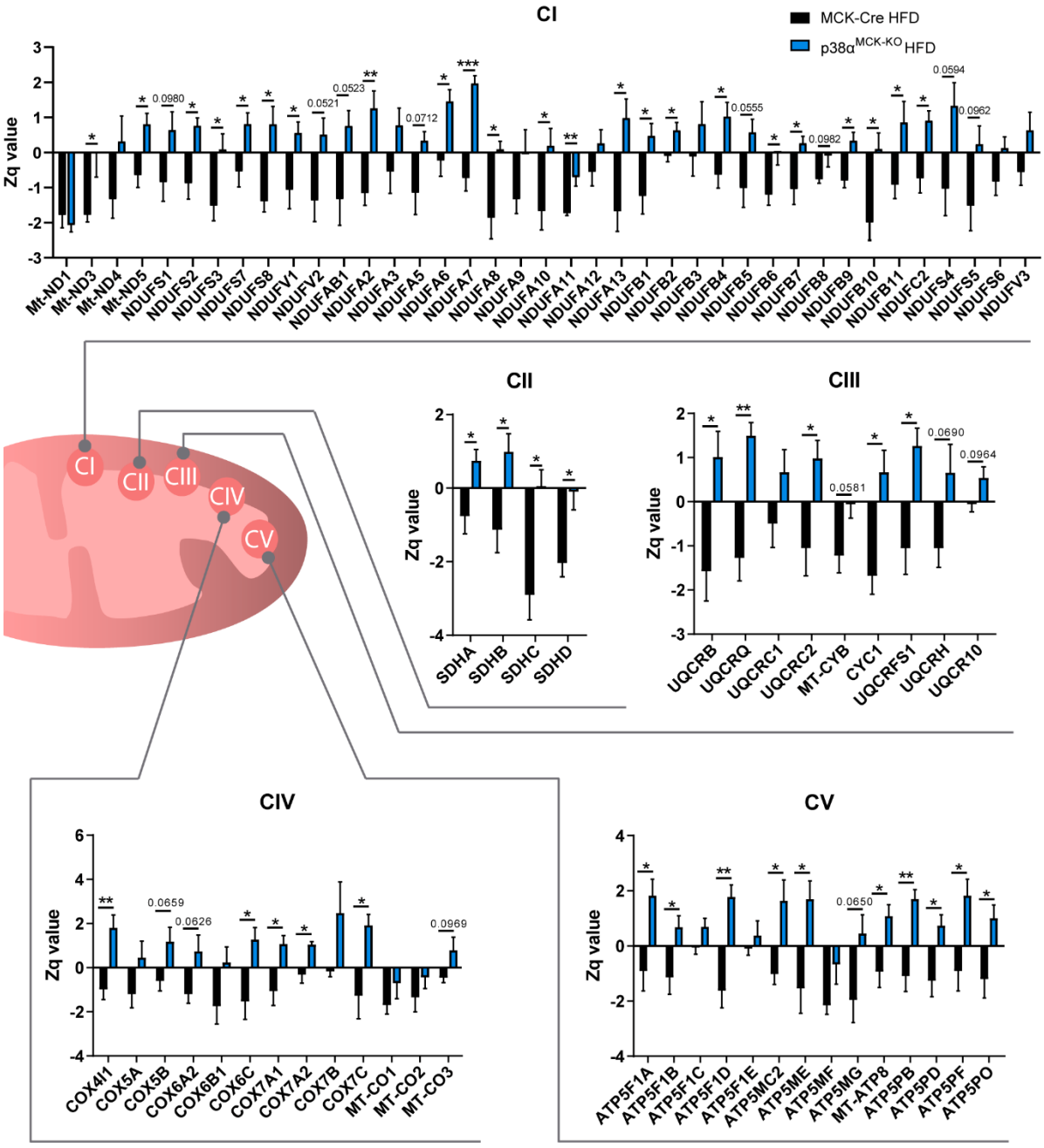

Figure R15. Lack of p38α in skeletal muscle upregulates subunits of mitochondrial electron transport chain. p38α^{MCK-KO} and MCK-Cre mice were fed a HFD for 14 weeks, fasted overnight and sacrificed. A quantitative proteomics analysis with gastrocnemius samples was performed. An analysis of subunits of NADH dehydrogenase (CI), succinate dehydrogenase (CII), ubiquinol-cytochrome c reductase (CIII), cytochrome c oxidase (CIV), and ATP synthase (CV) is represented. Zq values represent units of standard deviation according to the estimated variances. Data are shown as means ± SEM; **p* < 0.05; ***p* < 0.01; ****p* < 0.001; Student's *t*-test; *n* = 4-5.

1.9. p38α and p38γ control PGC1α in myotubes in a differential manner

p38s have been described to control PGC1α expression and activity (Fan et al., 2004; Pogozelski et al., 2009; Puigserver et al., 2001). To determine the effects of p38α or p38γ on PGC1α, we transfected HEK-293 cells with PGC1α alone or in combination with the constitutively active p38s (α, β, γ, δ). PGC1α phosphorylation was increased in HEK-293 cells when any of p38s were overexpressed, but it was higher in the case of p38γ (Figure R16A). To further understand the regulation of PGC1α by p38α and p38γ in skeletal muscle, we transduced myotubes differentiated from primary myoblasts with recombinant adenoviruses expressing GFP, PGC1α, or the constitutively active kinases p38α or p38γ, and we used tandem mass spectrometry after isobaric peptide tagging to compare protein abundance in the different conditions (Figure R16B). We first checked that the *in vitro* model was suitable, since a good overexpression of PGC1α and the p38 isoforms was achieved (Figures R16C, D). Interestingly, p38γ increased while p38α decreased MKK6 protein and mRNA levels (Figures R16E, F), which may indicate similarities between our *in vitro* e *in vivo* models (Figures R11H, J).

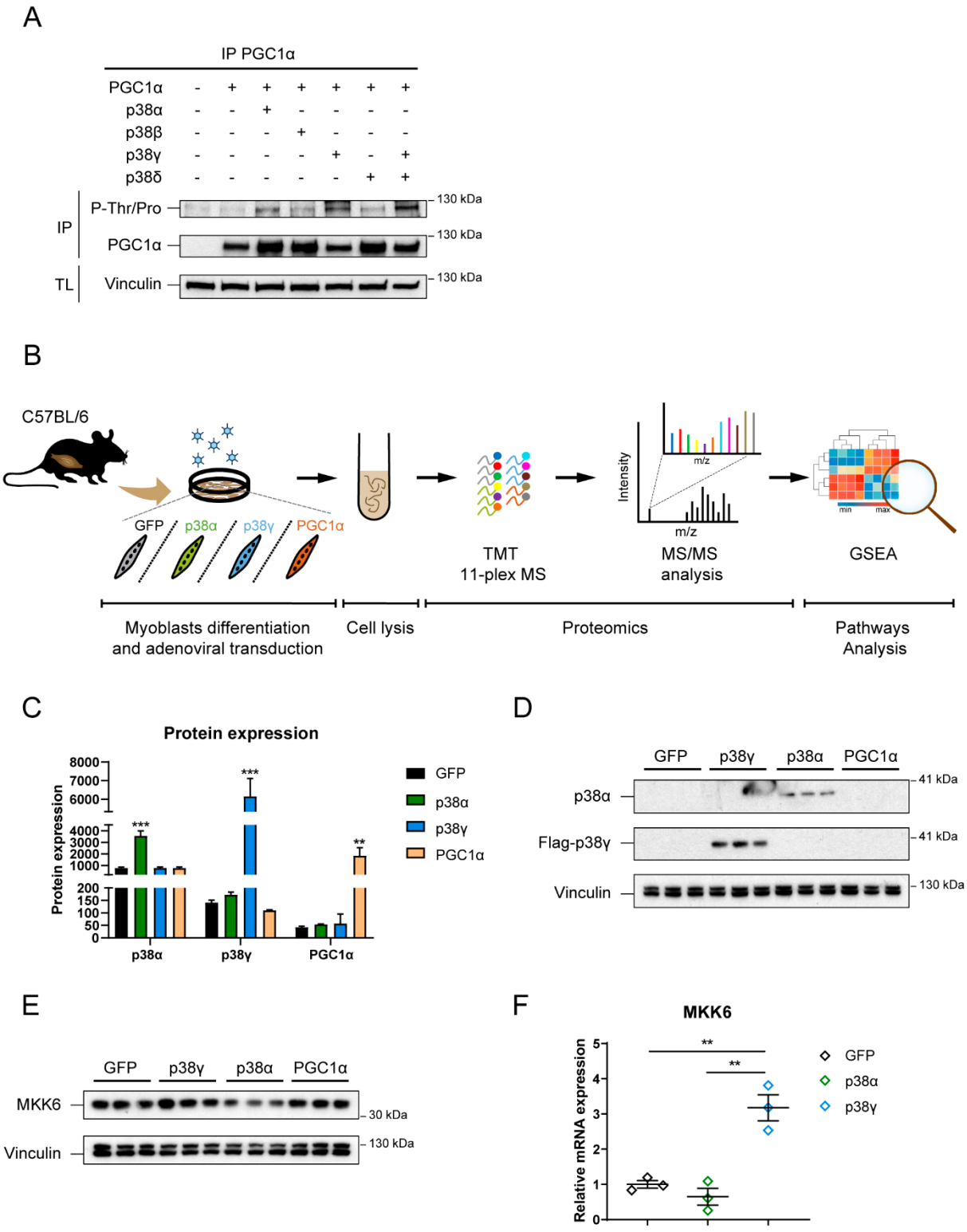

Figure R16. *In vitro* models to study the regulation of PGC1α by p38s. (A) HEK-293 cells were transfected with PGC1α either alone or in combination with any of the different active p38 family members (α, β, γ, δ, or γ plus δ). Extracts prepared from these cells were immunoprecipitated with an antibody targeting PGC1α, and immunoblots were probed with antibodies against phospho (P)-Thr/Pro and PGC1α. Vinculin was monitored as a loading control. *n* = 1. IP, immunoprecipitation; TL, total lysate. (B-F) Mouse primary myoblasts were differentiated and transduced with adenoviruses overexpressing GFP, PGC1α or the active forms of p38α or p38γ, and harvested 48 h later after 10 h of

serum starvation. The cells were processed to perform proteomics experiments. (B) Schematic representation of the proteomics experimental layout. Protein lysates of infected myotubes were labeled with isobaric tags and subjected to tandem mass spectrometry (MS/MS). *n* = 2-3. (C) Protein expression of overexpressed p38α, p38γ and PGC1α proteins quantified by MS (absolute values). Data are shown as means ± SEM; $^{**}p < 0.01$; $^{***}p < 0.001$, indicating significant differences among the indicated myotubes and all the other conditions; one-way ANOVA coupled to Bonferroni's multiple comparisons test; *n* = 2-3. (D) Confirmation of the overexpression of p38α and Flag-tagged p38γ. Extracts prepared from myotubes were examined by immunoblot analysis with antibodies against Flag-tag, p38α and vinculin. *n* = 3. (E) Immunoblot analysis of MKK6 in myotubes. Vinculin protein expression was monitored as a loading control. *n* = 3. (F) qRT-PCR analysis of *Map2k6* (MKK6) gene in myotubes. mRNA expression was normalized to the amount of *Tbp* mRNA in each sample. Data are normalized to GFP and shown as means ± SEM; $^{**}p < 0.01$; one-way ANOVA coupled to Bonferroni's multiple comparisons test; *n* = 3.

As expected, GSEA showed that oxidative phosphorylation was the topmost upregulated pathway in PGC1α-overexpressing myotubes (Figure R17A). The topmost significantly enriched pathway in myotubes transduced with p38α compared to other conditions was myogenesis (Figure R17B), which was found as one of the most downregulated ones in p38γ-overexpressing cells (Figure R17C). This confirmed the role of both kinases in promoting and inhibiting myoblasts differentiation, respectively (Lluís et al., 2006; Lovett et al., 2010). Importantly, oxidative phosphorylation was significantly depressed in myotubes transduced with active p38α or p38γ in comparison with GFP (Figures R17B, C). To obtain maximum distinctions between p38γ and p38α, we computed the fold change for each protein in p38γ-overexpressing cells as compared to p38α-overexpressing ones. GSEA revealed that p38α signaling was substantially more associated with myogenesis-related protein expression, whereas p38γ signaling was more associated with oxidative phosphorylation (Figure R17D). This suggests that the negative impact of p38 family members on the oxidative phosphorylation downstream pathway controlled by PGC1α is higher in the case of p38α than of p38γ.

A

PGC1α vs. GFP
HALLMARK pathways

Pathway	NES	*p*-value
Oxidative phosphorylation	4.90	<0.001
Adipogenesis	2.17	0.037
Inflammatory response	-2.22	0.026
G2M checkpoint	-2.10	0.055

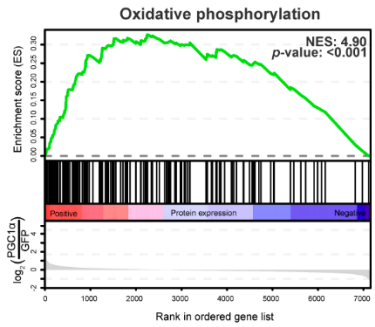

B

p38α vs. GFP
HALLMARK pathways

Pathway	NES	*p*-value
Myogenesis	3.29	<0.001
E2F targets	2.29	0.020
DNA repair	2.23	0.031
MYC targets V1	2.18	0.048
Xenobiotic metabolism	-2.39	0.006
Oxidative phosphorylation	-2.37	0.006
Protein secretion	-2.23	0.030
Bile acid metabolism	-2.23	0.030

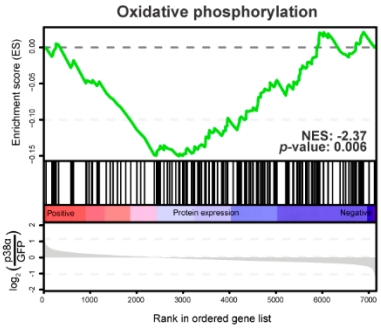

C

p38γ vs. GFP
HALLMARK pathways

Pathway	NES	*p*-value
MYC targets V1	4.38	<0.001
DNA repair	2.37	0.012
E2F targets	2.22	0.023
EMT	-3.20	<0.001
Myogenesis	-3.11	<0.001
Cholesterol homeostasis	-2.72	<0.001
Protein secretion	-2.43	0.007
Estrogen response early	-2.38	0.010
Estrogen response late	-2.38	0.010
Bile acid metabolism	-2.32	0.015
Fatty acid metabolism	-2.31	0.015
Xenobiotic metabolism	-2.30	0.018
Oxidative phosphorylation	-2.26	0.024
Inflammatory response	-2.20	0.040
Adipogenesis	-2.04	0.088

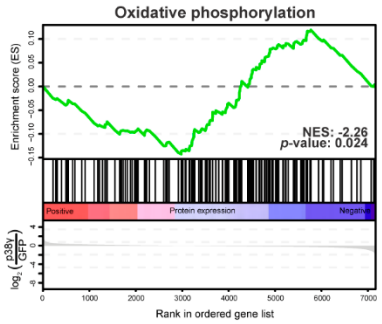

D

p38γ vs. p38α
HALLMARK pathways

Pathway	NES	*p*-value
MYC targets V1	2.82	0.002
Oxidative phosphorylation	2.80	0.002
Myogenesis	-5.91	<0.001
EMT	-3.81	<0.001
Cholesterol homeostasis	-2.78	<0.001
Coagulation	-2.57	<0.001
Fatty acid metabolism	-2.41	0.004
Estrogen response late	-2.22	0.021
UV response DN	-2.12	0.045

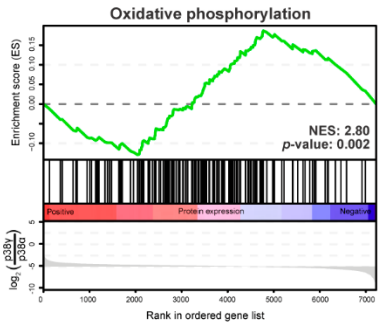

Figure R17. p38α and p38γ decrease oxidative phosphorylation pathway in myotubes. Mouse primary myoblasts were differentiated and transduced with adenoviruses overexpressing the active forms of p38α or p38γ and harvested 48 h later after 10 h of serum starvation. Cells were processed to perform proteomics experiments. MS analysis and gene set enrichment plots of HALLMARK oxidative phosphorylation of GFP-, PGC1α-, p38α- or p38γ-overexpressing myotubes are shown. Proteins

detected in MS were ranked based on relative amount in myotubes overexpressing PGC1α, p38α or p38γ versus GFP (A-C) or p38γ versus p38α (D), with the first ranked protein corresponding to the protein most upregulated in the first condition (log2 scale). Gene set enrichment analysis was used to determine whether any HALLMARK gene sets were enriched among proteins upregulated in myotubes overexpressing PGC1α (A), p38α (B) or p38γ (C) compared with GFP controls, or in p38γ compared with p38α (D). All gene sets enriched with an absolute value of normalized enrichment score (NES) greater than 2 are shown. Hash marks represent positions in the ranked list corresponding to members of oxidative phosphorylation HALLMARK gene set. NES indicates whether these members are enriched towards the upregulated end of this list (positive NES) or downregulated end of this list (negative NES) as compared to chance expectation. *n* = 2-3. E2F, eukaryotic transcription factor 2; EMT, epithelial-mesenchymal transition.

Surprisingly, qPCR analyses indicated that both p38 family members induce the mRNA expression of PGC1α-isoform a (PGC1α-a) and PGC1α-isoform b (PGC1α-b) in myotubes (Figure R18A). However, PGC1α protein expression was diminished in p38α- and p38γ-overexpressing myotubes (Figure R18B), indicating that the increase in PGC1α mRNA expression could be a compensatory mechanism for the downregulation of its protein levels, or that both p38α and p38γ exert a positive effect on PGC1α at the transcriptional level, but a negative effect at the posttranscriptional regulation. In contrast to p38α, p38γ increased PGC1α phosphorylation as compared to GFP controls, as shown by immunoprecipitation and Phos-Tag gels (Figures R18C, D). However, PGC1β phosphorylation (Figure R18E) or total protein levels (Figure R18F) were not altered when p38α or p38γ were overexpressed. Altogether, these results suggest that both p38 family members have a negative impact on PGC1α protein levels, albeit higher PGC1α phosphorylation is achieved with p38γ.

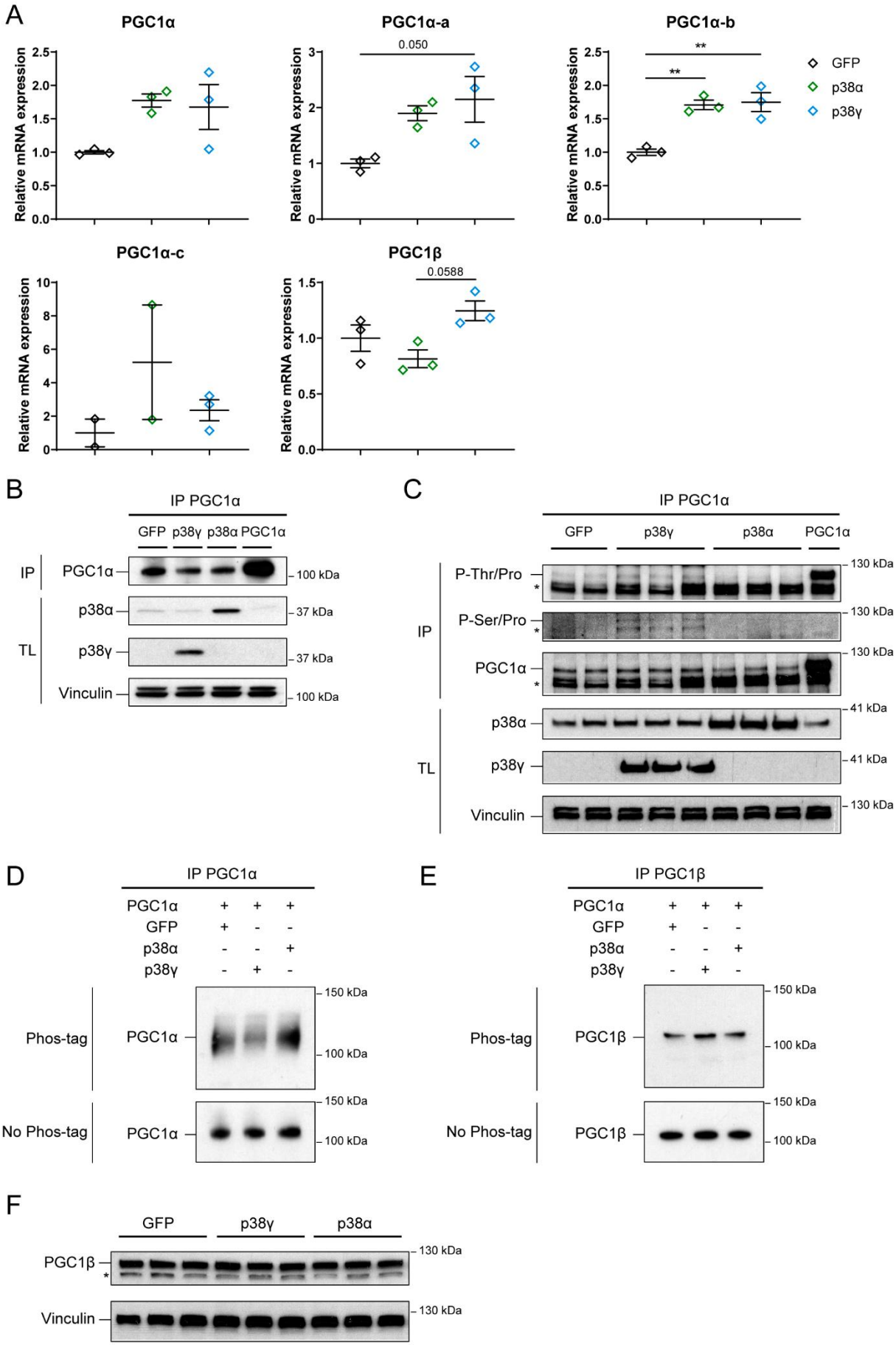
A
PGC1α
PGC1α-a
PGC1α-b
PGC1α-c
PGC1β
Relative mRNA expression
0.050
**
**
0.0588
GFP
p38α
p38γ
B
IP PGC1α
GFP p38γ p38α PGC1α
IP
TL
PGC1α
p38α
p38γ
Vinculin
100 kDa
37 kDa
C
IP PGC1α
GFP p38γ p38α PGC1α
P-Thr/Pro
P-Ser/Pro
PGC1α
p38α
p38γ
Vinculin
130 kDa
41 kDa
D
IP PGC1α
PGC1α + + +
GFP + - -
p38α - - +
p38γ - + -
Phos-tag
No Phos-tag
PGC1α
150 kDa
100 kDa
E
IP PGC1β
PGC1α + + +
GFP + - -
p38α - - +
p38γ - + -
Phos-tag
No Phos-tag
PGC1β
150 kDa
100 kDa
F
GFP p38γ p38α
PGC1β
Vinculin
130 kDa

Figure R18. p38α and p38γ increase PGC1α mRNA but decrease PGC1α protein levels in myotubes. Mouse primary myoblasts were differentiated and transduced with adenoviruses overexpressing GFP, PGC1α or the active forms of p38α or p38γ, and harvested 48 h later after 9 h of serum starvation. (A) qRT-PCR analysis of *Ppargc1a* (PGC1α), *Ppargc1b* (PGC1β) and PGC1α variants genes in myotubes samples. mRNA expression was normalized to the amount of *Tbp* mRNA in each sample. Data are normalized to GFP-overexpressing myotubes and shown as means ± SEM; ***p* < 0.01; one-way ANOVA coupled to Bonferroni's multiple comparisons test; *n* = 2-3. PGC1α-a, PGC1α-isoform a; PGC1α-b, PGC1α-isoform b; PGC1α-c, PGC1α-isoform c. (B, C) Extracts prepared from myotubes were immunoprecipitated with an antibody targeting PGC1α. Immunoblots were probed with the indicated antibodies. *n* = 3. IP, immunoprecipitation; TL, total lysate. * indicates non-specific bands. (D, E) Extracts prepared from myotubes were immunoprecipitated with an antibody targeting PGC1α (D) or PGC1β (E), and samples were loaded on a Phos-tag gel to check their phosphorylation. *n* = 1. (F) Immunoblot analysis of PGC1β in myotubes. Vinculin protein expression was monitored as a loading control. *n* = 3. * indicates non-specific band.

1.10. PGC1α upregulation in p38α-deficient muscles improves muscle strength

Increased oxidative metabolism (Jeong et al., 2019) and altered mitochondrial dynamics (Moore et al., 2019) have been linked to improved grip strength. According to this, muscle strength was increased in p38α^{MCK-KO} and p38α/γ^{MCK-KO} mice compared to controls (Figure R19A). To check whether PGC1α could be responsible for the improvement in muscle strength, we repeated this test with p38α/PGC1α^{MCK-KO} mice, observing no differences between MCK-Cre and p38α/PGC1α^{MCK-KO} mice, in contrast to p38α^{MCK-KO} or p38α/γ^{MCK-KO} mice (Figure R19B). These findings suggest that PGC1α and increased mitochondrial oxidative metabolism in p38α-deficient muscles are responsible for their higher strength.

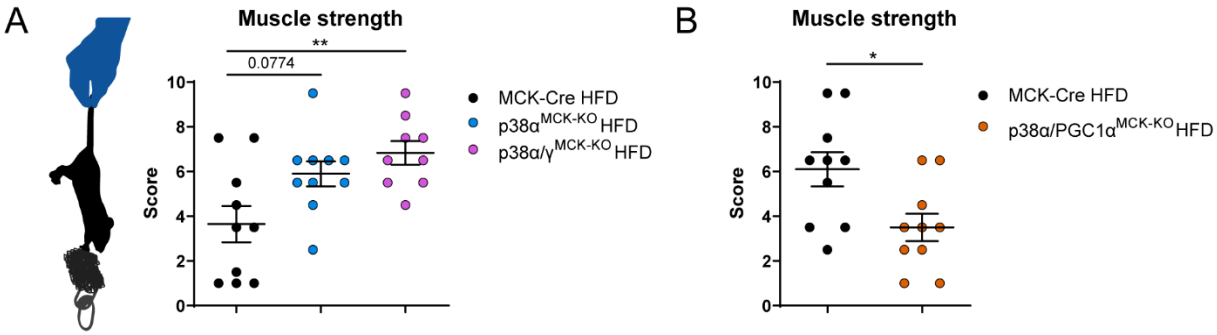

Figure R19. *In vivo* assessment of muscle strength. (A) p38α/γ^{MCK-KO}, p38α^{MCK-KO} and MCK-Cre mice were fed a HFD for 3 weeks, and muscle strength test was performed. A representation of the experimental procedure is shown: forelimb muscle strength is tested by allowing the mouse to grasp a wire scale collector attached to steel chain links as it is being hold by the tail. The mouse is hold steadily until it holds each weight for 3 s. The score is calculated based on the heaviest chain held. Data are shown as means ± SEM; ***p* < 0.01; Kruskal-Wallis test; *n* = 9-10. (B) p38α/PGC1α^{MCK-KO} and MCK-Cre mice were fed a HFD for 8 weeks, and muscle strength test was performed. Data are shown as means ± SEM; **p* < 0.05; Mann-Whitney test; *n* = 10.

Fiber type profile in skeletal muscle is associated with different metabolic characteristics, from a more oxidative metabolism in slow-twitch fibers (type I) to a more glycolytic one in fast-twitch fibers (type II) (Egan & Zierath, 2013). Importantly, PGC1α is thought to increase oxidative

muscle fibers and improve muscle endurance capacity (Handschin et al., 2007a; Lin et al., 2002), and MAPKs are also known to promote fiber type transformation (Boyer et al., 2019; Schiaffino & Reggiani, 2011). In order to check whether improved muscle strength in p38α-deficient muscles could be due to possible alterations in fiber type composition caused by PGC1α upregulation, we performed histological analyses in soleus muscles. Muscles lacking p38α had a tendency towards increased type IIA and decreased type I proportion of fibers compared with MCK-Cre controls, while no differences were observed between muscles of p38α^{MCK-KO} and p38α/PGC1α^{MCK-KO} mice (Figure R20). Conversely, muscles lacking both p38α and p38γ increased type I fibers while decreased type IIA, showing opposite fiber type proportion compared with the absence of p38α alone (Figure R20). These results suggest that increased muscle strength of muscles lacking p38α is caused by PGC1α upregulation independently of changes in fiber type composition.

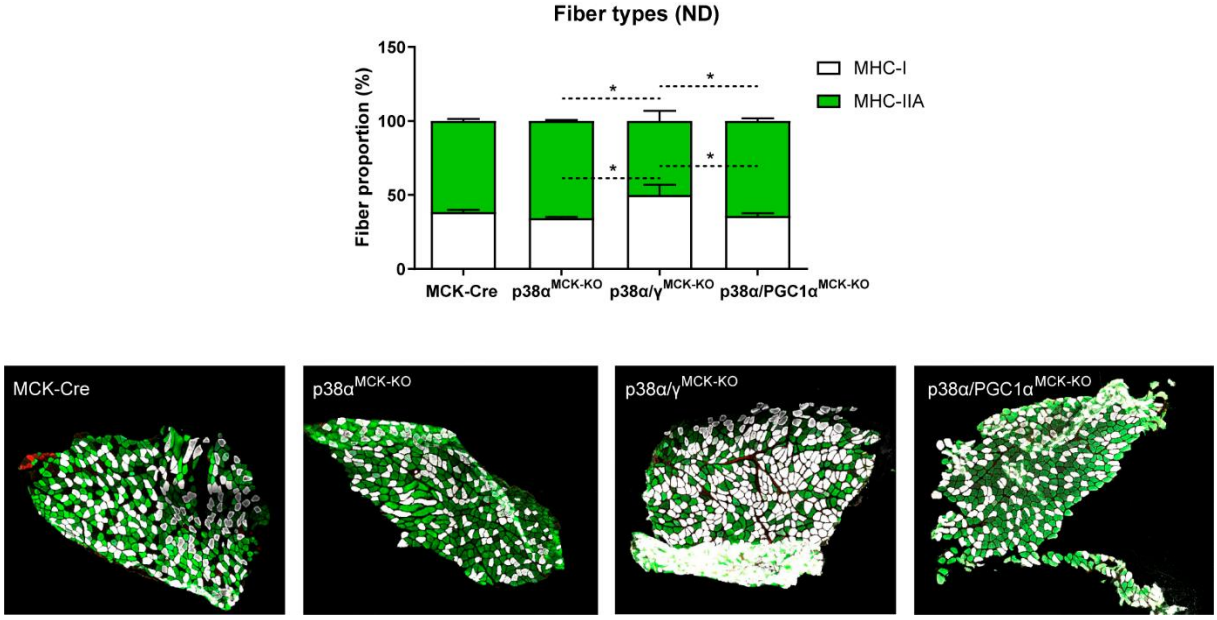

Figure R20. Muscles from p38α^{MCK-KO} and p38α/γ^{MCK-KO} mice show different fiber type profile. p38α^{MCK-KO}, p38α/γ^{MCK-KO}, p38α/PGC1α^{MCK-KO} and MCK-Cre mice were fed a ND, fasted overnight and sacrificed at 11-12 weeks of age. Immunofluorescence for fiber types staining in soleus muscle was performed. Quantification of the proportion of the different fiber types and representative immunofluorescence images are shown. Type I (white), type IIA (green) fibers. Data are shown as means ± SEM; *p < 0.05; one-way ANOVA coupled to Bonferroni's multiple comparisons test; n = 3-4. MHC, myosin heavy chain.

1.11. PGC1α does not control the locomotor activity-associated phenotype of p38α^{MCK-KO} mice

Muscle PGC1α has been described to control glucose and energy homeostasis (Handschin et al., 2007b), as well as exercise performance (Calvo et al., 2008). To decipher if higher PGC1α expression in p38α-deficient muscles could play a role in their protection against obesity,

p38α/PGC1α^{MCK-KO} mice were fed a HFD. There were no differences between p38α^{MCK-KO} and p38α/PGC1α^{MCK-KO} mice regarding body weight in HFD (Figures R21A, B), as well as in the weight of several organs, including muscle, liver and fat (Figure R21C).

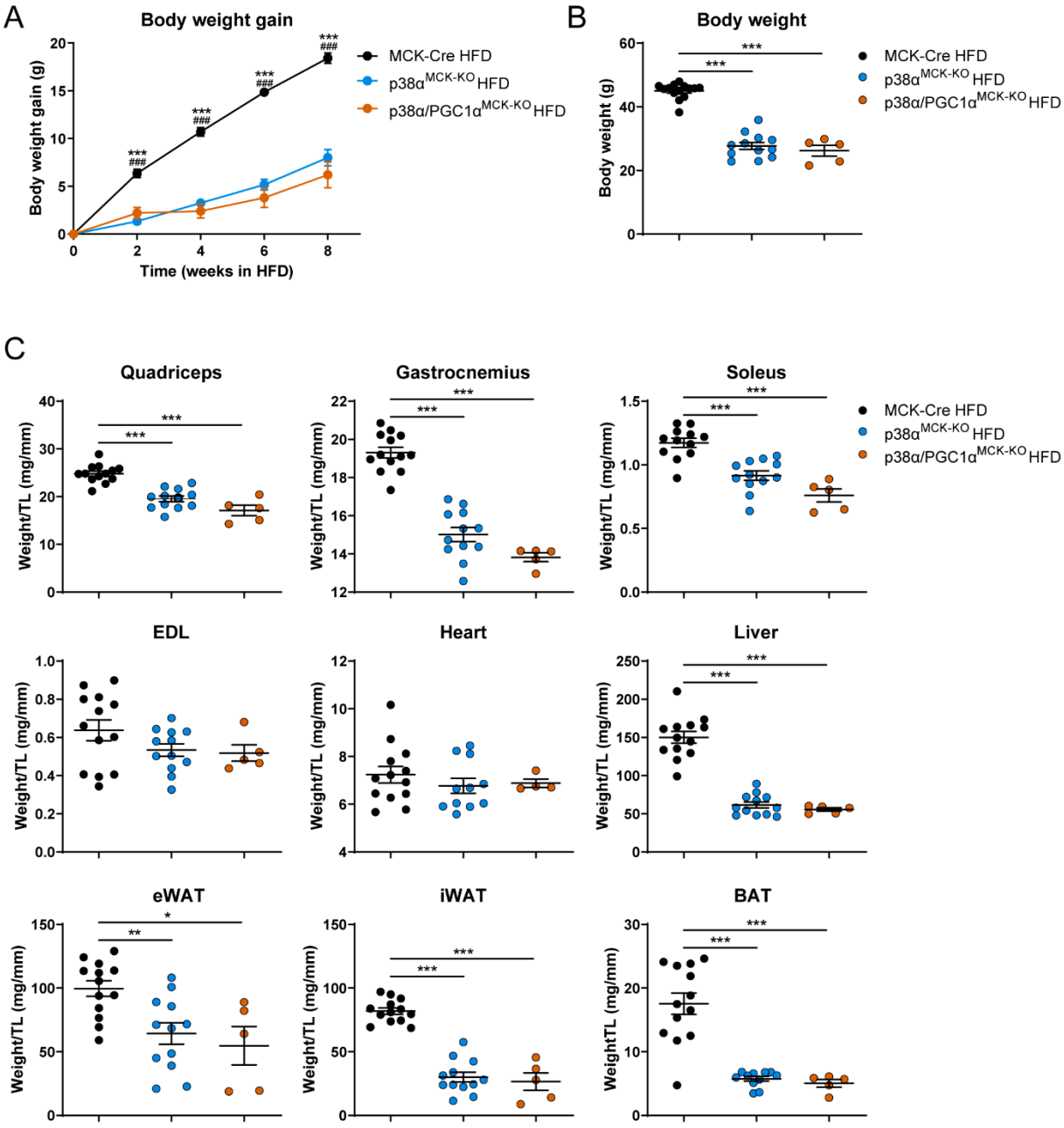

Figure R21. HFD-fed p38α/PGC1α^{MCK-KO} mice are protected against HFD-induced obesity. p38α^{MCK-KO}, p38α/PGC1α^{MCK-KO} and MCK-Cre mice were fed a HFD for 10 weeks. (A) Body weight gain measured at the indicated times during HFD treatment. (B) Body weight measured at sacrifice. (C) Relative weight of organs at sacrifice (measurements standardized to tibial length). Data are shown as means ± SEM; *p < 0.05; **p < 0.01; *** or $^{\#\#\#}p$ < 0.001; one-way (Figures B, C) or two-way ANOVA (body weight gain) coupled to Bonferroni's multiple comparisons test. n = 5-13. * symbols depict significant differences between p38α^{MCK-KO} and MCK-Cre mice, while $^{\#}$ symbols indicate significant differences between p38α/PGC1α^{MCK-KO} and MCK-Cre mice unless otherwise indicated. TL, tibia length; EDL, extensor digitorum longus; eWAT, epididymal white adipose tissue; iWAT, inguinal white adipose tissue; BAT, brown adipose tissue.

In concordance with body weight, energy expenditure was similarly increased in both knockout genotypes compared to MCK-Cre controls (Figure R22A), with no changes in RQ (Figure R22B). Locomotor activity was also higher in p38α/PGC1α^{MCK-KO} compared to MCK-Cre and p38α^{MCK-KO} mice (Figure R22C), while body or interscapular temperature did not differ between genotypes (Figures R22D, E). In addition, p38α/PGC1α^{MCK-KO} mice showed no differences in glucose homeostasis compared to p38α^{MCK-KO} mice, meaning that the effect of muscle p38α on whole-body homeostasis was not dependent on muscle PGC1α (Figures R22F-H).

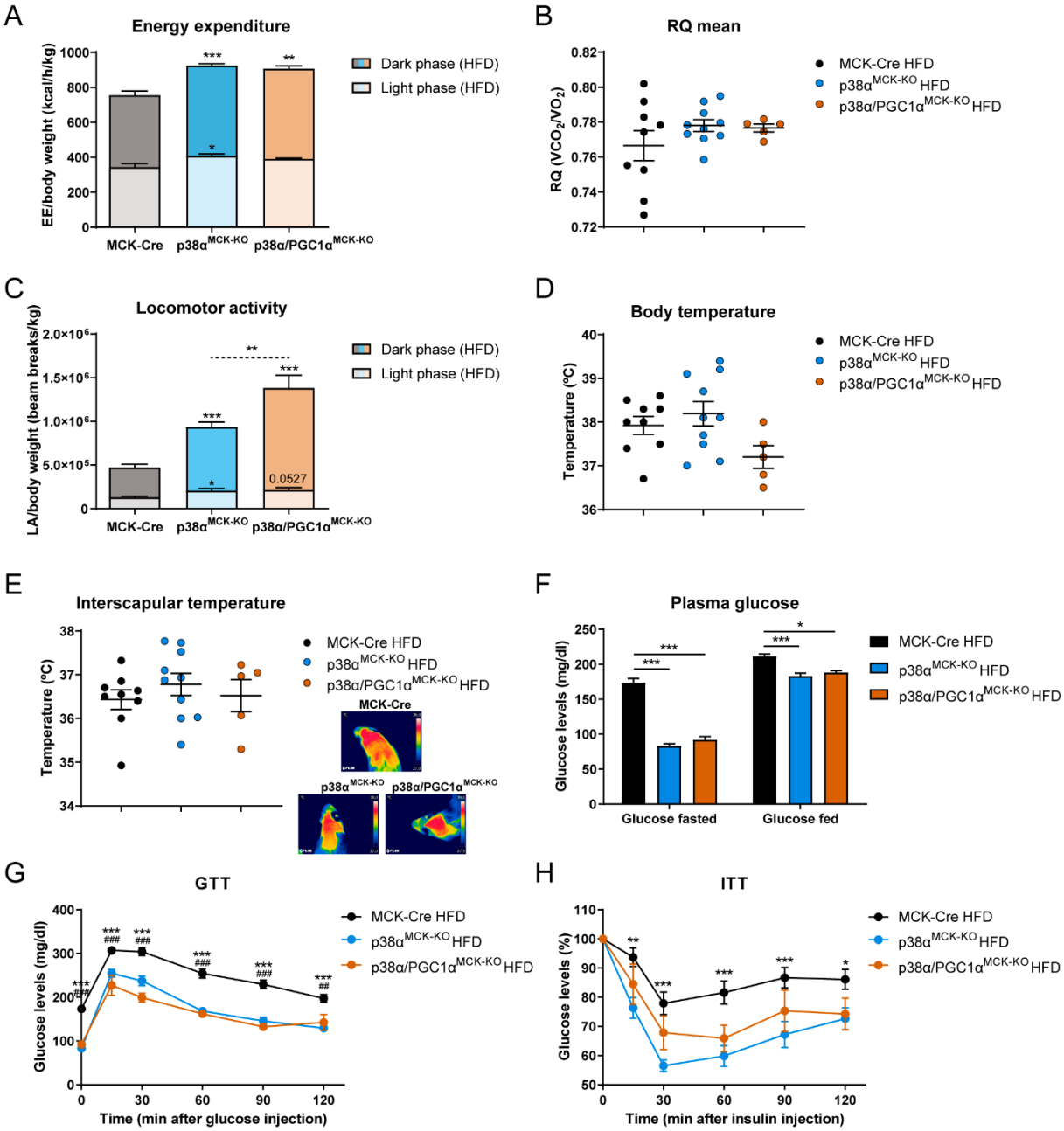

Figure R22. Higher energy expenditure, locomotor activity and improved glucose homeostasis is preserved in HFD-fed p38α/PGC1α^{MCK-KO} mice. (A-E) p38α^{MCK-KO}, p38α/PGC1α^{MCK-KO} and MCK-Cre were fed a HFD for 6 weeks, and metabolic parameters were assayed at the end of this period. (A) Energy expenditure (EE) corrected by body weight. (B) Average of respiratory quotient (RQ)

measured during 48 h. (C) Locomotor activity (LA) corrected by body weight during a 48 h period. (D) Rectal temperature measurement. (E) Interscapular temperature measurement and representative infrared thermal images. Scale range: 27 °C (lowest, blue)-39 °C (highest, white). Data are shown as means ± SEM; **p* < 0.05; ***p* < 0.01; ****p* < 0.001; one-way ANOVA coupled to Bonferroni's multiple comparisons test; *n* = 5-10. * symbols indicate differences between p38α^{MCK-KO} or p38α/PGC1α^{MCK-KO} mice compared with MCK-Cre controls unless otherwise indicated. (F-H) p38α^{MCK-KO}, p38α/PGC1α^{MCK-KO} and MCK-Cre were fed a HFD for 10 weeks. (F) Fasting and fed plasma glucose levels. (G) Glucose tolerance test (GTT). Mice fasted overnight were injected i.p. with glucose (1 g/kg). (H) Insulin tolerance test (ITT). Mice fed *ad libitum* were injected i.p. with insulin (0.75 U/kg). Blood glucose concentration was measured at the indicated points in GTT and ITT. Data are shown as means ± SEM; **p* < 0.05; ** or $^{\#\#}$*p* < 0.01; *** or $^{\#\#\#}$*p* < 0.001; one-way (plasma glucose) or two-way ANOVA (GTT, ITT) coupled to Bonferroni's multiple comparisons test; *n* = 5-13. * symbols depict significant differences between p38α^{MCK-KO} and MCK-Cre mice, while $^{\#}$ symbols indicate significant differences between p38α/PGC1α^{MCK-KO} and MCK-Cre mice unless otherwise indicated.

1.12. p38γ hyperactivation is responsible for the high locomotor activity and energy expenditure of p38α^{MCK-KO} mice

Although p38γ was found to be hyperactivated in p38α-deficient muscles, it was not responsible for the mitochondrial phenotype. However, since p38γ is known to have relevant functions in obesity comorbidities (González-Terán et al., 2016b; Koh et al., 2018), we sought to investigate the influence of p38γ hyperphosphorylation in the phenotype of striated muscle p38α-deficient mice by comparing MCK-Cre, p38α^{MCK-KO} and p38α/γ^{MCK-KO} mice. We first observed that p38α/γ^{MCK-KO} mice had higher body weight and body weight gain in HFD compared to p38α^{MCK-KO} mice (Figures R23A, B). In concordance with this, they had increased skeletal muscles, fat and liver weight (Figure R23C).

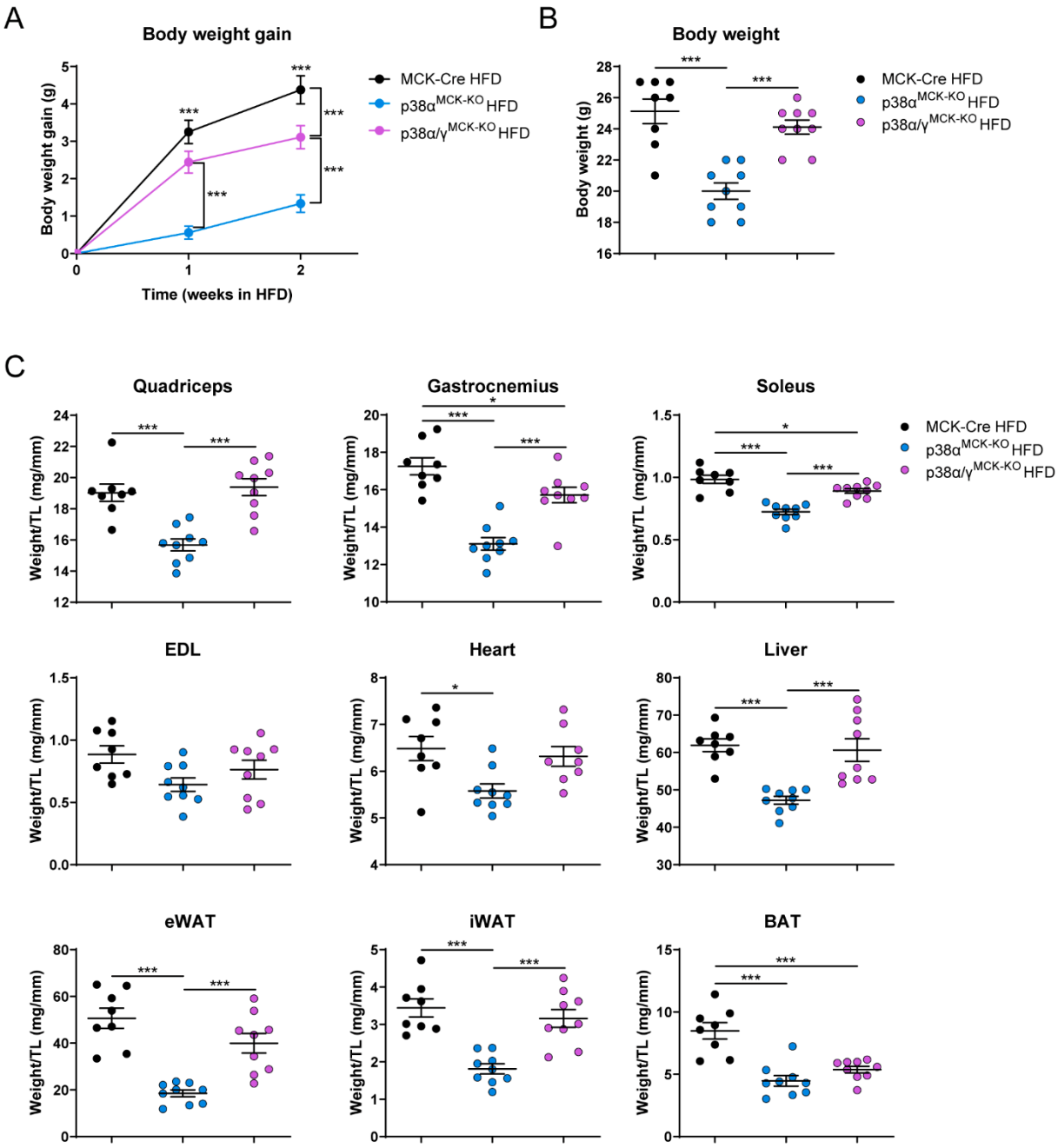

Figure R23. Lack of p38γ in p38α^{MCK-KO} mice loses their protection against HFD-induced obesity. p38α/γ^{MCK-KO}, p38α^{MCK-KO} and MCK-Cre mice were fed a HFD, and body weight was monitored for 2 weeks. (A) Body weight gain measured at the indicated times during HFD treatment. (B) Body weight measured before HFD feeding. (C) Relative weight of organs at sacrifice (measurements standardized to tibial length). Data are shown as means ± SEM; *$p < 0.05$; ***$p < 0.001$; one-way (Figures B, C) or two-way ANOVA (body weight gain) coupled to Bonferroni's multiple comparisons test; n = 8-9. TL, tibia length; EDL, extensor digitorum longus; eWAT, epididymal white adipose tissue; iWAT, inguinal white adipose tissue; BAT, brown adipose tissue. * symbols indicate differences between p38α^{MCK-KO} and MCK-Cre mice unless otherwise indicated.

In concordance with lack of protection against HFD-induced obesity, p38α/γ^{MCK-KO} mice also showed reduced energy expenditure compared to p38α^{MCK-KO} mice (Figure R24A), which was due to a decreased locomotor activity (Figure R24C), with no differences in RQ (Figure R24B)

or body temperature (Figure R24D, E). These results demonstrate that lack of p38γ in mice deficient for p38α in striated muscle reverses their global metabolic phenotype, losing their protection against obesity.

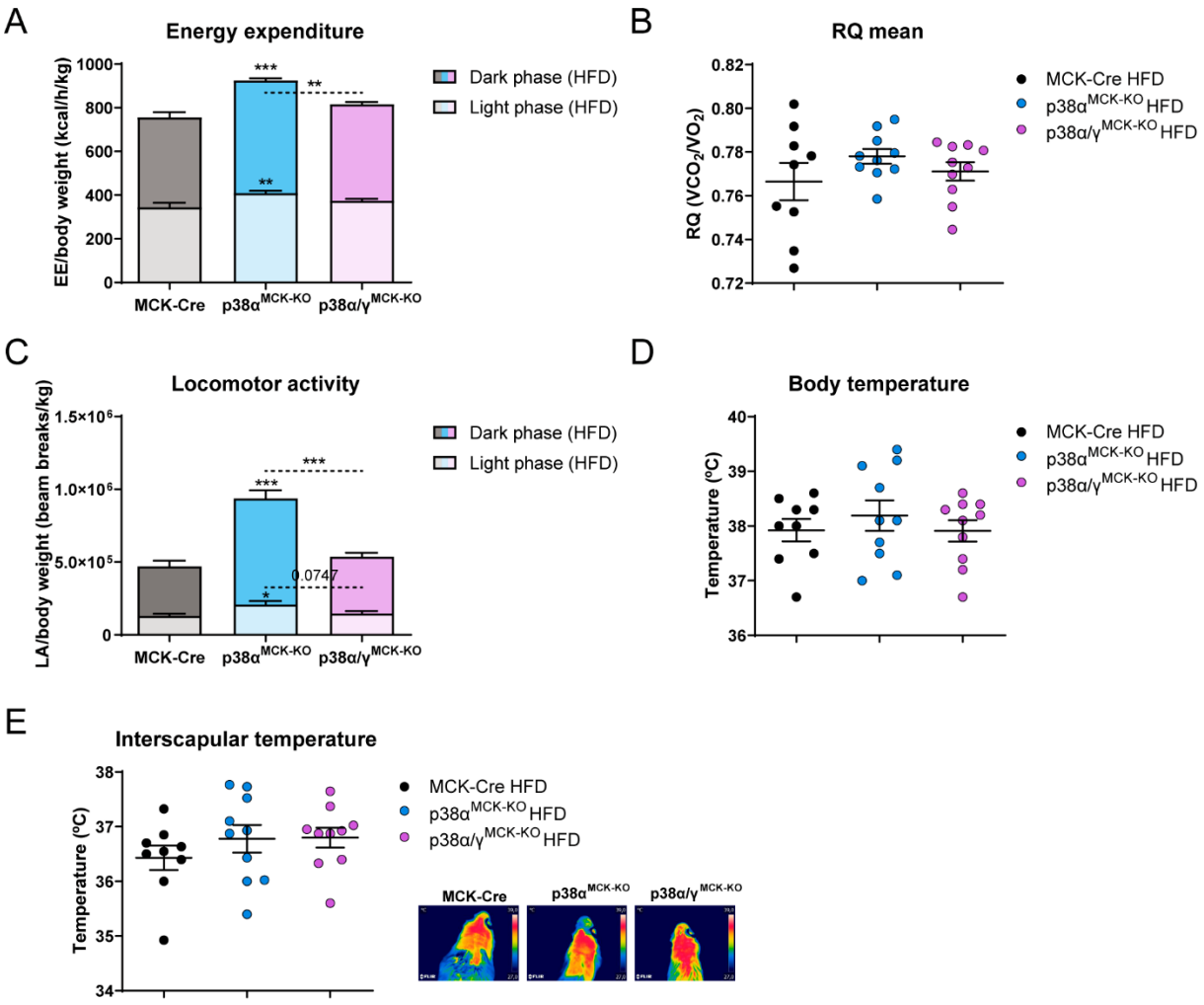

Figure R24. Lack of p38γ in p38α^{MCK-KO} mice decreases locomotor activity and energy expenditure. p38α/γ^{MCK-KO}, p38α^{MCK-KO} and MCK-Cre mice were fed a HFD for 6 weeks and metabolic parameters were assayed at the end of this period. (A) Energy expenditure (EE) corrected by body weight. (B) Average of respiratory quotient (RQ) measured during 48 h. (C) Locomotor activity (LA) corrected by body weight during a 48 h period. (D) Rectal temperature measurement. (E) Interscapular temperature measurement and representative infrared thermal images. Scale range: 27 °C (lowest, blue)-39 °C (highest, white). Data are shown as means ± SEM; *p < 0.05; **p < 0.01; ***p < 0.001; one-way ANOVA coupled to Bonferroni's multiple comparisons test; n = 9-10. * symbols indicate differences between p38α^{MCK-KO} and MCK-Cre mice unless otherwise indicated.

Importantly, muscle p38α/γ-deficient mice had similar glucose tolerance (Figure R25A) and impaired insulin sensitivity (Figure R25B) compared to MCK-Cre controls, indicating that p38γ hyperactivation in skeletal muscles of p38α^{MCK-KO} mice was responsible for their protection against diet-induced diabetes.

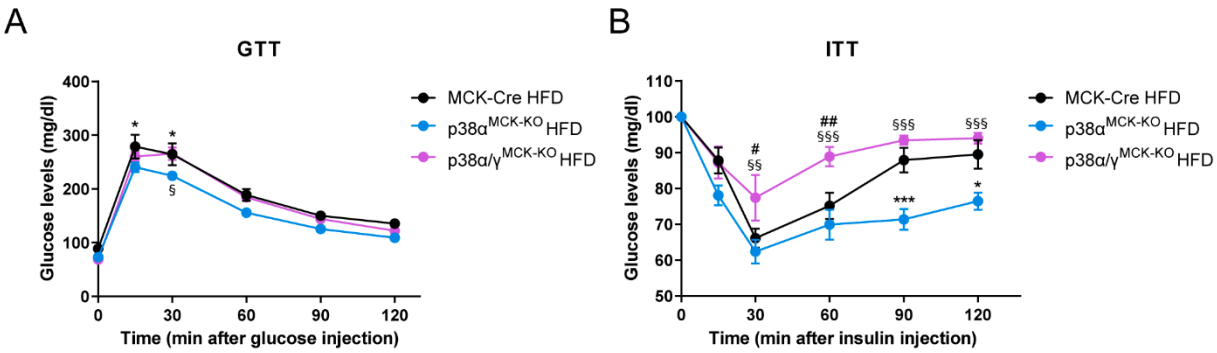

Figure R25. HFD-fed p38α/γ^{MCK-KO} have impaired glucose metabolism compared with p38α^{MCK-KO} mice. p38α/γ^{MCK-KO}, p38α^{MCK-KO} and MCK-Cre mice were fed a HFD for 3 weeks. (A) Glucose tolerance test (GTT). Mice fasted overnight were injected i.p. with glucose (1 g/kg). (B) Insulin tolerance test (ITT). Mice fed *ad libitum* were injected i.p. with insulin (0.75 U/kg). Blood glucose concentration was measured at the indicated points in GTT and ITT. Data are shown as means ± SEM; *, $^{\#}$ or $^{\S}p < 0.05$; $^{\#\#}$ or $^{\S\S}p < 0.01$; *** or $^{\S\S\S}p < 0.001$; two-way ANOVA coupled to Bonferroni's multiple comparisons test; n = 9-10. * symbols depict significant differences between p38α^{MCK-KO} and MCK-Cre mice; $^{\#}$ symbols indicate significant differences between p38α/γ^{MCK-KO} and MCK-Cre mice; and § symbols depict significant differences between p38α/γ^{MCK-KO} and p38α^{MCK-KO} mice.

1.13. Altered IL-15 signaling in p38α^{MCK-KO} mice controls their locomotor activity

Skeletal muscle is known to influence brain function by the action of peripheral factors termed myokines (Pedersen, 2019). To search for myokine candidates that could mediate the high locomotor activity under the control of skeletal muscle p38γ (Whitham & Febbraio, 2016), we used a combination of RNA-seq-based transcriptomic analysis of MCK-Cre, p38α^{MCK-KO} and p38α/γ^{MCK-KO} muscles, and secretome searching tools to filter genes encoding for proteins found to be secreted. Fifteen genes were identified as differentially expressed (DEGs) in muscles from p38α^{MCK-KO} mice compared with controls and as likely to encode for proteins that can be secreted, which did not differ between between p38α/γ^{MCK-KO} and MCK-Cre mice (Figures R26A, B). Among these hits, IL-15 is a well-known myokine which has been linked to the control of locomotor activity (Crane et al., 2015; He et al., 2010; Pistilli et al., 2011) and anxiety-related behaviors (X. Wu et al., 2010, 2011). Thus, we focused on this myokine and observed that *Il15* expression was only increased in muscles from p38α^{MCK-KO} mice, but not in the absence of p38γ (Figure R26C). This result was further confirmed by qPCR (Figure R26D). We also observed a tendency towards a higher activity and decreased depression-like behavior in p38α^{MCK-KO} mice compared with the other groups in the tail suspension test (Figure R26E). Conversely, a deeper analysis of IL-15 revealed lower concentrations in plasma from p38α^{MCK-KO} mice (Figure R26F). Some studies have reported an increase in circulating IL-15 concentration following exercise training (Crane et al., 2015; Tamura et al., 2011), while others have failed to do so (dos Santos et al., 2020; Ostrowski et al., 1998). Thus, IL-15 was also examined in plasma from MCK-Cre and p38α^{MCK-KO} mice before and after a controlled period of endurance exercise (Figure R26G). Interestingly, although p38α^{MCK-KO} mice presented lower

plasma IL-15 levels in basal conditions compared to controls, they showed a higher increase of this myokine in plasma after acute exercise (Figure R26H). These results suggested that p38γ hyperphosphorylation in skeletal muscle may improve IL-15 secretion upon exercise, but not in basal conditions.

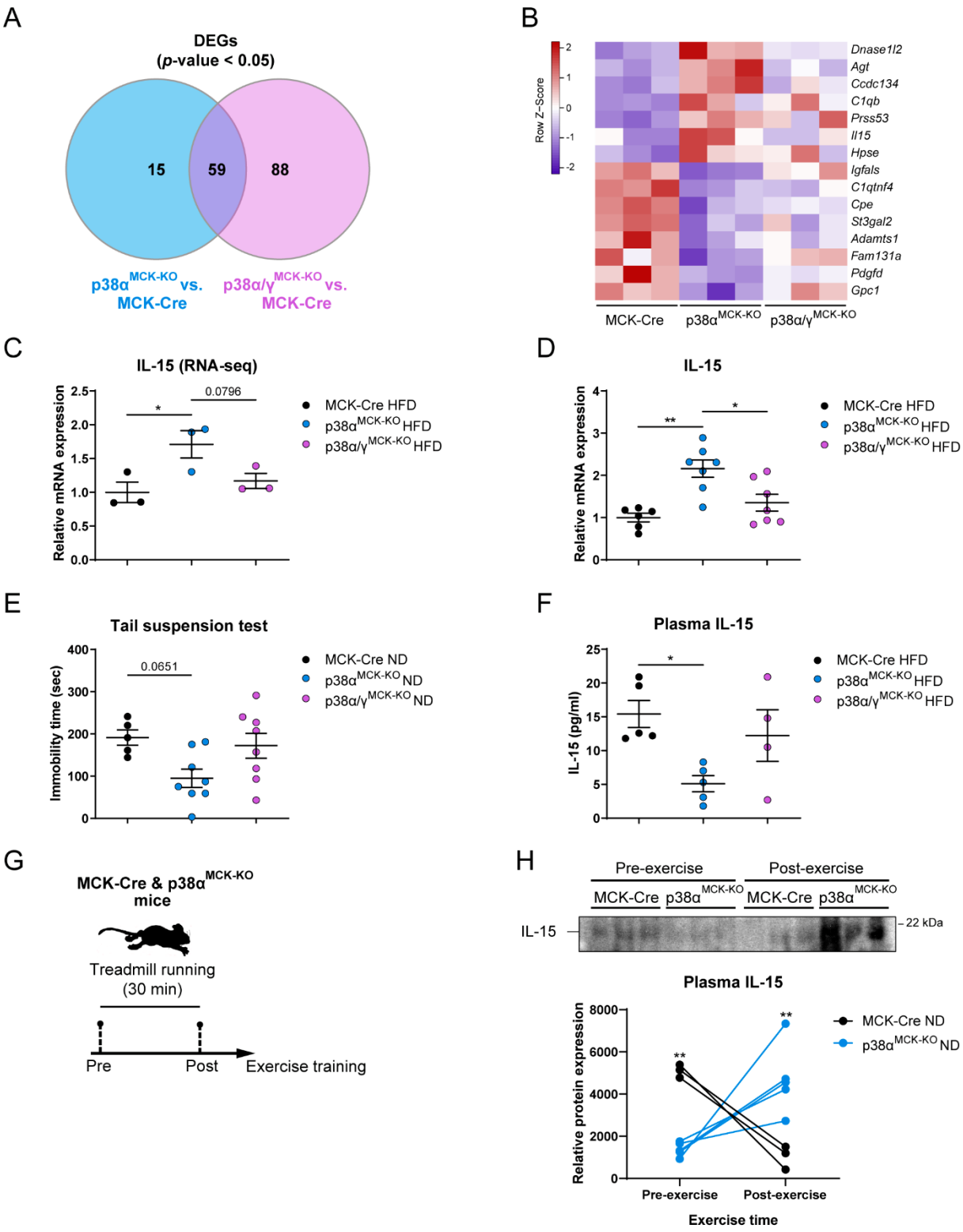

Figure R26. p38α^{MCK-KO} mice have higher muscle IL-15 expression and increased plasma IL-15 levels following exercise. (A-C) p38α^{MCK-KO}, p38α/γ^{MCK-KO} and MCK-Cre mice were fed a HFD for 6 weeks, fasted overnight and sacrificed, and an RNA-seq analysis with gastrocnemius samples was performed. (A) Venn diagram illustrating the number and overlap of differentially expressed genes (DEGs) with a positive or negative fold change (FC) when comparing muscles from p38α^{MCK-KO} or p38α/γ^{MCK-KO} mice with controls after filtering for those encoding for proteins predicted to be secreted. (B) Heatmap of all DEGs between gastrocnemius of p38α^{MCK-KO} and MCK-Cre mice with either a positive or a negative FC that are not considered DEGs between muscles of p38α/γ^{MCK-KO} and MCK-Cre mice, as determined by Student's *t*-test. (C) Quantification of *Il15* mRNA expression in RNA-seq of gastrocnemius samples. Data are normalized to MCK-Cre mice and shown as means ± SEM; **p* < 0.05; one-way ANOVA coupled with Bonferroni's multiple comparisons test; *n* = 3. (D) qRT-PCR analysis of *Il15* gene in gastrocnemius samples of p38α/γ^{MCK-KO}, p38α^{MCK-KO} and MCK-Cre mice fed a HFD for 2 weeks and sacrificed after overnight starvation. mRNA expression was normalized to the amount of *Rps18* mRNA in each sample. Data are normalized to MCK-Cre mice and shown as means ± SEM; **p* < 0.05; ***p* < 0.01; one-way ANOVA coupled to Bonferroni's multiple comparisons test; *n* = 6-7. (E) Tail suspension test performed in 18-23-week-old p38α/γ^{MCK-KO}, p38α^{MCK-KO} and MCK-Cre mice fed a ND. Data are shown as means ± SEM; one-way ANOVA coupled with Bonferroni's multiple comparisons test; *n* = 5-8. (F) IL-15 levels in plasma samples of p38α/γ^{MCK-KO}, p38α^{MCK-KO} and MCK-Cre mice fed a HFD for 4 weeks, measured by magnetic bead-based multiplex assay. Data are shown as means ± SEM; **p* < 0.05; one-way ANOVA coupled with Bonferroni's multiple comparisons test; *n* = 4-5. (G, H) 7-8-week-old p38α^{MCK-KO} and MCK-Cre mice were subjected to treadmill exercise for 30 min, and blood samples were extracted before and after training. (G) Schematic representation of the experimental procedure. (H) Immunoblot analysis and quantification of circulating IL-15 levels before and immediately after exercise. Data are shown as means ± SEM; ***p* < 0.01, indicating both between-genotype differences within each time, as well as differences in the comparison between pre- and post-exercise time within each genotype; two-way ANOVA coupled with Bonferroni's multiple comparisons test; *n* = 3-5.

We decided to check IL-15 signaling in the primary and secondary motor cortex (M1 and M2) in the brain, which are involved in locomotion (Grillner & El Manira, 2020). We found higher phosphorylation of ERK, signal transducer and activator of transcription 3 (STAT3) and 5 (STAT5) in these brain areas from p38α^{MCK-KO} mice (Figure R27A). These and previous results suggested that higher IL-15 signaling in the motor cortex of p38α^{MCK-KO} mice could contribute to their increased locomotor activity. To check this hypothesis, we performed a stereotaxic surgery in MCK-Cre and p38α^{MCK-KO} mice to diminish IL-15 signaling in the motor cortex by injecting an shRNA against the alpha subunit of the receptor of IL-15 (IL-15Rα; shIL-15Rα), or a control sequence (shScramble), specifically in M1 (Figure R27B). Four weeks after the surgery, p38α^{MCK-KO} mice with reduced IL-15Rα in the motor cortex showed decreased locomotor activity compared with p38α^{MCK-KO} controls (p38α^{MCK-KO} shScramble) (Figure R27C). All these results suggest that the higher exercise-induced IL-15 release by muscles hyperactivating p38γ might lead to increased IL-15 signaling in the motor cortex of p38α^{MCK-KO} mice, contributing to their high locomotor activity.

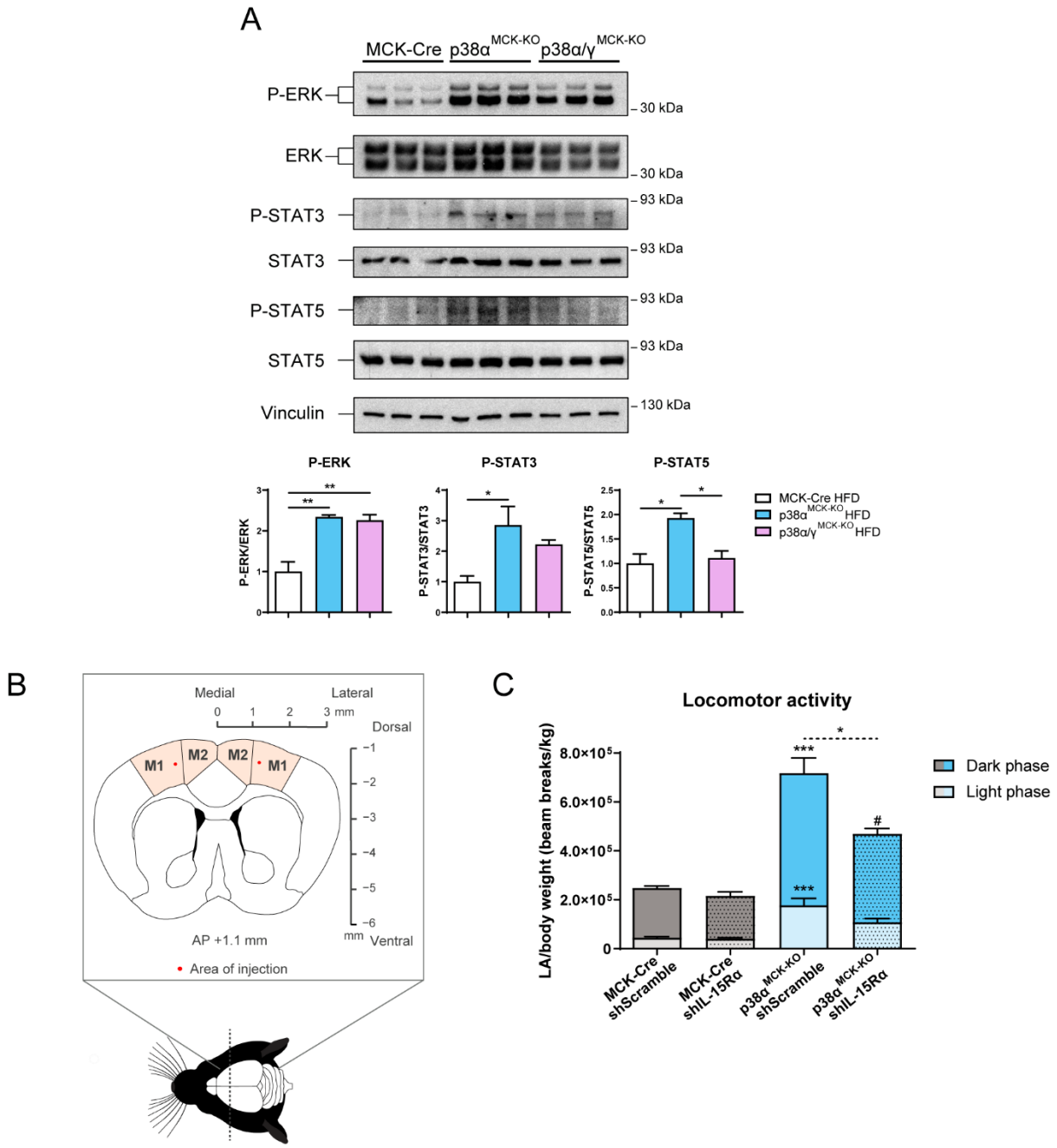

Figure R27. Increased IL-15 signaling in the motor cortex of p38α^{MCK-KO} mice controls their locomotor activity. (A) p38α/γ^{MCK-KO}, p38α^{MCK-KO} and MCK-Cre mice were fed a HFD for 6 weeks, fasted overnight and sacrificed. Extracts prepared from the motor cortex were examined by immunoblot analysis with antibodies against phospho (P)-ERK, P-STAT3, P-STAT5 and total protein levels. Vinculin protein expression was monitored as a loading control. Quantifications are shown. Data are normalized to MCK-Cre mice and shown as means ± SEM; *p < 0.05; **p < 0.01; one-way ANOVA coupled to Bonferroni's multiple comparisons test; n = 3. (B, C) 8-11-week-old p38α^{MCK-KO} and MCK-Cre mice were injected in the motor cortex with an shRNA targeting IL-15Rα (shIL-15Rα) or a control sequence (shScramble) by stereotaxic surgery. (B) Schematic representation of the brain area targeted during the surgical procedure. AP, antero-posterior. (C) Locomotor activity (LA) corrected by body weight during a 48 h period, 4 weeks after stereotaxic injection. Data are shown as means ± SEM; * or $^{\#}p$ < 0.05; ***p < 0.001; one-way ANOVA coupled to Bonferroni's multiple comparisons test; n = 5-9. * symbols indicate differences between MCK-Cre shScramble and p38α^{MCK-KO} shScramble unless otherwise indicated. $^{\#}$ symbols depict differences between MCK-Cre shIL-15Rα and p38α^{MCK-KO} shIL-15Rα.

2. Adipose tissue JNK1 and adiponectin in gender predisposition to hepatocellular carcinoma

Both obese individuals and male sex show a higher incidence of HCC (Bosch et al., 2004; Calle et al., 2003), which correlates with their decreased adiponectin levels (Arita et al., 1999; Yannakoulia et al., 2003). Therefore, by using human and rodent models, we wanted to understand the relevance of the differences in adiponectin circulating concentrations in the development of HCC, as well as the molecular and physiological mechanisms explaining these discrepancies.

2.1. Lean subjects, women and female rodents have increased circulating adiponectin levels

Using a cohort of obese and lean subjects, we confirmed the decrease of adiponectin levels in obesity (Figure R28A) and the higher adiponectin in healthy women compared with men (Figure R28B). In addition, quantification of circulating adiponectin in 11-12-week-old C57BL/6J mice confirmed previous findings, detecting more than twice the level in females than in males (Figure R28C). Similar results were obtained from the quantification of blood adiponectin in male and female rats (Figure R28D).

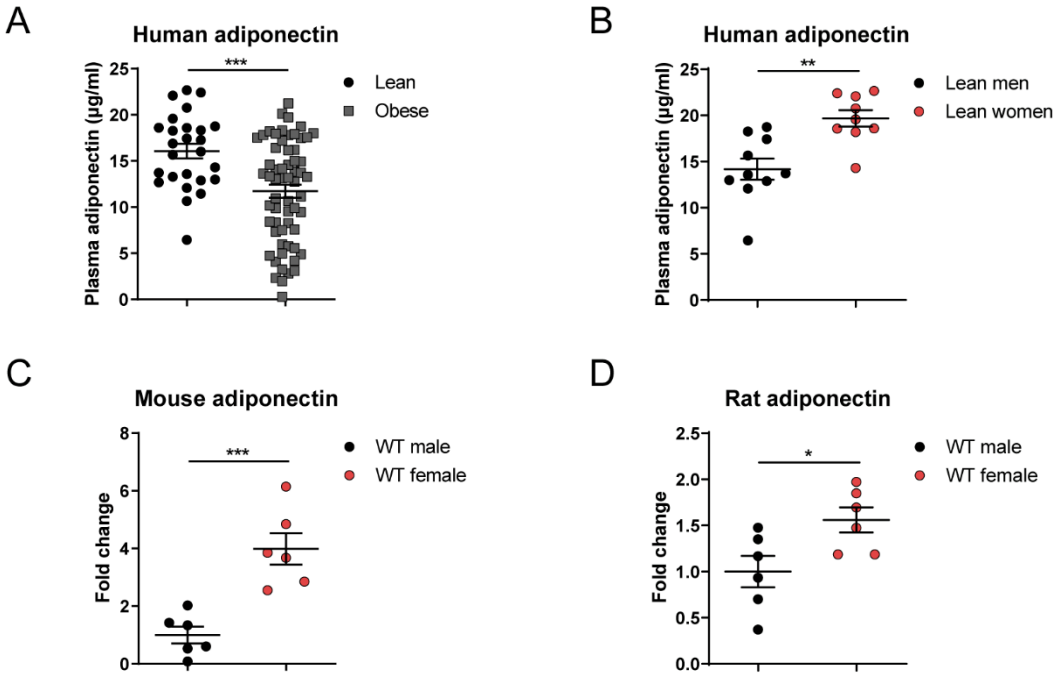

Figure R28. Gender differences in adiponectin levels in humans and rodents. (A) Quantification of circulating adiponectin levels in plasma samples from obese and lean individuals of both sexes. (B) Quantification of circulating adiponectin levels in plasma samples from lean men and women. (C) Circulating levels of adiponectin measured in 11-12-week-old female and male mice. (D) Circulating levels of adiponectin measured in 8-week-old Sprague-Dawley female and male rats. Adiponectin levels are normalized to WT male in Figures C and D. Data are shown as means ± SEM; *$p < 0.05$, **$p < 0.01$,

***p < 0.001; Student's *t*-test; n = 26-61 (lean vs. obese), n = 9-10 (lean men vs. lean women), n = 6 (male vs. female mice and rats).

2.2. Female mice are protected against liver cancer

In order to check whether hepatic tumor growth was different between male and female mice, we used Hep53.4 cells, an HCC-derived tumor cell line, in allograft models. Results showed that adiponectin levels in mice correlated with the stronger growth of subcutaneously implanted mouse HCC-derived tumor cells in males than in females (Figure R29A). In addition, these gender differences were HCC-specific, given that growth of subcutaneously injected colon adenocarcinoma-derived tumor cells (MC-38; Figure R29B) or melanoma-derived tumor cells (B16-F10; Figure R29C) was not different between males and females.

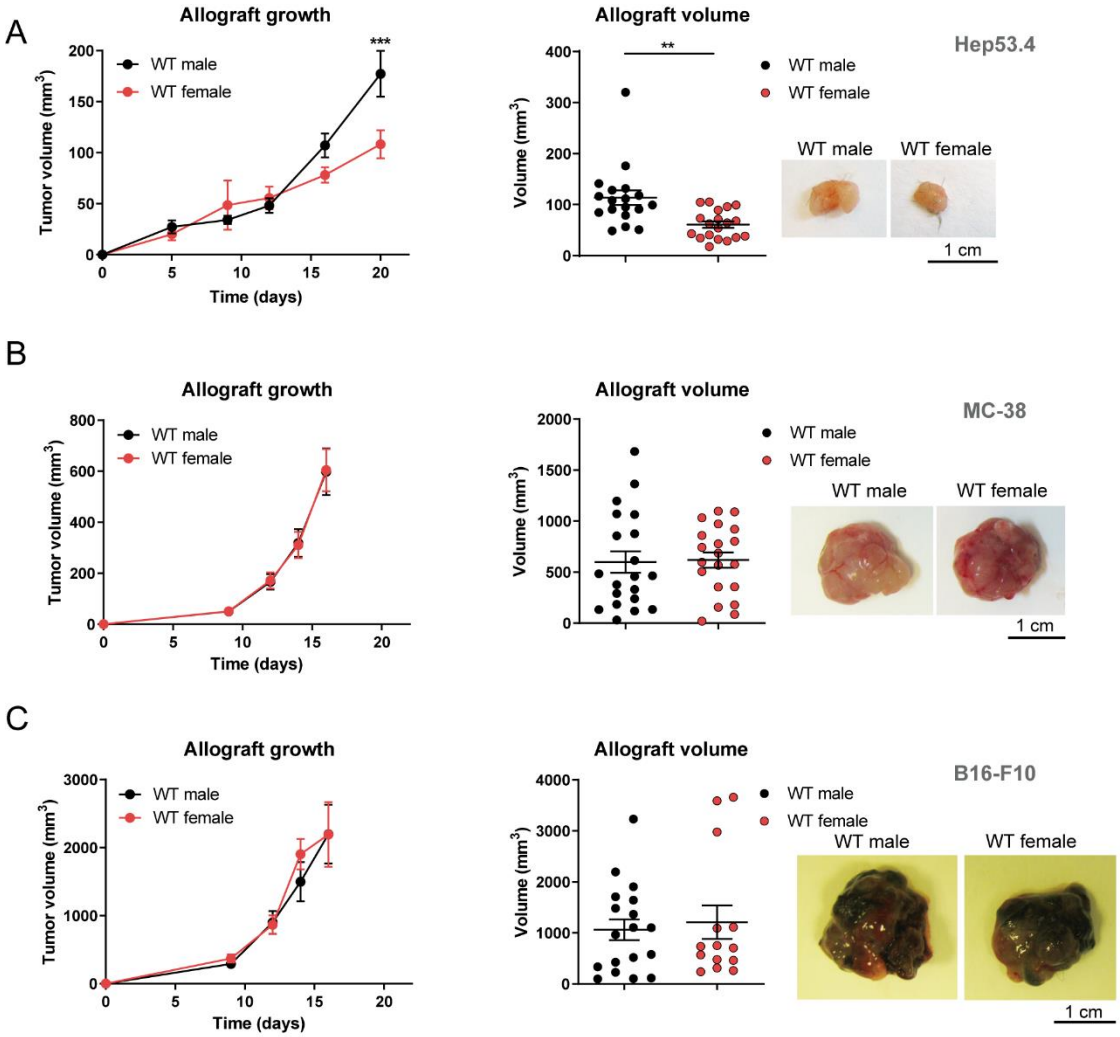

Figure R29. Gender differences in the growth of different tumor cell lines. WT male and female mice were used for allograft experiments with different tumor cell lines. Representative allografts and tumor volume quantification during the experiment and at sacrifice are shown. (A) Sacrifice was performed 3 weeks after subcutaneous injection with 5 x 10^4 Hep53.4 cells (HCC-derived cells) in each flank. Data are shown as means ± SEM; **p < 0.01, ***p < 0.001; two-way ANOVA coupled with Bonferroni's multiple comparisons test (allograft growth); Student's *t*-test (allograft volume); n = 18-19

tumors (10 mice per condition). (B) Sacrifice was performed 3 weeks after subcutaneous injection with 5 x 10^5 MC-38 cells (colon adenocarcinoma-derived cells) in each flank. Data are shown as means ± SEM; two-way ANOVA coupled with Bonferroni's multiple comparisons test (allograft growth); Student's *t*-test (allograft volume); *n* = 20 tumors (10 mice per condition). (C) Sacrifice was performed 2 weeks after subcutaneous injection with 5 x 10^5 B16-F10 cells (melanoma-derived cells) in each flank. Data are shown as means ± SEM; two-way ANOVA coupled with Bonferroni's multiple comparisons test (allograft growth); Student's *t*-test (allograft volume); *n* = 14-18 tumors (7-10 mice per condition).

2.3. Increased levels of adiponectin in females protect them against liver cancer

To determine whether the gender differences in adiponectin production influence tumor growth, we performed allograft experiments in male and female adiponectin knockout (Adipoq$^{-/-}$) and WT mice. Unlike the results observed in WT mice, in which we had observed larger tumors in males than in females (Figure R29A), Adipoq$^{-/-}$ mice showed no gender differences (Figure R30).

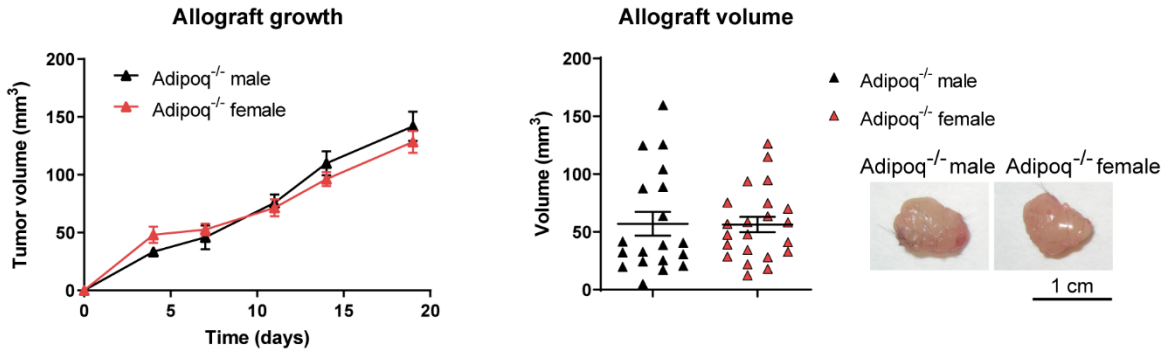

Figure R30. Mice lacking adiponectin show no gender differences in the growth of HCC cells. Representative allografts and tumor volume quantification in Adipoq$^{-/-}$ male and female mice during the experiment and at sacrifice 3 weeks after subcutaneous injection with 5 x 10^4 Hep53.4 cells in each flank. Data are shown as means ± SEM; two-way ANOVA coupled with Bonferroni's multiple comparisons test (allograft growth); Student's *t*-test (allograft volume); *n* = 19-22 tumors (10-11 mice per condition).

2.4. Alterations of adiponectin levels affect HCC development

The contribution of adiponectin to HCC development was evaluated by the DEN-induced hepatocarcinogenesis model (Heindryckx et al., 2009). Male mice were injected with a serotype 8 adeno-associated virus overexpressing adiponectin under the control of the adipocyte aP2 promoter (AAV aP2 Adipoq) or carrying an empty control vector (AAV aP2 CTRL), at P1. After 14 days, these mice received i.p. DEN injections to induce HCC (Figure R31A). Adiponectin overexpression was confirmed by measurement of adiponectin plasma levels 3 weeks after virus injection (Figure R31B), as well as 8.5 months after virus injection (Figure R31C). Quantification of tumors 8 months after DEN treatment revealed a significant reduction in the number of tumors in adiponectin-overexpressing males (Figures R31D-G),

indicating that adiponectin reduces tumor progression and may be a potential treatment for HCC.

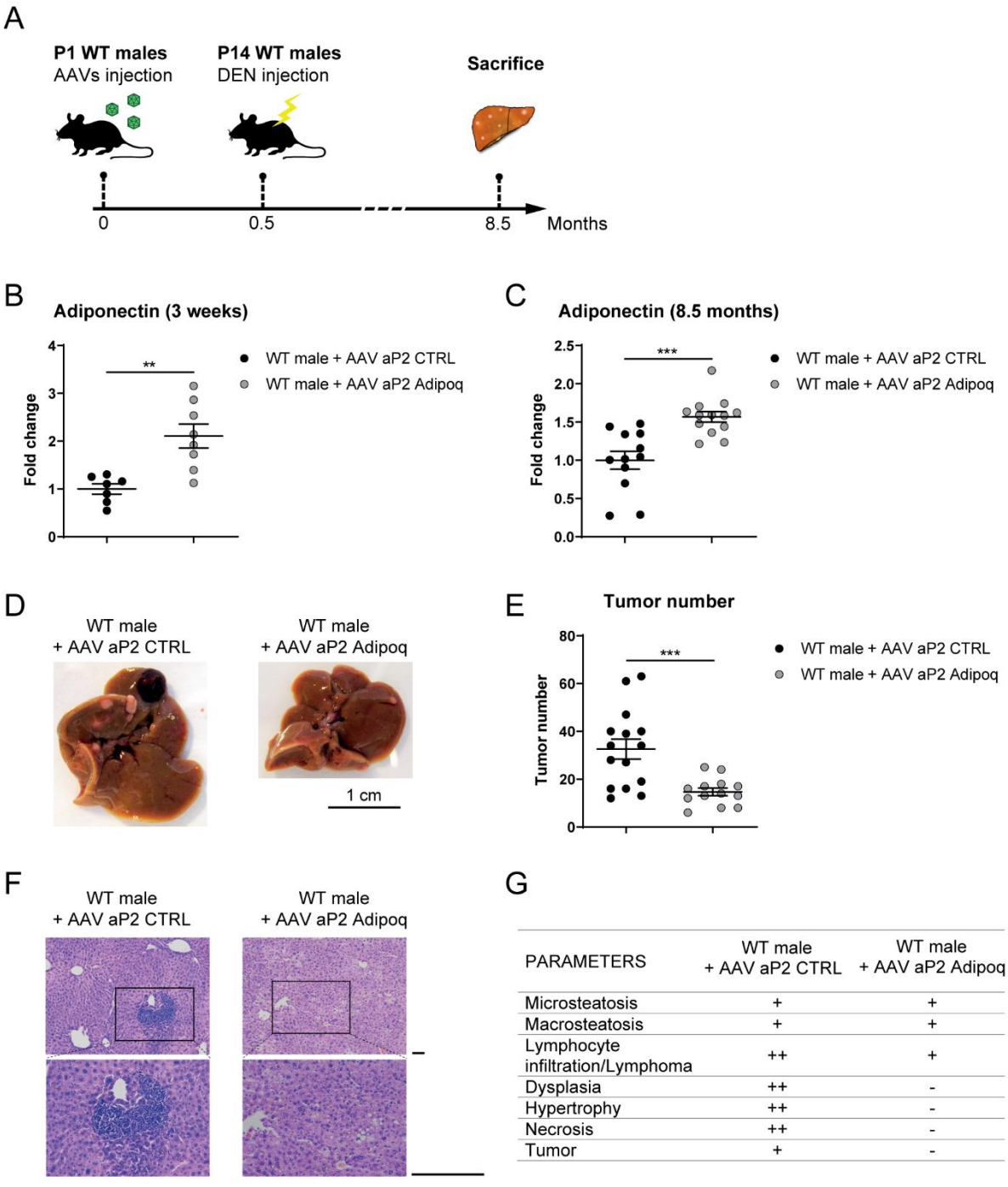

PARAMETERS	WT male + AAV aP2 CTRL	WT male + AAV aP2 Adipoq
Microsteatosis	+	+
Macrosteatosis	+	+
Lymphocyte infiltration/Lymphoma	++	+
Dysplasia	++	-
Hypertrophy	++	-
Necrosis	++	-
Tumor	+	-

Figure R31. Adiponectin overexpression reduces HCC progression. WT male mice were injected with adeno-associated viruses carrying a control sequence (WT male + AAV aP2 CTRL) or the adiponectin gene under control of the aP2 promoter (WT male + AAV aP2 Adipoq) at P1 and received an i.p. DEN injection (50 mg/kg body weight) 14 days later. (A) Schematic representation of the experimental procedure. (B) Quantification of circulating levels of adiponectin 3 weeks after virus injection. Data are normalized to controls and shown as means ± SEM; $^{**}p < 0.01$; Student's *t*-test with Welch's correction; $n = 7\text{-}8$. (C) Quantification of circulating levels of adiponectin 8.5 months after virus injection. Data are normalized to controls and shown as means ± SEM; $^{***}p < 0.001$; Student's *t*-test;

n = 12-13. (D) HCC development 8 months after i.p. injection with DEN. (E) Tumor number determined at sacrifice. Data are shown as means ± SEM; ***p < 0.001; Student's *t*-test; *n* = 13-15. (F) Representative photos of H&E-stained liver sections obtained from these DEN-injected mice at sacrifice. Scale bars: 100 µm. (G) Histopathological evaluation was performed in livers from these mice upon sacrifice. No injury (−) or different grades of injury (mild [+], moderate [++], or marked [+++]) were noted in at least seven view fields per slide. *n* = 10 per condition. AAV, adeno-associated virus; aP2, adipocyte protein 2; CTRL, control.

To further evaluate the protective effects of adiponectin, we used the DEN-induced HCC model in WT and Adipoq$^{-/-}$ mice. Results showed that lack of adiponectin increases tumor size 8 months after DEN treatment in males (Figures R32A, B) and slightly increases the number of tumors in females (Figure R32C, D). These results corroborated that high levels of adiponectin in females contribute to the protection against HCC.

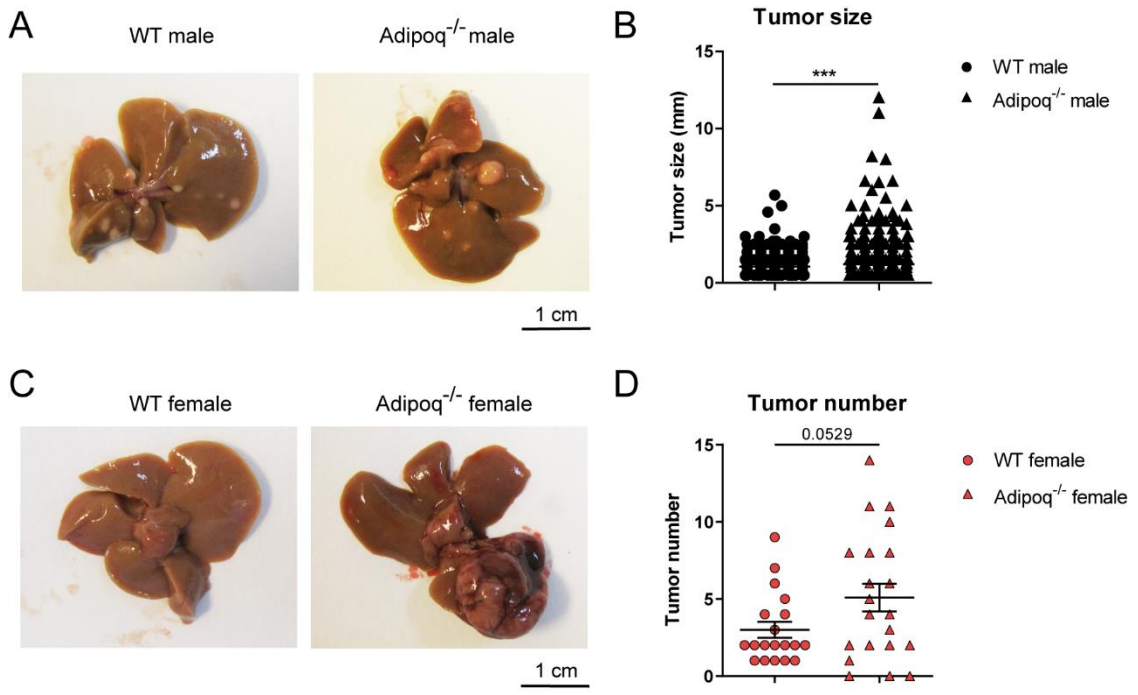

Figure R32. Adiponectin deficiency in male and female mice increases HCC development. 14-day-old WT and Adipoq$^{-/-}$ male and female mice were injected i.p. with DEN (50 mg/kg body weight). (A) HCC development in males, 8 months after i.p. injection with DEN. (B) Tumor size in male livers determined at sacrifice. Data are shown as means ± SEM; ***p < 0.001; Student's *t*-test with Welch's correction; *n* = 24-38. (C) HCC development in females, 8 months after i.p. injection with DEN. (D) Tumor number in female livers determined at sacrifice. Data are shown as means ± SEM; Student's *t*-test with Welch's correction; *n* = 19-21.

2.5. Adiponectin-mediated protection from HCC is mainly mediated by adiponectin receptor 2

The cellular function of adiponectin is mainly mediated by two transmembrane receptors, known as adiponectin receptors 1 and 2 (AdipoR1/2) (Wang & Scherer, 2016). Increased expression of both receptors was found in HCC-derived cells in comparison with colon

adenocarcinoma and melanoma cells (Figure R33A). In the liver, hepatocytes are the main source of AdipoR2, while AdipoR1 is expressed in hepatocytes, Kupffer cells (KCs) and endothelial cells (ECs; Figure R33B). In addition, hepatocytes increase the expression of both receptors when they become tumoral (Figure R33C).

To evaluate the importance of these receptors in the protection observed in females, we used shRNAs against them in Hep53.4 cells and confirmed their reduced expression before performing an allograft experiment in females (Figure R33D). We observed that only depletion of AdipoR2 was able to block the protection found in females, as no significant differences in tumor growth were found between males and females injected with Hep53.4 AdipoR2-shRNA-treated cells (Figure R33E).

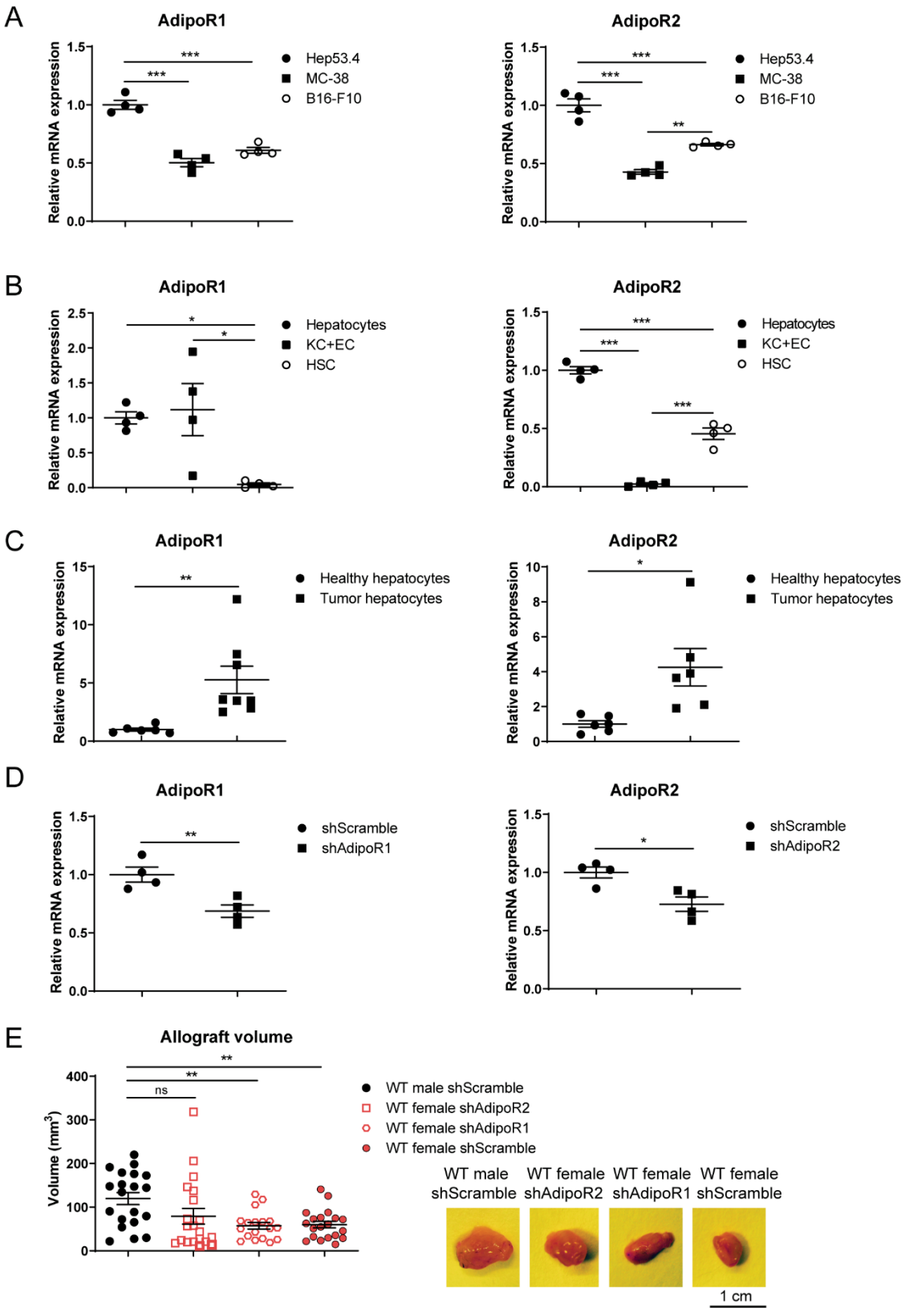

Figure R33. Analysis of adiponectin receptors expression and their role in tumor growth. (A) qRT-PCR analysis of adiponectin receptors 1 and 2 (*AdipoR1* and *AdipoR2*) genes in Hep53.4, MC-38, or B16-F10 tumor cells. mRNA expression was normalized to the amount of *Gapdh* mRNA in each sample. Data are normalized to Hep53.4 cells and shown as means ± SEM; $^{**}p < 0.01$; $^{***}p < 0.001$; one-way ANOVA coupled with Bonferroni's multiple comparisons test; $n = 4$. (B) qRT-PCR analysis of

AdipoR1 and *AdipoR2* in different liver cell populations. mRNA expression was normalized to the amount of *Gapdh* mRNA in each sample. Data are normalized to hepatocytes and shown as means ± SEM; **p* < 0.05; ****p* < 0.001; one-way ANOVA coupled with Bonferroni's multiple comparisons test; *n* = 4. KC, Kupffer cells; EC, endothelial cells; HSC, hepatic stellate cells. (C) qRT-PCR analysis of *AdipoR1* and *AdipoR2* in healthy hepatocytes and hepatocytes derived from hepatic tumors of C57BL/6J mice treated with DEN at P14 and 300 µg/l TAA administered in the drinking water for 26 weeks. mRNA expression was normalized to the amount of *Gapdh* mRNA in each sample. Data are normalized to healthy hepatocytes and shown as means ± SEM; **p* < 0.05; ***p* < 0.01; Student's *t*-test with Welch's correction; healthy hepatocytes, *n* = 6; tumor hepatocytes, *n* = 6-8. (D) qRT-PCR analysis of *AdipoR1* in Hep53.4 treated with an shRNA against AdipoR1 (shAdipoR1) or a scrambled control sequence, and analysis of *AdipoR2* in Hep53.4 cells treated with an shRNA against AdipoR2 (shAdipoR2) or a scrambled control sequence. mRNA expression was normalized to the amount of *Gapdh* mRNA in each sample. Data are normalized to shScramble cells and shown as means ± SEM; **p* < 0.05; ***p* < 0.01; Student's *t*-test; *n* = 4. (E) Representative allografts and tumor volume quantification in WT mice with hepatic tumors lacking AdipoR1 or AdipoR2 expression. Mice received subcutaneous injections with 1 x 10^6 Hep53.4 cells per flank, previously transduced with shRNA targeting AdipoR1, AdipoR2 or a control sequence (shScramble). Mice were sacrificed 3 weeks after Hep53.4 cell injection. Data are shown as means ± SEM; ***p* < 0.01; non-significant differences (ns); one-way ANOVA coupled with Bonferroni's multiple comparisons test; *n* = 18-20 tumors (10 mice per group).

2.6. Adiponectin levels increase in males after castration and partially protect them from tumor growth

It is already known that adiponectin levels significantly decrease with the progression of puberty in boys, but not in girls, and this decline is inversely related to testosterone levels (Böttner et al., 2004). Considering this inverse correlation between higher testosterone levels and lower adiponectin in males, we assessed the effect of castration on blood adiponectin levels in mice (Figure R34A). Castrated males had similar adiponectin levels to those found in females (Figure R34B) and developed smaller tumors in allograft experiments compared to non-castrated males (Figure R34C). These results demonstrated an effect of castration on adiponectin levels and subsequent tumor growth.

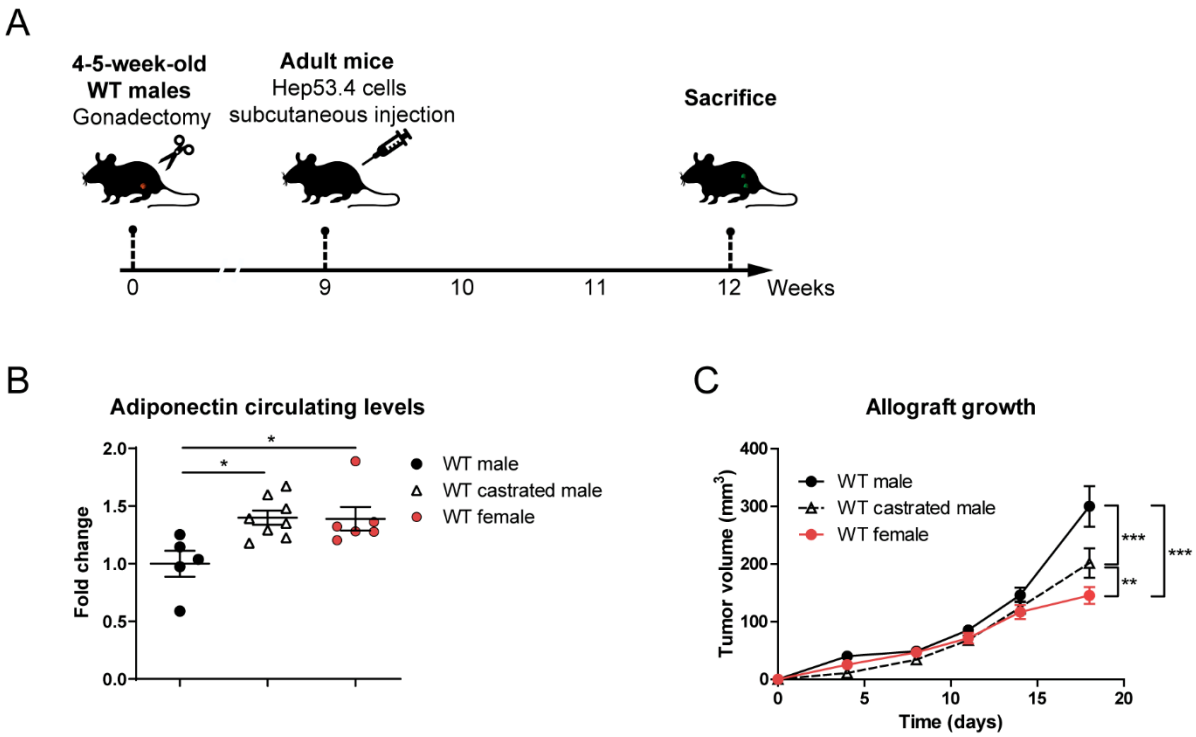

Figure R34. Castration in males increases adiponectin levels and reduces allograft growth. 4-5-week-old WT male mice were subjected to gonadectomy, and female, male and castrated mice were injected subcutaneously with 5 x 10^4 Hep53.4 cells in each flank 9 weeks later. (A) Schematic representation of the experimental procedure. (B) Quantification of circulating adiponectin levels in female, male, and castrated male mice 7 weeks after castration. Data are normalized to WT male and shown as means ± SEM; *p < 0.05; one-way ANOVA coupled with Bonferroni's multiple comparisons test; n = 5-8. (C) Tumor volume in male, female, and castrated male mice monitored over 3 weeks after injection of Hep53.4 cells. Data are shown as means ± SEM; **p < 0.01; ***p < 0.001; two-way ANOVA coupled with Bonferroni's multiple comparisons test; n = 18-20 tumors (9-10 mice per condition).

2.7. Testosterone controls adiponectin levels through adipose tissue JNK activation

It is known that adipose tissue JNK controls the production of important adipokines that regulate liver metabolism (Manieri & Sabio, 2015; Sabio et al., 2008). We therefore tested if there were sex-dependent differences in JNK activation in adipose tissue that could account for the higher adiponectin levels in females. Western blot analysis of JNK in adipose tissue revealed a higher activation of this stress kinase in males than in females, both in mouse and rat models, which correlated with their lower adiponectin levels (Figure R35 and Figures R28C and D). These data suggested that this was a general effect conserved among species.

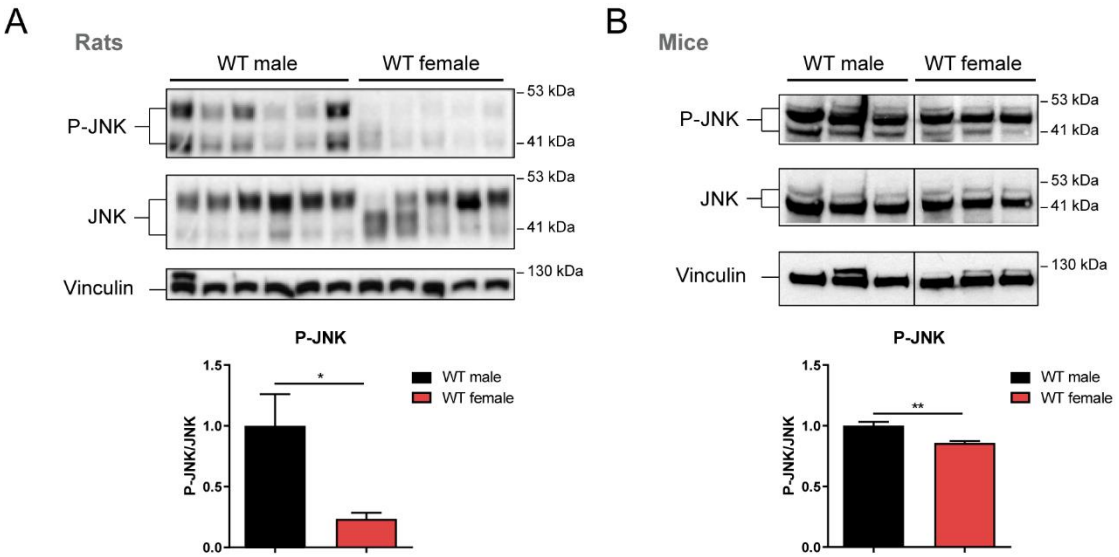

Figure R35. Adipose tissue JNK phosphorylation is higher in male rodents. (A) Immunoblot analysis and quantification of phospho (P)-JNK and JNK in adipose tissue from WT male and female rats. Vinculin protein expression was monitored as a loading control. Data are normalized to WT male and shown as means ± SEM; **p* < 0.05; Student's *t*-test; *n* = 5-6. (B) Immunoblot analysis and quantification of P-JNK and JNK in adipose tissue from WT male and female mice. Vinculin protein expression was monitored as a loading control. Data are normalized to WT male and shown as means ± SEM; ***p* < 0.01; Student's *t*-test; *n* = 3-4.

In line with these results, we found that testosterone activated JNK in both mouse and human adipocytes (Figures R36A, B). To check whether testosterone was also able to regulate JNK phosphorylation *in vivo*, we castrated WT male mice and performed testosterone replacement in them (Figure R36C). Results showed that adipose tissue JNK activation was significantly reduced in castrated males, whereas testosterone injection was enough to increase its activation to non-castrated mice levels within 2 weeks (Figure R36D). Importantly, the observed changes in JNK phosphorylation were in concordance with adiponectin levels, which decreased to the levels of non-castrated mice when testosterone replacement was performed (Figure R36E).

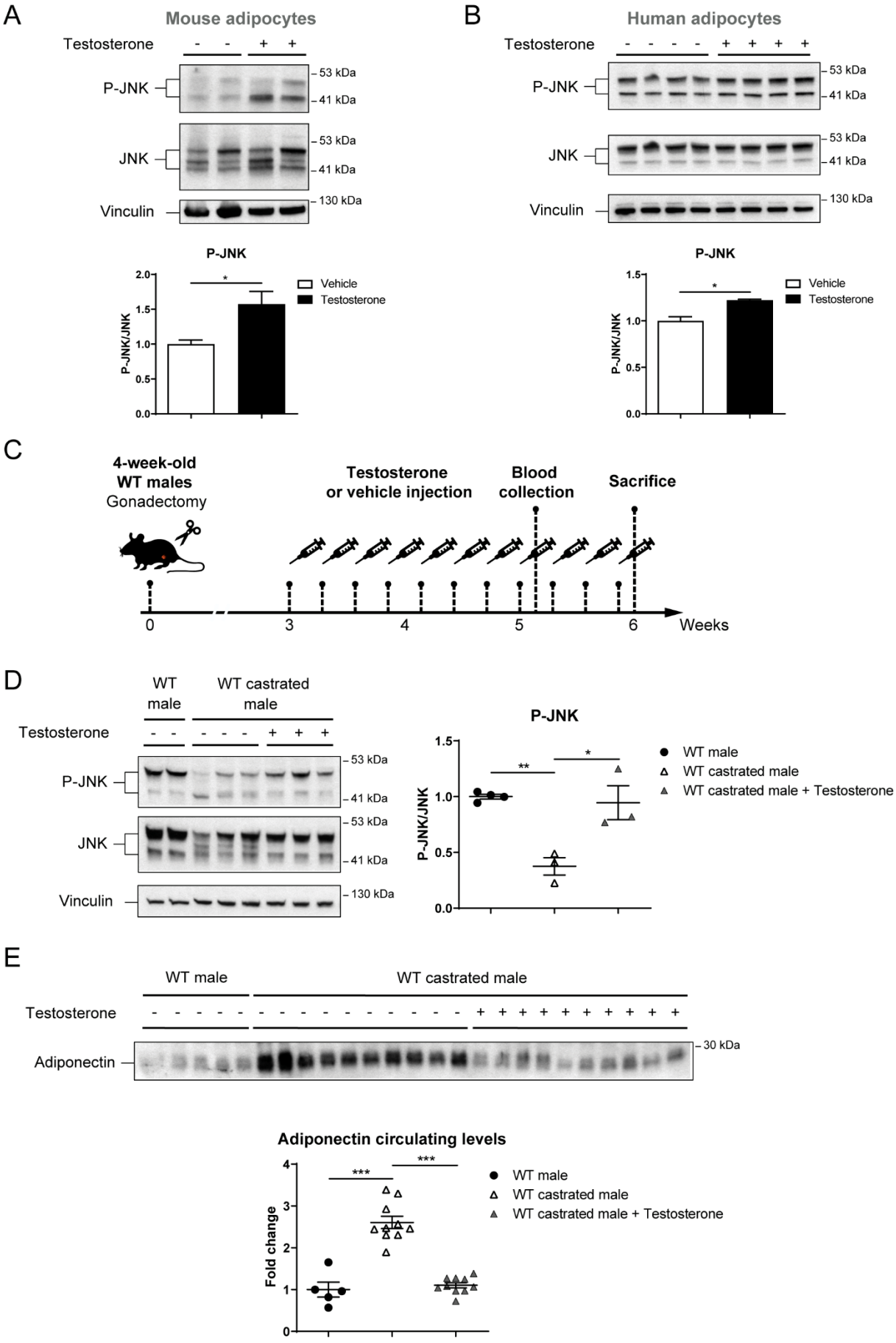
A
Mouse adipocytes
Testosterone
P-JNK
JNK
Vinculin
53 kDa
41 kDa
130 kDa
P-JNK
P-JNK/JNK
Vehicle
Testosterone
B
Human adipocytes
C
4-week-old
WT males
Gonadectomy
Testosterone
or vehicle injection
Blood
collection
Sacrifice
Weeks
D
WT
male
WT castrated
male
WT male
WT castrated male
WT castrated male + Testosterone
E
Adiponectin
30 kDa
Adiponectin circulating levels
Fold change

Figure R36. Testosterone controls adiponectin levels through adipose tissue JNK. (A) Immunoblot analysis and quantification of phospho (P)-JNK and JNK in mouse differentiated adipocytes after treatment with testosterone (300 nM for 120 min). Vinculin protein expression was monitored as a loading control. Data are normalized to vehicle and shown as means ± SEM; **p* < 0.05; Student's *t*-test; *n* = 3. (B) Immunoblot analysis and quantification of P-JNK and JNK in human differentiated adipocytes after treatment with testosterone (1.2 µM for 30 min). Vinculin protein expression was monitored as a loading control. Data are normalized to vehicle and shown as means ± SEM; **p* < 0.05; Student's *t*-test with Welch's correction; *n* = 4. (C-E) 4-week-old WT males were castrated or sham-operated and they were subcutaneously injected with testosterone propionate (5 µg/g body weight) or vehicle alone every other day for 3 weeks. (C) Schematic representation of the experimental procedure. (D) Immunoblot analysis and quantification of P-JNK and JNK in adipose tissue from these WT male mice, treated with testosterone propionate (50 µg/g body weight) or vehicle alone 30 min before sacrifice. Vinculin protein expression was monitored as a loading control. Data are normalized to WT male and shown as means ± SEM; **p* < 0.05; ***p* < 0.01; one-way ANOVA coupled with Bonferroni's multiple comparisons test; *n* = 3-4. (E) Immunoblot analysis and quantification of circulating adiponectin levels 2 weeks after the first testosterone injection. Data are normalized to WT male and shown as means ± SEM; ****p* < 0.001; one-way ANOVA coupled with Bonferroni's multiple comparisons test; *n* = 5-10.

2.8. Lack of JNK1 in the adipose tissue protects against HCC progression

We next examined plasma concentrations of adiponectin in males with adipose tissue-specific deletion of JNK1 (JNK1$^{Fabp\text{-}KO}$) or control mice (Fabp-Cre; Figure R37A). Blood adiponectin levels were significantly higher in JNK1$^{Fabp\text{-}KO}$ males than in Fabp-Cre males (Figure R37B), whereas no between-genotype differences were found in the levels of interleukin-1 beta (IL-1β), TNFα or IL-6 (Figure R37C).

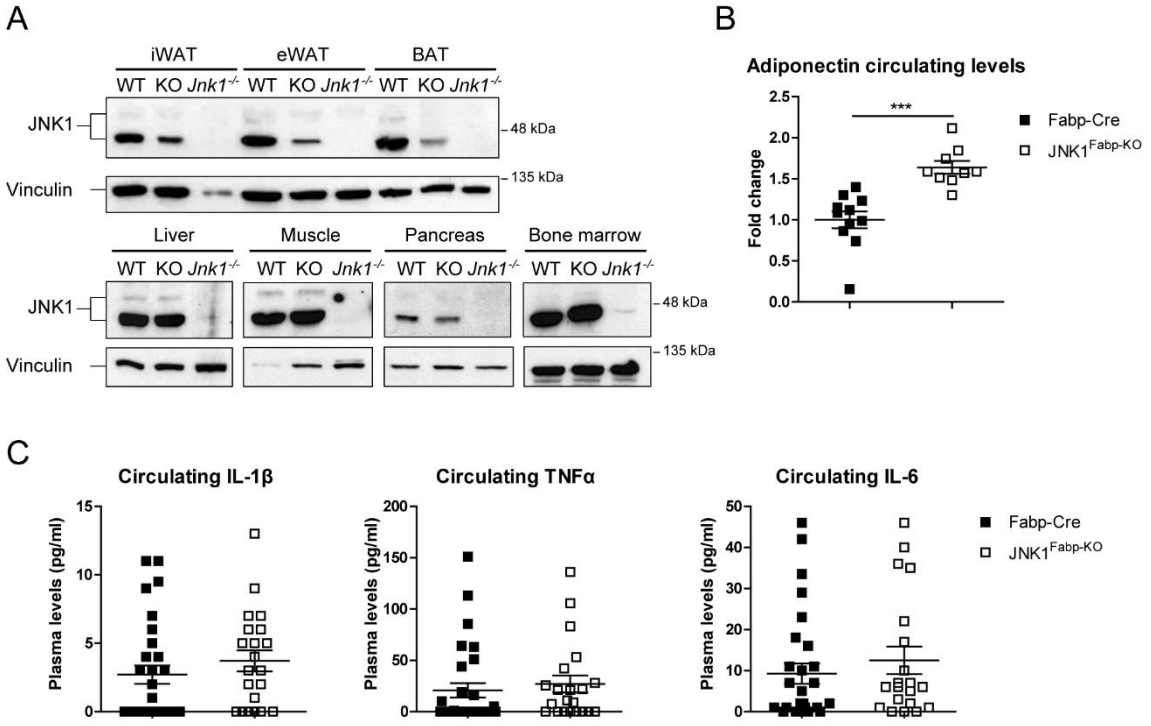

Figure R37. Deletion of JNK1 and cytokines levels in control (Fabp-Cre) and adipose tissue JNK1-deficient (JNK1$^{Fabp\text{-}KO}$) mice. (A) Fabp-Cre and JNK1$^{Fabp\text{-}KO}$ mice were sacrificed at 10 weeks, and different tissues were extracted and analyzed by immunoblotting with an antibody against JNK.

Vinculin protein expression was monitored as a loading control. Tissues from Jnk1$^{-/-}$ mice were used as a control. iWAT, inguinal adipose tissue; eWAT, epididymal white adipose tissue; BAT, brown adipose tissue; WT, Fabp-Cre; KO, JNK1$^{Fabp\text{-}KO}$. (B) Circulating levels of adiponectin were measured in Fabp-Cre and JNK1$^{Fabp\text{-}KO}$ mice. Data are normalized to Fabp-Cre adiponectin levels and shown as means ± SEM; ***$p < 0.001$; Student's *t*-test; $n = 9\text{-}11$. (C) Fabp-Cre and JNK1$^{Fabp\text{-}KO}$ mice were injected i.p. with DEN (50 mg/kg) at P14. Plasma was analyzed after 8 months on a Luminex platform to measure the levels of TNFα, IL-1β, and IL-6 adipokines. Data are shown as means ± SEM; Student's *t*-test; $n = 20\text{-}30$. (Results shared in Manieri, 2016 and Manieri & Herrera-Melle et al., 2019).

We next performed allograft tumor formation assays in Fabp-Cre and JNK1$^{Fabp\text{-}KO}$ males to investigate the role of adipose tissue JNK1 in tumor growth. Consistent with the higher adiponectin levels found in JNK1$^{Fabp\text{-}KO}$ males, tumor growth in these mice was slower than in Fabp-Cre controls, and postmortem inspection revealed smaller tumors (Figure R38A). To further evaluate these results, JNK1$^{Fabp\text{-}KO}$ and Fabp-Cre males were injected with DEN, and tumors were examined 8 months later. We found that HCC was strongly suppressed in JNK1$^{Fabp\text{-}KO}$ mice (Figure R38B). JNK1$^{Fabp\text{-}KO}$ mice had significantly fewer tumors than Fabp-Cre mice (Figure R38C), and tumor size and maximum tumor size were significantly lower in JNK1$^{Fabp\text{-}KO}$ mice (Figures R38D, E).

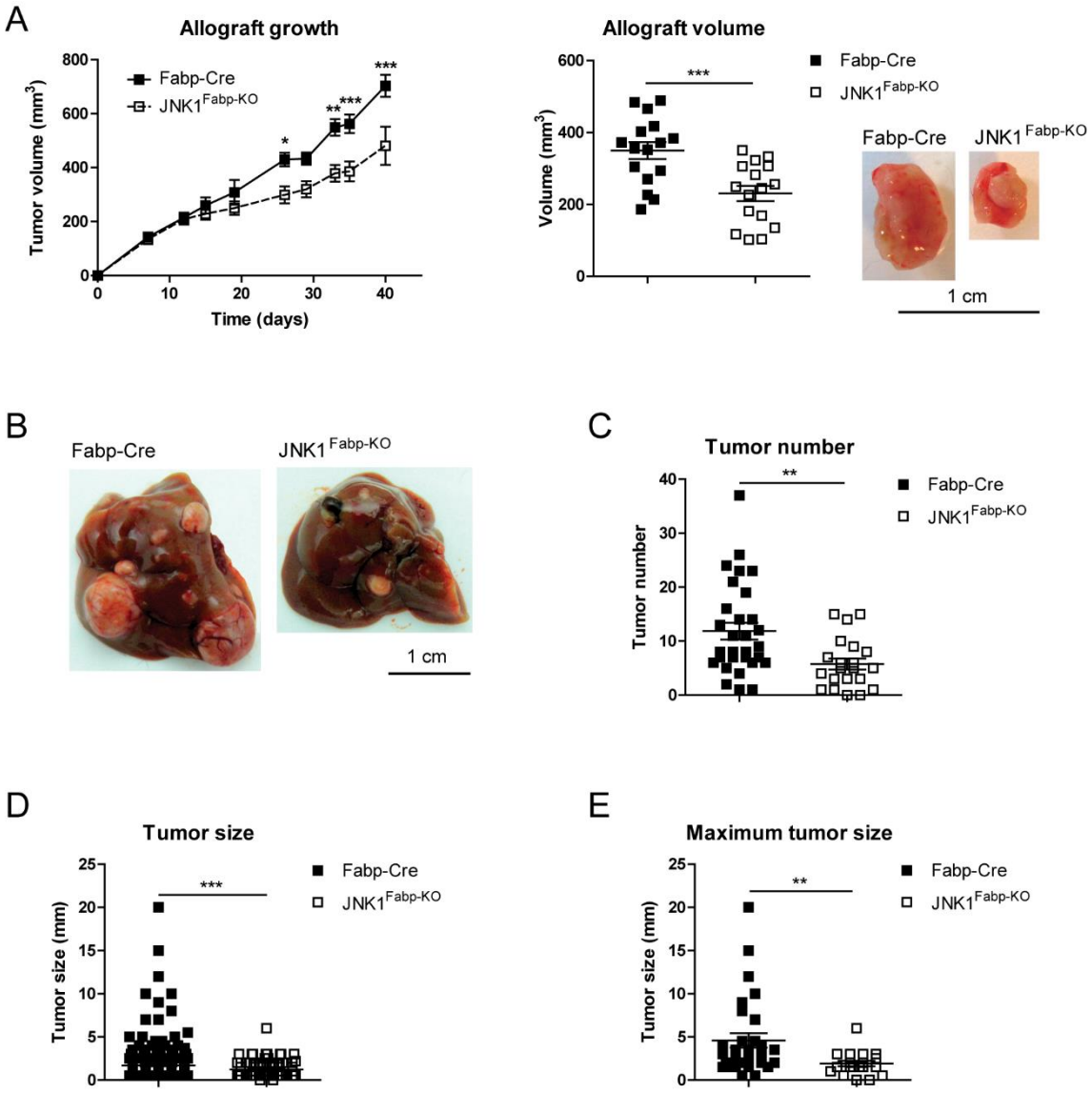

Figure R38. Adipose tissue JNK1 deficiency reduces HCC progression. (A) Representative allografts and tumor volume quantification in Fabp-Cre and JNK1$^{Fabp\text{-}KO}$ male mice during the experiment and at sacrifice 5 weeks after subcutaneous injection with 5 x 10^4 Hep53.4 cells in each flank. Data are shown as means ± SEM; **p* < 0.05; ***p* < 0.01; ****p* < 0.001; two-way ANOVA coupled with Bonferroni's multiple comparisons test (allograft growth); Student's *t*-test (allograft volume); *n* = 16-18 tumors (8-9 mice per genotype). (B-E) HCC progression analyzed in Fabp-Cre and JNK1$^{Fabp\text{-}KO}$ mice 8 months after i.p. injection with DEN (50 mg/kg body weight) at P14. (B) Representative images of liver tumors in Fabp-Cre and JNK1$^{Fabp\text{-}KO}$ mice. (C-E) Tumor number, tumor size and maximum tumor size. Data are shown as means ± SEM; ***p* < 0.01; ****p* < 0.001; Student's *t*-test (tumor number); Student's *t*-test with Welch's correction (tumor size and maximum tumor size); *n* = 21-30. (Results shared in Manieri, 2016 and Manieri & Herrera-Melle et al., 2019).

2.9. Higher levels of adiponectin in JNK1$^{Fabp\text{-}KO}$ mice are essential for their protection against HCC

In order to evaluate the potential role of adiponectin in the protection against HCC in JNK1$^{Fabp\text{-}KO}$ males, WT and JNK1-deficient mice were crossed with mice deficient in

adiponectin (Adipoq$^{-/-}$), and allograft assays were performed. Results revealed that tumor growth was similar in Fabp-Cre Adipoq$^{-/-}$ and JNK1$^{Fabp\text{-}KO}$ Adipoq$^{-/-}$ males (Figure R39A), consistent with a central role for adiponectin in the JNK1$^{Fabp\text{-}KO}$ phenotype, and suggesting that the elevated adiponectin levels in JNK1$^{Fabp\text{-}KO}$ males were responsible for their reduced tumor growth. To corroborate this hypothesis, we analyzed DEN-induced liver cancer in Fabp-Cre Adipoq$^{-/-}$ and JNK1$^{Fabp\text{-}KO}$ Adipoq$^{-/-}$ males. Tumor number, size, and maximum size after 8 months did not differ significantly between the two groups of mice, suggesting an important role for adiponectin in the protection of JNK1$^{Fabp\text{-}KO}$ males against DEN-induced HCC (Figures R39B-E).

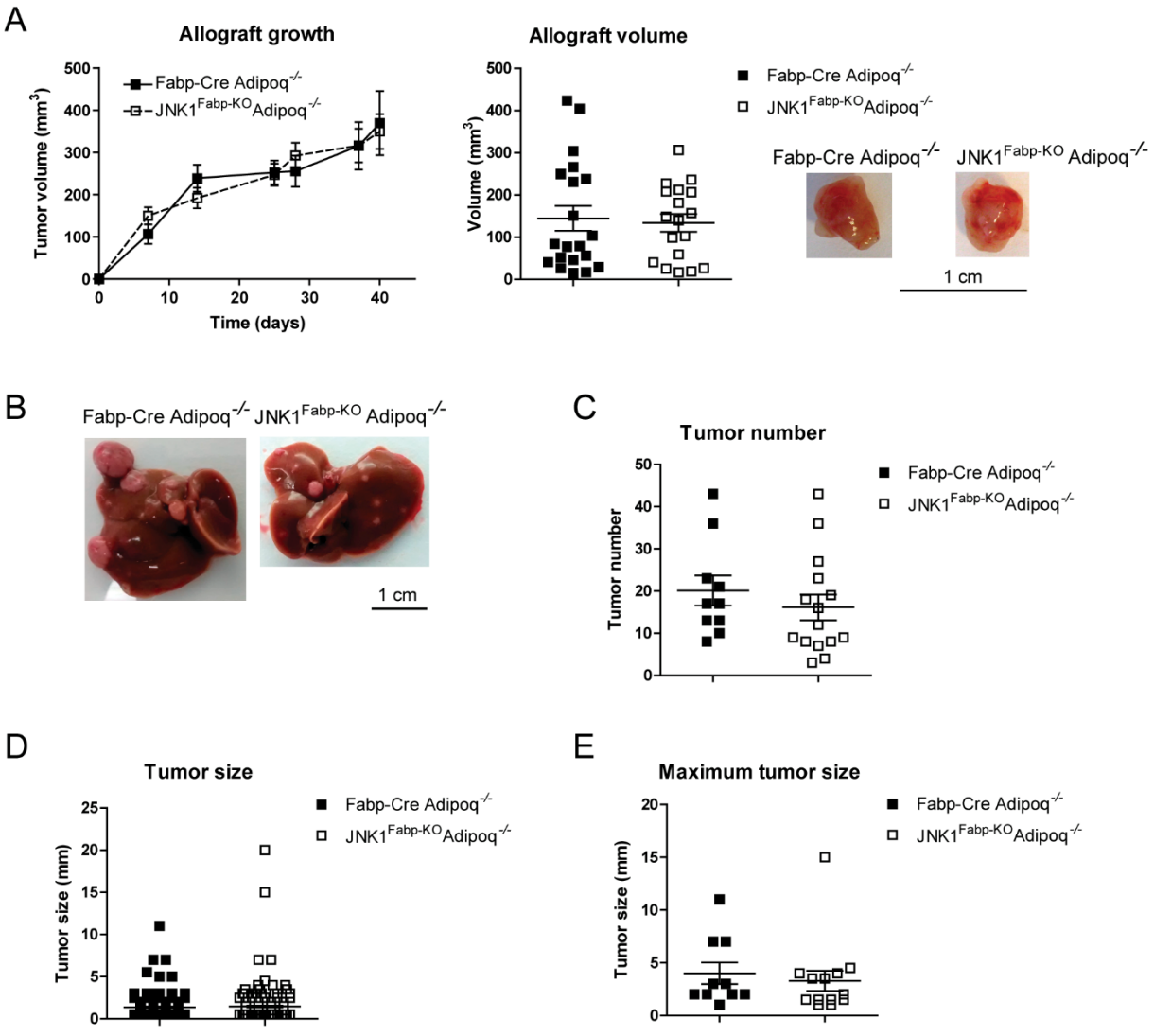

Figure R39. High levels of adiponectin in JNK1$^{Fabp\text{-}KO}$ mice are responsible for their protection against HCC. (A) Representative allografts and tumor volume quantification in Fabp-Cre adiponectin knockout male mice (Fabp-Cre Adipoq$^{-/-}$) and JNK1$^{Fabp\text{-}KO}$ adiponectin knockout male mice (JNK1$^{Fabp\text{-}KO}$ Adipoq$^{-/-}$) during the experiment and at sacrifice 5 weeks after subcutaneous injection of 5 x 10^4 Hep53.4 cells in each flank. Data are shown as means ± SEM; two-way ANOVA coupled with Bonferroni's multiple comparisons test (allograft growth); Student's *t*-test (allograft volume); *n* = 18-20 tumors (9-10 mice). (B-E) HCC progression analyzed in Fabp-Cre Adipoq$^{-/-}$ and JNK1$^{Fabp\text{-}KO}$ Adipoq$^{-/-}$

mice 8 months after i.p. injection with DEN (50 mg/kg body weight) at P14. (B) Representative images of liver tumors in Fabp-Cre Adipoq$^{-/-}$ and JNK1$^{Fabp\text{-}KO}$ Adipoq$^{-/-}$ mice. (C-E) Tumor number, tumor size and maximum tumor size. Data are shown as means ± SEM; Student's *t*-test; *n* = 10-15. (Results shared in Manieri, 2016 and Manieri & Herrera-Melle et al., 2019).

2.10. AMPK and p38α activation by adiponectin reduces tumor progression

Adiponectin transduces its signal in the liver through the activation of several pathways, incuding p38 MAPK (Combs & Marliss, 2014; Mao et al., 2006) and AMPK (Roy & Palaniyandi, 2021; Yamauchi et al., 2002). Both p38α and AMPK are known to suppress liver cancer development (L. Hui et al., 2007; Jiang et al., 2019). Therefore, we evaluated the activation of AMPK and p38α in allografts from male and female mice. Immunoblot analysis detected higher AMPK and p38α phosphorylation, and therefore activation, in females (Figure R40A), correlating with the higher adiponectin levels in female mice (Figure R28C). This gender difference in p38α or AMPK activation was not observed in Adipoq$^{-/-}$ mice (Figure R40B), suggesting that higher activation of these kinases in females is the result of the higher levels of circulating adiponectin. To evaluate whether p38α and AMPK activation is implicated in the protection against liver cancer in females, we implanted Hep53.4 cells subcutaneously into male mice and activated each pathway by two different strategies. In the first strategy, animals were treated with metformin to activate AMPK. In the second one, allografts were injected with a retrovirus containing active p38α or a control construct on days 9 and 22 after transplantation. As expected, metformin treatment significantly reduced tumor volume (Figure R40C), indicating that AMPK activation confers protection against HCC. Similarly, tumors infected with active p38α were significantly smaller (Figure R40D), suggesting that the adiponectin-mediated protection against HCC is also mediated by p38α activation.

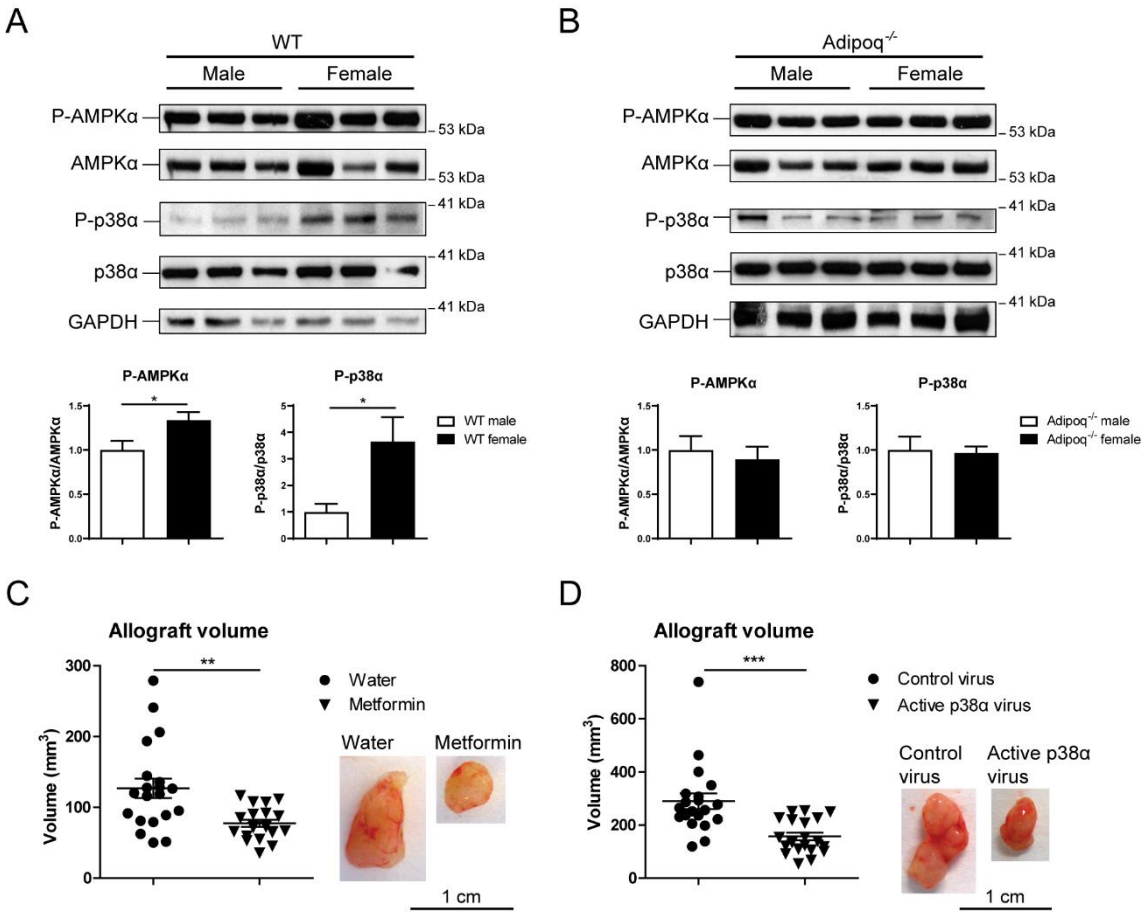

Figure R40. AMPKα and p38α activation protects against tumor growth. (A) Immunoblot analysis and quantification of phospho (P)-AMPKα, AMPKα, P-p38α, and p38α in tumor allografts obtained from WT male and female mice 21 days after implantation. GAPDH protein expression was monitored as a loading control. Data are normalized to WT male and shown as means ± SEM; **p* < 0.05; Student's *t*-test; *n* = 6-10. (B) Immunoblot analysis and quantification of P-AMPKα, AMPKα, P-p38α, and p38α in tumor allografts obtained from Adipoq$^{-/-}$ male and female mice 21 days after implantation. GAPDH protein expression was monitored as a loading control. Data are normalized to Adipoq$^{-/-}$ male and shown as means ± SEM; Student's *t*-test; *n* = 10-11. (C) Representative allografts and tumor volume quantification in WT male at sacrifice 5 weeks after subcutaneous injection with 5 x 10^4 Hep53.4 cells in each flank and treatment with 300 mg/day/kg body weight of metformin (supplied in the drinking water). Data are shown as means ± SEM; ***p* < 0.01; Student's *t*-test with Welch's correction; *n* = 20 tumors (10 mice per genotype). (D) Representative allografts and tumor volume quantification in WT male overexpressing p38α in hepatic tumors. Mice received subcutaneous injections in each flank with 5 x 10^4 Hep53.4 cells followed by intratumor injections on days 9 and 22 with retroviruses expressing active p38α or control viruses. Male mice were sacrificed 5 weeks after Hep53.4 cell injection. Data are shown as means ± SEM; ****p* < 0.001; Student's *t*-test with Welch's correction; *n* = 20 tumors (10 mice per genotype). (Results C and D shared in Manieri, 2016 and Manieri & Herrera-Melle et al., 2019).

We next investigated the extent of p38α and AMPK phosphorylation in livers of JNK1$^{Fabp\text{-}KO}$ mice. Consistent with the high levels of adiponectin in JNK1$^{Fabp\text{-}KO}$ males, liver activation of p38α and AMPK was significantly higher in DEN-treated JNK1$^{Fabp\text{-}KO}$ male mice than in their Fabp-Cre counterparts (Figures R41A, B). To evaluate whether AMPK activation is necessary for adiponectin-mediated protection in JNK1$^{Fabp\text{-}KO}$ mice, we treated Hep53.4 cells with an

shRNA against AMPK or a scrambled control sequence. As expected, AMPK knockdown in Hep53.4 cells resulted in larger tumors after implantation in Fabp-Cre animals. More importantly, JNK1$^{Fabp\text{-}KO}$ males were no longer protected against tumor growth, indicating that AMPK activation in hepatocytes is necessary for the protection observed in JNK1$^{Fabp\text{-}KO}$ mice (Figure R41C).

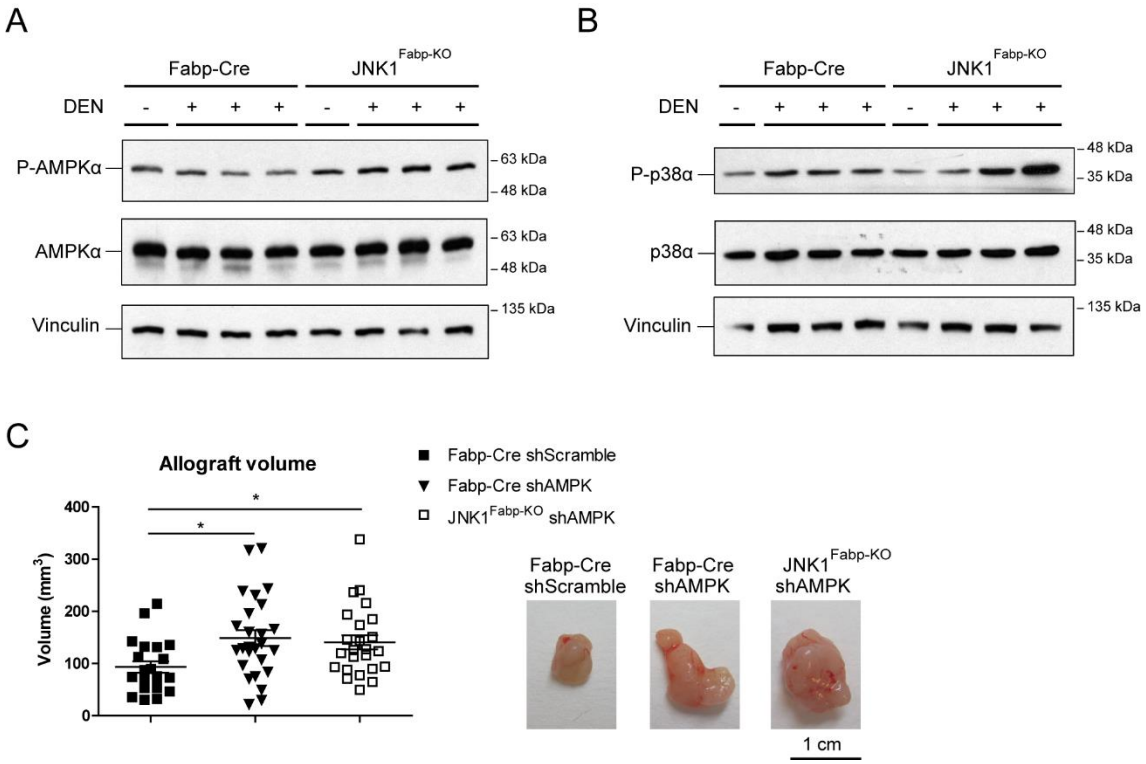

Figure R41. Adiponectin confers protection against tumor growth through AMPKα and p38α activation. (A, B) Fabp-Cre and JNK1$^{Fabp\text{-}KO}$ mice were injected i.p. with DEN (50 mg/kg) or saline (-) at P14. (A) Immunoblot analysis of phospho (P)-AMPKα, AMPKα and vinculin in livers obtained 15 days after DEN injection. (B) Immunoblot analysis of P-p38α, p38α, and vinculin in livers obtained one month after DEN injection. (C) Representative allografts and tumor volume quantification in male mice with hepatic tumors lacking AMPK expression. Mice received subcutaneous injections with 1 x 10^6 Hep53.4 cells in each flank, previously transduced with shRNA targeting AMPK or a control sequence (shScramble). Mice were sacrificed 5 weeks after Hep53.4 cell injection. Data are shown as means ± SEM; **p* < 0.05; one-way ANOVA coupled with Dunnett's multiple comparisons test. *n* = 21-26 tumors (11-13 mice). (Results A and B shared in Manieri, 2016 and Manieri & Herrera-Melle et al., 2019).

DISCUSSION

Obesity, which has emerged as a pandemic, is explained by the overlay of environmental changes and genetic and epigenetic mechanisms. Together with the rise in obesity worldwide, increasing trends of its comorbidities are also observed, which results in a relevant public health challenge (Upadhyay et al., 2018).

The metabolic stress observed in obesity has been linked to systemic alterations that lead to the activation of diverse signaling pathways, including the SAPKs pathway (Manieri & Sabio, 2015). Stress kinases are important regulators of cell adaptation to external changes, which makes them promising targets for the prevention and treatment of obesity and its complications (Nikolic et al., 2020). Remarkably, SAPKs have been identified as important modulators of whole-body energy homeostasis by the control of inter-organ communication (Cereijo et al., 2018; Sabio et al., 2008; Y. Wu et al., 2015). The main purpose of this thesis was to broaden our understanding of the functions of stress kinases in the control of whole-body metabolism and inter-organ crosstalk in the context of diseases whose prevalence increases in obese individuals. To that end, we analyzed the role of skeletal muscle p38α in the development of obesity and type 2 diabetes, and the implications of white adipose tissue JNK1 in HCC development, including gender-based differences. The results derived from this thesis significantly contribute to the understanding of the role of stress kinases in obesity and some of its associated diseases in a tissue-specific manner, and they also expand our knowledge of the intricate network through which SAPKs modulate inter-organ communication.

1. Muscle p38α in the control of energy balance

Energy homeostasis depends on the balance between energy intake and energy expenditure. High energy availability and low energy demand favor fat accumulation (Gehart et al., 2010). This evolutionary adaptation has become a great disadvantage nowadays, promoting the development of several metabolic disorders (Benton et al., 2021).

Among the different pathways that have been implicated in the control of energy balance, the SAPKs pathway has received special attention (Manieri & Sabio, 2015). While the role of JNK in obesity and insulin resistance has been extensively studied (Sabio & Davis, 2010), the implications of p38 in this context remain poorly understood. Nevertheless, there is ample evidence that the activation of p38s signaling in key metabolic tissues is crucial in the development of obesity comorbidities (Bernardo, 2017; Matesanz et al., 2017, 2018). However, its role in some organs, such as skeletal muscle, needs further understanding. Although p38α is the most widely studied p38 family member, its function in skeletal muscle is still far from clear. In this study, we attempted to identify the *in vivo* role of p38α in striated muscle by using striated muscle-specific p38α knockout mice, as well as its systemic implications.

1.1. Lack of p38α in striated muscle protects against HFD-induced obesity through increased locomotor activity

Our results show that mice deficient for p38α in striated muscle have reduced body weight and are protected against HFD-induced obesity compared to control mice (Figures R2, R4). This phenotype is mainly caused by an increase in locomotor activity and subsequent energy expenditure (Figures R5, R6), protecting mice against HFD-associated disorders, such as diabetes and liver steatosis (Figures R3, R7-9). Although differences in locomotor activity were higher in HFD than in ND, HFD was not necessary for them to appear (Figure R6C).

It was previously described that lack of the upstream p38 activator MKK6 ($MKK6^{-/-}$) protects mice against HFD-induced obesity due to an increase in energy expenditure caused by enhanced thermogenesis (Matesanz et al., 2017). In contrast, muscle p38α-deficient mice did not have differences in body or interscapular temperature (Figures R5D, E; R6D, E), which indicates that lack of p38α in striated muscle is not responsible for the phenotype of $MKK6^{-/-}$ animals. In contrast, absence of p38α in adipose tissue renders a similar phenotype (Matesanz et al., 2018). In addition, lack of MKK3 ($MKK3^{-/-}$) does not influence HFD-induced obesity, but it impairs insulin signaling, as happens similarly with full-body p38β knockout mice (Bernardo, 2017), an opposite phenotype to the one of $p38\alpha^{MCK\text{-}KO}$ mice (Figures R7, R8). It is known that lack of p38α in different cells renders opposing phenotypes, as happens with hepatocytes and macrophages, where it increases or decreases weight gain, respectively (X. Zhang et al., 2019), or in neurons, where it does not regulate body weight or glucose homeostasis (Stefanoska et al., 2018). All these results indicate that targeting certain p38 family members in a tissue-specific manner renders different results than using the upstream MKK3 and MKK6 proteins as potential therapeutic targets against obesity and diabetes. Here, we show a confirmation of the diverse roles of the same family members in different organs, which justifies the need to get a clear understanding of their function at the tissue or cellular level.

The increase in locomotor activity explains the protection against HFD-induced obesity in $p38\alpha^{MCK\text{-}KO}$ mice, which is accompanied by reduced insulin resistance and liver steatosis (Figures R7-9). Improved insulin signaling in skeletal muscle is crucial, since this organ is considered the earliest site of insulin resistance in individuals at high risk for type 2 diabetes (DeFronzo & Tripathy, 2009). In addition, protection against liver steatosis in these mice might contribute to their improved insulin signaling, indicating that the protection against obesity could be responsible for the better control of glucose and insulin levels. Thus, it seems that this phenotype is due to an interplay between the insulin responsiveness of skeletal muscle and liver, and glucose-stimulated insulin secretion by pancreatic β cells, which would improve glucose

tolerance. Moreover, the reduced levels of the “satiety hormone” leptin, which is secreted in direct proportion to the amount of fat mass (S. Zhao et al., 2020), seems to be controlling food intake, as its levels negatively correlate with food ingestion in ND and HFD (Figures R5G, R6H). In addition, it has been shown that an increase in energy expenditure increments energy intake, which compensates for the additional requirement (Westerterp, 2010). However, this high food consumption was not observed when mice were fed a ND (Figure R6G), suggesting that food intake was independent of the regulation of locomotor activity and energy balance. In fact, differences in food intake depending on the diet have also been described in other models, where they were essential for the development of obesity (Vernia et al., 2016b). This contrasts with our results, where high food intake in HFD was not enough to develop obesity in p38α^{MCK-KO} mice.

1.2. p38γ is hyperactivated in p38α-deficient muscles

One of the major findings of our study is the hyperactivation of p38γ in p38α-deficient skeletal muscles, which was responsible for their protection against HFD-induced obesity and diabetes (Figures R11A-E, R23-25). Although it is known that the increase in fatty acids, inflammatory cytokines and stress in HFD conditions can activate MAPKs signaling pathway (Gehart et al., 2010), a comparison between ND- and HFD-fed mice suggested that the HFD stressor was not responsible for p38γ activation. Therefore, this activation seems to be caused by increased levels and activity of the two main upstream regulators of p38s, MKK3 and MKK6, which could be compensating for p38α loss (Figures R11H-J). This is consistent with the previously described p38α-mediated negative feedback regulation of TAK1, a MAP3K that phosphorylates MKK3 and MKK6 (Cheung et al., 2003). In fact, this compensatory phosphorylation of p38γ has also been shown in skeletal muscle in different models (Brien et al., 2013; Odeh et al., 2020), as well as in other tissues (Matesanz et al., 2018). Although exercise is known to activate p38s (Egan & Zierath, 2013), the decrease in MKK6 protein levels in p38α-overexpressing myotubes (Figure R16E) suggests that p38α exerts a negative regulation over MKK6 in a cell-autonomous way, independent of locomotor activity. On the other hand, the hyperactivation of JNK in the absence of p38α has been described in other cell types (L. Hui et al., 2007), and our results indicate that it was not enough to impair insulin signaling in p38α-deficient muscles.

1.3. p38α-deficient skeletal muscles increase their mitochondrial metabolic pathways through PGC1α

Muscle contraction is powered by ATP hydrolysis, and ATP resynthesis can be achieved by several pathways: (1) phosphocreatine degradation; (2) anaerobic glycolysis; and (3) aerobic pathways including carbohydrate or lipid oxidation, in which mitochondria is involved (Egan & Zierath, 2013). p38α-deficient muscles showed downregulation of glycolytic pathways and

upregulation of mitochondrial ones (Figures R10, R12, R15), indicating that molecular alterations derived from p38α deficiency are linked to skeletal muscle metabolic remodeling, from a glycolytic to an oxidative phenotype dependent on mitochondrial activity. We confirmed the previously described role of PGC1α, one of the most important factors for mitochondrial biogenesis (Lin et al., 2005), in upregulating mitochondrial pathways in primary myotubes (Figure R17A) (Handschin et al., 2007b). Since PGC1α expression was increased in p38α-deficient muscles (Figure R13B), it was suggested as a possible candidate for the metabolic shift observed, including the increase in mitochondrial size and in the number of lipid droplets, as previously described (Choi et al., 2008). Although other mediators of mitochondrial biogenesis are known (Islam et al., 2020), the absence of differences in PGC1β levels in muscles lacking p38α (Figures R13C, D) and the reversion of the mitochondrial phenotype when PGC1α was not present in a context of p38α deficiency (Figure R14) indicate that these changes rely on PGC1α protein.

While p38γ is thought to be required for exercise-induced mitochondrial biogenesis through PGC1α (Pogozelski et al., 2009), its absence does not change PGC1α expression *in vivo* (Foster et al., 2012). Our results indicate that p38γ is not driving the mitochondrial phenotype of $p38\alpha^{MCK\text{-}KO}$ mice, since muscles from $p38\alpha/\gamma^{MCK\text{-}KO}$ mice also showed an upregulation of PGC1α and oxidative phosphorylation pathway (Figures R12C, E; R13B, F). Indeed, mitochondria were also bigger in skeletal muscles from $p38\alpha/\gamma^{MCK\text{-}KO}$ mice and contained a similarly high number of lipid droplets as muscles from $p38\alpha^{MCK\text{-}KO}$ mice, further corroborating the relevance of PGC1α in this phenotype (Figures R14A-C). Although exercise is known to increase muscle PGC1α expression (Pilegaard et al., 2003; Terada & Tabata, 2004), PGC1α upregulation in p38α-deficient muscles was not the consequence of high locomotor activity, since $p38\alpha/\gamma^{MCK\text{-}KO}$ mice displayed lower voluntary activity. Altogether, these results support the existence of an additional mechanism causing PGC1α upregulation in the absence of p38α.

p38α and p38γ have been described to stimulate mitochondrial biogenesis and respiration by positively affecting both transcription and activity of PGC1α (Fan et al., 2004; Pogozelski et al., 2009; Puigserver et al., 2001). It was therefore surprising to find an upregulation of this transcription factor in p38α-deficient muscles. Our *in vitro* results suggest that both p38s are negative regulators of PGC1α at the posttranscriptional level, in spite of their positive effect on PGC1α transcription (Figures R18A, B). The discrepancies between our study and others might be explained by the different strategies used to induce or repress p38s activity: while others simultaneously target several p38s by using the p38s constitutive activator MKK6E or the p38α/β inhibitor (T. Hong et al., 2011; Puigserver et al., 2001), we used a more p38 isoform-specific approach by using the constitutively active forms of p38α and p38γ. In addition, many mitochondrial genes have been shown to decrease in muscle cells infected with MKK6E when

PGC1α is not co-transduced, which might indicate that supraphysiological PGC1α levels are needed for MKK6E to promote cellular respiration (Puigserver et al., 2001). Indeed, we did not observe alterations in PGC1α protein when p38α or p38γ were transduced in myotubes overexpressing PGC1α (Figure R18D). In line with our results, activation of p38s by obesity stimuli such as saturated fatty acids or TNFα has been found to suppress PGC1α in different muscle cells (Crunkhorn et al., 2007; Palomer et al., 2009). In addition, p38s signaling has been shown to decrease mitochondrial proteins in the heart (Wall et al., 2006), and it has been involved in the negative regulation of the PGC1α target gene fibronectin type III domain-containing 5 (*Fndc5*) in C2C12 cells (M. Yang et al., 2013). Therefore, the controversial role of p38s in the control of PGC1α expression and activation might indicate a cell type- and context-specific regulation. According to our results, it is possible that both p38α and p38γ control PGC1α by decreasing its translation or increasing its degradation, while p38γ is also increasing its phosphorylation (Figures R18C, D). This differential regulation of PGC1α by different p38 family members opens new research avenues that may help us understand the exact mechanisms of PGC1α regulation, ranging from transcription to posttranslational modifications. Interestingly, p38-modified PGC1α has some qualitatively different activities compared to the wild-type protein (Puigserver et al., 2001), which suggests that p38α- or p38γ-modified PGC1α protein might have different target specificity, therefore causing different metabolic alterations.

1.4. PGC1α is not responsible for the protection against obesity and type 2 diabetes in mice lacking p38α in striated muscle

Mitochondrial dysfunction is connected to common diseases, such as diabetes, obesity, cancer and neurodegenerative disorders (Chandel, 2015). In contrast, high mitochondrial activity has been considered to reduce insulin resistance by decreasing intracellular fatty acids (Petersen & Shulman, 2018). In particular, reduced expression of PGC1α in skeletal muscle has been associated with type 2 diabetes (Mootha et al., 2003; Patti et al., 2003). In fact, lack of PGC1α in muscle worsens glucose homeostasis (Handschin et al., 2007b) and decreases physical activity (Handschin et al., 2007a). However, the absence of PGC1α in p38α-deficient muscles did not impair glucose homeostasis, nor did it decrease locomotor activity, since both p38α/PGC1α^{MCK-KO} and p38α^{MCK-KO} mice showed higher locomotor activity and energy expenditure (Figures R22A, C), glucose tolerance and insulin sensitivity (Figures R22G, H) compared with controls. All these results indicate that higher PGC1α expression is not responsible for the protection against obesity and improved systemic glucose homeostasis in p38α^{MCK-KO} mice and suggest that muscle p38γ activation may rescue some of the adverse consequences of PGC1α loss. Although PGC1α upregulation in p38α-deficient muscles does not seem to have systemic implications in energy balance, our results suggest that it is responsible for the increased strength observed in these

muscles (Figure R19). In fact, increased oxidative muscle metabolism has been shown to improve muscle functionality (Jeong et al., 2019), and muscle PGC1α is thought to improve exercise performance and grip strength (Calvo et al., 2008; Handschin et al., 2007a). Although many of these effects may be caused by the role of PGC1α in driving the formation of slow-twitch muscle fibers (Lin et al., 2002), the different fiber type composition in p38α^{MCK-KO} and p38α/γ^{MCK-KO} mice as well as the lack of differences between p38α^{MCK-KO} and p38α/PGC1α^{MCK-KO} mice suggest that higher PGC1α levels and mitochondrial metabolism in p38α-deficient muscles have functional implications at the local level independently of the fiber type profile. However, fiber type composition in other muscles should also be analyzed.

1.5. p38γ hyperactivation in p38α-deficient muscles is essential for the protection against HFD-induced obesity

In contrast to PGC1α, p38γ demonstrated to be essential in the protection against HFD-induced obesity and diabetes in mice lacking p38α in striated muscle by increasing locomotor activity and energy expenditure (Figures R23-25). Although many studies indicate that a higher activation of MAPKs signaling might be detrimental (Gehart et al., 2010), some MAPKs can also have protective roles in specific contexts, as skeletal muscle p38γ is doing. Stimuli such as muscle denervation (Odeh et al., 2020) or muscle contraction (Boppart et al., 2001; Coffey et al., 2006; M. Yu et al., 2003) are known to induce p38s activation in skeletal muscle. Although most of the studies do not discriminate between p38 isoforms, some have revealed the relevance of p38γ activation in response to exercise, in contrast to p38α (Boppart et al., 2000). Importantly, the opposite role of different p38 family members within the same tissue in energy homeostasis has been previously described, as happens with p38α and p38δ in BAT (Matesanz et al., 2018). Our results indicate that p38α and p38γ have opposite roles in muscle, not only regarding myogenesis (Lluís et al., 2006; Lovett et al., 2010) (Figures R17B-D), but also in the control of energy balance.

Although p38s are thought to be dispensable for endurance exercise-induced changes between type II fibers (Pogozelski et al., 2009), our results indicate that p38γ promotes I-to-IIA fiber type transformation in soleus muscle (Figure R20). This result is in concordance with previous findings of preferential activation of p38γ in slow muscles, as well as higher percentage of slow fibers while lower of fast fibers in the absence of p38γ (Foster et al., 2012). In fact, p38γ is thought to repress myosin heavy chain 7 (*Myh7*) gene, which encodes for the type I MHC, characteristic of slow fiber types (Pogozelski et al., 2009; Schiaffino & Reggiani, 2011).

It was described that skeletal muscle-specific deletion of MKP-1 and its subsequent increase in p38 and JNK activities protects against diet-induced obesity (Lawan et al., 2018), a phenotype which could be partly mediated by p38γ. Moreover, p38 MAPKs pathway has been involved in

the control of glucose metabolism in skeletal muscle (Bengal et al., 2020), and our results indicate that muscle p38γ contributes to improved glucose homeostasis by controlling inter-organ communication. Interestingly, p38s phosphorylation has been found to be higher in skeletal muscle from females compared to males (Nicoll et al., 2019), which highlights the need to understand the role of muscle p38s to find new connections between their differential activation and known gender disparities in metabolism and energy homeostasis (Maher et al., 2010; Tramunt et al., 2020).

Our results point at IL-15 as a possible candidate for contributing to the high locomotor activity of p38α^{MCK-KO} mice (Figures R26-27). Higher IL-15 mRNA expression in muscles hyperactivating p38γ, but not in the absence of this p38 member, indicates a relevant role for this protein in the control of IL-15 expression (Figures R26B-D). In spite of higher muscle IL-15 expression in p38α^{MCK-KO} mice, they had lower circulating IL-15 in basal conditions (Figure R26F). This discrepancy could be due to a compensatory mechanism in the blood to counteract the higher exercise-induced IL-15 release observed in p38α^{MCK-KO} mice (Figure R26H). However, since our blood collections in basal conditions occurred at the time of euthanasia, they may not reflect the presence of IL-15 in the circulation at other times of the day. In fact, IL-15 is a myokine usually elevated following exercise (Crane et al., 2015; Tamura et al., 2011), although this is not always the case (Nielsen et al., 2007). Our results suggest that higher muscle IL-15 expression could be facilitating IL-15 secretion after exercise stimulation, making it faster in the case of p38α^{MCK-KO} mice. This higher plasma IL-15 upon exercise could be signaling in the cerebral motor cortex to enhance locomotor activity (Figure R27A) and reduce depression-like behavior (Figure R26E). Importantly, a decrease in IL-15Rα in the motor cortex results in a reduction in locomotor activity in p38α^{MCK-KO} mice (Figures R27B, C), further reinforcing the relevant role of IL-15 signaling in this area for the control of voluntary movements. Interestingly, the higher permeability of the blood-brain barrier to IL-15 in inflammatory conditions could explain why the phenotype observed is more extreme in HFD compared to ND (Pan et al., 2008) (Figures R5, R6).

The regulation of muscle-derived IL-15 and its physiological consequences remain unclear. Although IL-15 has been linked to reductions in adiposity and protection against type 2 diabetes and fatty liver (Nielsen et al., 2008; Sun et al., 2016; Sun & Liu, 2015), inconsistency among studies has brought controversy, with some of them indicating a negative effect of IL-15 on obesity (Cepero-Donates et al., 2016; Lacraz et al., 2016; Loro et al., 2015). In fact, while some studies have found low plasma IL-15 levels in obesity (Nielsen et al., 2008), others found no differences (Pierce et al., 2015) or higher levels in overweight individuals (Dozio et al., 2014). Moreover, the role of IL-15 signaling in the control of locomotor activity is also controversial, with evidence indicating that IL-15 enhances (Crane et al., 2015) or decreases locomotor activity (He

et al., 2010; Pistilli et al., 2011), a controversy that is also found regarding its role in the modulation of anxiety and depression (L. Nguyen et al., 2017; X. Wu et al., 2010, 2011). Our results indicate that IL-15 signaling in the motor cortex contributes to the increased locomotor activity of p38α^{MCK-KO} mice, establishing a relevant crosstalk between the muscle and the brain.

Considering our data altogether, we can submit a presumptive model of local and systemic effects originated from striated muscle p38α deficiency, demonstrating a novel role of stress-activated kinases in activation of pathways linked to energy metabolism and mitochondrial respiration (Figure D1). This study places skeletal muscle p38α as a signaling hub that is involved in different metabolic alterations and reveals a critical role for muscle p38γ activation in the stimulation of locomotor activity and energy expenditure, providing a promising new target for the development of novel therapeutic approaches to the current obesity epidemic.

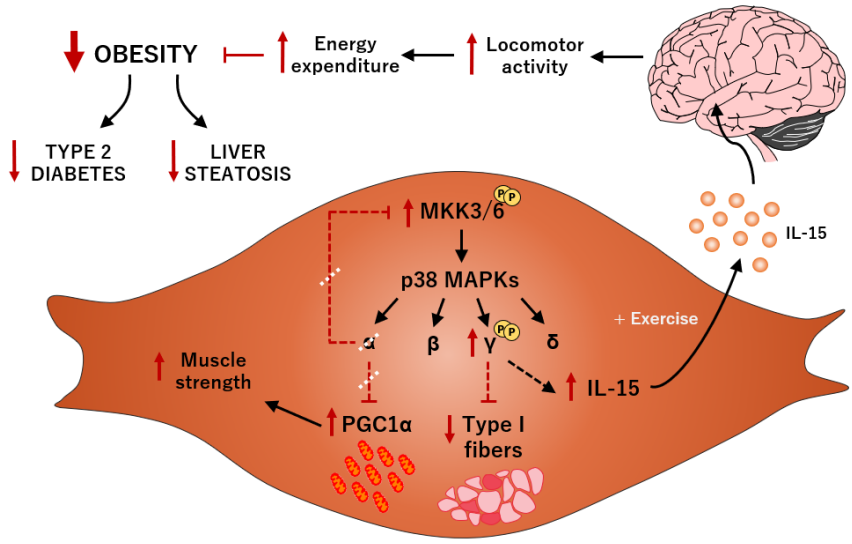

Figure D1. Proposed model for p38α action in muscle. As a result of the negative control of PGC1α by p38α in skeletal muscle, lack of p38α would lead to metabolic remodeling, increasing PGC1α and mitochondrial metabolism, which would enhance muscle strength. Moreover, due to the p38α-mediated control of upstream kinases, lack of p38α would result in the hyperactivation of MKK3 and MKK6 and, subsequently, of p38γ. p38γ hyperactivation represses type I fibers. Importantly, p38γ could be increasing IL-15 release upon exercise training, which would act on the motor cortex, increasing locomotor activity and energy expenditure, protecting against obesity and its adverse consequences.

2. Adipose tissue JNK1 and adiponectin in gender predisposition to hepatocellular carcinoma

Liver cancer is the third cause of death from cancer worldwide (Sung et al., 2021). The incidence and mortality rates of this cancer have increased rapidly, coinciding with the rising prevalence of obesity (Larsson & Wolk, 2007). Although epidemiological evidence indicates that excess body weight may be a risk factor for liver cancer, the definite link between both phenomena remains elusive (Vanni & Bugianesi, 2014). Adipose tissue is an active endocrine organ that mediates a

variety of physiological functions via secretion of adipokines, whose function is frequently altered in obesity. Interestingly, there are sex differences in the distribution and function of the adipose tissue, including changes in the secretion of adipokines, which make adipose tissue a sexually dimorphic organ. One example is the higher levels of adiponectin found in women compared to men (Yannakoulia et al., 2003), a hormone which is also decreased in obese individuals (Arita et al., 1999). Adiponectin has been described as a protective factor against many cancers (Parida et al., 2019), although its role in HCC remains controversial. Interestingly, men have 2 to 3 times more probability to develop liver cancer compared to women (Kim & Viatour, 2020). Accordingly, both male gender and obesity are accompanied by reduced plasma adiponectin levels, and both conditions increase the risk to develop HCC. Therefore, the main purpose of this project was to understand whether lower adiponectin levels are a risk factor for the development of HCC, as well as the physiological and molecular mechanisms linking obesity and gender with adiponectin and HCC.

2.1. Increased levels of adiponectin in females protect against liver cancer

The reduction of adiponectin levels in obesity, together with the gender dimorphism in humans (Yannakoulia et al., 2003) and rodents (Combs et al., 2003) were confirmed in our models (Figure R28). According to the increased probability to develop HCC and die from it in males (Bosch et al., 2004; S. Maeda et al., 2005; Naugler et al., 2007), we observed that WT female mice had reduced HCC tumor growth compared to males, a difference which was not observed in other types of tumors (Figure R29). Importantly, our results demonstrate that adiponectin is mainly responsible for these gender disparities in HCC development, indicating that higher adiponectin levels in females or adiponectin overexpression in males protect against HCC (Figures R30-32).

The connection between adiponectin and liver disease is not surprising, as liver is one of the main target organs for this adipokine (Moschen et al., 2012; Straub & Scherer, 2019). The beneficial effects of adiponectin on liver metabolism are clear, being considered a protective factor against NAFLD due to its role in the regulation of hepatic steatosis, insulin resistance, inflammation and fibrosis (Moschen et al., 2012). In fact, adiponectin is reduced in patients with non-alcoholic fatty liver (NAFL) and NASH (Polyzos et al., 2011). However, the role of this adipokine in liver cancer remained controversial (Dalamaga et al., 2012). Adiponectin has an anti-oncogenic potential in HCC cell lines (Saxena et al., 2010; Sharma et al., 2010). Besides, adiponectin knockout mice enhance the progression of NASH as well as hepatic tumor formation (Kamada et al., 2007), and they have impaired liver regeneration (Ezaki et al., 2009; Shu et al., 2009). Accordingly, adiponectin treatment inhibits liver tumor growth and metastasis (Man et al., 2010). In addition, some epidemiological studies have suggested the association between low

adiponectin levels and liver tumorigenesis (Saxena et al., 2010). However, no association (Nkontchou et al., 2010) or opposite results (Arano et al., 2011; M. J. Chen et al., 2012) have been reported for HCC associated with hepatitis C. Indeed, adiponectin is significantly elevated in other liver diseases apart from NAFL or NASH, especially in advanced stages, including chronic viral hepatitis (C. K. Hui et al., 2007) or viral hepatitis-related cirrhosis and HCC (C. J. Liu et al., 2009). These discrepancies in the connection between adiponectinemia and HCC may be attributable to the different HCC etiologies examined. Indeed, hyperadiponectinemia in viral hepatitis and associated liver malignancies might be due to secondary alterations to the hepatic disease, such as a response of the organism to counteract the inflammation and fibrosis through increased adiponectin. It may also be a secondary effect of adiponectin resistance that is commonly observed in cirrhosis or fibrosis (Corbetta et al., 2011). In this study, we have proved that adiponectin has a protective role in the development of HCC in both DEN and allograft models. Although the pathogenesis in the chemically induced HCC model differs from that in humans, it resembles some aspects of obesity-driven HCC, such as cell death, oxidative stress, inflammation and compensatory proliferation of hepatocytes (Heindryckx et al., 2009). Moreover, this mouse model of DEN-induced HCC shares histological and genetic signatures with human HCC with poor prognosis (J. S. Lee et al., 2004) and recapitulates the dependence on inflammation and gender disparity seen in humans (Naugler et al., 2007). With the results from this thesis, we confirm that the role of adiponectin in mediating the adipose tissue to liver crosstalk is not only relevant for the control of metabolic diseases, but also for liver cancer.

2.2. AdipoR2 is essential for gender differences in HCC development

Adiponectin acts mainly through its receptors AdipoR1 and AdipoR2, although T-cadherin has also been described as another receptor for this adipokine (Straub & Scherer, 2019). Our findings corroborate that AdipoR1 and AdipoR2 are expressed in the liver (Yamauchi et al., 2003) and indicate that hepatocytes are the liver cell type showing higher AdipoR2 expression compared to non-parenchymal cells, in contrast to AdipoR1 (Figure R33B). In particular, AdipoR2 is most abundantly expressed in the mouse liver compared with other organs (Yamauchi et al., 2003). Although hepatocytes account for most of AdipoR2 expression in the liver, this receptor is also relevant in other hepatic cells, such as HSCs, where it is responsible for their anti-fibrotic effects (Alzahrani et al., 2018), or KCs (Thakur et al., 2006). Moreover, our results indicate that tumoral hepatocytes have higher expression of these receptors compared to normal hepatocytes or to other tumoral cell lines (Figures R33A, C). In fact, other authors found AdipoRs expression in HCC cell lines (Miyazaki et al., 2005; Saxena et al., 2010). Since AdipoRs expression is positively correlated with adiponectin sensitivity (Yamauchi et al., 2007), their upregulation in HCC cells might be a mechanism to counteract lower adiponectin levels in liver cancer. In fact, AdipoR2

expression in HCC cells is of high relevance, since Hep53.4 tumor cells deficient for this receptor show faster proliferation when implanted into female mice, eliminating statistically significant differences in tumor volume between sexes (Figures R33D, E), in spite of higher adiponectin levels of females (Figure R28C). Besides hypoadiponectinemia, both obesity and NASH are characterized by reduced expression of adiponectin receptors in the liver of rodents (S. Liu et al., 2011; Peng et al., 2009; Yamauchi et al., 2007) and humans (Kaser et al., 2005; Shimizu et al., 2007), which has been shown to provoke a state of hepatic adiponectin resistance. Adiponectin resistance in the liver involves AdipoR2, since its inhibition aggravates liver disease, whereas its overexpression improves it (Tomita et al., 2008). With the present study, we confirmed the relevance of AdipoR2 for the protective effects of adiponectin in HCC tumor growth, being the AdipoR2 signaling pathway a promising target not only for fatty liver disease, but also for HCC.

2.3. Testosterone-dependent JNK1 activation in the adipose tissue controls adiponectin levels and HCC progression

It is known that adiponectin decreases with puberty in men, whereas its levels are maintained in women (Böttner et al., 2004). A similar gender disparity occurs in mice (Combs et al., 2003). The decline in adiponectin levels is inversely related to serum testosterone concentration (Böttner et al., 2004; Nishizawa et al., 2002). Accordingly, we found that changes in testosterone modified plasma adiponectin in male mice, increasing adiponectin concentration to the levels of females after castration, while decreasing it upon testosterone replacement (Figures R34B, R36E). Moreover, we showed that lack of testosterone protects against HCC (Figure R34C). Our results agree with previous findings in which testosterone decreased the secretion of adiponectin by 3T3-L1 adipocytes, confirming that androgens reduce plasma adiponectin through their effect on adipocytes (Nishizawa et al., 2002).

Several studies had addressed the question of gender disparities in HCC incidence. Liver tumors already proved to be sex hormones-responsive, since chemical or surgical reduction in testosterone levels decreased DEN-induced HCC incidence and size in males (T. Nakatani et al., 2001). Moreover, ovariectomy or testosterone administration in female mice increased tumor incidence, whereas administration of estrogens to orchiectomized mice further limited the development of HCC (T. Nakatani et al., 2001). These results and ours indicate that testosterone controls HCC tumor growth through adiponectin, whereas estrogens might have a protective effect through other mechanisms. Indeed, IL-6 was proposed as an important mediator of gender differences in HCC due to the higher IL-6 circulating levels after DEN administration in male mice compared to females (Naugler et al., 2007). Estrogens inhibited IL-6 production by KCs, thus decreasing liver cancer risk in females (Naugler et al., 2007). However, the role of estrogens in

the control of adiponectin is controversial, with some studies showing suppressive effects on adiponectin (Combs et al., 2003; S. C. Hong et al., 2007), or no association (Chalvatzas et al., 2009; Nishizawa et al., 2002; Sieminska et al., 2005). This indicates that androgens have a more relevant role in the control of adiponectin than estrogens. Although these results and others show that testosterone is a negative regulator of adiponectin, the mechanisms that underlie this regulation are still poorly understood (A. Xu et al., 2005). Testosterone might be affecting mechanisms that control adiponectin release instead of its expression, since neither adiponectin protein levels nor its mRNA expression are altered when testosterone levels are modified (Nishizawa et al., 2002). Besides, steroid hormones bind to intracellular receptors that enhance the transcription of genes by interacting with specific DNA sequences (Wilkenfeld et al., 2018). These facts suggested the existence of a factor involved in the secretion machinery of adiponectin, whose activity would be modulated by testosterone (Nishizawa et al., 2002). Indeed, it is known that steroid receptors can also signal via crosstalk with kinase signaling cascades through non-genomic mechanisms (Wilkenfeld et al., 2018). For instance, steroid receptors can lead to the activation of MAPKs such as ERK through these mechanisms (Ballaré et al., 2003; Peterziel et al., 1999; X. Zhang et al., 2014). Therefore, the participation of a kinase mediating the negative actions of testosterone on adiponectin release was inferred from these observations.

The activation of JNK in the adipose tissue of humans and mice is higher in conditions which are usually characterized by lower plasma adiponectin, such as obesity (Carvalho et al., 2013; Hirosumi et al., 2002) and type 2 diabetes (Carlson et al., 2003). More importantly, circulating adiponectin is higher in full-body JNK1 knockout mice ($JNK1^{-/-}$) compared to controls (Hirosumi et al., 2002). These observations suggested a possible role for adipose tissue JNK1 in the differential control of adiponectin levels between sexes. Our results indicate that the activation of JNK in the adipose tissue of male rodents is higher compared to females (Figure R35), and that testosterone leads to increased JNK phosphorylation in a cell-autonomous manner (Figures R36A, B). More importantly, *in vivo* JNK activation in adipose tissue is dependent on testosterone levels (Figure R36D) and inversely correlates with plasma adiponectin concentrations (Figure R36E). Thus, we suggest that testosterone decreases adiponectin circulating levels by activating JNK in the adipose tissue. We found higher plasma adiponectin in mice lacking JNK1 in the adipose tissue compared to controls (Figure R37B), confirming that lack of JNK1 exclusively in this tissue is able to reproduce the higher adiponectin concentrations found in $JNK1^{-/-}$ mice (Hirosumi et al., 2002). We demonstrated that JNK1 deficiency in the adipose tissue slows HCC tumor growth in both allografts and DEN-induced HCC models (Figure R38), an effect which is dependent on higher adiponectin concentrations in $JNK1^{Fabp\text{-}KO}$ mice (Figure R39). Therefore, these results corroborate our hypothesis that activation of adipose tissue JNK1 by testosterone

diminishes adiponectin secretion, being a risk factor for the development of HCC. It was known that JNK1$^{-/-}$ mice were protected against DEN-induced HCC (L. Hui et al., 2008), and the reduced JNK in myeloid cells was established as a possible cause for this phenotype (Das et al., 2011; Han et al., 2016). However, the results from this thesis indicate that the reduction of JNK1 in the adipose tissue also contributes to the protection against HCC observed in JNK1$^{-/-}$ mice. We therefore suggest that JNK1 is a factor linking testosterone to the reduced adiponectin release by adipocytes, whose existence had already been predicted (Nishizawa et al., 2002). There was previous evidence of the direct regulation of the JNK pathway by androgens *in vitro*. In fact, testosterone phosphorylates JNK in human umbilical vein endothelial cells (Jin et al., 2010; Powazniak et al., 2009) and in human kidney cells (Verzola et al., 2009). On the contrary, testosterone administration is known to transiently inhibit JNK phosphorylation in skeletal muscle of mice (Brown et al., 2009), indicating that testosterone-mediated JNK activation depends on the cell type. Our results demonstrate that testosterone promotes JNK activation in the adipose tissue, a pathway previously involved in the downregulation of adiponectin expression mediated by TNFα in 3T3-L1 adipocytes (Kim et al., 2005), but not in artificially hypertrophied 3T3-L1 adipocytes (Takahashi et al., 2008). Moreover, it was known that JNK1$^{-/-}$ mice have higher circulating adiponectin (Hirosumi et al., 2002), which also happens when JNK is inactivated specifically in the adipose tissue (X. Zhang et al., 2011). However, it was not known whether this effect was a secondary consequence of reduced fat mass in these mice. Here, we demonstrate a connection between adipose tissue JNK1 and adiponectin circulating levels independently of body weight (Sabio et al., 2008), which has been later confirmed (Han et al., 2021). Although the exact mechanism needs further understanding, a transcriptional event might be implicated in the process between testosterone action and adiponectin release, since a transcription inhibitor was able to restore the negative effect of testosterone on adiponectin secretion (A. Xu et al., 2005). Indeed, it has been very recently described that JNK can control adiponectin release by the adipocytes through a fibroblast growth factor 21 (FGF21)-dependent mechanism, since adipocyte JNK is thought to be a negative regulator of FGF21 expression in adipose tissue, a factor which increases the circulating concentration of adiponectin (Han et al., 2021).

This is not the first time that JNK1 in the adipose tissue has been described to control hepatic function. Adipose tissue JNK1 also controls the release of other adipokines, such as IL-6, an inflammatory cytokine that induces hepatic insulin resistance (Sabio et al., 2008). We found no differences in IL-6 or other pro-inflammatory cytokines between JNK1$^{Fabp\text{-}KO}$ and control mice (Figure R37C). Lack of changes in circulating IL-6 might be explained by the fact that HFD is necessary for them to appear between adipose JNK1 knockout mice and controls (Sabio et al., 2008). In addition, KCs are the main cells responsible for IL-6 production in the DEN model used,

and JNK in these cells has a relevant role in the production of these pro-inflammatory cytokines to induce HCC (Das et al., 2011; Han et al., 2016). As KCs have normal levels of JNK1 in JNK1$^{Fabp\text{-}KO}$ mice, the production of these cytokines might not be impaired and may mask any possible difference in IL-6 release from the adipose tissue. Therefore, we suggest that circulating IL-6 is not responsible for the differential HCC development between genotypes and that an additional and complementary mechanism to the one proposed by Naugler et al. might explain gender differences in HCC development. Thus, estrogens protect against HCC through the decreased release of IL-6 by KCs, whereas testosterone is a risk factor for HCC due to the lower adiponectin secretion by the adipose tissue. Interestingly, adiponectin levels inversely correlate with circulating IL-6 (Bruun et al., 2003), which establishes an interesting connection between these two secreted factors. It is possible that gender differences in IL-6 might not only be controlled by different estrogen levels in males and females, but also by testosterone through the decreased JNK1-mediated adiponectin release in males. In fact, adiponectin reduces JNK phosphorylation in macrophages (Folco et al., 2009), which could be an interesting link between adiponectin and JNK-mediated IL-6 production by macrophages and HCC (Das et al., 2011). Interestingly, IL-6 also downregulates adiponectin through a mechanism dependent on ERK MAPK (Fasshauer et al., 2003).

It is interesting to note that hepatic JNK also controls adiponectin, since higher blood FGF21 due to hepatic JNK deficiency increases adiponectin expression in the adipose tissue (Vernia et al., 2016c). Moreover, JNK signaling in adipocytes can also systemically control metabolism by regulating FGF21 expression (Han et al., 2021). These results and ours show that adipose tissue and liver have different ways to communicate through the release of several secreted factors in which JNK kinase is involved. By doing so, adipose tissue JNK can affect the liver, and hepatic JNK can alter adipose tissue function as observed by altered adiponectin expression, which can in turn have an impact on the liver and other tissues.

2.4. Adiponectin acts through AMPK and p38α activation to reduce tumor progression

Interaction of adiponectin with its receptors leads to the activation of several downstream targets, including AMPK (Yamauchi et al., 2002) and p38 (Mao et al., 2006). According to higher adiponectin levels in females, we observed stronger phosphorylation of AMPK and p38α in HCC tumors from them (Figure R40A), which was lost in the absence of this adipokine (Figure R40B). Indeed, livers from DEN-injected JNK1$^{Fabp\text{-}KO}$ mice also had higher AMPK and p38α activation (Figures R41A, B), in concordance with their higher circulating adiponectin (Figure R37B). Apart from their implications in metabolism (Achari & Jain, 2017), both AMPK and p38α have a role in cancer. p38α suppresses liver cancer development by reducing cell proliferation, and

consequently, mice with hepatic deletion of p38α show enhanced hepatocyte proliferation and tumor development (L. Hui et al., 2007; Sakurai et al., 2008, 2013). AMPK also suppresses HCC (Jiang et al., 2019), and treatment with the AMPK activator metformin reduces cancer incidence (H. P. Chen et al., 2013) and may improve survival among liver cancer patients (Ma et al., 2016). Consequently, AMPK has emerged as an important metabolic tumor suppressor and a promising target for cancer prevention and treatment (Larsson et al., 2012; Luo et al., 2010). The present study further corroborates the protective role of AMPK and p38α in HCC by showing decreased tumor growth when any of these kinases was activated (Figures R40C, D), or the relevance of AMPK activation for the protection against tumor growth in JNK1$^{Fabp\text{-}KO}$ mice (Figure R41C). It is known that activation of AMPK is a key step in mediating most of the effects of adiponectin at the cellular level (Achari & Jain, 2017), and these results suggest that the sole activation of AMPK in the liver might be a good therapeutic strategy for the prevention of HCC. Therefore, our results suggest that adiponectin and metformin could be used in the treatment of HCC.

In conclusion, we found that testosterone reduces the circulating concentrations of adiponectin by activating the stress kinase JNK in the adipose tissue, thus decreasing the protective role of adiponectin against HCC through p38α and AMPK activation in the liver (Figure D2). Our results indicate that gender differences in adipocytes are important players in HCC progression and can contribute to the increased incidence of HCC observed in males.

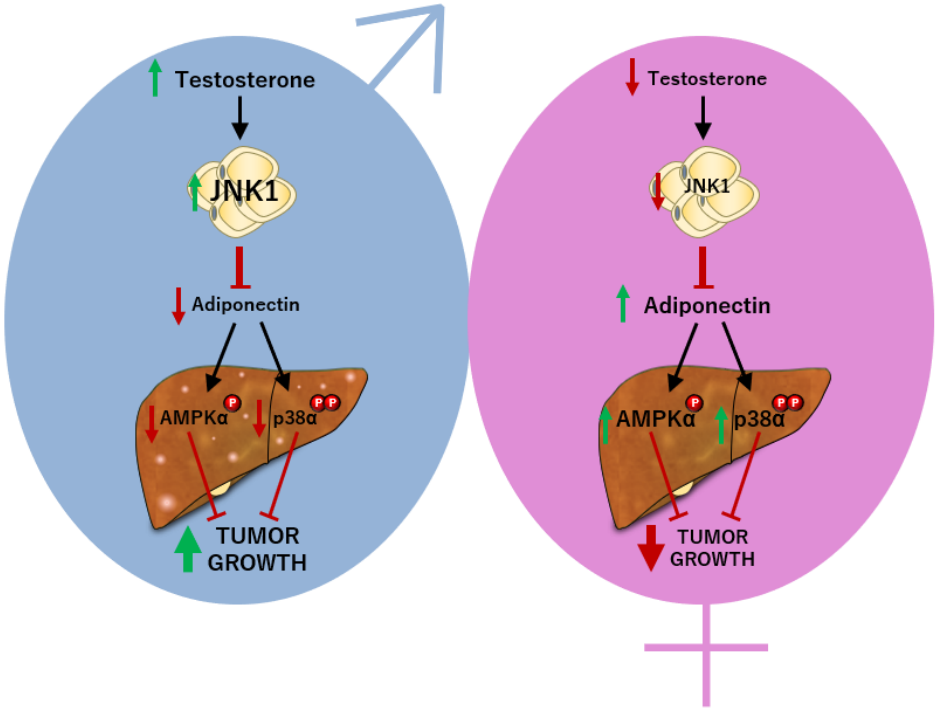

Figure D2. Proposed model for the gender differences in adiponectin levels and their role in HCC development. Testosterone-induced JNK1 activation in adipose tissue results in decreased levels of circulating adiponectin, which is responsible for the higher incidence of HCC in males due to the protective role of adiponectin against this cancer through AMPK and p38α activation in the liver.

CONCLUSIONS/CONCLUSIONES

1. Lack of p38α in striated muscle protects mice against HFD-induced obesity, type 2 diabetes and liver steatosis due to an increase in locomotor activity and subsequent energy expenditure.

2. Decreased p38α expression in skeletal muscle leads to p38γ hyperactivation through a mechanism dependent on the upstream kinases MKK3 and/or MKK6.

3. p38γ hyperactivation in p38α-deficient skeletal muscles is responsible for the increase in locomotor activity, energy expenditure and improved glucose homeostasis, which could be triggered by alterations in motor cortex signaling caused by the higher release of IL-15 by these muscles upon exercise.

4. The hyperactivation of p38γ in p38α-deficient soleus muscles leads to the transformation of type I fibers to type IIA, which does not impact muscle strength.

5. Lack of p38α in skeletal muscle increases its mitochondrial program as a consequence of PGC1α upregulation independently of p38γ hyperactivation. Although this increase in PGC1α does not have systemic consequences in glucose and energy homeostasis, it improves muscle strength.

6. The overexpression of the active proteins p38α or p38γ in myotubes decreases PGC1α protein levels and oxidative phosphorylation pathway, which suggests a relevant inhibitory role of p38s over this transcription factor.

7. Higher levels of adiponectin in females compared to males contribute to their protection against HCC development.

8. Testosterone is responsible for the decrease in plasma adiponectin observed in males through the activation of JNK in white adipocytes.

9. The decrease in plasma adiponectin caused by testosterone-mediated JNK1 activation in adipose tissue contributes to increased HCC development, which indicates a relevant adipose tissue-liver crosstalk.

10. The protective effects of adiponectin on liver cancer are mostly mediated by p38α and AMPK activation in this organ, being AdipoR2 essential for its function.

1. La deficiencia de p38α en músculo estriado protege a los ratones frente a la obesidad inducida por dieta rica en grasa, así como frente a la diabetes de tipo 2 y a la esteatosis hepática, debido a un incremento de la actividad locomotora, que a su vez aumenta el gasto energético.

2. La disminución en la expresión de p38α en músculo esquelético tiene como consecuencia la hiperactivación de p38γ debido a sus principales quinasas reguladoras, MKK3 y/o MKK6.

3. La hiperactivación de p38γ en músculos esqueléticos deficientes en p38α es responsable del aumento de la actividad locomotora, así como del incremento del gasto energético y mejora de la homeostasis de la glucosa. Este aumento de la actividad locomotora podría deberse a alteraciones en la señalización de la corteza motora ocasionadas por una mayor liberación de IL-15 por estos músculos después de hacer ejercicio.

4. La hiperactivación de p38γ en sóleos deficientes en p38α ocasiona una transformación del tipo de fibra muscular de tipo I a tipo IIA, que no afecta a la fuerza muscular.

5. La ausencia de p38α en músculo esquelético conduce a un incremento del programa mitocondrial debido al aumento de PGC1α, que es independiente de la hiperactivación de p38γ. Aunque este aumento en PGC1α no tiene consecuencias a nivel sistémico en la homeostasis energética y de la glucosa, ocasiona un aumento de la fuerza muscular.

6. La sobreexpresión de las formas activas de p38α o p38γ en miotubos disminuye la cantidad de proteína PGC1α y la vía de la fosforilación oxidativa, lo que sugiere un importante papel inhibitorio de estas p38s sobre este factor de transcripción.

7. Los mayores niveles de adiponectina en hembras en comparación con machos contribuyen a la protección frente al HCC observada en ellas.

8. La testosterona es responsable de la disminución de los niveles plasmáticos de adiponectina observada en machos por medio de la activación de JNK en adipocitos blancos.

9. La disminución de la adiponectina en sangre debido a la activación de JNK1 en el tejido adiposo contribuye a un aumento del desarrollo de HCC, estableciéndose una importante comunicación entre el tejido adiposo y el hígado.

10. Los efectos protectores de la adiponectina en el cáncer hepático se deben en gran parte a la activación de p38α y AMPK en este órgano, siendo el receptor AdipoR2 esencial para su función.

BIBLIOGRAPHY

Achari, A. E., & Jain, S. K. (2017). Adiponectin, a therapeutic target for obesity, diabetes, and endothelial dysfunction. *Int J Mol Sci*, *18*, 1321.

Adams, R. H., Porras, A., Alonso, G., Jones, M., Vintersten, K., Panelli, S., Valladares, A., Perez, L., Klein, R., & Nebreda, A. R. (2000). Essential role of p38alpha MAP kinase in placental but not embryonic cardiovascular development. *Mol Cell*, *6*, 109–116.

Aguirre, V., Uchida, T., Yenush, L., Davis, R., & White, M. F. (2000). The c-Jun NH(2)-terminal kinase promotes insulin resistance during association with insulin receptor substrate-1 and phosphorylation of Ser(307). *J Biol Chem*, *275*, 9047–9054.

Ahima, R. S., & Park, H. K. (2015). Connecting myokines and metabolism. *Endocrinol Metab (Seoul)*, *30*, 235–245.

Akagiri, S., Naito, Y., Ichikawa, H., Mizushima, K., Takagi, T., Handa, O., Kokura, S., & Yoshikawa, T. (2008). A mouse model of metabolic syndrome; increase in visceral adipose tissue precedes the development of fatty liver and insulin resistance in high-fat diet-fed male KK/Ta mice. *J Clin Biochem Nutr*, *42*, 150–157.

Alarcon-Vargas, D., & Ronai, Z. (2004). c-Jun-NH2 kinase (JNK) contributes to the regulation of c-Myc protein stability. *J Biol Chem*, *279*, 5008–5016.

Alessi, D. R., James, S. R., Downes, C. P., Holmes, A. B., Gaffney, P. R., Reese, C. B., & Cohen, P. (1997). Characterization of a 3-phosphoinositide-dependent protein kinase which phosphorylates and activates protein kinase Balpha. *Curr Biol*, *7*, 261–269.

Allen, D. L., Hittel, D. S., & McPherron, A. C. (2011). Expression and function of myostatin in obesity, diabetes, and exercise adaptation. *Med Sci Sports Exerc*, *43*, 1828–1835.

Allen Institute for Brain Science (2004). Allen Mouse Brain Atlas. https://mouse.brain-map.org/static/atlas

Alzahrani, B., Iseli, T., Ramezani-Moghadam, M., Ho, V., Wankell, M., Sun, E. J., Qiao, L., George, J., & Hebbard, L. W. (2018). The role of AdipoR1 and AdipoR2 in liver fibrosis. *Biochim Biophys Acta Mol Basis Dis*, *1864*, 700–708.

Andrews, S. (n.d.). A quality control application for high throughput sequence data. Babraham Institute. http://www.bioinformatics.babraham.ac.uk/projects/fastqc/

Aoi, W., Naito, Y., Takagi, T., Tanimura, Y., Takanami, Y., Kawai, Y., Sakuma, K., Hang, L. P., Mizushima, K., Hirai, Y., Koyama, R., Wada, S., Higashi, A., Kokura, S., Ichikawa, H., & Yoshikawa, T. (2013). A novel myokine, secreted protein acidic and rich in cysteine (SPARC), suppresses colon tumorigenesis via regular exercise. *Gut*, *62*, 882–889.

Arano, T., Nakagawa, H., Tateishi, R., Ikeda, H., Uchino, K., Enooku, K., Goto, E., Masuzaki,

R., Asaoka, Y., Kondo, Y., Goto, T., Shiina, S., Omata, M., Yoshida, H., & Koike, K. (2011). Serum level of adiponectin and the risk of liver cancer development in chronic hepatitis C patients. *Int J Cancer*, *129*, 2226–2235.

Arita, Y., Kihara, S., Ouchi, N., Takahashi, M., Maeda, K., Miyagawa, J., Hotta, K., Shimomura, I., Nakamura, T., Miyaoka, K., Kuriyama, H., Nishida, M., Yamashita, S., Okubo, K., Matsubara, K., Muraguchi, M., Ohmoto, Y., Funahashi, T., & Matsuzawa, Y. (1999). Paradoxical decrease of an adipose-specific protein, adiponectin, in obesity. *Biochem Biophys Res Commun*, *257*, 79–83.

Arnold, M., Pandeya, N., Byrnes, G., Renehan, P. A. G., Stevens, G. A., Ezzati, P. M., Ferlay, J., Miranda, J. J., Romieu, I., Dikshit, R., Forman, D., & Soerjomataram, I. (2015). Global burden of cancer attributable to high body-mass index in 2012: a population-based study. *Lancet Oncol*, *16*, 36–46.

Asih, P. R., Prikas, E., Stefanoska, K., Tan, A. R. P., Ahel, H. I., & Ittner, A. (2020). Functions of p38 MAP kinases in the central nervous system. *Front Mol Neurosci*, *13*, 570586.

Azzu, V., Vacca, M., Virtue, S., Allison, M., & Vidal-Puig, A. (2020). Adipose tissue-liver cross talk in the control of whole-body metabolism: implications in nonalcoholic fatty liver disease. *Gastroenterology*, *158*, 1899–1912.

Bakiri, L., & Wagner, E. F. (2013). Mouse models for liver cancer. *Mol Oncol*, *7*, 206–223.

Ballaré, C., Uhrig, M., Bechtold, T., Sancho, E., Di Domenico, M., Migliaccio, A., Auricchio, F., & Beato, M. (2003). Two domains of the progesterone receptor interact with the estrogen receptor and are required for progesterone activation of the c-Src/Erk pathway in mammalian cells. *Mol Cell Biol*, *23*, 1994–2008.

Barchetta, I., Cimini, F. A., Ciccarelli, G., Baroni, M. G., & Cavallo, M. G. (2019). Sick fat: the good and the bad of old and new circulating markers of adipose tissue inflammation. *J Endocrinol Invest*, *42*, 1257–1272.

Beardmore, V. A., Hinton, H. J., Eftychi, C., Apostolaki, M., Armaka, M., Darragh, J., McIlrath, J., Carr, J. M., Armit, L. J., Clacher, C., Malone, L., Kollias, G., & Arthur, J. S. (2005). Generation and characterization of p38beta (MAPK11) gene-targeted mice. *Mol Cell Biol*, *25*, 10454–10464.

Bengal, E., Aviram, S., & Hayek, T. (2020). p38 MAPK in glucose metabolism of skeletal muscle: beneficial or harmful? *Int J Mol Sci*, *21*, 6480.

Benton, M. L., Abraham, A., LaBella, A. L., Abbot, P., Rokas, A., & Capra, J. A. (2021). The influence of evolutionary history on human health and disease. *Nat Rev Genet*, *22*, 269–

283.

Bernardo, E. (2017). Role of MKK3 in diabetes development. Doctoral dissertation, *Autonomous University of Madrid*.

Betz, M. J., & Enerbäck, S. (2018). Targeting thermogenesis in brown fat and muscle to treat obesity and metabolic disease. *Nat Rev Endocrinol*, *14*, 77–87.

Blair, A. S., Hajduch, E., Litherland, G. J., & Hundal, H. S. (1999). Regulation of glucose transport and glycogen synthesis in L6 muscle cells during oxidative stress. Evidence for cross-talk between the insulin and SAPK2/p38 mitogen-activated protein kinase signaling pathways. *J Biol Chem*, *274*, 36293–36299.

Bloemberg, D., & Quadrilatero, J. (2012). Rapid determination of myosin heavy chain expression in rat, mouse, and human skeletal muscle using multicolor immunofluorescence analysis. *PLoS One*, *7*, e35273.

Boden, G., Duan, X., Homko, C., Molina, E. J., Song, W., Perez, O., Cheung, P., & Merali, S. (2008). Increase in endoplasmic reticulum stress-related proteins and genes in adipose tissue of obese, insulin-resistant individuals. *Diabetes*, *57*, 2438–2444.

Bogoyevitch, M. A., & Kobe, B. (2006). Uses for JNK: the many and varied substrates of the c-Jun N-terminal kinases. *Microbiol Mol Biol Rev*, *70*, 1061–1095.

Boppart, M. D., Asp, S., Wojtaszewski, J. F., Fielding, R. A., Mohr, T., & Goodyear, L. J. (2000). Marathon running transiently increases c-Jun NH2-terminal kinase and p38γ activities in human skeletal muscle. *J Physiol*, *526 Pt 3*, 663–669.

Boppart, M. D., Hirshman, M. F., Sakamoto, K., Fielding, R. A., & Goodyear, L. J. (2001). Static stretch increases c-Jun NH2-terminal kinase activity and p38 phosphorylation in rat skeletal muscle. *Am J Physiol Cell Physiol*, *280*, C352-358.

Bosch, F. X., Ribes, J., Diaz, M., & Cleries, R. (2004). Primary liver cancer: worldwide incidence and trends. *Gastroenterology*, *127*, S5–S16.

Boström, P., Wu, J., Jedrychowski, M. P., Korde, A., Ye, L., Lo, J. C., Rasbach, K. A., Böstrom, E. A., Choi, J. H., Long, J. Z., Kajimura, S., Zingaretti, M. C., Vind, B. F., Tu, H., Cinti, S., Hojlund, K., Gygi, S. P., & Spiegelman, B. M. (2012). A PGC1-alpha-dependent myokine that drives brown-fat-like development of white fat and thermogenesis. *Nature*, *481*, 463–468.

Böttner, A., Kratzsch, J., Muller, G., Kapellen, T. M., Bluher, S., Keller, E., Bluher, M., & Kiess, W. (2004). Gender differences of adiponectin levels develop during the progression of puberty and are related to serum androgen levels. *J Clin Endocrinol Metab*, *89*, 4053–

4061.

Bouskila, M., Hirshman, M. F., Jensen, J., Goodyear, L. J., & Sakamoto, K. (2008). Insulin promotes glycogen synthesis in the absence of GSK3 phosphorylation in skeletal muscle. *Am J Physiol Endocrinol Metab*, *294*, E28-35.

Boyer, J. G., Prasad, V., Song, T., Lee, D., Fu, X., Grimes, K. M., Sargent, M. A., Sadayappan, S., & Molkentin, J. D. (2019). ERK1/2 signaling induces skeletal muscle slow fiber-type switching and reduces muscular dystrophy disease severity. *JCI Insight*, *5*, e127356.

Bradford, M. M. (1976). A rapid and sensitive method for the quantitation of microgram quantities of protein utilizing the principle of protein-dye binding. *Anal Biochem*, *72*, 248–254.

Brien, P., Pugazhendhi, D., Woodhouse, S., Oxley, D., & Pell, J. M. (2013). p38alpha MAPK regulates adult muscle stem cell fate by restricting progenitor proliferation during postnatal growth and repair. *Stem Cells*, *31*, 1597–1610.

Brown, D., Hikim, A. P., Kovacheva, E. L., & Sinha-Hikim, I. (2009). Mouse model of testosterone-induced muscle fiber hypertrophy: involvement of p38 mitogen-activated protein kinase-mediated Notch signaling. *J Endocrinol*, *201*, 129–139.

Bruun, J. M., Lihn, A. S., Verdich, C., Pedersen, S. B., Toubro, S., Astrup, A., & Richelsen, B. (2003). Regulation of adiponectin by adipose tissue-derived cytokines: in vivo and in vitro investigations in humans. *Am J Physiol Endocrinol Metab*, *285*, E527-33.

Buschmann, T., Potapova, O., Bar-Shira, A., Ivanov, V. N., Fuchs, S. Y., Henderson, S., Fried, V. A., Minamoto, T., Alarcon-Vargas, D., Pincus, M. R., Gaarde, W. A., Holbrook, N. J., Shiloh, Y., & Ronai, Z. (2001). Jun NH2-terminal kinase phosphorylation of p53 on Thr-81 is important for p53 stabilization and transcriptional activities in response to stress. *Mol Cell Biol*, *21*, 2743–2754.

Calle, E. E., Rodriguez, C., Walker-Thurmond, K., & Thun, M. J. (2003). Overweight, obesity, and mortality from cancer in a prospectively studied cohort of U.S. adults. *N Engl J Med*, *348*, 1625–1638.

Calvo, J. A., Daniels, T. G., Wang, X., Paul, A., Lin, J., Spiegelman, B. M., Stevenson, S. C., & Rangwala, S. M. (2008). Muscle-specific expression of PPARgamma coactivator-1alpha improves exercise performance and increases peak oxygen uptake. *J Appl Physiol (1985)*, *104*, 1304–1312.

Campbell, P. T., Newton, C. C., Freedman, N. D., Koshiol, J., Alavanja, M. C., Beane Freeman, L. E., Buring, J. E., Chan, A. T., Chong, D. Q., Datta, M., Gaudet, M. M., Gaziano, J. M.,

Giovannucci, E. L., Graubard, B. I., Hollenbeck, A. R., King, L., Lee, I. M., Linet, M. S., Palmer, J. R., Petrick, J. L., Poynter, J. N., Purdue, M. P., Robien, K., Rosenberg, L., Sahasrabuddhe, V. V., Schairer, C., Sesso, H. D., Sigurdson, A. J., Stevens, V. L., Wactawski-Wende, J., Zeleniuch-Jacquotte, A., Renehan, A. G., & McGlynn, K. A. (2016). Body mass index, waist circumference, diabetes, and risk of liver cancer for U.S. adults. *Cancer Res*, *76*, 6076–6083.

Can, A., Dao, D. T., Terrillion, C. E., Piantadosi, S. C., Bhat, S., & Gould, T. D. (2012). The tail suspension test. *J Vis Exp*, *59*, e3769.

Canovas, B., & Nebreda, A. R. (2021). Diversity and versatility of p38 kinase signalling in health and disease. *Nat Rev Mol Cell Biol*, 1–21.

Cao, W., Daniel, K. W., Robidoux, J., Puigserver, P., Medvedev, A. V, Bai, X., Floering, L. M., Spiegelman, B. M., & Collins, S. (2004). p38 mitogen-activated protein kinase is the central regulator of cyclic AMP-dependent transcription of the brown fat uncoupling protein 1 gene. *Mol Cell Biol*, *24*, 3057–3067.

Carbó, N., López-Soriano, J., Costelli, P., Alvarez, B., Busquets, S., Baccino, F. M., Quinn, L. S., López-Soriano, F. J., & Argilés, J. M. (2001). Interleukin-15 mediates reciprocal regulation of adipose and muscle mass: a potential role in body weight control. *Biochim Biophys Acta*, *1526*, 17–24.

Cardona, M., López, J. A., Serafín, A., Rongvaux, A., Inserte, J., García-Dorado, D., Flavell, R., Llovera, M., Canas, X., Vázquez, J., & Sanchis, D. (2015). Executioner caspase-3 and 7 deficiency reduces myocyte number in the developing mouse heart. *PLoS One*, *10*, e0131411.

Carey, W. D. (2020). Nonalcoholic fatty liver disease. https://my.clevelandclinic.org/

Cargnello, M., & Roux, P. P. (2011). Activation and function of the MAPKs and their substrates, the MAPK-activated protein kinases. *Microbiol Mol Biol Rev*, *75*, 50–83.

Carlson, C. J., Koterski, S., Sciotti, R. J., Poccard, G. B., & Rondinone, C. M. (2003). Enhanced basal activation of mitogen-activated protein kinases in adipocytes from type 2 diabetes: potential role of p38 in the downregulation of GLUT4 expression. *Diabetes*, *52*, 634–641.

Carvalho, B. M., Oliveira, A. G., Ueno, M., Araujo, T. G., Guadagnini, D., Carvalho-Filho, M. A., Geloneze, B., Lima, M. M., Pareja, J. C., Carvalheira, J. B., & Saad, M. J. (2013). Modulation of double-stranded RNA-activated protein kinase in insulin sensitive tissues of obese humans. *Obesity (Silver Spring)*, *21*, 2452–2457.

Caunt, C. J., & Keyse, S. M. (2013). Dual-specificity MAP kinase phosphatases (MKPs):

shaping the outcome of MAP kinase signalling. *FEBS J*, *280*, 489–504.

Cepero-Donates, Y., Lacraz, G., Ghobadi, F., Rakotoarivelo, V., Orkhis, S., Mayhue, M., Chen, Y. G., Rola-Pleszczynski, M., Menendez, A., Ilangumaran, S., & Ramanathan, S. (2016). Interleukin-15-mediated inflammation promotes non-alcoholic fatty liver disease. *Cytokine*, *82*, 102–111.

Cereijo, R., Gavaldà-Navarro, A., Cairo, M., Quesada-López, T., Villarroya, J., Moron-Ros, S., Sánchez-Infantes, D., Peyrou, M., Iglesias, R., Mampel, T., Turatsinze, J. V, Eizirik, D. L., Giralt, M., & Villarroya, F. (2018). CXCL14, a brown adipokine that mediates brown-fat-to-macrophage communication in thermogenic adaptation. *Cell Metab*, *28*, 750-763 e6.

Chalvatzas, N., Dafopoulos, K., Kosmas, G., Kallitsaris, A., Pournaras, S., & Messinis, I. E. (2009). Effect of ovarian hormones on serum adiponectin and resistin concentrations. *Fertil Steril*, *91*, 1189–1194.

Chan, M. H., McGee, S. L., Watt, M. J., Hargreaves, M., & Febbraio, M. A. (2004). Altering dietary nutrient intake that reduces glycogen content leads to phosphorylation of nuclear p38 MAP kinase in human skeletal muscle: association with IL-6 gene transcription during contraction. *FASEB J*, *18*, 1785–1787.

Chandel, N. S. (2015). Navigating Metabolism. *Cold Spring Harbor Laboratory Press*.

Chang, L., & Karin, M. (2001). Mammalian MAP kinase signalling cascades. *Nature*, *410*, 37–40.

Chen, G., Ni, Y., Nagata, N., Xu, L., Zhuge, F., Nagashimada, M., Kaneko, S., & Ota, T. (2019). Pirfenidone prevents and reverses hepatic insulin resistance and steatohepatitis by polarizing M2 macrophages. *Lab Invest*, *99*, 1335–1348.

Chen, H. P., Shieh, J. J., Chang, C. C., Chen, T. T., Lin, J. T., Wu, M. S., Lin, J. H., & Wu, C. Y. (2013). Metformin decreases hepatocellular carcinoma risk in a dose-dependent manner: population-based and in vitro studies. *Gut*, *62*, 606–615.

Chen, M. J., Yeh, Y. T., Lee, K. T., Tsai, C. J., Lee, H. H., & Wang, S. N. (2012). The promoting effect of adiponectin in hepatocellular carcinoma. *J Surg Oncol*, *106*, 181–187.

Chen, Y., Wang, X., Wang, J., Yan, Z., & Luo, J. (2012). Excess body weight and the risk of primary liver cancer: an updated meta-analysis of prospective studies. *Eur J Cancer*, *48*, 2137–2145.

Cheung, P. C., Campbell, D. G., Nebreda, A. R., & Cohen, P. (2003). Feedback control of the protein kinase TAK1 by SAPK2a/p38alpha. *EMBO J*, *22*, 5793–5805.

Choi, C. S., Befroy, D. E., Codella, R., Kim, S., Reznick, R. M., Hwang, Y. J., Liu, Z. X., Lee,

H. Y., Distefano, A., Samuel, V. T., Zhang, D., Cline, G. W., Handschin, C., Lin, J., Petersen, K. F., Spiegelman, B. M., & Shulman, G. I. (2008). Paradoxical effects of increased expression of PGC-1alpha on muscle mitochondrial function and insulin-stimulated muscle glucose metabolism. *Proc Natl Acad Sci U S A*, *105*, 19926–19931.

Chomentowski, P., Coen, P. M., Radiková, Z., Goodpaster, B. H., & Toledo, F. G. S. (2011). Skeletal muscle mitochondria in insulin resistance: differences in intermyofibrillar versus subsarcolemmal subpopulations and relationship to metabolic flexibility. *J Clin Endocrinol Metab*, *96*, 494-503.

Chung, J., Nguyen, A. K., Henstridge, D. C., Holmes, A. G., Chan, M. H., Mesa, J. L., Lancaster, G. I., Southgate, R. J., Bruce, C. R., Duffy, S. J., Horvath, I., Mestril, R., Watt, M. J., Hooper, P. L., Kingwell, B. A., Vigh, L., Hevener, A., & Febbraio, M. A. (2008). HSP72 protects against obesity-induced insulin resistance. *Proc Natl Acad Sci U S A*, *105*, 1739–1744.

Clocchiatti, A., Cora, E., Zhang, Y., & Dotto, G. P. (2016). Sexual dimorphism in cancer. *Nat Rev Cancer*, *16*, 330–339.

Cnop, M., Havel, P. J., Utzschneider, K. M., Carr, D. B., Sinha, M. K., Boyko, E. J., Retzlaff, B. M., Knopp, R. H., Brunzell, J. D., & Kahn, S. E. (2003). Relationship of adiponectin to body fat distribution, insulin sensitivity and plasma lipoproteins: evidence for independent roles of age and sex. *Diabetologia*, *46*, 459–469.

Cnop, M., Landchild, M. J., Vidal, J., Havel, P. J., Knowles, N. G., Carr, D. R., Wang, F., Hull, R. L., Boyko, E. J., Retzlaff, B. M., Walden, C. E., Knopp, R. H., & Kahn, S. E. (2002). The concurrent accumulation of intra-abdominal and subcutaneous fat explains the association between insulin resistance and plasma leptin concentrations: distinct metabolic effects of two fat compartments. *Diabetes*, *51*, 1005–1015.

Coffey, V. G., Zhong, Z., Shield, A., Canny, B. J., Chibalin, A. V, Zierath, J. R., & Hawley, J. A. (2006). Early signaling responses to divergent exercise stimuli in skeletal muscle from well-trained humans. *FASEB J*, *20*, 190–192.

Cohen, P. (2002). The origins of protein phosphorylation. *Nature Cell Biology*, *4*, E127–130.

Combs, T. P., Berg, A. H., Rajala, M. W., Klebanov, S., Iyengar, P., Jimenez-Chillaron, J. C., Patti, M. E., Klein, S. L., Weinstein, R. S., & Scherer, P. E. (2003). Sexual differentiation, pregnancy, calorie restriction, and aging affect the adipocyte-specific secretory protein adiponectin. *Diabetes*, *52*, 268–276.

Combs, T. P., & Marliss, E. B. (2014). Adiponectin signaling in the liver. *Rev Endocr Metab Disord*, *15*, 137–147.

Corbetta, S., Redaelli, A., Pozzi, M., Bovo, G., Ratti, L., Redaelli, E., Pellegrini, C., Beck-Peccoz, P., & Spada, A. (2011). Fibrosis is associated with adiponectin resistance in chronic hepatitis C virus infection. *Eur J Clin Invest*, *41*, 898–905.

Crane, J. D., MacNeil, L. G., Lally, J. S., Ford, R. J., Bujak, A. L., Brar, I. K., Kemp, B. E., Raha, S., Steinberg, G. R., & Tarnopolsky, M. A. (2015). Exercise-stimulated interleukin-15 is controlled by AMPK and regulates skin metabolism and aging. *Aging Cell*, *14*, 625–634.

Crunkhorn, S., Dearie, F., Mantzoros, C., Gami, H., da Silva, W. S., Espinoza, D., Faucette, R., Barry, K., Bianco, A. C., & Patti, M. E. (2007). Peroxisome proliferator activator receptor gamma coactivator-1 expression is reduced in obesity: potential pathogenic role of saturated fatty acids and p38 mitogen-activated protein kinase activation. *J Biol Chem*, *282*, 15439–15450.

Cuadrado, A., & Nebreda, A. R. (2010). Mechanisms and functions of p38 MAPK signalling. *Biochem J*, *429*, 403–417.

Cubero, F. J., Mohamed, M. R., Woitok, M. M., Zhao, G., Hatting, M., Nevzorova, Y. A., Chen, C., Haybaeck, J., de Bruin, A., Avila, M. A., Boekschoten, M. V, Davis, R. J., & Trautwein, C. (2020). Loss of c-Jun N-terminal kinase 1 and 2 function in liver epithelial cells triggers biliary hyperproliferation resembling cholangiocarcinoma. *Hepatol Commun*, *4*, 834–851.

Cuenda, A., Cohen, P., Buee-Scherrer, V., & Goedert, M. (1997). Activation of stress-activated protein kinase-3 (SAPK3) by cytokines and cellular stresses is mediated via SAPKK3 (MKK6); comparison of the specificities of SAPK3 and SAPK2 (RK/p38). *EMBO J*, *16*, 295–305.

Cuenda, A., & Rousseau, S. (2007). p38 MAP-kinases pathway regulation, function and role in human diseases. *Biochim Biophys Acta*, *1773*, 1358–1375.

Cuenda, A., & Sanz-Ezquerro, J. J. (2017). p38gamma and p38delta: from spectators to key physiological players. *Trends Biochem Sci*, *42*, 431–442.

Czyzyk, T. A., Nogueiras, R., Lockwood, J. F., McKinzie, J. H., Coskun, T., Pintar, J. E., Hammond, C., Tschop, M. H., & Statnick, M. A. (2010). kappa-Opioid receptors control the metabolic response to a high-energy diet in mice. *FASEB J*, *24*, 1151–1159.

Dalamaga, M., Diakopoulos, K. N., & Mantzoros, C. S. (2012). The role of adiponectin in cancer: a review of current evidence. *Endocr Rev*, *33*, 547–594.

Dalamaga, M., Migdalis, I., Fargnoli, J. L., Papadavid, E., Bloom, E., Mitsiades, N., Karmaniolas, K., Pelecanos, N., Tseleni-Balafouta, S., Dionyssiou-Asteriou, A., & Mantzoros, C. S. (2009). Pancreatic cancer expresses adiponectin receptors and is

associated with hypoleptinemia and hyperadiponectinemia: a case-control study. *Cancer Causes Control*, *20*, 625–633.

Das, M., Garlick, D. S., Greiner, D. L., & Davis, R. J. (2011). The role of JNK in the development of hepatocellular carcinoma. *Genes Dev*, *25*, 634–645.

Davis, R. J. (2000). Signal transduction by the JNK group of MAP kinases. *Cell*, *103*, 239–252.

Dazai, S., Akita, S., Hirano, A., Rashid, M. A., Naito, S., Akino, K., & Fujii, T. (2000). Leukemia inhibitory factor enhances bone formation in calvarial bone defect. *J Craniofac Surg*, *11*, 513–520.

de Alvaro, C., Teruel, T., Hernández, R., & Lorenzo, M. (2004). Tumor necrosis factor alpha produces insulin resistance in skeletal muscle by activation of inhibitor kappaB kinase in a p38 MAPK-dependent manner. *J Biol Chem*, *279*, 17070–17078.

Deacon, R. M. (2013). Measuring the strength of mice. *J Vis Exp*, *76*, 2610.

DeFronzo, R. A., & Tripathy, D. (2009). Skeletal muscle insulin resistance is the primary defect in type 2 diabetes. *Diabetes Care*, *32 Suppl 2*, S157-63.

Del Reino, P., Alsina-Beauchamp, D., Escós, A., Cerezo-Guisado, M. I., Risco, A., Aparicio, N., Zur, R., Fernández-Estévez, M., Collantes, E., Montans, J., & Cuenda, A. (2014). Pro-oncogenic role of alternative p38 mitogen-activated protein kinases p38gamma and p38delta, linking inflammation and cancer in colitis-associated colon cancer. *Cancer Res*, *74*, 6150–6160.

Dérijard, B., Raingeaud, J., Barrett, T., Wu, I. H., Han, J., Ulevitch, R. J., & Davis, R. J. (1995). Independent human MAP kinase signal transduction pathways defined by MEK and MKK isoforms. *Science*, *267*, 682–685.

Diskin, R., Askari, N., Capone, R., Engelberg, D., & Livnah, O. (2004). Active mutants of the human p38alpha mitogen-activated protein kinase. *J Biol Chem*, *279*, 47040–47049.

Dong, C., Yang, D. D., Tournier, C., Whitmarsh, A. J., Xu, J., Davis, R. J., & Flavell, R. A. (2000). JNK is required for effector T-cell function but not for T-cell activation. *Nature*, *405*, 91–94.

Dong, C., Yang, D. D., Wysk, M., Whitmarsh, A. J., Davis, R. J., & Flavell, R. A. (1998). Defective T cell differentiation in the absence of Jnk1. *Science*, *282*, 2092–2095.

Donohoe, F., Wilkinson, M., Baxter, E., & Brennan, D. J. (2020). Mitogen-activated protein kinase (MAPK) and obesity-related cancer. *Int J Mol Sci*, *21*, 1241.

dos Santos, T., Lira, F. S., & Antunes, B. M. (2020). Interleukin-15 and creatine kinase response to high-intensity intermittent exercise training. *Sport Sci Health*, *16*, 479-484.

Dozio, E., Malavazos, A. E., Vianello, E., Briganti, S., Dogliotti, G., Bandera, F., Giacomazzi, F., Castelvecchio, S., Menicanti, L., Sigruener, A., Schmitz, G., & Corsi Romanelli, M. M. (2014). Interleukin-15 and soluble interleukin-15 receptor alpha in coronary artery disease patients: association with epicardial fat and indices of adipose tissue distribution. *PLoS One*, *9*, e90960.

Dumesic, P. A., Egan, D. F., Gut, P., Tran, M. T., Parisi, A., Chatterjee, N., Jedrychowski, M., Paschini, M., Kazak, L., Wilensky, S. E., Dou, F., Bogoslavski, D., Cartier, J. A., Perrimon, N., Kajimura, S., Parikh, S. M., & Spiegelman, B. M. (2019). An evolutionarily conserved uORF regulates PGC1alpha and oxidative metabolism in mice, flies, and bluefin tuna. *Cell Metab*, *30*, 190-200 e6.

Egan, B., & Zierath, J. R. (2013). Exercise metabolism and the molecular regulation of skeletal muscle adaptation. *Cell Metab*, *17*, 162–184.

El-Serag, H. B., & Rudolph, K. L. (2007). Hepatocellular carcinoma: epidemiology and molecular carcinogenesis. *Gastroenterology*, *132*, 2557–2576.

Ellingsgaard, H., Hauselmann, I., Schuler, B., Habib, A. M., Baggio, L. L., Meier, D. T., Eppler, E., Bouzakri, K., Wueest, S., Muller, Y. D., Hansen, A. M., Reinecke, M., Konrad, D., Gassmann, M., Reimann, F., Halban, P. A., Gromada, J., Drucker, D. J., Gribble, F. M., Ehses, J. A., & Donath, M. Y. (2011). Interleukin-6 enhances insulin secretion by increasing glucagon-like peptide-1 secretion from L cells and alpha cells. *Nat Med*, *17*, 1481–1489.

Emanuelsson, O., Brunak, S., von Heijne, G., & Nielsen, H. (2007). Locating proteins in the cell using TargetP, SignalP and related tools. *Nat Protoc*, *2*, 953–971.

Engel, F. B., Schebesta, M., Duong, M. T., Lu, G., Ren, S., Madwed, J. B., Jiang, H., Wang, Y., & Keating, M. T. (2005). p38 MAP kinase inhibition enables proliferation of adult mammalian cardiomyocytes. *Genes Dev*, *19*, 1175–1187.

Engin, A. (2017). Human protein kinases and obesity. *Adv Exp Med Biol*, *960*, 111–134.

Ezaki, H., Yoshida, Y., Saji, Y., Takemura, T., Fukushima, J., Matsumoto, H., Kamada, Y., Wada, A., Igura, T., Kihara, S., Funahashi, T., Shimomura, I., Tamura, S., Kiso, S., & Hayashi, N. (2009). Delayed liver regeneration after partial hepatectomy in adiponectin knockout mice. *Biochem Biophys Res Commun*, *378*, 68–72.

Fan, M., Rhee, J., St-Pierre, J., Handschin, C., Puigserver, P., Lin, J., Jaeger, S., Erdjument-Bromage, H., Tempst, P., & Spiegelman, B. M. (2004). Suppression of mitochondrial respiration through recruitment of p160 myb binding protein to PGC-1alpha: modulation by p38 MAPK. *Genes Dev*, *18*, 278–289.

Farese Jr., R. V, Zechner, R., Newgard, C. B., & Walther, T. C. (2012). The problem of establishing relationships between hepatic steatosis and hepatic insulin resistance. *Cell Metab*, *15*, 570–573.

Fasshauer, M., Kralisch, S., Klier, M., Lossner, U., Bluher, M., Klein, J., & Paschke, R. (2003). Adiponectin gene expression and secretion is inhibited by interleukin-6 in 3T3-L1 adipocytes. *Biochem Biophys Res Commun*, *301*, 1045-1050.

Feijoo, C., Campbell, D. G., Jakes, R., Goedert, M., & Cuenda, A. (2005). Evidence that phosphorylation of the microtubule-associated protein Tau by SAPK4/p38delta at Thr50 promotes microtubule assembly. *J Cell Sci*, *118*, 397–408.

Folco, E. J., Rocha, V. Z., Lopez-Ilasaca, M., & Libby, P. (2009). Adiponectin inhibits pro-inflammatory signaling in human macrophages independent of interleukin-10. *J Biol Chem*, *284*, 25569–25575.

Foster, W. H., Tidball, J. G., & Wang, Y. (2012). p38gamma activity is required for maintenance of slow skeletal muscle size. *Muscle Nerve*, *45*, 266–273.

Fuente-Martín, E., Argente-Arizón, P., Ros, P., Argente, J., & Chowen, J. A. (2013). Sex differences in adipose tissue: It is not only a question of quantity and distribution. *Adipocyte*, *2*, 128–134.

Fujishiro, M., Gotoh, Y., Katagiri, H., Sakoda, H., Ogihara, T., Anai, M., Onishi, Y., Ono, H., Funaki, M., Inukai, K., Fukushima, Y., Kikuchi, M., Oka, Y., & Asano, T. (2001). MKK6/3 and p38 MAPK pathway activation is not necessary for insulin-induced glucose uptake but regulates glucose transporter expression. *J Biol Chem*, *276*, 19800–19806.

Funcke, J. B., & Scherer, P. E. (2019). Beyond adiponectin and leptin: adipose tissue-derived mediators of inter-organ communication. *J Lipid Res*, *60*, 1648–1684.

Gallage, S., García-Beccaria, M., Szydlowska, M., Rahbari, M., Mohr, R., Tacke, F., & Heikenwalder, M. (2021). The therapeutic landscape of hepatocellular carcinoma. *Med*, *2*, 505–552.

Gatselis, N. K., Ntaios, G., Makaritsis, K., & Dalekos, G. N. (2014). Adiponectin: a key playmaker adipocytokine in non-alcoholic fatty liver disease. *Clin Exp Med*, *14*, 121–131.

Ge, B., Gram, H., Di Padova, F., Huang, B., New, L., Ulevitch, R. J., Luo, Y., & Han, J. (2002). MAPKK-independent activation of p38alpha mediated by TAB1-dependent autophosphorylation of p38alpha. *Science*, *295*, 1291–1294.

Ge, B., Xiong, X., Jing, Q., Mosley, J. L., Filose, A., Bian, D., Huang, S., & Han, J. (2003). TAB1beta (transforming growth factor-beta-activated protein kinase 1-binding protein

1beta), a novel splicing variant of TAB1 that interacts with p38alpha but not TAK1. *J Biol Chem*, *278*, 2286–2293.

Gehart, H., Kumpf, S., Ittner, A., & Ricci, R. (2010). MAPK signalling in cellular metabolism: stress or wellness? *EMBO Rep*, *11*, 834–840.

Ghebranious, N., & Sell, S. (1998). Hepatitis B injury, male gender, aflatoxin, and p53 expression each contribute to hepatocarcinogenesis in transgenic mice. *Hepatology*, *27*, 383–391.

Gills, J. J., Castillo, S. S., Zhang, C., Petukhov, P. A., Memmott, R. M., Hollingshead, M., Warfel, N., Han, J., Kozikowski, A. P., & Dennis, P. A. (2007). Phosphatidylinositol ether lipid analogues that inhibit AKT also independently activate the stress kinase, p38alpha, through MKK3/6-independent and -dependent mechanisms. *J Biol Chem*, *282*, 27020–27029.

González-Terán, B., Cortes, J. R., Manieri, E., Matesanz, N., Verdugo, A., Rodríguez, M. E., González-Rodríguez, A., Valverde, A. M., Martín, P., Davis, R. J., & Sabio, G. (2013). Eukaryotic elongation factor 2 controls TNF-alpha translation in LPS-induced hepatitis. *J Clin Invest*, *123*, 164–178.

González-Terán, B., López, J. A., Rodríguez, E., Leiva, L., Martínez-Martínez, S., Bernal, J. A., Jiménez-Borreguero, L. J., Redondo, J. M., Vázquez, J., & Sabio, G. (2016a). p38gamma and delta promote heart hypertrophy by targeting the mTOR-inhibitory protein DEPTOR for degradation. *Nat Commun*, *7*, 10477.

González-Terán, B., Matesanz, N., Nikolic, I., Verdugo, M. A., Sreeramkumar, V., Hernández-Cosido, L., Mora, A., Crainiciuc, G., Sáiz, M. L., Bernardo, E., Leiva-Vega, L., Rodríguez, E., Bondía, V., Torres, J. L., Pérez-Sieira, S., Ortega, L., Cuenda, A., Sánchez-Madrid, F., Nogueiras, R., Hidalgo, A., Marcos, M., & Sabio, G. (2016b). p38gamma and p38delta reprogram liver metabolism by modulating neutrophil infiltration. *EMBO J*, *35*, 536–552.

Goodman, Z. D. (2007). Grading and staging systems for inflammation and fibrosis in chronic liver diseases. *J Hepatol*, *47*, 598–607.

Greenblatt, M. B., Shim, J. H., Zou, W., Sitara, D., Schweitzer, M., Hu, D., Lotinun, S., Sano, Y., Baron, R., Park, J. M., Arthur, S., Xie, M., Schneider, M. D., Zhai, B., Gygi, S., Davis, R., & Glimcher, L. H. (2010). The p38 MAPK pathway is essential for skeletogenesis and bone homeostasis in mice. *J Clin Invest*, *120*, 2457–2473.

Gregor, M. F., & Hotamisligil, G. S. (2011). Inflammatory mechanisms in obesity. *Annu Rev Immunol*, *29*, 415–445.

Grillner, S., & El Manira, A. (2020). Current principles of motor control, with special reference to vertebrate locomotion. *Physiol Rev*, *100*, 271–320.

Gual, P., Le Marchand-Brustel, Y., & Tanti, J. F. (2005). Positive and negative regulation of insulin signaling through IRS-1 phosphorylation. *Biochimie*, *87*, 99–109.

Gupta, S., Barrett, T., Whitmarsh, A. J., Cavanagh, J., Sluss, H. K., Derijard, B., & Davis, R. J. (1996). Selective interaction of JNK protein kinase isoforms with transcription factors. *EMBO J*, *15*, 2760–2770.

Hassan, R. H., Bourron, O., & Hajduch, E. (2014). Defect of insulin signal in peripheral tissues: important role of ceramide. *World J Diabetes*, *5*, 244–257.

Hamrick, M. W. (2011). A role for myokines in muscle-bone interactions. *Exerc Sport Sci Rev*, *39*, 43–47.

Han, M. S., Barrett, T., Brehm, M. A., & Davis, R. J. (2016). Inflammation mediated by JNK in myeloid cells promotes the development of hepatitis and hepatocellular carcinoma. *Cell Rep*, *15*, 19–26.

Han, M. S., Perry, R. J., Camporez, J. P., Scherer, P. E., Shulman, G. I., Gao, G., & Davis, R. J. (2021). A feed-forward regulatory loop in adipose tissue promotes signaling by the hepatokine FGF21. *Genes Dev*, *35*, 133–146.

Hanahan, D., & Weinberg, R. A. (2011). Hallmarks of cancer: the next generation. *Cell*, *144*, 646–674.

Handschin, C., Chin, S., Li, P., Liu, F., Maratos-Flier, E., Lebrasseur, N. K., Yan, Z., & Spiegelman, B. M. (2007a). Skeletal muscle fiber-type switching, exercise intolerance, and myopathy in PGC-1alpha muscle-specific knock-out animals. *J Biol Chem*, *282*, 30014–30021.

Handschin, C., Choi, C. S., Chin, S., Kim, S., Kawamori, D., Kurpad, A. J., Neubauer, N., Hu, J., Mootha, V. K., Kim, Y. B., Kulkarni, R. N., Shulman, G. I., & Spiegelman, B. M. (2007b). Abnormal glucose homeostasis in skeletal muscle-specific PGC-1alpha knockout mice reveals skeletal muscle-pancreatic beta cell crosstalk. *J Clin Invest*, *117*, 3463–3474.

Handschin, C., & Spiegelman, B. M. (2006). Peroxisome proliferator-activated receptor gamma coactivator 1 coactivators, energy homeostasis, and metabolism. *Endocr Rev*, *27*, 728–735.

He, Y., Wu, X., Khan, R. S., Kastin, A. J., Cornelissen-Guillaume, G. G., Hsuchou, H., Robert, B., Halberg, F., & Pan, W. (2010). IL-15 receptor deletion results in circadian changes of locomotor and metabolic activity. *J Mol Neurosci*, *41*, 315–321.

Hebbard, L., & Ranscht, B. (2014). Multifaceted roles of adiponectin in cancer. *Best Pract Res Clin Endocrinol Metab*, *28*, 59–69.

Heindryckx, F., Colle, I., & Van Vlierberghe, H. (2009). Experimental mouse models for hepatocellular carcinoma research. *Int J Exp Pathol*, *90*, 367–386.

Henstridge, D. C., Bruce, C. R., Pang, C. P., Lancaster, G. I., Allen, T. L., Estevez, E., Gardner, T., Weir, J. M., Meikle, P. J., Lam, K. S. L., Xu, A., Fujii, N., Goodyear, L. J., & Febbraio, M. A. (2012). Skeletal muscle-specific overproduction of constitutively activated c-Jun N-terminal kinase (JNK) induces insulin resistance in mice. *Diabetologia*, *55*, 2769–2778.

Herrera-Melle, L., Crespo, M., Leiva, M., & Sabio, G. (2021). Stress-activated kinases signaling pathways in cancer development. *Curr Opin Physiol*, *19*, 22–31.

Hirosumi, J., Tuncman, G., Chang, L., Gorgun, C. Z., Uysal, K. T., Maeda, K., Karin, M., & Hotamisligil, G. S. (2002). A central role for JNK in obesity and insulin resistance. *Nature*, *420*, 333–336.

Ho, R. C., Alcazar, O., Fujii, N., Hirshman, M. F., & Goodyear, L. J. (2004). p38gamma MAPK regulation of glucose transporter expression and glucose uptake in L6 myotubes and mouse skeletal muscle. *Am J Physiol Regul Integr Comp Physiol*, *286*, R342-9.

Hong, S. C., Yoo, S. W., Cho, G. J., Kim, T., Hur, J. Y., Park, Y. K., Lee, K. W., & Kim, S. H. (2007). Correlation between estrogens and serum adipocytokines in premenopausal and postmenopausal women. *Menopause*, *14*, 835–840.

Hong, T., Ning, J., Yang, X., Liu, H. Y., Han, J., Liu, Z., & Cao, W. (2011). Fine-tuned regulation of the PGC-1alpha gene transcription by different intracellular signaling pathways. *Am J Physiol Endocrinol Metab*, *300*, E500-7.

Hotamisligil, G. S. (2006). Inflammation and metabolic disorders. *Nature*, *444*, 860–867.

Hu, E., Liang, P., & Spiegelman, B. M. (1996). AdipoQ is a novel adipose-specific gene dysregulated in obesity. *J Biol Chem*, *271*, 10697–10703.

Hui, C. K., Zhang, H. Y., Lee, N. P., Chan, W., Yueng, Y. H., Leung, K. W., Lu, L., Leung, N., Lo, C. M., Fan, S. T., Luk, J. M., Xu, A., Lam, K. S., Kwong, Y. L., Lau, G. K., & Hong Kong Liver Fibrosis Study Group. (2007). Serum adiponectin is increased in advancing liver fibrosis and declines with reduction in fibrosis in chronic hepatitis B. *J Hepatol*, *47*, 191–202.

Hui, L., Bakiri, L., Mairhorfer, A., Schweifer, N., Haslinger, C., Kenner, L., Komnenovic, V., Scheuch, H., Beug, H., & Wagner, E. F. (2007). p38alpha suppresses normal and cancer cell proliferation by antagonizing the JNK-c-Jun pathway. *Nat Genet*, *39*, 741–749.

Hui, L., Zatloukal, K., Scheuch, H., Stepniak, E., & Wagner, E. F. (2008). Proliferation of human HCC cells and chemically induced mouse liver cancers requires JNK1-dependent p21 downregulation. *J Clin Invest*, *118*, 3943–3953.

Ikeda, S. I., Tamura, Y., Kakehi, S., Sanada, H., Kawamori, R., & Watada, H. (2016). Exercise-induced increase in IL-6 level enhances GLUT4 expression and insulin sensitivity in mouse skeletal muscle. *Biochem Biophys Res Commun*, *473*, 947–952.

International Diabetes Federation (IDF). (2019). IDF Diabetes Atlas (9th edition). Brussels (Belgium).

Ip, Y. T., & Davis, R. J. (1998). Signal transduction by the c-Jun N-terminal kinase (JNK)--from inflammation to development. *Curr Opin Cell Biol*, *10*, 205–219.

Islam, H., Hood, D. A., & Gurd, B. J. (2020). Looking beyond PGC-1alpha: emerging regulators of exercise-induced skeletal muscle mitochondrial biogenesis and their activation by dietary compounds. *Appl Physiol Nutr Metab*, *45*, 11–23.

Ittner, A., Block, H., Reichel, C. A., Varjosalo, M., Gehart, H., Sumara, G., Gstaiger, M., Krombach, F., Zarbock, A., & Ricci, R. (2012). Regulation of PTEN activity by p38delta-PKD1 signaling in neutrophils confers inflammatory responses in the lung. *J Exp Med*, *209*, 2229–2246.

Ittner, A., Chua, S. W., Bertz, J., Volkerling, A., van der Hoven, J., Gladbach, A., Przybyla, M., Bi, M., van Hummel, A., Stevens, C. H., Ippati, S., Suh, L. S., Macmillan, A., Sutherland, G., Kril, J. J., Silva, A. P., Mackay, J. P., Poljak, A., Delerue, F., Ke, Y. D., & Ittner, L. M. (2016). Site-specific phosphorylation of tau inhibits amyloid-beta toxicity in Alzheimer's mice. *Science*, *354*, 904–908.

Iyoda, K., Sasaki, Y., Horimoto, M., Toyama, T., Yakushijin, T., Sakakibara, M., Takehara, T., Fujimoto, J., Hori, M., Wands, J. R., & Hayashi, N. (2003). Involvement of the p38 mitogen-activated protein kinase cascade in hepatocellular carcinoma. *Cancer*, *97*, 3017–3026.

Jaeschke, A., Rincon, M., Doran, B., Reilly, J., Neuberg, D., Greiner, D. L., Shultz, L. D., Rossini, A. A., Flavell, R. A., & Davis, R. J. (2005). Disruption of the Jnk2 (Mapk9) gene reduces destructive insulitis and diabetes in a mouse model of type I diabetes. *Proc Natl Acad Sci U S A*, *102*, 6931–6935.

Jeong, H. J., So, H. K., Jo, A., Kim, H. B., Lee, S. J., Bae, G. U., & Kang, J. S. (2019). Ginsenoside Rg1 augments oxidative metabolism and anabolic response of skeletal muscle in mice. *J Ginseng Res*, *43*, 475–481.

Jiang, X., Tan, H. Y., Teng, S., Chan, Y. T., Wang, D., & Wang, N. (2019). The role of AMP-activated protein kinase as a potential target of treatment of hepatocellular carcinoma. *Cancers (Basel)*, *11*, 647.

Jin, H., Wang, D. Y., Mei, Y. F., Qiu, W. B., Zhou, Y., Wang, D. M., Tan, X. R., & Li, Y. G. (2010). Mitogen-activated protein kinases pathway is involved in physiological testosterone-induced tissue factor pathway inhibitor expression in endothelial cells. *Blood Coagul Fibrinolysis*, *21*, 420–424.

Jing, Y., Liu, W., Cao, H., Zhang, D., Yao, X., Zhang, S., Xia, H., Li, D., Wang, Y. C., Yan, J., Hui, L., & Ying, H. (2015). Hepatic p38α regulates gluconeogenesis by suppressing AMPK. *J Hepatol*, *62*, 1319-1327.

Jirmanova, L., Sarma, D. N., Jankovic, D., Mittelstadt, P. R., & Ashwell, J. D. (2009). Genetic disruption of p38alpha Tyr323 phosphorylation prevents T-cell receptor-mediated p38alpha activation and impairs interferon-gamma production. *Blood*, *113*, 2229–2237.

Kadotani, A., Tsuchiya, Y., Hatakeyama, H., Katagiri, H., & Kanzaki, M. (2009). Different impacts of saturated and unsaturated free fatty acids on COX-2 expression in C2C12 myotubes. *Am J Physiol Endocrinol Metab*, *297*, E1291–303.

Kahn, C. R., Weir, G. C., King, G. L., Moses, A. C., Smith, R. J., Jacobson, A. M. (2005). Joslin's Diabetes Mellitus (14th edition). *Lippincott Williams & Wilkins.*

Kahn, S. E., Hull, R. L., & Utzschneider, K. M. (2006). Mechanisms linking obesity to insulin resistance and type 2 diabetes. *Nature*, *444*, 840–846.

Kamada, Y., Matsumoto, H., Tamura, S., Fukushima, J., Kiso, S., Fukui, K., Igura, T., Maeda, N., Kihara, S., Funahashi, T., Matsuzawa, Y., Shimomura, I., & Hayashi, N. (2007). Hypoadiponectinemia accelerates hepatic tumor formation in a nonalcoholic steatohepatitis mouse model. *J Hepatol*, *47*, 556–564.

Kaser, S., Moschen, A., Cayon, A., Kaser, A., Crespo, J., Pons-Romero, F., Ebenbichler, C. F., Patsch, J. R., & Tilg, H. (2005). Adiponectin and its receptors in non-alcoholic steatohepatitis. *Gut*, *54*, 117–121.

Kelly, T., Yang, W., Chen, C. S., Reynolds, K., & He, J. (2008). Global burden of obesity in 2005 and projections to 2030. *Int J Obes (Lond)*, *32*, 1431–1437.

Kerenidi, T., Lada, M., Tsaroucha, A., Georgoulias, P., Mystridou, P., & Gourgoulianis, K. I. (2013). Clinical significance of serum adipokines levels in lung cancer. *Med Oncol*, *30*, 507.

Khadir, A., Tiss, A., Abubaker, J., Abu-Farha, M., Al-Khairi, I., Cherian, P., John, J., Kavalakatt,

S., Warsame, S., Al-Madhoun, A., Al-Ghimlas, F., Elkum, N., Behbehani, K., Dermime, S., & Dehbi, M. (2015). MAP kinase phosphatase DUSP1 is overexpressed in obese humans and modulated by physical exercise. *Am J Physiol Endocrinol Metab*, *308*, E71-83.

Khandekar, M. J., Cohen, P., & Spiegelman, B. M. (2011). Molecular mechanisms of cancer development in obesity. *Nat Rev Cancer*, *11*, 886–895.

Kim, E., & Viatour, P. (2020). Hepatocellular carcinoma: old friends and new tricks. *Exp Mol Med*, *52*, 1898–1907.

Kim, K. Y., Kim, J. K., Jeon, J. H., Yoon, S. R., Choi, I., & Yang, Y. (2005). c-Jun N-terminal kinase is involved in the suppression of adiponectin expression by TNF-alpha in 3T3-L1 adipocytes. *Biochem Biophys Res Commun*, *327*, 460–467.

Kirsch, K., Zeke, A., Toke, O., Sok, P., Sethi, A., Sebo, A., Kumar, G. S., Egri, P., Poti, A. L., Gooley, P., Peti, W., Bento, I., Alexa, A., & Remenyi, A. (2020). Co-regulation of the transcription controlling ATF2 phosphoswitch by JNK and p38. *Nat Commun*, *11*, 5769.

Knebel, A., Morrice, N., & Cohen, P. (2001). A novel method to identify protein kinase substrates: eEF2 kinase is phosphorylated and inhibited by SAPK4/p38delta. *EMBO J*, *20*, 4360–4369.

Kodama, T., Yi, J., Newberg, J. Y., Tien, J. C., Wu, H., Finegold, M. J., Kodama, M., Wei, Z., Tamura, T., Takehara, T., Johnson, R. L., Jenkins, N. A., & Copeland, N. G. (2018). Molecular profiling of nonalcoholic fatty liver disease-associated hepatocellular carcinoma using SB transposon mutagenesis. *Proc Natl Acad Sci U S A*, *115*, E10417-E10426.

Koh, A., Molinaro, A., Stahlman, M., Khan, M. T., Schmidt, C., Manneras-Holm, L., Wu, H., Carreras, A., Jeong, H., Olofsson, L. E., Bergh, P. O., Gerdes, V., Hartstra, A., de Brauw, M., Perkins, R., Nieuwdorp, M., Bergstrom, G., & Backhed, F. (2018). Microbially produced imidazole propionate impairs insulin signaling through mTORC1. *Cell*, *175*, 947-961 e17.

Koistinen, H. A., Chibalin, A. V, & Zierath, J. R. (2003). Aberrant p38 mitogen-activated protein kinase signalling in skeletal muscle from type 2 diabetic patients. *Diabetologia*, *46*, 1324–1328.

Koliaki, C., Szendroedi, J., Kaul, K., Jelenik, T., Nowotny, P., Jankowiak, F., Herder, C., Carstensen, M., Krausch, M., Knoefel, W. T., Schlensak, M., & Roden, M. (2015). Adaptation of hepatic mitochondrial function in humans with non-alcoholic fatty liver is lost in steatohepatitis. *Cell Metab*, *21*, 739–746.

Kosova, F., Coskun, T., Kaya, Y., Kara, E., & Ari, Z. (2013). Adipocytokine levels of colon cancer patients before and after treatment. *Bratisl Lek Listy*, *114*, 394–397.

Kuan, C. Y., Yang, D. D., Samanta Roy, D. R., Davis, R. J., Rakic, P., & Flavell, R. A. (1999). The Jnk1 and Jnk2 protein kinases are required for regional specific apoptosis during early brain development. *Neuron*, *22*, 667–676.

Kuma, Y., Campbell, D. G., & Cuenda, A. (2004). Identification of glycogen synthase as a new substrate for stress-activated protein kinase 2b/p38beta. *Biochem J*, *379*, 133–139.

Kyriakis, J. M., & Avruch, J. (2012). Mammalian MAPK signal transduction pathways activated by stress and inflammation: a 10-year update. *Physiol Rev*, *92*, 689–737.

Lacraz, G., Rakotoarivelo, V., Labbe, S. M., Vernier, M., Noll, C., Mayhue, M., Stankova, J., Schwertani, A., Grenier, G., Carpentier, A., Richard, D., Ferbeyre, G., Fradette, J., Rola-Pleszczynski, M., Menendez, A., Langlois, M. F., Ilangumaran, S., & Ramanathan, S. (2016). Deficiency of interleukin-15 confers resistance to obesity by diminishing inflammation and enhancing the thermogenic function of adipose tissues. *PLoS One*, *11*, e0162995.

Lanna, A., Henson, S. M., Escors, D., & Akbar, A. N. (2014). The kinase p38 activated by the metabolic regulator AMPK and scaffold TAB1 drives the senescence of human T cells. *Nat Immunol*, *15*, 965–972.

Larsson, O., Morita, M., Topisirovic, I., Alain, T., Blouin, M. J., Pollak, M., & Sonenberg, N. (2012). Distinct perturbation of the translatome by the antidiabetic drug metformin. *Proc Natl Acad Sci U S A*, *109*, 8977–8982.

Larsson, S. C., & Wolk, A. (2007). Overweight, obesity and risk of liver cancer: a meta-analysis of cohort studies. *Br J Cancer*, *97*, 1005–1008.

Lauby-Secretan, B., Scoccianti, C., Loomis, D., Grosse, Y., Bianchini, F., Straif, K., & International Agency for Research on Cancer Handbook Working Group. (2016). Body fatness and cancer--viewpoint of the IARC working group. *N Engl J Med*, *375*, 794–798.

Lawan, A., Min, K., Zhang, L., Canfran-Duque, A., Jurczak, M. J., Camporez, J. P. G., Nie, Y., Gavin, T. P., Shulman, G. I., Fernández-Hernando, C., & Bennett, A. M. (2018). Skeletal muscle-specific deletion of MKP-1 reveals a p38 MAPK/JNK/AKT signaling node that regulates obesity-induced insulin resistance. *Diabetes*, *67*, 624–635.

Lawan, A., Zhang, L., Gatzke, F., Min, K., Jurczak, M. J., Al-Mutairi, M., Richter, P., Camporez, J. P., Couvillon, A., Pesta, D., Roth Flach, R. J., Shulman, G. I., & Bennett, A. M. (2015). Hepatic mitogen-activated protein kinase phosphatase 1 selectively regulates glucose

metabolism and energy homeostasis. *Mol Cell Biol*, *35*, 26–40.

Lee, J. S., Chu, I. S., Mikaelyan, A., Calvisi, D. F., Heo, J., Reddy, J. K., & Thorgeirsson, S. S. (2004). Application of comparative functional genomics to identify best-fit mouse models to study human cancer. *Nat Genet*, *36*, 1306–1311.

Lee, J., Sun, C., Zhou, Y., Lee, J., Gokalp, D., Herrema, H., Park, S. W., Davis, R. J., & Ozcan, U. (2011). p38 MAPK-mediated regulation of Xbp1s is crucial for glucose homeostasis. *Nat Med*, *17*, 1251–1260.

Leiva, M., Matesanz, N., Pulgarín-Alfaro, M., Nikolic, I., & Sabio, G. (2020). Uncovering the role of p38 family members in adipose tissue physiology. *Front Endocrinol (Lausanne)*, *11*, 572089.

Li, B., & Dewey, C. N. (2011). RSEM: accurate transcript quantification from RNA-Seq data with or without a reference genome. *BMC Bioinformatics*, *12*, 323.

Li, M., Liu, J., & Zhang, C. (2011). Evolutionary history of the vertebrate mitogen activated protein kinases family. *PLoS One*, *6*, e26999.

Liao, L. M., Schwartz, K., Pollak, M., Graubard, B. I., Li, Z., Ruterbusch, J., Rothman, N., Davis, F., Wacholder, S., Colt, J., Chow, W. H., & Purdue, M. P. (2013). Serum leptin and adiponectin levels and risk of renal cell carcinoma. *Obesity (Silver Spring)*, *21*, 1478–1485.

Liberzon, A., Birger, C., Thorvaldsdottir, H., Ghandi, M., Mesirov, J. P., & Tamayo, P. (2015). The Molecular Signatures Database (MSigDB) hallmark gene set collection. *Cell Syst*, *1*, 417–425.

Lin, J., Handschin, C., & Spiegelman, B. M. (2005). Metabolic control through the PGC-1 family of transcription coactivators. *Cell Metab*, *1*, 361–370.

Lin, J., Wu, H., Tarr, P. T., Zhang, C. Y., Wu, Z., Boss, O., Michael, L. F., Puigserver, P., Isotani, E., Olson, E. N., Lowell, B. B., Bassel-Duby, R., & Spiegelman, B. M. (2002). Transcriptional co-activator PGC-1 alpha drives the formation of slow-twitch muscle fibres. *Nature*, *418*, 797–801.

Lin, J., Wu, P. H., Tarr, P. T., Lindenberg, K. S., St-Pierre, J., Zhang, C. Y., Mootha, V. K., Jager, S., Vianna, C. R., Reznick, R. M., Cui, L., Manieri, M., Donovan, M. X., Wu, Z., Cooper, M. P., Fan, M. C., Rohas, L. M., Zavacki, A. M., Cinti, S., Shulman, G. I., Lowell, B. B., Krainc, D., & Spiegelman, B. M. (2004). Defects in adaptive energy metabolism with CNS-linked hyperactivity in PGC-1alpha null mice. *Cell*, *119*, 121–135.

Liu, C. J., Chen, P. J., Lai, M. Y., Liu, C. H., Chen, C. L., Kao, J. H., & Chen, D. S. (2009). High

serum adiponectin correlates with advanced liver disease in patients with chronic hepatitis B virus infection. *Hepatol Int*, *3*, 364–370.

Liu, J., & Lin, A. (2005). Role of JNK activation in apoptosis: a double-edged sword. *Cell Res*, *15*, 36–42.

Liu, M., Chen, H., Wei, L., Hu, D., Dong, K., Jia, W., Dong, L. Q., & Liu, F. (2015). Endoplasmic reticulum (ER) localization is critical for DsbA-L protein to suppress ER stress and adiponectin down-regulation in adipocytes. *J Biol Chem*, *290*, 10143–10148.

Liu, S., Wu, H. J., Zhang, Z. Q., Chen, Q., Liu, B., Wu, J. P., & Zhu, L. (2011). The ameliorating effect of rosiglitazone on experimental nonalcoholic steatohepatitis is associated with regulating adiponectin receptor expression in rats. *Eur J Pharmacol*, *650*, 384–389.

Lluís, F., Perdiguero, E., Nebreda, A. R., & Muñoz-Cánoves, P. (2006). Regulation of skeletal muscle gene expression by p38 MAP kinases. *Trends Cell Biol*, *16*, 36–44.

Loonat, A. A., Martin, E. D., Sarafraz-Shekary, N., Tilgner, K., Hertz, N. T., Levin, R., Shokat, K. M., Burlingame, A. L., Arabacilar, P., Uddin, S., Thomas, M., Marber, M. S., & Clark, J. E. (2019). p38gamma MAPK contributes to left ventricular remodeling after pathologic stress and disinhibits calpain through phosphorylation of calpastatin. *FASEB J*, *33*, 13131–13144.

Loro, E., Seifert, E. L., Moffat, C., Romero, F., Mishra, M. K., Sun, Z., Krajacic, P., Anokye-Danso, F., Summer, R. S., Ahima, R. S., & Khurana, T. S. (2015). IL-15Ralpha is a determinant of muscle fuel utilization, and its loss protects against obesity. *Am J Physiol Regul Integr Comp Physiol*, *309*, R835-44.

Lovett, F. A., Cosgrove, R. A., González, I., & Pell, J. M. (2010). Essential role for p38alpha MAPK but not p38gamma MAPK in Igf2 expression and myoblast differentiation. *Endocrinology*, *151*, 4368–4380.

Lowell, B. B., & Spiegelman, B. M. (2000). Towards a molecular understanding of adaptive thermogenesis. *Nature*, *404*, 652–660.

Lowell, B. B., V, S. S., Hamann, A., Lawitts, J. A., Himms-Hagen, J., Boyer, B. B., Kozak, L. P., & Flier, J. S. (1993). Development of obesity in transgenic mice after genetic ablation of brown adipose tissue. *Nature*, *366*, 740–742.

Loy, B., Apostolova, G., Dorn, R., McGuire, V. A., Arthur, J. S., & Dechant, G. (2011). p38alpha and p38beta mitogen-activated protein kinases determine cholinergic transdifferentiation of sympathetic neurons. *J Neurosci*, *31*, 12059–12067.

Lu, C. C., Chu, P. Y., Hsia, S. M., Wu, C. H., Tung, Y. T., & Yen, G. C. (2017). Insulin induction

instigates cell proliferation and metastasis in human colorectal cancer cells. *Int J Oncol*, *50*, 736–744.

Luo, Z., Zang, M., & Guo, W. (2010). AMPK as a metabolic tumor suppressor: control of metabolism and cell growth. *Future Oncol*, *6*, 457–470.

Ma, S. J., Zheng, Y. X., Zhou, P. C., Xiao, Y. N., & Tan, H. Z. (2016). Metformin use improves survival of diabetic liver cancer patients: systematic review and meta-analysis. *Oncotarget*, *7*, 66202–66211.

Maeda, K., Okubo, K., Shimomura, I., Funahashi, T., Matsuzawa, Y., & Matsubara, K. (1996). cDNA cloning and expression of a novel adipose specific collagen-like factor, apM1 (AdiPose Most abundant Gene transcript 1). *Biochem Biophys Res Commun*, *221*, 286–289.

Maeda, S., Kamata, H., Luo, J. L., Leffert, H., & Karin, M. (2005). IKKbeta couples hepatocyte death to cytokine-driven compensatory proliferation that promotes chemical hepatocarcinogenesis. *Cell*, *121*, 977–990.

Maher, A. C., Akhtar, M., Vockley, J., & Tarnopolsky, M. A. (2010). Women have higher protein content of beta-oxidation enzymes in skeletal muscle than men. *PLoS One*, *5*, e12025.

Man, K., Ng, K. T., Xu, A., Cheng, Q., Lo, C. M., Xiao, J. W., Sun, B. S., Lim, Z. X., Cheung, J. S., Wu, E. X., Sun, C. K., Poon, R. T., & Fan, S. T. (2010). Suppression of liver tumor growth and metastasis by adiponectin in nude mice through inhibition of tumor angiogenesis and downregulation of Rho kinase/IFN-inducible protein 10/matrix metalloproteinase 9 signaling. *Clin Cancer Res*, *16*, 967–977.

Manieri, E, & Sabio, G. (2015). Stress kinases in the modulation of metabolism and energy balance. *J Mol Endocrinol*, *55*, R11-22.

Manieri, E. (2016). Metabolic genes in hepatocellular carcinoma development. Doctoral dissertation, *Autonomous University of Madrid*.

Manieri, E., Folgueira, C., Rodríguez, M. E., Leiva-Vega, L., Esteban-Lafuente, L., Chen, C., Cubero, F. J., Barrett, T., Cavanagh-Kyros, J., Seruggia, D., Rosell, A., Sanchez-Cabo, F., Gómez, M. J., Monte, M. J., Marin, J. J. G., Davis, R. J., Mora, A., & Sabio, G. (2020). JNK-mediated disruption of bile acid homeostasis promotes intrahepatic cholangiocarcinoma. *Proc Natl Acad Sci U S A*, *117*, 16492-16499.

Manieri, E., Herrera-Melle, L., Mora, A., Tomás-Loba, A., Leiva-Vega, L., Fernández, D. I., Rodríguez, E., Morán, L., Hernández-Cosido, L., Torres, J. L., Seoane, L. M., Cubero, F. J., Marcos, M., & Sabio, G. (2019). Adiponectin accounts for gender differences in

hepatocellular carcinoma incidence. *J Exp Med*, *216*, 1108-1119.

Mantzoros, C., Petridou, E., Dessypris, N., Chavelas, C., Dalamaga, M., Alexe, D. M., Papadiamantis, Y., Markopoulos, C., Spanos, E., Chrousos, G., & Trichopoulos, D. (2004). Adiponectin and breast cancer risk. *J Clin Endocrinol Metab*, *89*, 1102–1107.

Mao, X., Kikani, C. K., Riojas, R. A., Langlais, P., Wang, L., Ramos, F. J., Fang, Q., Christ-Roberts, C. Y., Hong, J. Y., Kim, R. Y., Liu, F., & Dong, L. Q. (2006). APPL1 binds to adiponectin receptors and mediates adiponectin signalling and function. *Nat Cell Biol*, *8*, 516–523.

Marshall, C. J. (1995). Specificity of receptor tyrosine kinase signaling: transient versus sustained extracellular signal-regulated kinase activation. *Cell*, *80*, 179–185.

Matesanz, N., Bernardo, E., Acín-Perez, R., Manieri, E., Pérez-Sieira, S., Hernández-Cosido, L., Montalvo-Romeral, V., Mora, A., Rodríguez, E., Leiva-Vega, L., Lechuga-Vieco, A. V, Ruiz-Cabello, J., Torres, J. L., Crespo-Ruiz, M., Centeno, F., Álvarez, C. V, Marcos, M., Enríquez, J. A., Nogueiras, R., & Sabio, G. (2017). MKK6 controls T3-mediated browning of white adipose tissue. *Nat Commun*, *8*, 856.

Matesanz, N., Nikolic, I., Leiva, M., Pulgarín-Alfaro, M., Santamans, A. M., Bernardo, E., Mora, A., Herrera-Melle, L., Rodríguez, E., Beiroa, D., Caballero, A., Martín-García, E., Acín-Perez, R., Hernández-Cosido, L., Leiva-Vega, L., Torres, J. L., Centeno, F., Nebreda, A. R., Enríquez, J. A., Nogueiras, R., Marcos, M., & Sabio, G. (2018). p38alpha blocks brown adipose tissue thermogenesis through p38delta inhibition. *PLoS Biol*, *16*, e2004455.

McPherron, A. C., Lawler, A. M., & Lee, S. J. (1997). Regulation of skeletal muscle mass in mice by a new TGF-beta superfamily member. *Nature*, *387*, 83–90.

Mitsiades, N., Pazaitou-Panayiotou, K., Aronis, K. N., Moon, H. S., Chamberland, J. P., Liu, X., Diakopoulos, K. N., Kyttaris, V., Panagiotou, V., Mylvaganam, G., Tseleni-Balafouta, S., & Mantzoros, C. S. (2011). Circulating adiponectin is inversely associated with risk of thyroid cancer: in vivo and in vitro studies. *J Clin Endocrinol Metab*, *96*, E2023-8.

Miyazaki, T., Bub, J. D., Uzuki, M., & Iwamoto, Y. (2005). Adiponectin activates c-Jun NH2-terminal kinase and inhibits signal transducer and activator of transcription 3. *Biochem Biophys Res Commun*, *333*, 79–87.

Montalvo-Romeral, V. (2019). Role of hepatic p38delta MAPK in liver metabolism. Doctoral dissertation, *Autonomous University of Madrid*.

Montan, P. D., Sourlas, A., Olivero, J., Silverio, D., Guzman, E., & Kosmas, C. E. (2019). Pharmacologic therapy of obesity: mechanisms of action and cardiometabolic effects.

Ann Transl Med, *7*, 393.

Moore, T. M., Zhou, Z., Cohn, W., Norheim, F., Lin, A. J., Kalajian, N., Strumwasser, A. R., Cory, K., Whitney, K., Ho, T., Ho, T., Lee, J. L., Rucker, D. H., Shirihai, O., van der Bliek, A. M., Whitelegge, J. P., Seldin, M. M., Lusis, A. J., Lee, S., Drevon, C. A., Mahata, S. K., Turcotte, L. P., & Hevener, A. L. (2019). The impact of exercise on mitochondrial dynamics and the role of Drp1 in exercise performance and training adaptations in skeletal muscle. *Mol Metab*, *21*, 51–67.

Mootha, V. K., Lindgren, C. M., Eriksson, K. F., Subramanian, A., Sihag, S., Lehar, J., Puigserver, P., Carlsson, E., Ridderstrale, M., Laurila, E., Houstis, N., Daly, M. J., Patterson, N., Mesirov, J. P., Golub, T. R., Tamayo, P., Spiegelman, B., Lander, E. S., Hirschhorn, J. N., Altshuler, D., & Groop, L. C. (2003). PGC-1alpha-responsive genes involved in oxidative phosphorylation are coordinately downregulated in human diabetes. *Nat Genet*, *34*, 267–273.

Morrison, D. K., & Davis, R. J. (2003). Regulation of MAP kinase signaling modules by scaffold proteins in mammals. *Annu Rev Cell Dev Biol*, *19*, 91–118.

Moschen, A. R., Wieser, V., & Tilg, H. (2012). Adiponectin: key player in the adipose tissue-liver crosstalk. *Curr Med Chem*, *19*, 5467–5473.

Murphy, R. M., Watt, M. J., & Febbraio, M. A. (2020). Metabolic communication during exercise. *Nat Metab*, *2*, 805–816.

Nakajima, T. E., Yamada, Y., Hamano, T., Furuta, K., Gotoda, T., Katai, H., Kato, K., Hamaguchi, T., & Shimada, Y. (2009). Adipocytokine levels in gastric cancer patients: resistin and visfatin as biomarkers of gastric cancer. *J Gastroenterol*, *44*, 685–690.

Nakano, Y., Tobe, T., Choi-Miura, N. H., Mazda, T., & Tomita, M. (1996). Isolation and characterization of GBP28, a novel gelatin-binding protein purified from human plasma. *J Biochem*, *120*, 803–812.

Nakatani, T., Roy, G., Fujimoto, N., Asahara, T., & Ito, A. (2001). Sex hormone dependency of diethylnitrosamine-induced liver tumors in mice and chemoprevention by leuprorelin. *Jpn J Cancer Res*, *92*, 249–256.

Nakatani, Y., Kaneto, H., Kawamori, D., Hatazaki, M., Miyatsuka, T., Matsuoka, T. A., Kajimoto, Y., Matsuhisa, M., Yamasaki, Y., & Hori, M. (2004). Modulation of the JNK pathway in liver affects insulin resistance status. *J Biol Chem*, *279*, 45803–45809.

Naugler, W. E., Sakurai, T., Kim, S., Maeda, S., Kim, K., Elsharkawy, A. M., & Karin, M. (2007). Gender disparity in liver cancer due to sex differences in MyD88-dependent IL-6

production. *Science*, *317*, 121–124.

Navarro, P., & Vázquez, J. (2009). A refined method to calculate false discovery rates for peptide identification using decoy databases. *J Proteome Res*, *8*, 1792–1796.

Neufer, P. D., Bamman, M. M., Muoio, D. M., Bouchard, C., Cooper, D. M., Goodpaster, B. H., Booth, F. W., Kohrt, W. M., Gerszten, R. E., Mattson, M. P., Hepple, R. T., Kraus, W. E., Reid, M. B., Bodine, S. C., Jakicic, J. M., Fleg, J. L., Williams, J. P., Joseph, L., Evans, M., Maruvada, P., Rodgers, M., Roary, M., Boyce, A. T., Drugan, J. K., Koenig, J. I., Ingraham, R. H., Krotoski, D., Garcia-Cazarin, M., McGowan, J. A., & Laughlin, M. R. (2015). Understanding the cellular and molecular mechanisms of physical activity-induced health benefits. *Cell Metab*, *22*, 4–11.

Nguyen, L., Bohlen, J., Stricker, J., Chahal, I., Zhang, H., & Pistilli, E. E. (2017). Hippocampus-specific deficiency of IL-15Ralpha contributes to greater anxiety-like behaviors in mice. *Metab Brain Dis*, *32*, 297–302.

Nguyen, M. T., Satoh, H., Favelyukis, S., Babendure, J. L., Imamura, T., Sbodio, J. I., Zalevsky, J., Dahiyat, B. I., Chi, N. W., & Olefsky, J. M. (2005). JNK and tumor necrosis factor-alpha mediate free fatty acid-induced insulin resistance in 3T3-L1 adipocytes. *J Biol Chem*, *280*, 35361–35371.

Nicoll, J. X., Fry, A. C., & Mosier, E. M. (2019). Sex-based differences in resting MAPK, androgen, and glucocorticoid receptor phosphorylation in human skeletal muscle. *Steroids*, *141*, 23–29.

Nielsen, A. R., Hojman, P., Erikstrup, C., Fischer, C. P., Plomgaard, P., Mounier, R., Mortensen, O. H., Broholm, C., Taudorf, S., Krogh-Madsen, R., Lindegaard, B., Petersen, A. M., Gehl, J., & Pedersen, B. K. (2008). Association between interleukin-15 and obesity: interleukin-15 as a potential regulator of fat mass. *J Clin Endocrinol Metab*, *93*, 4486–4493.

Nielsen, A. R., Mounier, R., Plomgaard, P., Mortensen, O. H., Penkowa, M., Speerschneider, T., Pilegaard, H., & Pedersen, B. K. (2007). Expression of interleukin-15 in human skeletal muscle effect of exercise and muscle fibre type composition. *J Physiol*, *584*, 305–312.

Nikolic, I., Leiva, M., & Sabio, G. (2020). The role of stress kinases in metabolic disease. *Nat Rev Endocrinol*, *16*, 697–716.

Nishizawa, H., Shimomura, I., Kishida, K., Maeda, N., Kuriyama, H., Nagaretani, H., Matsuda, M., Kondo, H., Furuyama, N., Kihara, S., Nakamura, T., Tochino, Y., Funahashi, T., & Matsuzawa, Y. (2002). Androgens decrease plasma adiponectin, an insulin-sensitizing adipocyte-derived protein. *Diabetes*, *51*, 2734–2741.

Nkontchou, G., Bastard, J. P., Ziol, M., Aout, M., Cosson, E., Ganne-Carrie, N., Grando-Lemaire, V., Roulot, D., Capeau, J., Trinchet, J. C., Vicaut, E., & Beaugrand, M. (2010). Insulin resistance, serum leptin, and adiponectin levels and outcomes of viral hepatitis C cirrhosis. *J Hepatol*, *53*, 827–833.

Nogueiras, R., & Sabio, G. (2021). Brain JNK and metabolic disease. *Diabetologia*, *64*, 265–274.

Nomura, D. K., Long, J. Z., Niessen, S., Hoover, H. S., Ng, S. W., & Cravatt, B. F. (2010). Monoacylglycerol lipase regulates a fatty acid network that promotes cancer pathogenesis. *Cell*, *140*, 49–61.

Norrby, M., & Tågerud, S. (2010). Mitogen-activated protein kinase-activated protein kinase 2 (MK2) in skeletal muscle atrophy and hypertrophy. *J Cell Physiol*, *223*, 194–201.

O'Shea, D., Cawood, T. J., O'Farrelly, C., & Lynch, L. (2010). Natural killer cells in obesity: impaired function and increased susceptibility to the effects of cigarette smoke. *PLoS One*, *5*, e8660.

O'Shea, D., Corrigan, M., Dunne, M. R., Jackson, R., Woods, C., Gaoatswe, G., Moynagh, P. N., O'Connell, J., & Hogan, A. E. (2013). Changes in human dendritic cell number and function in severe obesity may contribute to increased susceptibility to viral infection. *Int J Obes (Lond)*, *37*, 1510–1513.

Odeh, M., Tamir-Livne, Y., Haas, T., & Bengal, E. (2020). P38alpha MAPK coordinates the activities of several metabolic pathways that together induce atrophy of denervated muscles. *FEBS J*, *287*, 73–93.

Ohbuchi, Y., Suzuki, Y., Hatakeyama, I., Nakao, Y., Fujito, A., Iwasaka, T., & Isaka, K. (2014). A lower serum level of middle-molecular-weight adiponectin is a risk factor for endometrial cancer. *Int J Clin Oncol*, *19*, 667–673.

Onuma, M., Bub, J. D., Rummel, T. L., & Iwamoto, Y. (2003). Prostate cancer cell-adipocyte interaction: leptin mediates androgen-independent prostate cancer cell proliferation through c-Jun NH2-terminal kinase. *J Biol Chem*, *278*, 42660–42667.

Ostrowski, K., Hermann, C., Bangash, A., Schjerling, P., Nielsen, J. N., & Pedersen, B. K. (1998). A trauma-like elevation of plasma cytokines in humans in response to treadmill running. *J Physiol*, *513*, 889–894.

Ouchi, N., Oshima, Y., Ohashi, K., Higuchi, A., Ikegami, C., Izumiya, Y., & Walsh, K. (2008). Follistatin-like 1, a secreted muscle protein, promotes endothelial cell function and revascularization in ischemic tissue through a nitric-oxide synthase-dependent

mechanism. *J Biol Chem*, *283*, 32802–32811.

Özcan, U., Cao, Q., Yilmaz, E., Lee, A. H., Iwakoshi, N. N., Ozdelen, E., Tuncman, G., Gorgun, C., Glimcher, L. H., & Hotamisligil, G. S. (2004). Endoplasmic reticulum stress links obesity, insulin action, and type 2 diabetes. *Science*, *306*, 457–461.

Pajvani, U. B., Du, X., Combs, T. P., Berg, A. H., Rajala, M. W., Schulthess, T., Engel, J., Brownlee, M., & Scherer, P. E. (2003). Structure-function studies of the adipocyte-secreted hormone Acrp30/adiponectin. Implications fpr metabolic regulation and bioactivity. *J Biol Chem*, *278*, 9073–9085.

Pal, M., Wunderlich, C. M., Spohn, G., Bronneke, H. S., Schmidt-Supprian, M., & Wunderlich, F. T. (2013). Alteration of JNK-1 signaling in skeletal muscle fails to affect glucose homeostasis and obesity-associated insulin resistance in mice. *PLoS One*, *8*, e54247.

Palomer, X., Alvarez-Guardia, D., Rodríguez-Calvo, R., Coll, T., Laguna, J. C., Davidson, M. M., Chan, T. O., Feldman, A. M., & Vázquez-Carrera, M. (2009). TNF-alpha reduces PGC-1alpha expression through NF-kappaB and p38 MAPK leading to increased glucose oxidation in a human cardiac cell model. *Cardiovasc Res*, *81*, 703–712.

Pan, W., Hsuchou, H., Yu, C., & Kastin, A. J. (2008). Permeation of blood-borne IL15 across the blood-brain barrier and the effect of LPS. *J Neurochem*, *106*, 313–319.

Panieri, E., & Santoro, M. M. (2016). ROS homeostasis and metabolism: a dangerous liason in cancer cells. *Cell Death Dis*, *7*, e2253.

Parekh, S., & Anania, F. A. (2007). Abnormal lipid and glucose metabolism in obesity: implications for nonalcoholic fatty liver disease. *Gastroenterology*, *132*, 2191–2207.

Parida, S., Siddharth, S., & Sharma, D. (2019). Adiponectin, obesity, and cancer: clash of the bigwigs in health and disease. *Int J Mol Sci*, *20*, 2519.

Patterson, K. I., Brummer, T., O'Brien, P. M., & Daly, R. J. (2009). Dual-specificity phosphatases: critical regulators with diverse cellular targets. *Biochem J*, *418*, 475–489.

Patti, M. E., Butte, A. J., Crunkhorn, S., Cusi, K., Berria, R., Kashyap, S., Miyazaki, Y., Kohane, I., Costello, M., Saccone, R., Landaker, E. J., Goldfine, A. B., Mun, E., DeFronzo, R., Finlayson, J., Kahn, C. R., & Mandarino, L. J. (2003). Coordinated reduction of genes of oxidative metabolism in humans with insulin resistance and diabetes: potential role of PGC1 and NRF1. *Proc Natl Acad Sci U S A*, *100*, 8466–8471.

Paul, A., Wilson, S., Belham, C. M., Robinson, C. J. M., Scott, P. H., Gould, G. W., & Plevin, R. (1997). Stress-activated protein kinases: activation, regulation and function. *Cell Signal*, *9*, 403–410.

Pedersen, B. K. (2019). Physical activity and muscle-brain crosstalk. *Nat Rev Endocrinol*, *15*, 383–392.

Pedersen, B. K., & Febbraio, M. A. (2012). Muscles, exercise and obesity: skeletal muscle as a secretory organ. *Nat Rev Endocrinol*, *8*, 457–465.

Peng, Y., Rideout, D., Rakita, S., Sajan, M., Farese, R., You, M., & Murr, M. M. (2009). Downregulation of adiponectin/AdipoR2 is associated with steatohepatitis in obese mice. *J Gastrointest Surg*, *13*, 2043–2049.

Perfettini, J. L., Castedo, M., Nardacci, R., Ciccosanti, F., Boya, P., Roumier, T., Larochette, N., Piacentini, M., & Kroemer, G. (2005). Essential role of p53 phosphorylation by p38 MAPK in apoptosis induction by the HIV-1 envelope. *J Exp Med*, *201*, 279–289.

Petersen, M. C., & Shulman, G. I. (2018). Mechanisms of insulin action and insulin resistance. *Physiol Rev*, *98*, 2133–2223.

Peterziel, H., Mink, S., Schonert, A., Becker, M., Klocker, H., & Cato, A. C. (1999). Rapid signalling by androgen receptor in prostate cancer cells. *Oncogene*, *18*, 6322–6329.

Petridou, E., Mantzoros, C. S., Dessypris, N., Dikalioti, S. K., & Trichopoulos, D. (2006). Adiponectin in relation to childhood myeloblastic leukaemia. *Br J Cancer*, *94*, 156–160.

Petridou, E. T., Dessypris, N., Panagopoulou, P., Sergentanis, T. N., Mentis, A. F., Pourtsidis, A., Polychronopoulou, S., Kalmanti, M., Athanasiadou-Piperopoulou, F., & Moschovi, M. (2010). Adipocytokines in relation to Hodgkin lymphoma in children. *Pediatr Blood Cancer*, *54*, 311–315.

Petridou, E. T., Mitsiades, N., Gialamas, S., Angelopoulos, M., Skalkidou, A., Dessypris, N., Hsi, A., Lazaris, N., Polyzos, A., Syrigos, C., Brennan, A. M., Tseleni-Balafouta, S., & Mantzoros, C. S. (2007). Circulating adiponectin levels and expression of adiponectin receptors in relation to lung cancer: two case-control studies. *Oncology*, *73*, 261–269.

Pierce, J. R., Maples, J. M., & Hickner, R. C. (2015). IL-15 concentrations in skeletal muscle and subcutaneous adipose tissue in lean and obese humans: local effects of IL-15 on adipose tissue lipolysis. *Am J Physiol Endocrinol Metab*, *308*, E1131-9.

Pilegaard, H., Saltin, B., & Neufer, P. D. (2003). Exercise induces transient transcriptional activation of the PGC-1alpha gene in human skeletal muscle. *J Physiol*, *546*, 851–858.

Pinti, M. V, Fink, G. K., Hathaway, Q. A., Durr, A. J., Kunovac, A., & Hollander, J. M. (2019). Mitochondrial dysfunction in type 2 diabetes mellitus: an organ-based analysis. *Am J Physiol Endocrinol Metab*, *316*, E268–E285.

Pistilli, E. E., Bogdanovich, S., Garton, F., Yang, N., Gulbin, J. P., Conner, J. D., Anderson, B.

G., Quinn, L. S., North, K., Ahima, R. S., & Khurana, T. S. (2011). Loss of IL-15 receptor alpha alters the endurance, fatigability, and metabolic characteristics of mouse fast skeletal muscles. *J Clin Invest*, *121*, 3120–3132.

Ploeger, J. M., Manivel, J. C., Boatner, L. N., & Mashek, D. G. (2017). Caloric restriction prevents carcinogen-initiated liver tumorigenesis in mice. *Cancer Prev Res (Phila)*, *10*, 660–670.

Pogozelski, A. R., Geng, T., Li, P., Yin, X., Lira, V. A., Zhang, M., Chi, J. T., & Yan, Z. (2009). p38gamma mitogen-activated protein kinase is a key regulator in skeletal muscle metabolic adaptation in mice. *PLoS One*, *4*, e7934.

Pollard, J. W. (2004). Tumour-educated macrophages promote tumour progression and metastasis. *Nat Rev Cancer*, *4*, 71–78.

Polyzos, S. A., Toulis, K. A., Goulis, D. G., Zavos, C., & Kountouras, J. (2011). Serum total adiponectin in nonalcoholic fatty liver disease: a systematic review and meta-analysis. *Metabolism*, *60*, 313–326.

Powazniak, Y., Kempfer, A. C., de la Paz Dominguez, M., Farias, C., Keller, L., Calderazzo, J. C., & Lazzari, M. A. (2009). Effect of estradiol, progesterone and testosterone on apoptosis- and proliferation-induced MAPK signaling in human umbilical vein endothelial cells. *Mol Med Rep*, *2*, 441–447.

Prada, P. O., Zecchin, H. G., Gasparetti, A. L., Torsoni, M. A., Ueno, M., Hirata, A. E., Corezola do Amaral, M. E., Hoer, N. F., Boschero, A. C., & Saad, M. J. (2005). Western diet modulates insulin signaling, c-Jun N-terminal kinase activity, and insulin receptor substrate-1ser307 phosphorylation in a tissue-specific fashion. *Endocrinology*, *146*, 1576–1587.

Priest, C., & Tontonoz, P. (2019). Inter-organ cross-talk in metabolic syndrome. *Nat Metab*, *1*, 1177–1188.

Puigserver, P., Rhee, J., Lin, J., Wu, Z., Yoon, J. C., Zhang, C. Y., Krauss, S., Mootha, V. K., Lowell, B. B., & Spiegelman, B. M. (2001). Cytokine stimulation of energy expenditure through p38 MAP kinase activation of PPARgamma coactivator-1. *Mol Cell*, *8*, 971–982.

Qatanani, M., & Lazar, M. A. (2007). Mechanisms of obesity-associated insulin resistance: many choices on the menu. *Genes Dev*, *21*, 1443–1455.

Qi, Y., Takahashi, N., Hileman, S. M., Patel, H. R., Berg, A. H., Pajvani, U. B., Scherer, P. E., & Ahima, R. S. (2004). Adiponectin acts in the brain to decrease body weight. *Nat Med*, *10*, 524–529.

Rajamäki, K., Mayranpaa, M. I., Risco, A., Tuimala, J., Nurmi, K., Cuenda, A., Eklund, K. K., Oorni, K., & Kovanen, P. T. (2016). p38delta MAPK: a novel regulator of NLRP3 inflammasome activation with increased expression in coronary atherogenesis. *Arterioscler Thromb Vasc Biol*, *36*, 1937–1946.

Raman, M., Chen, W., & Cobb, M. H. (2007). Differential regulation and properties of MAPKs. *Oncogene*, *26*, 3100–3112.

Rao, R. R., Long, J. Z., White, J. P., Svensson, K. J., Lou, J., Lokurkar, I., Jedrychowski, M. P., Ruas, J. L., Wrann, C. D., Lo, J. C., Camera, D. M., Lachey, J., Gygi, S., Seehra, J., Hawley, J. A., & Spiegelman, B. M. (2014). Meteorin-like is a hormone that regulates immune-adipose interactions to increase beige fat thermogenesis. *Cell*, *157*, 1279–1291.

Risco, A., del Fresno, C., Mambol, A., Alsina-Beauchamp, D., MacKenzie, K. F., Yang, H. T., Barber, D. F., Morcelle, C., Arthur, J. S., Ley, S. C., Ardavin, C., & Cuenda, A. (2012). p38gamma and p38delta kinases regulate the Toll-like receptor 4 (TLR4)-induced cytokine production by controlling ERK1/2 protein kinase pathway activation. *Proc Natl Acad Sci U S A*, *109*, 11200–11205.

Ritchie, M. E., Phipson, B., Wu, D., Hu, Y., Law, C. W., Shi, W., & Smyth, G. K. (2015). limma powers differential expression analyses for RNA-sequencing and microarray studies. *Nucleic Acids Res*, *43*, e47.

Roche, O., Fernández-Aroca, D. M., Arconada-Luque, E., García-Flores, N., Mellor, L. F., Ruiz-Hidalgo, M. J., & Sánchez-Prieto, R. (2020). p38beta and cancer: the beginning of the road. *Int J Mol Sci*, *21*, 7524.

Rodríguez-Fdez, S., Lorenzo-Martín, L. F., Fernández-Pisonero, I., Porteiro, B., Veyrat-Durebex, C., Beiroa, D., Al-Massadi, O., Abad, A., Diéguez, C., Coppari, R., Nogueiras, R., & Bustelo, X. R. (2020). Vav2 catalysis-dependent pathways contribute to skeletal muscle growth and metabolic homeostasis. *Nat Commun*, *11*, 5808.

Rodriguez, A., & Flemington, E. K. (1999). Transfection-mediated cell-cycle signaling: considerations for transient transfection-based cell-cycle studies. *Anal Biochem*, *272*, 171–181.

Romieu, I., Dossus, L., Barquera, S., Blottière, H. M., Franks, P. W., Gunter, M., Hwalla, N., Hursting, S. D., Leitzmann, M., Margetts, B., Nishida, C., Potischman, N., Seidell, J., Stepien, M., Wang, Y., Westerterp, K., Winichagoon, P., Wiseman, M., Willett, W. C. (2017). Energy balance and obesity: what are the main drivers? *Cancer Causes Control*, *28*, 247–258.

Rosen, E. D., & Spiegelman, B. M. (2014). What we talk about when we talk about fat. *Cell*,

156, 20–44.

Roy, B., & Palaniyandi, S. S. (2021). Tissue-specific role and associated downstream signaling pathways of adiponectin. *Cell Biosci*, *11*, 77.

Ruas, J. L., White, J. P., Rao, R. R., Kleiner, S., Brannan, K. T., Harrison, B. C., Greene, N. P., Wu, J., Estall, J. L., Irving, B. A., Lanza, I. R., Rasbach, K. A., Okutsu, M., Nair, K. S., Yan, Z., Leinwand, L. A., & Spiegelman, B. M. (2012). A PGC-1alpha isoform induced by resistance training regulates skeletal muscle hypertrophy. *Cell*, *151*, 1319–1331.

Rubin, J. B., Lagas, J. S., Broestl, L., Sponagel, J., Rockwell, N., Rhee, G., Rosen, S. F., Chen, S., Klein, R. S., Imoukhuede, P., & Luo, J. (2020). Sex differences in cancer mechanisms. *Biol Sex Differ*, *11*, 17.

Rutkowski, J. M., Wang, Z. V, Park, A. S., Zhang, J., Zhang, D., Hu, M. C., Moe, O. W., Susztak, K., & Scherer, P. E. (2013). Adiponectin promotes functional recovery after podocyte ablation. *J Am Soc Nephrol*, *24*, 268–282.

Sabapathy, K., Jochum, W., Hochedlinger, K., Chang, L., Karin, M., & Wagner, E. F. (1999). Defective neural tube morphogenesis and altered apoptosis in the absence of both JNK1 and JNK2. *Mech Dev*, *89*, 115–124.

Sabio, G., Arthur, J. S., Kuma, Y., Peggie, M., Carr, J., Murray-Tait, V., Centeno, F., Goedert, M., Morrice, N. A., & Cuenda, A. (2005). p38gamma regulates the localisation of SAP97 in the cytoskeleton by modulating its interaction with GKAP. *EMBO J*, *24*, 1134–1145.

Sabio, G., Cavanagh-Kyros, J., Barrett, T., Jung, D. Y., Ko, H. J., Ong, H., Morel, C., Mora, A., Reilly, J., Kim, J. K., & Davis, R. J. (2010a). Role of the hypothalamic-pituitary-thyroid axis in metabolic regulation by JNK1. *Genes Dev*, *24*, 256–264.

Sabio, G., Das, M., Mora, A., Zhang, Z., Jun, J. Y., Ko, H. J., Barrett, T., Kim, J. K., & Davis, R. J. (2008). A stress signaling pathway in adipose tissue regulates hepatic insulin resistance. *Science*, *322*, 1539–1543.

Sabio, G., & Davis, R. J. (2010). cJun NH2-terminal kinase 1 (JNK1): roles in metabolic regulation of insulin resistance. *Trends Biochem Sci*, *35*, 490–496.

Sabio, G., & Davis, R. J. (2014). TNF and MAP kinase signalling pathways. *Semin Immunol*, *26*, 237–245.

Sabio, G., Kennedy, N. J., Cavanagh-Kyros, J., Jung, D. Y., Ko, H. J., Ong, H., Barrett, T., Kim, J. K., & Davis, R. J. (2010b). Role of muscle c-Jun NH2-terminal kinase 1 in obesity-induced insulin resistance. *Mol Cell Biol*, *30*, 106–115.

Sabio, G., Reuver, S., Feijoo, C., Hasegawa, M., Thomas, G. M., Centeno, F., Kuhlendahl, S.,

Leal-Ortiz, S., Goedert, M., Garner, C., & Cuenda, A. (2004). Stress- and mitogen-induced phosphorylation of the synapse-associated protein SAP90/PSD-95 by activation of SAPK3/p38gamma and ERK1/ERK2. *Biochem J*, *380*, 19–30.

Sabio, G., Cavanagh-Kyros, J., Ko, H. J., Jung, D. Y., Gray, S., Jun, J. Y., Barrett, T., Mora, A., Kim, J. K., & Davis, R. J. (2009). Prevention of steatosis by hepatic JNK1. *Cell Metab*, *10*, 491-498.

Saito, M., Okamatsu-Ogura, Y., Matsushita, M., Watanabe, K., Yoneshiro, T., Nio-Kobayashi, J., Iwanaga, T., Miyagawa, M., Kameya, T., Nakada, K., Kawai, Y., & Tsujisaki, M. (2009). High incidence of metabolically active brown adipose tissue in healthy adult humans: effects of cold exposure and adiposity. *Diabetes*, *58*, 1526–1531.

Sakurai, T., He, G., Matsuzawa, A., Yu, G. Y., Maeda, S., Hardiman, G., & Karin, M. (2008). Hepatocyte necrosis induced by oxidative stress and IL-1 alpha release mediate carcinogen-induced compensatory proliferation and liver tumorigenesis. *Cancer Cell*, *14*, 156–165.

Sakurai, T., Kudo, M., Umemura, A., He, G., Elsharkawy, A. M., Seki, E., & Karin, M. (2013). p38alpha inhibits liver fibrogenesis and consequent hepatocarcinogenesis by curtailing accumulation of reactive oxygen species. *Cancer Res*, *73*, 215–224.

Salguero Palacios, R., Roderfeld, M., Hemmann, S., Rath, T., Atanasova, S., Tschuschner, A., Gressner, O. A., Weiskirchen, R., Graf, J., & Roeb, E. (2008). Activation of hepatic stellate cells is associated with cytokine expression in thioacetamide-induced hepatic fibrosis in mice. *Lab Invest*, *88*, 1192–1203.

Salvador, J. M., Mittelstadt, P. R., Guszczynski, T., Copeland, T. D., Yamaguchi, H., Appella, E., Fornace Jr., A. J., & Ashwell, J. D. (2005). Alternative p38 activation pathway mediated by T cell receptor-proximal tyrosine kinases. *Nat Immunol*, *6*, 390–395.

Santos, F. R., Diamond-Stanic, M. K., Prasannarong, M., & Henriksen, E. J. (2012). Contribution of the serine kinase c-Jun N-terminal kinase (JNK) to oxidant-induced insulin resistance in isolated rat skeletal muscle. *Arch Physiol Biochem*, *118*, 231–236.

Sarbassov, D. D., Guertin, D. A., Ali, S. M., & Sabatini, D. M. (2005). Phosphorylation and regulation of Akt/PKB by the rictor-mTOR complex. *Science*, *307*, 1098–1101.

Saxena, N. K., Fu, P. P., Nagalingam, A., Wang, J., Handy, J., Cohen, C., Tighiouart, M., Sharma, D., & Anania, F. A. (2010). Adiponectin modulates C-jun N-terminal kinase and mammalian target of rapamycin and inhibits hepatocellular carcinoma. *Gastroenterology*, *139*, 1762–1773.

Schattenberg, J. M., Singh, R., Wang, Y., Lefkowitch, J. H., Rigoli, R. M., Scherer, P. E., & Czaja, M. J. (2006). JNK1 but not JNK2 promotes the development of steatohepatitis in mice. *Hepatology*, *43*, 163–172.

Scheja, L., & Heeren, J. (2019). The endocrine function of adipose tissues in health and cardiometabolic disease. *Nat Rev Endocrinol*, *15*, 507–524.

Scherer, P. E., Williams, S., Fogliano, M., Baldini, G., & Lodish, H. F. (1995). A novel serum protein similar to C1q, produced exclusively in adipocytes. *J Biol Chem*, *270*, 26746–26749.

Schiaffino, S., & Reggiani, C. (2011). Fiber types in mammalian skeletal muscles. *Physiol Rev*, *91*, 1447–1531.

Schraw, T., Wang, Z. V., Halberg, N., Hawkins, M., & Scherer, P. E. (2008). Plasma adiponectin complexes have distinct biochemical characteristics. *Endocrinology*, 149, 2270–2282.

Sharma, D., Wang, J., Fu, P. P., Sharma, S., Nagalingam, A., Mells, J., Handy, J., Page, A. J., Cohen, C., Anania, F. A., & Saxena, N. K. (2010). Adiponectin antagonizes the oncogenic actions of leptin in hepatocellular carcinogenesis. *Hepatology*, *52*, 1713–1722.

Shibata, R., Sato, K., Pimentel, D. R., Takemura, Y., Kihara, S., Ohashi, K., Funahashi, T., Ouchi, N., & Walsh, K. (2005). Adiponectin protects against myocardial ischemia-reperfusion injury through AMPK- and COX-2-dependent mechanisms. *Nat Med*, *11*, 1096–1103.

Shimizu, A., Takamura, T., Matsuzawa, N., Nakamura, S., Nabemoto, S., Takeshita, Y., Misu, H., Kurita, S., Sakurai, M., Yokoyama, M., Zen, Y., Sasaki, M., Nakanuma, Y., & Kaneko, S. (2007). Regulation of adiponectin receptor expression in human liver and a hepatocyte cell line. *Metabolism*, *56*, 1478–1485.

Shu, R. Z., Zhang, F., Wang, F., Feng, D. C., Li, X. H., Ren, W. H., Wu, X. L., Yang, X., Liao, X. D., Huang, L., & Wang, Z. G. (2009). Adiponectin deficiency impairs liver regeneration through attenuating STAT3 phosphorylation in mice. *Lab Invest*, *89*, 1043–1052.

Sieminska, L., Wojciechowska, C., Niedziolka, D., Marek, B., Kos-Kudla, B., Kajdaniuk, D., & Nowak, M. (2005). Effect of postmenopause and hormone replacement therapy on serum adiponectin levels. *Metabolism*, *54*, 1610–1614.

Singh, R., Wang, Y., Xiang, Y., Tanaka, K. E., Gaarde, W. A., & Czaja, M. J. (2009). Differential effects of JNK1 and JNK2 inhibition on murine steatohepatitis and insulin resistance. *Hepatology*, *49*, 87–96.

Somwar, R., Koterski, S., Sweeney, G., Sciotti, R., Djuric, S., Berg, C., Trevillyan, J., Scherer, P. E., Rondinone, C. M., & Klip, A. (2002). A dominant-negative p38 MAPK mutant and novel selective inhibitors of p38 MAPK reduce insulin-stimulated glucose uptake in 3T3-L1 adipocytes without affecting GLUT4 translocation. *J Biol Chem*, *277*, 50386–50395.

Speakman, J. R. (2004). Obesity: the integrated roles of environment and genetics. *J Nutr*, *134*, 2090S-2105S.

Speakman, J. R. (2013). Evolutionary perspectives on the obesity epidemic: adaptive, maladaptive, and neutral viewpoints. *Annu Rev Nutr*, *33*, 289–317.

Springer, M. L., Rando, T. A., & Blau, H. M. (2002). Gene delivery to muscle. *Curr Protoc Hum Genet*, *Chapter 13*, 13.4.1-13.4.19.

Spyridopoulos, T. N., Petridou, E. T., Skalkidou, A., Dessypris, N., Chrousos, G. P., Mantzoros, C. S., Obesity, & Cancer Oncology Group. (2007). Low adiponectin levels are associated with renal cell carcinoma: a case-control study. *Int J Cancer*, *120*, 1573–1578.

Starley, B. Q., Calcagno, C. J., & Harrison, S. A. (2010). Nonalcoholic fatty liver disease and hepatocellular carcinoma: a weighty connection. *Hepatology*, *51*, 1820–1832.

Stefan, N., Birkenfeld, A. L., Schulze, M. B., & Ludwig, D. S. (2020). Obesity and impaired metabolic health in patients with COVID-19. *Nat Rev Endocrinol*, *16*, 341–342.

Stefanoska, K., Bertz, J., Volkerling, A. M., van der Hoven, J., Ittner, L. M., & Ittner, A. (2018). Neuronal MAP kinase p38alpha inhibits c-Jun N-terminal kinase to modulate anxiety-related behaviour. *Sci Rep*, *8*, 14296.

Straub, L. G., & Scherer, P. E. (2019). Metabolic messengers: adiponectin. *Nat Metab*, *1*, 334–339.

Subramanian, A., Tamayo, P., Mootha, V. K., Mukherjee, S., Ebert, B. L., Gillette, M. A., Paulovich, A., Pomeroy, S. L., Golub, T. R., Lander, E. S., & Mesirov, J. P. (2005). Gene set enrichment analysis: a knowledge-based approach for interpreting genome-wide expression profiles. *Proc Natl Acad Sci U S A*, *102*, 15545–15550.

Sumara, G., Formentini, I., Collins, S., Sumara, I., Windak, R., Bodenmiller, B., Ramracheya, R., Caille, D., Jiang, H., Platt, K. A., Meda, P., Aebersold, R., Rorsman, P., & Ricci, R. (2009). Regulation of PKD by the MAPK p38delta in insulin secretion and glucose homeostasis. *Cell*, *136*, 235–248.

Sun, H., & Liu, D. (2015). Hydrodynamic delivery of interleukin 15 gene promotes resistance to high fat diet-induced obesity, fatty liver and improves glucose homeostasis. *Gene Ther*, *22*, 341–347.

Sun, H., Ma, Y., Gao, M., & Liu, D. (2016). IL-15/sIL-15Ralpha gene transfer induces weight loss and improves glucose homeostasis in obese mice. *Gene Ther*, *23*, 349–356.

Sung, H., Ferlay, J., Siegel, R. L., Laversanne, M., Soerjomataram, I., Jemal, A., & Bray, F. (2021). Global Cancer Statistics 2020: GLOBOCAN estimates of incidence and mortality worldwide for 36 cancers in 185 countries. *CA Cancer J Clin*, *71*, 209–249.

Takahashi, K., Yamaguchi, S., Shimoyama, T., Seki, H., Miyokawa, K., Katsuta, H., Tanaka, T., Yoshimoto, K., Ohno, H., Nagamatsu, S., & Ishida, H. (2008). JNK- and IkappaB-dependent pathways regulate MCP-1 but not adiponectin release from artificially hypertrophied 3T3-L1 adipocytes preloaded with palmitate in vitro. *Am J Physiol Endocrinol Metab*, *294*, E898-909.

Tamura, Y., Watanabe, K., Kantani, T., Hayashi, J., Ishida, N., & Kaneki, M. (2011). Upregulation of circulating IL-15 by treadmill running in healthy individuals: is IL-15 an endocrine mediator of the beneficial effects of endurance exercise? *Endocr J*, *58*, 211–215.

Tan, Y., Rouse, J., Zhang, A., Cariati, S., Cohen, P., & Comb, M. J. (1996). FGF and stress regulate CREB and ATF-1 via a pathway involving p38 MAP kinase and MAPKAP kinase-2. *EMBO J*, *15*, 4629–4642.

Tang, P., Low, H. B., Png, C. W., Torta, F., Kumar, J. K., Lim, H. Y., Zhou, Y., Yang, H., Angeli, V., Shabbir, A., Tai, E. S., Flavell, R. A., Dong, C., Wenk, M. R., Yang, D. Y., & Zhang, Y. (2019). Protective function of mitogen-activated protein kinase phosphatase 5 in aging- and diet-induced hepatic steatosis and steatohepatitis. *Hepatol Commun*, *3*, 748–762.

Terada, S., & Tabata, I. (2004). Effects of acute bouts of running and swimming exercise on PGC-1alpha protein expression in rat epitrochlearis and soleus muscle. *Am J Physiol Endocrinol Metab*, *286*, E208-16.

Thakur, V., Pritchard, M. T., McMullen, M. R., & Nagy, L. E. (2006). Adiponectin normalizes LPS-stimulated TNF-alpha production by rat Kupffer cells after chronic ethanol feeding. *Am J Physiol Gastrointest Liver Physiol*, *290*, G998-1007.

Tomás-Loba, A., Manieri, E., González-Terán, B., Mora, A., Leiva-Vega, L., Santamans, A. M., Romero-Becerra, R., Rodríguez, E., Pintor-Chocano, A., Feixas, F., López, J. A., Caballero, B., Trakala, M., Blanco, O., Torres, J. L., Hernández-Cosido, L., Montalvo-Romeral, V., Matesanz, N., Roche-Molina, M., Bernal, J. A., Mischo, H., León, M., Caballero, A., Miranda-Saavedra, D., Ruiz-Cabello, J., Nevzorova, Y. A., Cubero, F. J., Bravo, J., Vázquez, J., Malumbres, M., Marcos, M., Osuna, S, & Sabio, G. (2019). p38gamma is essential for cell cycle progression and liver tumorigenesis. *Nature*, *568*,

557–560.

Tomita, K., Oike, Y., Teratani, T., Taguchi, T., Noguchi, M., Suzuki, T., Mizutani, A., Yokoyama, H., Irie, R., Sumimoto, H., Takayanagi, A., Miyashita, K., Akao, M., Tabata, M., Tamiya, G., Ohkura, T., & Hibi, T. (2008). Hepatic AdipoR2 signaling plays a protective role against progression of nonalcoholic steatohepatitis in mice. *Hepatology*, *48*, 458–473.

Tramunt, B., Smati, S., Grandgeorge, N., Lenfant, F., Arnal, J. F., Montagner, A., & Gourdy, P. (2020). Sex differences in metabolic regulation and diabetes susceptibility. *Diabetologia*, *63*, 453–461.

Tuncman, G., Hirosumi, J., Solinas, G., Chang, L., Karin, M., & Hotamisligil, G. S. (2006). Functional in vivo interactions between JNK1 and JNK2 isoforms in obesity and insulin resistance. *Proc Natl Acad Sci U S A*, *103*, 10741–10746.

Upadhyay, J., Farr, O., Perakakis, N., Ghaly, W., & Mantzoros, C. (2018). Obesity as a Disease. *Med Clin North Am*, *102*, 13–33.

Urso, K., Alfranca, A., Martínez-Martínez, S., Escolano, A., Ortega, I., Rodríguez, A., & Redondo, J. M. (2011). NFATc3 regulates the transcription of genes involved in T-cell activation and angiogenesis. *Blood*, *118*(3), 795–803.

van Hall, G., Steensberg, A., Sacchetti, M., Fischer, C., Keller, C., Schjerling, P., Hiscock, N., Moller, K., Saltin, B., Febbraio, M. A., & Pedersen, B. K. (2003). Interleukin-6 stimulates lipolysis and fat oxidation in humans. *J Clin Endocrinol Metab*, *88*, 3005–3010.

van Marken Lichtenbelt, W. D., Vanhommerig, J. W., Smulders, N. M., Drossaerts, J. M., Kemerink, G. J., Bouvy, N. D., Schrauwen, P., & Teule, G. J. (2009). Cold-activated brown adipose tissue in healthy men. *N Engl J Med*, *360*, 1500–1508.

Vanni, E., & Bugianesi, E. (2014). Obesity and liver cancer. *Clin Liver Dis*, *18*, 191–203.

Ventura, J. J., Tenbaum, S., Perdiguero, E., Huth, M., Guerra, C., Barbacid, M., Pasparakis, M., & Nebreda, A. R. (2007). p38alpha MAP kinase is essential in lung stem and progenitor cell proliferation and differentiation. *Nat Genet*, *39*, 750–758.

Vernia, S, Cavanagh-Kyros, J., Garcia-Haro, L., Sabio, G., Barrett, T., Jung, D. Y., Kim, J. K., Xu, J., Shulha, H. P., Garber, M., Gao, G., & Davis, R. J. (2014). The PPARalpha-FGF21 hormone axis contributes to metabolic regulation by the hepatic JNK signaling pathway. *Cell Metab*, *20*, 512–525.

Vernia, S., Edwards, Y. J., Han, M. S., Cavanagh-Kyros, J., Barrett, T., Kim, J. K., & Davis, R. J. (2016a). An alternative splicing program promotes adipose tissue thermogenesis. *Elife*, *5*, e17672.

Vernia, S., Morel, C., Madara, J. C., Cavanagh-Kyros, J., Barrett, T., Chase, K., Kennedy, N. J., Jung, D. Y., Kim, J. K., Aronin, N., Flavell, R. A., Lowell, B. B., & Davis, R. J. (2016b). Excitatory transmission onto AgRP neurons is regulated by cJun NH2-terminal kinase 3 in response to metabolic stress. *Elife*, *5*, e10031.

Vernia, S., Cavanagh-Kyros, J., Barrett, T., Tournier, C., & Davis, R. J. (2016c). Fibroblast growth factor 21 mediates glycemic regulation by hepatic JNK. *Cell Rep*, *14*, 2273-2280.

Verzola, D., Villaggio, B., Procopio, V., Gandolfo, M. T., Gianiorio, F., Fama, A., Tosetti, F., Traverso, P., Deferrari, G., & Garibotto, G. (2009). Androgen-mediated apoptosis of kidney tubule cells: role of c-Jun amino terminal kinase. *Biochem Biophys Res Commun*, *387*, 531–536.

Vitos-Faleato, J., Real, S. M., Gutierrez-Prat, N., Villanueva, A., Llonch, E., Drosten, M., Barbacid, M., & Nebreda, A. R. (2020). Requirement for epithelial p38alpha in KRAS-driven lung tumor progression. *Proc Natl Acad Sci U S A*, *117*, 2588–2596.

Wall, J. A., Wei, J., Ly, M., Belmont, P., Martindale, J. J., Tran, D., Sun, J., Chen, W. J., Yu, W., Oeller, P., Briggs, S., Gustafsson, A. B., Sayen, M. R., Gottlieb, R. A., & Glembotski, C. C. (2006). Alterations in oxidative phosphorylation complex proteins in the hearts of transgenic mice that overexpress the p38 MAP kinase activator, MAP kinase kinase 6. *Am J Physiol Heart Circ Physiol*, *291*, H2462-72.

Wang, F., Qi, X. M., Wertz, R., Mortensen, M., Hagen, C., Evans, J., Sheinin, Y., James, M., Liu, P., Tsai, S., Thomas, J., Mackinnon, A., Dwinell, M., Myers, C. R., Bartrons Bach, R., Fu, L., & Chen, G. (2020). p38gamma MAPK is essential for aerobic glycolysis and pancreatic tumorigenesis. *Cancer Res*, *80*, 3251–3264.

Wang, Z. V, & Scherer, P. E. (2016). Adiponectin, the past two decades. *J Mol Cell Biol*, *8*, 93–100.

Wang, Z. V, Schraw, T. D., Kim, J. Y., Khan, T., Rajala, M. W., Follenzi, A., & Scherer, P. E. (2007). Secretion of the adipocyte-specific secretory protein adiponectin critically depends on thiol-mediated protein retention. *Mol Cell Biol*, *27*, 3716–3731.

Wang, X. Z., & Ron, D. (1996). Stress-induced phosphorylation and activation of the transcription factor CHOP (GADD153) by p38 MAP Kinase. *Science*, *272*, 1347–1349.

Wei, E. K., Giovannucci, E., Fuchs, C. S., Willett, W. C., & Mantzoros, C. S. (2005). Low plasma adiponectin levels and risk of colorectal cancer in men: a prospective study. *J Natl Cancer Inst*, *97*, 1688–1694.

Wellen, K. E., & Hotamisligil, G. S. (2005). Inflammation, stress, and diabetes. *J Clin Invest*,

115, 1111–1119.

Westerterp, K. R. (2010). Physical activity, food intake, and body weight regulation: insights from doubly labeled water studies. *Nutr Rev*, *68*, 148–154.

Westerterp, K. R. (2017). Control of energy expenditure in humans. *Eur J Clin Nutr*, *71*, 340–344.

White, M. F. (2002). IRS proteins and the common path to diabetes. *Am J Physiol Endocrinol Metab*, *283*, E413-22.

Whitham, M., Chan, M. H., Pal, M., Matthews, V. B., Prelovsek, O., Lunke, S., El-Osta, A., Broenneke, H., Alber, J., Bruning, J. C., Wunderlich, F. T., Lancaster, G. I., & Febbraio, M. A. (2012). Contraction-induced interleukin-6 gene transcription in skeletal muscle is regulated by c-Jun terminal kinase/activator protein-1. *J Biol Chem*, *287*, 10771–10779.

Whitham, M., & Febbraio, M. A. (2016). The ever-expanding myokinome: discovery challenges and therapeutic implications. *Nat Rev Drug Discov*, *15*, 719–729.

Wilkenfeld, S. R., Lin, C., & Frigo, D. E. (2018). Communication between genomic and non-genomic signaling events coordinate steroid hormone actions. *Steroids*, *133*, 2–7.

World Health Organization (WHO). (2020, April 1). Obesity and overweight. https://www.who.int/news-room/fact-sheets/detail/obesity-and-overweight

Wu, X., He, Y., Hsuchou, H., Kastin, A. J., Rood, J. C., & Pan, W. (2010). Essential role of interleukin-15 receptor in normal anxiety behavior. *Brain Behav Immun*, *24*, 1340–1346.

Wu, X., Hsuchou, H., Kastin, A. J., He, Y., Khan, R. S., Stone, K. P., Cash, M. S., & Pan, W. (2011). Interleukin-15 affects serotonin system and exerts antidepressive effects through IL15Ralpha receptor. *Psychoneuroendocrinology*, *36*, 266–278.

Wu, Y., Song, P., Zhang, W., Liu, J., Dai, X., Liu, Z., Lu, Q., Ouyang, C., Xie, Z., Zhao, Z., Zhuo, X., Viollet, B., Foretz, M., Wu, J., Yuan, Z., & Zou, M. H. (2015). Activation of AMPKalpha2 in adipocytes is essential for nicotine-induced insulin resistance in vivo. *Nat Med*, *21*, 373–382.

Xiong, Y., Collins, Q. F., An, J., Lupo Jr., E., Liu, H. Y., Liu, D., Robidoux, J., Liu, Z., & Cao, W. (2007). p38 mitogen-activated protein kinase plays an inhibitory role in hepatic lipogenesis. *J Biol Chem*, *282*, 4975–4982.

Xu, A., Chan, K. W., Hoo, R. L., Wang, Y., Tan, K. C., Zhang, J., Chen, B., Lam, M. C., Tse, C., Cooper, G. J., & Lam, K. S. (2005). Testosterone selectively reduces the high molecular weight form of adiponectin by inhibiting its secretion from adipocytes. *J Biol Chem*, *280*, 18073–18080.

Xu, L., Chen, S., & Bergan, R. C. (2006). MAPKAPK2 and HSP27 are downstream effectors of p38 MAP kinase-mediated matrix metalloproteinase type 2 activation and cell invasion in human prostate cancer. *Oncogene*, *25*, 2987–2998.

Yamauchi, T., Kamon, J., Ito, Y., Tsuchida, A., Yokomizo, T., Kita, S., Sugiyama, T., Miyagishi, M., Hara, K., Tsunoda, M., Murakami, K., Ohteki, T., Uchida, S., Takekawa, S., Waki, H., Tsuno, N. H., Shibata, Y., Terauchi, Y., Froguel, P., Tobe, K., Koyasu, S., Taira, K., Kitamura, T., Shimizu, T., Nagai, R., & Kadowaki, T. (2003). Cloning of adiponectin receptors that mediate antidiabetic metabolic effects. *Nature*, *423*, 762–769.

Yamauchi, T., Kamon, J., Minokoshi, Y., Ito, Y., Waki, H., Uchida, S., Yamashita, S., Noda, M., Kita, S., Ueki, K., Eto, K., Akanuma, Y., Froguel, P., Foufelle, F., Ferre, P., Carling, D., Kimura, S., Nagai, R., Kahn, B. B., & Kadowaki, T. (2002). Adiponectin stimulates glucose utilization and fatty-acid oxidation by activating AMP-activated protein kinase. *Nat Med*, *8*, 1288–1295.

Yamauchi, T., Kamon, J., Waki, H., Terauchi, Y., Kubota, N., Hara, K., Mori, Y., Ide, T., Murakami, K., Tsuboyama-Kasaoka, N., Ezaki, O., Akanuma, Y., Gavrilova, O., Vinson, C., Reitman, M. L., Kagechika, H., Shudo, K., Yoda, M., Nakano, Y., Tobe, K., Nagai, R., Kimura, S., Tomita, M., Froguel, P., & Kadowaki, T. (2001). The fat-derived hormone adiponectin reverses insulin resistance associated with both lipoatrophy and obesity. *Nat Med*, *7*, 941–946.

Yamauchi, T., Nio, Y., Maki, T., Kobayashi, M., Takazawa, T., Iwabu, M., Okada-Iwabu, M., Kawamoto, S., Kubota, N., Kubota, T., Ito, Y., Kamon, J., Tsuchida, A., Kumagai, K., Kozono, H., Hada, Y., Ogata, H., Tokuyama, K., Tsunoda, M., Ide, T., Murakami, K., Awazawa, M., Takamoto, I., Froguel, P., Hara, K., Tobe, K., Nagai, R., Ueki, K., & Kadowaki, T. (2007). Targeted disruption of AdipoR1 and AdipoR2 causes abrogation of adiponectin binding and metabolic actions. *Nat Med*, *13*, 332–339.

Yang, D. D., Conze, D., Whitmarsh, A. J., Barrett, T., Davis, R. J., Rincon, M., & Flavell, R. A. (1998). Differentiation of CD4+ T cells to Th1 cells requires MAP kinase JNK2. *Immunity*, *9*, 575–585.

Yang, D. D., Kuan, C. Y., Whitmarsh, A. J., Rincon, M., Zheng, T. S., Davis, R. J., Rakic, P., & Flavell, R. A. (1997). Absence of excitotoxicity-induced apoptosis in the hippocampus of mice lacking the Jnk3 gene. *Nature*, *389*, 865–870.

Yang, J., Hu, J., & Zhu, C. (2021). Obesity aggravates COVID-19: a systematic review and meta-analysis. *J Med Virol*, *93*, 257–261.

Yang, M., Wei, D., Mo, C., Zhang, J., Wang, X., Han, X., Wang, Z., & Xiao, H. (2013). Saturated

fatty acid palmitate-induced insulin resistance is accompanied with myotube loss and the impaired expression of health benefit myokine genes in C2C12 myotubes. *Lipids Health Dis*, *12*, 104.

Yang, R., Wilcox, D. M., Haasch, D. L., Jung, P. M., Nguyen, P. T., Voorbach, M. J., Doktor, S., Brodjian, S., Bush, E. N., Lin, E., Jacobson, P. B., Collins, C. A., Landschulz, K. T., Trevillyan, J. M., Rondinone, C. M., & Surowy, T. K. (2007). Liver-specific knockdown of JNK1 up-regulates proliferator-activated receptor gamma coactivator 1 beta and increases plasma triglyceride despite reduced glucose and insulin levels in diet-induced obese mice. *J Biol Chem*, *282*, 22765–22774.

Yang, S. H., Galanis, A., & Sharrocks, A. D. (1999). Targeting of p38 mitogen-activated protein kinases to MEF2 transcription factors. *Mol Cell Biol*, *19*, 4028–4038.

Yang, S. H., Whitmarsh, A. J., Davis, R. J., & Sharrocks, A. D. (1998). Differential targeting of MAP kinases to the ETS-domain transcription factor Elk-1. *EMBO J*, *17*, 1740–1749.

Yannakoulia, M., Yiannakouris, N., Bluher, S., Matalas, A. L., Klimis-Zacas, D., & Mantzoros, C. S. (2003). Body fat mass and macronutrient intake in relation to circulating soluble leptin receptor, free leptin index, adiponectin, and resistin concentrations in healthy humans. *J Clin Endocrinol Metab*, *88*, 1730–1736.

Yu, M., Blomstrand, E., Chibalin, A. V, Krook, A., & Zierath, J. R. (2001). Marathon running increases ERK1/2 and p38 MAP kinase signalling to downstream targets in human skeletal muscle. *J Physiol*, *536*, 273–282.

Yu, M., Fu, Y., Liang, Y., Song, H., Yao, Y., Wu, P., Yao, Y., Pan, Y., Wen, X., Ma, L., Hexige, S., Ding, Y., Luo, S., & Lu, B. (2017). Suppression of MAPK11 or HIPK3 reduces mutant Huntingtin levels in Huntington's disease models. *Cell Res*, *27*, 1441–1465.

Yu, M., Stepto, N. K., Chibalin, A. V, Fryer, L. G., Carling, D., Krook, A., Hawley, J. A., & Zierath, J. R. (2003). Metabolic and mitogenic signal transduction in human skeletal muscle after intense cycling exercise. *J Physiol*, *546*, 327–335.

Zhang, S., Weinheimer, C., Courtois, M., Kovacs, A., Zhang, C. E., Cheng, A. M., Wang, Y., & Muslin, A. J. (2003). The role of the Grb2-p38 MAPK signaling pathway in cardiac hypertrophy and fibrosis. *J Clin Invest*, *111*, 833–841.

Zhang, X., Deng, H., & Wang, Z. Y. (2014). Estrogen activation of the mitogen-activated protein kinase is mediated by ER-alpha36 in ER-positive breast cancer cells. *J Steroid Biochem Mol Biol*, *143*, 434–443.

Zhang, X., Fan, L., Wu, J., Xu, H., Leung, W. Y., Fu, K., Wu, J., Liu, K., Man, K., Yang, X.,

Han, J., Ren, J., & Yu, J. (2019). Macrophage p38alpha promotes nutritional steatohepatitis through M1 polarization. *J Hepatol*, *71*, 163–174.

Zhang, X., Xu, A., Chung, S. K., Cresser, J. H., Sweeney, G., Wong, R. L., Lin, A., & Lam, K. S. (2011). Selective inactivation of c-Jun NH2-terminal kinase in adipose tissue protects against diet-induced obesity and improves insulin sensitivity in both liver and skeletal muscle in mice. *Diabetes*, *60*, 486–495.

Zhang, Y., Bellows, C. F., & Kolonin, M. G. (2010). Adipose tissue-derived progenitor cells and cancer. *World J Stem Cells*, *2*, 103–113.

Zhao, G., Hatting, M., Nevzorova, Y. A., Peng, J., Hu, W., Boekschoten, M. V, Roskams, T., Muller, M., Gassler, N., Liedtke, C., Davis, R. J., Cubero, F. J., & Trautwein, C. (2014). Jnk1 in murine hepatic stellate cells is a crucial mediator of liver fibrogenesis. *Gut*, *63*, 1159–1172.

Zhao, S., Kusminski, C. M., Elmquist, J. K., & Scherer, P. E. (2020). Leptin: less is more. *Diabetes*, *69*, 823–829.

Zur, R., Garcia-Ibanez, L., Nunez-Buiza, A., Aparicio, N., Liappas, G., Escós, A., Risco, A., Page, A., Saiz-Ladera, C., Alsina-Beauchamp, D., Montans, J., Paramio, J. M., & Cuenda, A. (2015). Combined deletion of p38gamma and p38delta reduces skin inflammation and protects from carcinogenesis. *Oncotarget*, *6*, 12920–12935.

APPENDICES

APPENDIX I: Supplementary material

Gene/protein sets used for gene set enrichment analysis

Table S1. PGC1α muscle gene set

Gene set name: PGC1α muscle gene set.

Inclusion criteria: genes upregulated > 2-fold in gastrocnemius muscle of MCK-PGC1α transgenic mouse (Lin et al., 2002).

Included genes:

BC049352	VAV2	FAM69B	LIMD2	ATP5F1	SP140
TMPRSS4	PANK1	EPHX2	LRMP	ETFA	ACOT2
CHST8	CD53	DNAJC6	NDUFB6	NAB1	6820408C15RIK
CDS1	TSTD3	NDUFAB1	GPR65	COX7B	KBTBD11
MAP3K9	NUDT7	FAM195A	1110058L19RIK	ITGB2	ATP5E
SLC24A1	2310039L15RIK	GNB5	COX6C	CIITA	MYBPH
RGS9BP	IRAK4	TNFAIP2	GLIPR1	CYBB	MTX2
HSBP1L1	GOT1	UQCRQ	CD48	2410015M20RIK	SUCLG1
TM6SF1	LOC100503676	NDUFA4	KCTD1	ENDOG	GLRX5
PPARGC1A	COL24A1	GNG2	AI450353	RND3	LPXN
SH2D4A	FADS6	COX5A	SLC15A5	HYAL1	HEMK1
SRRM4	DLAT	PYHIN1	CRLF3	PLIN5	PCNXL2
APOL8	SERPINB1A	HCCS	KLHDC8A	CASQ2	HELT
P2RY1	CTSS	BLNK	43160	POC1A	PMAIP1
KCNK1	RAP1GAP2	LYZ2	PIK3CG	RETSAT	CACNB3
SNPH	IDNK	WNT11	RSAD1	ACOT13	ARHGAP4
PAQR4	MPPE1	TNFSF10	OSBPL1A	GM166	HIBCH
AI118078	MSRB2	SLC16A1	FZD5	FUOM	CXCR4
MFSD4	RGL3	FAM196B	CTSF	CDK18	CASC1
ESRRB	H2-AA	2310016D03RIK	NDUFB10	MRPL12	TLR3
ADIG	PLCE1	LACC1	NACAD	DPYD	THEM4
CIDEA	RBPMS2	TES	ICAM4	MRPS35	CEP83OS

VOPP1	CYTIP	CD83	ZFP930	IL21R	MDH2
PLBD1	ITGAL	COX7C	MAGIX	NDUFB8	LTBP2
NCEH1	DPP6	VAV1	TMSB4X	CD40	PTPRC
IL15	RAVER2	LRG1	NDUFB5	STAP1	SAMSN1
CAR2	PRDX5	CRYBB1	LY86	COX7A1	AKAP17B
BC048679	PFN4	SDHD	ZFP827	C230035I16RIK	FAM210A
SEC14L2	ACAA2	PRDX6	YARS2	RNF128	ECHDC3
2010300C02RIK	ATP5G3	ABHD3	SPN	CAR14	TREML2
GDPD1	ACADL	ADAMTSL5	UQCC1	PPA2	DNAJC28
ARHGAP15	UQCRFS1	CLEC4N	MRM1	NDUFA8	LYZ1
SCO2	MPC2	RALGPS2	UQCRC2	FAHD1	ATP5A1
CCNJL	SOD2	ADCK1	MS4A6B	QRSL1	NDUFC2
CISH	NRG4	BTC	COQ5	SLFN8	TOMM5
IQCG	PTPN18	ROM1	MYO1G	ZDBF2	GUF1
NKX6-3	MTERFD3	MYO5B	HSDL2	CYC1	MB
AK4	CYB561D1	NUDT8	AMIGO3	TCF7	TMEM70
PHYHIP	EPSTI1	TIFA	FAM63B	CCR2	AIG1
GPR162	ACADVL	2010107E04RIK	NTNG2	RANGRF	COQ6
GMNN	SMIM3	NDUFC1	FYB	UQCRC1	MYH1
TMEM184A	TMEM25	GM5420	SMOC1	BC021891	LMO2
CKMT2	UNG	NDUFAF6	ATP5J2	KCNN2	SLC25A5
SYN2	USMG5	LAPTM5	LCP2	NXPE2	ST8SIA4
DCAF12L1	SLC25A20	CD2	EGR3	SUCLA2	TTPA
PDSS1	ALDH5A1	DNASE1L3	MKI67	HCLS1	TRP53I11
GYK	CYCS	TSPAN12	NRTN	AGBL2	SLC27A1
ASPA	ATP1B4	SNN	EFCAB6	GM14403	DAP3
KCNG4	FDX1	XKRX	LACE1	SLC41A1	PTCD2
SOWAHA	RRM2	TLR2	PTPRK	TLR1	CASP6
ARHGAP9	KIT	CMC2	ATP5SL	CD72	PACSIN1
USH1G	43344	MKLN1OS	INPP5D	AGPAT2	DECR1
FNDC5	RMDN1	ATP5G1	1110001J03RIK	DOCK10	ATP5K

SLC25A34	DOCK5	ECHS1	NAPRT1	NDUFV2	NDUFS8
PHYH	H2-EB1	DLD	SLC25A3	NDUFAF1	FAM179A
KCTD8	ZFP750	PFKFB2	ETFB	NUDT17	1810021B22RIK
PPIF	TTC39B	WDFY4	NDUFB9	NCKAP1L	ETHE1
5031414D18RIK	CIAPIN1	VEGFB	SLFN2	TMEM74B	PLCB2
SH3BP1	GOT2	COX4I1	POLN	PM20D2	RTN4IP1
APLN	CD84	TMEM229B	TANGO2	GLRX	NDUFA5
HRH2	SDHB	TLDC1	ESRRA	ETFDH	TSFM
CCBL2	HPDL	GSTK1	SLA	OXCT1	STARD7
TMEM132B	NEURL3	HSPA4L	PTK2B	UNC13C	RCAN2
GRM1	BCL11B	MRPL47	AK3	NDUFV1	
FBXO44	SLC25A13	OSTM1	MRPL45	PDHB	
MDH1	MPEG1	ATP5B	0610040J01RIK	PDHX	
MTFP1	SIRT5	NME1	CMSS1	PGBD1	
FGF9	SIRT3	DLST	NCF1	MCEE	
GCA	ABCB9	ARL4C	NDUFA9	CHMP4C	

Table S2. PGC1α myotubes protein set

Protein set name: PGC1α myotubes protein set.

Inclusion criteria: proteins upregulated > 1.4-fold in myotubes overexpressing PGC1α (Figure R17A).

Included proteins:

PPARGC1A	NUDT19	CSRNP1	PDSS1	ATN1	HCCS
SPP1	NCEH1	FGB	GSKIP	MYCBP	EXT1
HPDL	FUOM	TRAK1	TRPT1	METTL17	PEX19
PCOLCE	WIPF3	GALT	MTPN	RNASET2	RNF149
STARD5	PSAP	SLC20A1	HK1	ALAS1	COA5
SEMA3A	PDK4	ZFP655	CMC2	OXNAD1	MCFD2
RILP	GOT1	POLRMT	ZNF768	RGCC	GK
ESRRA	ADAMTSL5	EIF1AD	COX10	PKN1	GINM1

MYL2	TCN2	PDXK	RND3	LARP1B	ACTR6
ASPA	SDHAF4	ENDOG	DESI1	TMX2	IRAK4
NDRG2	ACACB	FV1	THEM4	S100A13	EIF4EBP1
ATP1B1	PNPLA2	TIMM10B	BC025446	HYKK	LPGAT1
CPT1B	SNN	FBLIM1	TNNC2	MRPL12	MRPS36
UPP1	SYNPO	ATP5G1	FAM104A	MYH6	MBNL1
MUP2	GLRX5	MT1	PRELID3B	COA6	RPGRIP1L
TRAK2	DPH3	COX5A	TIMM13	RGS10	SDHC
CKMT2	PPP3R1	LIFR	MIF4GD	TEF	URM1
COL1A1	PPIF	TALPID3	GPT	MTFR1L	TMOD3
FABP3	CIAPIN1	LUZP1	SCO2	LARP4	COX20
MCRIP2	VAT1L	DLAT	GATC	TXN2	SMPDL3B
SLC37A2	RANGRF	FNTB	CASP6	ADIPOR2	GFM1
SEMA3E	SLC16A1	GRN	CEP68	S100A6	RPLP1
SLC6A17	HSDL2	TRIAP1	MCEE	TMEM106B	MPC2
SMTNL1	TFEB	MPP7	FABP4	ARRB1	ASAP3
GLRX	COX7A1	NDRG3	UOX	EIF1	COA4
SLC12A7	ALDH1B1	COX11	CTNNBIP1	MYH2	NDUFAF3
FDX1	NDRG4	SLC1A5	LBH	BLOC1S2	BSG
NTN1	DPY30	IMPA2	CPLX1	FXN	PRSS23
MYZAP	PPTC7	FN1	RCAN1	SLC27A4	COX17
CTSF	GRSF1	CYR61	FAM234A	CHCHD7	COX5B
TIMM8A1	AKAP1	TNNC1	CD97	BORCS8	FEZ2
LDHB	DHRS11	ERRFI1	TSTD3	EPDR1	KIAA1522
PYURF	MOCS2	UBXN2A	PFKP	S100A4	DYNLRB1
PANK1	LENG1	MITF	GTF2H5	TULP3	TTC39B
ABRA	RNF115	CTSL	IGFBP2	LPIN1	ETHE1
TPM3	USP25	CST3	CALM1	DBI	DUSP6
OSBPL1A	MSRB2	SIRT5	RHOT2	FAHD1	SLC25A26
SERPINF1	SNX21	CAVIN2	KIAA0232	CADM4	PSTK
SEMA3D	NUDT7	TWF2	ALKBH7	CHCHD4	HMGCS1

ATP5J	TIMM10	PCYT1A	FAM13A	COX19	AKAP8
HSBP1	CA2	AG2	ALB	CCPG1	PDE4A
FAM69B	LTBP3	TIMM9	ZC3H10	GRPEL1	TXNDC17
TACC2	CLUH	GATA4	NDUFAB1	ISCA2	HAGH

APPENDIX II: List of publications

Publications derived from this Thesis

Manieri, E.*, **Herrera-Melle, L.***, Mora, A., Tomás-Loba, A., Leiva-Vega, L., Fernández, D. I., Rodríguez, M. E., Morán, L., Hernández-Cosido, L., Torres, J. L., Seoane, L. M., Cubero, F. J., Marcos, M., Sabio, G. (2019). Adiponectin accounts for gender differences in hepatocellular carcinoma incidence. *J Exp Med*, *216*, 1108-1119. *Equal contribution.

Herrera-Melle, L., Crespo, M., Leiva, M., Sabio, G. (2021). Stress-activated kinases signaling pathways in cancer development. *Curr Opin Physiol*, *19*, 22-31.

Herrera-Melle, L., Folgueira, C., López, J. A., Dumesic, P. A., Rodríguez, M. E., Leiva-Vega, L., Beiroa, D., Spiegelman, B. M., Vázquez, J., Mora, A., Sabio, G. Muscle-to-brain communication is controlled by p38 stress kinases. *Paper in preparation.*

Other publications during the doctoral training period

Matesanz, N., Nikolic, I., Leiva, M., Pulgarín-Alfaro, M., Santamans, A. M., Bernardo, E., Mora, A., **Herrera-Melle, L.**, Rodríguez, E., Beiroa, D., Caballero, A., Martín-García, E., Acín-Pérez, R., Hernández-Cosido, L., Leiva-Vega, L., Torres, J. L., Centeno, F., Nebreda, A. R., Enríquez, J. A., Nogueiras, R., Marcos, M., Sabio, G. (2018). p38α blocks brown adipose tissue thermogenesis through p38δ inhibition. *PLoS Biol*, *16*, e2004455.

Published Online: 3 April, 2019 | Supp Info: http://doi.org/10.1084/jem.20181288
Downloaded from jem.rupress.org on April 3, 2019

JEM Journal of Experimental Medicine

ARTICLE

Adiponectin accounts for gender differences in hepatocellular carcinoma incidence

Elisa Manieri[1,2*], Leticia Herrera-Melle[1*], Alfonso Mora[1], Antonia Tomás-Loba[1], Luis Leiva-Vega[1], Delia I. Fernández[1], Elena Rodríguez[1], Laura Morán[3,4], Lourdes Hernández-Cosido[5], Jorge L. Torres[5], Luisa M. Seoane[6,7], Francisco Javier Cubero[3,4], Miguel Marcos[5], and Guadalupe Sabio[1]

Hepatocellular carcinoma (HCC) is the sixth most common cancer type and the fourth leading cause of cancer-related death. This cancer appears with higher incidence in men and during obesity; however, the specific mechanisms underlying this correlation are unknown. Adipose tissue, a key organ in metabolic syndrome, shows evident gender disparities in the production of adipokines. Levels of the important adipokine adiponectin decrease in men during puberty, as well as in the obese state. Here, we show that this decrease in adiponectin levels is responsible for the increased liver cancer risk in males. We found that testosterone activates the protein JNK in mouse and human adipocytes. JNK-mediated inhibition of adiponectin secretion increases liver cancer cell proliferation, since adiponectin protects against liver cancer development through the activation of AMP-activated protein kinase (AMPK) and p38α. This study provides insight into adipose tissue to liver crosstalk and its gender relation during cancer development, having the potential to guide strategies for new cancer therapeutics.

Introduction

Hepatocellular carcinoma (HCC) is the fourth leading cause of cancer-related death (Bray et al., 2018), and its incidence is rising worldwide due to the increased prevalence of obesity (Parkin et al., 2005). Therapeutic options for HCC are limited, and survival after diagnosis is poor. Better preventive, diagnostic, and therapeutic tools are therefore urgently needed, particularly in view of the important contribution of obesity to HCC incidence worldwide (Bakiri and Wagner, 2013). In addition, epidemiological studies have shown a higher incidence of HCC in men than in women (Bosch et al., 2004), a dimorphism also observed in mouse models (Ghebranious and Sell, 1998; Naugler et al., 2007). Adipose tissue is one of the most important players in the adaptation to obesity, through the regulation of fuel metabolism storage, the release of nutrients and, indirectly, the production of circulating adipokines (Havel, 2002). However, this tissue responds differently in males and females, due to the different genetic make-up and differences in the inputs that act on it (Fuente-Martín et al., 2013). The adipokine adiponectin improves hepatic insulin sensitivity and fuel oxidation (Whitehead et al., 2006) and is considered to play a protective role in cancer (Dalamaga et al., 2012). However, its role in HCC is controversial and requires further investigation (Cheung and Cheng, 2016). Circulating adiponectin levels have been reported to show a gender disparity, being higher in females than in males (Yannakoulia et al., 2003). It has been suggested that testosterone might play a role in adiponectin levels, whereas estrogens do not seem to mediate this effect (Nishizawa et al., 2002). Here, we demonstrate that lower adiponectin levels in males account for their higher prevalence of liver cancer. We show that p38α and AMP-activated protein kinase (AMPK) activation in hepatocytes by adiponectin results in a protective effect against tumor growth. Furthermore, we found that testosterone activates JNK in human and mouse adipocytes, and genetic deletion of JNK1 in mouse adipose tissue results in higher adiponectin levels and protection against HCC. Our results unravel a clear crosstalk between sex hormones and adipocytes signaling and physiology, clarifying the mechanism underlying gender disparity in liver cancer development.

[1]Centro Nacional de Investigaciones Cardiovasculares (CNIC), Madrid, Spain; [2]Centro Nacional de Biotecnología, Madrid, Spain; [3]Department of Immunology, Ophthalmology and Otorhinolaryngology, Complutense University School of Medicine, Madrid, Spain; [4]12 de Octubre Health Research Institute, Madrid, Spain; [5]University of Salamanca, University Hospital of Salamanca–Instituto de Investigación Biomédica de Salamanca, Salamanca, Spain; [6]Fisiopatología Endocrina, Instituto de Investigación Sanitaria de Santiago, Hospital Clínico Universitario de Santiago de Compostela Servicio Gallego de Salud, Santiago de Compostela, Spain; [7]Centro de Investigación Biomédica en Red (CIBER), Fisiopatología Obesidad y Nutrición, Instituto Salud Carlos III, Spain.

*E. Manieri and L. Herrera-Melle contributed equally to this paper; Correspondence to Guadalupe Sabio: gsabio@cnic.es; E. Manieri's present address is Dana-Farber Cancer Institute, Boston, MA.

© 2019 Manieri et al. This article is distributed under the terms of an Attribution–Noncommercial–Share Alike–No Mirror Sites license for the first six months after the publication date (see http://www.rupress.org/terms/). After six months it is available under a Creative Commons License (Attribution–Noncommercial–Share Alike 4.0 International license, as described at https://creativecommons.org/licenses/by-nc-sa/4.0/).

Results

Increased levels of adiponectin in females protect against liver cancer

Using a cohort of healthy subjects, we found that adiponectin levels are higher in women compared with men (Fig. 1 a). Quantification of circulating adiponectin in 11–12-wk-old C57BL/6J mice confirmed previous findings, detecting more than twice the level in females than in males (Fig. S1 a). This correlated with the stronger growth of subcutaneously implanted mouse HCC-derived tumor cells in males than in females (Fig. 1 b). In addition, gender differences were HCC-specific, given that growth of subcutaneously injected colon adenocarcinoma-derived tumor cells (Fig. S1 b) or melanoma-derived tumor cells (Fig. S1 c) was not different between males and females. To further study how gender could affect adiponectin levels and, as a consequence, tumor growth, we assessed the effect of castration on blood adiponectin levels. Castrated males presented similar adiponectin levels to those found in females (Fig. 1 c). In line with the important role of adiponectin in gender disparity, castrated males developed smaller tumors in allograft experiments (Fig. 1 d). To determine whether the gender differences in adiponectin production influences tumor growth, we performed allograft experiments in male and female adiponectin KO (*Adipoq*$^{-/-}$) and WT mice. In WT mice, we observed larger tumors in males than in females, whereas *Adipoq*$^{-/-}$ mice showed no gender differences (Fig. 1 e). Adiponectin cellular function is mainly mediated by two transmembrane receptors, known as adiponectin receptors 1 and 2 (AdipoR1/2; Wang and Scherer, 2016). Increased expression of both receptors were found in HCC-derived cells in comparison with colon adenocarcinoma and melanoma cells (Fig. S2 a). In the liver, hepatocytes are the main source of AdipoR2, while AdipoR1 is expressed in hepatocytes, Kupffer cells (KCs), and endothelial cells (ECs; Fig. S2 b). In addition, hepatocytes increase the expression of both receptors when they become tumoral (Fig. S2 c).

To evaluate the importance of these receptors in the protection observed in females, we used shRNAs against them in Hep53.4 cells and performed an allograft experiment in females (Fig. S2 d). Only depletion of AdipoR2 was sufficient to block the protection found in females, as no differences in tumor growth were found between males and females injected with Hep53.4 AdipoR2-shRNA–treated cells (Fig. S2 e).

The contribution of adiponectin to HCC development was evaluated by the diethylnitrosamine (DEN)-induced hepatocarcinogenesis model (Heindryckx et al., 2009). At postnatal day (P) 1, male mice were injected with a serotype 8 adeno-associated virus overexpressing adiponectin under the control of the adipocyte aP2 promoter (AAV-aP2-Adipoq) or carrying an empty control vector (AAV-aP2-CTRL). After 14 d, these mice received i.p. DEN injections to induce HCC. Adiponectin overexpression was confirmed by measurement of adiponectin plasma levels 3 wk after virus injection (Fig. S3 a), as well as 8.5 mo after virus injection (Fig. S3 b). Quantification of tumors 8 mo after DEN treatment revealed a significant reduction in the number of tumors in adiponectin-overexpressing males (Fig. 1, f–i), indicating that adiponectin reduces tumor progression and may be a potential treatment for HCC. To further evaluate the protective effects of adiponectin in females, we used the DEN-induced HCC model in WT and *Adipoq*$^{-/-}$ mice. Results showed that lack of adiponectin slightly increases the number of tumors 8 mo after DEN treatment (Fig. S3, c and d), corroborating that high levels of adiponectin in females contribute to the protection against HCC.

Lack of JNK1 in the adipose tissue protects against HCC progression

It is known that adipose tissue JNK controls the production of important adipokines that regulate liver metabolism (Sabio et al., 2008; Manieri and Sabio, 2015). We therefore tested whether sex-dependent differences in JNK activation in adipose tissue could account for the higher adiponectin levels in females. Western blot analysis revealed a higher activation of adipose tissue JNK in males than in females, both in mouse and rat models, which correlated with lower adiponectin levels (Fig. 2 a; Fig. S1 a; and Fig. S4, a and b), suggesting a general effect conserved among species. In line with these results, testosterone activated JNK in both mouse and human adipocytes (Fig. 2 b and Fig. S4 c). To check whether testosterone was also able to regulate JNK phosphorylation in vivo, we castrated WT male mice and performed testosterone replacement. Adipose tissue JNK activation was significantly reduced in castrated males, whereas testosterone injection was enough to increase its activation to noncastrated mice levels within 2 wk (Fig. 2 c). Importantly, the observed changes in JNK phosphorylation were in concordance with adiponectin levels, which decreased to the levels of noncastrated mice when testosterone replacement was performed (Fig. 2 d). We next examined serum concentrations of adiponectin in males with adipose tissue-specific deletion of JNK1 (F^{KO}) or control mice (F^{WT}; Fig. S5 a). Blood adiponectin levels were significantly higher in F^{KO} males than in F^{WT} males (Fig. S5 b), whereas no between-genotype differences were found in the levels of TNFα, IL-1β, or IL-6 (Fig. S5 c). We next performed allograft tumor formation assays in F^{WT} and F^{KO} males to investigate the role of adipose tissue JNK1 in tumor growth. Consistent with the higher adiponectin levels found in F^{KO} males (Fig. S5 b), tumor growth in these mice was slower than in F^{WT} controls, and postmortem inspection revealed smaller tumors (Fig. 3 a). To further evaluate these results, F^{KO} and F^{WT} males were injected with DEN, and tumors were examined 8 mo later. We found that HCC was strongly suppressed in F^{KO} mice (Fig. 3 b). Moreover, F^{KO} mice had significantly fewer tumors than F^{WT} mice (Fig. 3 c), and tumor size and maximum tumor size were significantly lower in F^{KO} mice (Fig. 3, d and e).

Higher levels of adiponectin in F^{KO} mice are essential for their protection against HCC

To evaluate the potential role of adiponectin in the protection against HCC in F^{KO} males, we crossed WT and JNK1-deficient mice with mice deficient in adiponectin (*Adipoq*$^{-/-}$),

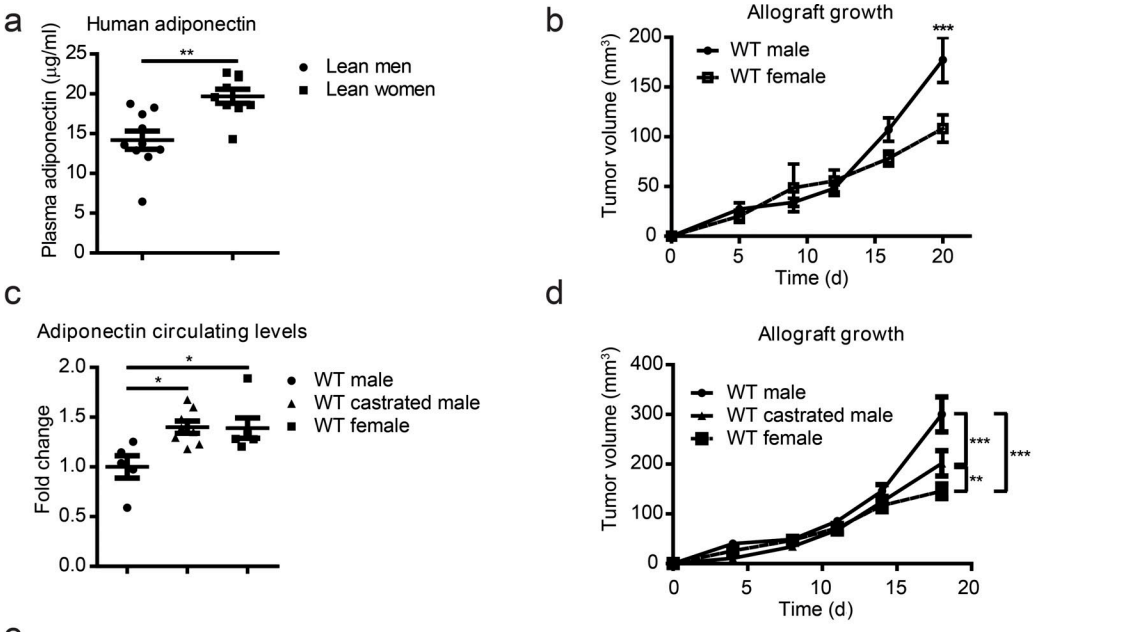

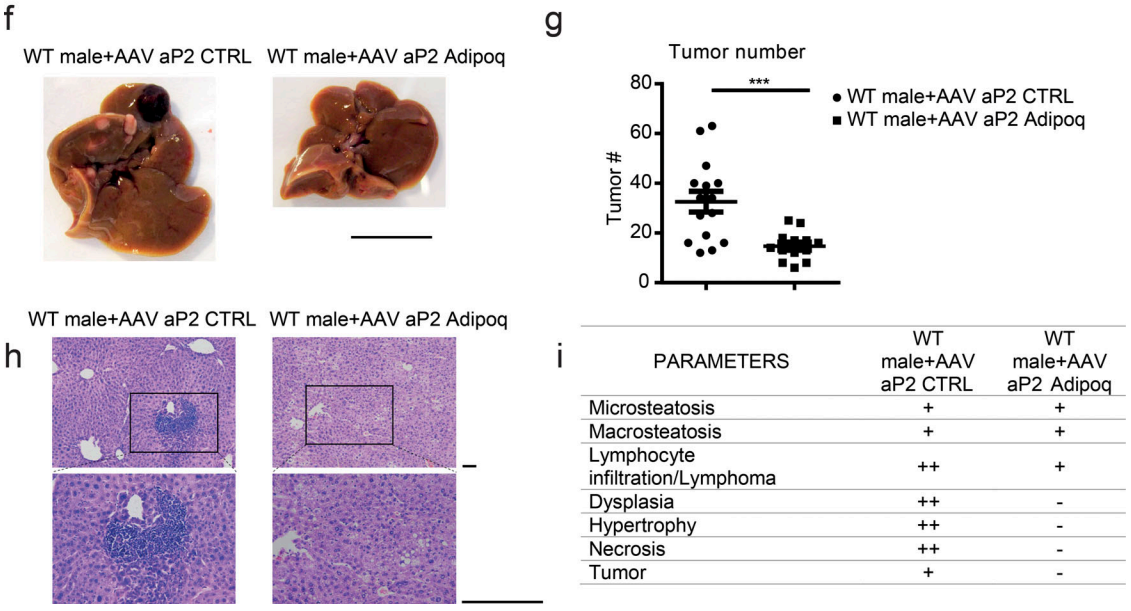

i

PARAMETERS	WT male+AAV aP2 CTRL	WT male+AAV aP2 Adipoq
Microsteatosis	+	+
Macrosteatosis	+	+
Lymphocyte infiltration/Lymphoma	++	+
Dysplasia	++	-
Hypertrophy	++	-
Necrosis	++	-
Tumor	+	-

Figure 1. **Adiponectin gender disparity and the effect on HCC development. (a)** Quantification of circulating adiponectin levels in plasma samples from lean men and women. Data are shown as means ± SEM; **, P < 0.01; Student's *t* test; men *n* = 10; women *n* = 9. **(b)** Tumor volume in WT male and female mice monitored over 3 wk after subcutaneous injection with 5 × 10^4 Hep53.4 cells in each flank. Data are shown as means ± SEM; ***, P < 0.001; two-way ANOVA coupled with Bonferroni's multiple comparisons test; *n* = 18–19 tumors (10 mice per condition). **(c)** Quantification of circulating adiponectin levels in 11–12-wk-old female, male, and castrated male mice. Data are normalized to WT male and are shown as means ± SEM; *, P < 0.05; one-way ANOVA coupled with Bonferroni's multiple comparisons test; WT male *n* = 5; WT castrated male *n* = 8; WT female *n* = 6. **(d)** Tumor volume in male, female, and castrated male mice monitored over 3 wk after subcutaneous injection with 5 × 10^4 Hep53.4 cells in each flank. Data are shown as means ± SEM; **, P < 0.01; ***, P < 0.001; two-way ANOVA coupled with Bonferroni's multiple comparisons test; *n* = 20 tumors (10 mice per condition), except WT castrated males *n* = 18 (9 mice). **(e)** Representative allografts and tumor volume quantification in WT and *Adipoq*$^{-/-}$ male and female mice at sacrifice, 3 wk after subcutaneous

injection with 5 × 10^4 Hep53.4 cells in each flank. Data are shown as means ± SEM; **, P < 0.01; nonsignificant differences in *Adipoq*$^{-/-}$ mice were found (ns); Student's *t* test; WT *n* = 18–19 tumors (10 mice per gender); *Adipoq*$^{-/-}$ *n* = 19–22 tumors (10 male and 11 female mice). Bar, 1 cm. **(f–i)** WT mice were injected at P1 with adeno-associated virus carrying a control sequence (AAV aP2 CTRL) or the adiponectin gene under control of the aP2 promoter (AAV aP2 Adipoq). **(f)** HCC development 8 mo after i.p. injection with DEN (50 mg/kg) on P14. Bar, 1 cm. **(g)** Tumor number was determined at sacrifice. Data are shown as means ± SEM; ***, P < 0.001; Student´s *t* test; WT male+AAV aP2 CTRL *n* = 15; WT male+AAV aP2 Adipoq *n* = 13. AAV, adeno-associated virus; CTRL, control. **(h)** Representative photos of H&E-stained liver sections obtained from these DEN-injected mice at sacrifice (upper panels: 10×; lower panels: 20×; bars, 100 µm). **(i)** Histopathological evaluation was performed in livers from these mice upon sacrifice. No injury (–) or different grades of injury (mild [+], moderate [++], or marked [+++]) were noted in at least seven view fields per slide. *n* = 10 per condition.

and repeated the allograft assays. Tumor growth was identical in F^{WT}*Adipoq*$^{-/-}$ and F^{KO}*Adipoq*$^{-/-}$ males (Fig. 4 a), consistent with a central role for adiponectin in the F^{KO} phenotype, and suggesting that the elevated adiponectin levels in F^{KO} males were responsible for their reduced tumor growth. To corroborate this hypothesis, we analyzed DEN-induced liver cancer in F^{WT}*Adipoq*$^{-/-}$ and F^{KO}*Adipoq*$^{-/-}$ males. Tumor number, size, and maximum size after 8 mo did not differ significantly between the two groups of mice, suggesting an important role for adiponectin in the protection of F^{KO} males against DEN-induced HCC (Fig. 4, b–e).

AMPKα and p38α activation by adiponectin reduces tumor progression

Adiponectin transduces its signal in the liver through the activation of two pathways: p38 MAPK (Mao et al., 2006a,b) and AMPK (Yamauchi et al., 2002; Polyzos et al., 2010). p38α suppresses liver cancer development by reducing cell proliferation, and consequently, mice with hepatic deletion of p38α show enhanced hepatocyte proliferation and tumor development (Hui et al., 2007). AMPK also suppresses cancer, and treatment with the AMPK activator metformin reduces cancer incidence (Chen et al., 2013) and may improve survival among liver cancer patients (Ma et al., 2016). Consequently, AMPK is emerging as an important metabolic tumor suppressor and a promising target for cancer prevention and therapy (Luo et al., 2010). We evaluated the activation of AMPK and p38α in allografts from male and female mice. Immunoblot analysis detected higher levels of AMPK and p38α activation (phosphorylation) in females (Fig. 5 a), correlating with the higher adiponectin levels in female mice (Fig. S1 a). This gender difference in p38α or AMPK activation was not observed in *Adipoq*$^{-/-}$ mice (Fig. 5 b), suggesting that higher activation of these kinases in females is the result of the higher levels of circulating adiponectin. To evaluate whether p38α and AMPK activation is implicated in the protection against liver cancer in females, we implanted Hep53.4 cells subcutaneously into male mice and activated each pathway by two different strategies. In the first strategy, animals were treated with metformin to activate AMPK. In the second one, allografts were injected with a retrovirus containing active p38α or a control construct on days 9 and 22 after transplantation. As expected, metformin treatment significantly reduced tumor volume (Fig. 5 c), indicating that AMPK activation confers protection against HCC. Similarly, tumors infected with active p38α were significantly smaller (Fig. 5 d), suggesting that the adiponectin-mediated protection against HCC is also mediated by p38α activation.

We next investigated the extent of p38α and AMPK phosphorylation in livers of F^{KO} mice. Consistent with the high levels of adiponectin in F^{KO} males, liver activation of p38α and AMPK was significantly higher in DEN-treated F^{KO} male mice than in their F^{WT} counterparts (Fig. S5, d and e). To evaluate whether AMPK activation is necessary for adiponectin-mediated protection in F^{KO} mice, we treated Hep53.4 cells with shRNA against AMPK or a scrambled control sequence. As expected, AMPK knockdown in Hep53.4 cells resulted in larger tumors after implantation in F^{WT} animals. More importantly, F^{KO} males were no longer protected against tumor growth, indicating that AMPK activation in hepatocytes is necessary for the protection observed in F^{KO} mice (Fig. 5 e).

Discussion

Liver cancer is the fourth most common cause of death from cancer worldwide (Marquardt et al., 2015). The incidence and mortality rates of liver cancer have increased rapidly, coinciding with the rising prevalence of obesity (Larsson and Wolk, 2007). Accumulating epidemiological evidence indicates that excess of body weight may be a risk factor for liver cancer; however, the link between both phenomena remains elusive.

Adipose tissue is recognized as an active endocrine organ that mediates a variety of physiological functions via secretion of adipokines. Here, we found that gender differences in adipocytes are important players in HCC progression and can contribute to the increased incidence of HCC observed in males. Our study demonstrates that adiponectin plays an important role in protecting female mice against HCC. In men, adiponectin levels decrease with puberty, whereas its levels are maintained in women (Böttner et al., 2004). A similar gender disparity occurs in mice (Combs et al., 2003). We found that the gender bias in tumor growth is strongly dependent on adiponectin, and that adiponectin KO mice showed no gender differences in tumor progression. We also demonstrate that activation of JNK in adipose tissue correlates with reduced levels of adiponectin in males, and that males with JNK1 deficiency in adipose tissue have increased adiponectin secretion, protecting against HCC. Moreover, castration reduces JNK phosphorylation in the adipose tissue while testosterone replacement increases it, together with a reduction in adiponectin to the levels before castration.

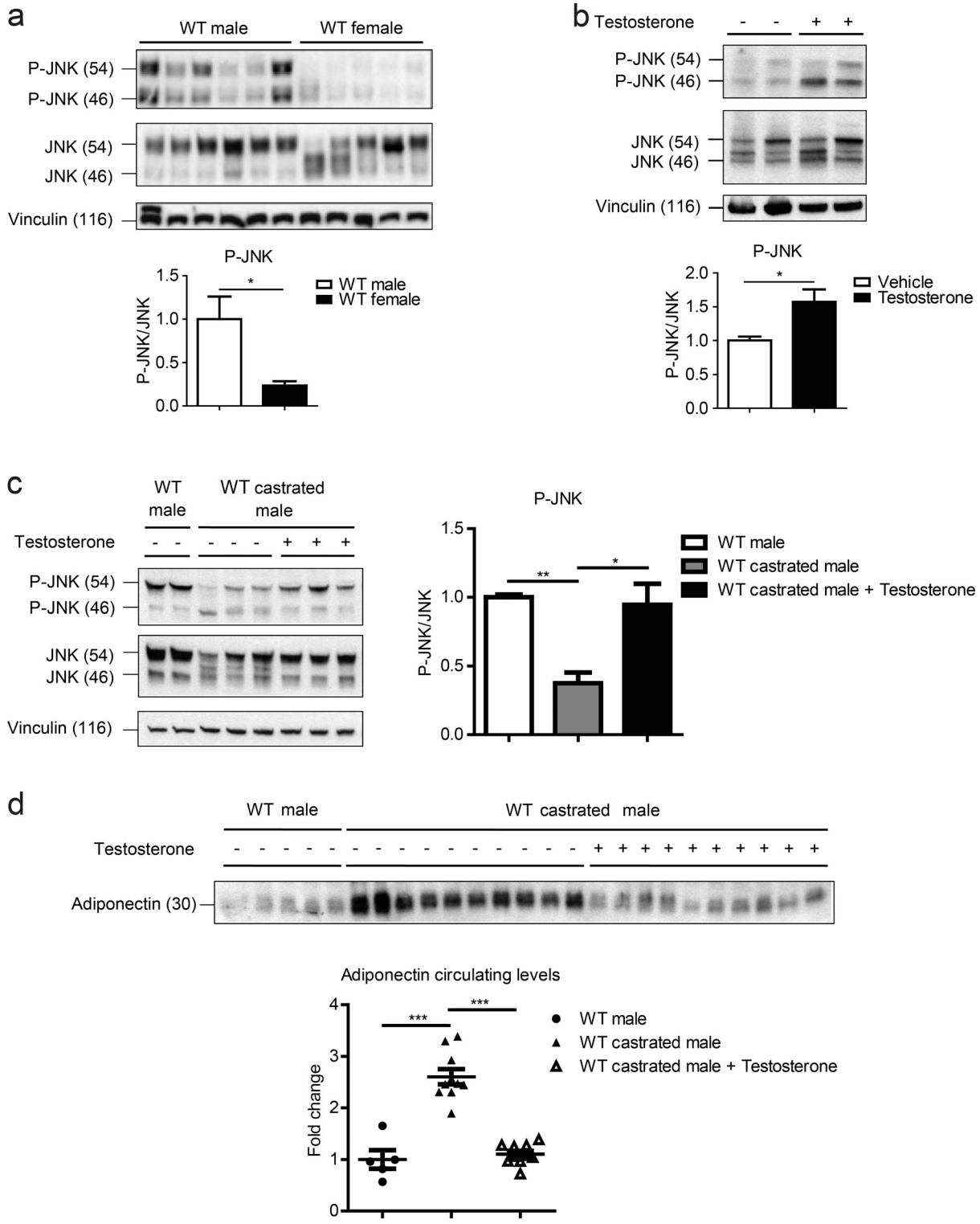

Figure 2. **Effect of testosterone on the control of adiponectin levels through adipose tissue JNK. (a)** Immunoblot analysis and quantification of phospho (P)-JNK and JNK in adipose tissue from WT male and female rats. Vinculin protein expression was monitored as a loading control. Data are shown as means ± SEM; *, P < 0.05; Student's *t* test; WT male *n* = 6; WT female *n* = 5. **(b)** Immunoblot analysis and quantification of phospho-JNK and JNK in mouse differentiated adipocytes after treatment with testosterone (300 nM for 120 min). Vinculin protein expression was monitored as a loading control. Data are shown as means ± SEM; *, P < 0.05; Student's *t* test; *n* = 3. **(c and d)** 4-wk-old WT males were castrated or sham-operated and they were subcutaneously injected with testosterone propionate (5 µg/g body weight) or vehicle alone every other day for 3 wk. **(c)** Immunoblot analysis and quantification of phospho-JNK and JNK in adipose tissue from these WT male mice, treated with testosterone propionate (50 µg/g body weight) or vehicle alone, 30 min before sacrifice. Vinculin protein expression was monitored as a loading control. Data are normalized to WT male and are shown as means ± SEM; *, P < 0.05; **, P < 0.01; one-way ANOVA coupled with Bonferroni's multiple comparisons test; *n* = 3, except WT sham males *n* = 4. **(d)** Immunoblot analysis and quantification of circulating adiponectin levels 2 wk after the first testosterone injection. Data are normalized to WT male and are shown as means ± SEM; ***, P < 0.001; one-way ANOVA coupled with Bonferroni's multiple comparisons test; *n* = 10, except WT sham males *n* = 5.

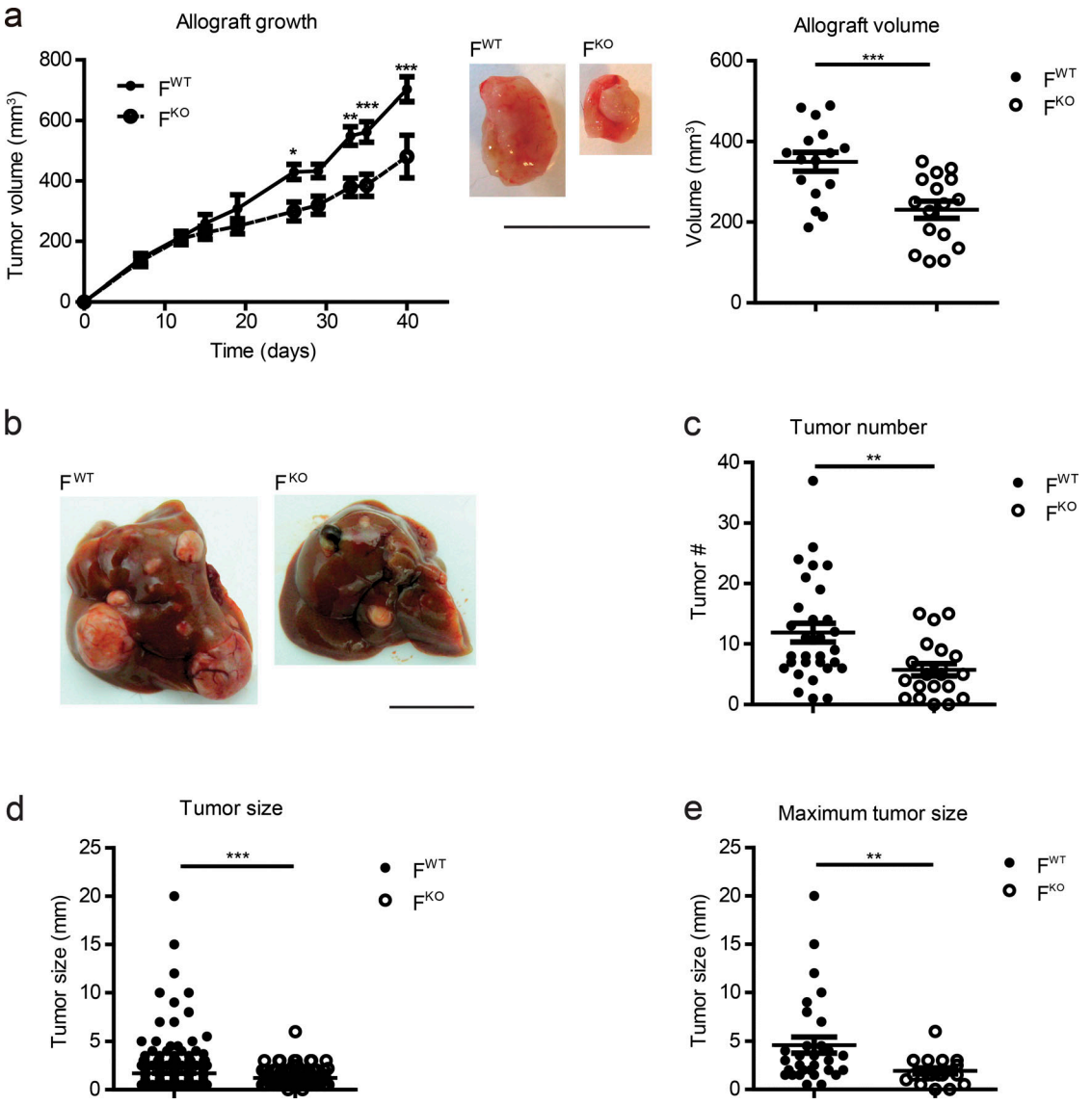

Figure 3. **Effect of adipose tissue JNK1 deficiency on HCC progression. (a)** Representative allografts and tumor volume quantification in F^{WT} and F^{KO} male mice during the experiment and at sacrifice 5 wk after subcutaneous injection with 5×10^4 Hep53.4 cells in each flank. Data are shown as means ± SEM; *, P < 0.05; **, P < 0.01; ***, P < 0.001; two-way ANOVA coupled with Bonferroni's multiple comparisons test (allograft growth); Student's *t* test (allograft volume); *n* = 16–18 tumors (8–9 mice per genotype). Bar, 1 cm. **(b–e)** HCC progression analyzed in control (F^{WT}) and adipose tissue JNK1-deficient (F^{KO}) mice 8 mo after i.p. injection with DEN (50 mg/kg body weight) on P14. **(b)** Representative images of liver tumors in F^{WT} and F^{KO} mice. Bar, 1 cm. **(c–e)** Tumor number, tumor size, and maximum tumor size. Data are shown as means ± SEM; **, P < 0.01; ***, P < 0.001; Student's *t* test (tumor number); Student's *t* test with Welch's correction (tumor size and maximum tumor size); F^{WT} *n* = 30; F^{KO} *n* = 20–21.

These results indicate that activation of JNK in adipose tissue inhibits adiponectin secretion, promoting tumor growth in males. Epidemiological studies suggest the association between low adiponectin levels and liver tumorigenesis (Kotani et al., 2009). In line with this, adiponectin has an anti-oncogenic potential in HCC cell lines (Sharma et al., 2010). However, opposite results were reported for HCC associated with hepatitis C (Arano et al., 2011). These discrepancies may be attributable to the different HCC etiologies examined in those studies (Dalamaga et al., 2012). Here, using mouse models, we demonstrated that adiponectin protects against HCC by activating p38α and AMPK. Our results suggest that adiponectin and metformin could be of use in the treatment of HCC.

Materials and methods

Study population and sample collection

For the analysis of human levels of blood adiponectin, individuals were recruited among patients who underwent laparoscopic cholecystectomy for gallstone disease.

Blood was extracted using straight needles (21G butterfly) and Vacuette Z Serum Sep Clot Activator tubes. After 30 min, these tubes were centrifuged at 1,500 rpm for 10 min at room temperature to separate serum, which was divided into aliquots and stored at −80°C until further analysis. The study was approved by the Ethics Committee of the University Hospital of Salamanca, and all subjects provided written informed consent to participate. Fasting blood samples were

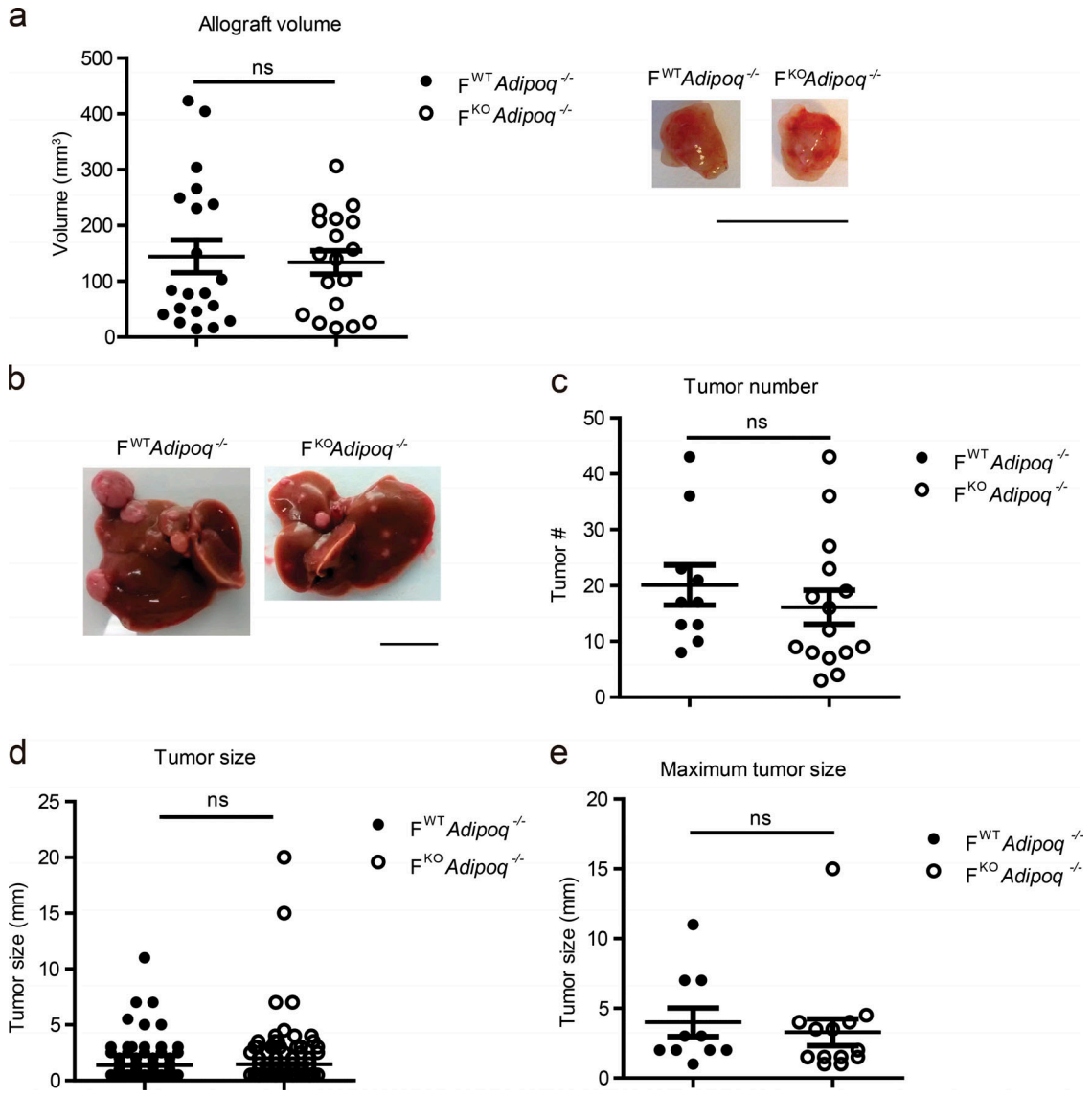

Figure 4. **High levels of adiponectin in F^{KO} mice are responsible for the protection against HCC. (a)** Tumor volume quantification and representative allografts in male F^{WT} adiponectin KO mice (F^{WT}*Adipoq*$^{-/-}$) and male F^{KO} adiponectin KO mice (F^{KO}*Adipoq*$^{-/-}$) at sacrifice 5 wk after subcutaneous injection of 5×10^4 Hep53.4 cells in each flank. Data are shown as means ± SEM; nonsignificant differences were found (ns); Student's *t* test; F^{WT}*Adipoq*$^{-/-}$ $n = 20$ tumors (10 mice); F^{KO}*Adipoq*$^{-/-}$ $n = 18$ tumors (9 mice). Bar, 1 cm. **(b–e)** HCC progression analyzed in F^{WT}*Adipoq*$^{-/-}$ and F^{KO}*Adipoq*$^{-/-}$ mice 8 mo after i.p. injection with DEN (50 mg/kg body weight) on P14. **(b)** Representative images of liver tumors in F^{WT}*Adipoq*$^{-/-}$ and F^{KO}*Adipoq*$^{-/-}$ mice. Bar, 1 cm. **(c–e)** Tumor number, tumor size, and maximum tumor size. Data are shown as means ± SEM; nonsignificant differences were found (ns); Student's *t* test; F^{WT}*Adipoq*$^{-/-}$ $n = 10$; F^{KO}*Adipoq*$^{-/-}$ $n = 15$.

collected for adiponectin, glucose, and lipid analysis. Patients were excluded if they had a history of alcohol use disorders or excessive alcohol consumption (>30 g/d in men and >20 g/d in women), chronic hepatitis C or B, or body mass index ≥ 35 (Table S1).

Animals

Adiponectin KO mice (B6;129-*Adipoq*^{tm1Chan}/J) and FabP4 cre mice (B6.Cg-Tg(Fabp4-cre)1Rev/J) were purchased from the Jackson Laboratory and backcrossed to the C57BL/6 background for 10 generations. Mice with specific deletion of JNK1 in adipocytes (F^{KO}) were as described (Sabio et al., 2008), and F^{WT} littermates were used as controls. Mice were housed randomly in a pathogen-free animal facility and maintained on a 12-h light/dark cycle at constant temperature and humidity. Genotypes were identified by PCR analysis of genomic DNA isolated from mouse tails. For tumor studies, mice at P14 received one i.p. injection of DEN (Sigma-Aldrich) at 50 mg/kg body weight dissolved in saline. After 8 mo, tumors were extracted and measured with a caliper. In all cases, mice were euthanized after overnight starvation. For testosterone deprivation studies, castration or sham operations were performed in mice at 4–5 wk of age. 23 d after castration, testosterone propionate (Desma) diluted in corn oil (5 µg/g body weight) or vehicle alone was subcutaneously injected in castrated or sham-operated mice, every other day for 3 wk. Blood samples were collected 2 wk

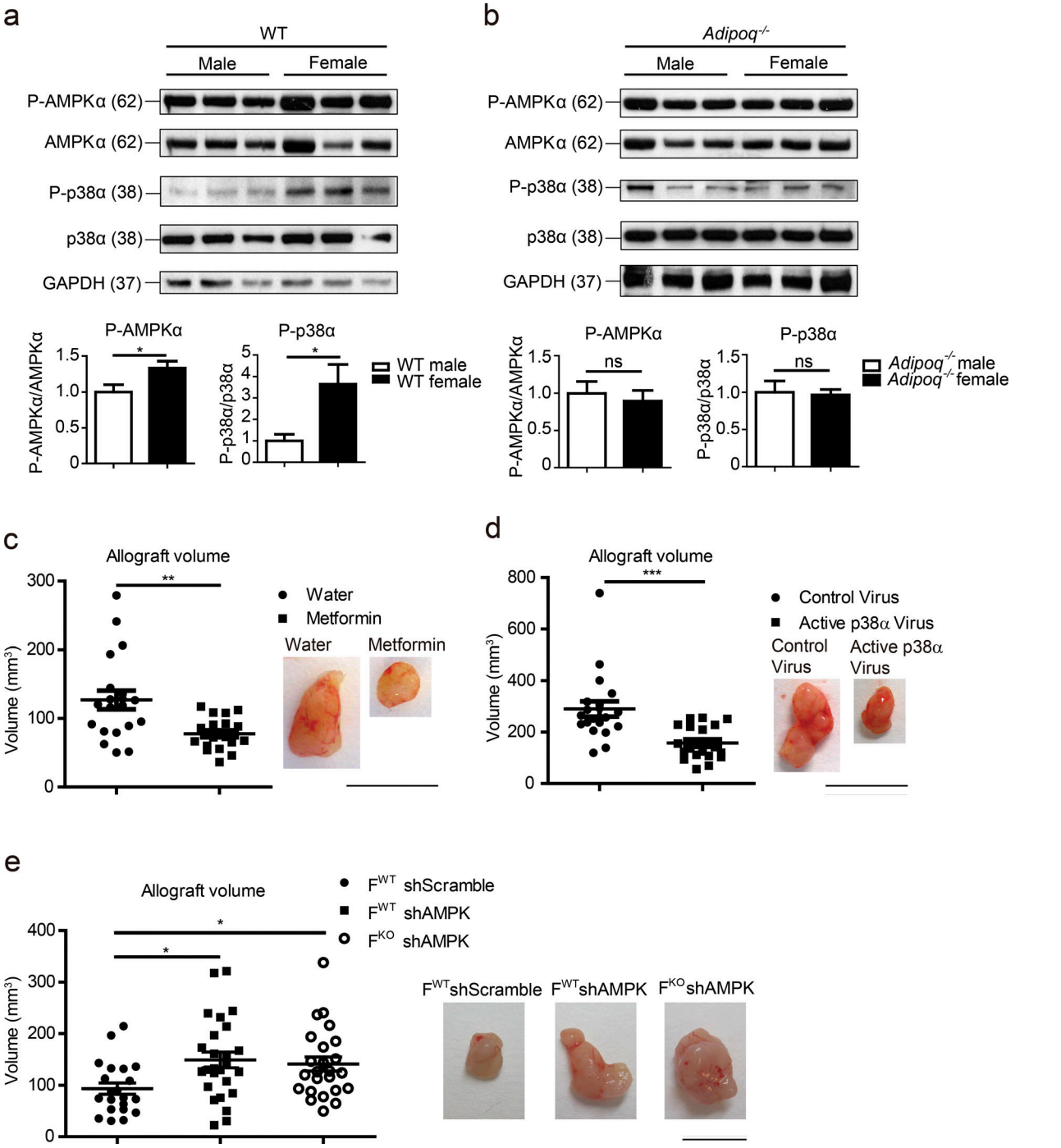

Figure 5. **AMPKα and p38α activation protects against tumor growth. (a)** Immunoblot analysis and quantification of phospho-AMPKα, AMPKα, phospho-p38α, and p38α in tumor allografts obtained from WT male and female mice 21 d after implantation. GAPDH protein expression was monitored as a loading control. Data are shown as means ± SEM; *, P < 0.05; Student's *t* test; WT male *n* = 10; WT female *n* = 6–9. **(b)** Immunoblot analysis and quantification of phospho-AMPKα, AMPKα, phospho-p38α, and p38α in tumor allografts obtained from *Adipoq*$^{-/-}$ male and female mice 21 d after implantation. GAPDH protein expression was monitored as a loading control. Data are shown as means ± SEM; nonsignificant differences were found (ns); Student's *t* test; *Adipoq*$^{-/-}$ male *n* = 10; *Adipoq*$^{-/-}$ female *n* = 11. **(c)** Representative allografts and tumor volume quantification in WT male at sacrifice 5 wk after subcutaneous injection with 5 × 10^4 Hep53.4 cells in each flank and treatment with 300 mg/d · kg body weight of metformin (supplied in the drinking water). Data are shown as means ± SEM; **, P < 0.01; Student's *t* test with Welch's correction; *n* = 20 tumors (10 mice per genotype). Bar, 1 cm. **(d)** Representative allografts and tumor volume quantification in WT male overexpressing p38α in hepatic tumors. Mice received subcutaneous injections in each flank with 5 × 10^4 Hep53.4 cells followed by intratumor injections on days 9 and 22 with retrovirus expressing active p38α or control virus. Male mice were sacrificed 5 wk after Hep53.4 cell injection. Data are shown as means ± SEM; ***, P < 0.001; Student's *t* test with Welch's correction; *n* = 20 tumors (10 mice per genotype). Bar, 1 cm. **(e)** Representative allografts and tumor volume quantification in WT male with hepatic tumors lacking AMPK expression. Mice received subcutaneous injections in each flank with 1 × 10^6 Hep53.4 cells in each flank, previously transduced with shRNA targeting AMPK or a control sequence (shScramble). Mice were sacrificed 5 wk after Hep53.4 cell injection. Data are shown as means ± SEM; *, P < 0.05; one-way ANOVA coupled with Dunnett's multiple comparisons test. F^{WT}shScramble *n* = 21 tumors (11 mice); F^{WT}shAMPK *n* = 26 tumors (13 mice); F^{KO}shAMPK *n* = 24 tumors (12 mice). Bar, 1 cm.

after the first injection, and testosterone propionate (50 µg/g body weight) was injected into some castrated mice 30 min before sacrifice, at the end of the experiment. For healthy and tumor hepatocytes analysis, C57BL/6J mice were injected with a single dose of DEN at day 14 postnatally, followed by administration of thioacetamide (TAA; 300 µg/liter) in the drinking water during 26 wk as described in Salguero Palacios et al. (2008). Control mice received a single injection of PBS at day 14 and normal drinking water. The parenchymal and the non-parenchymal compartment was isolated from vehicle (healthy) or DEN/TAA (tumor) mice. All animal experiments conformed to European Union Directive 2010/63EU and Recommendation 2007/526/EC, enforced in Spanish law under Real Decreto 1386/2018. All experiments were approved for the Centro Nacional de Investigaciones Cardiovasculares Carlos III ethics committee and Comunidad de Madrid.

Adeno-associated virus

Male mice were injected intravenously at P1 with 0.5×10^{11} viral particles of a serotype 8 adeno-associated virus overexpressing adiponectin under the control of the adipocyte-specific aP2 mini promoter (lentiviral vector tailor-designed and purchased from Vector Builder) or carrying an empty control vector.

Serum analysis

Serum cytokine concentrations were measured by multiplexed ELISA in a Luminex 200 analyzer (Millipore).

Adiponectin was detected in plasma samples by Western blot. Samples were diluted in PBS (1:10) and buffered with 2× Native Tris-Glycine Sample Buffer (Invitrogen). Diluted samples were loaded on precast native gels to preserve adiponectin multimers (NativePAGE Bis-Tris gel system; Thermo Fisher Scientific) and run with Novex Tris-Glycine Native Running Buffer (Invitrogen). In other cases, plasma samples were prepared as described but diluted in PBS, Milli-Q water, and Laemmli Sample Buffer and separated by SDS-PAGE. Membranes were blocked with 10% milk prepared in PBS without detergents (in the first case) or with PBS-Tween 0.1% (in the second case), and probed with a primary antibody to adiponectin (1:500 dilution; PA1-054; Thermo Fisher Scientific). After washing, membranes were incubated with a fluorescent secondary antibody (goat anti-rabbit 680 nm 926–32221; Odyssey) or a horseradish peroxidase–conjugated secondary antibody (GE Healthcare), and proteins were visualized and quantified using the Odyssey LI-COR imaging system (LI-COR) or an enhanced chemiluminescent substrate (Clarity Western ECL substrate; Bio-Rad), respectively. We assured the specificity of the antibody using serum from *Adiponectin* KO mice. Results were normalized to the control group (male mice or F^{WT} or control mice, as indicated in the figure legends).

Biochemical analysis

Total proteins from different organs or from adipocytes were extracted in lysis buffer (50 mM Tris-HCl, pH 7.5, 1 mM EGTA, 1 mM EDTA, pH 8.0, 50 mM NaF, 1 mM sodium glycerophosphate, 5 mM pyrophosphate, 0.27 M sucrose, 1% Triton X-100, 0.1 mM PMSF, 0.1% 2-mercaptoethanol, 1 mM sodium orthovanadate, 1 µg/ml leupeptin, and 1 µg/ml aprotinin) and centrifuged at 8,600 × *g* for 20 min at 4°C. Extracts were separated by SDS-PAGE and transferred to 0.2-µm-pore-size nitrocellulose membranes (Bio-Rad). Blots were probed with primary antibodies to phospho-JNK (Thr183/Tyr185; 4668), total JNK (9252), phospho-AMPKα (Thr172; 2531), total AMPKα (2603), and phospho-p38 (Thr180/Tyr182; 9211; all from Cell Signaling Technology), p38 from Santa Cruz Biotechnology (sc-535), and GAPDH (sc-25778) and vinculin (V4505; Sigma-Aldrich). All antibodies were used at 1:1,000. After washes, membranes were incubated with an appropriate horseradish peroxidase–conjugated secondary antibody (GE Healthcare), and signals were detected using an enhanced chemiluminescent substrate (Clarity Western ECL substrate; Bio-Rad). Protein levels were analyzed by optical density measured with ImageJ (National Institutes of Health). Results were normalized to the not phosphorylated form.

Allografts

The Hep53.4 cell line was purchased from CLS-Cell Lines Service and tested against *Mycoplasma* (MycoAlert Detection Kit; Lonza). Cells were cultured in DMEM supplemented with 10% FBS, L-glutamine, and antibiotics. The MC-38 and B16-F10 cell lines originally were tested against *Mycoplasma*. MC-38 cells were cultured in DMEM supplemented with 10% FBS, non-essential amino acids, sodium pyruvate, Hepes, L-glutamine, and antibiotics, whereas B16-10's culture medium only contained DMEM supplemented with 10% FBS, sodium pyruvate, and antibiotics. For allograft assays, Hep53.4 cells (5×10^4 cells for usual experiments, or 1×10^6 for short hairpin RNA experiments) were mixed 1:1 with Matrigel Matrix (Corning) and subcutaneously injected into each flank of anesthetized 8–12-wk-old mice. For MC-38 or B16-F10 allograft assays, 5×10^5 cells without Matrigel were subcutaneously injected into each flank. In both cases, tumor growth was monitored by measuring length and width every 3–4 d for a period of 2, 3, or 5 wk. At the end of the experiment, mice were sacrificed and tumors extracted and measured. To study AMPKα activation by metformin, mice were treated with metformin (300 mg/d · kg body weight), starting 1 wk before allograft injection. In allografts treated with active p38α, pBABE p38α D176A/F327S retrovirus was injected intratumorally on days 9 and 22.

Adipocytes cell culture

Immortalized white preadipocytes from C57BL/6 male mice were maintained in DMEM-F12 medium with 8% FBS, 200 mM L-glutamine, and 10,000 U/ml penicillin/streptomycin. These cells were differentiated to white adipocytes for 10 d with the previous medium supplemented with 5 µg/ml insulin, 25 µg/ml 3-isobutyl-1-methylxanthine, 1 µg/ml dexamethasone, and 1 µM troglitazone. The cells were starved overnight and treated with 300 nM testosterone (Sigma-Aldrich) for 2 h.

Human visceral white preadipocytes were purchased from Innoprot, and culture was set up following the manufacturer's instructions. Preadipocyte differentiation medium from Innoprot was used for the differentiation to white

adipocytes during 8 d, followed by an overnight starvation and treatment with 1,200 nM testosterone or vehicle for 30 min.

Liver cell populations isolation

To isolate the different hepatic cell types, a perfusion was performed in a C57BL/6 mouse. The liver was perfused with each solution (A, B, and C; see Table S3) separately for 5 min or 25 ml. After the final solution C, the perfusion was stopped and the liver was dissected and transferred into solution D and incubated for 20 min at 37°C. To ensure proper digestion of the liver, solution D was inverted several times during the incubation time. Next, solution D containing the digested liver was filtered through a 70-µm cell strainer, and the filtered solution was centrifuged at 50 × *g* for 1 min at 4°C. The pellet containing hepatocytes was kept for further analysis, and the supernatant was transferred to a new conical tube and subsequently centrifuged at 720 × *g* for 8 min at 4°C. The supernatant was removed and the pellet was resuspended in 10 ml Gey's Balanced Salt Solution buffer (GBSS-B) solution containing 150 µl DNase I stock solution, and the conical tube was filled up to 50 ml with GBSS-B solution. In the next step, the solution was centrifuged at 720 × *g* for 8 min at 4°C, and the supernatant was removed. Next, the pellet was resuspended in 10 ml GBSS-B containing 150 µl DNase I stock solution. In addition, 24 ml GBSS-B and 14 ml of the Nycodenz 1 solution were added, and the solution was carefully mixed. Further, 4 ml of the Nycodenz 2 solution was transferred into six 15-ml falcon tubes. Next, 8.3 ml of the mixed cell solution containing GBSS-B, DNase, and Nycodenz 1 was carefully laid onto the Nycodenz 2 solution, and the GBSS-B solution was used to gently overlay the cell suspension to obtain a final volume of 15 ml. Consequently, the gradient solution was centrifuged without brakes at 3,000 × *g* for 20 min at 4°C. After the centrifugation step, hepatic stellate cells (HSCs) are found in the upper gradient phase as a white ring, and KCs are found in the lower gradient phase. Each cell type was carefully transferred to a new tube and washed with GBSS-B solution and subsequently centrifuged at 720 × *g* for 8 min at 4°C to pellet the cells. The supernatant was removed, and the cells were checked for their purity under a microscope and subsequently frozen in liquid nitrogen and stored at −80°C for further RNA isolation. See Tables S3 and S4 to check the solutions used for the isolation of different hepatic cell types.

Histological analysis

Histopathological examination of H&E-stained livers was performed in an Eclipse CiL light microscope (Nikon), using 10–20× magnification with a numerical aperture of 0.25–0.40 of the optic lenses. Microphotographs were taken with a Nikon Camera DS-Fi3 and acquired using the NIS-Elements Microscope Imaging Software (Nikon). Histopathological grading of chronic liver disease was assessed based on the score system previously published (Goodman, 2007), but modified for nonalcoholic fatty liver disease and HCC. No insult (–) or different grades of injury (mild [+], moderate [++], or marked [+++]) were noted in at least seven view fields per slide.

RNA analysis

Total RNA was isolated from healthy or tumorigenic hepatocytes, other cell populations in the liver (KCs, ECs, and HSCs), as well as from different tumor cell lines (Hep53.4, MC-38, and B16-F10) using the RNeasy Mini Kit (Qiagen). Complementary DNA was synthesized with the High-Capacity Complementary DNA Reverse Transcription Kit (Applied Biosystems). Sequences of primers used for quantitative real-time PCR (qRT-PCR) are provided in Table S2. Expression levels were normalized to *Gapdh* mRNA. qRT-PCR was performed using Fast SYBR Green.

Statistical analysis

Differences between groups were examined for statistical significance using the two-tailed Student's *t* test, Student's *t* test coupled with Welch's correction in case of not equal variances, or one- or two-way ANOVA coupled to Bonferroni's or Dunnett's post-test.

Online supplemental material

Fig. S1 shows the mouse gender differences of adiponectin levels and the lack of differences in the growth of colon adenocarcinoma and melanoma cells between males and females. Fig. S2 shows the analysis of adiponectin receptors expression in different tumor cells and liver cell populations, along with the growth of HCC-derived tumor cells with reduced AdipoR1 or AdipoR2 levels. Fig. S3 shows the increased adiponectin levels observed in males infected with the adeno-associated virus overexpressing adiponectin and the maintenance of these high levels until the end of the experiment, as well as the effect of lack of adiponectin in females on tumor number. Fig. S4 shows the rat gender differences of adiponectin levels, the mouse gender differences in fat JNK activation, and its activation in human adipocytes upon testosterone stimuli. Fig. S5 shows the specific deletion of JNK1 in the adipose tissue, adiponectin and cytokine levels in F^{WT} and F^{KO} mice, and higher AMPKα and p38α activation in F^{KO} compared with F^{WT} mice. Table S1 shows the characteristics of women and men population used in the study. Table S2 shows the sequences of the primers used for the qRT-PCRs. Tables S3 and S4 show the solutions used for the isolation of different hepatic cell types, for both hepatic perfusion and hepatic cell isolation.

Acknowledgments

We thank K. McCreath and S. Bartlett for English editing. We are grateful to Dr. R.J. Davis (University of Massachusetts Medical School, Worcester, MA) for the F^{KO} animals and critical reading of the manuscript. We thank Dr. A. Nebreda (Institute for Research in Biomedicine, Barcelona, Spain) for the active pBABE p38α D176A/F327S plasmid. We also thank Dr. David Sancho (Centro Nacional de Investigaciones Cardiovasculares [CNIC], Madrid, Spain) for the MC-38 and B16-F10 cell lines, and Centro Nacional de Investigaciones Cardiovasculares Carlos III Animal Facility for the castration of mice.

G. Sabio is an investigator on the Ramón y Cajal Program. E. Manieri is a La Caixa Foundation fellow. L. Herrera-Melle is a fellow of the Ministerio de Educación, Cultura y Deporte (FPU15-05802). This study was funded by the following grants: G. Sabio was funded by the European Research Council (ERC 260464), European Foundation for the Study of Diabetes–Lilly, Ministerio de Ciencia, Innovación y Universidades (MICINN/SAF2016-79126-R), Comunidad de Madrid (B2017/BMD-3733), and BBVA Becas Leonardo a Investigadores y Creadores Culturales (Investigadores-BBVA-2017; IN[17]_BBM_BAS_0066); M. Marcos was funded by Instituto de Salud Carlos III and Federación Española de Enfermedades Raras (PI16/01548); and J.L. Torres was funded by Junta de Castilla y León GRS (1587/A/17). F.J. Cubero is a Ramón y Cajal Researcher (RYC-2014-15242) and a Gilead Liver Research Scholar 2018, and his work is supported by the Ministerio de Economia y Competitividad Retos (SAF2016-78711), Comunidad de Madrid (S2017/BMD-3727), The Alan Moremen Memorial Fund Cholangiocarcinoma Charity (2018/117), the European Cooperation in Science and Technology Action (CA17112), and the European Foundation for Alcohol Research (EA14/18). L. Morán is a Comunidad de Madrid fellow (S2017/BMD-3727). The CNIC is supported by the Ministerio de Ciencia, Innovación y Universidades and the Pro CNIC Foundation, and is a Severo Ochoa Center of Excellence (SEV-2015-0505).

The authors declare no competing financial interests.

Author contributions: G. Sabio conceived, designed, and supervised this project. E. Manieri, L. Herrera-Melle, and A. Mora designed the project, developed the hypothesis, performed the experiments, analyzed the data, and prepared figures. A. Tomás-Loba, L. Leiva-Vega, D.I. Fernández, M.E. Rodríguez, L. Morán, L. Hernández-Cosido, J.L. Torres, L.M. Seoane, F.J. Cubero, and M. Marcos participated in the experiments. E. Manieri, L. Herrera-Melle, and G. Sabio wrote the manuscript with input from all authors.

Submitted: 9 July 2018
Revised: 11 January 2019
Accepted: 8 February 2019

References

Arano, T., H. Nakagawa, R. Tateishi, H. Ikeda, K. Uchino, K. Enooku, E. Goto, R. Masuzaki, Y. Asaoka, Y. Kondo, et al. 2011. Serum level of adiponectin and the risk of liver cancer development in chronic hepatitis C patients. *Int. J. Cancer*. 129:2226–2235. https://doi.org/10.1002/ijc.25861

Bakiri, L., and E.F. Wagner. 2013. Mouse models for liver cancer. *Mol. Oncol.* 7: 206–223. https://doi.org/10.1016/j.molonc.2013.01.005

Bosch, F.X., J. Ribes, M. Díaz, and R. Cléries. 2004. Primary liver cancer: worldwide incidence and trends. *Gastroenterology*. 127(5, Suppl 1): S5–S16. https://doi.org/10.1053/j.gastro.2004.09.011

Böttner, A., J. Kratzsch, G. Müller, T.M. Kapellen, S. Blüher, E. Keller, M. Blüher, and W. Kiess. 2004. Gender differences of adiponectin levels develop during the progression of puberty and are related to serum androgen levels. *J. Clin. Endocrinol. Metab.* 89:4053–4061. https://doi.org/10.1210/jc.2004-0303

Bray, F., J. Ferlay, I. Soerjomataram, R.L. Siegel, L.A. Torre, and A. Jemal. 2018. Global cancer statistics 2018: GLOBOCAN estimates of incidence and mortality worldwide for 36 cancers in 185 countries. *CA Cancer J. Clin.* 68:394–424. https://doi.org/10.3322/caac.21492

Chen, H.P., J.J. Shieh, C.C. Chang, T.T. Chen, J.T. Lin, M.S. Wu, J.H. Lin, and C. Y. Wu. 2013. Metformin decreases hepatocellular carcinoma risk in a dose-dependent manner: population-based and in vitro studies. *Gut*. 62: 606–615. https://doi.org/10.1136/gutjnl-2011-301708

Cheung, O.K., and A.S. Cheng. 2016. Gender Differences in Adipocyte Metabolism and Liver Cancer Progression. *Front. Genet.* 7:168. https://doi.org/10.3389/fgene.2016.00168

Combs, T.P., A.H. Berg, M.W. Rajala, S. Klebanov, P. Iyengar, J.C. Jimenez-Chillaron, M.E. Patti, S.L. Klein, R.S. Weinstein, and P.E. Scherer. 2003. Sexual differentiation, pregnancy, calorie restriction, and aging affect the adipocyte-specific secretory protein adiponectin. *Diabetes*. 52: 268–276. https://doi.org/10.2337/diabetes.52.2.268

Dalamaga, M., K.N. Diakopoulos, and C.S. Mantzoros. 2012. The role of adiponectin in cancer: a review of current evidence. *Endocr. Rev.* 33: 547–594. https://doi.org/10.1210/er.2011-1015

Fuente-Martín, E., P. Argente-Arizón, P. Ros, J. Argente, and J.A. Chowen. 2013. Sex differences in adipose tissue: It is not only a question of quantity and distribution. *Adipocyte*. 2:128–134. https://doi.org/10.4161/adip.24075

Ghebranious, N., and S. Sell. 1998. Hepatitis B injury, male gender, aflatoxin, and p53 expression each contribute to hepatocarcinogenesis in transgenic mice. *Hepatology*. 27:383–391. https://doi.org/10.1002/hep.510270211

Goodman, Z.D. 2007. Grading and staging systems for inflammation and fibrosis in chronic liver diseases. *J. Hepatol.* 47:598–607. https://doi.org/10.1016/j.jhep.2007.07.006

Havel, P.J. 2002. Control of energy homeostasis and insulin action by adipocyte hormones: leptin, acylation stimulating protein, and adiponectin. *Curr. Opin. Lipidol.* 13:51–59. https://doi.org/10.1097/00041433-200202000-00008

Heindryckx, F., I. Colle, and H. Van Vlierberghe. 2009. Experimental mouse models for hepatocellular carcinoma research. *Int. J. Exp. Pathol.* 90: 367–386. https://doi.org/10.1111/j.1365-2613.2009.00656.x

Hui, L., L. Bakiri, A. Mairhorfer, N. Schweifer, C. Haslinger, L. Kenner, V. Komnenovic, H. Scheuch, H. Beug, and E.F. Wagner. 2007. p38alpha suppresses normal and cancer cell proliferation by antagonizing the JNK-c-Jun pathway. *Nat. Genet.* 39:741–749. https://doi.org/10.1038/ng2033

Kotani, K., K. Wakai, A. Shibata, Y. Fujita, I. Ogimoto, M. Naito, Y. Kurozawa, H. Suzuki, T. Yoshimura, A. Tamakoshi, and J.S. Group. JACC Study Group. 2009. Serum adiponectin multimer complexes and liver cancer risk in a large cohort study in Japan. *Asian Pac. J. Cancer Prev.* 10(suppl): 87–90.

Larsson, S.C., and A. Wolk. 2007. Overweight, obesity and risk of liver cancer: a meta-analysis of cohort studies. *Br. J. Cancer*. 97:1005–1008. https://doi.org/10.1038/sj.bjc.6603932

Luo, Z., M. Zang, and W. Guo. 2010. AMPK as a metabolic tumor suppressor: control of metabolism and cell growth. *Future Oncol.* 6:457–470. https://doi.org/10.2217/fon.09.174

Ma, S.J., Y.X. Zheng, P.C. Zhou, Y.N. Xiao, and H.Z. Tan. 2016. Metformin use improves survival of diabetic liver cancer patients: systematic review and meta-analysis. *Oncotarget*. 7:66202–66211.

Manieri, E., and G. Sabio. 2015. Stress kinases in the modulation of metabolism and energy balance. *J. Mol. Endocrinol.* 55:R11–R22. https://doi.org/10.1530/JME-15-0146

Mao, X., J.Y. Hong, and L.Q. Dong. 2006a. The adiponectin signaling pathway as a novel pharmacological target. *Mini Rev. Med. Chem.* 6:1331–1340. https://doi.org/10.2174/138955706778992978

Mao, X., C.K. Kikani, R.A. Riojas, P. Langlais, L. Wang, F.J. Ramos, Q. Fang, C. Y. Christ-Roberts, J.Y. Hong, R.Y. Kim, et al. 2006b. APPL1 binds to adiponectin receptors and mediates adiponectin signalling and function. *Nat. Cell Biol.* 8:516–523. https://doi.org/10.1038/ncb1404

Marquardt, J.U., J.B. Andersen, and S.S. Thorgeirsson. 2015. Functional and genetic deconstruction of the cellular origin in liver cancer. *Nat. Rev. Cancer*. 15:653–667. https://doi.org/10.1038/nrc4017

Naugler, W.E., T. Sakurai, S. Kim, S. Maeda, K. Kim, A.M. Elsharkawy, and M. Karin. 2007. Gender disparity in liver cancer due to sex differences in MyD88-dependent IL-6 production. *Science*. 317:121–124. https://doi.org/10.1126/science.1140485

Nishizawa, H., I. Shimomura, K. Kishida, N. Maeda, H. Kuriyama, H. Nagaretani, M. Matsuda, H. Kondo, N. Furuyama, S. Kihara, et al. 2002. Androgens decrease plasma adiponectin, an insulin-sensitizing adipocyte-derived protein. *Diabetes*. 51:2734–2741.

Parkin, D.M., F. Bray, J. Ferlay, and P. Pisani. 2005. Global cancer statistics, 2002. *CA Cancer J. Clin.* 55:74–108. https://doi.org/10.3322/canjclin.55.2.74

Polyzos, S.A., J. Kountouras, C. Zavos, and E. Tsiaousi. 2010. The role of adiponectin in the pathogenesis and treatment of non-alcoholic fatty liver disease. *Diabetes Obes. Metab.* 12:365–383. https://doi.org/10.1111/j.1463-1326.2009.01176.x

Sabio, G., M. Das, A. Mora, Z. Zhang, J.Y. Jun, H.J. Ko, T. Barrett, J.K. Kim, and R.J. Davis. 2008. A stress signaling pathway in adipose tissue regulates hepatic insulin resistance. *Science.* 322:1539–1543. https://doi.org/10.1126/science.1160794

Salguero Palacios, R., M. Roderfeld, S. Hemmann, T. Rath, S. Atanasova, A. Tschuschner, O.A. Gressner, R. Weiskirchen, J. Graf, and E. Roeb. 2008. Activation of hepatic stellate cells is associated with cytokine expression in thioacetamide-induced hepatic fibrosis in mice. *Lab. Invest.* 88:1192–1203. https://doi.org/10.1038/labinvest.2008.91

Sharma, D., J. Wang, P.P. Fu, S. Sharma, A. Nagalingam, J. Mells, J. Handy, A.J. Page, C. Cohen, F.A. Anania, and N.K. Saxena. 2010. Adiponectin antagonizes the oncogenic actions of leptin in hepatocellular carcinogenesis. *Hepatology.* 52:1713–1722. https://doi.org/10.1002/hep.23892

Wang, Z.V., and P.E. Scherer. 2016. Adiponectin, the past two decades. *J. Mol. Cell Biol.* 8:93–100. https://doi.org/10.1093/jmcb/mjw011

Whitehead, J.P., A.A. Richards, I.J. Hickman, G.A. Macdonald, and J.B. Prins. 2006. Adiponectin–a key adipokine in the metabolic syndrome. *Diabetes Obes. Metab.* 8:264–280. https://doi.org/10.1111/j.1463-1326.2005.00510.x

Yamauchi, T., J. Kamon, Y. Minokoshi, Y. Ito, H. Waki, S. Uchida, S. Yamashita, M. Noda, S. Kita, K. Ueki, et al. 2002. Adiponectin stimulates glucose utilization and fatty-acid oxidation by activating AMP-activated protein kinase. *Nat. Med.* 8:1288–1295. https://doi.org/10.1038/nm788

Yannakoulia, M., N. Yiannakouris, S. Blüher, A.L. Matalas, D. Klimis-Zacas, and C.S. Mantzoros. 2003. Body fat mass and macronutrient intake in relation to circulating soluble leptin receptor, free leptin index, adiponectin, and resistin concentrations in healthy humans. *J. Clin. Endocrinol. Metab.* 88:1730–1736. https://doi.org/10.1210/jc.2002-021604

JEM

Supplemental material

Manieri et al., https://doi.org/10.1084/jem.20181288

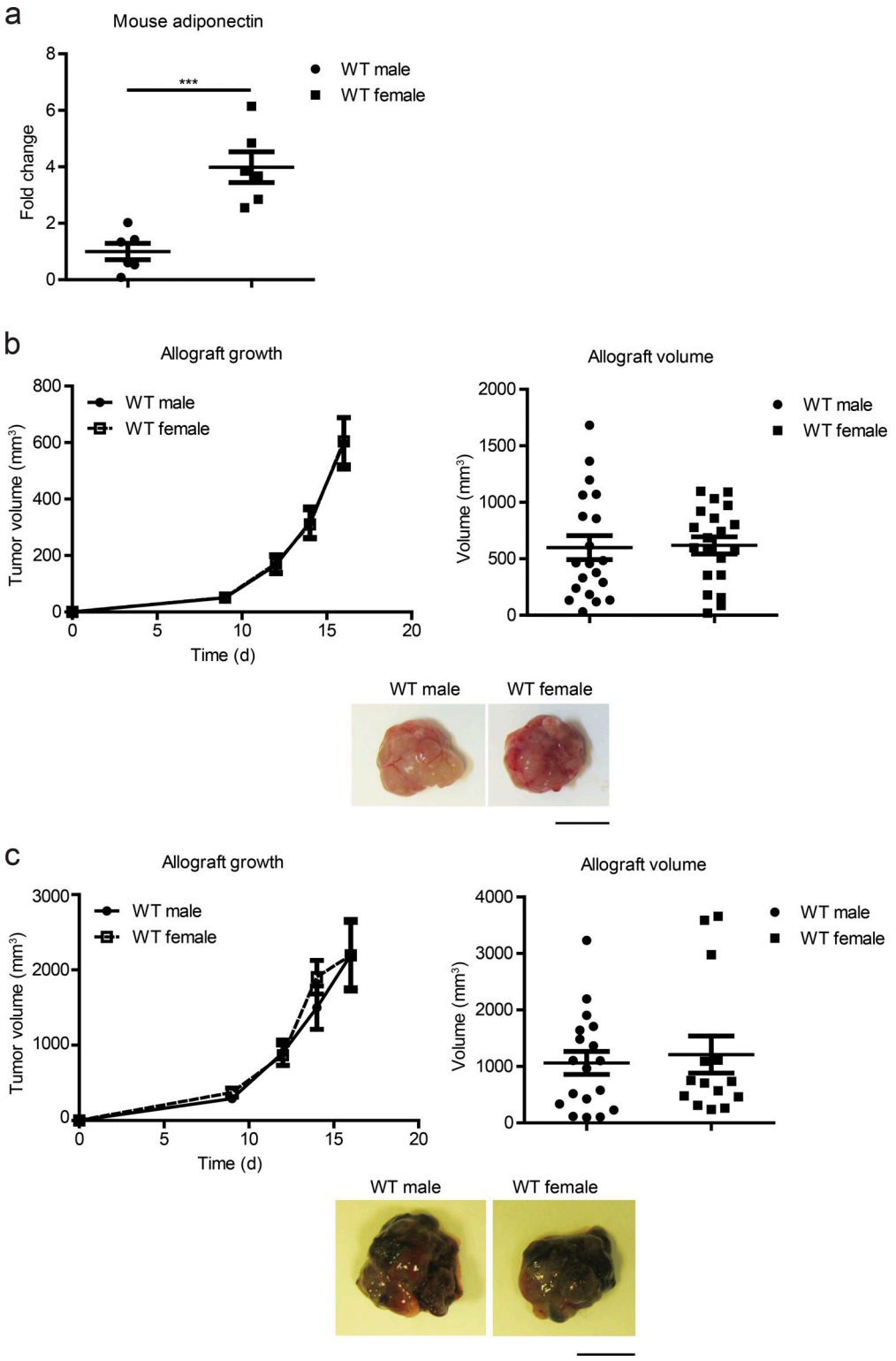

Figure S1. **Adiponectin quantification and specificity of gender differences in HCC. (a)** Circulating levels of adiponectin were measured in 11–12-wk-old female and male mice. Data are normalized to male mice and shown as means ± SEM; ***, P < 0.001; Student´s *t* test; *n* = 6. **(b)** Representative allografts and tumor volume quantification in WT male and female mice during the experiment and at sacrifice 3 wk after subcutaneous injection with 5 × 10^5 MC-38 cells (colon adenocarcinoma–derived cells) in each flank. Data are shown as means ± SEM; nonsignificant differences were found; two-way ANOVA coupled with Bonferroni's multiple comparisons test (allograft growth); Student's *t* test (allograft volume); *n* = 20 tumors (10 mice per genotype). Bar, 1 cm. **(c)** Representative allografts and tumor volume quantification in WT male and female mice during the experiment and at sacrifice 2 wk after subcutaneous injection with 5 × 10^5 B16-F10 cells (melanoma-derived cells) in each flank. Data are shown as means ± SEM; nonsignificant differences were found; two-way ANOVA coupled with Bonferroni's multiple comparisons test (allograft growth); Student's *t* test (allograft volume); WT male *n* = 18 tumors (10 mice); WT female *n* = 14 tumors (7 mice). Bar, 1 cm.

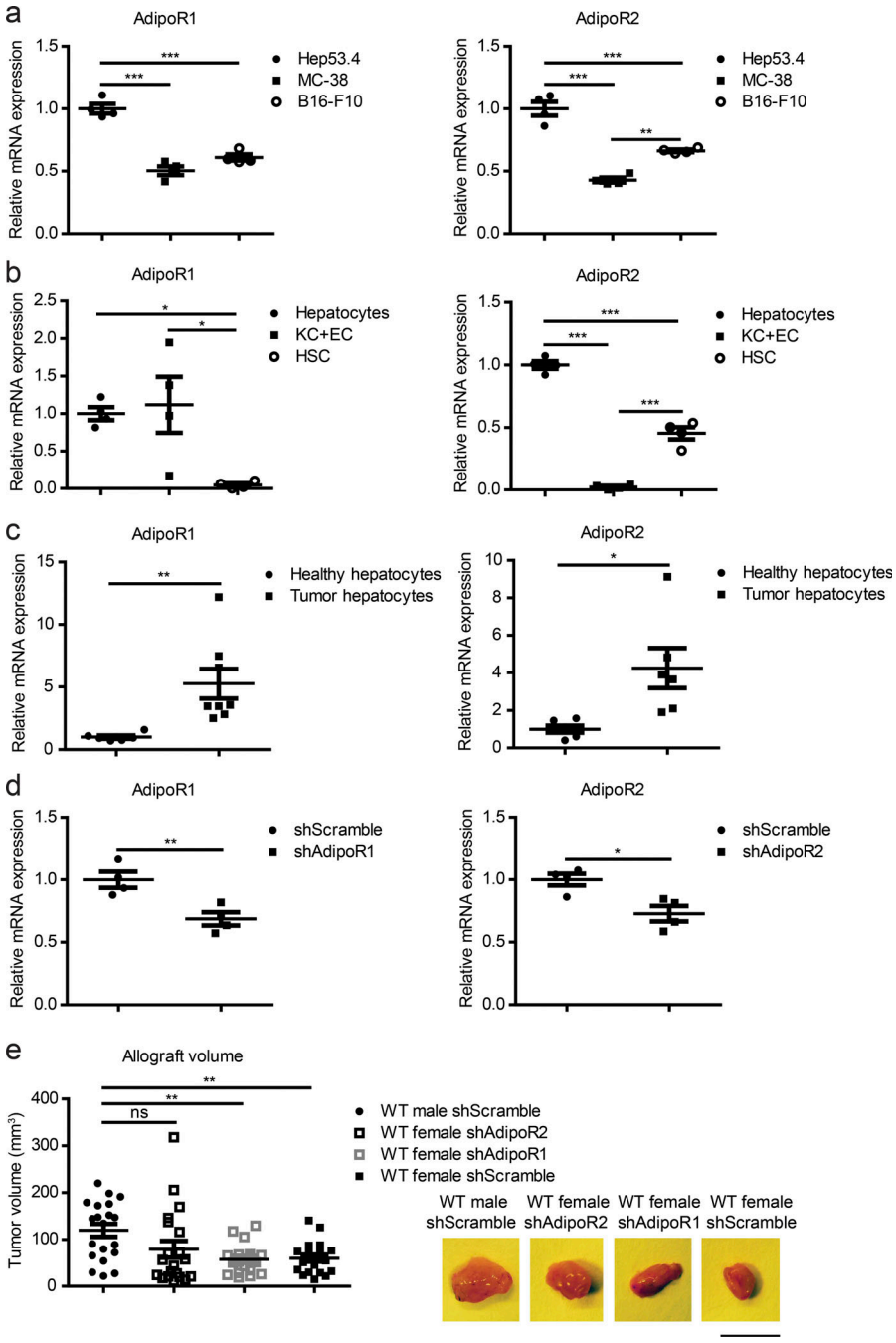

Figure S2. **Analysis of adiponectin receptors expression and their role in tumor growth. (a)** qRT-PCR analysis of adiponectin receptors 1 and 2 (*AdipoR1* and *AdipoR2*) in Hep53.4, MC-38, or B16-F10 tumor cells. mRNA expression was normalized to the amount of *Gapdh* mRNA in each sample. Data are normalized to Hep53.4 cells and shown as means ± SEM; **, P < 0.01; ***, P < 0.001; one-way ANOVA coupled with Bonferroni's multiple comparisons test; *n* = 4. **(b)** qRT-PCR analysis of *AdipoR1* and *AdipoR2* in different liver cell populations. mRNA expression was normalized to the amount of *Gapdh* mRNA in each sample. Data are normalized to hepatocytes and shown as means ± SEM; *, P < 0.05; ***, P < 0.001; one-way ANOVA coupled with Bonferroni's multiple comparisons test; *n* = 4. **(c)** qRT-PCR analysis of *AdipoR1* and *AdipoR2* in healthy hepatocytes and hepatocytes derived from hepatic tumors of C57BL/6J mice treated with DEN at P14 and 300 µg/liter TAA administered in the drinking water for 26 wk. mRNA expression was normalized to the amount of *Gapdh* mRNA in each sample. Data are normalized to healthy hepatocytes and shown as means ± SEM; *, P < 0.05; **, P < 0.01; Student's *t* test with Welch's correction; healthy hepatocytes *n* = 6; tumor hepatocytes *n* = 6–8. **(d)** qRT-PCR analysis of *AdipoR1* in Hep53.4 treated with a shRNA against AdipoR1 (shAdipoR1) or a scrambled control sequence, and analysis of *AdipoR2* in Hep53.4 cells treated with a shRNA against AdipoR2 (shAdipoR2) or a scrambled control sequence. mRNA expression was normalized to the amount of *Gapdh* mRNA in each sample. Data are normalized to shScramble cells and shown as means ± SEM; *, P < 0.05; **, P < 0.01; Student's *t* test; *n* = 4. **(e)** Representative allografts and tumor volume quantification in WT mice with hepatic tumors lacking AdipoR1 or AdipoR2 expression. Mice received subcutaneous injections with 1 × 10^6 Hep53.4 cells per flank, previously transduced with shRNA targeting AdipoR1, AdipoR2 or a control sequence (shScramble). Mice were sacrificed 3 wk after Hep53.4 cell injection. Data are shown as means ± SEM; **, P < 0.01; nonsignificant differences (ns); one-way ANOVA coupled with Bonferroni's multiple comparisons test; WT *n* = 20 tumors (10 mice per group), except WT female shAdipoR1 *n* = 18 tumors (10 mice). Bar, 1 cm.

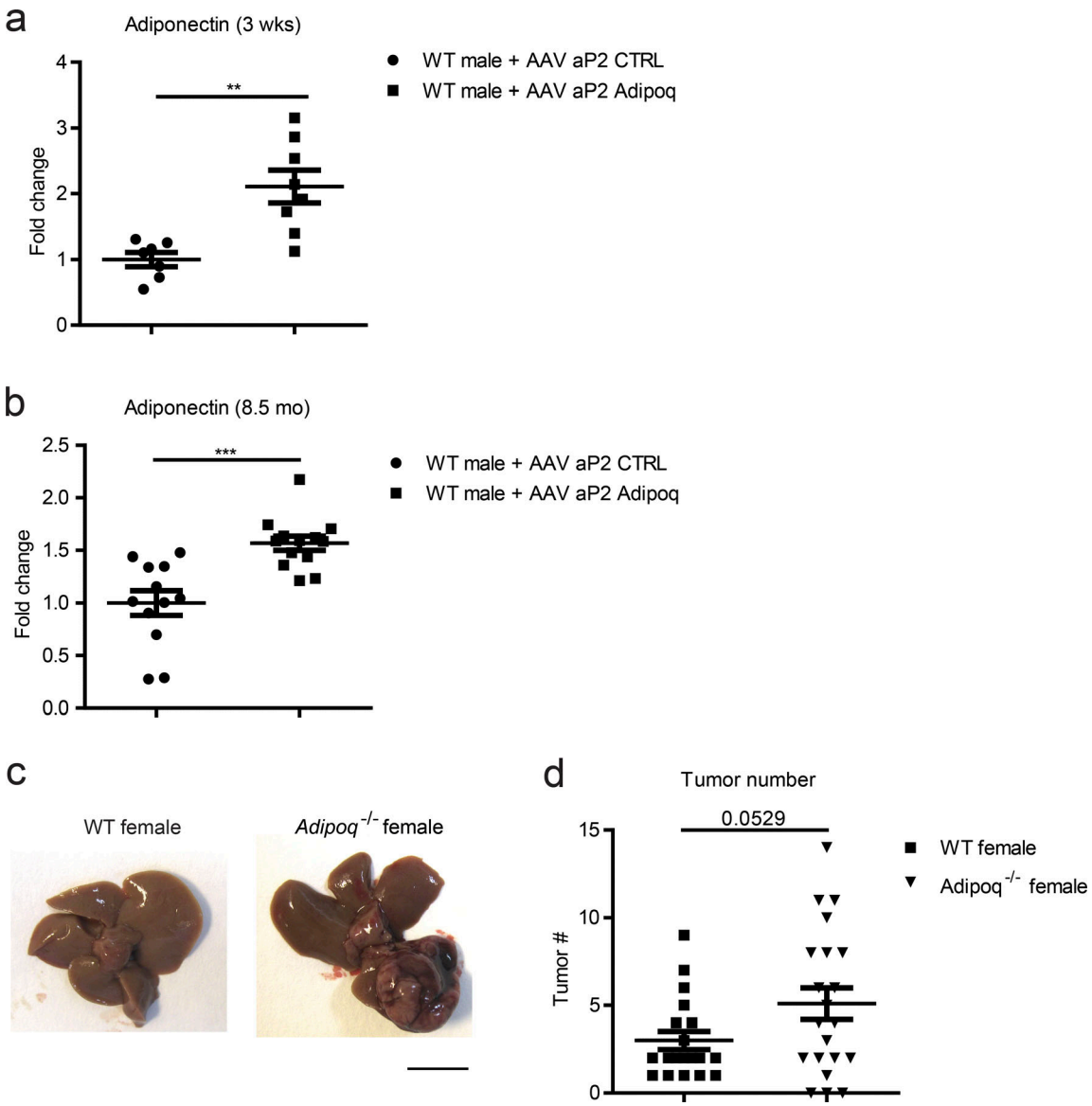

Figure S3. **Adiponectin quantification and overexpression in mice and effect of adiponectin deficiency in female mice. (a and b)** 6–7-wk-old WT male mice were injected with adeno-associated virus carrying a control sequence (WT male + AAV aP2 CTRL) or the adiponectin gene under control of the aP2 promoter (WT male + AAV aP2 Adipoq) at P1 and received an i.p. DEN injection (50 mg/kg body weight) 14 d later. AAV, adeno-associated virus; CTRL, control. **(a)** Quantification of circulating levels of adiponectin 3 wk after virus injection. Data are shown as means ± SEM; **, P < 0.01; Student´s *t* test with Welch's correction; WT male + AAV aP2 CTRL *n* = 7; WT male + AAV aP2 Adipoq *n* = 8. **(b)** Quantification of circulating levels of adiponectin 8.5 mo after virus injection. Data are shown as means ± SEM; ***, P < 0.001; Student's *t* test; WT male + AAV aP2 CTRL *n* = 12; WT male + AAV aP2 Adipoq *n* = 13. **(c)** HCC development 8 mo after i.p. injection with DEN (50 mg/kg) on P14 in WT and *Adipoq*$^{-/-}$ female mice. Bar, 1 cm. **(d)** Tumor number was determined at sacrifice. Data are shown as means ± SEM; Student's *t* test with Welch's correction; WT female *n* = 19; *Adipoq*$^{-/-}$ female *n* = 21.

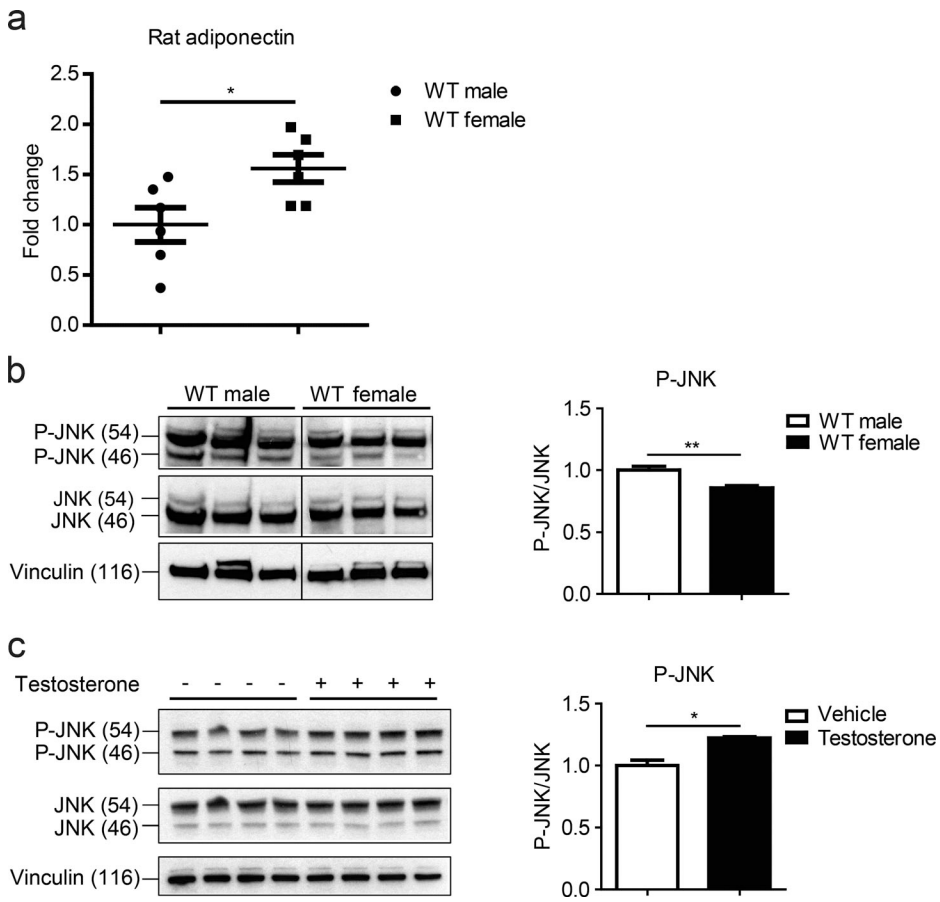

Figure S4. **Gender disparity in rat adiponectin, mice adipose tissue, and human adipocytes JNK phosphorylation. (a)** Circulating levels of adiponectin were measured in WT male and female rats. Data are normalized to male rats. Data are shown as means ± SEM; *, P < 0.05; Student's *t* test; *n* = 6. **(b)** Immunoblot analysis and quantification of phospho-JNK and JNK in adipose tissue from WT male and female mice. Vinculin protein expression was monitored as a loading control. Data are shown as means ± SEM; **, P < 0.01; Student's *t* test; WT male *n* = 3; WT female *n* = 4. **(c)** Immunoblot analysis and quantification of phospho-JNK and JNK in human differentiated adipocytes after treatment with testosterone (1,200 nM for 30 min). Vinculin protein expression was monitored as a loading control. Data are shown as means ± SEM; *, P < 0.05; Student's *t* test with Welch's correction; *n* = 4.

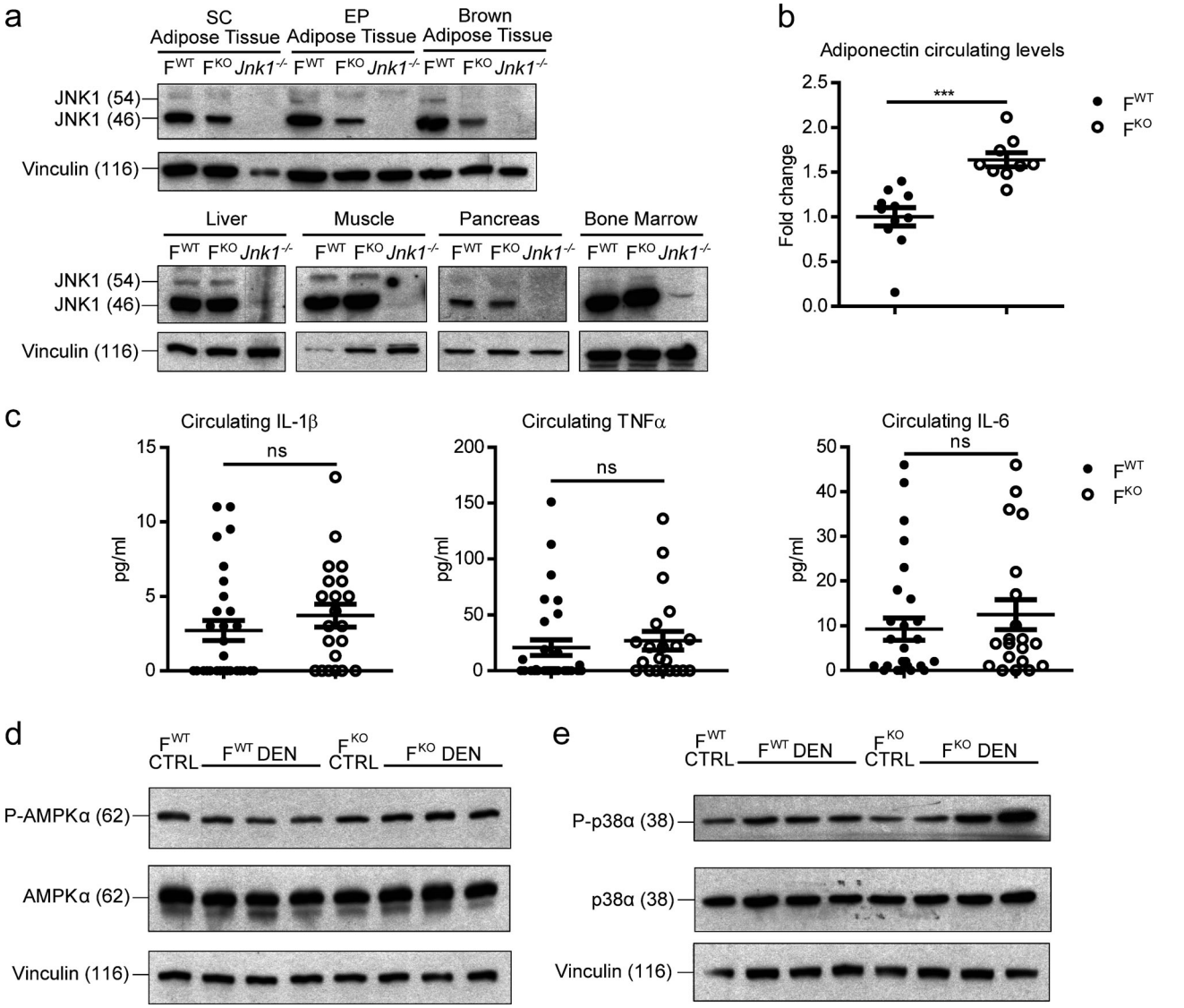

Figure S5. **Deletion of JNK1, cytokines levels in F^{WT} and F^{KO} mice, and adiponectin protection through AMPKα and p38α activation. (a)** Control (F^{WT}) and adipose tissue JNK1-deficient (F^{KO}) mice were sacrificed at 10 wk, and different tissues were extracted and analyzed by immunoblotting. Tissues from *Jnk1*$^{-/-}$ mice were used as a control. EP, epididymal; SC, subcutaneous. Vinculin protein expression was monitored as a loading control. **(b)** Circulating levels of adiponectin were measured in control (F^{WT}) and adipose tissue JNK1-deficient (F^{KO}) mice. Data are normalized to F^{WT} adiponectin levels and are shown as means ± SEM; ***, $P < 0.001$; Student's *t* test; F^{WT} $n = 11$; F^{KO} $n = 9$. **(c)** Control (F^{WT}) and adipose tissue JNK1-deficient (F^{KO}) mice were injected i.p. with DEN (50 mg/kg) on P14. Serum was analyzed after 8 mo on a Luminex platform to measure the levels of TNFα, IL-1β, and IL-6 adipokines. Data are shown as means ± SEM; nonsignificant differences were found (ns); Student's *t* test; $n = 20–30$. **(d and e)** F^{WT} and F^{KO} mice were injected i.p. with DEN (50 mg/kg) or saline (CTRL) on P14. **(d)** Immunoblot analysis of phospho-AMPKα, AMPKα and vinculin in livers obtained 15 d after DEN injection. **(e)** Immunoblot analysis of phospho-p38α, p38α, and vinculin in livers obtained 1 mo after DEN injection.

Table S1. **Characteristics of women and men**

Variable	Women (*n* = 9)	Men (*n* = 10)	P value
Age (yr)	49.7 (14.3)	58.1 (14.3)	0.278
Hypertension (n)	1 (11.1)	2 (20)	0.542
Diabetes mellitus (n)	0	0	–
BMI (kg/m^2)	25.8 (3.5)	26.8 (4.5)	0.905
Fasting blood sugar (mg/dl)	86.1 (12.8)	99 (10.5)	0.046
AST (IU/liter)	24.3 (12.9)	21.1 (5.1)	0.798
ALT (IU/liter)	32.5 (32.2)	30.3 (20.7)	0.878
Alkaline phosphatase (IU/liter)	77.4 (21.4)	95.3 (35.3)	0.536
Bilirubin (mg/dl)	0.5 (0.3)	0.9 (0.5)	0.059
Albumin (mg/dl)	4.5 (0.3)	4.5 (0.6)	0.607
Total cholesterol (mg/dl)	205.9 (50)	189.9 (47.9)	0.383
Triglycerides (mg/dl)	118.7 (67.5)	116 (49.7)	0.902
LDL-cholesterol (mg/dl)	121.7 (44.5)	123.7 (43.7)	0.945
HDL-cholesterol (mg/dl)	62.1 (14.6)	42.9 (12.7)	0.035
Adiponectin (µg/ml)	19.69 (2.663)	14.18 (3.620)	0.0016

Variables are presented as mean (SD) or absolute frequency (%) and are compared by means of Mann–Whitney *U* test or χ^2 test. ALT, alanine aminotransferase; AST, aspartate aminotransferase; BMI, body mass index; HDL, high-density lipoprotein; LDL, low-density lipoprotein.

Table S2. **qRT-PCR primers**

Gene	Forward primer (5′→3′)	Reverse primer (5′→3′)
AdipoR1	AATGGGGCTCCTTCTGGTAAC	GGATGACTCTCCAACGTCCCT
AdipoR2	GGCCCATCATGCTATGGAAC	GTGAGGGATCACTCGCCATC
Gapdh	TGAAGCAGGCATCTGAGGG	CGAAGGTGGAAGAGTGGGA

Table S3. **Solutions for hepatic perfusion**

Solution (ml)	A	B	C	D
SC-1	100	–	–	–
SC-2	–	100	100	100
DNAse I (stock solution)	–	–	–	1[a]
Collagenase D (mg)	–	–	110	80
Pronase E (mg)	–	40	–	50

[a]DNase I stock solution: 2 mg/ml in GBSS-B.

Table S4. **Stock solutions for hepatic cell isolation**

Stock solution (mg)	SC1	SC2	GBSS-A	GBSS-B
EGTA	95	-	-	-
Glucose	450	-	495.5	495.5
HEPES	1,190	1,190	-	-
KCl	200	200	185	185
$Na_2HPO_4 \cdot 2H_2O$	75.5	75.5	37.5	37.5
NaCl	4,000	4,000	-	4,000
$NaH_2PO_4 \cdot H_2O$	39	39	-	-
$NaHCO_3$	175	175	113.5	113.5
Phenol Red	3	3	3	3
$CaCl_2 \cdot 2H_2O$	-	280	112.5	112.5
KH_2PO_4	-	-	15	15
$MgCl_2 \cdot 6H_2O$	-	-	105	105
$MgSO_4 \cdot 7H_2O$	-	-	35	35
H_2O to (ml)	500	500	500	500

For the density gradient medium, the following solutions were prepared before starting the perfusion of the liver: Nycodenz 1: 5.18 g/total volume 15 ml GBSS-A; Nycodenz 2: 3.63 g/total volume 25 ml GBSS-A.

Available online at www.sciencedirect.com

ScienceDirect

Current Opinion in Physiology

Stress-activated kinases signaling pathways in cancer development

Leticia Herrera-Melle, María Crespo, Magdalena Leiva and Guadalupe Sabio

Cancer is a large group of diseases characterized by abnormal cell growth that can lead to metastasis. It is the second leading cause of death worldwide, and its incidence is expected to rise over the next decades. Stress-activated protein kinases (SAPK) are important players in its regulation. Several studies have tried to unravel their role; however, their pro-tumorigenic or anti-tumorigenic properties are sometimes controversial. In this review, we will discuss the main roles of the different SAPK in the control of tumor development through essential processes such as cell proliferation, apoptosis or invasiveness. We will also show the latest discoveries regarding the contribution of SAPK in shaping tumor microenvironment through the regulation of organ crosstalk and immune cell response during cancer progression. All these studies are relevant examples of how SAPK offer new therapeutic avenues for cancer patients that may help increase their survival.

Address
Centro Nacional de Investigaciones Cardiovasculares (CNIC), 28029 Madrid, Spain

Corresponding authors: Leiva, Magdalena (magdalena.leiva@cnic.es), Sabio, Guadalupe (gsabio@cnic.es)

Current Opinion in Physiology 2021, **19**:22–31

This review comes from a themed issue on **Inflammation**

Edited by **Pilar Alcaide** and **Michael Schnoor**

Available online 21st August 2020

For complete overview of the section, please refer the article collection - Inflammation

https://doi.org/10.1016/j.cophys.2020.08.005

2468-8673/ 2020 Elsevier Ltd. All rights reserved.

Introduction of stress kinases

The stress-activated protein kinases (SAPK) relay, amplify and integrate signals, mainly associated with cellular stress, to allow cell adaptation [1]. Its prolonged and disturbed activation has been implicated in the development of several diseases such as diabetes and cancer [2]. In order to promote signal amplification and fidelity, SAPK cascades are triple kinase pathways that include a MKKK (MAPK kinase kinase), a MKK (MAPK kinase) and a terminal MAPK [3]. There are two major groups of distinctly regulated SAPK: c-Jun N-terminal kinase (JNK) and p38. The SAPK are activated upon dual phosphorylation of tyrosine and threonine residues in a conserved Thr-X-Tyr loop sequence, where X is proline for JNKs and glycine for p38s [4]. It is described that the activation of p38 pathway is primarily driven by MKK3/6, while the JNKs are regulated by MKK4/7 [5]. The JNK family has three members, JNK1, 2 and 3 [6], whereas the p38 has four, p38α, β, γ and δ [1].

SAPK in tumor cells

Deregulation of SAPK signaling underlies different types of cancers affecting cellular homeostatic processes such as proliferation or apoptosis. Besides, SAPK can also control detachment, migration and invasion of malignant cells, playing a crucial role in metastasis [7].

p38 in tumor cells

The role of p38 in cell proliferation in different types of cancer has been widely demonstrated. However, these effects could be opposite depending on the p38 family member and the cancer cell type. For instance, in several glioblastoma cell lines, the activation of p38 is responsible for the clonogenic growth of the tumor through the activation of the upstream kinase ASK1 [8]. This over-activation is associated with an elevated expression of the FK506-binding protein 9 (FKBP9), which is related to poor prognosis in glioma patients [8]. Besides, inhibition of p38α/β with several chemical inhibitors or genetic silencing of p38α is enough to block these proliferative effects [8]. Interestingly, the selective inhibition of p38α significantly reduced cell invasiveness of a glioblastoma cell line in another study [9], indicating an additional role of this p38 family member. This dual effect of p38 is also observed in pancreatic ductal adenocarcinoma, in which it has been reported that the oncogene-associated protein Leucin-rich-alpha-2-glycoprotein-1 (LRG-1) promotes cell proliferation and migration activating the EGFR-p38α/β signaling axis [10]. On the contrary, the activation of Trib2-p38 axis has been proposed to be required in myeloid leukemia to induce cell cycle arrest and an adequate stress response in drug-treated leukemic cells [11]. Given that as a pseudokinase Trib2 is not able to phosphorylate p38, further investigations are needed to define this mechanism.

The activation of p38 pathway has also been linked with pro-metastatic and anti-metastatic functions in different tumors, and the involved mechanisms are starting to be defined. For instance, in human colorectal cancer (CRC)

p38α/β inhibits ubiquitination and degradation of the oncoprotein Forkhead box C1 (FOXC1), promoting its stability and consequently increasing migration and invasion of tumor cells [12]. In contrast, in a previous study, p38α downregulation resulted in increased levels of the cytokine parathyroid hormone-like hormone, which is associated with the capacity of CRC to colonize the lung [13].

In the last decade, multiple efforts have been done to define the role of each p38 family member in different types of cancers (Figure 1). p38α has been recently shown to be an important contributor to breast cancer development. Del Barco Barrantes *et al.* demonstrated that p38α is critical for controlling the luminal progenitor cell fate by affecting mammary tumor formation in mice [14]. Additionally, the same research group showed that p38α activates CtBP-interacting protein, regulating DNA repair and restricting chromosome instability, thus increasing cancer cell survival in breast tumors [15•]. It is also notable that p38α has a great impact in CRC development. Gupta et al. found that p38α acts as a tumor suppressor or a promoter in function of the healthy or malignant status, respectively, of the intestinal epithelial cells in mice [16]. In fact, p38α ablation in intestinal epithelial cells increases the colitis-associated CRC by altering the homeostasis of intestinal barrier. However, this deletion in transformed colon epithelial cells reduces colon tumor burden. Indeed, later on, it was shown that chemical inhibition of p38α/β might be a potential therapeutic strategy for the treatment of CRC in humans, alone or in combination with mTOR kinase inhibitors in function of protein phosphatase 2AC (PP2AC) levels [17].

Recently, it has been demonstrated that p38γ triggers the cell cycle acting as a CDK-like kinase in the hepatocyte and, as a consequence, lack of hepatic p38γ protects mice against hepatocellular carcinoma (HCC) [18•]. p38γ is activated in hepatocytes by stress and phosphorylates retinoblastoma protein (RB), inducing proliferation. This mechanism to control cell cycle might be a specific response of the cell after the stress where the mitogenic stimuli that induce cyclins are absent and, in consequence, CDKs are inactive [18•]. The authors showed that p38γ is activated in different animal models of HCC, suggesting a key role of this kinase controlling stress-induced proliferation in hepatocytes [18•]. Moreover, human HCC highly expresses p38γ, highlighting the potential of this kinase as a therapeutic target [18•]. This pro-tumorigenic activity of p38γ has been also seen in cutaneous-T cell lymphoma in which its activation is crucial for T cell transformation. Indeed, the treatment

Figure 1

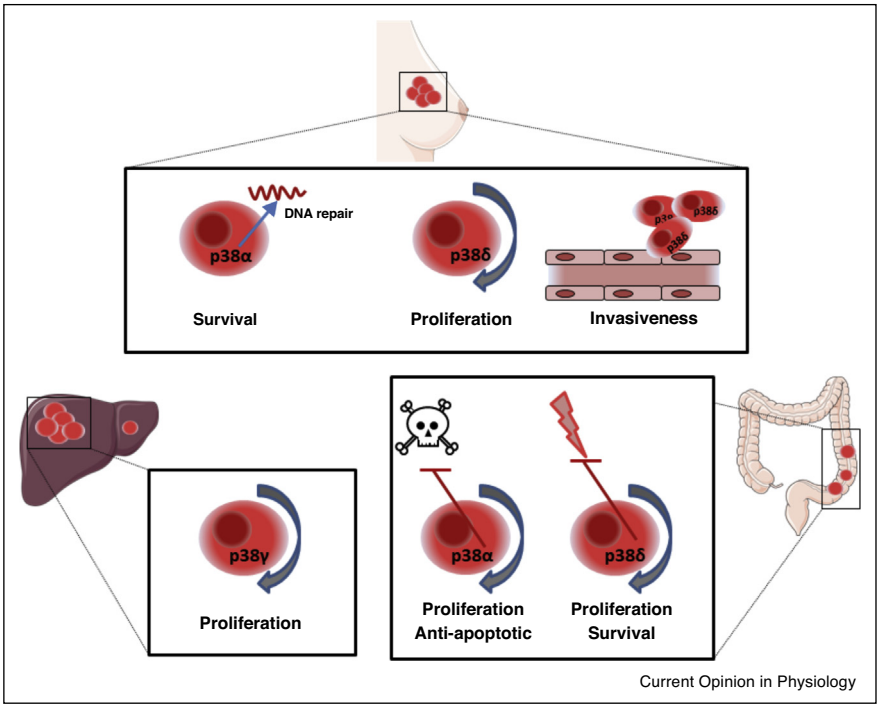

Overview of p38 family members in distinct types of cancer. In breast tumors, while p38α coordinates the DNA damage response increasing the survival of tumor cells, p38δ displays proliferative and invasive properties. In hepatocellular carcinoma (HCC), p38γ acts as a CDK-like kinase inducing cell proliferation. In colorectal cancer (CRC), p38α has proliferative functions and inhibits apoptosis of transformed colon epithelial cells, while p38δ contributes to CRC by supporting proliferation and protecting against drug-induced cell death.

of T cancerous cells with the p38γ inhibitor F7/PIK75 reduced tumor growth [19]. However, the molecular mechanism underlying the T cell alterations needs to be clarified.

p38δ is highly expressed in all types of human breast cancers, suggesting a pro-tumoral role of this kinase. In a mouse model of metastatic breast cancer, p38δ played proliferative and cell detachment functions [20], affecting the tumor growth and promoting metastasis. A proliferative function of p38δ has also been described in CRC [21]. Depletion of p38δ in tumor xenografted CRC mouse models impairs tumor growth. Additionally, p38δ induces pro-survival signaling and protects against drug-induced cell death, suggesting that p38δ inhibition could be a promising therapeutic strategy to use in combination for CRC treatment. All these findings support the identification of the role of the different p38 family members as a promising strategy to develop novel cancer therapies.

JNK in tumor cells

JNK can act either as a positive or a negative regulator in tumorigenesis (Figure 2). While it has been proposed that transient JNK activation promotes cell survival, prolonged JNK activation has anti-tumorigenic effects, although further studies with animal models will be needed to fully understand the dual function of these kinases [22].

JNK has been shown to promote cell proliferation and survival through the activation of AP1 transcription factor [23]. Colleoni et al. demonstrated that both JNK1 and JNK2, and possibly JNK3, can act as CDK4-activating kinases through the independent phosphorylation of CDK4 and p21 [24]. Since JNKs inhibition decreases cell cycle entry through a reduced activation of cyclin D1-CDK4 complexes, therapeutic approaches targeting JNKs might control the deregulated CDK4 activation found in some cancers [24]. The tumor-promoting function of JNK has been shown in several tumor types. For instance, JNK is required for Ras-induced lung tumor formation, mainly due to increased proliferation [25]. In addition, mitochondrial dysfunction and oxidative stress promote an increase in TNFα production by Kupffer cells, which then causes JNK-mediated intrahepatic cholangiocellular proliferation and transformation [26]. Apart

Figure 2

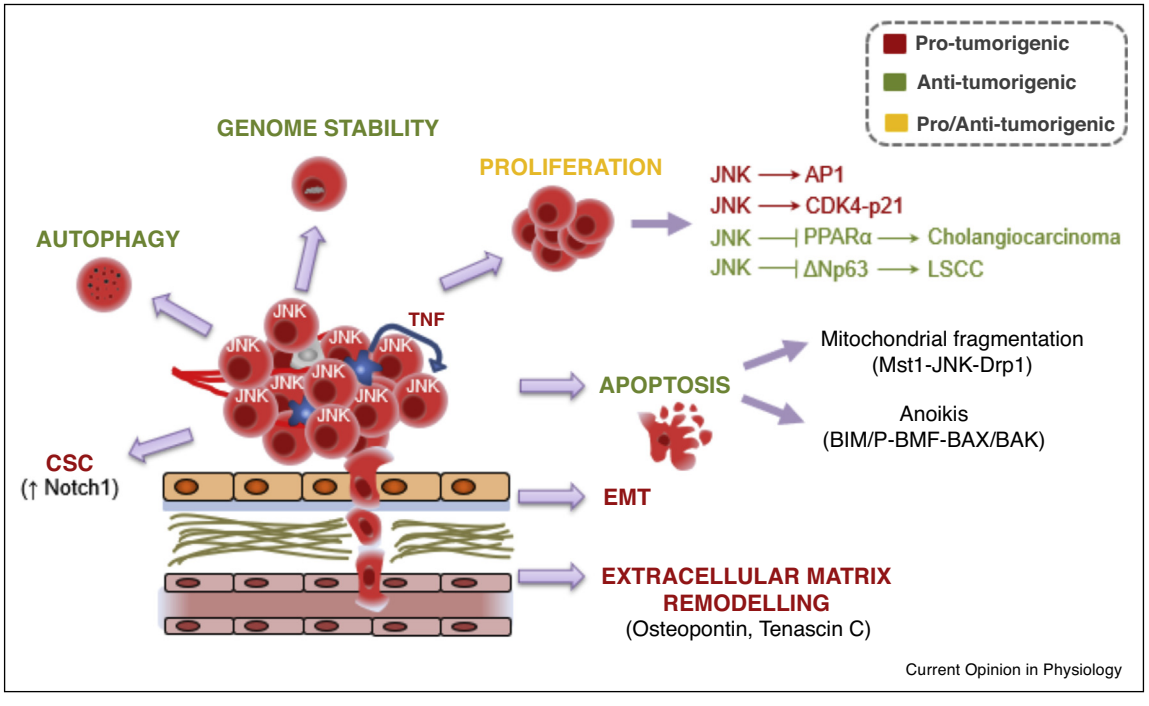

Overview of JNK function in the regulation of tumorigenesis. JNK regulates different processes with a tumor-promoting function (red), with a tumor suppressor role (green), or both (yellow), depending on the type of tumor and on the context. JNK promotes genome stability in breast cancer but abrogates breast cancer progression by the induction of autophagy or apoptosis through mitochondrial fragmentation. JNK also promotes anoikis by increasing BIM expression and phosphorylating BMF, whereas it provokes cancer stem cell (CSC) maintenance. JNK also contributes to metastatic dissemination, mediating epithelial-mesenchymal transition (EMT) and extracellular matrix remodeling through the upregulation of osteopontin or tenascin C. Regarding proliferation, JNK can have a pro-tumorigenic role phosphorylating AP1, CDK4 or p21, or an anti-tumorigenic function by inhibiting PPARα or the ΔNp63 pathway, which are involved in cholangiocarcinoma or lung squamous cell carcinoma (LSCC) development, respectively. The relevance of the tumor microenvironment in the control of JNK function is also depicted as TNF-mediated JNK activation.

from the effect of direct JNK1/2 deletion in the liver, this study highlights the importance of altering the tumor microenvironment to prevent stress kinases-mediated proliferation [26]. Conversely, a recent study has shown that deletion of both JNK1 and JNK2 in hepatocytes promotes intrahepatic cholangiocarcinoma by deregulating bile acid production and increasing the proliferation of cholangiocytes, showing that, in this context, hepatocyte JNK1/2 have an opposite role compared to other situations [27•]. Manieri *et al.* found that hepatic JNK deficiency promotes spontaneous cholangiocarcinoma development through PPARα-dependent alterations in bile acid metabolism and elevated FXR/FGF15/FGR4, subsequently increasing ERK signaling in cholangiocytes [27•]. This protective role of JNK1/2 in hepatocytes has been confirmed by an independent group using DEN and NEMO liver cancer models, also finding a hyperactivation of ERK pathway in these tumors [28]. These studies might indicate that although reduction of hepatic JNK activation after tissue damage would be protective against liver cancer, complete deletion of this pathway might be deleterious as it is necessary for the physiological control of bile acid production.

The role of JNK in metastasis has also been described. JNK has been shown to decrease the intercellular adhesion of cells by negatively controlling the expression of E-cadherin, thus contributing to epithelial-mesenchymal transition (EMT) [25]. Moreover, Insua-Rodríguez *et al.* found that JNK signaling increases the expression of extracellular matrix remodeling and stem cell niche components that promote lung metastasis [29]. In addition, JNK pathway also mediates EMT and stemness in CRC [30], as well as stem cell phenotype in breast cancer through Notch1 upregulation [31].

Other studies have identified opposite functions for different JNK family members. For instance, while JNK1 has been related to tumor-suppressive activity, JNK2 is implicated in melanoma cell proliferation, invasiveness and resistance to BRAF inhibitors, and this activity is more important when JNK1 is suppressed [32].

The role of JNK in breast cancer is controversial. Some studies have linked elevated JNK activity with poor clinical outcome in breast cancer patients [29,31], while others have shown that *loss-of-function* mutations of the JNK pathway are found in human breast cancer [33•]. Accordingly, it has been shown that JNK controls genome stability, thus preventing tumor formation, with no anti-proliferative effect in the growth of established tumors of the breast epithelium [33•]. Besides, the activation of JNK can promote autophagy and prevent breast cancer progression [34]. The tumor-suppressive role of JNK is also due to the promotion of apoptosis in several tumor cell types. A recent study shows that Mst1 overexpression in breast cancer activates the JNK-Drp1 axis, which causes apoptosis due to mitochondrial fragmentation [35]. In addition, JNK promotes apoptosis induced by epithelial cell detachment (anoikis) by increasing BIM expression and BMF phosphorylation leading to BAX/BAK-dependent apoptosis, a process which constitutes a barrier to metastatic dissemination [36]. Furthermore, JNK signaling has been shown to reduce the development of invasive adenocarcinoma in the PTEN-deficient model of prostate cancer [37]. Moreover, JNK inactivation is also frequent in lung squamous cell carcinoma (LSCC) and negatively correlates with the survival rates of LSCC patients, which has helped to identify another suppressive role of MKK7-JNK1/2 by acting downstream of the tumor suppressor *Lkb1* and inhibiting the oncogenic ΔNp63 pathway [38].

SAPK in tumor microenvironment

Tumor development can be controlled by cytotoxic innate and adaptive immune cells, together with other metabolic and endocrine factors. SAPK play different roles within the tumor microenvironment, including the induction of cytokine expression and the production of growth factors, adipokines and other metabolites, important for intracellular signaling during tumor development [25,39].

p38 in tumor microenvironment

In the vast majority of the studies, p38 presents a protumorigenic function through the promotion of innate inflammation and suppression of T cell activity in the tumor. However, there are some exceptions in which p38 presents the opposite role (Figure 3). Tumor-associated macrophages (TAMs) are crucial for cancer progression, and p38 is determinant in the polarization and function of these cells. The activation of the main downstream effector of p38α, MK2, in TAMs promotes the switch from tumor-inhibiting phenotype (M1) to tumor-promoting phenotype (M2) in CRC. Moreover, myeloid p38α-MK2 pathway is involved in the production of pro-angiogenic factors by M2 macrophages that increase tumor vascularization [40]. Contrary to this finding, p38α exhibits anti-angiogenic activity in mesenchymal and perivascular cells (MSCs) of the vessels surrounding the tumor [41]. Myeloid p38α is also necessary for the secretion of insulin-like growth factor-1 (IGF-1) by M2 macrophages in CRC. IGF-1 works as a chemoattractant that promotes $Ly6C^{high}CCR2^{+}$ monocyte infiltration into tumors. Besides, p38α in $Ly6C^{high}CCR2^{+}$ monocytes, induces their egress from the bone-marrow to the tumor. Thus, deletion of myeloid p38α decreases inflammation and protects against CRC progression [42•]. These results agree with the finding that lack of p38α substrate, MK2, in the myeloid compartment exerts an anti-inflammatory and anti-tumoral effect, while its deletion in epithelial cells is not protective [40]. Myeloid p38δ ablation also protects against tumor growth in skin carcinogenesis. However, the molecular mechanism underlying these

Figure 3

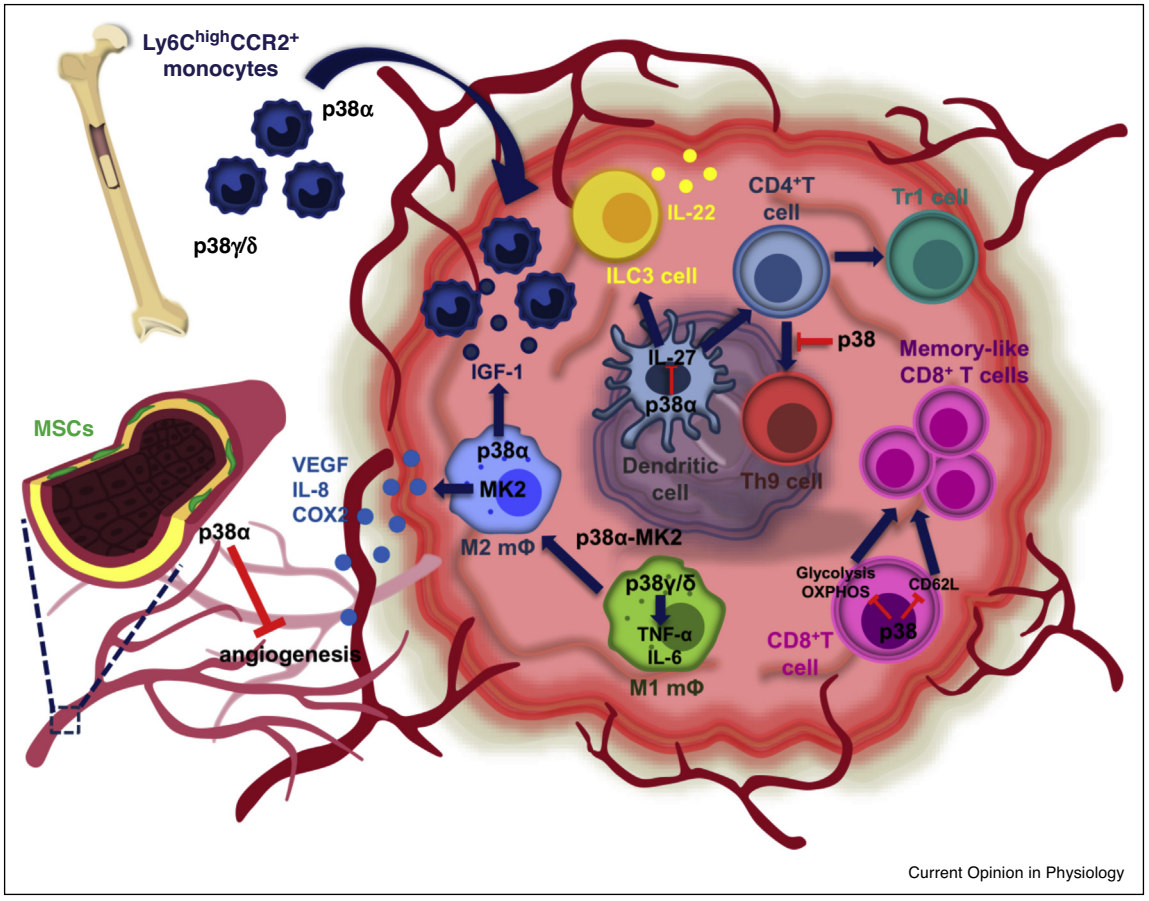

Overview of p38 functions in the control of tumor microenvironment. p38α, γ and δ in the myeloid compartment promote monocyte recruitment to the tumor. In tumor-associated macrophages (mΦ), p38α-MK2 induces transition from anti-tumor (M1) to tumor-promoting (M2) phenotype, and p38γ/δ control TNFα and IL-6 expression in macrophages, increasing inflammation. While myeloid p38α activates angiogenesis, p38α in mesenchymal and perivascular cells (MSCs) of the vessels inhibits it. p38α in dendritic cells suppresses the expression of IL-27, affecting the activation and the anti-tumor function of CD4+ T cells. In T cells, p38 inhibits CD4+ T cell differentiation into Th9 and reduces CD8 + T cell anti-tumor function by decreasing their memory-like phenotype.

preventive effects remains undefined [43]. In concordance with the important role of p38γ and p38δ controlling neutrophil migration [44•] and proinflammatory cytokine expression by macrophages [45], it has been demonstrated that these kinases contribute to the recruitment of these myeloid cells into the tumor, inducing CRC progression by promoting inflammation and endothelial cell proliferation [46•].

The malignant role of p38γ in CRC was also reported in the epithelial compartment, where p38γ is necessary for the transduction of inflammatory signals in intestinal epithelial cells and for the subsequent induction of inflammatory cytokines [47].

The pro-tumoral immune environment driven by p38α in CRC development has also been demonstrated in dendritic cells (DCs), where p38α inhibits the expression of IL-27, a cytokine required for Tr1 differentiation and the IL-22 secretion by ILC3 cells in the intestine. These processes are crucial to avoid aberrant immune responses and to maintain a proper epithelial function in the intestine [48].

Regarding the role of p38 in T cell function during cancer, it was shown that activated p38 is part of the negative feedback loop of Fas-induced $CD4^+$ T cell differentiation into the tumor suppressor Th9 cell type [49]. On the other hand, in $CD8^+$ T cells, p38 inhibition improves the anti-tumor activity of these cells by increasing their memory-like phenotype at transcriptional and metabolic levels. Thus, *ex vivo* inhibition of p38 in T cells and later adoptive transfer in a mouse model of melanoma enhanced $CD8^+$ T cell expansion and infiltration into tumor, increasing the survival rate and reducing tumor growth [50•].

Figure 4

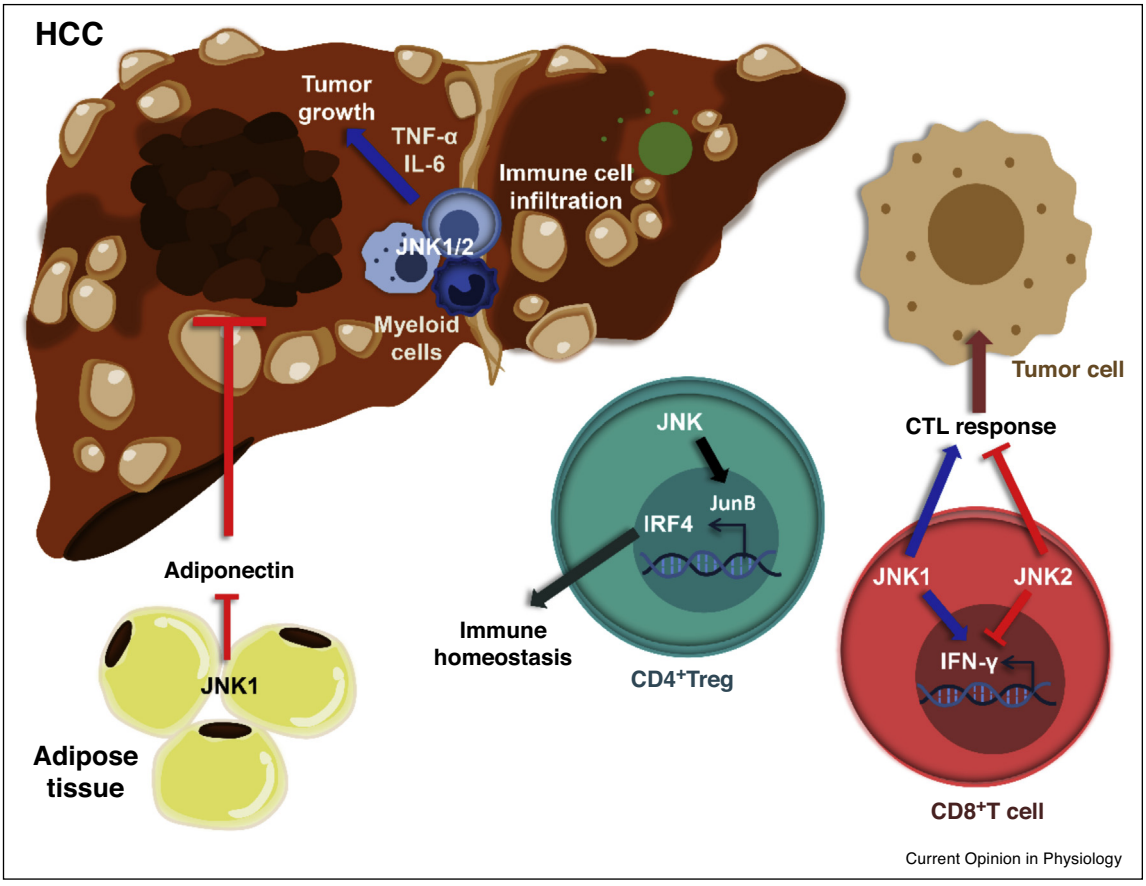

Overview of JNK function in the control of tumor microenvironment. JNK1 and JNK2 have opposite roles in $CD8^+$ T cells regulating IFN-γ production. Lack of JNK1 increases tumor susceptibility. In contrast, depletion of JNK2 in $CD8^+$ T cells enhances $CD8^+$ T cell-mediated anti-tumor immune response. JNK substrate JunB is a critical regulator of interferon regulatory factor 4 (IRF4) and, in consequence, of Treg-mediated immune homeostasis. JNK1/2 in macrophages and Kupffer cells control TNFα and IL-6 production promoting HCC. JNK1 in adipose tissue inhibits adiponectin secretion and, in consequence, its activation in male adipose tissue increases their susceptibility to develop HCC. Cytotoxic T lymphocyte (CTL).

JNK in tumor microenvironment

On one hand, JNK1 and JNK2 have divergent roles in regulating the effector functions of $CD4^+$ and $CD8^+$ T cells (Figure 4). Their function in $CD8^+$ T cell-mediated tumor immunosurveillance has been demonstrated in animal models [51,52]. Lack of JNK1 increases tumor susceptibility, and this effect is mediated by the role of JNK1 in regulating IFN-γ transcription program and effector functions of $CD8^+$ T cells [51]. In contrast to JNK1, JNK2 negatively regulates antigen-specific $CD8^+$ T cell proliferation, IFN-γ production and cytotoxic T lymphocyte function, and depletion of JNK2 in $CD8^+$ T cells enhances $CD8^+$ T cell-mediated anti-tumor immune response [52]. These results suggest that while inhibition of JNK1 would increase tumor burden, selective block of JNK2 in $CD8^+$ T cells may potentially enhance anti-tumor immunity [52]. Moreover, in $CD4^+$ cells, the JNK substrate JunB is a critical regulator of interferon regulatory factor 4-dependent Treg effector transcription program. These data highlight JunB as a critical regulator of Treg-mediated immune homeostasis [53].

On the other hand, the role of JNK pathway controlling innate immune system and its effects in tumor progression have been mainly studied in HCC development (Fig. 4). It was demonstrated that the effect of JNK1 deficiency to suppress carcinogen-induced HCC was mediated by lack of JNK1 in the myeloid compartment [54]. Lack of JNK1 might account for the decreased expression of inflammatory cytokines such as TNFα and IL-6 by hepatic innate immune cells [55]. These results have been corroborated later using conditional deletion of JNK1/2 in myeloid cells [56]. Finally, it has been recently demonstrated that JNK1 can also regulate liver cancer development by controlling adipose tissue secretion of the most abundant adipokine, adiponectin [57•]. Adiponectin activates protective signaling

pathways in the liver, such as AMPK and p38α. Activation of JNK1 by testosterone inhibits adiponectin secretion, resulting in increased susceptibility to liver cancer development in males [57•].

Future remarks

The role of stress kinases in cancer development has been extensively studied, mainly in cell culture experiments and using inhibitors. However, little is known about the role of the different family members. Recent studies using conditional mice lacking specific p38 or JNK family members highlight the contrary functions of this kinases belonging to the same family. Then, future studies should focus on the specific roles of the each SAPK family member in cancer development. Animal studies are encouraged, since most of the current findings are based on *in vitro* studies. In addition, more specific inhibitors would be needed as an important tool to understand these pathways and to use these kinases as therapeutic targets for cancer treatment.

A recent report has identified the role of SAPK pathway in controlling not only the secretome of immune cells [39], but also metabolites secreted by other important tissues such as adipose tissue [57•]. Analyzing the effects of SAPK in tissue secretome would be of interest in order to find pro-tumorigenic or anti-tumorigenic molecules useful for the treatment and diagnosis of cancer.

Author contribution

All authors were responsible for drafting the article and revising it critically for important intellectual content. All authors approved this version to be published.

Conflict of interest statement

Nothing declared.

Acknowledgements

L.H-M and M.C are fellows of the FPU (FPU15-05802) and FPI (BES-2017-079711), respectively. GS is granted by funds from European Regional Development Fund (ERDF): to G.S. European Union's Seventh Framework Programme (FP7/2007-2013) ERC 260464, EFSD/Lilly European Diabetes Research Programme Dr Sabio, 2017 Leonardo Grant for Researchers and Cultural Creators, BBVA Foundation (Investigadores-BBVA-2017) IN[17]_BBM_BAS_0066, MINECO-FEDER SAF2016-79126-R, Fundación AECC PROYE19047SABI and Comunidad de Madrid IMMUNOTHERCAN-CM S2010/BMD-2326 and B2017/BMD-3733; ML is granted by Fundación AECC INVES20026LEIV. The CNIC is supported by the Ministerio de Ciencia, Innovación y Universidades (MCNU) and the Pro CNIC Foundation, and is a Severo Ochoa Center of Excellence (SEV-2015-0505). We thank our collaborators and the students and fellows who contributed to the studies in Sabio's group over the years. We regret the inadvertent omission of important references due to space limitations.

References and recommended reading

Papers of particular interest, published within the period of review, have been highlighted as:

- • of special interest

1. Sabio G, Davis RJ: **TNF and MAP kinase signalling pathways**. *Semin Immunol* 2014, **26**:237-245 http://dx.doi.org/10.1016/j.smim.2014.02.009 Epub 2014/03/22. S1044-5323(14)00022-0 [pii]. PubMed PMID: 24647229; PubMed Central PMCID: PMC4099309.

2. Gehart H, Kumpf S, Ittner A, Ricci R: **MAPK signalling in cellular metabolism: stress or wellness?** *EMBO Rep* 2010, **11**:834-840 http://dx.doi.org/10.1038/embor.2010.160 Epub 2010/10/12. PubMed PMID: 20930846; PubMed Central PMCID: PMCPMC2966959..

3. Manieri E, Sabio G: **Stress kinases in the modulation of metabolism and energy balance**. *J Mol Endocrinol* 2015, **55**: R11-22 http://dx.doi.org/10.1530/jme-15-0146 Epub 2015/09/13. PubMed PMID: 26363062; PubMed Central PMCID: PMCPMC5176079.

4. Cuenda A, Rousseau S: **p38 MAP-kinases pathway regulation, function and role in human diseases**. *Biochim Biophys Acta* 2007, **1773**:1358-1375 http://dx.doi.org/10.1016/j.bbamcr.2007.03.010 Epub 2007/05/08. doi: S0167-4889(07)00070-5 [pii] PubMed PMID: 17481747.

5. Remy G, Risco AM, Inesta-Vaquera FA, Gonzalez-Teran B, Sabio G, Davis RJ *et al.*: **Differential activation of p38MAPK isoforms by MKK6 and MKK3**. *Cell Signal* 2010, **22**:660-667 http://dx.doi.org/10.1016/j.cellsig.2009.11.020 Epub 2009/12/17. PubMed PMID: 20004242.

6. Sabio G, Davis RJ: **cJun NH2-terminal kinase 1 (JNK1): roles in metabolic regulation of insulin resistance**. *Trends Biochem Sci* 2010, **35**:490-496 http://dx.doi.org/10.1016/j.tibs.2010.04.004 Epub 2010/05/11. PubMed PMID: 20452774; PubMed Central PMCID: PMCPMC2975251.

7. Huang C, Jacobson K, Schaller MD: **MAP kinases and cell migration**. *J Cell Sci* 2004, **117**:4619-4628 http://dx.doi.org/10.1242/jcs.01481 Epub 2004/09/17. PubMed PMID: 15371522.

8. Xu H, Liu P, Yan Y, Fang K, Liang D, Hou X *et al.*: **FKBP9 promotes the malignant behavior of glioblastoma cells and confers resistance to endoplasmic reticulum stress inducers**. *J Exp Clin Cancer Res* 2020, **39**:44 http://dx.doi.org/10.1186/s13046-020-1541-0 Epub 2020/03/01. PubMed PMID: 32111229; PubMed Central PMCID: PMCPMC7048151.

9. Goldsmith CS, Kim SM, Karunarathna N, Neuendorff N, Toussaint LG, Earnest DJ *et al.*: **Inhibition of p38 MAPK activity leads to cell type-specific effects on the molecular circadian clock and time-dependent reduction of glioma cell invasiveness**. *BMC Cancer* 2018, **18**:43 http://dx.doi.org/10.1186/s12885-017-3896-y Epub 2018/01/11. PubMed PMID: 29316898; PubMed Central PMCID: PMCPMC5761097.

10. Xie ZB, Zhang YF, Jin C, Mao YS, Fu DL: **LRG-1 promotes pancreatic cancer growth and metastasis via modulation of the EGFR/p38 signaling**. *J Exp Clin Cancer Res* 2019, **38**:75 http://dx.doi.org/10.1186/s13046-019-1088-0 Epub 2019/02/15. PubMed PMID: 30760292; PubMed Central PMCID: PMCPMC6374912.

11. Salome M, Magee A, Yalla K, Chaudhury S, Sarrou E, Carmody RJ *et al.*: **A Trib2-p38 axis controls myeloid leukaemia cell cycle and stress response signalling**. *Cell Death Dis* 2018, **9**:443 http://dx.doi.org/10.1038/s41419-018-0467-3 Epub 2018/04/20. PubMed PMID: 29670085; PubMed Central PMCID: PMCPMC5906628.

12. Zhang Y, Liao Y, Chen C, Sun W, Sun X, Liu Y *et al.*: **p38-regulated FOXC1 stability is required for colorectal cancer metastasis**. *J Pathol* 2020, **250**:217-230 http://dx.doi.org/10.1002/path.5362 Epub 2019/10/28. PubMed PMID: 31650548.

13. Urosevic J, Garcia-Albeniz X, Planet E, Real S, Cespedes MV, Guiu M *et al.*: **Colon cancer cells colonize the lung from established liver metastases through p38 MAPK signalling and PTHLH**. *Nat Cell Biol* 2014, **16**:685-694 http://dx.doi.org/10.1038/ncb2977 Epub 2014/06/02. PubMed PMID: 24880666.

14. Del Barco Barrantes I, Stephan-Otto Attolini C, Slobodnyuk K, Igea A, Gregorio S, Gawrzak S *et al.*: **Regulation of mammary luminal cell fate and tumorigenesis by p38alpha**. *Stem Cell Rep* 2018, **10**:257-271 http://dx.doi.org/10.1016/j.stemcr.2017.11.021 Epub 2018/01/02. PubMed PMID: 29290625; PubMed Central PMCID: PMCPMC5768988.

15. Canovas B, Igea A, Sartori AA, Gomis RR, Paull TT, Isoda M *et al.*:
• **Targeting p38alpha Increases DNA damage, chromosome instability, and the anti-tumoral response to Taxanes in breast cancer cells**. *Cancer Cell* 2018, **33**:1094-1110 e8 http://dx.doi.org/10.1016/j.ccell.2018.04.010 Epub 2018/05/29. PubMed PMID: 29805078
The authors describe how p38α controls the DNA repair and chromosome instability in breast cancer cells increasing their survival and their tumorigenic capacity. They identified the DNA damage response protein CtIP as a new substrate of p38α, and how its phosphorylation orchestrated DNA repair machinery through the DNA double strand breaks (DSB) repair pathway. Pharmacological inhibition of p38α in combination with the cytostatic drugs taxanes to target breast cancer cell increases the tumor cell death. This study suggests that this therapeutic strategy could be very encouraging for the treatment of breast cancer and others susceptible to be treated with DNA-damage therapies.

16. Gupta J, del Barco Barrantes I, Igea A, Sakellariou S, Pateras IS, Gorgoulis VG *et al.*: **Dual function of p38alpha MAPK in colon cancer: suppression of colitis-associated tumor initiation but requirement for cancer cell survival**. *Cancer Cell* 2014, **25**:484-500 http://dx.doi.org/10.1016/j.ccr.2014.02.019 Epub 2014/04/02. PubMed PMID: 24684847.

17. Zhang Y, Wang X, Qin X, Wang X, Liu F, White E *et al.*: **PP2AC level determines differential programming of p38-tsc-mtor signaling and therapeutic Response to p38-targeted therapy in colorectal cancer**. *EBioMedicine* 2015, **2**:1944-1956 http://dx.doi.org/10.1016/j.ebiom.2015.11.031 Epub 2016/02/05. PubMed PMID: 26844273; PubMed Central PMCID: PMCPMC4703732.

18. Tomas-Loba A, Manieri E, Gonzalez-Teran B, Mora A, Leiva-
• Vega L, Santamans AM *et al.*: **p38gamma is essential for cell cycle progression and liver tumorigenesis**. *Nature* 2019, **568**:557-560 http://dx.doi.org/10.1038/s41586-019-1112-8 Epub 2019/04/12. PubMed PMID: 30971822
This study highlights the potential role of SAPK to play non-canonical functions. Tomás-Loba *et al.* demonstrated that p38γ acts as a CDK-like kinase in the hepatocyte after partial hepatectomy. p38γ phosphorylated the retinoblastoma tumor suppressor (Rb), a CDK substrate, to induce entry into the cell cycle. Remarkably, inhibition or lack of p38γ protects against diethylnitrosamine (DEN)-induced liver tumors in mice. This protumorigenic role of p38γ was supported by the high expression levels of this kinase found in biopsies of human hepatocellular carcinoma, suggesting that p38γ inhibition could be a therapeutic target for this type of cancer.

19. Zhang XH, Nam S, Wu J, Chen CH, Liu X, Li H *et al.*: **Multi-kinase inhibitor with anti-p38gamma activity in cutaneous T-cell lymphoma**. *J Invest Dermatol* 2018, **138**:2377-2387 http://dx.doi.org/10.1016/j.jid.2018.04.030 Epub 2018/05/15. PubMed PMID: 29758280.

20. Wada M, Canals D, Adada M, Coant N, Salama MF, Helke KL *et al.*: **P38 delta MAPK promotes breast cancer progression and lung metastasis by enhancing cell proliferation and cell detachment**. *Oncogene* 2017, **36**:6649-6657 http://dx.doi.org/10.1038/onc.2017.274 Epub 2017/08/08. PubMed PMID: 28783172; PubMed Central PMCID: PMCPMC5746050.

21. Stramucci L, Pranteda A, Stravato A, Amoreo CA, Pennetti A, Diodoro MG *et al.*: **MKK3 sustains cell proliferation and survival through p38DELTA MAPK activation in colorectal cancer**. *Cell Death Dis* 2019, **10**:842 http://dx.doi.org/10.1038/s41419-019-2083-2 Epub 2019/11/07. PubMed PMID: 31695024; PubMed Central PMCID: PMCPMC6834673..

22. Wu Q, Wu W, Fu B, Shi L, Wang X, Kuca K: **JNK signaling in cancer cell survival**. *Med Res Rev* 2019, **39**:2082-2104 http://dx.doi.org/10.1002/med.21574 Epub 2019/03/27. PubMed PMID: 30912203.

23. Ding X, Wang X, Zhu X, Zhang J, Zhu Y, Shao X *et al.*: **JNK/AP1 pathway regulates MYC expression and BCR signaling through Ig enhancers in burkitt lymphoma cells**. *J Cancer* 2020, **11**:610-618 http://dx.doi.org/10.7150/jca.34055 Epub 2020/01/17. PubMed PMID: 31942184; PubMed Central PMCID: PMCPMC6959055.

24. Colleoni B, Paternot S, Pita JM, Bisteau X, Coulonval K, Davis RJ *et al.*: **JNKs function as CDK4-activating kinases by phosphorylating CDK4 and p21**. *Oncogene* 2017, **36**:4349-4361 http://dx.doi.org/10.1038/onc.2017.7 Epub 2017/04/04. PubMed PMID: 28368408; PubMed Central PMCID: PMCPMC5537611.

25. Cellurale C, Sabio G, Kennedy NJ, Das M, Barlow M, Sandy P *et al.*: **Requirement of c-Jun NH(2)-terminal kinase for Ras-initiated tumor formation**. *Mol Cell Biol* 2011, **31**:1565-1576 http://dx.doi.org/10.1128/MCB.01122-10 Epub 2011/02/02. PubMed PMID: 21282468; PubMed Central PMCID: PMC3135291.

26. Yuan D, Huang S, Berger E, Liu L, Gross N, Heinzmann F *et al.*: **Kupffer cell-derived Tnf triggers cholangiocellular tumorigenesis through JNK due to chronic mitochondrial dysfunction and ROS**. *Cancer Cell* 2017, **31**:771-789 e6 http://dx.doi.org/10.1016/j.ccell.2017.05.006 Epub 2017/06/14. PubMed PMID: 28609656.

27. Manieri E, Folgueira C, Rodriguez ME, Leiva-Vega L, Esteban-
• Lafuente L, Chen C *et al.*: **JNK-mediated disruption of bile acid homeostasis promotes intrahepatic cholangiocarcinoma**. *Proc Natl Acad Sci U S A* 2020 http://dx.doi.org/10.1073/pnas.2002672117. Epub 2020/07/01. PubMed PMID: 32601222
Hepatic JNK represses PPARα and causes changes in bile acid homeostasis, thus suppressing cholangiocyte proliferation. Therefore, hepatic JNK deficiency promotes alterations in bile acid metabolism through a mechanism dependent on PPARα, and it also increases the hepatic expression of FXR/FGF15/FGR4, driving the activation of ERK in cholangiocytes and causing cholangiocarcinoma. This study highlights the relevance of reconsidering the use of JNK inhibitors or PPAR agonists for the treatment of metabolic syndrome.

28. Cubero FJ, Mohamed MR, Woitok MM, Zhao G, Hatting M, Nevzorova YA *et al.*: **Loss of c-Jun N-terminal Kinase 1 and 2 function in liver epithelial cells triggers biliary hyperproliferation resembling cholangiocarcinoma**. *Hepatol Commun* 2020 http://dx.doi.org/10.1002/hep4.1495. n/a(n/a).

29. Insua-Rodriguez J, Pein M, Hongu T, Meier J, Descot A, Lowy CM *et al.*: **Stress signaling in breast cancer cells induces matrix components that promote chemoresistant metastasis**. *EMBO Mol Med* 2018, **10** http://dx.doi.org/10.15252/emmm.201809003 Epub 2018/09/08. PubMed PMID: 30190333; PubMed Central PMCID: PMCPMC6180299.

30. Tam SY, Wu VWC, Law HKW: **JNK pathway mediates low oxygen level induced epithelial-mesenchymal transition and stemness maintenance in colorectal cancer cells**. *Cancers* 2020, **12** http://dx.doi.org/10.3390/cancers12010224 Epub 2020/01/23. PubMed PMID: 31963305; PubMed Central PMCID: PMCPMC7017419.

31. Xie X, Kaoud TS, Edupuganti R, Zhang T, Kogawa T, Zhao Y *et al.*: **c-Jun N-terminal kinase promotes stem cell phenotype in triple-negative breast cancer through upregulation of Notch1 via activation of c-Jun**. *Oncogene* 2017, **36**:2599-2608 http://dx.doi.org/10.1038/onc.2016.417 Epub 2016/12/13. PubMed PMID: 27941886; PubMed Central PMCID: PMCPMC6116358.

32. Du L, Anderson A, Nguyen K, Ojeda SS, Ortiz-Rivera I, Nguyen TN *et al.*: **JNK2 is required for the tumorigenic properties of melanoma cells**. *ACS Chem Biol* 2019, **14**:1426-1435 http://dx.doi.org/10.1021/acschembio.9b00083 Epub 2019/05/08. PubMed PMID: 31063355.

33. Girnius N, Edwards YJ, Garlick DS, Davis RJ: **The cJUN NH2-**
• **terminal kinase (JNK) signaling pathway promotes genome stability and prevents tumor initiation**. *eLife* 2018, **7** http://dx.doi.org/10.7554/eLife.36389 Epub 2018/06/02. PubMed PMID: 29856313; PubMed Central PMCID: PMCPMC5984035
The authors identify a function of JNK in the control of genome stability in murine breast cancer tumors. Frequent loss-of-function mutations in the JNK signaling pathway are present in breast cancer, thus confirming an important role of this pathway in this type of tumor. Indeed, JNK deficiency in the mammary epithelium increases murine breast cancer initiation, accelerating tumor development. Although this deficiency promotes tumor cell survival, it has no effects on tumor cell proliferation or tumor stem cell activity, and it does not have an influence on the growth of established tumors.

34. Deng L, Gao X, Liu B, He X, Xu J, Qiang J *et al.*: **NMT1 inhibition modulates breast cancer progression through stress-triggered JNK pathway**. *Cell Death Dis* 2018, **9**:1143 http://dx.doi.org/10.1038/s41419-018-1201-x Epub 2018/11/18. PubMed PMID: 30446635; PubMed Central PMCID: PMCPMC6240078.

35. Ouyang H, Zhou E, Wang H: **Mst1-hippo pathway triggers breast cancer apoptosis via inducing mitochondrial fragmentation in a manner dependent on JNK-Drp1 axis**. *Onco*

Targets Ther 2019, **12**:1147-1159 http://dx.doi.org/10.2147/OTT.S193787 Epub 2019/02/28. PubMed PMID: 30809096; PubMed Central PMCID: PMCPMC6376886.

36. Girnius N, Davis RJ: **JNK promotes epithelial cell anoikis by transcriptional and post-translational regulation of BH3-only proteins**. *Cell Rep* 2017, **21**:1910-1921 http://dx.doi.org/10.1016/j.celrep.2017.10.067 Epub 2017/11/16. PubMed PMID: 29141222; PubMed Central PMCID: PMCPMC5711519..

37. Hubner A, Mulholland DJ, Standen CL, Karasarides M, Cavanagh-Kyros J, Barrett T *et al.*: **JNK and PTEN cooperatively control the development of invasive adenocarcinoma of the prostate**. *Proc Natl Acad Sci U S A* 2012, **109**:12046-12051 http://dx.doi.org/10.1073/pnas.1209660109 Epub 2012/07/04. PubMed PMID: 22753496; PubMed Central PMCID: PMCPMC3409732.

38. Liu J, Wang T, Creighton CJ, Wu SP, Ray M, Janardhan KS *et al.*: **JNK(1/2) represses Lkb(1)-deficiency-induced lung squamous cell carcinoma progression**. *Nat Commun* 2019, **10**:2148 http://dx.doi.org/10.1038/s41467-019-09843-1 Epub 2019/05/16. PubMed PMID: 31089135; PubMed Central PMCID: PMCPMC6517592.

39. Rincon M, Davis RJ: **Regulation of the immune response by stress-activated protein kinases**. *Immunol Rev* 2009, **228**:212-224 http://dx.doi.org/10.1111/j.1600-065X.2008.00744.x Epub 2009/03/18. PubMed PMID: 19290930.

40. Suarez-Lopez L, Sriram G, Kong YW, Morandell S, Merrick KA, Hernandez Y *et al.*: **MK2 contributes to tumor progression by promoting M2 macrophage polarization and tumor angiogenesis**. *Proc Natl Acad Sci U S A* 2018, **115**:E4236-E4244 http://dx.doi.org/10.1073/pnas.1722020115 Epub 2018/04/19. PubMed PMID: 29666270; PubMed Central PMCID: PMCPMC5939099.

41. Batlle R, Andres E, Gonzalez L, Llonch E, Igea A, Gutierrez-Prat N *et al.*: **Regulation of tumor angiogenesis and mesenchymal-endothelial transition by p38alpha through TGF-beta and JNK signaling**. *Nat Commun* 2019, **10**:3071 http://dx.doi.org/10.1038/s41467-019-10946-y Epub 2019/07/13. PubMed PMID: 31296856; PubMed Central PMCID: PMCPMC6624205.

42. • Youssif C, Cubillos-Rojas M, Comalada M, Llonch E, Perna C, Djouder N *et al.*: **Myeloid p38alpha signaling promotes intestinal IGF-1 production and inflammation-associated tumorigenesis**. *EMBO Mol Med* 2018, **10** http://dx.doi.org/10.15252/emmm.201708403 Epub 2018/06/17. PubMed PMID: 29907597; PubMed Central PMCID: PMCPMC6034132

Authors found the peptidic hormone IGF-1 as a novel target of p38α in macrophages during inflammation-associated colon tumorigenesis. IGF-1 released by macrophages in the tumor acts as a chemoattractant for the recruitment of other immune cells enhancing the tumor-promoting microenvironment. Indeed, IGF-1 deficiency in myeloid cells protects against inflammation and cancer progression. Authors found a direct correlation between p38α/IGF-1 activation and infiltration of myeloid cells in human colon tumor samples, thus confirming the importance of this pathway during colon cancer progression and its potential clinical relevance as a novel therapeutic target.

43. Kiss A, Koppel AC, Murphy E, Sall M, Barlas M, Kissling G *et al.*: **Cell type-specific p38delta targeting reveals a context-, stage-, and sex-dependent regulation of skin carcinogenesis**. *Int J Mol Sci* 2019, **20** http://dx.doi.org/10.3390/ijms20071532 Epub 2019/04/03. PubMed PMID: 30934690; PubMed Central PMCID: PMCPMC6479675.

44. • Gonzalez-Teran B, Matesanz N, Nikolic I, Verdugo MA, Sreeramkumar V, Hernandez-Cosido L *et al.*: **p38gamma and p38delta reprogram liver metabolism by modulating neutrophil infiltration**. *EMBO J* 2016, **35**:536-552 http://dx.doi.org/10.15252/embj.201591857 Epub 2016/02/05. PubMed PMID: 26843485; PubMed Central PMCID: PMCPMC4772851

The authors demonstrated that alternative p38 mitogen-activated kinases (p38γ and p38δ) are highly expressed in liver of obese patients with steatosis. Accordingly, mice fed with methionine choline diet that develop liver steatosis presented high levels of p38γ/δ. Moreover, mice lacking p38γ/δ in myeloid cells are resistant to diet-induced fatty liver, hepatic triglyceride accumulation and glucose intolerance. This protective effect is due to defective migration of p38γ/δ-deficient neutrophils to the damaged liver. They further show that neutrophil infiltration in wild-type mice contributes to steatosis development by means of inflammation and liver metabolic changes.

45. Gonzalez-Teran B, Cortes JR, Manieri E, Matesanz N, Verdugo A, Rodriguez ME *et al.*: **Eukaryotic elongation factor 2 controls TNF-alpha translation in LPS-induced hepatitis**. *J Clin Invest* 2013, **123**:164-178 http://dx.doi.org/10.1172/JCI65124 Epub 2012/12/04. PubMed PMID: 23202732; PubMed Central PMCID: PMCPMC3533299.

46. • Del Reino P, Alsina-Beauchamp D, Escos A, Cerezo-Guisado MI, Risco A, Aparicio N *et al.*: **Pro-oncogenic role of alternative p38 mitogen-activated protein kinases p38gamma and p38delta, linking inflammation and cancer in colitis-associated colon cancer**. *Cancer Res* 2014, **74**:6150-6160 http://dx.doi.org/10.1158/0008-5472.CAN-14-0870 Epub 2014/09/14. PubMed PMID: 25217523

This study highlights the important role of p38γ and p38δ in driving a pro-tumoral microenvironment during colorectal cancer. These kinases regulate the expression of inflammatory cytokines and chemokines in the tumor site, promoting leukocyte recruitment, and inducing colon tumor formation. Authors demonstrated that p38γ/δ in the hematopoietic compartment was responsible for these effects, although the implication of p38γ/δ from other cell types cannot be discarded. This finding opens new insights about the role of other p38 isoforms rather than p38α in controlling inflammation-associated colon tumorigenesis.

47. Yin N, Qi X, Tsai S, Lu Y, Basir Z, Oshima K *et al.*: **p38gamma MAPK is required for inflammation-associated colon tumorigenesis**. *Oncogene* 2016, **35**:1039-1048 http://dx.doi.org/10.1038/onc.2015.158 Epub 2015/05/12. PubMed PMID: 25961922.

48. Zheng T, Zhang B, Chen C, Ma J, Meng D, Huang J *et al.*: **Protein kinase p38alpha signaling in dendritic cells regulates colon inflammation and tumorigenesis**. *Proc Natl Acad Sci U S A* 2018, **115**:E12313-E12322 http://dx.doi.org/10.1073/pnas.1814705115 Epub 2018/12/14. PubMed PMID: 30541887; PubMed Central PMCID: PMCPMC6310843.

49. Shen Y, Song Z, Lu X, Ma Z, Lu C, Zhang B *et al.*: **Fas signaling-mediated TH9 cell differentiation favors bowel inflammation and antitumor functions**. *Nat Commun* 2019, **10**:2924 http://dx.doi.org/10.1038/s41467-019-10889-4 Epub 2019/07/04. PubMed PMID: 31266950; PubMed Central PMCID: PMCPMC6606754.

50. • Gurusamy D, Henning AN, Yamamoto TN, Yu Z, Zacharakis N, Krishna S *et al.*: **Multi-phenotype CRISPR-Cas9 screen identifies p38 kinase as a target for adoptive immunotherapies**. *Cancer Cell* 2020, **37**:818-833 e9 http://dx.doi.org/10.1016/j.ccell.2020.05.004 Epub 2020/06/10. PubMed PMID: 32516591

This recent and elegant work reveals a new therapeutic approach for cancer treatment using p38 inhibitor combined with adoptive T cell transfer immunotherapy. Authors first demonstrated that p38 is a negative regulator of $CD8^+$ T cell memory signature by downregulating the expression of important markers and altering the metabolic T cell status related to this memory-like phenotype. Treatment of human and murine $CD8^+$ T cells with p38 inhibitor enhances the memory function of these cells and improved their capacity to infiltrate and reduced tumor growth after adoptive T cell transfer. This novel use of p38 inhibitor uncovers the relevance of these family of kinases in cancer development and the importance to continue studying the molecular mechanisms through which they contribute to this pathology.

51. Gao Y, Tao J, Li MO, Zhang D, Chi H, Henegariu O *et al.*: **JNK1 is essential for CD8+ T cell-mediated tumor immune surveillance**. *J Immunol* 2005, **175**:5783-5789 http://dx.doi.org/10.4049/jimmunol.175.9.5783 Epub 2005/10/21. PubMed PMID: 16237070.

52. Tao J, Gao Y, Li MO, He W, Chen L, Harvev B *et al.*: **JNK2 negatively regulates CD8+ T cell effector function and anti-tumor immune response**. *Eur J Immunol* 2007, **37**:818-829 http://dx.doi.org/10.1002/eji.200636726 Epub 2007/02/16. PubMed PMID: 17301952.

53. Koizumi SI, Sasaki D, Hsieh TH, Taira N, Arakaki N, Yamasaki S *et al.*: **JunB regulates homeostasis and suppressive functions of effector regulatory T cells**. *Nat Commun* 2018, **9**:5344 http://dx.doi.org/10.1038/s41467-018-07735-4 Epub 2018/12/19. PubMed PMID: 30559442; PubMed Central PMCID: PMCPMC6297218.

54. Das M, Garlick DS, Greiner DL, Davis RJ: **The role of JNK in the development of hepatocellular carcinoma**. *Genes Dev* 2011, **25**:634-645 http://dx.doi.org/10.1101/gad.1989311 Epub 2011/

03/17. PubMed PMID: 21406557; PubMed Central PMCID: PMC3059836.

55. Das M, Sabio G, Jiang F, Rincon M, Flavell RA, Davis RJ: **Induction of hepatitis by JNK-mediated expression of TNF-alpha**. *Cell* 2009, **136**:249-260 Epub 2009/01/27. doi: S0092-8674(08)01492-X [pii] 10.1016/j.cell.2008.11.017. PubMed PMID: 19167327; PubMed Central PMCID: PMC2794880.

56. Han MS, Barrett T, Brehm MA, Davis RJ: **Inflammation mediated by JNK in myeloid cells promotes the development of hepatitis and hepatocellular carcinoma**. *Cell Rep* 2016, **15**:19-26 http://dx.doi.org/10.1016/j.celrep.2016.03.008 Epub 2016/04/08. PubMed PMID: 27052181; PubMed Central PMCID: PMCPMC4826851.

57. • Manieri E, Herrera-Melle L, Mora A, Tomas-Loba A, Leiva-Vega L, Fernandez DI *et al.*: **Adiponectin accounts for gender differences in hepatocellular carcinoma incidence**. *J Exp Med* 2019, **216**:1108-1119 http://dx.doi.org/10.1084/jem.20181288 Epub 2019/04/05. PubMed PMID: 30944152; PubMed Central PMCID: PMCPMC6504215

In this study, the authors demonstrated that JNK1 in adipose tissue is responsible of the gender dimorphism in the susceptibility to develop hepatocellular carcinoma (HCC). They showed that JNK1 is activated in adipocytes by testosterone, resulting in reduced adiponectin levels in males and, in consequence, higher HCC. Mice lacking adiponectin did not present differences in HCC susceptibility and castration of males also protects them against this cancer. The authors decipher the molecular mechanism of these effects as they found that adiponectin activates p38α and AMPKα in liver. In fact the activation of these signalling pathways is higher in liver from WT females than males, while there were no sex differences in mice lacking adiponectin. In summary, this paper demonstrates that stress in adipose tissue might control liver cancer predisposition.

RESEARCH ARTICLE (*In preparation*)

Muscle-to-brain communication is controlled by p38 stress kinases

Leticia Herrera-Melle[1], Cintia Folgueira[1], Juan Antonio López[2], Phillip A. Dumesic[3], María Elena Rodríguez[1], Luis Leiva-Vega[1], Daniel Beiroa[4], Bruce M. Spiegelman[3], Jesús Vázquez[2], Alfonso Mora[1*], Guadalupe Sabio[1*]

[1]Stress kinases in diabetes, cancer and cardiovascular disease Lab, Centro Nacional de Investigaciones Cardiovasculares (CNIC), 28029 Madrid, Spain. [2]Cardiovascular Proteomics Unit, CNIC, 28029 Madrid, Spain. [3]Dana-Farber Cancer Institute (DFCI); Department of Cell Biology, Harvard University Medical School, Boston, United States of America. [4]Department of Physiology, CiMUS, University of Santiago de Compostela-Instituto de Investigación Sanitaria, Santiago de Compostela 15782, Spain; CIBER Fisiopatología de la Obesidad y Nutrición (CIBERobn), 15706 Santiago de Compostela, Spain.

*Corresponding authors:
Guadalupe Sabio, Stress kinases in diabetes, cancer and cardiovascular disease Lab, Centro Nacional de Investigaciones Cardiovasculares (CNIC), 28029 Madrid, Spain. E-mail: guadalupe.sabio@cnic.es
Alfonso Mora, Stress kinases in diabetes, cancer and cardiovascular disease Lab, Centro Nacional de Investigaciones Cardiovasculares (CNIC), 28029 Madrid, Spain. E-mail: alfonso.mora@cnic.es

Abstract

Physical inactivity and changes in dietary habits have increased the prevalence of obesity in current societies, which has become a major health problem. It is well known that exercise has the capacity to improve the metabolic status in obesity and type 2 diabetes. However, the molecular mechanisms underlying the response to exercise and inactivity are not fully understood. Among the different metabolic organs, skeletal muscle is considered an important regulator of glucose homeostasis and an essential contributor to exercise-induced changes in metabolism, in part through the release of secreted factors termed myokines. Although the endocrine function of skeletal muscle is well accepted, the mechanisms explaining its communication with other organs are not well understood. Several signaling pathways have been studied in the context of obesity and insulin resistance, including stress kinases. However, the systemic implications of the activation of these kinases in specific tissues is starting to be addressed, as occurs with p38s family. In this work, using a conditional mouse model lacking p38α in striated muscle, we found that muscle p38α deletion protects mice against high-fat diet (HFD)-induced obesity by increasing energy expenditure, together with skeletal muscle metabolic remodeling. Lack of p38α results in the hyperactivation of p38γ, which improves glucose and energy homeostasis through an increase in locomotor activity, a process in which interleukin-15 (IL-15) is involved. This effect decreases the risk of developing diabetes and liver steatosis, therefore linking local and systemic manifestations of muscle p38α deficiency and showing a new muscle-to-brain crosstalk with potential clinical implications.

Introduction

Obesity is the most common metabolic disorder worldwide, with growing incidence and prevalence as reflected by the over 650 million obese adults in 2016 (WHO, 2020). Exercise is a vital tool in the fight against the global epidemic of obesity-induced metabolic diseases. Healthy lifestyle, including calorie restriction and regular exercise, is an effective strategy for the prevention and treatment of obesity. Apart from the benefits of reducing adiposity and circulating lipids by regular exercise, recent evidence has identified skeletal muscle as an endocrine organ that produces and secretes factors that participate in inter-organ communication (Atakan et al., 2021). These secreted factors include protein hormones, small molecules, lipids and other factors such as exosomes that are released from contracting skeletal muscle (Priest & Tontonoz, 2019). These molecules are called

myokines, and their secretion in response to exercise may play a significant role in preventing obesity. Importantly, the alteration of this crosstalk can result in metabolic disease, leading to many disorders, including type 2 diabetes, cardiovascular disease, fatty liver disease and cancer. In fact, alterations in skeletal muscle signaling can compromise metabolic homeostasis (Rodríguez-Fdez et al., 2020). Indeed, physical inactivity alters the responses to myokines, which has been related to an increased risk of several chronic disorders (Pedersen & Febbraio, 2012). Despite the profound benefit of exercise for the treatment and prevention of metabolic disease, knowledge of the mechanisms by which exercise improves metabolic health is insufficient. Among others, p38s signaling pathway is known to be activated after intermittent or continuous exercise in human skeletal muscle (Combes et al., 2015), driving metabolic adaptation (Bengal et al., 2020). Although activation of p38s increases insulin-independent glucose uptake and oxidative metabolism in muscle during exercise, this pathway promotes insulin resistance and glucose intolerance during metabolic syndrome (de Alvaro et al., 2004). These opposite effects of p38s activation during exercise and obesity might reflect different functions of the members of this family. p38s family includes four members: alpha, beta, gamma and delta, which are encoded by four different genes and present different tissue expression patterns (Nikolic et al., 2020). Hence, each p38 may lead to diverse responses in skeletal muscle, but their contributions to the metabolic adaptation of skeletal muscle are not clear. Although some studies have suggested the implications of p38s activation in myokines production and inter-organ communication (Chan et al., 2004; Yang et al., 2013), none of them has focused on the systemic metabolic implications of the muscle-specific p38 deficiency. Importantly, a better understanding of the metabolic and cellular effects of exercise, coupled with advances in the characterization of the human genome, could lead to improved personalized or targeted exercise interventions. In addition, elucidation of the myriad of molecular changes induced by divergent exercise modalities may accelerate the discovery of pharmaceutical targets to improve metabolic health and help in the fight against obesity-associated disorders.

Results

p38α^{MCK-KO} mice have decreased body weight and improved glucose homeostasis in normal chow diet

To test the contribution of muscle p38α in the development of obesity and its comorbidities, we generated conditional knockout mice for p38α in striated muscle by expressing the Cre recombinase under the muscle creatine kinase (MCK) promoter in mice with the first exon of p38α gene flanked by loxP sequences (p38α^{MCK-KO}). Mice expressing this Cre recombinase were used as controls (MCK-Cre). Immunoblot images confirmed the deficiency of p38α in the skeletal muscles analyzed (quadriceps, gastrocnemius, soleus and extensor digitorum longus [EDL]) and in hearts of p38α^{MCK-KO} mice, whereas no changes in the level of p38α were observed in other tissues (Figure 1A). These results indicate specific deletion of p38α. We observed that mice lacking p38α in striated muscle presented reduced body weight when fed a normal chow diet (ND) (Figure 1B), which correlated with a decrease in blood glucose levels both in the fasted and fed state (Figure 1C), as well as with improved glucose tolerance (Figure 1D).

In order to elucidate the reason for the reduced body weight of p38α^{MCK-KO} mice, they were housed in metabolic cages. p38α^{MCK-KO} mice presented slightly higher energy expenditure than MCK-Cre mice, with no differences in the respiratory quotient (RQ) (Figures 1E and S1A), indicating that lack of muscle p38α increases energy expenditure without affecting nutrient partitioning. In concordance with increased energy expenditure, locomotor activity was also higher in p38α^{MCK-KO} mice (Figure 1F), while no differences were found in body temperature, interscapular temperature or rectal temperature after cold exposure (Figures S1B-D). In addition, food intake was decreased in p38α^{MCK-KO} mice, probably due to a tendency towards higher leptin circulating levels (Figures S1E, F). These data suggest that reduced body weight of p38α^{MCK-KO} mice was mediated by their increased energy expenditure due to their higher locomotor activity and reduced food intake.

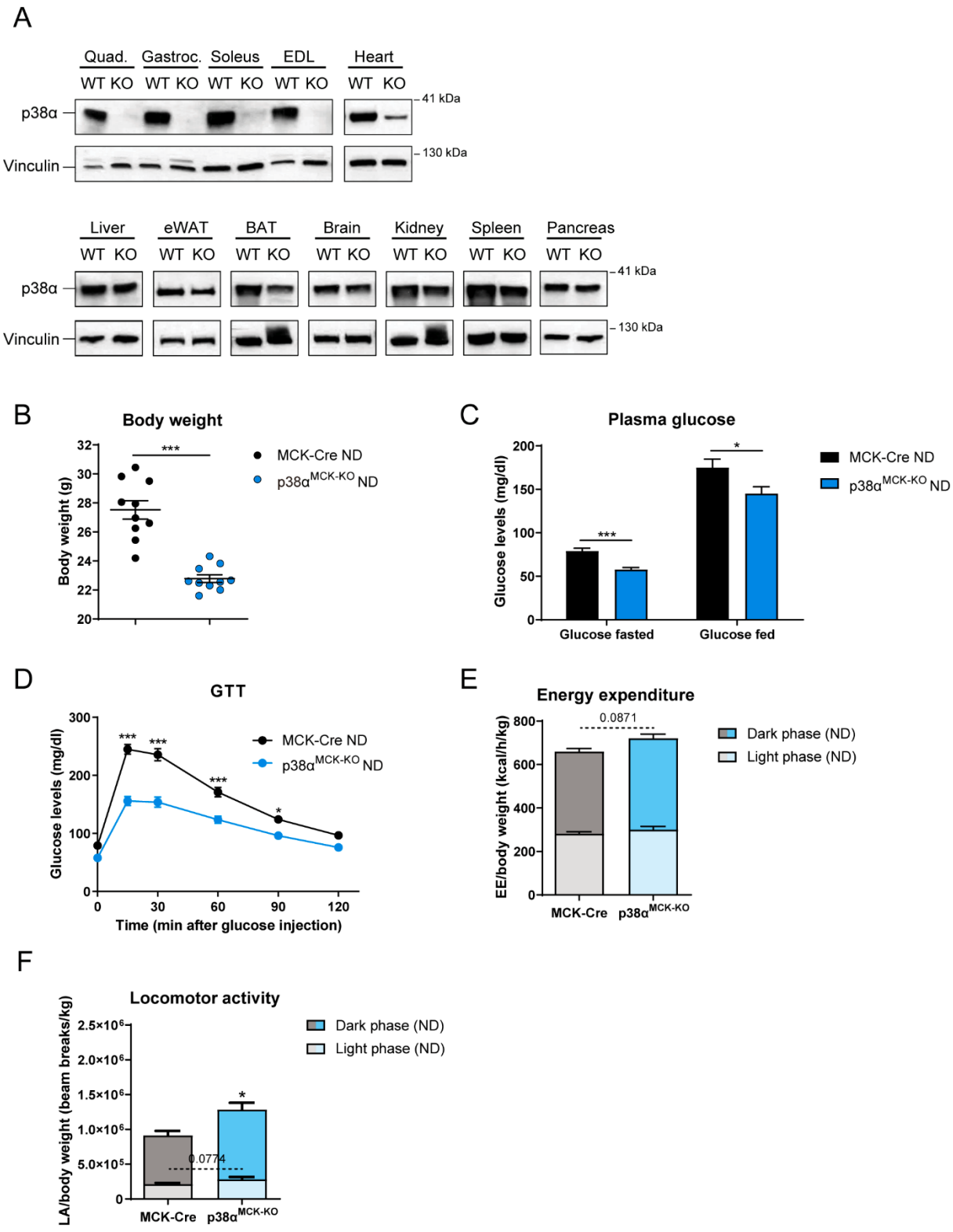

Figure 1. Lack of p38α in striated muscle decreases body weight and improves glucose homeostasis in mice fed a normal chow diet. (**A**) Analysis of p38α expression in tissues derived from MCK-Cre or p38α^{MCK-KO} mice by immunoblot analysis using antibodies against p38α and vinculin as loading control. *n* = 2-4. Quad., quadriceps; Gastroc., gastrocnemius; EDL, extensor digitorum longus; eWAT, epididymal white adipose tissue; BAT, brown adipose tissue; WT, MCK-Cre; KO, p38α^{MCK-KO}. (**B-F**) 8-week-old p38α^{MCK-KO} and MCK-Cre mice were fed a ND. (**B**) Body weight measured at sacrifice. (**C**) Fasting and fed plasma glucose levels at 16 weeks old. (**D**) Glucose tolerance test (GTT). Mice fasted overnight were injected intraperitoneally (i.p.) with glucose (1 g/kg) and blood glucose concentration was measured at the indicated time points. (**E**) Energy expenditure (EE) corrected by body weight at 21 weeks old. (**F**) Locomotor activity (LA) corrected by body weight during a 48 h period at 21 weeks old. Data are shown as means ± SEM; **p* < 0.05; ****p* < 0.001; Student's t-test (Figures B, C, E, F); two-way ANOVA coupled to Bonferroni's multiple comparisons test (Figure D); *n* = 9-13.

Mice deficient for p38α in striated muscle are protected against high-fat diet-induced obesity through an increase in locomotor activity

The decreased body weight and higher locomotor activity found in ND-fed mice led us to check whether the absence of p38α in striated muscle protected mice against high-fat diet (HFD)-induced obesity. p38α^{MCK-KO} mice fed a HFD showed decreased body weight gain and, consequently, presented lower weight at sacrifice (Figures 2A, B). These data indicate that muscle-specific p38α deficiency protects mice against HFD-induced obesity. In agreement with our results in ND, HFD-fed p38α^{MCK-KO} mice presented higher energy expenditure than MCK-Cre mice, with no differences in the RQ (Figures 2C and S2A). Locomotor activity was also higher in p38α^{MCK-KO} mice (Figure 2D). Surprisingly, despite their lower body weight, p38α^{MCK-KO} mice showed a significant increase in food intake (Figure S2B). To find the mechanism underlying this higher food intake, we analyzed plasma levels of the anorexigenic hormone leptin and the orexigenic hormone ghrelin. p38α^{MCK-KO} mice presented lower leptin levels, which correlated with their increased food intake, whereas no differences were observed in ghrelin (Figure S2C). No differences were found in body or interscapular temperature (Figures S2D, E). In summary, the results presented here support a role for muscle p38α in the regulation of energy balance in HFD.

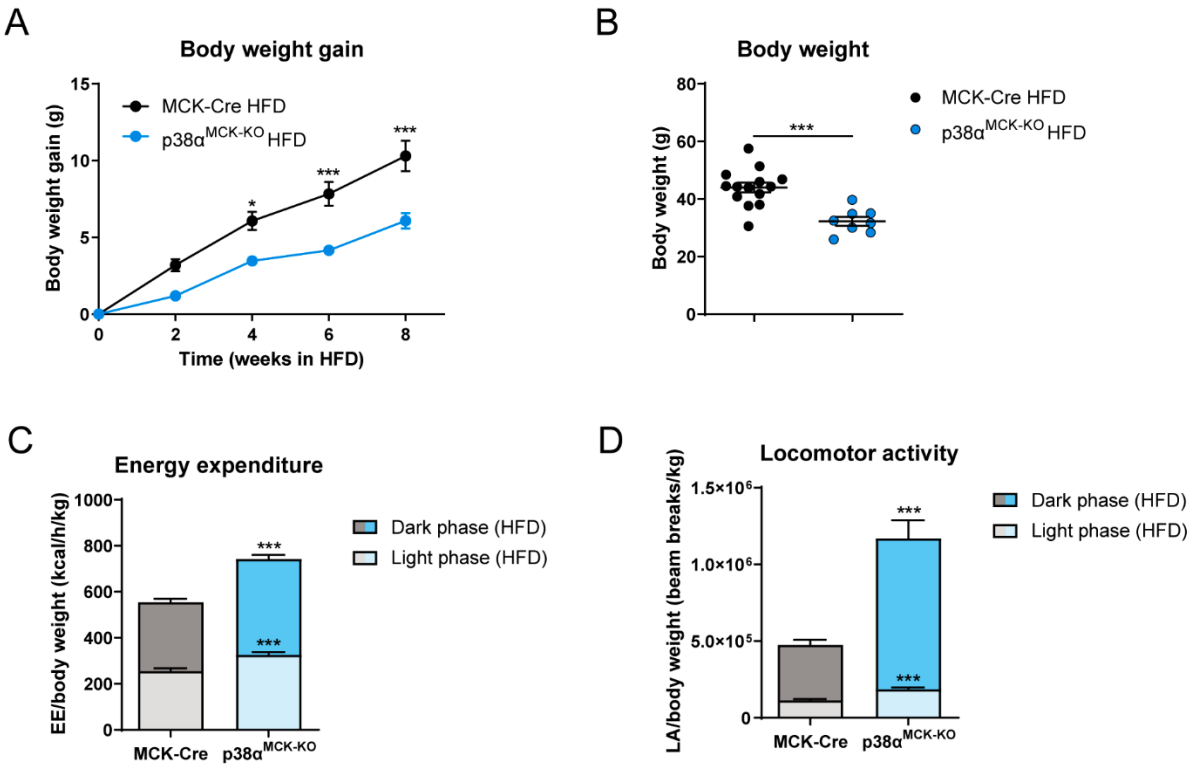

Figure 2. Lack of p38α in striated muscle protects against HFD-induced obesity. p38α^{MCK-KO} and MCK-Cre mice were fed a HFD, and body weight was monitored for 8 weeks. (**A**) Body weight gain measured at the indicated times during HFD treatment. (**B**) Body weight measured at sacrifice. (**C**) Energy expenditure (EE) corrected by body weight measured after 12 weeks on HFD. (**D**) Locomotor activity (LA) corrected by body weight during a 48 h period after 12 weeks on HFD. Data are shown as means ± SEM; *$p < 0.05$; ***$p < 0.001$; two-way ANOVA coupled to Bonferroni's multiple comparisons test (Figure A); Student's *t*-test (with Welch's correction for LA-dark phase) (Figures B-D); n = 7-14.

Striated muscle p38α-deficient mice are protected against diet-induced diabetes and liver steatosis

Feeding a HFD causes hyperglycemia and hyperinsulinemia in mice, which can lead to an increased propensity of developing insulin resistance and diabetes (Kahn et al., 2006). The reduced fat accumulation in p38α^{MCK-KO} mice prompted us to investigate whether these mice were also protected against HFD-induced diabetes. Analysis of plasma samples indicated that p38α^{MCK-KO} mice had significantly lower levels of HFD-induced hyperglycemia and hyperinsulinemia than wild-type mice (Figures 3A, B), as well as a decreased HOMA-IR index, indicative of lower insulin resistance (Figure 3C). Moreover, HFD-fed p38α^{MCK-KO} mice showed enhanced glucose tolerance (Figure 3D), correlating with higher glucose-induced insulin release (Figure 3E). In addition, higher insulin sensitivity in knockout mice was corroborated by insulin tolerance test (Figure 3F). Western blot analysis of AKT phosphorylation, an appropriate method to assay insulin resistance (Kahn et al., 2006), showed that p38α^{MCK-KO} mice presented higher AKT phosphorylation after insulin injection in liver and skeletal muscle compared to MCK-Cre mice, indicative of protection against insulin resistance in these two organs (Figure S3). To evaluate if this protection in hepatic insulin resistance was associated with a protection against liver steatosis, we performed a histological analysis of the liver. Our results revealed a reduction in hepatic steatosis in p38α^{MCK-KO} mice as evaluated by hematoxylin and eosin (H&E) and Oil Red staining compared with MCK-Cre mice (Figures 3G, H). These results suggest that the deficiency of p38α in muscle also protects against HFD-induced hepatic steatosis.

Lack of p38α in skeletal muscle increases its mitochondrial metabolism

To gain further insights into the altered protein expression caused by the lack of p38α that could influence insulin signaling, we performed a quantitative proteomics analysis, using isobaric labeling and subsequent liquid chromatography with tandem mass spectrometry (LC-MS/MS) analysis of gastrocnemius muscles from HFD-fed mice (Figure 4A). A total of 188 statistically significant pathways were detected by Ingenuity Pathway Analysis (IPA) ($p < 0.05$). The most enriched pathway associated with upregulated proteins in p38α^{MCK-KO} mice compared to control mice was mitochondrial oxidative phosphorylation (Figure 4B), while glycolysis was the most enriched one associated with downregulated proteins (Figure 4C). Similar results were found by gene set enrichment analysis (GSEA) (Figure 4D). A further analysis revealed that 61 proteins of oxidative phosphorylation, 14 of tricarboxylic acid (TCA) cycle and 13 of fatty acid β-oxidation were significantly upregulated in p38α^{MCK-KO} mice, while 17 glycolytic proteins and 13 gluconeogenic proteins were downregulated in comparison with MCK-Cre mice (Figure 4E). These data suggest that p38α-deficient myocytes rely on the production of ATP by mitochondrial metabolic pathways rather than by glycolysis.

p38α-deficient muscles hyperactivate p38γ and MAP2Ks

To unveil the mechanism linking p38α deficiency and the metabolic remodeling observed in skeletal muscle, we analyzed p38s activation by their state of phosphorylation in skeletal muscle samples of MCK-Cre and p38α^{MCK-KO} mice. Results showed a hyperactivation of p38γ in different skeletal muscles of HFD-fed p38α^{MCK-KO} mice (Figures 5A and S4A, B), which was conserved both in ND and HFD (Figure 5B). This increase was not accompanied by an increase in total p38γ mRNA (Figure S4C) or protein levels (Figures 5A, B and S4A, B). As expected, MAPK-activated protein kinase 2 (MK2), a well-known specific p38α/β substrate (Cuenda et al., 1997), and its substrate Hsp27, were not phosphorylated in HFD-fed p38α^{MCK-KO} mice, suggesting that p38β kinase activity was not compensating for p38α loss (Figure 5C). Moreover, in concordance with the higher p38γ activation, the deficiency of p38α resulted in the hyperactivation of the two main MAP2Ks of p38 signaling pathway, MKK3 and MKK6, linked to an increase in their mRNA and total protein levels (Figures 5D and S4D, E), suggesting a negative feedback regulation of p38α over its upstream kinases. Taken together, these results indicate that lack of muscle p38α results in higher activation of its upstream kinases and subsequent p38γ hyperphosphorylation.

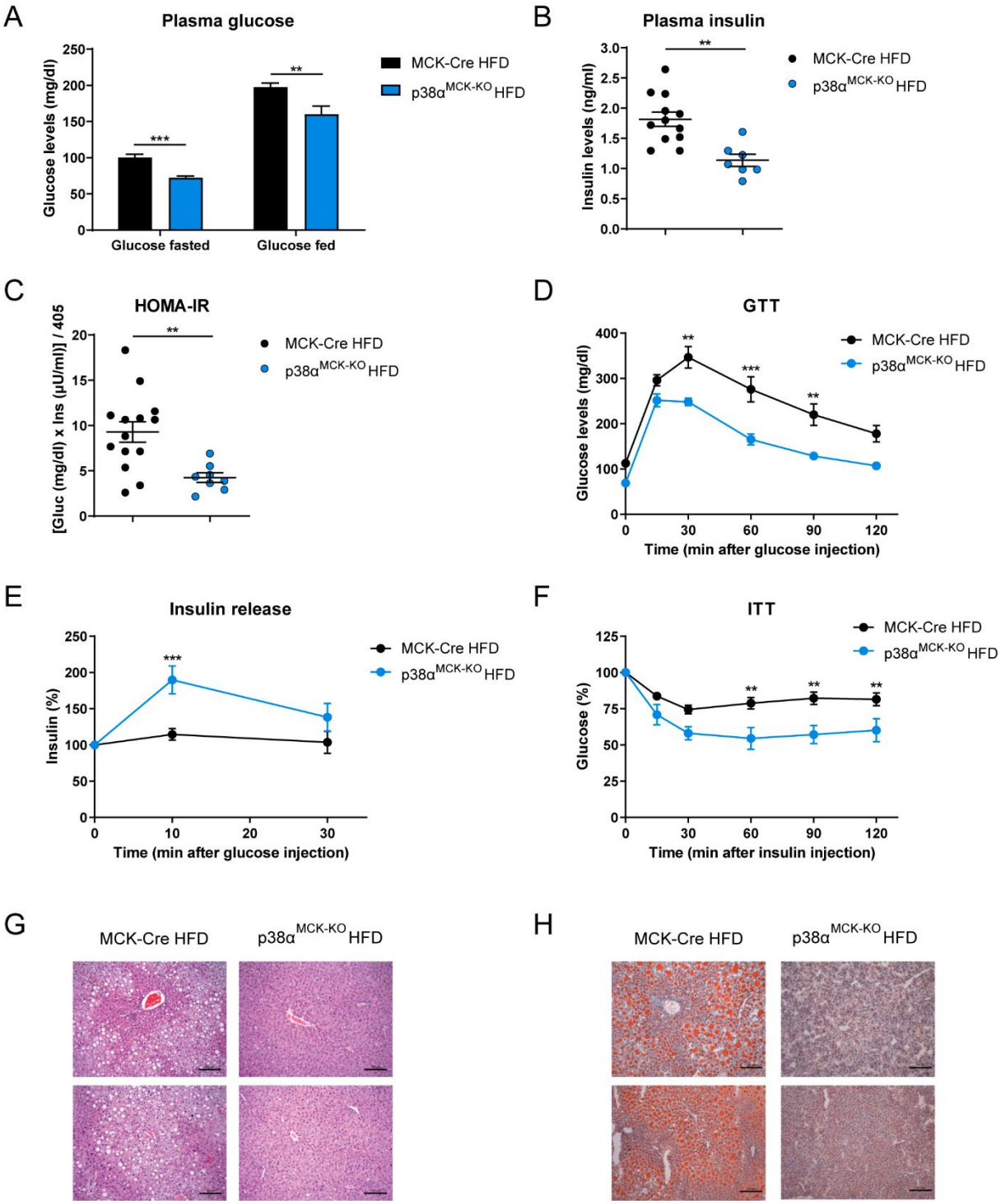

Figure 3. HFD-fed p38α^{MCK-KO} mice present improved glucose metabolism and reduced hepatic steatosis. (**A-F**) p38α^{MCK-KO} and MCK-Cre mice were fed a HFD for 8 weeks. (**A**) Fasting and fed plasma glucose levels. (**B**) Fasting plasma insulin levels. (**C**) Insulin resistance rate calculated as HOMA-IR ratio. (**D**) Glucose tolerance test (GTT). Mice fasted overnight were injected i.p. with glucose (1 g/kg). (**E**) Insulin release assay. Mice fasted overnight were injected i.p. with glucose (2 g/kg) and insulin levels were measured at the indicated points. (**F**) Insulin tolerance test (ITT). Mice fed *ad libitum* were injected i.p. with insulin (0.75 U/kg). Blood glucose concentration was measured at the indicated points in GTT and ITT. Data are shown as means ± SEM; $^{**}p < 0.01$; $^{***}p < 0.001$; Student's *t*-test (Figures A-C), with Welch's correction for glucose (fasted) and HOMA-IR; two-way ANOVA coupled to Bonferroni's multiple comparisons test (Figures D-F); n = 7-14. Gluc, glucose; Ins, insulin. (**G-H**) p38α^{MCK-KO} and MCK-Cre mice were fed a HFD for 14 weeks, fasted overnight and sacrificed. Representative H&E- (**G**) and Oil Red O- (**H**) stained liver sections are presented. Scale bar: 150 μm. n = 5.

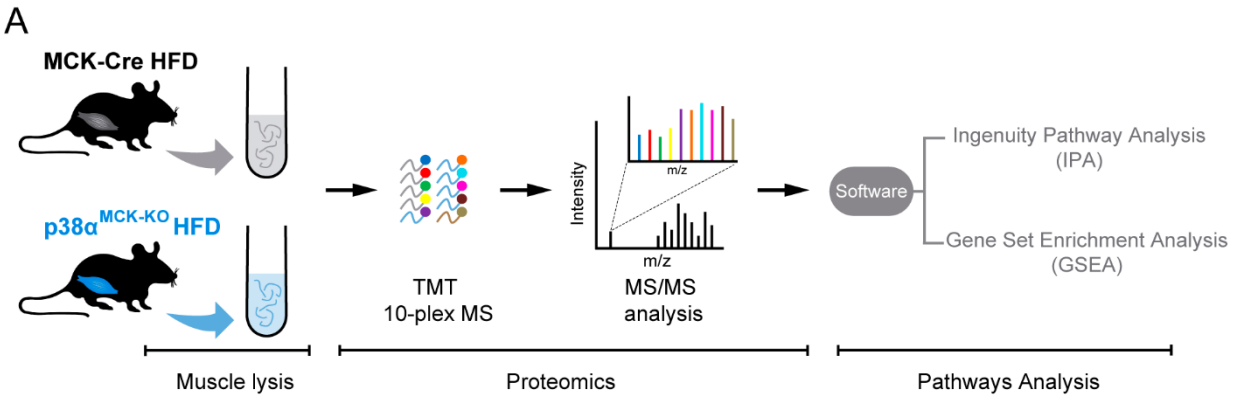
A
MCK-Cre HFD
p38α MCK-KO HFD
TMT
10-plex MS
Intensity
m/z
MS/MS
analysis
Software
Ingenuity Pathway Analysis
(IPA)
Gene Set Enrichment Analysis
(GSEA)
Muscle lysis
Proteomics
Pathways Analysis

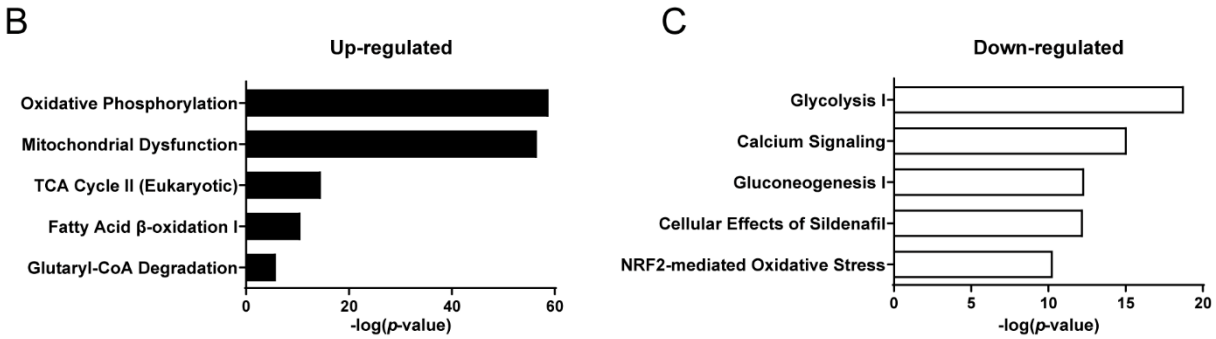
B
Up-regulated
Oxidative Phosphorylation
Mitochondrial Dysfunction
TCA Cycle II (Eukaryotic)
Fatty Acid β-oxidation I
Glutaryl-CoA Degradation
0
20
40
60
-log(p-value)
C
Down-regulated
Glycolysis I
Calcium Signaling
Gluconeogenesis I
Cellular Effects of Sildenafil
NRF2-mediated Oxidative Stress
0
5
10
15
20
-log(p-value)

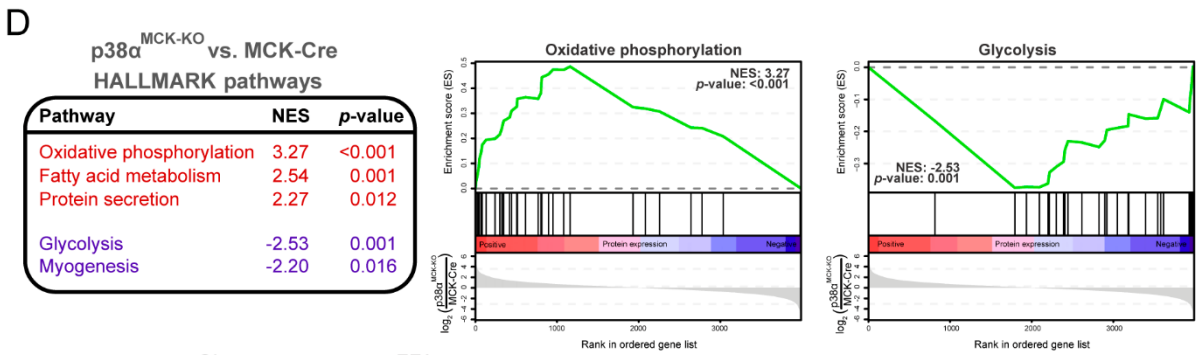
D
p38α MCK-KO vs. MCK-Cre
HALLMARK pathways
Pathway | NES | p-value
Oxidative phosphorylation | 3.27 | <0.001
Fatty acid metabolism | 2.54 | 0.001
Protein secretion | 2.27 | 0.012
Glycolysis | -2.53 | 0.001
Myogenesis | -2.20 | 0.016
Oxidative phosphorylation
NES: 3.27
p-value: <0.001
Glycolysis
NES: -2.53
p-value: 0.001
Enrichment score (ES)
Positive
Protein expression
Negative
Rank in ordered gene list

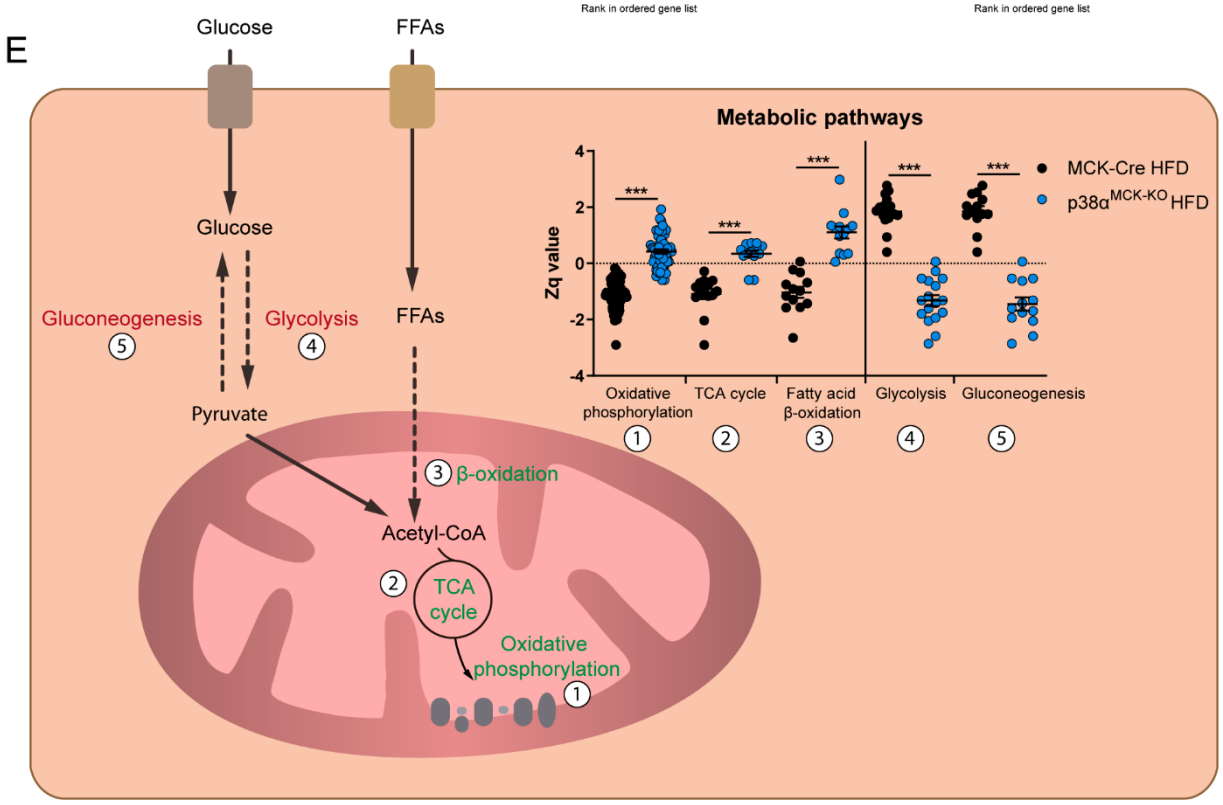
E
Glucose
FFAs
Glucose
Gluconeogenesis
5
Glycolysis
4
FFAs
Pyruvate
3 β-oxidation
Acetyl-CoA
2
TCA
cycle
Oxidative
phosphorylation
1
Metabolic pathways
Zq value
MCK-Cre HFD
p38α MCK-KO HFD
***
Oxidative
phosphorylation
TCA cycle
Fatty acid
β-oxidation
Glycolysis
Gluconeogenesis
1
2
3
4
5

Figure 4. Pathway enrichment analysis of differentially expressed proteins between p38α^{MCK-KO} and MCK-Cre mice. p38α^{MCK-KO} and MCK-Cre mice were fed a HFD for 14 weeks, fasted overnight and sacrificed. A quantitative proteomics analysis with gastrocnemius samples was performed. (**A**) Schematic representation of the proteomics experimental layout. (**B, C**) Top 5 significantly enriched pathways shown by Ingenuity Pathway Analysis derived through comparison of proteins differentially expressed between MCK-Cre and p38α^{MCK-KO} mice. Bars show enriched pathways for upregulated (B) or downregulated (C) proteins in p38α^{MCK-KO} mice compared to controls. NRF2, nuclear factor erythroid 2-related factor 2; CoA, coenzyme A. (**D**) MS analysis by GSEA and gene set enrichment plots of HALLMARK oxidative phosphorylation and glycolysis of p38α^{MCK-KO} and MCK-Cre mice. Proteins detected in MS were ranked based on relative amount in muscles from p38α^{MCK-KO} mice versus MCK-Cre mice, with the first ranked protein corresponding to the protein most upregulated in those conditions (log2 scale). GSEA was used to determine whether any HALLMARK gene sets were enriched among proteins upregulated or downregulated in p38α^{MCK-KO} mice compared with MCK-Cre controls. All gene sets enriched with an absolute value of normalized enrichment score (NES) greater than 2 are shown. Hash marks represent positions in the ranked list corresponding to members of oxidative phosphorylation (left) or glycolysis (right) HALLMARK gene sets. NES indicates whether these members are enriched towards the upregulated end of this list (positive NES) or downregulated end of this list (negative NES) as compared to chance expectation. (**E**) Analysis of proteins of oxidative phosphorylation, TCA cycle, fatty acid β-oxidation, glycolysis and gluconeogenesis in MCK-Cre and p38α^{MCK-KO} mice. Each point in the graph corresponds to a protein of the pathway. Zq values represent units of standard deviation according to the estimated variances. Data are shown as means ± SEM; ***$p < 0.001$; Student's *t*-test; $n = 4$-5.

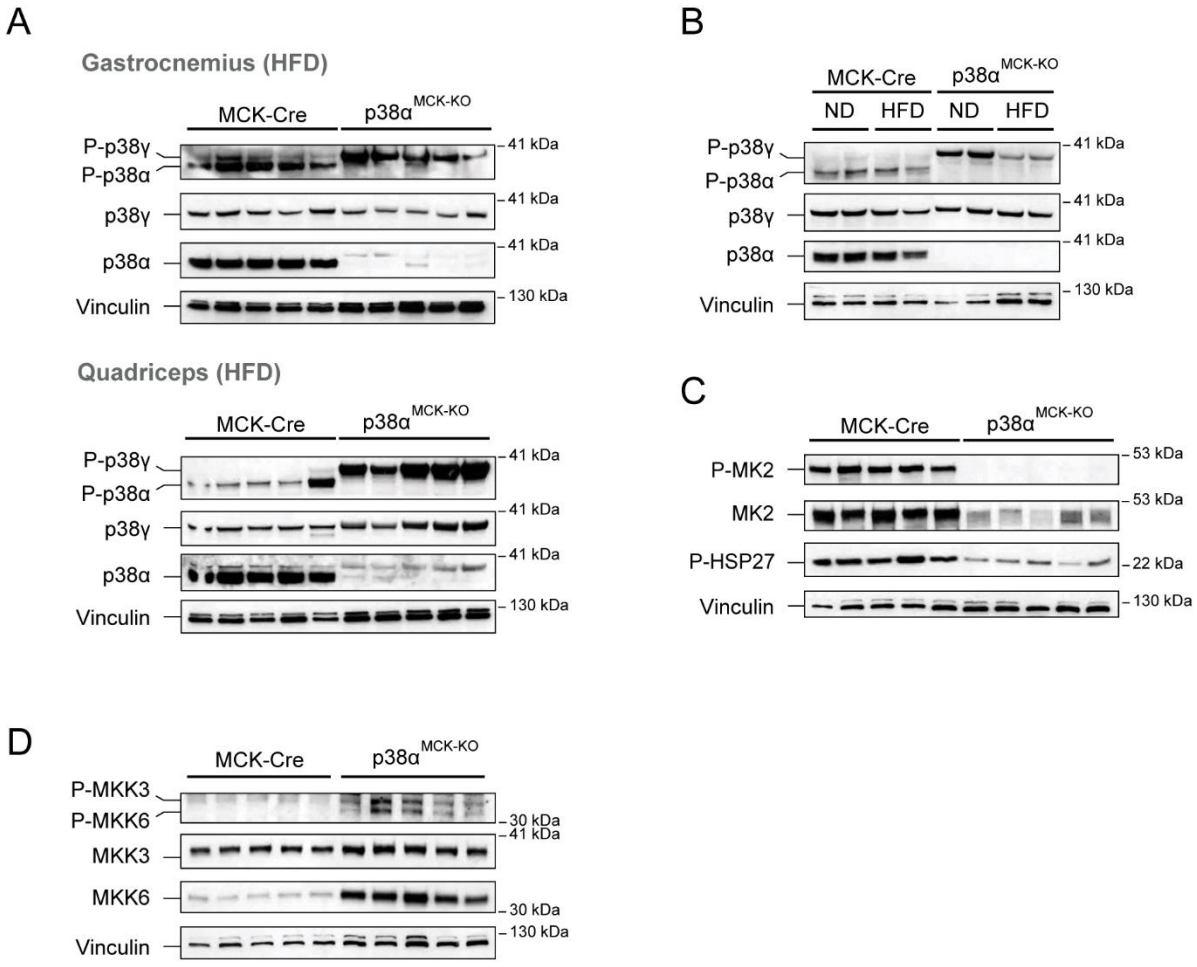

Figure 5. Biochemical analysis of the p38 signaling pathway in p38α^{MCK-KO} and MCK-Cre mice. 8-week-old p38α^{MCK-KO} and MCK-Cre mice were fed a HFD or a ND (B) for 14 weeks, fasted overnight and sacrificed. Extracts prepared from gastrocnemius (**A-D**), and quadriceps (**A**) muscles were examined by immunoblot analysis with antibodies against phospho (P)-p38, P-MK2, P-Hsp27, P-MKK3/6 and total protein levels. Vinculin protein expression was monitored as a loading control. $n = 4$-5.

p38γ hyperactivation in p38α-deficient muscles is responsible for the protection against obesity of p38α^{MCK-KO} mice

Given the relevance of p38γ in obesity comorbidities (González-Terán et al., 2016; Koh et al., 2018), we decided to investigate the influence of p38γ hyperphosphorylation in the phenotype of striated muscle p38α-deficient mice. For that, we created striated muscle p38α-deficient mice that also lacked p38γ (p38α/γ^{MCK-KO}) and fed MCK-Cre, p38α^{MCK-KO} and p38α/γ^{MCK-KO} mice with HFD. Interestingly, we found that lack of p38γ reverted the phenotype observed in p38α^{MCK-KO}, since p38α/γ^{MCK-KO} mice presented higher body weight and body weight gain compared to p38α^{MCK-KO} mice (Figures 6A, B). In concordance with the lack of protection against HFD-induced obesity, p38α/γ^{MCK-KO} mice also showed reduced energy expenditure compared to p38α^{MCK-KO} mice (Figure 6C) due to a decreased locomotor activity (Figure 6D), with no differences in RQ or body temperature (Figure S5). Importantly, muscle p38α/γ-deficient mice had similar glucose tolerance (Figure 6E) and impaired insulin sensitivity (Figure 6F) compared to MCK-Cre controls. These results indicate that p38γ hyperactivation in skeletal muscles of p38α^{MCK-KO} mice was responsible for their protection against obesity and diet-induced diabetes.

Altered IL-15 signaling in p38α^{MCK-KO} mice controls their locomotor activity

Skeletal muscle is known to influence brain function by the action of peripheral factors termed myokines (Pedersen, 2019). To search for myokine candidates that could mediate the high locomotor activity under the control of skeletal muscle p38γ (Whitham & Febbraio, 2016), we used a combination of RNA-seq-based transcriptomic analysis of MCK-Cre, p38α^{MCK-KO} and p38α/γ^{MCK-KO} muscles, and secretome searching tools to filter genes encoding for proteins found to be secreted. Fifteen genes were identified as differentially expressed (DEGs) in muscles from p38α^{MCK-KO} mice compared with controls and as likely to encode for proteins that can be secreted, which did not differ between p38α/γ^{MCK-KO} and MCK-Cre mice (Figures 7A, B). Among these hits, interleukin-15 (IL-15) is a well-known myokine which has been linked to the control of locomotor activity (Crane et al., 2015; He et al., 2010; Pistilli et al., 2011) and anxiety-related behaviors (Wu et al., 2010, 2011). Thus, we focused on this myokine and observed that *Il15* expression was only increased in muscles from p38α^{MCK-KO} mice, but not in the absence of p38γ (Figure 7C). This result was further confirmed by qPCR (Figure 7D). We also observed a tendency towards a higher activity and decreased depression-like behavior in p38α^{MCK-KO} mice compared with the other groups in the tail suspension test (Figure 7E). In addition, p38α^{MCK-KO} mice presented higher IL-15 concentrations in plasma compared with MCK-Cre mice (Figure 7F). These results suggested that lack of p38α in skeletal muscle may improve IL-15 secretion.

IL-15 signaling in the primary and secondary motor cortex (M1 and M2) in the brain has been shown to control movements (Grillner & El Manira, 2020). Thus, we decided to evaluate whether higher levels of muscle IL-15 secretion might affect motor cortex signaling. We found higher phosphorylation of extracellular signal-regulated kinase (ERK), signal transducer and activator of transcription 3 (STAT3) and 5 (STAT5) in these brain areas from p38α^{MCK-KO} mice (Figure 8A). These results suggested that higher IL-15 signaling in the motor cortex of p38α^{MCK-KO} mice could contribute to their increased locomotor activity. To check this hypothesis, we performed a stereotaxic surgery in MCK-Cre and p38α^{MCK-KO} mice to diminish IL-15 signaling in the motor cortex by injecting an shRNA against the alpha subunit of the receptor of IL-15 (IL-15Rα; shIL-15Rα), or a control sequence (shScramble), specifically in M1 (Figure 8B). Four weeks after the surgery, p38α^{MCK-KO} with reduced IL-15Rα in the motor cortex showed decreased locomotor activity compared with p38α^{MCK-KO} controls (p38α^{MCK-KO} shScramble) (Figure 8C). All these results suggest that the higher exercise-induced IL-15 release by muscles hyperactivating p38γ might lead to increased IL-15 signaling in the motor cortex of p38α^{MCK-KO} mice, contributing to their high locomotor activity.

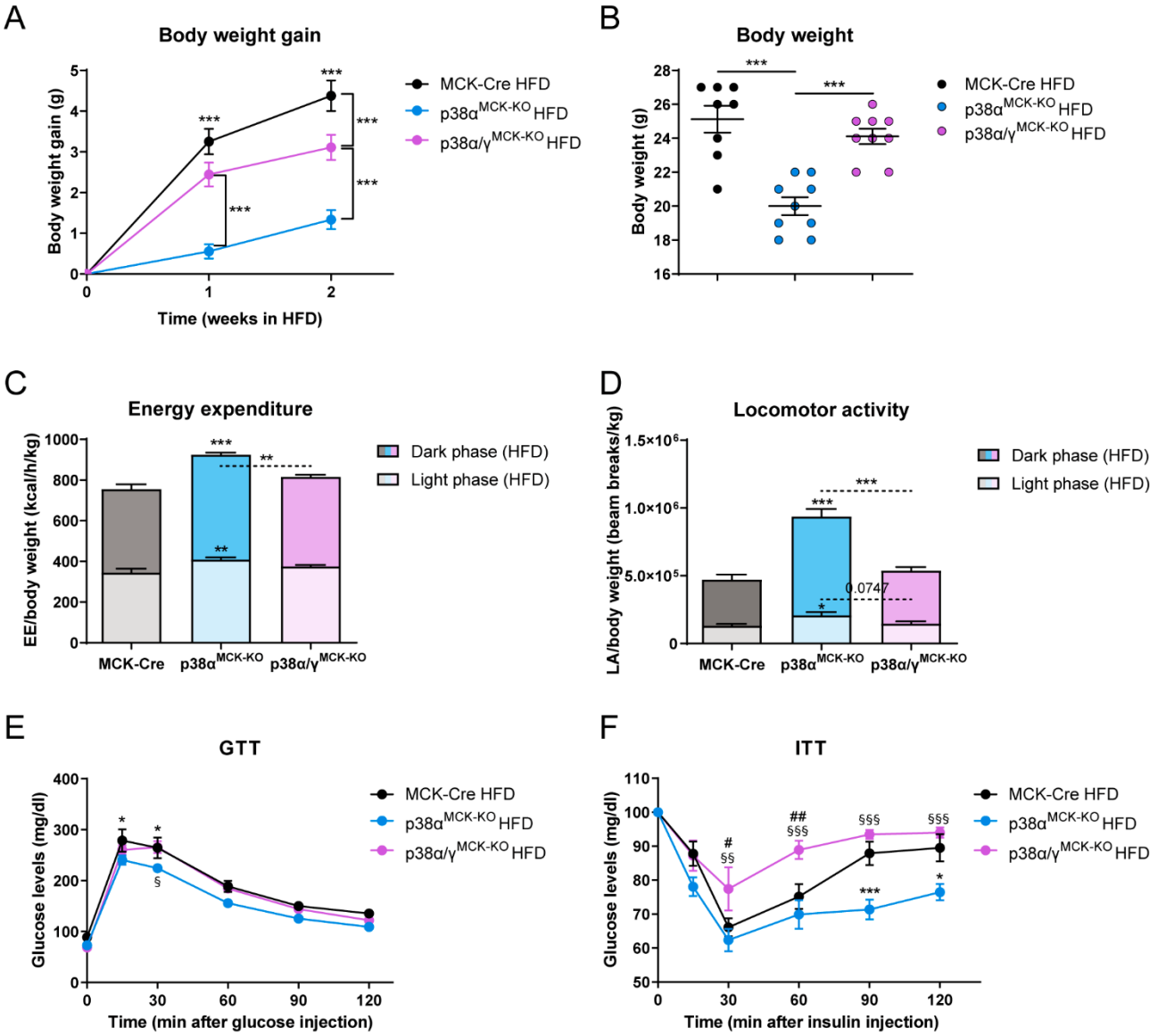

Figure 6. Lack of p38γ in p38α^{MCK-KO} mice loses their protection against HFD-induced obesity and diabetes. (**A-B**) p38α/γ^{MCK-KO}, p38α^{MCK-KO} and MCK-Cre mice were fed a HFD, and body weight was monitored for 2 weeks. (**A**) Body weight gain measured at the indicated times during HFD treatment. (**B**) Body weight measured before HFD feeding. Data are shown as means ± SEM; ***p < 0.001; one-way (Figure B) or two-way ANOVA (Figure A) coupled to Bonferroni's multiple comparisons test; n = 8-9. * symbols indicate differences between p38α^{MCK-KO} and MCK-Cre mice unless otherwise indicated. (**C, D**) p38α/γ^{MCK-KO}, p38α^{MCK-KO} and MCK-Cre mice were fed a HFD for 6 weeks and metabolic parameters were assayed at the end of this period. (**C**) Energy expenditure (EE) corrected by body weight. (**D**) Locomotor activity (LA) corrected by body weight during a 48 h period. Data are shown as means ± SEM; *p < 0.05; **p < 0.01; ***p < 0.001; one-way ANOVA coupled to Bonferroni's multiple comparisons test; n = 9-10. * symbols indicate differences between p38α^{MCK-KO} and MCK-Cre mice unless otherwise indicated. (**E, F**) p38α/γ^{MCK-KO}, p38α^{MCK-KO} and MCK-Cre mice were fed a HFD for 3 weeks. (**E**) Glucose tolerance test (GTT). Mice fasted overnight were injected i.p. with glucose (1 g/kg). (**F**) Insulin tolerance test (ITT). Mice fed *ad libitum* were injected i.p. with insulin (0.75 U/kg). Blood glucose concentration was measured at the indicated points in GTT and ITT. Data are shown as means ± SEM; *, $^{\#}$ or $^{\S}p$ < 0.05; $^{\#\#}$ or $^{\S\S}p$ < 0.01; *** or $^{\S\S\S}p$ < 0.001; two-way ANOVA coupled to Bonferroni's multiple comparisons test; n = 9-10. * symbols depict significant differences between p38α^{MCK-KO} and MCK-Cre mice; $^{\#}$ symbols indicate significant differences between p38α/γ^{MCK-KO} and MCK-Cre mice; and § symbols depict significant differences between p38α/γ^{MCK-KO} and p38α^{MCK-KO} mice.

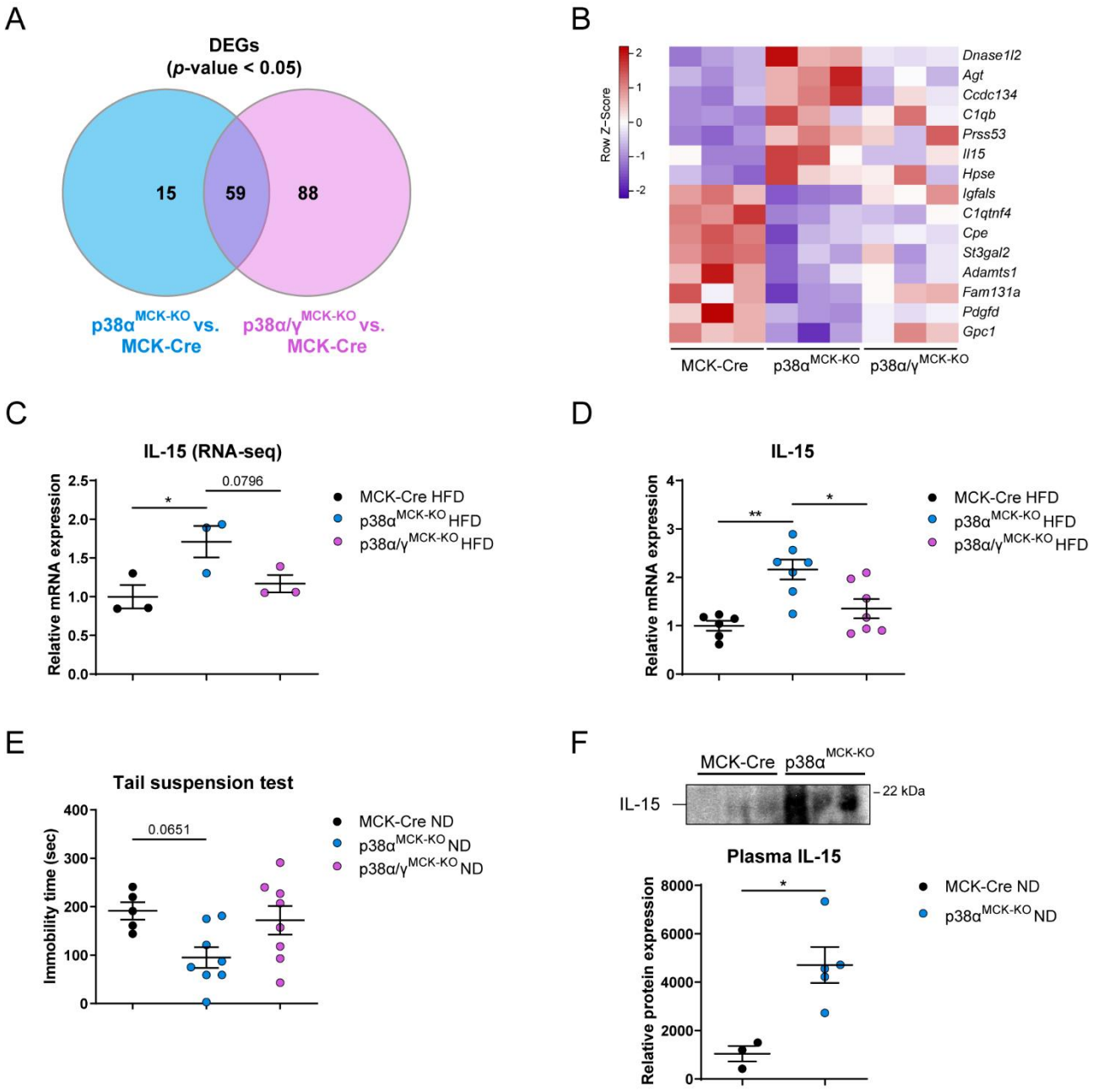

Figure 7. p38α^{MCK-KO} mice have higher muscle IL-15 expression and increased plasma IL-15 levels following exercise. (**A-C**) p38α^{MCK-KO}, p38α/γ^{MCK-KO} and MCK-Cre mice were fed a HFD for 6 weeks, fasted overnight and sacrificed, and an RNA-seq analysis with gastrocnemius samples was performed. (**A**) Venn diagram illustrating the number and overlap of differentially expressed genes (DEGs) with a positive or negative fold change (FC) when comparing muscles from p38α^{MCK-KO} or p38α/γ^{MCK-KO} mice with controls after filtering for those encoding for proteins predicted to be secreted. (**B**) Heatmap of all DEGs between gastrocnemius of p38α^{MCK-KO} and MCK-Cre mice with either a positive or a negative FC that are not considered DEGs between muscles of p38α/γ^{MCK-KO} and MCK-Cre mice, as determined by Student's *t*-test. (**C**) Quantification of *Il15* mRNA expression in RNA-seq of gastrocnemius samples. Data are normalized to MCK-Cre mice and shown as means ± SEM; **p* < 0.05; one-way ANOVA coupled with Bonferroni's multiple comparisons test; *n* = 3. (**D**) qRT-PCR analysis of *Il15* gene in gastrocnemius samples of p38α/γ^{MCK-KO}, p38α^{MCK-KO} and MCK-Cre mice fed a HFD for 2 weeks and sacrificed after overnight starvation. mRNA expression was normalized to the amount of *Rps18* mRNA in each sample. Data are normalized to MCK-Cre mice and shown as means ± SEM; **p* < 0.05; ***p* < 0.01; one-way ANOVA coupled to Bonferroni's multiple comparisons test; *n* = 6-7. (**E**) Tail suspension test performed in 18-23-week-old p38α/γ^{MCK-KO}, p38α^{MCK-KO} and MCK-Cre mice fed a ND. Data are shown as means ± SEM; one-way ANOVA coupled with Bonferroni's multiple comparisons test; *n* = 5-8. (**F**) 7-8-week-old p38α^{MCK-KO} and MCK-Cre mice were subjected to treadmill exercise for 30 min, and blood samples were extracted after training. Immunoblot analysis and quantification of circulating IL-15 levels immediately after exercise are shown. Data are shown as means ± SEM; **p* < 0.05, Student's *t*-test; *n* = 3-5.

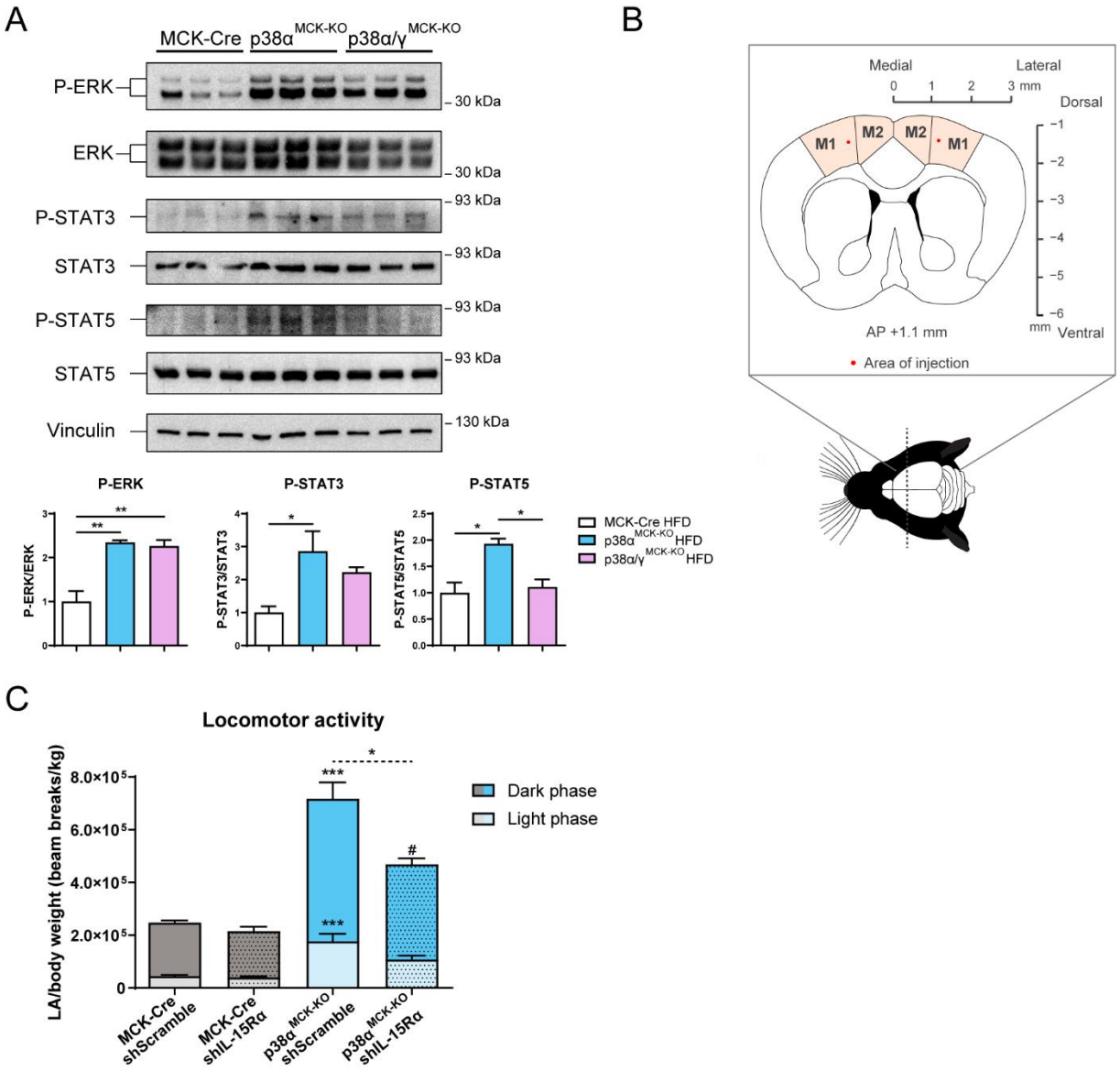

Figure 8. Increased IL-15 signaling in the motor cortex of p38α^{MCK-KO} mice controls their locomotor activity. (**A**) p38α/γ^{MCK-KO}, p38α^{MCK-KO} and MCK-Cre mice were fed a HFD for 6 weeks, fasted overnight and sacrificed. Extracts prepared from the motor cortex were examined by immunoblot analysis with antibodies against phospho (P)-ERK, P-STAT3, P-STAT5 and total protein levels. Vinculin protein expression was monitored as a loading control. Quantifications are shown. Data are normalized to MCK-Cre mice and shown as means ± SEM; *p < 0.05; **p < 0.01; one-way ANOVA coupled to Bonferroni's multiple comparisons test; n = 3. (**B, C**) 8-11-week-old p38α^{MCK-KO} and MCK-Cre mice were injected in the motor cortex with an shRNA targeting IL-15Rα (shIL-15Rα) or a control sequence (shScramble) by stereotaxic surgery. (**B**) Schematic representation of the brain area targeted during the surgical procedure. (**C**) Locomotor activity (LA) corrected by body weight during a 48 h period, 4 weeks after stereotaxic injection. Data are shown as means ± SEM; * or $^{\#}p$ < 0.05; ***p < 0.001; one-way ANOVA coupled to Bonferroni's multiple comparisons test; n = 5-9. * symbols indicate differences between MCK-Cre shScramble and p38α^{MCK-KO} shScramble unless otherwise indicated. $^{\#}$ symbols depict significant differences between MCK-Cre shIL-15Rα and p38α^{MCK-KO} shIL-15Rα.

Discussion

Exercise has been proposed as a physiological way to fight against obesity. In fact, exercise is associated with the secretion of myokines that improve metabolic homeostasis. Interestingly, it has also been described that p38γ is activated in human muscle after exercise (Boppart et al., 2000), suggesting that the activation of this kinase might have beneficial effects in metabolic homeostasis. Here, we show that p38γ in skeletal muscle controls the production and secretion of IL-15 by the muscle and, in consequence, the activation of the motor cortex, increasing locomotor activity. This increase

in locomotor activity results in higher energy expenditure, protecting against obesity, diabetes and liver steatosis.

Although many studies indicate that a higher activation of stress kinases signaling might be detrimental (Gehart et al., 2010), some of these kinases can also have protective roles in specific contexts, as skeletal muscle p38γ is doing. Stimuli such as muscle denervation (Odeh et al., 2020) or muscle contraction (Boppart et al., 2001; Coffey et al., 2006; Yu et al., 2003) are known to induce p38s activation in skeletal muscle. Although most of the studies do not discriminate between p38 isoforms, some have revealed the relevance of p38γ activation in response to exercise, in contrast to p38α (Boppart et al., 2000). Importantly, the opposite role of different p38 family members within the same tissue in energy homeostasis has been previously described, as happens with p38α and p38δ in brown adipose tissue (BAT) (Matesanz et al., 2018). Our results indicate that p38α and p38γ have opposite roles in muscle, not only regarding myogenesis (Lluís et al., 2006; Lovett et al., 2010), but also in the control of energy balance.

Our results point at IL-15 as a possible candidate for contributing to the high locomotor activity of p38α$^{MCK\text{-}KO}$ mice. In fact, IL-15 is a myokine usually elevated following exercise (Crane et al., 2015; Tamura et al., 2011), when p38γ is activated (Boppart et al., 2000). Our results suggest that higher muscle IL-15 expression could be facilitating IL-15 secretion after exercise stimulation, making it faster in the case of p38α$^{MCK\text{-}KO}$ mice. This higher plasma IL-15 upon exercise could signal in the cerebral motor cortex to enhance locomotor activity and reduce depression-like behavior. Importantly, a decrease in IL-15Rα in the motor cortex results in a reduction in locomotor activity in p38α$^{MCK\text{-}KO}$ mice, further reinforcing the relevant role of IL-15 signaling in this area for the control of voluntary movements. Interestingly, the higher permeability of the blood-brain barrier to IL-15 in inflammatory conditions could explain why the phenotype observed is more extreme in HFD compared to ND (Pan et al., 2008).

The regulation of muscle-derived IL-15 and its physiological consequences remains unclear. Although IL-15 has been linked to reductions in adiposity and protection against type 2 diabetes and fatty liver (Nielsen et al., 2008; Sun et al., 2016; Sun & Liu, 2015), inconsistency among studies has brought controversy, with some of them indicating a negative effect of IL-15 on obesity (Cepero-Donates et al., 2016; Lacraz et al., 2016; Loro et al., 2015). In fact, while some studies have found low plasma IL-15 levels in obesity (Nielsen et al., 2008), others found no differences (Pierce et al., 2015) or higher levels in overweight individuals (Dozio et al., 2014). Moreover, the role of IL-15 signaling in the control of locomotor activity is also controversial, with evidence indicating that IL-15 enhances (Crane et al., 2015) or decreases locomotor activity (He et al., 2010; Pistilli et al., 2011). This controversy is also found regarding its role in the modulation of anxiety and depression (Nguyen et al., 2017; Wu et al., 2010, 2011). Our results indicate that IL-15 signaling in the motor cortex contributes to the increased locomotor activity of p38α$^{MCK\text{-}KO}$ mice, establishing a relevant crosstalk between the muscle and the brain.

Considering our data altogether, we propose a novel role of stress-activated kinases in activation of pathways linked to energy metabolism and mitochondrial respiration. This study places skeletal muscle p38α as a signaling hub involved in different metabolic alterations and reveals a critical role for muscle p38γ activation in the stimulation of locomotor activity and energy expenditure, providing a promising new target for the development of novel therapeutic approaches to the current obesity epidemic.

Materials and methods

Mouse model

Mice carrying the floxed p38α alleles (B6.129-*Mapk14*$^{tm2.1}$/N) were generated by Boehringer Ingelheim Pharmaceuticals and have been described previously (Hui et al., 2007). These mice were crossed to mice expressing the Cre recombinase under the MCK promoter (FVB-*Tg(Ckmm-cre)5Khn*/N; MCK-Cre in the text) to conditionally delete p38α from striated muscle (*Mapk14*$^{MCK\text{-}cre}$; designated as p38α$^{MCK\text{-}KO}$ in the text). To generate double knockout mice for p38α and p38γ, p38α$^{MCK\text{-}KO}$ mice were crossed to whole-body knockout mice for p38γ (B6.129-*Mapk12*^{tm1}), generating full-body knockout mice for p38γ and conditional for p38α in striated muscle (p38α/γ$^{MCK\text{-}KO}$ in the text).

Mice were backcrossed for at least 10 generations to the C57BL/6N background and

genotyped by PCR analysis of genomic DNA isolated from mouse tails. All studies were performed using male mice (8-29 weeks old). Mice were housed randomly in a pathogen-free animal facility and maintained on a 12-h light/dark cycle at constant temperature and humidity. Mice were fed a normal chow diet (ND) (breeding and maintenance diets: D183, SAFE; and 1410, Altromin) or a high-fat diet (HFD) (high-fat diet with 60% kcal fat and 1.5% cholesterol: D11103002i, Research Diets, Inc.) *ad libitum* for 8-29 weeks. Experiments in HFD started at 8 weeks of age. All animal procedures conformed to European Union Directive 2010/63/EU and Recommendation 2007/526/EC regarding the protection of animals used for experimental and other scientific purposes, enforced in Spanish law under Real Decreto 53/2013. All experiments were approved by the Spanish National Center for Cardiovascular Research (CNIC) Animal Care and Use Committee and Comunidad de Madrid.

Determination of body composition and energy balance

For determination of energy expenditure, food intake, locomotor activity and respiratory quotient (RQ), animals were monitored in a custom 12-cage indirect calorimetry, food intake and locomotor activity monitoring system (TSE LabMaster, TSE Systems; and Panlab, Harvard Apparatus) as previously described (Czyzyk et al., 2010). Mice were acclimated during 48 h to the metabolic cages and then were monitored for an additional 48 h. The indirect calorimetry system collected information about food intake, locomotor activity and respiratory gas exchange (oxygen consumption, vO_2, and carbon dioxide production, vCO_2) every 30 min. Data collected from the last 48 h were used to calculate all parameters for which results are reported. RQ was calculated by dividing vCO_2 produced by vO_2 consumed (vCO_2/vO_2), thus determining the preferential macronutrient oxidation. Energy expenditure was calculated from O_2 consumption and CO_2 production measurements with standard analysis software provided with the calorimeter system. Energy expenditure (kcal/48 h) was normalized to body weight measured at the end of the procedure (energy expenditure/kg body weight). Locomotor activity was determined with infrared sensors that register horizontal and vertical movements. The total number of beam breaks was determined and normalized to body weight measured at the end of the procedure (locomotor activity/kg body weight).

Temperature measurement

Body temperature was measured by a rectal thermometer (AZ 8851 K/J/T Handheld Digital Thermometer-Single from AZ Instruments Corp.; and BAT-12 Microprobe Thermometer from Physitemp). For determination of interscapular temperature as a representation of BAT temperature, mice were shaved in the interscapular region, and a thermographic camera was used to capture images (E60bx: Compact Infrared Thermal Imaging Camera, FLIR). Images were analyzed with FLIR Tools software.

For cold exposure test, temperature was measured with a rectal thermometer (BAT-12 Microprobe Thermometer, Physitemp), and mice were placed in a cold room at 4 °C. Rectal temperature was measured every 60 min, being the last measurement 6 h after the beginning of the test.

***In vivo* metabolic tests**

Glucose tolerance test (GTT), insulin tolerance test (ITT) and insulin release test were performed as described (Sabio et al., 2009). For GTT, mice were fasted overnight (16 h), and basal glucose levels were measured by collecting blood from the tail tip and using a glucometer (Ascensia BREEZE 2 from Bayer and Contour Next One from Ascensia). Then, mice were injected intraperitoneally (i.p.) with glucose (1 g/kg body weight) (D(+)-glucose monohydrate, Merck) dissolved in PBS, and blood glucose concentration was measured at 15, 30, 60, 90 and 120 min post-injection. For ITT, mice were fed *ad libitum*, and basal glucose levels were measured as described for GTT. Then, mice were injected i.p. with insulin (0.75 U/kg body weight) (Lilly). Blood glucose concentration was measured at 15, 30, 60, 90 and 120 min after insulin injection. Glucose levels were normalized to basal glucose and shown as percentage. For insulin release test, mice were fasted overnight (16 h), and 100 µl of blood samples from the submandibular vein were collected in EDTA blood collection tubes (Microvette). Mice were injected i.p. with glucose (2 g/kg), and 100 µl of blood were collected using the same procedure, 10 and 30 min after glucose injection. Plasma samples were obtained by centrifuging the samples at 9,600 x *g* for 20 min at 4 °C.

Determination of homeostasis model assessment of insulin resistance (HOMA-IR)

The homeostasis model assessment of insulin resistance (HOMA-IR) was calculated as described (Akagiri et al., 2008). Glucose and insulin concentrations obtained after 16 h of food withdrawal were measured and used in the following formula:

$$\frac{\text{Fasting blood glucose (mg/dl) x Fasting insulin (µU/ml)}}{405}$$

Tail suspension test

Tail suspension test was performed as previously described (Can et al., 2012), with minor modifications. Mice were acclimated to the experimental room for 15 min. A white 42 cm height x 56 cm width x 17.5 cm depth tail suspension box was used, which was divided in 4 three-walled rectangular compartments (42 cm height x 14 cm width x 17.5 cm depth) to prevent mice from observing other animals. A suspension bar (1 cm height x 1 cm width x 60 cm length) was placed on the top of the box. A 17 cm tape was used to adhere the end of mouse's tail at one end and the suspension bar at the other end in a parallel way. Hollow cylinders (4 cm length, 1.6 cm outside diameter, 1.2 cm inside diameter, 4.15 g) were placed around the tails of mice to prevent climbing behavior. Mice were suspended by the tail in the middle of their compartments with an approximate distance between their noses and the apparatus floor of 15 cm. A digital camera was used to record 6 min sessions with 4 mice tested simultaneously. An on-screen stopwatch software (Xnote Stopwatch, dnSoft Research Group) was used to measure the time that each mouse spends as mobile, excluding small movements confined to the front legs but without involvement of the hind legs, as well as oscillations due to the momentum gained during the earlier mobility, which were considered as immobility. Immobility time was calculated by subtracting the time the mouse spends as mobile to the total 6 min of the session. All analyses were done in a blinded fashion.

Treadmill exercise

7-8-week-old ND-fed mice were exercised during 30 min with forced treadmill running training at a speed of 10 cm/s for 5 min, 15 cm/s for 20 min and 20 cm/s for 5 min, at a 20° uphill inclination of the treadmill (5-lane LE8710 treadmill, Harvard Apparatus, Panlab). Intensity of the electrical stimulation was set to 0.2 mA. The same exercise protocol was repeated two days later. Blood was obtained from the submandibular vein immediately after exercise and collected in EDTA blood collection tubes (Microvette). Plasma was obtained after centrifugation at 9,600 x *g* for 20 min at 4 °C.

Lentivirus vector production and stereotaxic microinjections

Lentiviruses were produced as described (Urso et al., 2011), with some modifications. Human embryonic kidney (HEK)-293T cells were plated at 25-35% confluence in Dulbecco's Modified Eagle Medium (DMEM) (Gibco) supplemented with 10% fetal bovine serum (FBS) (Sigma), 200 mM L-glutamine (Lonza), and 10,000 U/ml penicillin/streptomycin (1:1, Lonza). Transient calcium phosphate co-transfection of HEK-293T cells was done with the pGIPZ empty vector or short hairpin RNAs (shRNAs) against the alpha subunit of IL-15 receptor (pGIPZ.shIL15Rα vector, V3LMM_451921, Dharmacon), together with pΔ8.9 and pVSV-G packaging plasmids. The supernatants containing the lentiviral particles were collected 48 h after removal of the calcium phosphate precipitate, filtered through 0.45-µm filters and concentrated by ultracentrifugation at 115,500 x *g* for 2 h at 4 °C (Ultra-Clear Tubes, SW28 rotor and Optima L-100 XP Ultracentrifuge; Beckman Coulter).

Mice were injected in the primary motor cortex (M1) with 1 µl of lentiviral particles suspended in sterile PBS, with a speed of 100 nl/min. For that, mice were placed in a stereotaxic frame (World Precision Instruments) under ketamine-xylazine anesthesia injected i.p. (42.5% ketamine [Richter Pharma AG] and 20% xylazine hydrochloride [Bayer] in NaCl). A longitudinal incision in the skin over the cranium was performed, and lentiviruses were injected stereotaxically in M1 area with a 32-gauge needle (Hamilton) connected to a 1 µl syringe. The coordinates used to reach the M1 area were: anterior to the bregma (AP), +1.1 mm; lateral to the sagittal suture (ML), ±1.2 mm; and ventral from the surface of the skull (DV), -1.5 mm. The incision was closed with sutures, and buprenorphine (0.1 mg/kg body weight) (Richter Pharma AG) was injected i.p. after surgery as a painkiller.

Blood and organs collection

At sacrifice, blood samples were obtained from the submandibular vein and collected in EDTA blood collection tubes (Microvette), and plasma was obtained after centrifugation at 9,600 x *g* for 20 min at 4 °C. Mice were fasted overnight for most of the experiments, euthanized by cervical dislocation, and organs were removed, weighed and frozen in liquid nitrogen. For insulin signaling analysis, mice were injected i.p. with 1.5 U kg insulin (Lilly) 15 min prior to removal of the organs. Liver samples were collected in 10% formalin (Bio-Optica) for hematoxylin and eosin (H&E) staining, or frozen in dry ice after being embedded in optimal cutting temperature (OCT) compound (Tissue-Tek) for Oil Red staining. Brain samples were frozen in dry ice to preserve their anatomy. The primary and secondary motor cortex (M1 and M2) was removed from the whole brain by cutting at the caudal part of the hippocampus parallel to the base of the hypothalamus and 1.2 mm to each lateral side of the corpus callosum. The depth of each section isolated was around 1 mm thick and according to the Allen Brain reference Atlas (Allen Institute for Brain Science, 2004).

Plasma analysis

Plasma insulin, leptin and ghrelin concentrations were measured by magnetic bead-based multiplex assay (Bio-Rad) with a Luminex 200 analyzer, following manufacturer's instructions. IL-15 was detected in plasma samples by Western blot. Samples were diluted in PBS (1/5), Milli-Q water (H_2O_{mq}), and Laemmli Sample Buffer, and separated by sodium dodecyl sulfate (SDS)-polyacrylamide gel electrophoresis (PAGE) using AnykD Criterion TGX Precast gels (Bio-Rad) as indicated in immunoblot analysis.

Immunoblot analysis

Tissue extracts were prepared in lysis buffer (50 mM Tris-HCl pH 7.5, 1 mM EGTA, 1 mM EDTA, 50 mM NaF, 1 mM sodium glycerophosphate, 5 mM sodium pyrophosphate, 0.27 M sucrose, 1% Triton X-100, 0.1% β-mercaptoethanol, 0.1 mM phenylmethylsulfonyl fluoride [PMSF], 1 mM sodium orthovanadate, 1 µg/ml leupeptin, and 1 µg/ml aprotinin) by using T 10 Ultra-Turrax (IKA). Lysates were centrifuged at 19,000 x *g* for 20 min at 4 °C, and protein concentration in supernatants was quantified by Bradford method (Bio-Rad Protein Assay). Samples were denatured in loading buffer (0.24 M Tris-HCl pH 6.8, 40% glycerol, 8% SDS, 5% β-mercaptoethanol, 0.04% bromophenol blue) at 95 °C for 5 min. Equal amounts of protein (20-50 µg) were loaded in 10% polyacrylamide gels (30% Acrylamide/Bis Solution, 29:1, Bio-Rad) or AnykD Criterion TGX Precast gels for IL-15 detection (Bio-Rad) and separated by SDS-PAGE. Gels were transferred to 0.2 µm pore-size nitrocellulose membranes (Bio-Rad), blocked with 10% fat-free milk powder for 45 min. Membranes were probed overnight with primary antibodies against phospho-p38 (T180/Y182; 9211), p38α (Santa Cruz Biotechnology; sc-535), p38γ (2307), phospho-MKK3 (S189)/MKK6 (S207) (9231), MKK3b (9238), MKK6 (Enzo Life Sciences; ADI-KAP-MA014-E), phospho-MK2 (T334; 3007), MK2 (3042), phospho-HSP27 (S82; 9709), phospho-AKT (T308; 2965), phospho-AKT (S473; 9271), AKT (9272), IL-15 (Abcam; ab273625), phospho-ERK1/2 (T202/Y204; 3101), ERK1/2 (9102), phospho-STAT3 (Y705; 9145), STAT3 (12640), phospho-STAT5 (Y694; 9359), STAT5 (94205) and vinculin (Sigma-Aldrich; V4505). All primary antibodies were used at 1:1,000, except from vinculin (1:2,000) and are from Cell Signaling, unless otherwise indicated. Horseradish peroxidase (HRP)-conjugated goat anti-rabbit and sheep anti-mouse from GE Healthcare were used as secondary antibodies (1:5,000) for a 1-h incubation at room temperature (RT). Membranes were washed with PBS-0.1% Tween, and reactive bands were detected by enhanced chemiluminescence (ECL, GE Healthcare) and quantified by ImageJ software (National Institutes of Health, NIH). In certain instances, membranes probed for phospho-proteins were stripped by incubating them at 55 °C for 15 min with stripping buffer (68 mM Tris-HCl pH 6.8, 1% SDS, 0.7% β-mercaptoethanol) and reprobed for total protein. Results were normalized to the non-phosphorylated form.

Quantitative proteomics by isobaric labeling

Quantitative proteomic analysis was performed in collaboration with the Proteomics Unit of CNIC. Gastrocnemius muscle samples from HFD-fed mice were homogenized by using the MagNA Lyser. 120 µg of total protein for each sample were digested using the filter aided sample preparation (FASP) protocol as previously described (Cardona et al., 2015). The dried peptides were dissolved in 100 mM triethylammonium bicarbonate (TEAB)

buffer. Equal amounts of each peptide sample were labeled using the 10-plex tandem mass tag (TMT) Kit (Thermo Scientific). Labeled peptides were subjected to liquid chromatography with tandem mass spectrometry (LC-MS/MS) analysis using a C-18 reversed phase EASY nano-column (75 µm I.D. x 50 cm, 2 µm particle size, Acclaim PepMap RSLC, 100 C18; Thermo Scientific) in a continuous gradient consisting of 0-30% B in 360 min, 50-90% B in 3 min (A = 0.5% formic acid; B = 90% acetonitrile, 0.5% formic acid). Peptides were eluted from the reverse-phase nano-column to an emitter nanospray needle for real time ionization and peptide fragmentation on an Orbitrap Trybrid Fusion mass spectrometer (Thermo Fisher). An enhanced Fourier transform-resolution spectrum (resolution = 70.000) followed by the MS/MS spectra from the 15 most intense parent ions was performed. All spectra were analyzed with Proteome Discoverer (version 2.1, Thermo Fisher Scientific) using SEQUEST-HT (Thermo Fisher Scientific). Data were searched against a Uniprot database (48,644 sequences), and peptide identification was performed as described previously (Navarro & Vázquez, 2009). Identified peptides had a false discovery rate (FDR) equal or lower than 1% FDR. Protein quantification and statistical analysis were performed using QuiXoT based on the weighted spectrum, peptide and protein (WSPP) statistical model. Proteins were annotated using Ingenuity Knowledge Database (Ingenuity Pathway Analysis, IPA).

RNA isolation and quantitative real-time-PCR analyses (qRT-PCR)

RNA from gastrocnemius samples was extracted with RNeasy Fibrous Tissue Mini kit (Qiagen) following manufacturer's instructions. T 10 Ultra-Turrax (IKA) was used to homogenize muscles. RNA concentration was measured with a NanoDrop 1000 spectrophotometer (Thermo Fisher Scientific). From 200 ng to 1 µg RNA were retrotranscribed using High-Capacity cDNA Reverse Transcription Kit (Applied Biosystems) following manufacturer's instructions. The following program was used: 10 min at 25 °C, 2 h at 37 °C, 5 min at 85 °C. Samples were diluted 1/5, and the expression of mRNA was examined by qRT-PCR using a 7900HT Fast Real-Time PCR System and FAST SYBR GREEN assays (Applied Biosystems). For that, 2 µl of diluted complementary DNA (cDNA) were added to 384-well MicroAmp Optical plates (Applied Biosystems), together with the following mix per well: 4 µl Fast SYBR Green Master Mix (Applied Biosystems), 0.16 µl each primer and 2 µl ribonuclease (RNase)-free water. An 8-point standard curve created by 5-fold serial dilution was included. The following PCR program in SDS 2.4 software was used: 1 cycle of 20 s at 95 °C and 40 cycles of 1 s at 95 °C plus 20 s at 60 °C. A dissociation curve was used after each reaction to verify primer specificity and purity of the PCR products. Relative mRNA expression was normalized to ribosomal protein S18 (*Rps18*) or glyceraldehyde-3-phosphate dehydrogenase (*Gapdh*) mRNA measured in each sample. The following genes were amplified using primers purchased from Sigma-Aldrich (F, forward; R, reverse):

Map2k3 F: GCCTCAGACCAAAGGAAAATCC
Map2k3 R: GGTGTGGGGTTGGACACAG
Map2k6 F: ATGTCTCAGTCGAAAGGCAAG
Map2k6 R: TTGGAGTCTAAATCCCGAGGC
Mapk12 F: ATGCGCTACACGCAGACA
Mapk12 R: TGGTCATTGCCTTTGAACAG
Rps18 F: CAGCTCCAAGCGTTCCTGG
Rps18 R: GGCCTTCAATTACAGTCGTCTTC
Gapdh F: TGAAGCAGGCATCTGAGGG
Gapdh R: CGAAGGTGGAAGAGTGGGA
Il15 F: CATCCATCTCGTGCTACTTGTG
Il15 R: GCCTCTGTTTTAGGGAGACCT

RNA-sequencing (RNA-seq) library preparation, sequencing and generation of FastQ files

Total RNA was isolated from gastrocnemius samples of mice fed a HFD for 6 weeks using the RNeasy Fibrous Tissue Mini Kit (Qiagen) as previously described. RNA quality was verified using Agilent 2100 Bioanalyzer, and individual samples with RNA Integrity Number (RIN) > 8 were included in the study. Samples were pooled from two individual samples to obtain 200 ng of total RNA (100 ng from each pooled sample) in 100 µl RNase-free water. RNA sequencing was performed in the CNIC Genomics Unit. Total RNA was used to generate barcoded RNA-seq libraries using the NEBNext Ultra II Directional RNA Library preparation kit (New England Biolabs) according to manufacturer's instructions. First, poly A+ RNA was purified using poly-T oligo-attached magnetic beads followed by fragmentation and first and second cDNA strand synthesis. Next, cDNA ends were repaired and adenylated. The NEBNext adaptor

was then ligated followed by second strand removal, uracile excision from the adaptor and PCR amplification. The size of the libraries was checked using the Agilent 2100 Bioanalyzer, and the concentration was determined using the Qubit® fluorometer (Thermo Fisher). Libraries were sequenced on a HiSeq2500 (Illumina) to generate 60 bases single reads. FastQ files for each sample were obtained using CASAVA v1.8 software (Illumina).

RNA-seq data analysis was performed by the Bioinformatics Unit of CNIC. The number of reads per sample was between 25 and 30 million. After evaluating their quality with FastQC (Andrews, n.d.), reads were mapped against mouse transcriptome GRCm38.76, and gene expression levels were estimated with RNA-seq by Expectation Maximization (RSEM) (Li & Dewey, 2011). Parameter "strandedness reverse" was included to calculate expression from directional RNA-seq data. The percentage of aligned reads was between 91% and 94% for all samples. Expression count matrices were then processed with an analysis pipeline that used Bioconductor package limma (Ritchie et al., 2015) for normalization (using trimmed mean of M-values [TMM] method) and differential expression testing, taking into account only those genes expressed with at least one count per million in at least three samples (the number of samples available for each condition). Three pairwise contrasts were performed: $p38\alpha^{MCK\text{-}KO}$ vs. MCK-Cre, $p38\alpha/\gamma^{MCK\text{-}KO}$ vs. MCK-Cre, and $p38\alpha^{MCK\text{-}KO}$ vs. $p38\alpha/\gamma^{MCK\text{-}KO}$. Changes in gene expression were considered significant if associated to Benjamini and Hochberg adjusted p-value < 0.05.

Histological analysis

Liver tissue samples were fixed in 10% formalin (Bio-Optica) for 48 h, dehydrated and embedded in paraffin. 8 µm sections were cut and stained with H&E (American Master Tech Scientific).

For Oil Red staining, 8 µm sections were prepared from tissue frozen in OCT compound (Tissue-Tek) using a cryostat (Leica CM 1950). Sections were fixed in 10% formalin (Bio-Optica) during 10 min at 4 °C and rinsed with distilled water. Sections were embedded in propylene glycol (Sigma-Aldrich) for 5 min at RT, changed to new propylene glycol and left 5 additional min. Samples were stained with pre-warmed (60 °C) Oil Red O solution (7 mg/ml Oil Red O from Sigma-Aldrich in propylene glycol) for 10 min. 85% propylene glycol was added for 3 min, and samples were rinsed in distilled water and embedded in hematoxylin for 1 min, washed in water and introduced in Bluing solution. Sections were washed in tap water, rinsed in distilled water and mounted in aqueous mounting agent Aquatex (Merck).

All samples were examined in Leica DM2500 microscope at different magnifications and imaged using the software Leica Application Suite v4.3 (LAS v4.3).

Gene set enrichment analysis (GSEA)

Fold change (FC) values were used to generate pre-ranked protein lists for gene set enrichment analysis (Subramanian et al., 2005). GSEA was done using GSEA software version 4.0.1, which uses predefined gene sets from the Molecular Signatures Database (MSigDB v7.2) (Liberzon et al., 2015). For unbiased discovery of enriched gene sets in proteomics study, we used the HALLMARK gene sets as queries and a list of ranked proteins based on a score calculated as difference between Zq means for each protein for every comparison. The minimum and maximum criteria for selection of gene sets from the collection were 15 and 500 genes, respectively. "Classic" mode was used for enrichment statistic calculation. GSEA graphs were replotted using replot GSEA package in R.

Ingenuity Pathway Analysis (IPA)

The list of differentially expressed proteins in proteomics analyses of skeletal muscles, containing protein identifiers and corresponding expression values, was uploaded into the IPA software (Qiagen) to discover overrepresented protein lists derived from Ingenuity's proprietary knowledge-base (IPAKB). Enrichments associated to a p-value < 0.05 were considered statistically significant and included. Each protein identifier was mapped to its corresponding gene object in the Ingenuity Pathway Knowledge Base. The "core analysis" function included in the software was used to interpret the differentially expressed data, which included biological processes, canonical pathways, upstream transcriptional regulators, and gene networks.

Identification of secreted proteins

All potential p38γ-induced genes as judged from gene expression analysis in the comparison of muscles from p38α^{MCK-KO} or p38α/γ^{MCK-KO} mice with MCK-Cre controls with a *p*-value < 0.05 were filtered for those encoding for secreted proteins by using the SignalP, SecretomeP and TargetP software (http://www.cbs.dtu.dk/services/) as described (Emanuelsson et al., 2007). Heatmap representation was created using Heatmapper tool.

Statistical analysis

Values are presented as means ± standard error of the mean (SEM). Differences between groups were examined for statistical significance using two-tailed unpaired Student's *t*-test (with Welch's correction when variances were different), or one- or two-way analysis of variance (ANOVA) coupled to Bonferroni's post-test. Statistical significance was determined as a two-sided *p*-value < 0.05 (GraphPad Prism 8.0). Family-wise error rate (FWER) *p*-values are displayed for GSEA to correct for multiple hypothesis testing. Statistical details and experimental *n* are specified in figure legends.

Acknowledgments

We thank Dr. R. J. Davis (University of Massachusetts Medical School, Worcester, MA) for IL-15Rα plasmid. L. Herrera-Melle is a fellow of the Ministerio de Educación, Cultura y Deporte (FPU15-05802). This work was funded by the following grants: MINECO-PID2019-104399RB-I00, Fundación Jesús Serra, EFSD/Lilly European Diabetes Research Programme, Fundación AECC PROYE19047SABI and Comunidad de Madrid IMMUNOTHERCAN-CM S2010/BMD-2326 and B2017/BMD-3733. The CNIC is supported by the Ministerio de Ciencia, Innovación y Universidades and the Pro CNIC Foundation.

The authors declare no competing financial interests.

References

World Health Organization (WHO). (2020). Obesity and overweight. https://www.who.int/news-room/fact-sheets/detail/obesity-and-overweight

Akagiri, S., Naito, Y., Ichikawa, H., Mizushima, K., Takagi, T., Handa, O., Kokura, S., & Yoshikawa, T. (2008). A Mouse Model of Metabolic Syndrome; Increase in Visceral Adipose Tissue Precedes the Development of Fatty Liver and Insulin Resistance in High-Fat Diet-Fed Male KK/Ta Mice. *J Clin Biochem Nutr*, *42*(2), 150–157.

Allen Institute for Brain Science (2004). Allen Mouse Brain Atlas. https://mouse.brain-map.org/static/atlas

Andrews, S. (n.d.). A quality control application for high throughput sequence data. Babraham Institute. http://www.bioinformatics.babraham.ac.uk/projects/fastqc/

Atakan, M. M., Kosar, S. N., Guzel, Y., Tin, H. T., & Yan, X. (2021). The Role of Exercise, Diet, and Cytokines in Preventing Obesity and Improving Adipose Tissue. *Nutrients*, *13*(5).

Bengal, E., Aviram, S., & Hayek, T. (2020). p38 MAPK in Glucose Metabolism of Skeletal Muscle: Beneficial or Harmful? *Int J Mol Sci*, *21*(18).

Boppart, M. D., Asp, S., Wojtaszewski, J. F., Fielding, R. A., Mohr, T., & Goodyear, L. J. (2000). Marathon running transiently increases c-Jun NH2-terminal kinase and p38 activities in human skeletal muscle. *J Physiol*, *526 Pt 3*, 663–669.

Boppart, M. D., Hirshman, M. F., Sakamoto, K., Fielding, R. A., & Goodyear, L. J. (2001). Static stretch increases c-Jun NH2-terminal kinase activity and p38 phosphorylation in rat skeletal muscle. *Am J Physiol Cell Physiol*, *280*(2), C352-8.

Can, A., Dao, D. T., Terrillion, C. E., Piantadosi, S. C., Bhat, S., & Gould, T. D. (2012). The tail suspension test. *J Vis Exp*, *59*, e3769.

Cardona, M., López, J. A., Serafín, A., Rongvaux, A., Inserte, J., García-Dorado, D., Flavell, R., Llovera, M., Canas, X., Vázquez, J., & Sanchis, D. (2015). Executioner Caspase-3 and 7 Deficiency Reduces Myocyte Number in the Developing Mouse Heart. *PLoS One*, *10*(6), e0131411.

Cepero-Donates, Y., Lacraz, G., Ghobadi, F., Rakotoarivelo, V., Orkhis, S., Mayhue, M., Chen, Y. G., Rola-Pleszczynski, M., Menendez, A., Ilangumaran, S., & Ramanathan, S. (2016). Interleukin-15-mediated inflammation promotes non-alcoholic fatty liver disease. *Cytokine*, *82*, 102–111.

Chan, M. H., McGee, S. L., Watt, M. J., Hargreaves, M., & Febbraio, M. A. (2004). Altering dietary nutrient intake that reduces glycogen content leads to phosphorylation of nuclear p38 MAP kinase in human skeletal muscle: association with IL-6 gene transcription during contraction. *FASEB J*, *18*(14), 1785–1787.

Coffey, V. G., Zhong, Z., Shield, A., Canny, B. J., Chibalin, A. V, Zierath, J. R., & Hawley, J. A. (2006). Early signaling responses to divergent exercise stimuli in skeletal muscle from well-trained humans. *FASEB J*, *20*(1), 190–192.

Combes, A., Dekerle, J., Webborn, N., Watt, P., Bougault, V., & Daussin, F. N. (2015). Exercise-induced metabolic fluctuations influence AMPK, p38-MAPK and CaMKII phosphorylation in human skeletal muscle. *Physiol Rep*, *3*(9).

Crane, J. D., MacNeil, L. G., Lally, J. S., Ford, R. J., Bujak, A. L., Brar, I. K., Kemp, B. E., Raha, S., Steinberg, G. R., & Tarnopolsky, M. A. (2015). Exercise-stimulated interleukin-15 is controlled by AMPK and regulates skin metabolism and aging. *Aging Cell*, *14*(4), 625–634.

Cuenda, A., Cohen, P., Buee-Scherrer, V., & Goedert, M. (1997). Activation of stress-activated protein kinase-3 (SAPK3) by cytokines and cellular stresses is mediated via SAPKK3 (MKK6); comparison of the specificities of SAPK3 and SAPK2 (RK/p38). *EMBO J*, *16*(2), 295–305.

Czyzyk, T. A., Nogueiras, R., Lockwood, J. F., McKinzie, J.

H., Coskun, T., Pintar, J. E., Hammond, C., Tschop, M. H., & Statnick, M. A. (2010). kappa-Opioid receptors control the metabolic response to a high-energy diet in mice. *FASEB J*, *24*(4), 1151–1159.

de Alvaro, C., Teruel, T., Hernandez, R., & Lorenzo, M. (2004). Tumor necrosis factor alpha produces insulin resistance in skeletal muscle by activation of inhibitor kappaB kinase in a p38 MAPK-dependent manner. *J Biol Chem*, *279*(17), 17070–17078.

Dozio, E., Malavazos, A. E., Vianello, E., Briganti, S., Dogliotti, G., Bandera, F., Giacomazzi, F., Castelvecchio, S., Menicanti, L., Sigruener, A., Schmitz, G., & Corsi Romanelli, M. M. (2014). Interleukin-15 and soluble interleukin-15 receptor alpha in coronary artery disease patients: association with epicardial fat and indices of adipose tissue distribution. *PLoS One*, *9*(3), e90960.

Emanuelsson, O., Brunak, S., von Heijne, G., & Nielsen, H. (2007). Locating proteins in the cell using TargetP, SignalP and related tools. *Nat Protoc*, *2*(4), 953–971.

Gehart, H., Kumpf, S., Ittner, A., & Ricci, R. (2010). MAPK signalling in cellular metabolism: stress or wellness? *EMBO Rep*, *11*(11), 834–840.

González-Terán, B., Matesanz, N., Nikolic, I., Verdugo, M. A., Sreeramkumar, V., Hernández-Cosido, L., Mora, A., Crainiciuc, G., Saiz, M. L., Bernardo, E., Leiva-Vega, L., Rodríguez, E., Bondia, V., Torres, J. L., Pérez-Sieira, S., Ortega, L., Cuenda, A., Sánchez-Madrid, F., Nogueiras, R., … Sabio, G. (2016). p38gamma and p38delta reprogram liver metabolism by modulating neutrophil infiltration. *EMBO J*, *35*(5), 536–552.

Grillner, S., & El Manira, A. (2020). Current Principles of Motor Control, with Special Reference to Vertebrate Locomotion. *Physiol Rev*, *100*(1), 271–320.

He, Y., Wu, X., Khan, R. S., Kastin, A. J., Cornelissen-Guillaume, G. G., Hsuchou, H., Robert, B., Halberg, F., & Pan, W. (2010). IL-15 receptor deletion results in circadian changes of locomotor and metabolic activity. *J Mol Neurosci*, *41*(2), 315–321.

Hui, L., Bakiri, L., Mairhorfer, A., Schweifer, N., Haslinger, C., Kenner, L., Komnenovic, V., Scheuch, H., Beug, H., & Wagner, E. F. (2007). p38alpha suppresses normal and cancer cell proliferation by antagonizing the JNK-c-Jun pathway. *Nat Genet*, *39*(6), 741–749.

Kahn, S. E., Hull, R. L., & Utzschneider, K. M. (2006). Mechanisms linking obesity to insulin resistance and type 2 diabetes. *Nature*, *444*(7121), 840–846.

Koh, A., Molinaro, A., Stahlman, M., Khan, M. T., Schmidt, C., Manneras-Holm, L., Wu, H., Carreras, A., Jeong, H., Olofsson, L. E., Bergh, P. O., Gerdes, V., Hartstra, A., de Brauw, M., Perkins, R., Nieuwdorp, M., Bergstrom, G., & Backhed, F. (2018). Microbially Produced Imidazole Propionate Impairs Insulin Signaling through mTORC1. *Cell*, *175*(4), 947-961 e17.

Lacraz, G., Rakotoarivelo, V., Labbe, S. M., Vernier, M., Noll, C., Mayhue, M., Stankova, J., Schwertani, A., Grenier, G., Carpentier, A., Richard, D., Ferbeyre, G., Fradette, J., Rola-Pleszczynski, M., Menendez, A., Langlois, M. F., Ilangumaran, S., & Ramanathan, S. (2016). Deficiency of Interleukin-15 Confers Resistance to Obesity by Diminishing Inflammation and Enhancing the Thermogenic Function of Adipose Tissues. *PLoS One*, *11*(9), e0162995.

Li, B., & Dewey, C. N. (2011). RSEM: accurate transcript quantification from RNA-Seq data with or without a reference genome. *BMC Bioinformatics*, *12*, 323.

Liberzon, A., Birger, C., Thorvaldsdottir, H., Ghandi, M., Mesirov, J. P., & Tamayo, P. (2015). The Molecular Signatures Database (MSigDB) hallmark gene set collection. *Cell Syst*, *1*(6), 417–425.

Lluís, F., Perdiguero, E., Nebreda, A. R., & Muñoz-Cánoves, P. (2006). Regulation of skeletal muscle gene expression by p38 MAP kinases. *Trends Cell Biol*, *16*(1), 36–44.

Loro, E., Seifert, E. L., Moffat, C., Romero, F., Mishra, M. K., Sun, Z., Krajacic, P., Anokye-Danso, F., Summer, R. S., Ahima, R. S., & Khurana, T. S. (2015). IL-15Ralpha is a determinant of muscle fuel utilization, and its loss protects against obesity. *Am J Physiol Regul Integr Comp Physiol*, *309*(8), R835-44.

Lovett, F. A., Cosgrove, R. A., Gonzalez, I., & Pell, J. M. (2010). Essential role for p38alpha MAPK but not p38gamma MAPK in Igf2 expression and myoblast differentiation. *Endocrinology*, *151*(9), 4368–4380.

Matesanz, N., Nikolic, I., Leiva, M., Pulgarin-Alfaro, M., Santamans, A. M., Bernardo, E., Mora, A., Herrera-Melle, L., Rodríguez, E., Beiroa, D., Caballero, A., Martín-García, E., Acín-Pérez, R., Hernández-Cosido, L., Leiva-Vega, L., Torres, J. L., Centeno, F., Nebreda, A. R., Enríquez, J. A., … Sabio, G. (2018). p38alpha blocks brown adipose tissue thermogenesis through p38delta inhibition. *PLoS Biol*, *16*(7), e2004455.

Navarro, P., & Vázquez, J. (2009). A refined method to calculate false discovery rates for peptide identification using decoy databases. *J Proteome Res*, *8*(4), 1792–1796.

Nguyen, L., Bohlen, J., Stricker, J., Chahal, I., Zhang, H., & Pistilli, E. E. (2017). Hippocampus-specific deficiency of IL-15Ralpha contributes to greater anxiety-like behaviors in mice. *Metab Brain Dis*, *32*(2), 297–302.

Nielsen, A. R., Hojman, P., Erikstrup, C., Fischer, C. P., Plomgaard, P., Mounier, R., Mortensen, O. H., Broholm, C., Taudorf, S., Krogh-Madsen, R., Lindegaard, B., Petersen, A. M., Gehl, J., & Pedersen, B. K. (2008). Association between interleukin-15 and obesity: interleukin-15 as a potential regulator of fat mass. *J Clin Endocrinol Metab*, *93*(11), 4486–4493.

Nikolic, I., Leiva, M., & Sabio, G. (2020). The role of stress kinases in metabolic disease. *Nat Rev Endocrinol*, *16*(12), 697–716.

Odeh, M., Tamir-Livne, Y., Haas, T., & Bengal, E. (2020). P38alpha MAPK coordinates the activities of several metabolic pathways that together induce atrophy of denervated muscles. *FEBS J*, *287*(1), 73–93.

Pan, W., Hsuchou, H., Yu, C., & Kastin, A. J. (2008). Permeation of blood-borne IL15 across the blood-brain barrier and the effect of LPS. *J Neurochem*, *106*(1), 313–319.

Pedersen, B. K. (2019). Physical activity and muscle-brain crosstalk. *Nat Rev Endocrinol*, *15*(7), 383–392.

Pedersen, B. K., & Febbraio, M. A. (2012). Muscles, exercise and obesity: skeletal muscle as a secretory organ. *Nat Rev Endocrinol*, *8*(8), 457–465.

Pierce, J. R., Maples, J. M., & Hickner, R. C. (2015). IL-15 concentrations in skeletal muscle and subcutaneous adipose tissue in lean and obese humans: local effects of IL-15 on adipose tissue lipolysis. *Am J Physiol Endocrinol Metab*, *308*(12), E1131-9.

Pistilli, E. E., Bogdanovich, S., Garton, F., Yang, N., Gulbin, J. P., Conner, J. D., Anderson, B. G., Quinn, L. S., North, K., Ahima, R. S., & Khurana, T. S. (2011). Loss of IL-15 receptor alpha alters the endurance, fatigability, and metabolic characteristics of mouse fast skeletal muscles. *J Clin Invest*, *121*(8), 3120–3132.

Priest, C., & Tontonoz, P. (2019). Inter-organ cross-talk in metabolic syndrome. *Nat Metab*, *1*(12), 1177–1188.

Ritchie, M. E., Phipson, B., Wu, D., Hu, Y., Law, C. W., Shi, W., & Smyth, G. K. (2015). limma powers differential

expression analyses for RNA-sequencing and microarray studies. *Nucleic Acids Res*, *43*(7), e47.

Rodríguez-Fdez, S., Lorenzo-Martín, L. F., Fernández-Pisonero, I., Porteiro, B., Veyrat-Durebex, C., Beiroa, D., Al-Massadi, O., Abad, A., Diéguez, C., Coppari, R., Nogueiras, R., & Bustelo, X. R. (2020). Vav2 catalysis-dependent pathways contribute to skeletal muscle growth and metabolic homeostasis. *Nat Commun*, *11*(1), 5808.

Sabio, G., Cavanagh-Kyros, J., Ko, H. J., Jung, D. Y., Gray, S., Jun, J. Y., Barrett, T., Mora, A., Kim, J. K., & Davis, R. J. (2009). Prevention of Steatosis by Hepatic JNK1. *Cell Metabolism*.

Subramanian, A., Tamayo, P., Mootha, V. K., Mukherjee, S., Ebert, B. L., Gillette, M. A., Paulovich, A., Pomeroy, S. L., Golub, T. R., Lander, E. S., & Mesirov, J. P. (2005). Gene set enrichment analysis: a knowledge-based approach for interpreting genome-wide expression profiles. *Proc Natl Acad Sci U S A*, *102*(43), 15545–15550.

Sun, H., & Liu, D. (2015). Hydrodynamic delivery of interleukin 15 gene promotes resistance to high fat diet-induced obesity, fatty liver and improves glucose homeostasis. *Gene Ther*, *22*(4), 341–347.

Sun, H., Ma, Y., Gao, M., & Liu, D. (2016). IL-15/sIL-15Ralpha gene transfer induces weight loss and improves glucose homeostasis in obese mice. *Gene Ther*, *23*(4), 349–356.

Tamura, Y., Watanabe, K., Kantani, T., Hayashi, J., Ishida, N., & Kaneki, M. (2011). Upregulation of circulating IL-15 by treadmill running in healthy individuals: is IL-15 an endocrine mediator of the beneficial effects of endurance exercise? *Endocr J*, *58*(3), 211–215.

Urso, K., Alfranca, A., Martínez-Martínez, S., Escolano, A., Ortega, I., Rodríguez, A., & Redondo, J. M. (2011). NFATc3 regulates the transcription of genes involved in T-cell activation and angiogenesis. *Blood*, *118*(3), 795–803.

Whitham, M., & Febbraio, M. A. (2016). The ever-expanding myokinome: discovery challenges and therapeutic implications. *Nat Rev Drug Discov*, *15*(10), 719–729.

Wu, X., He, Y., Hsuchou, H., Kastin, A. J., Rood, J. C., & Pan, W. (2010). Essential role of interleukin-15 receptor in normal anxiety behavior. *Brain Behav Immun*, *24*(8), 1340–1346.

Wu, X., Hsuchou, H., Kastin, A. J., He, Y., Khan, R. S., Stone, K. P., Cash, M. S., & Pan, W. (2011). Interleukin-15 affects serotonin system and exerts antidepressive effects through IL15Ralpha receptor. *Psychoneuroendocrinology*, *36*(2), 266–278.

Yang, M., Wei, D., Mo, C., Zhang, J., Wang, X., Han, X., Wang, Z., & Xiao, H. (2013). Saturated fatty acid palmitate-induced insulin resistance is accompanied with myotube loss and the impaired expression of health benefit myokine genes in C2C12 myotubes. *Lipids Health Dis*, *12*, 104.

Yu, M., Stepto, N. K., Chibalin, A. V, Fryer, L. G., Carling, D., Krook, A., Hawley, J. A., & Zierath, J. R. (2003). Metabolic and mitogenic signal transduction in human skeletal muscle after intense cycling exercise. *J Physiol*, *546*(Pt 2), 327–335.

Supplemental material

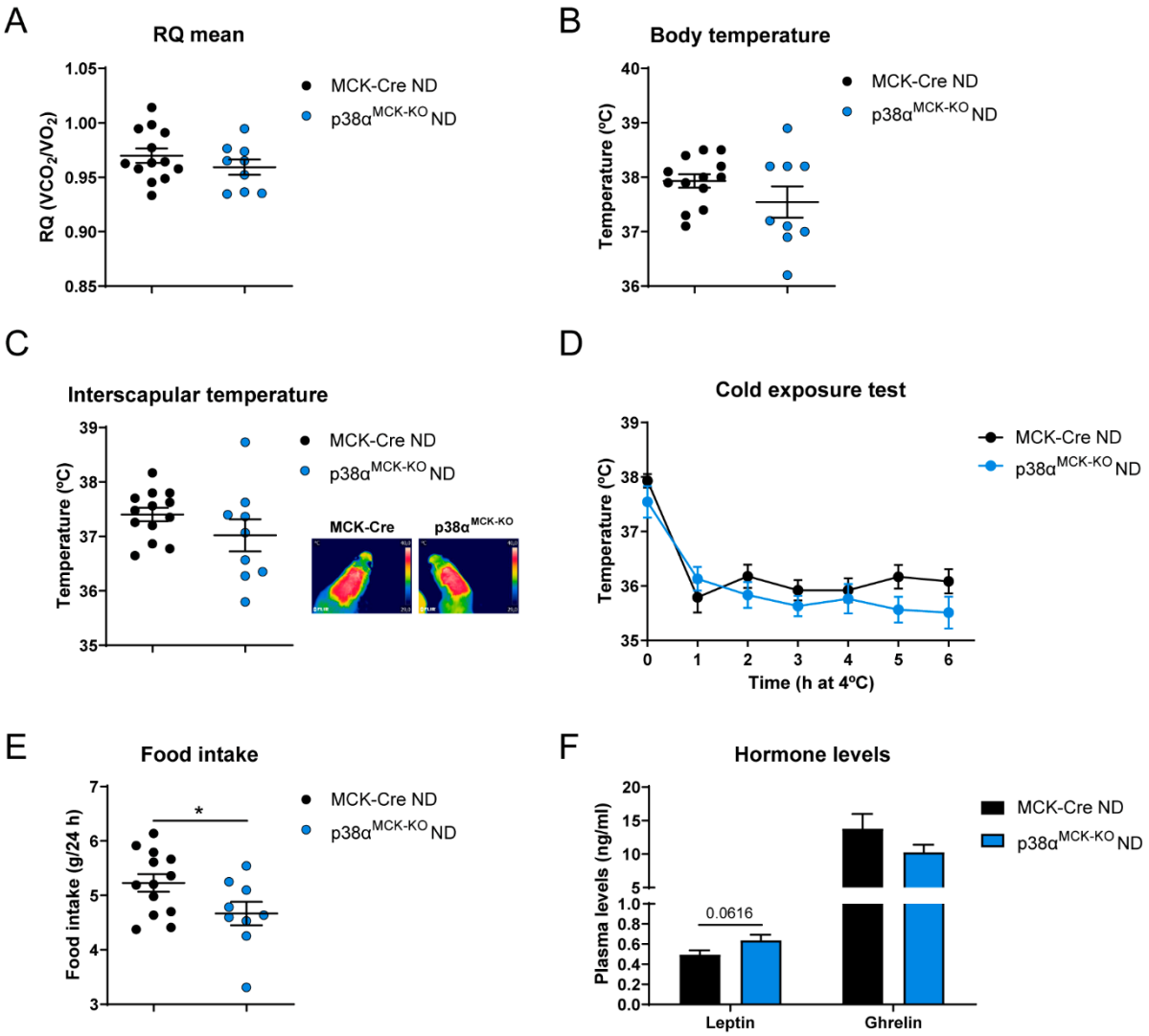

Figure S1. ND-fed p38α^{MCK-KO} mice have decreased food intake but similar temperature compared with MCK-Cre mice. p38α^{MCK-KO} and MCK-Cre mice were fed a ND, and metabolic parameters were assayed in 21-week-old mice. (**A**) Average of respiratory quotient (RQ) measured during 48 h. (**B**) Rectal temperature measurement. (**C**) Interscapular temperature measurement and representative infrared thermal images. (**D**) Effect of cold exposure (4 °C during 6 h) on body temperature at different time points. (**E**) Total food intake in 24 h. (**F**) Fasting leptin and ghrelin levels in plasma. Data are shown as means ± SEM; *$p < 0.05$; Student's *t*-test (Figures A-C, E-F), with Welch's correction for body and interscapular temperature; two-way ANOVA coupled to Bonferroni's multiple comparisons test (cold exposure test); n = 9-13.

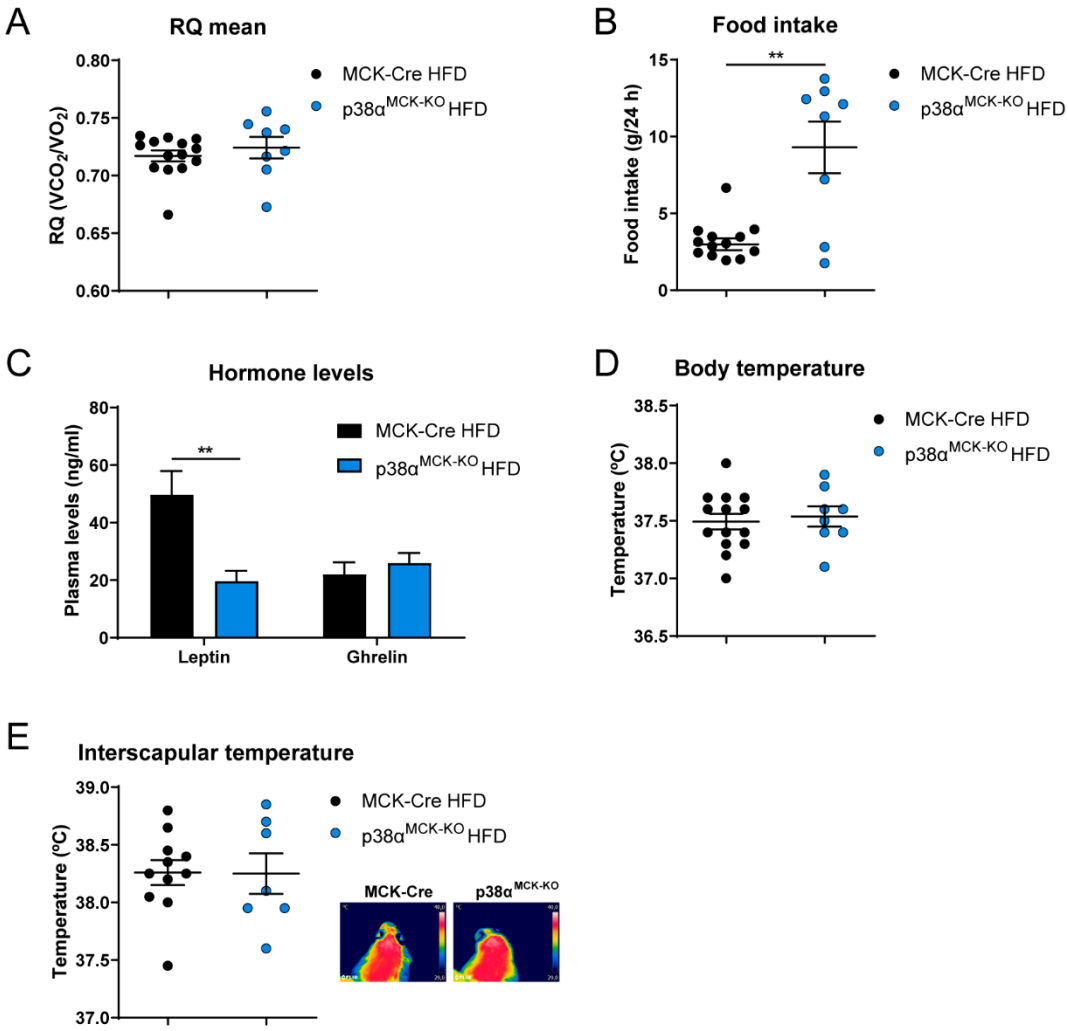

Figure S2. HFD-fed p38α^{MCK-KO} mice have increased food intake but similar temperature compared with MCK-Cre mice. p38α^{MCK-KO} and MCK-Cre mice were fed a HFD for 12 weeks, and metabolic parameters were assayed at the end of this period. (**A**) Average of respiratory quotient (RQ) measured during 48 h. (**B**) Total food intake in 24 h. (**C**) Fasting leptin and ghrelin levels in plasma. (**D**) Rectal temperature measurement. (**E**) Interscapular temperature measurement and representative infrared thermal images. Data are shown as means ± SEM; ***p* < 0.01; Student's *t*-test (with Welch's correction for food intake and leptin); *n* = 7-14.

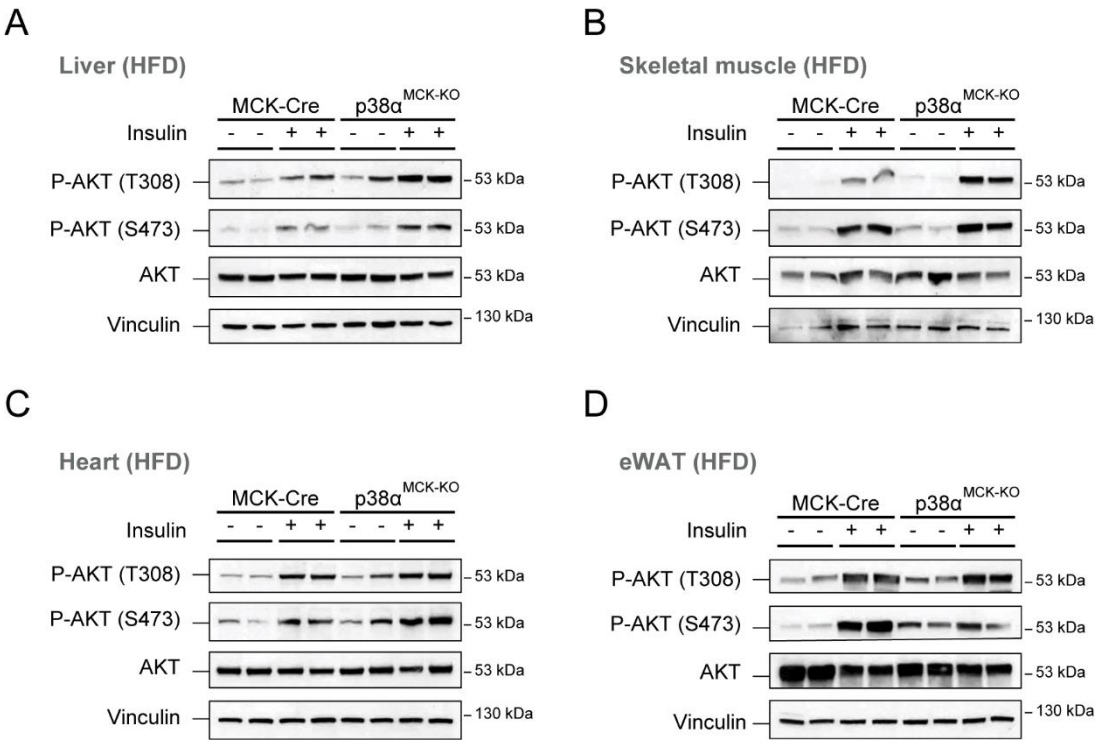

Figure S3. Mice lacking p38α in striated muscle are protected against insulin resistance in liver and skeletal muscle under HFD condition. p38α^{MCK-KO} and MCK-Cre mice were fed a HFD for 14 weeks, fasted overnight and injected (+) or not (-) with insulin (1.5 U/kg) before sacrifice. Extracts prepared from liver (A), quadriceps (B), heart (C) and epididymal white adipose tissue (eWAT) (D) at 15 min post-injection were examined by immunoblot analysis with antibodies against phospho (P)-AKT and total AKT. Vinculin protein expression was monitored as a loading control. *n* = 4.

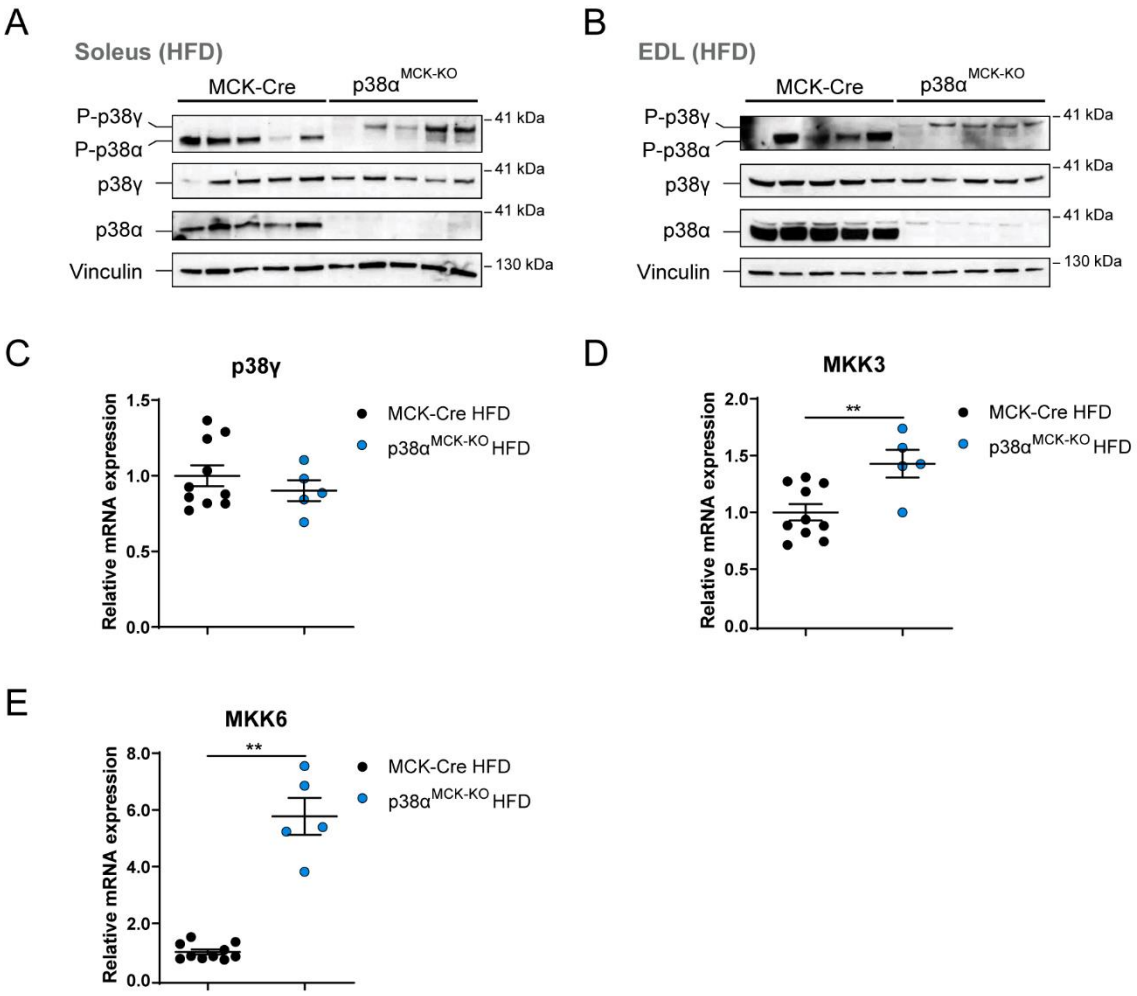

Figure S4. Biochemical analysis of the p38 signaling pathway in p38α^{MCK-KO} and MCK-Cre mice. 8-week-old p38α^{MCK-KO} and MCK-Cre mice were fed a HFD for 14 weeks, fasted overnight and sacrificed. Extracts prepared from soleus (**A**) and extensor digitorum longus (EDL) (**B**) muscles were examined by immunoblot analysis with antibodies against phospho (P)-p38 and total protein levels. Vinculin protein expression was monitored as a loading control. *n* = 4-5. (**C-E**) qRT-PCR analysis of *Mapk12* (p38γ), *Map2k3* (MKK3) and *Map2k6* (MKK6) genes in gastrocnemius samples. mRNA expression was normalized to the amount of *Gapdh* mRNA in each sample. Data are normalized to MCK-Cre mice and shown as means ± SEM; ***p* < 0.01; Student's *t*-test (with Welch's correction for MKK6); *n* = 5-10.

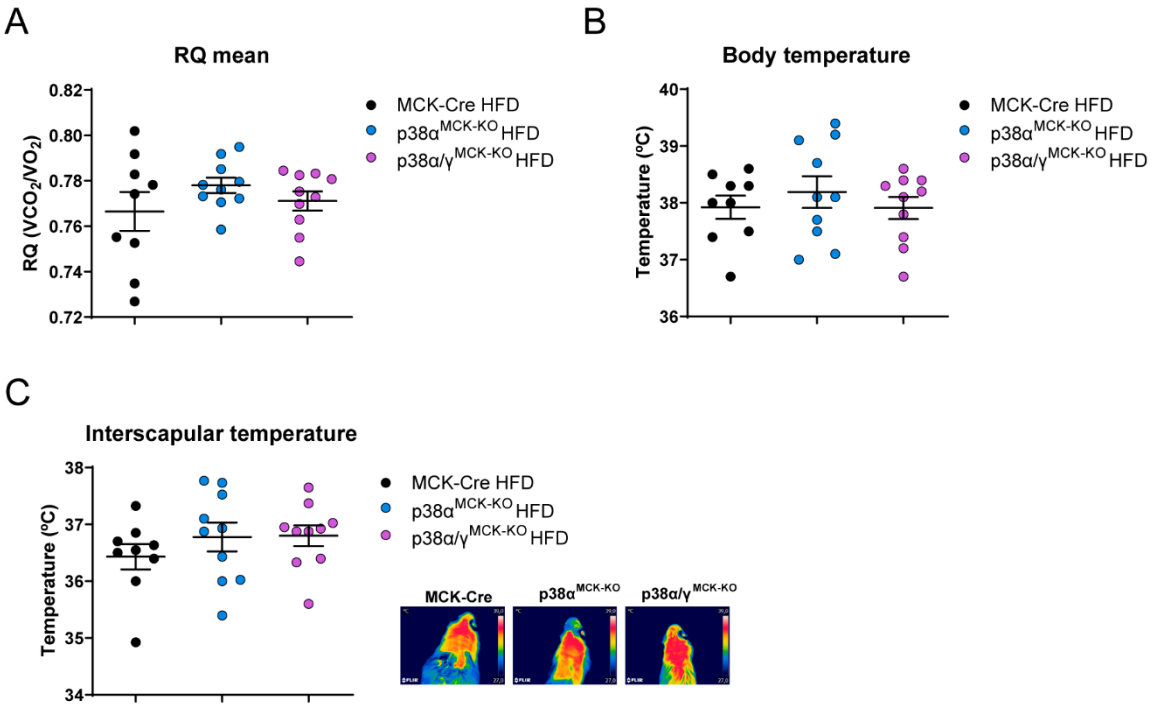

Figure S5. HFD-fed p38α/γ^{MCK-KO}, p38α^{MCK-KO} and MCK-Cre mice do not show differences in RQ or temperature. p38α/γ^{MCK-KO}, p38α^{MCK-KO} and MCK-Cre mice were fed a HFD for 6 weeks and metabolic parameters were assayed at the end of this period. (**A**) Average of respiratory quotient (RQ) measured during 48 h. (**B**) Rectal temperature measurement. (**C**) Interscapular temperature measurement and representative infrared thermal images. Data are shown as means ± SEM; one-way ANOVA coupled to Bonferroni's multiple comparisons test; *n* = 9-10.

PLOS BIOLOGY

RESEARCH ARTICLE

p38α blocks brown adipose tissue thermogenesis through p38δ inhibition

Nuria Matesanz[1☯], Ivana Nikolic[1☯], Magdalena Leiva[1], Marta Pulgarín-Alfaro[1], Ayelén M. Santamans[1], Edgar Bernardo[1], Alfonso Mora[1], Leticia Herrera-Melle[1], Elena Rodríguez[1], Daniel Beiroa[2,3], Ainoa Caballero[1], Elena Martín-García[1], Rebeca Acín-Pérez[1], Lourdes Hernández-Cosido[4], Luis Leiva-Vega[1], Jorge L. Torres[5], Francisco Centeno[6], Angel R. Nebreda[7,8], José Antonio Enríquez[1,9], Rubén Nogueiras[2,3], Miguel Marcos[5], Guadalupe Sabio[1]*

1 Fundación Centro Nacional de Investigaciones Cardiovasculares Carlos III, Madrid, Spain, **2** Department of Physiology, CIMUS, University of Santiago de Compostela-Instituto de Investigación Sanitaria, Santiago de Compostela, Spain, **3** CIBER Fisiopatología de la Obesidad y Nutrición (CIBERobn), Santiago de Compostela, Spain, **4** Bariatric Surgery Unit, Department of General Surgery, University Hospital of Salamanca, Salamanca, Spain, **5** Department of Internal Medicine, University Hospital of Salamanca-IBSAL, Department of Medicine, University of Salamanca, Salamanca, Spain, **6** Facultad de Ciencias, University of Extremadura, Grupo GIEN (Grupo de Investigación en Enfermedades Neurodegenerativas), Badajoz, Spain, **7** Institute for Research in Biomedicine (IRB Barcelona), The Barcelona Institute of Science and Technology, Barcelona, Spain, **8** ICREA, Barcelona, Spain, **9** CIBER Fragilidad y Envejecimiento Saludable (CIBERFES), Madrid, Spain

☯ These authors contributed equally to this work.
* gsabio@cnic.es

Check for updates

OPEN ACCESS

Citation: Matesanz N, Nikolic I, Leiva M, Pulgarín-Alfaro M, Santamans AM, Bernardo E, et al. (2018) p38α blocks brown adipose tissue thermogenesis through p38δ inhibition. PLoS Biol 16(7): e2004455. https://doi.org/10.1371/journal.pbio.2004455

Academic Editor: Gokhan Hotamisligil, Harvard School of Public Health, United States of America

Received: October 7, 2017

Accepted: June 15, 2018

Published: July 6, 2018

Copyright: © 2018 Matesanz et al. This is an open access article distributed under the terms of the Creative Commons Attribution License, which permits unrestricted use, distribution, and reproduction in any medium, provided the original author and source are credited.

Data Availability Statement: All relevant data are within the paper and its Supporting information files.

Funding: EFSD/Lilly Reseach Fellowship. Received by IN. The funder had no role in study design, data collection and analysis, decision to publish, or preparation of the manuscript. CNIC IPP FP7 Marie Curie Programme (grant number PCOFUND-2012-600396). Received by IN. The funder had no role in study design, data collection and analysis, decision to publish, or preparation of the manuscript.

Abstract

Adipose tissue has emerged as an important regulator of whole-body metabolism, and its capacity to dissipate energy in the form of heat has acquired a special relevance in recent years as potential treatment for obesity. In this context, the p38MAPK pathway has arisen as a key player in the thermogenic program because it is required for the activation of brown adipose tissue (BAT) thermogenesis and participates also in the transformation of white adipose tissue (WAT) into BAT-like depot called beige/brite tissue. Here, using mice that are deficient in p38α specifically in adipose tissue ($p38\alpha^{Fab\text{-}KO}$), we unexpectedly found that lack of p38α protected against high-fat diet (HFD)-induced obesity. We also showed that $p38\alpha^{Fab\text{-}KO}$ mice presented higher energy expenditure due to increased BAT thermogenesis. Mechanistically, we found that lack of p38α resulted in the activation of the related protein kinase family member p38δ. Our results showed that p38δ is activated in BAT by cold exposure, and lack of this kinase specifically in adipose tissue ($p38\delta^{Fab\text{-}KO}$) resulted in overweight together with reduced energy expenditure and lower body and skin surface temperature in the BAT region. These observations indicate that p38α probably blocks BAT thermogenesis through p38δ inhibition. Consistent with the results obtained in animals, p38α was reduced in visceral and subcutaneous adipose tissue of subjects with obesity and was inversely correlated with body mass index (BMI). Altogether, we have elucidated a mechanism implicated in physiological BAT activation that has potential clinical implications for the treatment of obesity and related diseases such as diabetes.

MINECO -FEDER (grant number SAF2015-74112-JIN). Received by ML. The funder had no role in study design, data collection and analysis, decision to publish, or preparation of the manuscript. Ramón y Cajal Programme (grant number RYC-2011-07826). Received by RAP. The funder had no role in study design, data collection and analysis, decision to publish, or preparation of the manuscript. MINECO FPI-FEDER (grant number FPI BES-2011-043428 and FPI-SO BES-2016-077635). Received by EB and AS. The funder had no role in study design, data collection and analysis, decision to publish, or preparation of the manuscript. European Union's Seventh Framework Programme (FP7/2007-2013) (grant number ERC 260464). Received by GS. The funder had no role in study design, data collection and analysis, decision to publish, or preparation of the manuscript. EFSD/Lilly European Diabetes Research Programme (grant number Dr Sabio, 2017). Received by GS. The funder had no role in study design, data collection and analysis, decision to publish, or preparation of the manuscript. Leonardo Grant for Researchers and Cultural Creators, BBVA Foundation (grant number Investigadores-BBVA-2017 IN[17]_BBM_BAS_0066). Received by GS. The funder had no role in study design, data collection and analysis, decision to publish, or preparation of the manuscript. MINECO-FEDER (grant number SAF2016-79126-R). Received by GS. The funder had no role in study design, data collection and analysis, decision to publish, or preparation of the manuscript. Comunidad de Madrid-FEDER (grant number IMMUNOTHERCAN-CM S2010/BMD-2326 and B2017/BMD-3733). Received by GS. The funder had no role in study design, data collection and analysis, decision to publish, or preparation of the manuscript. ISCIII and FEDER (grant number PI16/01548). Received by MM. The funder had no role in study design, data collection and analysis, decision to publish, or preparation of the manuscript. Junta de Castilla y León (grant number GRS 1362/A/16, INT/M/17/17, GRS 1356/A/16). Received by MM and JLT. The funder had no role in study design, data collection and analysis, decision to publish, or preparation of the manuscript. MINECO -FEDER (grant number BFU2015-70664-R). Received by RN. The funder had no role in study design, data collection and analysis, decision to publish, or preparation of the manuscript. Xunta de Galicia (grant number 2015-CP080 and PIE13/00024). Received by RN. The funder had no role in study design, data collection and analysis, decision to publish, or preparation of the manuscript. European grants (grant number ERC281408, UE0/MCA1108, UE0/MCA1201).

Author summary

Accumulation of fat in adipose tissue is essential to store energy and insulate the body; however, excessive body fat leads to obesity. Of the 2 existing types of adipose tissue, white adipose tissue (WAT) stores energy, whereas brown adipose tissue (BAT) can produce heat. Activation of BAT and transformation of WAT into brown-like 'brite/beige' adipocytes have recently emerged as novel strategies against obesity. The uncoupling protein 1 (UCP1) is a hallmark of BAT and is responsible for triggering these 2 processes under the regulation of the p38 MAP kinase (p38MAPK) pathway, but the underlying mechanisms remain unknown. Here, we have analysed this process in detail and demonstrate that a protein kinase called p38α directly correlates with UCP1 levels in human adipose tissue, while it inversely correlates with body mass index (BMI). We find that mice lacking p38α in adipose tissue are protected against diet-induced obesity due to increased body temperature. In addition, another p38 family member, p38δ, is activated in these adipocytes lacking p38α and reduces their thermogenic capacity. Our results suggest that these 2 members of the p38 family have opposite roles in controlling thermogenesis.

Obesity is a serious worldwide health problem, associated with a higher risk of life-threatening diseases [2], that has had a dramatic increase in prevalence [1]. As the main organ for fat storage, adipose tissue has a fundamental role in metabolism [3]. Whereas white adipose tissue (WAT) stores energy in the form of triglycerides and releases free fatty acids on demand, brown adipose tissue (BAT) burns fat to maintain the temperature in a process called non-shivering thermogenesis [4]. Classically, it was assumed that in adult humans BAT played a minor role in energy metabolism. However, recent findings have indicated that this tissue can be modulated by several stimuli presenting lower activity in individuals with obesity [5–7]. Additionally, under certain stimuli, WAT can increase its thermogenic capacity in a process called browning [8–11]. This remodelling of WAT has acquired special interest because it has important therapeutic implications in the treatment of obesity [12, 13].

The p38MAPK pathway is activated during browning, and it has been suggested that this drives adipose tissue remodelling [14, 15]. There are 4 p38 isoforms: p38α, p38β, p38γ, and p38δ, all of which are activated by stress stimuli in a cell-dependent manner, controlling cellular fate [16–20]. It has been extensively described that p38MAPK triggers browning and BAT activation through the transcription of uncoupling protein 1 (UCP1) via cAMP response element-binding (CREB), activating transcription factor 2 (ATF2), and peroxisome proliferator-activated receptor gamma coactivator 1α (PGC1α) activation. In fact, β-adrenergic stimulation and other browning agents stimulate the p38MAPK cascade, promoting thermogenesis [18, 21–23]. Although most of these studies assumed that the phenotype is driven by p38α, the specific role of the isoform p38α and other p38 isoforms in the development and transformation of adipose tissue has not been elucidated yet using genetically modified mouse models.

Using conditional animals for p38α ($p38\alpha^{Fab\text{-}KO}$), unexpectedly, we found that deletion of this kinase in adipose tissue protected animals against high-fat diet (HFD)-induced obesity together with increased energy expenditure followed by higher BAT thermogenesis. Lack of p38α in BAT resulted in higher activation of p38δ. In agreement with this, conditional deletion of p38δ in adipose tissue led to obesity, with higher body weight and reduced energy expenditure due to a lower body and skin surface temperature in the BAT region. Besides, lack of p38α in inguinal fat (iWAT) increased p38γ activation and UCP1 expression. Our results indicate

Received by RN. The funder had no role in study design, data collection and analysis, decision to publish, or preparation of the manuscript. Junta de Extremadura-FEDER (grant number BR15164). Received by FC. The funder had no role in study design, data collection and analysis, decision to publish, or preparation of the manuscript. Ministerio de Economía, Industria y Competitividad (MEIC) and the Pro CNIC Foundation (grant number SEV-2015-0505). The CNIC is supported by the Ministerio de Economía, Industria y Competitividad (MEIC) and the Pro CNIC Foundation, and is a Severo Ochoa Center of Excellence (SEV-2015-0505). The funder had no role in study design, data collection and analysis, decision to publish, or preparation of the manuscript.

Competing interests: The authors have declared that no competing interests exist.

Abbreviations: AMPK, 5' adenosine monophosphate-activated protein kinase; ALT, alanine aminotransferase; AST, aspartate aminotransferase; ATF2, activating transcription factor 2; BAT, brown adipose tissue; BM, bone marrow; BMI, body mass index; BrdU, bromodeoxyuridine; Creb, cAMP response element-binding; eWAT, epididymal fat; FACS, fluorescence-assisted cell sorting; FCCP, carbonyl cyanide-4-(trifluoromethoxy)phenylhydrazone; GLUT4, glucose transporter type 4; GTT, glucose tolerance test; HFD, high-fat diet; IR temperature, infrared temperature; ISO, isoproterenol; ITT, insulin tolerance test; iWAT, inguinal fat; ND, normal-chow diet; NE, norepinephrine; NMR, nuclear magnetic resonance; OCR, oxygen consumption rate; PGC1α, proliferator-activated receptor gamma coactivator 1α; PKA, protein kinase A; pWAT, perirenal fat; qRT-PCR, quantitative real-time polymerase chain reaction; sWAT, subcutaneous fat; UCP1, uncoupling protein 1; WAT, white adipose tissue; WT, wild-type.

that p38α controls p38δ activation in BAT, regulating thermogenesis and energy expenditure. In contrast, in WAT, p38α would have opposite effects depending on the fat depot, blocking browning through inhibition of p38γ in iWAT and promoting browning in epididymal fat (eWAT). Thus, these findings challenge the classical view of p38α as an activator of BAT thermogenesis. These studies provided important insights into p38δ and p38α function in BAT regulation that could have therapeutic implications to efficiently fight obesity.

Results

p38α has emerged as one of the main player that could activate the thermogenic capacity of adipose tissue. Because the thermogenesis of adipose tissue is reduced in obesity [6, 7, 21], we wondered whether expression of this kinase changes in human WAT during obesity. Using 2 cohorts for visceral fat and subcutaneous fat (sWAT) of adult patients with 80 and 170 samples, respectively, we found that the expression of p38α (*Mapk14*) in visceral fat and sWAT from individuals with obesity was reduced compared with those without obesity (Fig 1A and 1D). In fact, mRNA levels of *Mapk14* in visceral fat inversely correlated with body mass index (BMI) (Fig 1B). It has been suggested that p38α in WAT activates browning by triggering the expression of UCP1 [18], the main protein responsible for adipose tissue thermogenic capacity [22]. In visceral fat and sWAT from individuals with obesity and those without obesity, we found that expression of *Mapk14* correlated positively with the levels of *Ucp1* (Fig 1C and 1E). This correlation reinforced the idea that p38α in visceral fat and sWAT controls the levels of UCP1 and could regulate browning in humans.

Then, we evaluated the function of p38α in adipose tissue using conditional mice ($p38\alpha^{Fab\text{-}KO}$), which lacked p38α in WAT and BAT (S1 Fig). Under normal-chow diet (ND), $p38\alpha^{Fab\text{-}KO}$ mice had the same weight gain as the control Fab-Cre mice (S2A Fig). However, they presented reduced fat mass, in concordance with lower eWAT, perirenal WAT (pWAT), and BAT weight (S2B and S2C Fig). This reduction in fat accumulation was associated with higher energy expenditure and slight increase of body temperature (S2G and S2H Fig). In fact, these mice presented lower blood glucose levels in fasted and fed conditions (S2D Fig) and increased glucose tolerance (S2E Fig), with no differences in insulin sensitivity or insulin-stimulated glucose transporter type 4 (GLUT4) translocation in adipose tissue (S2E and S2F Fig). These data suggest that lack of p38α might protect against type 2 diabetes. Moreover, we evaluated whether lack of p38α affects adipogenesis, browning, and metabolism in eWAT and BAT. BAT from $p38\alpha^{Fab\text{-}KO}$ mice presented an increase of *Cidea*, a marker of browning, together with higher expression of glycolytic and β oxidation genes (S3 Fig).

To further evaluate the role of p38α in adipose tissue, mice were fed an HFD, and we observed that $p38\alpha^{Fab\text{-}KO}$ mice were completely protected from diet-induced obesity because their weight was identical to the weight of the control animals in ND (Fig 2A). This reduced weight gain was in line with lower fat mass (Fig 2B) and reduced weight of the different fat depots, including eWAT, sWAT, iWAT, pWAT, and BAT (S4A Fig). Moreover, liver weight was also reduced in agreement with protection against HFD-induced liver steatosis in $p38\alpha^{Fab\text{-}KO}$ mice (Fig 2C and S4A Fig). The protection against HFD-induced obesity was associated with reduced fasted and fed hyperglycaemia in $p38\alpha^{Fab\text{-}KO}$ mice, with no differences in triglyceridemia (Fig 2D and S4E Fig). In addition, $p38\alpha^{Fab\text{-}KO}$ mice were protected against HFD-induced glucose intolerance even when glucose dose was adjusted to lean mass (Fig 2E, S4B Fig.) and insulin resistance as shown by the reduced glucose levels during the insulin tolerance test (ITT) (Fig 2E). HFD-induced obesity was associated with liver insulin resistance and reduced insulin-stimulated Akt phosphorylation in livers from HFD-fed Fab-Cre mice (S4C Fig). Evaluation of insulin sensitivity in several tissues indicated that HFD-fed $p38\alpha^{Fab\text{-}KO}$

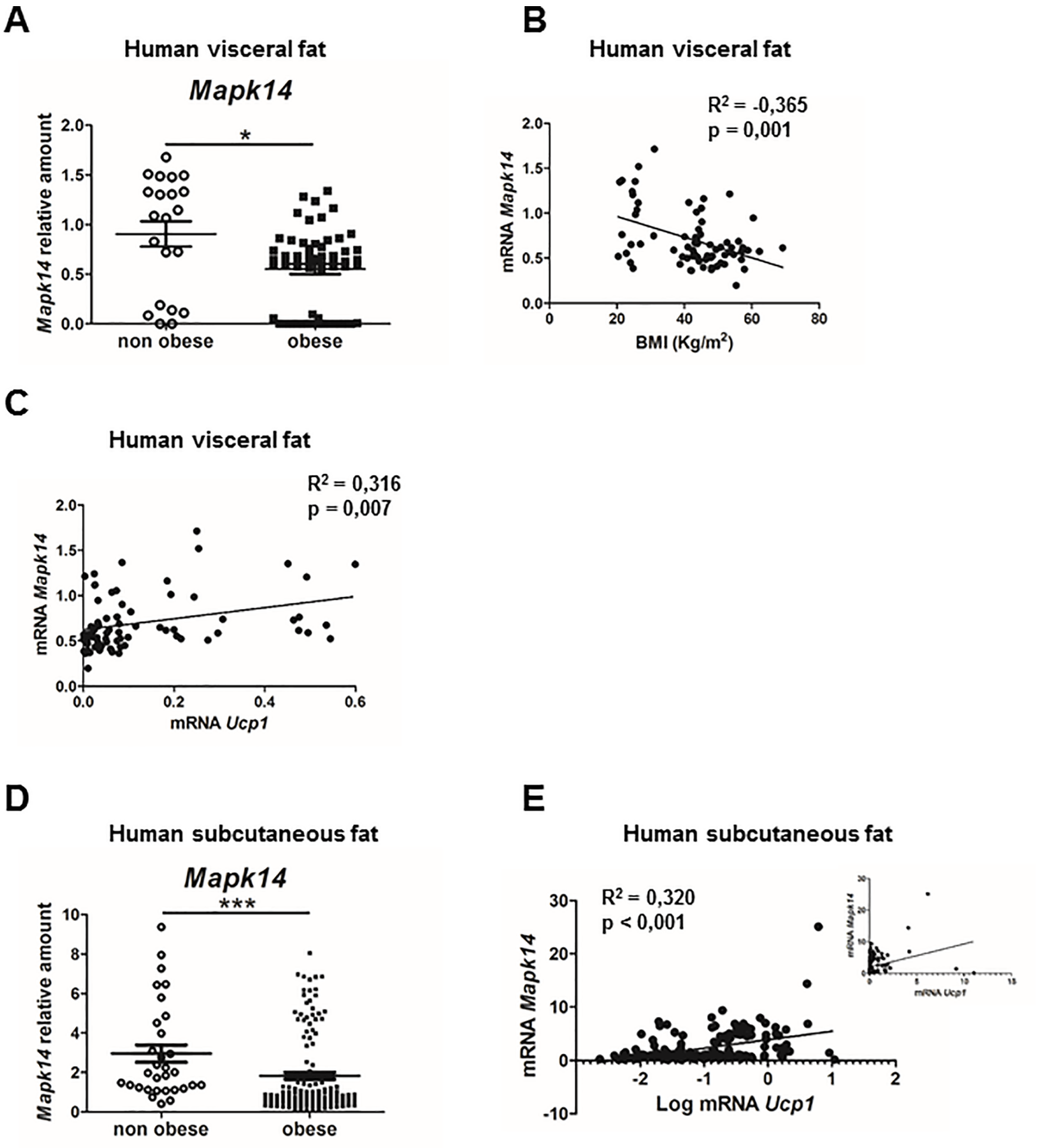

Fig 1. p38α in human visceral fat inversely correlated with BMI and directly correlated with UCP1 in human visceral fat and sWAT. (A) mRNA levels of *Mapk14* (p38α) in visceral fat from lean individuals and individuals with obesity—mRNA expression was normalised to the amount of *Gapdh* mRNA. (B) Correlation between mRNA levels of *Mapk14* (p38α) and BMI ($r^2 = -0{,}365$; $p = 0.001$) or (C) *Ucp1* in visceral fat ($r^2 = 0.316$; $p = 0.007$). The mRNA levels of *Mapk14* (p38α) and *Ucp1* were determined by qRT-PCR ($n = 71$). (D) mRNA levels of *Mapk14* (p38α) in sWAT from lean individuals and individuals with obesity. mRNA expression was normalised to the amount of *Gapdh* mRNA. (E) Correlation between mRNA levels of *Mapk14* (p38α) and *Ucp1* in sWAT ($r^2 = 0.320$; $p < 0.0001$). Graph correlating mRNA *Mapk14* and log mRNA *Ucp1* is also shown. The mRNA levels of *Mapk14* (p38α) and *Ucp1* were determined by qRT-PCR ($n = 168$). See also S1 Data. Linear relationships between variables were tested using Pearson's correlation coefficient. BMI, body mass index; qRT-PCR, quantitative real-time polymerase chain reaction; UCP1, uncoupling protein 1.

https://doi.org/10.1371/journal.pbio.2004455.g001

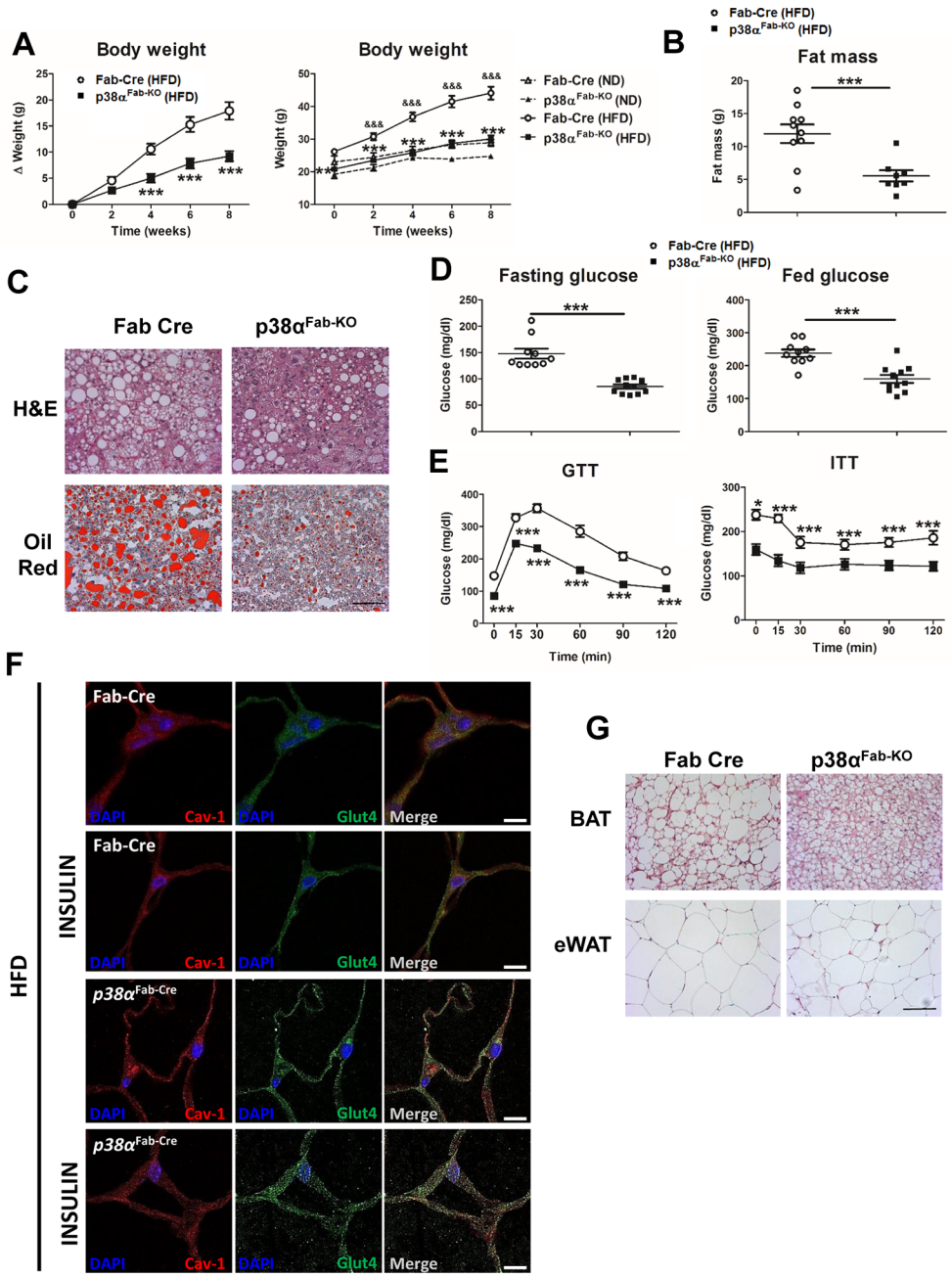

Fig 2. p38α$^{Fab\text{-}KO}$ mice are protected against diet-induced obesity and diabetes. (A) Body weight time course in Fab-Cre and p38α$^{Fab\text{-}KO}$ male (8–10-wk-old) mice fed an HFD over 8 weeks. Data are presented as the increase above initial weight (left panel) or as total weight comparing mice fed an HDF with mice fed an ND (right panel). HFD-induced weight gain was significantly higher in Fab-Cre than p38α$^{Fab\text{-}KO}$ mice (mean ± SEM; Fab-Cre HFD $n = 10$ mice; p38α$^{Fab\text{-}KO}$ HFD $n = 11$ mice; Fab-Cre ND $n = 9$ mice; p38α$^{Fab\text{-}KO}$ ND $n = 8$ mice). (B) NMR analysis of fat mass in p38α$^{Fab\text{-}KO}$ and Fab-Cre mice after 8 weeks of HFD (mean ± SEM; Fab-Cre $n = 10$ mice; p38α$^{Fab\text{-}KO}$ $n = 8$ mice). (C) Representative haematoxylin–eosin and oil red O staining of liver sections (Fab-Cre $n = 6$ mice; p38α$^{Fab\text{-}KO}$ $n = 6$ mice; and 3 pictures from each mouse). Scale bar: 50 μm. (D) Fasting and fed blood glucose in Fab-Cre and p38α$^{Fab\text{-}KO}$ mice fed the HFD (8 weeks) (mean ± SEM; Fab-Cre $n = 10$ mice; p38α$^{Fab\text{-}KO}$ $n = 11$ mice). (E) GTT and ITT in Fab-Cre and p38α$^{Fab\text{-}KO}$ mice fed the HFD for 8 weeks. Mice were fasted overnight (for GTT) or 1 hour (for ITT), and blood glucose concentration was measured in mice given intraperitoneal injections of glucose (1 g/kg of total body weight) or insulin (0.75 U/kg of total body weight) (mean ± SEM; Fab-Cre $n = 10$ mice; p38α$^{Fab\text{-}KO}$ $n = 11$ mice). (F) Immunohistochemistry of eWAT sections using anti-GLUT4 (green), anti-Cav-1 (red) antibodies, and the nuclear dye DAPI (blue). Location of GLUT4 was analysed in mice treated without or with insulin (1.5 IU/kg) for 15 minutes after overnight fasting. Scale bar: 20 μm. (G) Representative haematoxylin–eosin BAT and eWAT sections (Fab-Cre $n = 6$

mice; p38α$^{Fab\text{-}KO}$ $n = 6$ mice; and 3 pictures from each mouse). Scale bar: 50 μm. $^{*}p < 0.05$, $^{***}p < 0.001$ Fab-Cre versus p38α$^{Fab\text{-}KO}$. '&&' indicates $p < 0.01$, '&&&' indicates $p < 0.001$ Fab-Cre ND versus Fab-Cre HFD (2-way ANOVA coupled with Bonferroni's post-tests or *t* test or Welch's test when variances were different). See also S1 Data. BAT, brown adipose tissue; Cav-1, caveolin-1; eWAT, epididymal fat; GLUT4, glucose transporter type 4; GTT, glucose tolerance test; HFD, high-fat diet; ITT, insulin tolerance test; ND, normal-chow diet; WAT, white adipose tissue.

https://doi.org/10.1371/journal.pbio.2004455.g002

mice presented higher insulin-induced phosphorylation of Akt at Thr308 and Ser473 than HFD-fed Fab-Cre mice in liver and muscle but not in eWAT nor BAT (S4D Fig). Furthermore, we observed a slight increase of insulin-stimulated GLUT4 translocation in eWAT (Fig 2F). Together, these results demonstrate that p38α$^{Fab\text{-}KO}$ mice are protected against diet-induced obesity and diabetes.

Histological analysis showed that interscapular BAT depot from HFD-fed p38α$^{Fab\text{-}KO}$ mice had small multilocular adipocytes (Fig 2G), whereas in eWAT, we observed a slight decrease of adipocyte size (Fig 2G), which correlates to reduced cell size in BAT and WAT adipocytes from HFD-fed p38α$^{Fab\text{-}KO}$ with respect to HFD-fed Fab-Cre (S5A and S5C Fig). Then, we evaluated HFD-induced WAT adipocyte expansion by bromodeoxyuridine (BrdU) staining [23], observing reduced expansion in p38α$^{Fab\text{-}KO}$ (Fig 3A). However, no differences in Ki67 staining were observed after HFD in WAT or BAT adipocytes (S5A and S5C Fig).

To further investigate the mechanism by which lack of p38α in adipose tissue could protect against HFD-induced obesity, we evaluated whole-body metabolism using metabolic cages. HFD-fed p38α$^{Fab\text{-}KO}$ mice showed a significant increase in whole-body energy expenditure analysed by ANCOVA, with no changes in food intake or respiratory exchange ratio (Fig 3B). These data are consistent with the observation that HFD-fed p38α$^{Fab\text{-}KO}$ mice have higher skin temperature in the region of BAT compared with Fab-Cre mice (Fig 3C). Western blot analysis of BAT indicated that HFD-fed p38α$^{Fab\text{-}KO}$ mice presented a slight increase of UCP1 expression associated with higher AMPK and Creb phosphorylation (Fig 3D and 3E). In addition, higher expression of UCP1 levels was observed in iWAT from HFD-fed p38α$^{Fab\text{-}KO}$ mice (S5B and S7A Figs), suggesting an increased browning of this adipose depot. In contrast with the up-regulated UCP1 levels in iWAT, analysis of eWAT by western blot and immunohistochemistry showed that HFD-fed p38α$^{Fab\text{-}KO}$ mice have reduced UCP1 levels in this tissue (S6 and S7B Figs). These results are in agreement with the results found in human visceral fat (Fig 1C) suggesting that, in visceral fat, p38α directly correlates with UCP1.

In vitro–differentiated brown adipocytes from p38α$^{Fab\text{-}KO}$ mice confirmed a key role of this kinase inhibiting browning in a cell-autonomous manner because several browning markers (UCP1, PGC1b, Cidea, Cox7a1, Cox7a2, and Cox8b) were up-regulated in p38α$^{Fab\text{-}KO}$ brown adipocytes (S8A Fig). In concordance with the results observed in the BAT tissue, glycolytic genes were also up-regulated, while many lipogenic genes that correlated with the lower triglyceride content in p38α$^{Fab\text{-}KO}$ brown adipocytes were down-regulated (S8B, S8C, S8D and S8E Fig). In addition, p38α$^{Fab\text{-}KO}$ brown adipocytes have increased expression of perilipin with no changes in adiponectin, suggesting same differentiation capacity but smaller and more abundant lipid droplets (S8B Fig). On the other hand, p38α$^{Fab\text{-}KO}$ white adipocytes presented the same in vitro differentiation rate judging by red-oil staining and the expression levels of adipocyte markers such as adiponectin and perilipin (S8F and S8G Fig). However, p38α$^{Fab\text{-}KO}$ white adipocytes have increased expression of leptin (S8F Fig). To further confirm the autonomous role of p38α in BAT, we crossed p38α loxP mice with UCP1-Cre mice [24], which express Cre recombinase specifically in the interscapular brown fat at room temperature, generating p38α$^{UCP1\text{-}KO}$ mice. In agreement with our previous results, these mice were protected against HFD-induced obesity and presented lower fat mass and increased temperature.

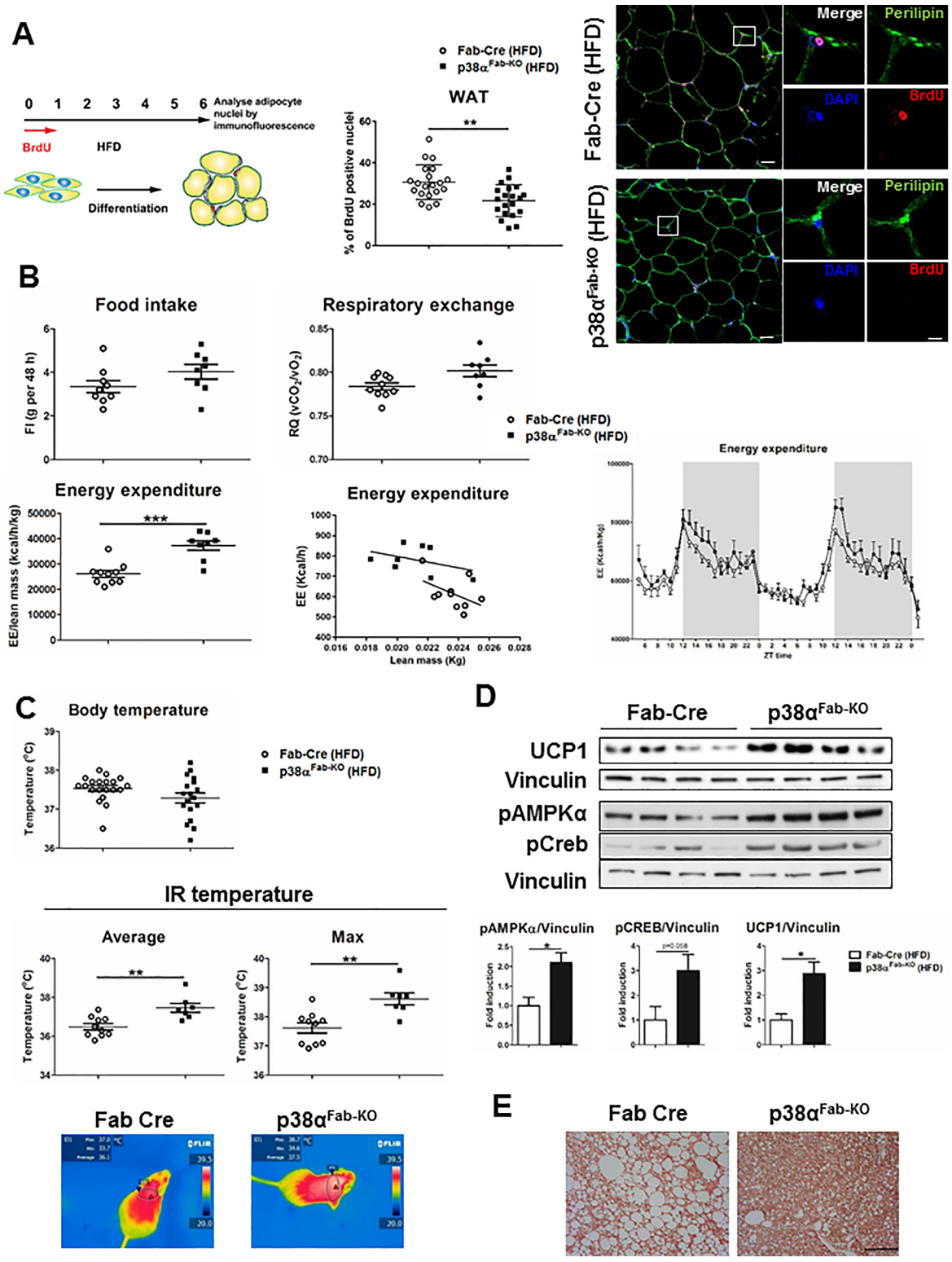

Fig 3. p38α$^{Fab\text{-}KO}$ mice have higher energy expenditure and increased BAT thermogenesis. Fab-Cre and p38α$^{Fab\text{-}KO}$ mice were fed an HFD for 8 weeks. (A) Analysis of eWAT expansion in HFD-fed Fab-Cre and p38α$^{Fab\text{-}KO}$ mice. Animals were treated with BrdU in the drinking water during the first week of a 6-week HFD. Cartoon explaining the protocol is shown in the left panel. BrdU incorporation into the nuclei was detected by immunofluorescence in eWAT sections (right panel). Cell outlines were stained with anti-perilipin antibody (green) and nuclei, with DAPI (blue). Scale bar: 20 μm. A cell in detail is shown in a bigger magnification for each genotype.

Quantification of positive BrdU nuclei is showed in the middle panel. (B) Comparison of energy balance between HFD-fed Fab-Cre and p38α$^{Fab\text{-}KO}$ mice. HFD-fed mice were examined in a metabolic cage over a 2-day period to measure FI, respiratory exchange, and EE. FI and EE (left) over 2 days were corrected by lean mass. EE expressed as ANCOVA analysis (middle panel) and hour by hour over 48-h period (right panel) are also shown (mean ± SEM; Fab-Cre $n = 10$ mice; p38α$^{Fab\text{-}KO}$ $n = 8$ mice). (C) Body (mean ± SEM; Fab-Cre $n = 20$ mice; p38α$^{Fab\text{-}KO}$ $n = 18$ mice) and skin temperature of surrounding interscapular BAT (mean ± SEM; Fab-Cre $n = 10$ mice; p38α$^{Fab\text{-}KO}$ $n = 7$ mice). Lower panels show representative infrared thermal images. (D) Immunoblot analysis of UCP1 levels and Creb and AMPK phosphorylation in lysates from BAT. Quantification is shown in the lower panel. (E) Immunohistochemistry staining of UCP1 after 8 weeks of HFD in BAT. Scale bar: 50 μm. Statistically significant differences between Fab-Cre and p38α$^{Fab\text{-}KO}$ mice are indicated: $^{**}p < 0.01$ (*t* test or Welch's test when variances were different). See also S1 Data. AMPK, 5' adenosine monophosphate-activated protein kinase; BAT, brown adipose tissue; BrdU, bromodeoxyuridine; Creb, cAMP response element-binding; EE, energy expenditure; eWAT, epididymal fat; FI, food intake; HFD, high-fat diet; IR temperature, infrared temperature; UCP1, uncoupling protein 1; WAT, white adipose tissue.

https://doi.org/10.1371/journal.pbio.2004455.g003

Furthermore, they had lower blood glucose levels and partial glucose tolerance, indicating that they were protected against HFD-induced diabetes (Fig 4A–4F).

Our data at 23 ˚C demonstrated that lack of p38α resulted in increased whole-body energy expenditure due to the activation of BAT and iWAT thermogenesis. At this temperature, BAT is already fully differentiated; because it is complicated to detect an even higher level of UCP1, genetic modifications that up-regulate UCP1 levels cannot be easily detected [25]. For this reason, we therefore evaluated p38α$^{Fab\text{-}KO}$ phenotype in thermoneutrality (30 ˚C) because it has been suggested to be more similar to the human situation [25]. At 30 ˚C, p38α$^{Fab\text{-}KO}$ mice were also protected against HFD-induced obesity (Fig 5A) and presented lower body fat mass and increased BAT thermogenesis (Fig 5B and 5C), indicating that, even at temperatures at which BAT is impeded, these mice maintain BAT activation. In fact, UCP1 expression was much higher in BAT from p38α$^{Fab\text{-}KO}$ than in the control Fab-Cre mice at 30 ˚C (Fig 5D). In addition, p38α$^{Fab\text{-}KO}$ were also protected from HFD-induced diabetes at thermoneutrality (Fig 5E and 5F). Together, these data confirm that lack of p38α protects against HFD-induced obesity and diabetes due to an activation of BAT thermogenesis.

To gain insight into the molecular mechanism that might account for increased UCP1 levels and thermogenic capacity, we studied the signalling in the different adipose tissue depots. The p38MAPK pathway has been shown to trigger BAT activation in several models [18, 26–28]. Additionally, it has been found that p38α can inhibit the other p38 isoforms by a negative feedback loop that blocks the activation of the upstream kinases of this pathway [29]. Therefore, we evaluated the expression and phosphorylation state of the other p38s, with a phospho-p38 antibody that recognises all p38 isoforms [30]. Using adipocytes lacking p38γ/δ, we confirmed that p38α/β run around 38 kDa, while p38γ/δ run higher—around 41 kDa—allowing us to distinguish the phosphorylation of these kinases (S9A Fig). Under ND condition, p38δ and p38γ were hyperactivated in eWAT and iWAT from p38α$^{Fab\text{-}KO}$ (S9B Fig). In agreement, p38δ/γ were activated more when cells were treated with sorbitol and p38α inhibitor SB203580 (S9C Fig). HFD resulted in reduced RNA expression of all the p38 isoforms in BAT, while in eWAT, only p38δ and p38γ decreased (S9D Fig). p38δ and p38γ were hyperactivated in iWAT and BAT from HFD-fed p38α$^{Fab\text{-}KO}$, whereas elevated p38δ (*Mapk13*) RNA levels were also found in BAT and eWAT from HFD-fed p38α$^{Fab\text{-}KO}$ animals (Fig 6A, 6B and S7, S9E and S9F Figs). Activation of p38δ in BAT was diminished when mice were maintained at 30 ˚C (Fig 6A), suggesting that this p38 isoform might activate BAT thermogenesis. To further evaluate this hypothesis, mice lacking p38δ in adipose tissue (p38δ$^{Fab\text{-}KO}$) were generated. In agreement with the importance of this kinase in BAT activation, p38δ$^{Fab\text{-}KO}$ mice fed with ND presented higher body weight, associated with increased fat mass and weight of all fat depots (Fig 6C and 6D and S10A Fig). In concordance, p38δ$^{Fab\text{-}KO}$ presented reduced energy expenditure, whole-body temperature, and decreased BAT thermogenesis (Fig 6E and 6F) as well as lower

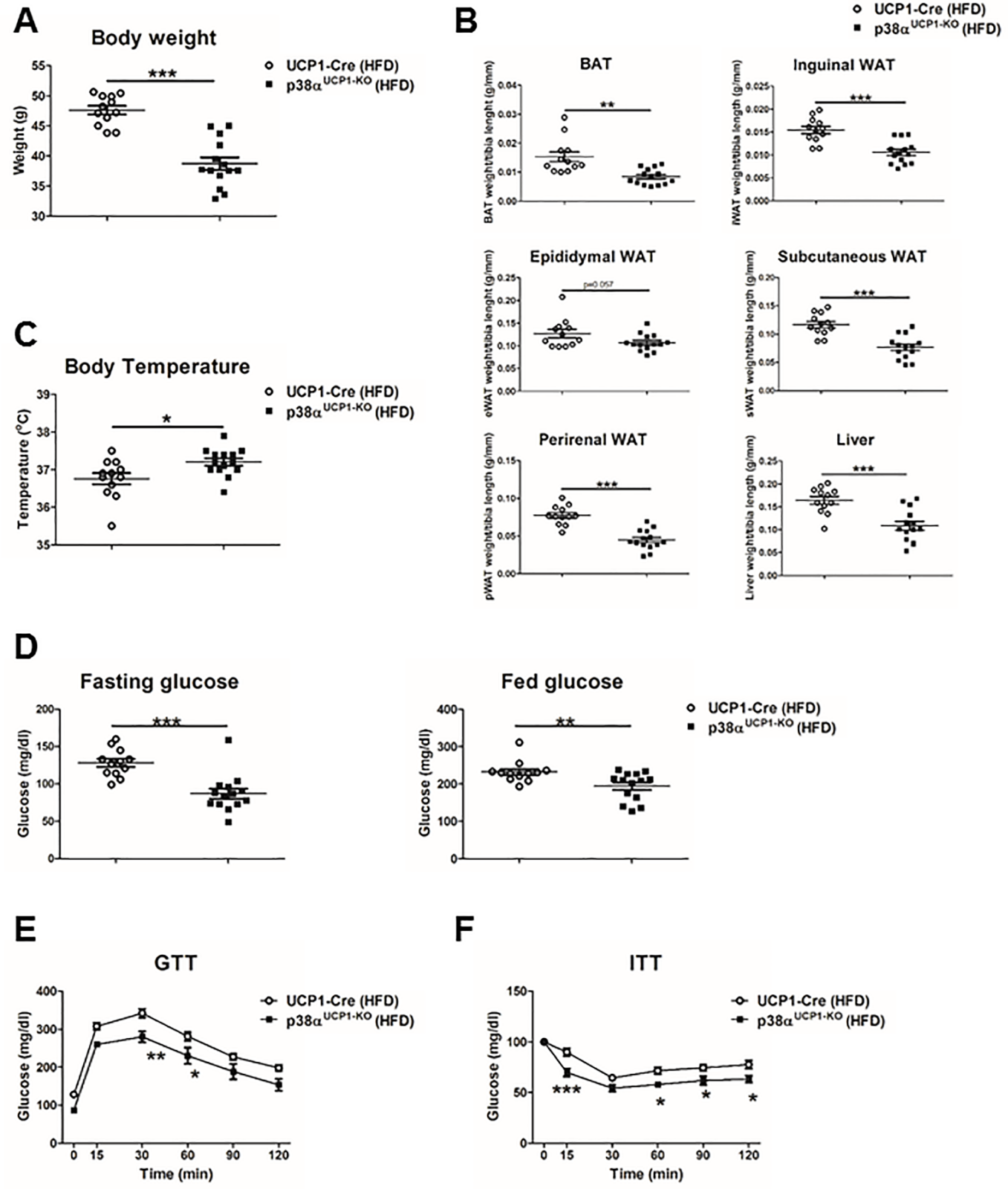

Fig 4. p38α controls BAT thermogenesis. UCP1-Cre and p38α$^{UCP1-KO}$ mice were fed with HFD for 8 weeks. (A) Body weight at the end of the treatment (mean ± SEM; UCP1-Cre $n = 12$ mice; p38α$^{UCP1-KO}$ $n = 14$ mice). (B) Weight of BAT, eWAT, sWAT, iWAT, pWAT, and liver relativised to tibia length

(mean ± SEM; UCP1-Cre $n = 12$ mice; $p38\alpha^{UCP1\text{-}KO}$ $n = 14$ mice). (C) Body temperature of HFD-fed UCP1-Cre and $p38\alpha^{UCP1\text{-}KO}$ mice (mean ± SEM; UCP1-Cre $n = 12$ mice; $p38\alpha^{UCP1\text{-}KO}$ $n = 14$ mice). (D) Fasting and fed blood glucose in UCP1-Cre and $p38\alpha^{UCP1\text{-}KO}$ mice fed an HFD (8 weeks) (mean ± SEM; UCP1-Cre $n = 12$ mice; $p38\alpha^{UCP1\text{-}KO}$ $n = 14$ mice). (E) GTT and (F) ITT in UCP1-Cre and $p38\alpha^{UCP1\text{-}KO}$ mice fed HFD for 8 weeks. Mice were fasted overnight (for GTT) or 1 hour (for ITT), and blood glucose concentration was measured in mice given intraperitoneal injections of glucose (1 g/kg of total body weight) or insulin (0.75 U/kg of total body weight) (mean ± SEM; UCP1-Cre $n = 12$ mice; $p38\alpha^{UCP1\text{-}KO}$ $n = 14$ mice). $^{*}p < 0.05$; $^{**}p < 0.01$; $^{***}p < 0.001$ UCP1-Cre versus $p38\alpha^{UCP1\text{-}KO}$ (2-way ANOVA coupled with Bonferroni's post-tests or *t* test or Welch's test when variances were different). See also S1 Data. BAT, brown adipose tissue; eWAT, epididymal fat; GTT, glucose tolerance test; HFD, high-fat diet; ITT, insulin tolerance test; iWAT, inguinal fat; pWAT, perirenal fat; sWAT, subcutaneous fat; UCP1, uncoupling protein 1; WAT, white adipose tissue.

https://doi.org/10.1371/journal.pbio.2004455.g004

expression levels of *Ucp1* and *Ppargc1*β in BAT (S10B Fig) with no differences in protein kinase A (PKA) phosphorylation (S10C Fig).

p38δ is activated in BAT upon cold exposure and in adipocytes after stimulation with the thyroid hormone T3 or norepinephrine (NE) (Fig 6G and 6H), suggesting that this p38 isoform might activate BAT thermogenesis. In fact, at 4 ˚C, $p38\delta^{Fab\text{-}KO}$ mice have lower body and skin temperature in the BAT region (Fig 6I). Moreover, HFD-fed $p38\delta^{Fab\text{-}KO}$ mice were more obese with higher fat mass and weight of all fat depots (S11A–S11C Fig). This increased adiposity correlated with lower BAT thermogenesis and lower UCP1, *Ppargc1a*, and *Cidea* levels in BAT (S11D–S11F Fig).

Our data indicated that p38δ was triggering thermogenesis because in vitro–differentiated brown adipocytes lacking p38δ have reduced expression of important genes implicated in BAT thermogenesis (*Ppargc1b*, *Ppargc1a*, *Cidea*, and *Cox8b*) and a slight decrease of *Ucp1* and *Cox7a1* supporting the cell-autonomous effect of p38δ in BAT thermogenesis (Fig 7A), with no differences in amount of mitochondrial DNA (Fig 7B and 7C).

Therefore, we evaluated respiration profiles in brown adipocytes lacking p38α and p38δ. Brown adipocytes lacking p38α presented higher leak respiration after isoproterenol (ISO) or NE treatment (Fig 7D). However, this augmented respiration capacity induced by NE or ISO was diminished when p38δ was chemically inhibited by BIRB796, a known inhibitor p38δ [31], as well as in p38δ-deficient brown adipocytes (Fig 7E and 7F), supporting the important role of this kinase in brown adipocyte activation.

In conclusion, we demonstrated that p38α in BAT inhibits p38δ activation, which in turn regulates BAT thermogenesis, energy expenditure, and body weight. We demonstrated that p38α and p38δ have opposite roles in BAT: whereas p38α inhibits BAT thermogenesis, p38δ induces it upon several physiological stimuli (Fig 8).

Discussion

Adipose tissue has become an important target for the treatment of obesity, not only because its dysfunction could be responsible for diabetes development but also because increasing BAT thermogenesis and/or browning of WAT could lead to new therapeutic approaches against obesity [32, 33]. In this scenario, p38MAPK signalling has been proposed to be a key activator of these processes. Consequently, there is an increasing interest to understand the function of this pathway in the regulation of adipose tissue metabolism, remodelling, and browning.

A growing number of studies have defined p38MAPK as one of the main pathways that stimulates browning and BAT thermogenesis [18,21–23]. However, using genetically modified mice lacking specific p38 family members in adipose tissue, we have shown that lack of p38α in adipose tissue protects against HFD-induced obesity by increasing energy expenditure through the activation of BAT thermogenesis. Mechanistically, lack of p38α results in hyperactivation of p38δ in BAT together with increased UCP1 expression and higher Creb and AMPK phosphorylation. Negative feedback controls by p38α through the regulation of upstream activators of the pathway—such as TAB1 phosphorylation or MKK6 expression—have been

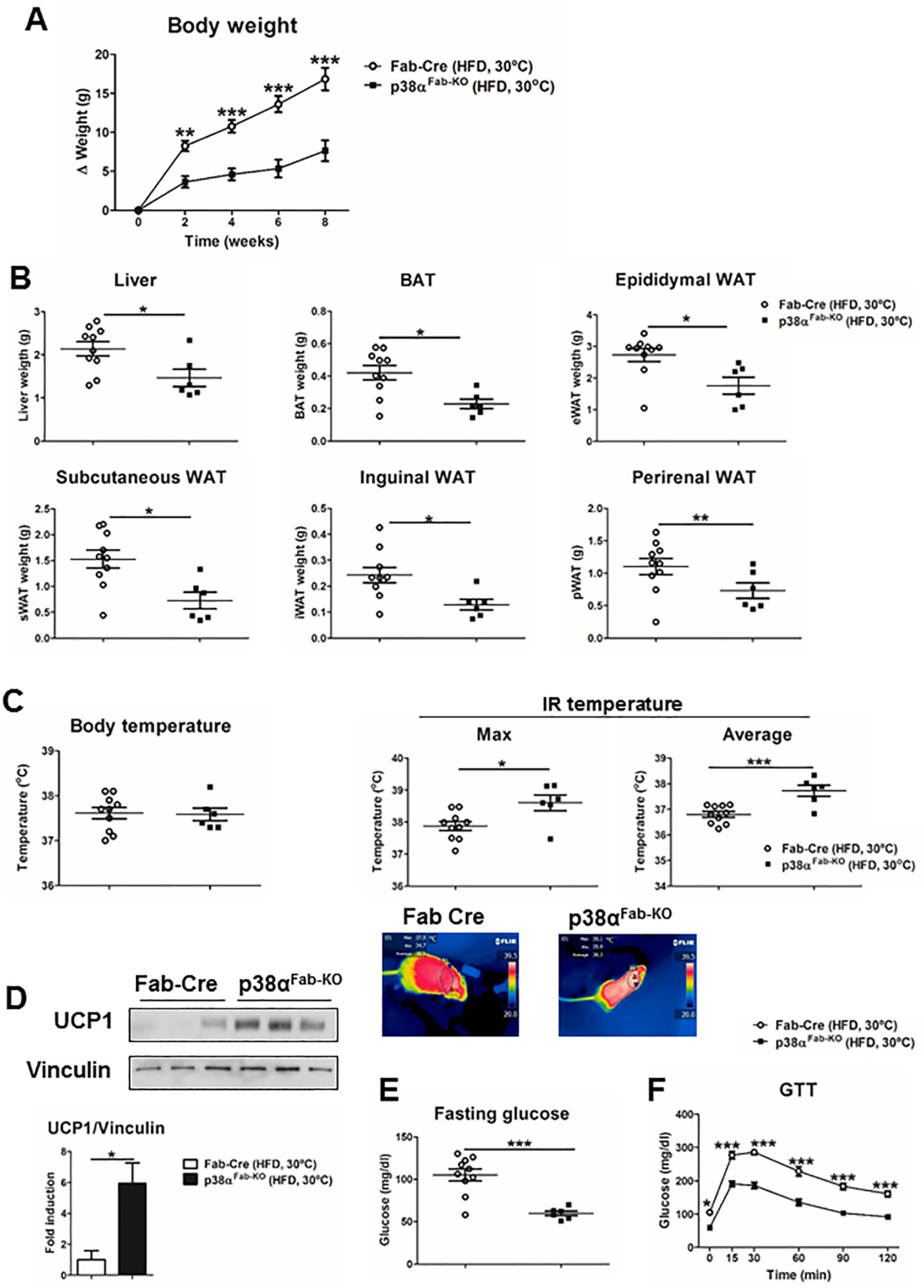

Fig 5. p38α$^{Fab\text{-}KO}$ mice have increased BAT thermogenesis under thermoneutrality conditions. Fab-Cre and p38α$^{Fab\text{-}KO}$ mice were fed an HFD for 8 weeks and housed at 30 ˚C. (A) Body weight time course in Fab-Cre and p38α$^{Fab\text{-}KO}$ male (8–10-wk-old) mice fed a HFD over 8 weeks. Data are presented as the increase above initial weight (mean ± SEM; Fab-Cre $n = 10$ mice; p38α$^{Fab\text{-}KO}$ $n = 6$ mice). (B) Weight of liver, BAT, eWAT, sWAT, iWAT, and pWAT (mean ± SEM; Fab-Cre $n = 10$ mice; p38α$^{Fab\text{-}KO}$ $n = 6$ mice). (C) Body and skin temperature of surrounding interscapular BAT from HFD-fed Fab-Cre and p38α$^{Fab\text{-}KO}$ mice (mean ± SEM; Fab-Cre

$n = 10$ mice; p38α$^{Fab\text{-}KO}$ $n = 6$ mice). Lower panels show representative infrared thermal images. (D) Immunoblot analysis of UCP1 protein levels in lysates from BAT. Quantification is shown in the lower panel. (E) Fasting and fed blood glucose in Fab-Cre and p38α$^{Fab\text{-}KO}$ mice fed the HFD at 30 ˚C (mean ± SEM; Fab-Cre $n = 10$ mice; p38α$^{Fab\text{-}KO}$ $n = 6$ mice). (F) GTT in HFD-fed Fab-Cre and p38α$^{Fab\text{-}KO}$ at 30 ˚C. Blood glucose concentration was measured in mice given intraperitoneal injections of glucose (1 g/kg of total body weight) (mean ± SEM; Fab-Cre $n = 10$ mice; p38α$^{Fab\text{-}KO}$ $n = 6$ mice). Statistically significant differences between Fab-Cre and p38α$^{Fab\text{-}KO}$ mice are indicated: $^{*}p < 0.05$; $^{**}p < 0.01$; $^{***}p < 0.001$ (*t* test or Welch's test when variances were different). See also S1 Data. BAT, brown adipose tissue; eWAT, epididymal fat; GTT, glucose tolerance test; HFD, high-fat diet; IR temperature, infrared temperature; iWAT, inguinal fat; pWAT, perirenal fat; sWAT, subcutaneous fat; UCP1, uncoupling protein 1; WAT, white adipose tissue.

https://doi.org/10.1371/journal.pbio.2004455.g005

previously reported [29, 34]. Here, we show that negative control of the pathway by p38α has biological and pathological implications. However, it would be interesting to examine the epistatic relationship between p38α and p38δ genetically in future studies.

We also demonstrated that p38δ is activated in BAT by 3 stimuli widely known to activate this tissue: cold exposure, NE, and thyroid hormone treatment [35, 36], whereas its phosphorylation is reduced under thermoneutrality conditions. In addition, p38δ expression in BAT was reduced in obese mice, while this down-regulation was ablated in p38α$^{Fab\text{-}KO}$ mice, suggesting that activation of p38δ in p38α$^{Fab\text{-}KO}$ mice is responsible for the protection against diet-induced obesity observed in these mice. Indeed, inhibition of p38δ in p38α$^{Fab\text{-}KO}$ brown adipocytes abolished the increased respiratory capacity induced by β3-adrenergic stimuli. In agreement with the role of p38δ-promoting thermogenesis, mice lacking this kinase in adipose tissue developed overweight, even in ND, and showed decreased whole-body energy expenditure associated with lower temperature and reduced BAT activation. Moreover, we confirmed the cell-autonomous role of p38δ inducing browning using differentiated adipocytes.

Our results were completely unexpected because the p38MAPK pathway has been shown to trigger BAT activation in several models [18, 26–28], and—until now—it was thought that the only implicated family member was p38α. Moreover, we have recently found that hyperactivation of p38α in MKK6-deficient animals induces browning of eWAT [37]. These finding might indicate opposite effects of p38α in eWAT versus iWAT or BAT. While p38α would activate browning in eWAT—increasing energy expenditure—it would prevent it in iWAT, and it would block thermogenesis through the negative regulation of p38δ in BAT. In agreement with this hypothesis, we observed reduced levels of UCP1 in epididymal fat lacking p38α. In fact, our data from human samples indicated that the p38α mRNA levels in visceral fat directly correlates with UCP1 expression and inversely correlates with the BMI, suggesting that p38α triggers visceral fat browning. We also found that p38α in sWAT inversely correlates with UCP1. This is in accordance with results observed in mouse models, in which we found a decrease of all p38s after HFD in all fat depots. However, the levels of UCP1 expression in these human fat depots is quite low judging by the low Ct obtained (higher than 29), and evaluation of UCP1 protein expression in human fat depots would be necessary. Moreover, further studies to determinate the expression of p38 family members and upstream kinases in other human fat depots would help us to understand the role of these kinases in human adipocytes.

It has been proposed that p38α induces adipogenesis [38–40]. However, using genetically modified animals, we showed here that lack of p38α in preadipocytes did not affect their differentiation to adipocytes, nor did it affect changes in the differentiation markers evaluated in the major fat depots. This capacity of cells lacking p38α to still differentiate to adipocytes could be due to the hyperactivation of the other members of the family: p38γ and p38δ. In fact, it has been shown that p38 isoforms can compensate for each other [30]. Here, we demonstrated the cell-autonomous and opposite effects of 2 p38 isoforms in adipocytes, p38α and p38δ. The cell-specific actions of p38α in each fat depot could be explained by the specific expression pattern of p38 family members—p38α being the main isoform expressed in eWAT, whereas p38δ

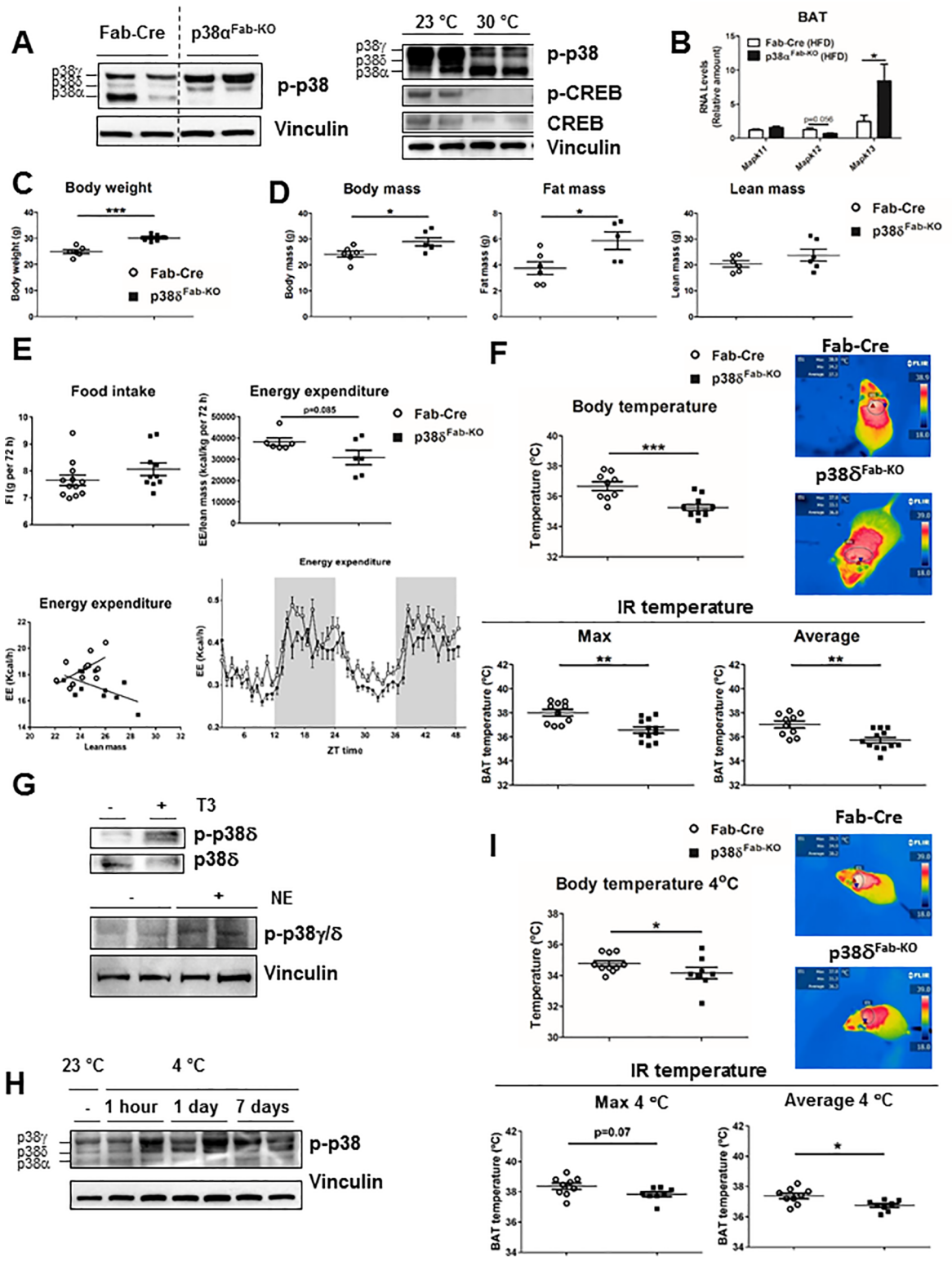

Fig 6. Activation of p38δ is responsible for BAT activation. (A) Immunoblot analysis of BAT lysate from Fab-Cre and p38α$^{Fab\text{-}KO}$ mice fed an HFD for 8 weeks. Left: 23 ˚C; right: comparison of 23 ˚C versus 30 ˚C. (B) qRT-PCR analysis of mRNA expression of p38β (*Mapk11*), p38γ (*Mapk12*), and p38δ (*Mapk13*) in BAT Fab-Cre and p38α$^{Fab\text{-}KO}$ mice fed an HFD for 8 weeks. mRNA was normalised to level of *Gapdh* mRNA (mean ± SEM, Fab-Cre $n = 15$ mice; p38α$^{Fab\text{-}KO}$ $n = 9$ mice) (C) Body weight in Fab-Cre and p38δ$^{Fab\text{-}KO}$ male (8–10-wk-old) mice fed an ND over 8 weeks (mean ± SEM; Fab-Cre $n = 6$ mice; p38δ$^{Fab\text{-}KO}$ $n = 6$ mice). (D) Body, fat, and lean mass in p38δ$^{Fab\text{-}KO}$ and Fab-Cre

mice after 8 weeks of ND measured by NMR (mean ± SEM; Fab-Cre $n = 6$ mice; $p38\delta^{Fab\text{-}KO}$ $n = 5$ mice). (E) Comparison of energy balance between ND-fed Fab-Cre and $p38\delta^{Fab\text{-}KO}$ mice. ND-fed mice were examined in a metabolic cage over a 3-day period to measure FI and EE. FI (upper left panel; mean ± SEM; Fab-Cre $n = 12$ mice; $p38\delta^{Fab\text{-}KO}$ $n = 10$ mice) and EE (upper right panel; mean ± SEM; Fab-Cre $n = 6$ mice; $p38\delta^{Fab\text{-}KO}$ $n = 6$ mice) over 2 days were corrected by lean mass. EE expressed as ANCOVA analysis (lower left panel; mean ± SEM; Fab-Cre $n = 9$ mice; $p38\delta^{Fab\text{-}KO}$ $n = 12$ mice) and hour by hour over a 48-hour period (lower right panel; mean ± SEM; Fab-Cre $n = 12$ mice; $p38\delta^{Fab\text{-}KO}$ $n = 12$ mice) are also shown. (F) Body temperature of ND-fed Fab-Cre and $p38\delta^{Fab\text{-}KO}$ mice (mean ± SEM; Fab-Cre $n = 9$ mice; $p38\delta^{Fab\text{-}KO}$ $n = 11$ mice). Skin temperature surrounding interscapular BAT in ND-fed Fab-Cre and $p38\delta^{Fab\text{-}KO}$. Right panels show representative infrared thermal images (mean ± SEM; Fab-Cre $n = 10$ mice; $p38\delta^{Fab\text{-}KO}$ $n = 12$ mice). (G) Adipocytes differentiated from interscapular BAT were stimulated with 100 nM T3 for 48 hours. Immunoprecipitation from cell lysates of p38δ were evaluated by immunoblot with antibodies against phospho-p38 and p38δ. Adipocytes differentiated from sWAT were stimulated with 1 μM NE for 1 hour, and p38 phosphorylation was analysed by immunoblot. (H) Control mice (C57BL/6) were exposed to cold (4 ˚C) for the indicated time, and phosphorylation of the different p38s in BAT was evaluated by immunoblot ($n = 5$ for each group; representative blot presented). (I) Body temperature of ND-fed Fab-Cre and $p38\delta^{Fab\text{-}KO}$ mice exposed to cold (4 ˚C) for 1 hour (mean ± SEM; Fab-Cre $n = 10$ mice; $p38\delta^{Fab\text{-}KO}$ $n = 8$ mice). Skin temperature surrounding interscapular BAT in ND-fed Fab-Cre and $p38\delta^{Fab\text{-}KO}$ after 1 hour of cold exposure. Right panels show representative infrared thermal images (mean ± SEM; Fab-Cre $n = 9$ mice; $p38\delta^{Fab\text{-}KO}$ $n = 8$ mice). $^{*}p < 0.05$; $^{**}p < 0.01$; $^{***}p < 0.001$ (*t* test). See also S1 Data. BAT, brown adipose tissue; Creb, cAMP response element-binding; EE, energy expenditure; FI, food intake; HFD, high-fat diet; IR temperature, infrared temperature; ND, normal-chow diet; NE, norepinephrine; NMR, nuclear magnetic resonance; qRT-PCR, quantitative real-time polymerase chain reaction; sWAT, subcutaneous fat.

https://doi.org/10.1371/journal.pbio.2004455.g006

or p38γ are abundant in BAT or iWAT. Furthermore, our results suggest a different regulation of p38s expression in adipose tissue during obesity, with only decrease of p38δ and p38γ in eWAT and no effects in p38α or p38β. More studies would be necessary to elucidate the function of p38γ in adipose tissue.

We also evaluated the controversial role of p38α in GLUT4 translocation [41–43]. Under ND, insulin-induced GLUT4 translocation was the same in both control and $p38\alpha^{Fab\text{-}KO}$ mice. However, $p38\alpha^{Fab\text{-}KO}$ mice maintained the insulin-induced translocation after the HFD, perhaps due to the fact that these animals did not gain weight and were protected against diet-induced insulin resistance. In fact, our data suggest that these mice are more glucose tolerant using a dose of glucose based on their total body weight.

Due to the potential clinical implications of these results, it would be necessary to further evaluate the function of each p38 family member in browning to better understand how this pathway controls adipose tissue metabolism.

In summary, we have demonstrated that p38α and p38δ in adipose tissue have opposite roles: p38α negatively regulates BAT thermogenesis, energy expenditure, and body weight, while p38δ induces thermogenesis in BAT in response to several physiological stimuli. These results have potential clinical implications because inhibition of p38α or activation of p38δ might be of therapeutic interest against obesity.

Material and methods

Ethics statement

This population study was approved by the Ethics Committee of the University Hospital of Salamanca and the Carlos III (CEI PI 09_2017-v3) with the all subjects providing written informed consent to undergo visceral fat biopsy under direct vision during surgery. Data were collected on demographic information (age, sex, and ethnicity), anthropomorphic measurements (BMI), smoking and alcohol history, coexisting medical conditions, and medication use.

All animal procedures conformed to EU Directive 86/609/EEC and Recommendation 2007/526/EC regarding the protection of animals used for experimental and other scientific purposes, enacted under Spanish law 1201/2005. The protocols are CNIC 08/13 and PROEX 49/13.

Study population and sample collection

For the analysis of visceral fat, the study population included 71 patients (58 adult patients with BMI $\geq$35), while for the analysis of sWAT, the study population included 170 patients

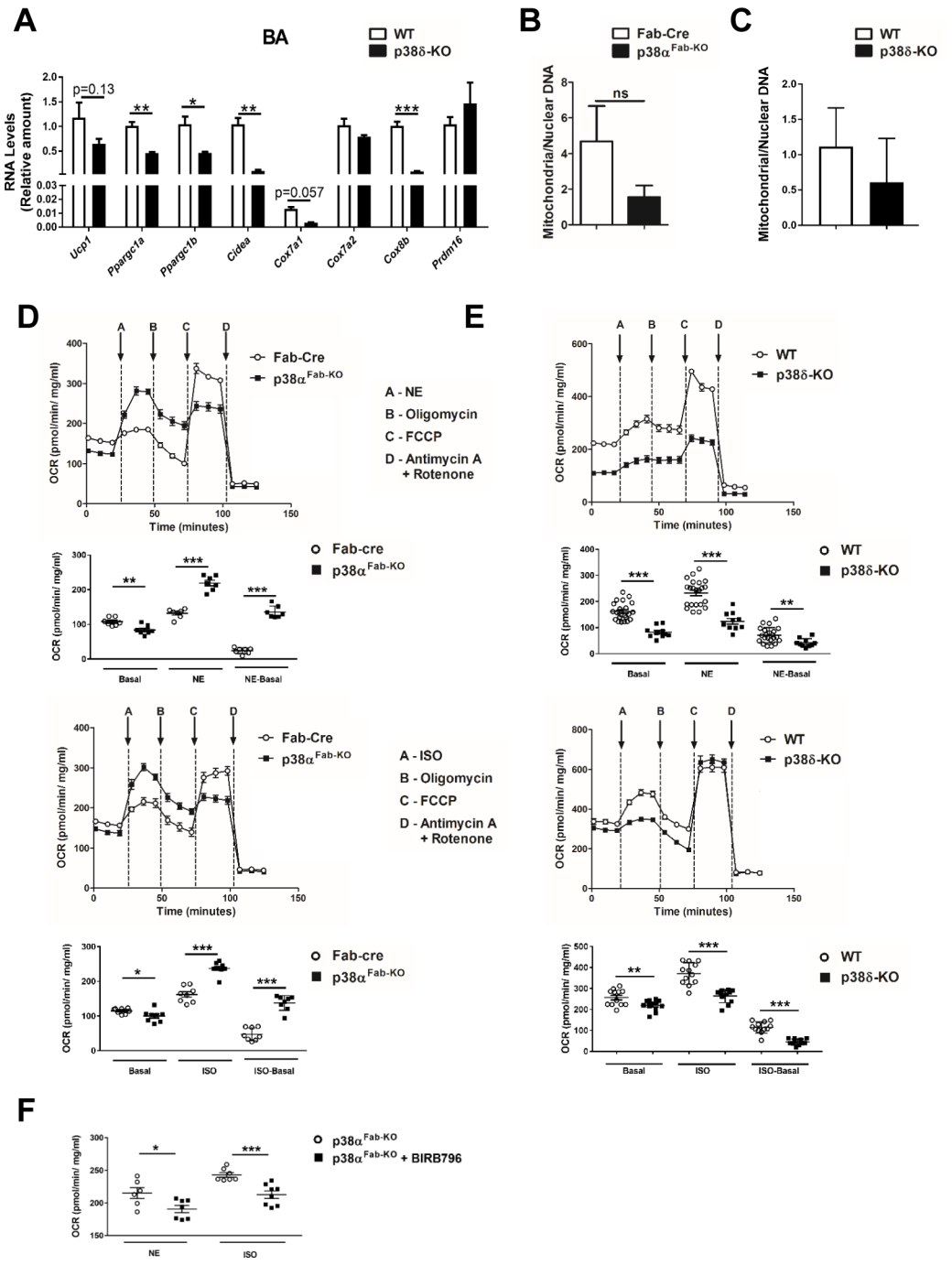

Fig 7. p38s regulate respiratory capacity of brown adipocytes. Primary adipocytes isolated from intercapsular BAT were differentiated in vitro. (A) qRT-PCR analysis of browning genes mRNA expression from primary adipocytes isolated from WT or p38δ$^{-/-}$ mice. mRNA expression was normalised to the amount of *Gapdh* mRNA (mean ± SEM; WT $n = 5$ wells; p38δ$^{-/-}$ $n = 5$ wells). (B) Analysis of mitochondrial DNA content with respect to nuclear DNA by RT-PCR in adipocytes isolated from BAT of Fab-cre or p38α$^{Fab\text{-}KO}$ mice (mean ± SEM; Fab-Cre $n = 3$ wells; p38α$^{Fab\text{-}KO}$ $n = 5$ wells) and of (C) WT or p38δ$^{-/-}$ mice (mean ± SEM; WT $n = 3$ wells; p38δ$^{-/-}$ $n = 4$ wells). (D–E) OCR to NE (1 μM) and ISO (1 μM) in differentiated brown adipocytes from Fab-Cre and p38α$^{Fab\text{-}KO}$ mice (mean ± SEM; Fab-Cre $n = 7$ or p38α$^{Fab\text{-}KO}$ $n = 7$ wells treated with NE; and Fab-Cre $n = 8$ or p38α$^{Fab\text{-}KO}$ $n = 8$ wells treated with ISO) (panel D) or from WT or p38δ$^{-/-}$ mice (mean ± SEM; WT $n = 22$ or p38δ$^{-/-}$ $n = 12$ wells treated with NE; and WT $n = 12$ or p38δ$^{-/-}$ $n = 12$ wells treated with ISO) (panel E) analysed by Seahorse assay. Nonmitochondrial respiration was subtracted from OCR values, and all values were normalised to protein content. Upper panels show OCR over time upon different drugs injections: oligomycin (1 μM), FCCP (1 μM), and antimycin A (1 μM) with rotenone (1 μM). Lower panels show basal and NE/ISO-

induced OCR. (F) OCR induced by NE and ISO in differentiated brown adipocytes from Fab-Cre and p38α$^{Fab\text{-}KO}$ mice was abolished by pretreatment with BIRB796 (10 μM) for 1 hour (mean ± SEM; Fab-Cre $n = 6$ or p38α$^{Fab\text{-}KO}$ $n = 7$ wells treated with NE; and Fab-Cre $n = 7$ or p38α$^{Fab\text{-}KO}$ $n = 8$ wells treated with ISO). See also S1 Data. BAT, brown adipose tissue; FCCP, carbonyl cyanide-4-(trifluoromethoxy)phenylhydrazone; ISO, isoproterenol; NE, norepinephrine; OCR, oxygen consumption rate; qRT-PCR, quantitative real-time polymerase chain reaction; WT, wild-type.

https://doi.org/10.1371/journal.pbio.2004455.g007

(140 adult patients with BMI ≥35), recruited from patients who underwent elective bariatric surgery at the University Hospital of Salamanca. Patients were excluded if they had a history of alcohol use disorders or excessive alcohol consumption (>30 g/day in men and >20 g/day in women) or had chronic hepatitis C or B. Control subjects ($n = 13$ for visceral fat study; $n = 30$ for sWAT study) were recruited among patients who underwent laparoscopic cholecystectomy for gallstone disease. Before surgery, fasting venous blood samples were collected for measuring complete cell blood count, total bilirubin, aspartate aminotransferase (AST), alanine aminotransferase (ALT), total cholesterol, high-density lipoprotein, low-density lipoprotein, triglycerides, creatinine, glucose, and albumin (S1 and S2 Tables).

Animal models

Mice with a germ-line mutation in *Mapk14* (*p38α*) and *Mapk13* (*p38δ*) have been reported before [44, 45]. These animals were crossed with Tg (Fabp4-cre)1Rev/J [46] line or B6.FVB-Tg (Ucp1-cre)1Evdr/J [24] on the C57BL/6J background (Jackson Laboratory) to generate the mice lacking p38α or p38δ in adipose tissue (both WAT and BAT or just in BAT, respectively). All mice were maintained on a C57BL/6J background (back-crossed 10 generations). Genotype was confirmed by PCR analysis of genomic DNA. Mice were fed with an ND or an HFD, Research Diets Inc.) for 8 weeks ad libitum. For fat expansion measurement, mice were treated with BrdU (0.4 mg/ml; Sigma) in the drinking water (water was refreshed every 3 days) during the first week of a 6-week HFD. For temperature experiments, mice were housed at 30 ˚C for 8 weeks while feeding an HFD in case of thermoneutrality analysis. Mice were exposed to 4 ˚C for 1 hour, 1 day, or 1 week in case of cold adaptation studies.

Cell culture

Immortalised and primary brown preadipocytes from WT, Fab-Cre, p38α$^{Fab\text{-}KO}$, and p38δ-KO mice were differentiated to brown adipocytes in 10% FCS medium supplemented with 20 nM insulin, 1 nM T3, 125 μM indomethacin, 2 μg/ml dexamethasone, and 50 mM IBMX for 48 hours and maintained with 20 nM of insulin and 1 nM of T3 for 8 days. For some experiments, cultures were incubated with 100 nM T3 for 48 hours before extraction.

Immortalised white preadipocytes from Fab-Cre and p38α$^{Fab\text{-}KO}$ mice were differentiated to adipocytes for 9 days in 8% FCS medium supplemented with 5 μg/ml insulin, 25 μg/ml IBMX, 1 μg/ml dexamethasone, and 1 μM troglitazone. For some experiments, cultures were incubated with 1 μM NE for 1 hour before extraction.

Analysis of mitochondrial function

Primary brown preadipocytes were plated and differentiated in gelatin-coated (0.1%) 96 seahorse plates. MitoStress oxygen consumption rate (OCR) was assessed in XF medium containing 25 mM glucose, 2 mM L-glutamine, and 1 mM sodium pyruvate using a XF-96 Extracellular Flux Analyzers (Seahorse Bioscience, Agilent Technologies). Cells were stimulated with following drugs: NE or ISO, oligomycin, FCCP, and antimycin A plus rotenone (1 μM finally; all from Sigma Aldrich). The protocol for the all drugs followed a 3-minute mix, 2-minute wait, and 3-minute measure cycle that was repeated 3 times. After the analysis, data were

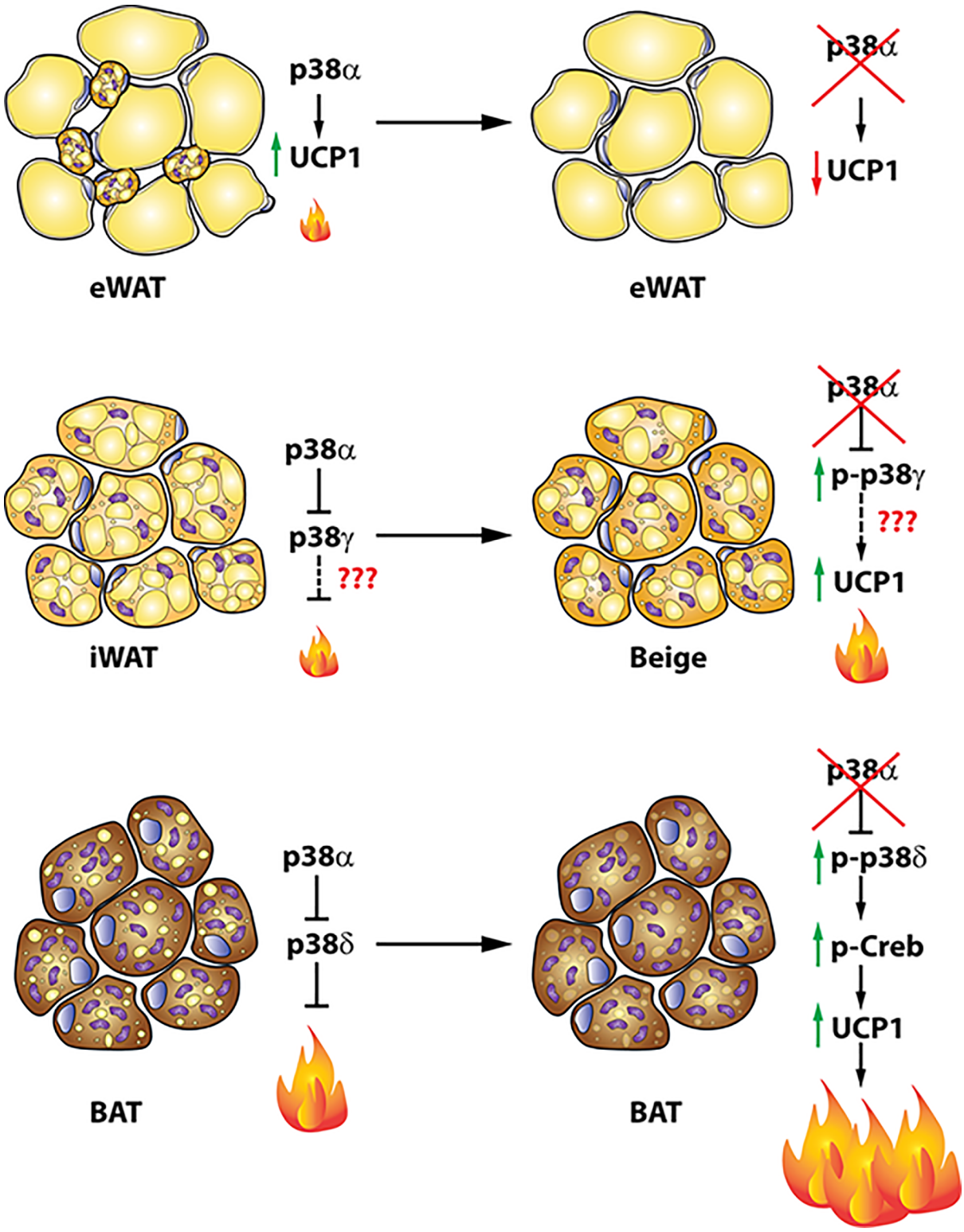

Fig 8. Regulation of browning and BAT activation by p38 pathway. Graphical abstract summarising the role of p38 isoforms in adipose tissue. In eWAT, p38α activates browning through the phosphorylation of Creb and ATF2 increasing UCP1 expression. In iWAT and BAT, p38α activation inhibits p38γ and p38δ and in consequence reduces browning and BAT activation, respectively, by down-regulation of UCP1. ATF2, activating transcription factor 2; BAT, brown adipose tissue; Creb, cAMP response element-binding; eWAT, epididymal fat; iWAT, inguinal fat; UCP1, uncoupling protein 1.

https://doi.org/10.1371/journal.pbio.2004455.g008

normalised to protein level assessed by Bradford quantification. Basal Respiration Capacity (OCR basal − OCR nonmitochondrial) and oxygen consumption in response to NE (OCR NE − OCR basal) or ISO (OCR ISO–OCR basal) were calculated. For some experiments, cultures were pretreated with 10 μM BIRB796 for 1 hour.

Western blot

Samples were lysed with RIPA buffer containing protease and phosphatase inhibitors (Tris-Hcl 50 mM [pH 7.5]; Triton X-100 1%; EDTA 1 mM [pH 8]; EGTA 1 mM; NaF 50 mM; β-glycerophosphate-Na 1 mM; sodium pirophosphate 5 mM; orthovanadate-Na 1 mM; sucrose 0.27 M; PMSF 0.1 mM; β-mercaptoethanol 1 mM; aprotinin 10 μg/ml; leupeptin 5 μg/ml). Lysates were separated by SDS-PAGE and incubated with antibodies diluted 1/1,000 against P-Akt308 (Cell Signaling, 9275s), P-Akt473 (Cell Signaling, 9271s), Akt (Cell Signaling, 9272s), UCP1 (Abcam, AB10983), P-ATF2 (Cell Signaling, 9225s), ATF2 (Cell Signaling, 9226s), P-CREB (Cell Signaling, 9198), CREB (Cell Signaling, 4820s), P-p38 (Cell Signaling, 9211s)—which recognises the phosphorylation in the activation sites of all the p38 isoforms—p38α (Santa Cruz, sc-535), P-AMPKα (Cell Signaling, 2531s), AMPKα (Cell Signaling, 2603s), P-ACC (Cell Signaling, 3661s), ACC (Cell Signaling, 3676s), PGC1α (Santa Cruz, sc13067), GAPDH (Santa Cruz, sc25778), tubulin (Sigma, T6199), and vinculin (Sigma, V9131), followed by an incubation with a secondary antibody conjugated with HRP. Reactive bands were detected by chemiluminescence and quantified by Image J software. Specificity of UCP1 antibody was evaluated using brown and eWAT from UCP1 KO animals [47].

For the immunoprecipitation assay, cell extracts were incubated with 4 μg of anti-p38 delta coupled with protein-G-Sepharose. After an overnight incubation at 4˚C, the captured proteins were centrifuged at 10,000 g, the supernatants discarded, and the beads washed 4 times in lysis buffer. Beads were boiled for 5 minutes at 95 ˚C in 10 μl sample buffer. The antibodies employed were anti-phospho p38 and anti-p38δ (Santa Cruz, sc7585). Immune complexes were detected by enhanced chemiluminescence (NEN).

Fluorescence-assisted cell sorting

Mouse bone marrow (BM) and spleens were collected, and single-cell suspension was obtained. Erythrocytes were lysed with a red cell lysis buffer incubation for 3 minutes on ice. Spleen samples were enriched using CD3 (BioLegend 79751 clone 145-2C11) and B220 (BioLegend 79752 clone RA3-6B2) biotinylated antibodies and magnetic Dynabeads Myone streptavidin T1 (invitrogen). Myeloid cells from spleen were labelled by surface staining with FITC-conjugated CD11b (BioLegend 79749 clone M1/70), PE-conjugated Gr1 (Ly6G/Ly6C) (BDBioscience 79750 clone RB6-8C5), and APC-conjugated F4/80 (eBiosciences 25-4801-82 clone BM8) antibodies, and myeloid cells from BM were labelled by FITC-conjugated Gr1 (Ly6G/Ly6C) (Invitrogen 11-5931-82 clone RB6-8C5), PE-conjugated CD115 (eBioscience 12-1152-82 clone AFS98), and APC-conjugated F4/80 (eBiosciences 25-4801-82 clone BM8) antibodies. Nuclei were stained with DAPI. Cells were sorted with a fluorescence-assisted cell sorting (FACS) Aria (BD) as follows: spleen macrophages ($Gr1^{-}$ $Cd11b^{medium}$ $F4/80^{+}$), spleen neutrophils ($Gr1^{high}$ $Cd11b^{+}$), and BM monocytes ($CD115^{+}$ $F4/80^{-}$). Isolated myeloid cells were lysed and analysed by western blot.

GTT

Overnight-starved mice were injected intraperitoneally with 1 g/kg of body weight of glucose, and blood glucose levels were quantified with an Ascensia Breeze 2 glucose meter at 0, 15, 30, 60, 90, and 120 minutes post injection. Alternatively, GTT was performed injecting intraperitoneally 1 g/kg of lean mass of glucose.

ITT

ITT was performed by injecting intraperitoneally 0.75 IU/kg of insulin at mice starved for 1 hour and detecting blood glucose levels with a glucometer at 0, 15, 30, 60, 90, and 120 minutes post injection.

Indirect calorimetry system

Energy expenditure, respiratory exchange, and food intake were quantified using the indirect calorimetry system (TSE LabMaster, TSE Systems, Germany) for 3 days.

Temperature

Body temperature was detected by a rectal thermometer (AZ 8851 K/J/T Handheld Digital Thermometer-Single, AZ Instruments Corp., Taiwan).

BAT-adjacent interscapular temperature was quantified by thermographic images using a FLIR T430sc Infrared Camera (FLIR Systems, Inc., Wilsonville, OR) and analysed through FlirIR software.

Nuclear magnetic resonance analysis

Body, fat, and lean mass were quantified by nuclear magnetic resonance (Whole Body Composition Analyzer; EchoMRI, Houston, TX) and analysed by ImageJ software.

Triglyceride measurement

Blood triglyceride content was quantified using a Dimension RxL Max analyser (Siemens). For triglyceride analysis in cells, brown adipocyte cultures were lysed in isopropanol, centrifuged at 10,000 g for 15 minutes at 4 ˚C, and triglycerides were detected in the supernatant with a commercial kit (Sigma).

DNA isolation

Brown adipocyte cells were scraped in PBS and pellet lysed in TNES buffer supplemented with Proteinase K (20 mg/ml) overnight at 55 ˚C. Reaction was stopped with sodium chloride 6 M and samples centrifuged 5 minutes at 13,000 g. DNA was precipitated in supernatants with 100% ethanol and washed with 70% ethanol. After drying, DNA was resuspended in DNase free water, quantified, and analysed by RT-PCR. Mitochondrial DNA was detected using primers for COII and nuclear DNA, using primers for Sdh1 (S3 Table).

qRT-PCR

RNA 500ng—extracted with RNeasy Plus Mini kit (Quiagen) following manufacturer instructions—was transcribed to cDNA, and qRT-PCR was performed using Fast Sybr Green probe (Applied Biosystems) and the appropriated primers in the 7900 Fast Real Time thermocycler (Applied Biosystems). Relative mRNA expression was normalised to *Gapdh* mRNA measured in each sample. Primers used are listed in S3 Table.

Histology staining

Fresh livers, brown, and epididymal white fat were fixed with formalin 10%, included in paraffin, and cut in 5 μm slides followed by a haematoxylin–eosin staining.

Fat droplets were detected by oil red staining (0.7% in propylenglycol) in 8 mm slides included in OCT compound (Tissue-Tek) and in differentiated brown and white adipocytes.

Immunostaining

Brown adipocytes were stained with Mito Tracker Deep Red (Invitrogen) and Bodipy (Invitrogen). Images were captured using Leica SPE confocal microcope (Leica Microsystems, Wetzlar, Germany).

For UCP1 immunostaining, brown and epididymal white fat were fixed with formalin 10%, included in paraffin, cut in 5 μm slides, and sequentially stained with a UCP1 antibody (1/500, Abcam, AB10983), a biotinylated goat anti-rabbit secondary antibody (1/500, Jackson Immuno Research Laboratories), a streptavidin-conjugated ABC complex (Vector Laboratories), and the substrate 3,3'-diaminobenzidene conjugated with horseradish peroxidase (Vector Laboratories), followed by brief counterstaining with Nuclear Fast Red haematoxylin (Sigma).

For immunofluorescence analysis, the 5 μm tissue sections were deparaffinised and rehydrated, followed by antigen retrieval in 10 mM sodium citrate (pH 6.0) under pressure in a CertoClav EL (CertoClav Sterilizer GmbH). For BrdU staining, sections were treated with DNase 30 minutes at 37 ˚C. Blocking and staining was performed in 5% BSA in PBS. Sections were incubated in primary antibodies including rat-anti-Ki67 (eBioscience, 14-5698-82; clone: SolA15) (1:100), rabbit-anti-GLUT4 (Abcam, ab654) (1:1000), mouse-anti-Caveolin-1 (Sigma, SAB4200216) (1:500), rat anti-BrdU (Abcam, Ab6326; clone: BU1/75 [ICR1]) (1:200), and rabbit anti-Perilipin (Cell Signaling, 9349; clone: D1D8) (1:400) overnight at 4 ˚C. Secondary antibodies including goat anti-rabbit-A488, goat anti-rat-A647, and chicken anti-mouse-A647—all used at 1:500—were purchased from Molecular Probes and incubated with tissue for 1 hour at room temperature. Nuclei were stained with DAPI, and slides were mounted with Vectashield mounting medium (Vector Laboratories) and examined using SP5 multi-line inverted confocal microscope. Several confocal images of each tissue section were acquired and analysed for the translocation of GLUT4 or the presence of Ki67 or BrdU in adipocyte nuclei. BAT and WAT cellularity were quantified using Fiji software. Adipocyte nuclei were identified by their location inside adipocyte membranes as described [23].

Statistical analysis

Results are expressed as mean ± SEM. Statistical analysis was evaluated by student *t* test and 2-way ANOVA coupled with Bonferroni's post-tests with values of $p < 0.05$ considered significant. When variances were different, Welch's test was used. For human studies, variables were compared by means of Mann-Whitney U test or χ^2 test.

Supporting information

S1 Fig. Deletion of p38α in white and BAT from p38α$^{Fab\text{-}KO}$ mice, related to Fig 2. (a) Western blot analysis of p38α expression in BAT, eWAT, spleen, BM, and liver isolated from p38α$^{Fab\text{-}KO}$ and control (Fab-Cre) mice. (b) Western blot analysis of p38α expression in BM, Mϕ, Neutros, and Mono. Mϕ and Neutros were sorted from spleen, and Mono from BM by FACS. BAT, brown adipose tissue; BM, bone marrow; eWAT, epididymal white adipose tissue; FACS, fluorescence assisted-cell sorting; Mϕ, macrophages; Mono, monocytes; Neutros, neutrophils.
(TIF)

S2 Fig. Lower fat mass and improved glucose tolerance in ND-fed p38α$^{Fab\text{-}KO}$ mice, related to Fig 2. (a) Body weight time course in Fab-Cre and p38α$^{Fab\text{-}KO}$ male (8- to 10-week-old) mice fed an ND over 8 weeks. Data are presented as the increase above initial weight (mean ± SEM, Fab-Cre $n = 9$ mice; p38α$^{Fab\text{-}KO}$ $n = 8$ mice). (b) NMR analysis of fat mass in p38α$^{Fab\text{-}KO}$ and

Fab-Cre mice after 8 weeks of ND (mean ± SEM, Fab-Cre $n = 9$ mice; p38α$^{Fab\text{-}KO}$ $n = 7$ mice). (c) Weight of eWAT, pWAT, sWAT, iWAT, BAT, and liver relativized to tibia length (mean ± SEM, Fab-Cre $n = 8$ mice; p38α$^{Fab\text{-}KO}$ $n = 7$ mice). (d) Fasting and fed blood glucose in Fab-Cre and p38α$^{Fab\text{-}KO}$ mice fed an ND (8 weeks) (mean ± SEM, Fab-Cre $n = 9$ mice; p38α$^{Fab\text{-}KO}$ $n = 8$ mice). (e) GTT and ITT in Fab-Cre and p38α$^{Fab\text{-}KO}$ mice fed HFD for 8 weeks. Mice were fasted overnight (for GTT) or 1 hour (for ITT), and blood glucose concentration was measured in mice given intraperitoneal injections of glucose (1 g/kg of total body weight) or insulin (0.75 U/kg of total body weight). (mean ± SEM, Fab-Cre $n = 9$ mice; p38α$^{Fab\text{-}KO}$ $n = 8$ mice). (f) Immunohistochemistry of eWAT sections using anti-GLUT4 (green), anti-Cav-1 (red) antibodies, and the nuclear dye DAPI (blue). Location of GLUT4 was analysed in mice treated with or without insulin (1.5 IU/kg) for 15 minutes after overnight fasting. Scale bar: 20 μm. (g) Comparison of energy balance between ND-fed Fab-Cre and p38α$^{Fab\text{-}KO}$ mice. ND-fed mice were examined in a metabolic cage over a 3-day period to measure EE. EE levels corrected by lean mass (left panel), expressed as ANCOVA analysis (right panel) and hour by hour over a 48-hour period (lower panel) are shown (mean ± SEM, Fab-Cre $n = 9$ mice; p38α$^{Fab\text{-}KO}$ $n = 7$ mice). (h) Body temperature of ND-fed Fab-Cre and p38α$^{Fab\text{-}KO}$ mice (mean ± SEM, Fab-Cre $n = 7$ mice; p38α$^{Fab\text{-}KO}$ $n = 5$ mice). $^{*}p < 0.05$; $^{**}p < 0.01$; $^{***}p < 0.001$ Fab-Cre versus p38α$^{Fab\text{-}KO}$ (2-way ANOVA coupled with Bonferroni's post-tests or *t* test or Welch's test when variances were different). See also S1 Data. BAT, brown adipose tissue; Cav-1, caveolin-1; EE, energy expenditure; eWAT, epididymal fat; GLUT4, glucose transporter type 4; GTT, glucose tolerance test; HFD, high-fat diet; iWAT, inguinal fat; ITT, insulin tolerance test; ND, normal-chow diet; pWAT, perirenal fat; sWAT, subcutaneous fat.
(TIF)

S3 Fig. ND-fed p38α$^{Fab\text{-}KO}$ mice present increased expression of metabolic genes, related to Fig 2. (a) qRT-PCR analysis of mRNA expression of browning, adipogenic, glycolytic, β-oxidation and lipogenic genes from BAT of ND-fed Fab-Cre and p38α$^{Fab\text{-}KO}$ mice. mRNA expression was normalized to the amount of *Gapdh* mRNA. (b) Immunoblot analysis of PGC1α protein levels in BAT of ND-fed Fab-Cre and p38α$^{Fab\text{-}KO}$ mice (c) qRT-PCR analysis of mRNA expression of browning, adipogenic, glycolytic, β-oxidation and lipogenic genes from eWAT of ND-fed Fab-Cre and p38α$^{Fab\text{-}KO}$ mice. mRNA expression was normalized to the amount of *Gapdh* mRNA (mean ± SEM, Fab-Cre $n = 7$ mice; p38α$^{Fab\text{-}KO}$ $n = 7$ mice). $^{*}p < 0.05$; $^{**}p < 0.01$. Fab-Cre versus p38α$^{Fab\text{-}KO}$ (*t* test or Welch's test when variances were different). See also S1 Data. Acaca, acetyl-CoA carboxylase 1; Acox1, acyl-CoA oxidase 1; Adipoq, Adiponectin; BAT, brown adipose tissue; cidea, cell death activator; Cpt1a, carnitine palmitoyltransferase 1A; Cpt2, carnitine palmitoyltransferase 2; Dgat1, diacylglycerol acyltransferase-1; Dgat2, diacylglycerol acyltransferase-2; Elovl, fatty acid elongase 6; eWAT, epididymal fat; Fasn, fatty acid synthase; G6pc, glucose-6-phosphatase catalytic subunit; Glys2, glycogen synthase 2; ND, normal-chow diet; Pepck, phosphoenolpyruvate carboxykinase; PGC1α, proliferator-activated receptor gamma coactivator 1α; Plin1, perilipin 1; Ppard, peroxisome proliferator-activated receptor delta; Pparg, peroxisome proliferator-activated receptor gamma; Prdm16, PR domain zinc finger protein 16; qRT-PCR, quantitative real-time polymerase chain reaction; Scd1, stearoyl-CoA desaturase-1.
(TIF)

S4 Fig. HFD-fed p38α$^{Fab\text{-}KO}$ mice are protected against diet-induced diabetes, related to Fig 2. Fab-Cre and p38α$^{Fab\text{-}KO}$ mice were fed an HFD for 8 weeks. (a) Weight of eWAT, sWAT, iWAT, pWAT, BAT, and liver relativized to tibia length (mean ± SEM, Fab-Cre $n = 10$ mice; p38α$^{Fab\text{-}KO}$ $n = 8$ mice). (b) GTT in Fab-Cre and p38α$^{Fab\text{-}KO}$ mice fed the HFD for 8 weeks. Mice were fasted overnight, and blood glucose concentration was measured in mice

given intraperitoneal injections of glucose (1 g/kg of lean mass) (mean ± SEM, Fab-Cre $n = 5$ mice; p38α$^{Fab\text{-}KO}$ $n = 6$ mice). (c) Western blot analysis of Akt activation in the liver from Fab-Cre mice fed with ND or HFD. Mice were treated without or with insulin (1.5 IU/kg) for 15 minutes after overnight fasting. Each line represents a different mouse. (d) Western blot analysis of Akt activation in the liver, skeletal muscle, eWAT, and BAT from mice fed with HFD. Mice were treated without or with insulin (1.5 IU/kg) for 15 minutes after overnight fasting. Each line represents a different mouse. (e) Triglyceride content in blood samples from Fab-Cre and p38α$^{Fab\text{-}KO}$ mice (mean ± SEM, Fab-Cre $n = 12$ mice; p38α$^{Fab\text{-}KO}$ $n = 8$ mice). $^{*}p < 0.05$, $^{***}p < 0.001$ Fab-Cre versus p38α$^{Fab\text{-}KO}$ (2-way ANOVA coupled with Bonferroni's post-tests or *t* test or Welch's test when variances were different). See also S1 Data. BAT, brown adipose tissue; eWAT, epididymal white fat; GTT, glucose tolerance test; Fts, Fasted; HFD, high-fat diet; iWAT, inguinal fat; ND, normal-chow diet; pWAT, perirenal WAT; sWAT, subcutaneous fat.
(TIF)

S5 Fig. Fat depots from HFD-fed p38α$^{Fab\text{-}KO}$ mice present smaller adipocytes, related to Fig 3. Fab-Cre and p38α$^{Fab\text{-}KO}$ mice were fed an HFD for 8 weeks. (a) Immunohistochemistry of eWAT sections using anti-Ki67 (red), anti-perilipin (green) antibodies, and the nuclear dye DAPI (blue) (upper panel). Scale bar: 20 μm. A positive cell is shown in a bigger magnification for each genotype. Quantification of proliferation and adipocyte size are shown (lower panel) (mean ± SEM, Fab-Cre $n = 5$ mice; p38α$^{Fab\text{-}KO}$ $n = 5$ mice and 5 pictures of each mouse). (b) Staining of UCP1 after 8 weeks of HFD in eWAT. Representative pictures are shown from Fab-Cre $n = 6$ mice; p38α$^{Fab\text{-}KO}$ $n = 6$ mice with 3 pictures of each mouse. Scale bar: 50 μm. (c) Immunohistochemistry of BAT sections using anti-Ki67 (red), anti-perilipin (green) antibodies, and the nuclear dye DAPI (blue) (upper panel). Scale bar: 20 μm. A positive cell is shown in a bigger magnification for each genotype. Quantification of proliferation and adipocyte size are shown (lower panel) (mean ± SEM, Fab-Cre $n = 5$ mice; p38α$^{Fab\text{-}KO}$ $n = 5$ mice and 5 pictures of each mouse). $^{*}p < 0.05$, $^{***}p < 0.001$ Fab-Cre versus p38α$^{Fab\text{-}KO}$ (*t* test or Welch's test when variances were different). See also S1 Data. BAT, brown adipose tissue; eWAT, epididymal white fat; HFD, high-fat diet; UCP1, uncoupling protein 1.
(TIF)

S6 Fig. Specificity of UCP1 antibody, related to Fig 3. Western blot analysis of UCP1 in eWAT from Fab-Cre and p38α$^{Fab\text{-}KO}$ mice fed with an HFD. BAT from control mice (diluted 1/10) was used as positive control. Nondiluted BAT and eWAT from UCP1$^{-/-}$ mice were used as negative controls. Each line represents a different mouse. Two different exposures are showed. BAT, brown adipose tissue; eWAT, epididymal white fat; HFD, high-fat diet; UCP1, uncoupling protein 1.
(TIF)

S7 Fig. HFD-fed p38α$^{Fab\text{-}KO}$ mice have higher iWAT and lower eWAT browning, related to Fig 3. Fab-Cre and p38α$^{Fab\text{-}KO}$ mice were fed with HFD for 8 weeks. Immunoblot analysis of UCP1 protein levels and Creb, ATF2, p38, AMPK, and ACC phosphorylation in lysates from iWAT (panel a) or eWAT (panel b). Quantifications are shown in lower panels (mean ± SEM, Fab-Cre $n = 4$–10 mice; p38α$^{Fab\text{-}KO}$ $n = 4$–10 mice). $^{*}p < 0.05$, Fab-Cre versus p38α$^{Fab\text{-}KO}$ (*t* test or Welch's test when variances were different). See also S1 Data. ACC, acetyl-CoA carboxylase; AMPK, 5' adenosine monophosphate-activated protein kinase; ATF2, activating transcription factor 2; Creb, cAMP response element-binding; eWAT, epididymal white fat; HFD, high-fat diet; iWAT, inguinal fat; UCP1, uncoupling protein 1.
(TIF)

S8 Fig. p38α controls brown adipocyte differentiation in vitro, related to Fig 3. (a–e) Primary adipocytes isolated from interscapular BAT of Fab-Cre and p38α$^{Fab\text{-}KO}$ were differentiated in vitro. (a) Immunoblot analysis of PGC1α and UCP1 protein levels (left panel) and qRT-PCR analysis of browning genes mRNA expression (right panel). mRNA expression was normalized to the amount of *Gapdh* mRNA. (mean ± SEM, Fab-Cre $n = 6$ mice; p38α$^{Fab\text{-}KO}$ $n = 6$ wells from 2 independent experiments). qRT-PCR analysis of mRNA expression of adipogenic (panel b), glycolytic (panel b), β-oxidation (panel c), and lipogenic (panel c) genes in in vitro–differentiated primary brown adipocytes. mRNA expression was normalized to the amount of *Gapdh* mRNA (mean ± SEM, a representative experiment is shown; Fab-Cre $n = 6$ wells; p38α$^{Fab\text{-}KO}$ $n = 6$ wells). (d) Oil red O staining of primary brown adipocytes after 10 days of differentiation in vitro. (e) Confocal imaging of Fab-Cre and p38α$^{Fab\text{-}KO}$ primary brown adipocytes stained with Mitotracker Deep Red (red) and Bodipy (green). Scale bar: 10 μm (left panel). Quantification of cellular triglyceride content in in vitro–differentiated primary brown adipocytes (right panel) (mean ± SEM, a representative experiment is shown; Fab-Cre $n = 4$ wells; p38α$^{Fab\text{-}KO}$ $n = 5$ wells). Statistically significant differences between Fab-Cre and p38α$^{Fab\text{-}KO}$ brown adipocytes are indicated: $^{*}p < 0.05$; $^{**}p < 0.01$; $^{***}p < 0.001$ (*t* test or Welch's test when variances were different). (f, g) Primary adipocytes isolated from subcutaneous white fat of Fab-Cre and p38α$^{Fab\text{-}KO}$ were differentiated in vitro. (f) qRT-PCR analysis of mRNA expression of adipogenic genes in in vitro–differentiated primary white adipocytes. mRNA expression was normalized to the amount of *Gapdh* mRNA (mean ± SEM, a representative experiment is shown; Fab-Cre $n = 9$ wells; p38α$^{Fab\text{-}KO}$ $n = 8$ wells from 3 independent experiments), $^{*}p < 0.05$ (Welch's test). (g) Oil red O staining of primary white adipocytes after 9 days of differentiation in vitro. See also S1 Data. Acaca, acetyl-CoA carboxylase 1; Acox1, acyl-CoA oxidase 1; Adipoq, adiponectin; BAT, brown adipose tissue; Cidea, Cell death activator CIDE-A; Cox7a1, cytochrome C oxidase subunit 7a1; Cpt1a, carnitine palmitoyltransferase 1a; Dgat1, diacylglycerol acyltransferase-1; Fasn; fatty acid synthase; G6pc, glucose-6-phosphatase catalytic subunit; Glys2, glycogen synthase 2; Pepck, phosphoenolpyruvate carboxykinase; PGC1α, proliferator-activated receptor gamma coactivator 1α; Plin1, perilipin 1; Ppard, peroxisome proliferator-activated receptor delta; Pparg, peroxisome proliferator-activated receptor gamma; Ppargc1a, peroxisome proliferator-activated receptor gamma coactivator 1-alpha; Ppargc1b, peroxisome proliferator-activated receptor gamma coactivator 1-beta; Prdm16, PR domain zinc finger protein 16; qRT-PCR quantitative real-time polymerase chain reaction; Scd1, stearoyl-CoA desaturase-1; UCP1, uncoupling protein 1.
(TIF)

S9 Fig. Activation of p38 isoforms in Fab-Cre and p38α$^{Fab\text{-}KO}$ mice after HFD, related to Fig 3. (a) Phosphorylation of p38 isoforms in adipocytes detected with cell signal antibody #9211. Western blot analysis of the different p38 isoforms activation in adipocytes from WT and p38γ/δ$^{-/-}$ cells. (b) Immunoblot analysis of p38 phosphorylation in BAT, eWAT, iWAT, sWAT, and pWAT lysates from ND-fed Fab-Cre and p38α$^{Fab\text{-}KO}$ mice. (c) Effect of SB203580 on phosphorylation of p38 isoforms. Western blot analysis of phospho p38 in brown preadipocytes from Fab-Cre mice treated with DMSO, sorbitol (0.5 M, 15 minutes), or sorbitol with SB203580 (10 μM, 1 hour pre treatment) or from p38α$^{Fab\text{-}KO}$ mice with DMSO. (d) qRT-PCR analysis of different isoforms of p38 mRNA expression (p38α [*Mapk14*], p38β [*Mapk11*], p38γ [*Mapk12*], p38δ [*Mapk13*]) in BAT and eWAT from control mice (Fab-Cre) after an ND or an HFD for 8 weeks. mRNA expression was normalized to the amount of *Gapdh* mRNA (mean ± SEM, ND $n = 6$–9 mice; HFD $n = 14$ mice). (e) Comparison of p38 isoforms mRNA expression by qRT-PCR analysis in BAT from ND-fed Fab-Cre and p38α$^{Fab\text{-}KO}$ mice. mRNA expression was normalized to the amount of *Gapdh* mRNA (mean ± SEM, Fab-Cre $n = 6$ mice;

p38α$^{Fab\text{-}KO}$ $n = 7$ mice). (f) Comparison of p38 isoforms mRNA expression by qRT-PCR analysis in eWAT from ND- and HFD-fed Fab-Cre and p38α$^{Fab\text{-}KO}$ mice. mRNA expression was normalized to the amount of *Gapdh* mRNA (mean ± SEM, Fab-Cre $n = 7$–14 mice; p38α$^{Fab\text{-}KO}$ $n = 7$–9 mice). $^{*}p < 0.05$; $^{**}p < 0.01$; $^{***}p < 0.001$; Fab-Cre versus p38δ$^{Fab\text{-}KO}$ (*t* test or Welch's test when variances were different). See also S1 Data. BAT, brown adipose tissue; eWAT, epididymal white fat; GTT, glucose tolerance test; HFD, high-fat diet; iWAT, inguinal fat; ND, normal-chow diet; pWAT, perirenal WAT; qRT-PCR, quantitative real-time polymerase chain reaction; sWAT, subcutaneous fat; WT, wild type.
(TIF)

S10 Fig. Brown fat from p38δ$^{Fab\text{-}KO}$ mice presents a decrease in BAT activity, related to Fig 6. Fab-Cre and p38δ$^{Fab\text{-}KO}$ mice were fed with an ND for 8 weeks. (a) Weight of eWAT, sWAT, iWAT, pWAT, BAT, and liver with respect to tibia length in ND-fed Fab-Cre and p38δ$^{Fab\text{-}KO}$ mice (mean ± SEM, Fab-Cre $n = 6$ mice; p38δ$^{Fab\text{-}KO}$ $n = 6$ mice). (b) qRT-PCR analysis of mRNA expression of browning genes in BAT isolated from ND-fed Fab-Cre and p38δ$^{Fab\text{-}KO}$ mice. mRNA expression was normalized to the amount of *Gapdh* mRNA. (c) Western blot analysis of PKA activation in BAT from Fab-Cre and p38δ$^{Fab\text{-}KO}$. Each line represents a different mouse ($n = 6$) (mean ± SEM, Fab-Cre $n = 6$ mice; p38δ$^{Fab\text{-}KO}$ $n = 6$ mice). $^{*}p < 0.05$; $^{**}p < 0.01$; Fab-Cre versus p38δ$^{Fab\text{-}KO}$ (*t* test or Welch's test when variances were different). See also S1 Data. BAT, brown adipose tissue; Cidea, Cell death activator CIDE-A; eWAT, epididymal white fat; GTT, glucose tolerance test; iWAT, inguinal fat; ND, normal-chow diet; pWAT, perirenal WAT; PKA, protein kinase A; Ppargc1a, peroxisome proliferator-activated receptor gamma coactivator 1-alpha; Prdm16, PR domain zinc finger protein 16; qRT-PCR quantitative real-time polymerase chain reaction; sWAT, subcutaneous fat; UCP1, uncoupling protein 1.
(TIF)

S11 Fig. p38δ$^{Fab\text{-}KO}$ mice have higher body weight and lower temperature when fed an HFD, related to Fig 6. Fab-Cre and p38δ$^{Fab\text{-}KO}$ mice were fed with an HFD for 8 weeks. (a) Body weight at the end of the treatment (mean ± SEM, Fab-Cre $n = 8$ mice; p38δ$^{Fab\text{-}KO}$ $n = 7$ mice). (b) NMR analysis of body mass and fat mass in p38δ$^{Fab\text{-}KO}$ and Fab-Cre mice after 8 weeks of HFD (mean ± SEM, Fab-Cre $n = 8$ mice; p38δ$^{Fab\text{-}KO}$ $n = 7$ mice). (c) Weight of eWAT, sWAT, iWAT, pWAT, BAT, and liver with respect to tibia length (mean ± SEM, Fab-Cre $n = 8$ mice; p38δ$^{Fab\text{-}KO}$ $n = 7$ mice). (d) Skin temperature surrounding interscapular BAT in HFD-fed Fab-Cre and p38δ$^{Fab\text{-}KO}$. Right panels show representative infrared thermal images (mean ± SEM, Fab-Cre $n = 8$ mice; p38δ$^{Fab\text{-}KO}$ $n = 7$ mice). (e) qRT-PCR analysis of mRNA expression of browning genes in BAT isolated from HFD-fed Fab-Cre and p38δ$^{Fab\text{-}KO}$ mice. mRNA expression was normalized to the amount of *Gapdh* mRNA (mean ± SEM, Fab-Cre $n = 5$ mice; p38δ$^{Fab\text{-}KO}$ $n = 6$ mice). (f) Immunoblot of UCP1 protein levels in p38δ$^{Fab\text{-}KO}$ and Fab-Cre mice after 8 weeks of HFD. Quantification is shown on the right panel (mean ± SEM, Fab-Cre $n = 5$ mice; p38δ$^{Fab\text{-}KO}$ $n = 6$ mice). $^{*}p < 0.05$; $^{**}p < 0.01$; $^{***}p < 0.001$; Fab-Cre versus p38δ$^{Fab\text{-}KO}$ (*t* test or Welch's test when variances were different). See also S1 Data. BAT, brown adipose tissue; Cidea, Cell death activator CIDE-A; eWAT, epididymal white fat; GTT, glucose tolerance test; HFD, high-fat diet; IR temperature, infrared temperature; iWAT, inguinal fat; Ppargc1a, peroxisome proliferator-activated receptor gamma coactivator 1-alpha; Ppargc1b, peroxisome proliferator-activated receptor gamma coactivator 1-beta; Prdm16, PR domain zinc finger protein 16; pWAT, perirenal WAT; qRT-PCR quantitative real-time polymerase chain reaction; sWAT, subcutaneous fat; UCP1, uncoupling protein 1.
(TIF)

S1 Table. Characteristics of patients and controls for human visceral fat samples.
(DOCX)

S2 Table. Characteristics of patients and controls for human sWAT samples. sWAT, subcutaneous fat.
(DOCX)

S3 Table. Primers used for gene amplification.
(DOCX)

S1 Data. Numerical data used in figures.
(XLSX)

S1 Text. Figure legend from S1 Fig.
(DOCX)

S2 Text. Figure legend from S2 Fig.
(DOCX)

S3 Text. Figure legend from S3 Fig.
(DOCX)

S4 Text. Figure legend from S4 Fig.
(DOCX)

S5 Text. Figure legend from S5 Fig.
(DOCX)

S6 Text. Figure legend from S6 Fig.
(DOCX)

S7 Text. Figure legend from S7 Fig.
(DOCX)

S8 Text. Figure legend from S8 Fig.
(DOCX)

S9 Text. Figure legend from S9 Fig.
(DOCX)

S10 Text. Figure legend from S10 Fig.
(DOCX)

S11 Text. Figure legend from S11 Fig.
(DOCX)

Acknowledgments

We thank to Dr. Miguel Lopez, Dr. Barbara Cannon and Dr. Jan Nedergaard who kindly provided the western blot samples from UCP1 KO mice (Brown fat and eWAT). We thank S. Bartlett for English editing. We thank the staff at the CNIC Animal facility and S. Pérez-Romero for technical assistance.

Author Contributions

Conceptualization: Nuria Matesanz, Ivana Nikolic, Magdalena Leiva, Edgar Bernardo, Guadalupe Sabio.

Data curation: Nuria Matesanz, Ivana Nikolic, Magdalena Leiva, Marta Pulgarín-Alfaro, Ayelén M. Santamans, Edgar Bernardo, Alfonso Mora, Leticia Herrera-Melle, Elena Rodríguez, Guadalupe Sabio.

Formal analysis: Nuria Matesanz, Ivana Nikolic, Magdalena Leiva, Ayelén M. Santamans, Edgar Bernardo, Leticia Herrera-Melle, Miguel Marcos, Guadalupe Sabio.

Funding acquisition: Ivana Nikolic, Magdalena Leiva, Francisco Centeno, Angel R. Nebreda, José Antonio Enríquez, Rubén Nogueiras, Miguel Marcos, Guadalupe Sabio.

Investigation: Nuria Matesanz, Ivana Nikolic, Magdalena Leiva, Marta Pulgarín-Alfaro, Ayelén M. Santamans, Edgar Bernardo, Alfonso Mora, Leticia Herrera-Melle, Daniel Beiroa, Ainoa Caballero, Elena Martín-García, Rebeca Acín-Pérez, Lourdes Hernández-Cosido, Luis Leiva-Vega, Jorge L. Torres, Francisco Centeno, Angel R. Nebreda, José Antonio Enríquez, Rubén Nogueiras, Miguel Marcos, Guadalupe Sabio.

Methodology: Nuria Matesanz, Ivana Nikolic, Magdalena Leiva, Marta Pulgarín-Alfaro, Ayelén M. Santamans, Edgar Bernardo, Alfonso Mora, Leticia Herrera-Melle, Elena Rodríguez, Daniel Beiroa, Ainoa Caballero, Elena Martín-García, Rebeca Acín-Pérez, Luis Leiva-Vega, Jorge L. Torres, Francisco Centeno, Rubén Nogueiras, Guadalupe Sabio.

Project administration: Guadalupe Sabio.

Resources: Angel R. Nebreda, José Antonio Enríquez, Rubén Nogueiras, Miguel Marcos, Guadalupe Sabio.

Supervision: Nuria Matesanz, Ivana Nikolic, Magdalena Leiva, Alfonso Mora, Rubén Nogueiras, Miguel Marcos, Guadalupe Sabio.

Validation: Nuria Matesanz, Ivana Nikolic, Magdalena Leiva, Marta Pulgarín-Alfaro, Ayelén M. Santamans, Edgar Bernardo, Alfonso Mora, José Antonio Enríquez, Rubén Nogueiras, Miguel Marcos, Guadalupe Sabio.

Visualization: Nuria Matesanz, Ivana Nikolic, Magdalena Leiva, Rubén Nogueiras, Guadalupe Sabio.

Writing – original draft: Nuria Matesanz, Ivana Nikolic, Guadalupe Sabio.

Writing – review & editing: Nuria Matesanz, Ivana Nikolic, Magdalena Leiva, Marta Pulgarín-Alfaro, Ayelén M. Santamans, Edgar Bernardo, Alfonso Mora, Leticia Herrera-Melle, Angel R. Nebreda, Rubén Nogueiras, Miguel Marcos, Guadalupe Sabio.

References

1. Bhurosy T, Jeewon R. Overweight and obesity epidemic in developing countries: a problem with diet, physical activity, or socioeconomic status? ScientificWorldJournal. 2014; 2014:964236. https://doi.org/10.1155/2014/964236 PMID: 25379554; PubMed Central PMCID: PMCPMC4212551.
2. Kearns K, Dee A, Fitzgerald AP, Doherty E, Perry IJ. Chronic disease burden associated with overweight and obesity in Ireland: the effects of a small BMI reduction at population level. BMC Public Health. 2014; 14:143. https://doi.org/10.1186/1471-2458-14-143 PMID: 24512151; PubMed Central PMCID: PMCPMC3929131.
3. Rosen ED, Spiegelman BM. Adipocytes as regulators of energy balance and glucose homeostasis. Nature. 2006; 444(7121):847–53. https://doi.org/10.1038/nature05483 PMID: 17167472; PubMed Central PMCID: PMCPMC3212857.
4. Wang W, Seale P. Control of brown and beige fat development. Nature reviews Molecular cell biology. 2016; 17(11):691–702. https://doi.org/10.1038/nrm.2016.96 PMID: 27552974.
5. Cypess AM, Lehman S, Williams G, Tal I, Rodman D, Goldfine AB, et al. Identification and importance of brown adipose tissue in adult humans. The New England journal of medicine. 2009; 360(15):1509–

17. Epub 2009/04/10. https://doi.org/10.1056/NEJMoa0810780 PMID: 19357406; PubMed Central PMCID: PMC2859951.

6. Nedergaard J, Bengtsson T, Cannon B. Unexpected evidence for active brown adipose tissue in adult humans. American journal of physiology Endocrinology and metabolism. 2007; 293(2):E444–52. https://doi.org/10.1152/ajpendo.00691.2006 PMID: 17473055.

7. van Marken Lichtenbelt WD, Vanhommerig JW, Smulders NM, Drossaerts JM, Kemerink GJ, Bouvy ND, et al. Cold-activated brown adipose tissue in healthy men. The New England journal of medicine. 2009; 360(15):1500–8. https://doi.org/10.1056/NEJMoa0808718 PMID: 19357405.

8. Cousin B, Cinti S, Morroni M, Raimbault S, Ricquier D, Penicaud L, et al. Occurrence of brown adipocytes in rat white adipose tissue: molecular and morphological characterization. Journal of cell science. 1992; 103 (Pt 4):931–42. Epub 1992/12/01. PMID: 1362571.

9. Lee JY, Takahashi N, Yasubuchi M, Kim YI, Hashizaki H, Kim MJ, et al. Triiodothyronine induces UCP-1 expression and mitochondrial biogenesis in human adipocytes. American journal of physiology Cell physiology. 2012; 302(2):C463–72. Epub 2011/11/15. https://doi.org/10.1152/ajpcell.00010.2011 PMID: 22075692.

10. Guerra C, Koza RA, Yamashita H, Walsh K, Kozak LP. Emergence of brown adipocytes in white fat in mice is under genetic control. Effects on body weight and adiposity. The Journal of clinical investigation. 1998; 102(2):412–20. Epub 1998/07/17. https://doi.org/10.1172/JCI3155 PMID: 9664083; PubMed Central PMCID: PMC508900.

11. Barbatelli G, Murano I, Madsen L, Hao Q, Jimenez M, Kristiansen K, et al. The emergence of cold-induced brown adipocytes in mouse white fat depots is determined predominantly by white to brown adipocyte transdifferentiation. American journal of physiology Endocrinology and metabolism. 2010; 298 (6):E1244–53. Epub 2010/04/01. https://doi.org/10.1152/ajpendo.00600.2009 PMID: 20354155.

12. Iyengar P, Scherer PE. Obesity: Slim without the gym—the magic of chilling out. Nat Rev Endocrinol. 2016; 12(5):252–4. https://doi.org/10.1038/nrendo.2016.20 PMID: 26915527.

13. Schrauwen P, van Marken Lichtenbelt WD, Spiegelman BM. The future of brown adipose tissues in the treatment of type 2 diabetes. Diabetologia. 2015; 58(8):1704–7. https://doi.org/10.1007/s00125-015-3611-y PMID: 25957230.

14. Cao W, Medvedev AV, Daniel KW, Collins S. beta-Adrenergic activation of p38 MAP kinase in adipocytes: cAMP induction of the uncoupling protein 1 (UCP1) gene requires p38 MAP kinase. The Journal of biological chemistry. 2001; 276(29):27077–82. Epub 2001/05/23. https://doi.org/10.1074/jbc.M101049200 PMID: 11369767.

15. Gantner ML, Hazen BC, Conkright J, Kralli A. GADD45gamma regulates the thermogenic capacity of brown adipose tissue. Proceedings of the National Academy of Sciences of the United States of America. 2014; 111(32):11870–5. https://doi.org/10.1073/pnas.1406638111 PMID: 25071184; PubMed Central PMCID: PMCPMC4136592.

16. Sabio G, Davis RJ. TNF and MAP kinase signalling pathways. Seminars in immunology. 2014; 26 (3):237–45. Epub 2014/03/22. https://doi.org/10.1016/j.smim.2014.02.009 PMID: 24647229; PubMed Central PMCID: PMC4099309.

17. Manieri E, Sabio G. Stress kinases in the modulation of metabolism and energy balance. Journal of molecular endocrinology. 2015; 55(2):R11–22. Epub 2015/09/13. https://doi.org/10.1530/JME-15-0146 PMID: 26363062.

18. Cao W, Daniel KW, Robidoux J, Puigserver P, Medvedev AV, Bai X, et al. p38 mitogen-activated protein kinase is the central regulator of cyclic AMP-dependent transcription of the brown fat uncoupling protein 1 gene. Molecular and cellular biology. 2004; 24(7):3057–67. Epub 2004/03/17. https://doi.org/10.1128/MCB.24.7.3057-3067.2004 PMID: 15024092; PubMed Central PMCID: PMC371122.

19. Zhang Y, Li R, Meng Y, Li S, Donelan W, Zhao Y, et al. Irisin stimulates browning of white adipocytes through mitogen-activated protein kinase p38 MAP kinase and ERK MAP kinase signaling. Diabetes. 2014; 63(2):514–25. Epub 2013/10/24. https://doi.org/10.2337/db13-1106 PMID: 24150604.

20. Wagner EF, Nebreda AR. Signal integration by JNK and p38 MAPK pathways in cancer development. Nature reviews Cancer. 2009; 9(8):537–49. https://doi.org/10.1038/nrc2694 PMID: 19629069.

21. Whittle AJ, Carobbio S, Martins L, Slawik M, Hondares E, Vazquez MJ, et al. BMP8B increases brown adipose tissue thermogenesis through both central and peripheral actions. Cell. 2012; 149(4):871–85. https://doi.org/10.1016/j.cell.2012.02.066 PMID: 22579288; PubMed Central PMCID: PMCPMC3383997.

22. Hondares E, Iglesias R, Giralt A, Gonzalez FJ, Giralt M, Mampel T, et al. Thermogenic activation induces FGF21 expression and release in brown adipose tissue. The Journal of biological chemistry. 2011; 286(15):12983–90. https://doi.org/10.1074/jbc.M110.215889 PMID: 21317437; PubMed Central PMCID: PMCPMC3075644.

23. Tseng YH, Kokkotou E, Schulz TJ, Huang TL, Winnay JN, Taniguchi CM, et al. New role of bone morphogenetic protein 7 in brown adipogenesis and energy expenditure. Nature. 2008; 454(7207):1000–4. Epub 2008/08/23. https://doi.org/10.1038/nature07221 PMID: 18719589; PubMed Central PMCID: PMC2745972.

24. Nedergaard J, Cannon B. The changed metabolic world with human brown adipose tissue: therapeutic visions. Cell metabolism. 2010; 11(4):268–72. https://doi.org/10.1016/j.cmet.2010.03.007 PMID: 20374959.

25. Kozak LP, Harper ME. Mitochondrial uncoupling proteins in energy expenditure. Annual review of nutrition. 2000; 20:339–63. Epub 2000/08/15. https://doi.org/10.1146/annurev.nutr.20.1.339 PMID: 10940338.

26. Jeffery E, Church CD, Holtrup B, Colman L, Rodeheffer MS. Rapid depot-specific activation of adipocyte precursor cells at the onset of obesity. Nature cell biology. 2015; 17(4):376–85. https://doi.org/10.1038/ncb3122 PMID: 25730471; PubMed Central PMCID: PMCPMC4380653.

27. Kong X, Banks A, Liu T, Kazak L, Rao RR, Cohen P, et al. IRF4 is a key thermogenic transcriptional partner of PGC-1alpha. Cell. 2014; 158(1):69–83. https://doi.org/10.1016/j.cell.2014.04.049 PMID: 24995979; PubMed Central PMCID: PMCPMC4116691.

28. Kalinovich AV, de Jong JM, Cannon B, Nedergaard J. UCP1 in adipose tissues: two steps to full browning. Biochimie. 2017; 134:127–37. https://doi.org/10.1016/j.biochi.2017.01.007 PMID: 28109720.

29. Cheung PC, Campbell DG, Nebreda AR, Cohen P. Feedback control of the protein kinase TAK1 by SAPK2a/p38alpha. The EMBO journal. 2003; 22(21):5793–805. https://doi.org/10.1093/emboj/cdg552 PMID: 14592977; PubMed Central PMCID: PMCPMC275409.

30. Sabio G, Arthur JS, Kuma Y, Peggie M, Carr J, Murray-Tait V, et al. p38gamma regulates the localisation of SAP97 in the cytoskeleton by modulating its interaction with GKAP. The EMBO journal. 2005; 24(6):1134–45. Epub 2005/02/25. https://doi.org/10.1038/sj.emboj.7600578 PMID: 15729360; PubMed Central PMCID: PMC556394.

31. Kuma Y, Campbell DG, Cuenda A. Identification of glycogen synthase as a new substrate for stress-activated protein kinase 2b/p38beta. The Biochemical journal. 2004; 379(Pt 1):133–9. Epub 2003/12/19. https://doi.org/10.1042/BJ20031559 PMID: 14680475; PubMed Central PMCID: PMC1224046.

32. Harms M, Seale P. Brown and beige fat: development, function and therapeutic potential. Nature medicine. 2013; 19(10):1252–63. https://doi.org/10.1038/nm.3361 PMID: 24100998.

33. Peschechera A, Eckel J. "Browning" of adipose tissue—regulation and therapeutic perspectives. Arch Physiol Biochem. 2013; 119(4):151–60. https://doi.org/10.3109/13813455.2013.796995 PMID: 23721302.

34. Ambrosino C, Mace G, Galban S, Fritsch C, Vintersten K, Black E, et al. Negative feedback regulation of MKK6 mRNA stability by p38alpha mitogen-activated protein kinase. Molecular and cellular biology. 2003; 23(1):370–81. Epub 2002/12/17. https://doi.org/10.1128/MCB.23.1.370-381.2003 PMID: 12482988; PubMed Central PMCID: PMC140674.

35. Branco M, Ribeiro M, Negrao N, Bianco AC. 3,5,3'-Triiodothyronine actively stimulates UCP in brown fat under minimal sympathetic activity. The American journal of physiology. 1999; 276(1 Pt 1):E179–87. PMID: 9886965.

36. van der Lans AA, Hoeks J, Brans B, Vijgen GH, Visser MG, Vosselman MJ, et al. Cold acclimation recruits human brown fat and increases nonshivering thermogenesis. The Journal of clinical investigation. 2013; 123(8):3395–403. https://doi.org/10.1172/JCI68993 PMID: 23867626; PubMed Central PMCID: PMCPMC3726172.

37. Matesanz N BE, Acín-Pérez R, Pérez-Sieira S, Hernández-Cosido L, Moltalvo V, Mora A, et al. MKK6 controls T3-mediated browning of white adipose tissue. Nature communications. 2017. https://doi.org/10.1038/s41467-017-00948-z PMID: 29021624

38. Aouadi M, Laurent K, Prot M, Le Marchand-Brustel Y, Binetruy B, Bost F. Inhibition of p38MAPK increases adipogenesis from embryonic to adult stages. Diabetes. 2006; 55(2):281–9. PMID: 16443758.

39. Engelman JA, Berg AH, Lewis RY, Lin A, Lisanti MP, Scherer PE. Constitutively active mitogen-activated protein kinase kinase 6 (MKK6) or salicylate induces spontaneous 3T3-L1 adipogenesis. The Journal of biological chemistry. 1999; 274(50):35630–8. PMID: 10585441.

40. Engelman JA, Lisanti MP, Scherer PE. Specific inhibitors of p38 mitogen-activated protein kinase block 3T3-L1 adipogenesis. The Journal of biological chemistry. 1998; 273(48):32111–20. PMID: 9822687.

41. Fujishiro M, Gotoh Y, Katagiri H, Sakoda H, Ogihara T, Anai M, et al. MKK6/3 and p38 MAPK pathway activation is not necessary for insulin-induced glucose uptake but regulates glucose transporter expression. The Journal of biological chemistry. 2001; 276(23):19800–6. https://doi.org/10.1074/jbc.M101087200 PMID: 11279172.

42. Somwar R, Koterski S, Sweeney G, Sciotti R, Djuric S, Berg C, et al. A dominant-negative p38 MAPK mutant and novel selective inhibitors of p38 MAPK reduce insulin-stimulated glucose uptake in 3T3-L1 adipocytes without affecting GLUT4 translocation. The Journal of biological chemistry. 2002; 277 (52):50386–95. https://doi.org/10.1074/jbc.M205277200 PMID: 12393894.

43. Antonescu CN, Huang C, Niu W, Liu Z, Eyers PA, Heidenreich KA, et al. Reduction of insulin-stimulated glucose uptake in L6 myotubes by the protein kinase inhibitor SB203580 is independent of p38MAPK activity. Endocrinology. 2005; 146(9):3773–81. https://doi.org/10.1210/en.2005-0404 PMID: 15947002.

44. Gonzalez-Teran B, Cortes JR, Manieri E, Matesanz N, Verdugo A, Rodriguez ME, et al. Eukaryotic elongation factor 2 controls TNF-alpha translation in LPS-induced hepatitis. The Journal of clinical investigation. 2013; 123(1):164–78. Epub 2012/12/04. https://doi.org/10.1172/JCI65124 PMID: 23202732; PubMed Central PMCID: PMC3533299.

45. Hui L, Bakiri L, Mairhorfer A, Schweifer N, Haslinger C, Kenner L, et al. p38alpha suppresses normal and cancer cell proliferation by antagonizing the JNK-c-Jun pathway. Nature genetics. 2007; 39 (6):741–9. Epub 2007/05/01. https://doi.org/10.1038/ng2033 PMID: 17468757.

46. He W, Barak Y, Hevener A, Olson P, Liao D, Le J, et al. Adipose-specific peroxisome proliferator-activated receptor gamma knockout causes insulin resistance in fat and liver but not in muscle. Proceedings of the National Academy of Sciences of the United States of America. 2003; 100(26):15712–7. https://doi.org/10.1073/pnas.2536828100 PMID: 14660788; PubMed Central PMCID: PMCPMC307633.

47. Alvarez-Crespo M, Csikasz RI, Martinez-Sanchez N, Dieguez C, Cannon B, Nedergaard J, et al. Essential role of UCP1 modulating the central effects of thyroid hormones on energy balance. Mol Metab. 2016; 5(4):271–82. https://doi.org/10.1016/j.molmet.2016.01.008 PMID: 27069867; PubMed Central PMCID: PMCPMC4812006.